

Robert B. Heimann

WILEY-VCH

Plasma Spray Coating

Principles and Applications

Second, Completely Revised and Enlarged Edition



Plasma- Spray Coating

by. Robert B. Heimann

Copyright© VCH Verlagsgesellschaft mbH. 1996

Robert B. Heimann

Plasma-Spray Coating



Related Reading

Brook, R. J.

Processing of Ceramics

Volumes 17 A and B from the series *Materials Science and Technology*, R. W. Cahn, P. Haasen, E. J. Kramer (eds.), VCH, 1995, ISBN 3-527-26830-8 and 3-527-29356-6.

Cahn, R. W. (ed.)

Processing of Metals and Alloys

Volumes 15 from the series *Materials Science and Technology*, R. W. Cahn, P. Haasen, E. J. Kramer (eds.), VCH, 1992, ISBN 3-527-26828-6.

A. C. Jones, P. O'Brian

CVD of Compound Semiconductors. Precursor Synthesis, Development and Applications. VCH, 1996, ISBN 3-527-29294-2.

T. Kodas, M. Hampden-Smith

The Chemistry of Metal CVD. VCH, 1994, ISBN 3-527-29071-0.

Materialwissenschaften und Werkstofftechnik. Entwicklung, Fertigung, Prüfung, Eigenschaften und Anwendungen technischer Werkstoffe. VCH, Volume 27, 1996, ISSN 0933-5137.

Materials and Corrosion. VCH, Volume 47, 1996, ISSN 0043-2822.

Chemical Vapor Deposition. Published bimonthly as part of **Advanced Materials.** VCH, Volume 2, 1996, ISSN 0948-1907

© VCH Verlagsgesellschaft mbH, D-69451 Weinheim (Federal Republic of Germany), 1996

Distribution:

VCH, P.O. Box 10 11 61, D-69451 Weinheim (Federal Republic of Germany)

Switzerland: VCH, P.O. Box, CH-4020 Basel (Switzerland)

United Kingdom and Ireland: VCH (UK) Ltd., 8 Wellington Court, Cambridge CB1 1HZ (England)

USA and Canada: VCH, 220 East 23rd Street, New York, NY 10010-4606 (USA)

Japan: VCH, Eikow Building, 10-9 Hongo 1-chome, Bunkyo-ku, Tokyo 113 (Japan)

ISBN 3-527-29430-9

Robert B. Heimann

Plasma-Spray Coating

Principles and Applications



Weinheim • New York • Basel • Cambridge • Tokyo

Prof. Dr. Robert B. Heimann
Institut für Mineralogie
TU Bergakademie Freiberg
Brennhausgasse 14
09596 Freiberg
Germany

This book was carefully produced. Nevertheless, author and publisher do not warrant the information contained therein to be free of errors. Readers are advised to keep in mind that statements, data, illustrations, procedural details or other items may inadvertently be inaccurate.

Published jointly by
VCH Verlagsgesellschaft mbH, Weinheim (Federal Republic of Germany)
VCH Publishers, Inc., New York, NY (USA)

Editorial Directors: Dr. Peter Gregory, Dr. Ute Anton
Production Manager: Dipl.-Ing. (FH) Hans Jörg Maier

Every effort has been made to trace the owners of copyrighted material; however, in some cases this has proved impossible. We take this opportunity to offer our apologies to any copyright holders whose rights we may have unwittingly infringed.

Library of Congress Card No. applied for.

A catalogue record for this book is available from the British Library.

Deutsche Bibliothek Cataloguing-in-Publication Data:

Heimann, Robert B.:

Plasma spray coating: principles and applications / Robert B. Heimann. – Weinheim; New York; Basel; Cambridge; Tokyo: VCH, 1996

ISBN 3-527-29430-9

© VCH Verlagsgesellschaft mbH. D-69451 Weinheim (Federal Republic of Germany), 1996
Printed on acid-free and chlorine-free paper.

All rights reserved (including those of translation into other languages). No part of this book may be reproduced in any form – by photoprinting, microfilm, or any other means – nor transmitted or translated into a machine-readable language without written permission from the publishers. Registered names, trademarks, etc. used in this book, even when not specifically marked as such, are not to be considered unprotected by law.

Composition: Asco Trade Typesetting Limited, Hong Kong. Printing: betz druck gmbh, D-64291 Darmstadt

Printed in the Federal Republic of Germany.

Preface

Thermal spraying encompasses a variety of apparently simple surface engineering processes by which solid materials (wire, rods, particles) are rapidly heated by a plasma jet or a combustion flame, melted and propelled against the substrate to be coated. Rapid solidification of the molten particles at the substrate surface builds up, splat by splat, into a layer which may have various functions including protection against wear, erosion, corrosion and thermal or chemical degradation. The coating may also impart special electrical, magnetic or decorative properties to the substrate. Thick coatings are applied in many industrial areas to restore or attain desired workpiece dimensions and specifications.

The text has been written bearing in mind the theoretical and practical requirements of students of materials engineering and materials science. It has been developed from the topics presented to classes of Master students of the Materials Engineering Program at the School of Energy and Materials, King Mongkut's Institute of Technology Thonburi, Bangkok, Thailand between 1991 and 1995 as well as to students of Technical (Applied) Mineralogy at Freiberg University of Mining and Technology since 1993. The author has also gained experience in plasma spray technology during his work from 1987 to 1988 as the head of the Industrial Products and Materials Section of the Industrial Technologies Department of the Alberta Research Council, Edmonton, Alberta, Canada, and from 1988 to 1993 as the manager of the Institutional and International Programs Group of the Manufacturing Technologies Department of the same organization.

It is nearly impossible to consider the entire body of literature on the subject of thermal spraying. Therefore, instead of an exhaustive coverage of applications of plasma-sprayed coatings only typical examples and case studies will be given to illustrate the various physical processes and phenomena occurring within the realm of this technology.

Many colleagues and friends helped with the production of this text. I owe thanks to Professor Dr. Dr. h.c. Walter Heywang, formerly director of Corporate Research and Development of Siemens AG in Munich for suggesting the idea of this book. I am much indebted to Mr. Liang Huguang, Dr. Ulrich Kreher and Mr. Dirk Kurlenbach who prepared diligently the numerous diagrams and graphs. The critical comments of my graduate students and Professor Jürgen Niklas, Institute of Experimental Physics, Freiberg University of Mining and Technology were most

welcome. My wife Giesela patiently endured my idiosyncrasies and irritations during some phases of the preparation of this text, and suffered through many lonely weekends. Last but not least, VCH Weinheim, represented by Frau Dr. Ute Anton, supported and encouraged me in the endeavour to complete the manuscript. Special thanks are due to Tommaso Albinoni and Antonio Vivaldi.

Robert B. Heimann

Freiberg, March 1996

Contents

List of Symbols and Abbreviations	xiii
1 Introduction	1
1.1 Coatings in the Industrial Environment	2
1.2 Surface Coating Techniques	3
1.3 Brief History of Thermal Spraying	8
1.4 Synergistic Nature of Coatings.	13
1.5 Applications of Thermally Sprayed Coatings	14
References	15
2 Principles of Thermal Spraying.	17
2.1 Characterization of Flame versus Plasma Spraying	21
2.2 Concept of Energy Transfer Processes	22
2.3 Unique Features of the Plasma Spray Process	22
References	25
3 The First Energy Transfer Process: Electron–Gas Interactions	27
3.1 The Plasma State	27
3.1.1 Characteristic Plasma Parameters	28
3.1.1.1 Langmuir Plasma Frequency	28
3.1.1.2 Debye Screening Length	29
3.1.1.3 Landau Length	29
3.1.1.4 Collision Path Length	30
3.1.1.5 Collision Frequency	31
3.1.2 Classification of Plasmas	31
3.1.2.1 Low Density Plasmas.	32
3.1.2.2 Medium Density Plasmas	32

3.1.2.3	High Density Plasmas	35
3.1.3	Equilibrium and Nonequilibrium Plasmas.	35
3.1.4	Maxwellian Distribution of Plasma Energies	37
3.1.5	Equilibrium Compositions of Plasma Gases (Phase Diagrams).	38
3.2	Plasma Generation	38
3.2.1	Plasma Generation through Application of Heat.	40
3.2.2	Plasma Generation through Compression	43
3.2.3	Plasma Generation by Radiation.	43
3.2.4	Plasma Generation by Electric Currents (Gas Discharges).	44
3.2.4.1	Glow Discharges.	45
3.2.4.2	Arc Discharges	46
3.2.4.3	Modeling of the Arc Column	48
3.2.4.4	Structure of the Arc Column	50
3.3	Design of Plasmatrons	55
3.3.1	Arc Discharge Generators and their Applications	57
3.3.1.1	Electrode-supported Plasmas	59
3.3.1.2	Electrodeless Plasmas.	63
3.3.1.3	Hybrid Devices	66
3.3.2	Stabilization of Plasma Arcs.	68
3.3.2.1	Wall-stabilized Arcs	68
3.3.2.2	Convection-stabilized Arcs	68
3.3.2.3	Electrode-stabilized Arcs	69
3.3.2.4	Other Stabilization Methods	69
3.3.3	Temperature and Velocity Distribution in a Plasma Jet	70
3.3.3.1	Turbulent Jets	70
3.3.3.2	Quasi-laminar Jets	74
3.4	Plasma Diagnostics: Temperature, Enthalpy, and Velocity Measurements	77
3.4.1	Temperature Measurements	77
3.4.1.1	Spectroscopic Methods	77
3.4.1.2	Two-wavelength Pyrometry	80
3.4.2	Velocity Measurements	81
3.4.2.1	Enthalpy Probe and Pitot Tube Techniques	81
3.4.2.2	Laser Doppler Anemometry (LDA)	83
3.4.2.3	Other Methods	88
	References	88
4	The Second Energy Transfer Process: Plasma–Particle Interactions	91
4.1	Injection of Powders	91
4.2	Feed Material Characteristics	91

4.2.1	Solid Wires, Rods and Filled Wires.	94
4.2.2	Powders	94
4.2.2.1	Atomization.	97
4.2.2.2	Fusion and Crushing	97
4.2.2.3	Compositing	100
4.2.2.4	Agglomeration	100
4.3	Momentum Transfer	100
4.3.1	Connected Energy Transmission	100
4.3.2	Modeling of Momentum Transfer	101
4.3.3	Estimation of the Drag Coefficient	103
4.3.4	Surface Ablation of Particles	104
4.4	Heat Transfer	106
4.4.1	Heat Transfer under Low Loading Conditions.	106
4.4.2	Exact Solution of Heat Transfer Equations	113
4.4.2.1	Particle Heating without Evaporation	114
4.4.2.2	Particle Heating with Evaporation	117
4.4.2.3	Evaporation Time of a Particle	118
4.4.3	Heat Transfer under Dense Loading Conditions	119
4.4.3.1	Conservation Equations	121
4.4.3.2	Results of Modeling under Dense Loading Conditions	122
4.4.4	Heat Transfer Catastrophy	122
4.4.5	Energy Economy	126
4.5	Particle Diagnostics: Velocity, Temperature, and Number Densities	128
4.5.1	Particle Velocity Determination	128
4.5.2	Particle Temperature Determination	132
4.5.3	Particle Number Density Determination	132
	References	134
5	The Third Energy Transfer Process: Particle–Substrate Interactions.	137
5.1	Basic Considerations	137
5.2	Estimation of Particle Number Density	138
5.3	Momentum Transfer from Particles to Substrate	141
5.4	Heat Transfer from Particles to Substrate	149
5.4.1	Generalized Heat Transfer Equation	150
5.4.2	Heat Transfer from Coating to Substrate	151
5.5	Coating Diagnostics: Microstructure, Porosity, Adhesion, and Residual Stresses.	153

5.5.1	Microstructure of Coatings	153
5.5.1.1	Splat Configuration	154
5.5.1.2	Surface Roughness of Coatings	155
5.5.1.3	Fractal Properties of Surfaces	158
5.5.2	Porosity of Coatings	164
5.5.2.1	Point Counting	165
5.5.2.2	Mercury Pressure Porosimetry	166
5.5.2.3	Archimedes' Method	166
5.5.3	Adhesion of Coatings.	167
5.5.4	Chemical Changes	168
5.5.5	Residual Stresses.	169
5.5.5.1	Blind Hole Test	170
5.5.5.2	X-ray Diffraction Measurements ($\sin^2 \psi$ -Technique)	171
5.5.5.3	Almen-type Test	174
5.5.5.4	Theoretical Analysis of Residual Stresses	175
	References	178
6	The Technology Transfer Process: Solutions to Industrial Problems . .	181
6.1	Wear- and Corrosion-Resistant Coatings	181
6.1.1	Pure Carbides	181
6.1.2	Cemented Carbides	182
6.1.2.1	Tungsten Carbide/Cobalt Coatings.	183
6.1.2.2	Titanium Carbide-based Coatings	191
6.1.2.3	Chromium Carbide-based Coatings	196
6.1.2.4	Boride-based Coatings	200
6.1.3	Oxide Coatings	201
6.1.3.1	Alumina-based Coatings	202
6.1.3.2	Chromia-based Coatings	204
6.1.4	Metallic Coatings	205
6.1.4.1	Refractory Metal Coatings	205
6.1.4.2	Superalloy Coatings	206
6.1.5	Diamond Coatings	207
6.2	Thermal and Chemical Barrier Coatings	209
6.2.1	Yttria-Partially Stabilized Zirconia Coatings (Y-PSZ)	209
6.2.1.1	Stress Control and Modeling	213
6.2.1.2	Sealing of As-sprayed Surfaces.	218
6.2.1.3	Laser Surface Remelting of Y-PSZ Coatings	218
6.2.2	Other Thermal Barrier Coatings	223
6.3	Bioceramic Coatings	224
6.3.1	Thin Film Techniques for HAp Coatings	225
6.3.1.1	Ion Beam Dynamic Mixing	225

6.3.1.2	RF Sputtering	225
6.3.1.3	Liquid Immersion Techniques	225
6.3.1.4	Electrophoretic Deposition	225
6.3.2	Thick HAp Coatings	226
6.3.2.1	Plasma Sprayed HAp Coatings	226
6.4	Functional Plasma-Sprayed Coatings.	232
6.4.1	HT-superconducting (HTSC) Coatings	232
6.4.2	Coating for Solid Oxide Fuel Cells (SOFCs).	233
	References	237
7	Quality Control and Assurance Procedures.	243
7.1	Quality Implementation	243
7.1.1	Total Quality Management	243
7.1.1.1	Quality Tools	243
7.1.1.2	Quality Philosophy.	244
7.1.1.3	Management Style	245
7.1.2	Qualification Procedures	245
7.1.3	Powder Characterization	246
7.2	Characterization and Test Procedures	247
7.2.1	Mechanical Properties	248
7.2.1.1	Bond Strength	248
7.2.1.2	Macro- and Microhardness Tests	261
7.2.1.3	Fracture Toughness	266
7.2.2	Tribological Properties	268
7.2.2.1	Simulation of Basic Wear Mechanisms	269
7.2.3	Chemical Properties	275
7.2.3.1	Chemical Corrosion Evaluation Tests	279
7.2.3.2	Burner Rig Test	279
	References	282
8	Design of Novel Coatings	285
8.1	Coating Requirements	285
8.2	Design of Novel Advanced Layered Coatings	286
8.2.1	Gradient Layers	287
8.2.2	Layered Materials in Thermodynamic Equilibrium.	288
8.2.3	Extended Solid Solution	288
8.2.4	Multilayers	288
8.3	Principles of Statistical Design of Experiments.	288

8.3.1	The Experimental Environment and its Evolution	288
8.3.1.1	Screening Designs	289
8.3.1.2	Response Surface Designs.	290
8.3.1.3	Theoretical Models.	290
8.3.2	Screening Designs	291
8.3.3	Factorial Designs	293
8.3.3.1	Full Factorial Designs	293
8.3.3.2	Fractional Factorial Designs	293
8.3.4	Box–Behnken Designs	294
8.3.5	Designs of Higher Dimensionality	295
8.4	Optimization of Coating Properties: Case Studies	296
8.4.1	Plackett–Burman (Taguchi) Screening Designs	296
8.4.2	Full Factorial Designs	297
8.4.3	Fractional Factorial Designs	299
8.4.3.1	Tungsten Carbide/Cobalt Coatings.	299
8.4.3.2	Ferrosilicon Coatings.	303
8.4.3.3	Alumina/titania Coatings	305
8.4.3.4	Stellite Coatings	308
8.4.3.5	Titanium Coatings	309
8.5	Future Developments.	310
	References	314
A	Appendix A: Dimensionless Groups	317
	References	318
B	Appendix B: Calculation of Temperature Profiles of Coatings	319
B.1	Heat Conduction Equations.	319
B.2	Solutions of the Equations	320
B.2.1	Substrate Temperature Profile	320
B.2.2	Deposit Temperature Profile	320
B.3	Real Temperature Profiles.	322
	References	322
C	Appendix C: Calculation of Factor Effects for a Fractional Factorial Design 2^{8-4}	323
Index	327

List of Symbols and Abbreviations

a.c. = alternating current
AE = acoustic emission
AJD = anode jet dominated
APS = air plasma spraying
BE = back wall echo
CAPS = controlled atmosphere plasma spraying
CBC = chemical barrier coatings
CCF = cross-correlation function
CFC = carbon fiber composite
CJD = cathode jet dominated
CSZ = completely stabilized zirconia
CTE = coefficient of thermal expansion
CVD = chemical vapor deposition
CW-PTR = continuous wave photothermal radiometry
d.c. = direct current
E, EM, M, T, and S = plasma types
EB-PVD = electron beam PVD
ECM = electrochemical machining
EMI = electromagnetic interference
EP = electrode plasma
f.c.c. = face centered cubic
FFT = fast Fourier transform
FGM = functional gradient material
FPA = fracture profile analysis
FTIR = Fourier transformed infrared
HAp = hydroxyapatite
HOSP = hollow-spherical-powder
HPPS = high power plasma spraying
HRC = Rockwell hardness
HTSC = high temperature superconducting coatings
HV = Vickers' hardness
HVOF = hypervelocity oxyfuel gun
ICP = inductively coupled plasma

IE = interfacial echo
 IGPS = inert gas plasma spraying
 IPS = inductive plasma spraying
 JIT = just-in-time
 LCF = low cycle fatigue
 LDA = laser Doppler anemometry
 LPPS = low pressure plasma spraying
 LPS = laser plasma spraying
 LTE = local thermodynamic equilibrium
 MHD = magnetohydrodynamic
 MRP = main regime parameters
 OCTA = oxide-cobalt-titanium anodes
 ORTA = oxide-ruthenium-titanium anodes
 p.p.m. = parts per million
 PA-CVD = plasma assisted CVD
 PAVD = plasma assisted vapor deposition
 PEN = positive electrode-electrolyte-negative electrode
 PLZT = lead lanthanum zirconate titanate
 PMMA = polymethylmethacrylate
 PMRS = plasma melted rapidly solidified
 PSI = particle-source-in (model)
 PSZ = partially stabilized zirconia
 PTA = plasma transferred arc
 PVD = physical vapor deposition
 PZT = lead zirconate titanate
 QFD = quality function deployment
 RFS = radio frequency spraying
 RT = room temperature
 SCFH = standard cubic feet per hour
 SDE = statistical design of experiments
 SEM = scanning electron microscopy
 SES = statistical experimental strategy
 SIA = slit island analysis
 SLPM = standard litres per minute
 SME = small and medium sized enterprises
 SOFC = solid oxide fuel cell
 SPC = statistical process control
 SPE = solid particle erosion
 SPS = shrouded plasma spraying
 SQA = statistical quality assurance
 SQC = statistical quality control
 STF = strain to fracture
 TBC = thermal barrier coatings
 TEM = transmission electron microscopy
 TI = transmitted impulse
 TQM = total quality management

TRIR = time resolved infrared radiometry
TTBCs = thick TBCs
TTT = temperature-time-transformation (diagram)
ULSI = ultra large scale integration
UPS = underwater plasma spraying
UTS = ultimate tensile strength
VPS = vacuum plasma spraying
Y-PSZ = yttria-partially stabilized zirconia

1 Introduction

Thermal spraying has emerged as an important tool of increasingly sophisticated surface engineering technology. Research and development are increasing rapidly, and many applications are being commercialized. An indication of this rapid development is the fact that over 80% of the advances made over the last 90 years were made in the last two decades, a corollary to Pareto's 80/20 rule! [1] Many exciting niches are opening up for metallic and ceramic surface coatings that include such well established markets as aerospace and consumer industries but also more slowly developing coating markets in the automotive, computer and telecommunications industries.

The goal of this text is to give students and researchers in materials engineering and materials science an appreciation of the fundamental physical processes governing plasma spray technology, to provide familiarization with advantages and disadvantages of the technology compared to other surface coating techniques, to discuss basic equipment requirements and limitations, to present case studies and typical applications of plasma spray technology to solve industrial problems, and to lay a foundation for future research and development work in this field.

The material covered will discuss the basic nature of the plasma state, plasma-particle interactions, heat and momentum transfer, particle-substrate interactions, analyses of the microstructure, adhesion strength and residual stresses of coatings, optimization of coatings by SDE (statistical design of experiments) and SPC (statistical process control) methods, modeling of the plasma spray process, and an account of a novel fractal approach to coating properties, and other nonlinear considerations. The fundamental physical processes underlying plasma spraying have been treated in detail. It was felt that many other texts neglect this topic even though this knowledge is crucial to the understanding of the process and, most importantly will enable the materials and maintenance engineer to choose the most appropriate combination of materials, equipment and parameter selection to lay down coatings with high performance, new functional properties, and improved service life.

It should be emphasized, however, that this text can not cover the totality of this fast developing field. In particular, limitations on space and reliable information, and the wide variety of types of equipment and coatings as well as applications, prevented covering some aspects of plasma spray technology in detail. For those rea-

sons, differences in the type of plasma spray systems used successfully in many applications have not been given much consideration. However, the following text will give brief references to the most pertinent aspects of plasma spray technology, and will enable the reader to build on this knowledge in order to perform research and development work.

Collaboration between universities or government research organizations and industry in the resource and manufacturing sectors will lead increasingly to strategic alliances that enable industry to perform more competitively and in an environmentally compatible way within the framework of a global concept of sustained development. Process control, including 3D-modeling of complex plasma-particle-substrate interactions, on-line process diagnostics, and development of novel coatings with improved performance are areas rich in research needs and opportunities. Specialists in plasma processing, including plasma spray technology, will find a rewarding field of endeavour in the 1990s and beyond.

1.1 Coatings in the Industrial Environment

There is increasing worldwide interest in thermal spray coatings. According to a study conducted by the Gorham Advanced Materials Institute [2], the sales of advanced ceramics are expected to topple US \$4 billion in 1995, 80% of which will be in ceramic coatings (Figs 1-1, 1-2). The 1986 world sales for ceramic coatings (total sales: US \$1.1 billion) were achieved predominantly in the construction industry (36%), metal fabrication industries (21%), military (12%), and other industries (31%): chemical processing, internal combustion engines, petrochemical and metal producing industries. Of the ceramic coatings, 39% were produced by physical vapor deposition techniques (PVD), 26% by chemical vapor deposition (CVD), 23% by thermal spraying, and 12% by wet processing including sol-gel technique [3]. Recent predictions show that these markets are expected to triple to more than US \$3 billion by the year 2000 with an annual average growth rate of 12%. The industrial segments with the largest predicted individual annual growth rates are engines (28%), marine equipment (18%), chemical processing (15%), military (11%)¹, and construction (11%). A field of application with a large potential is bioceramic coatings based on plasma-sprayed hydroxyapatite. Such biocompatible coatings for prosthetic implants in bone promise to have a rapidly growing market in an aging population [4]. High-temperature superconductive and diamond coatings are on the verge of making technological breakthroughs in the microelectronics industry [5].

Besides high-technology applications a major market exists in the resource industries including oil and gas, mining, forestry, pulp, paper and agricultural industries, manufacturing and electronics, automotive and aerospace industries. In partic-

¹ This figure does not contain a presumed reduction in spending caused by the recent reduction in political tension between the two large military blocks.

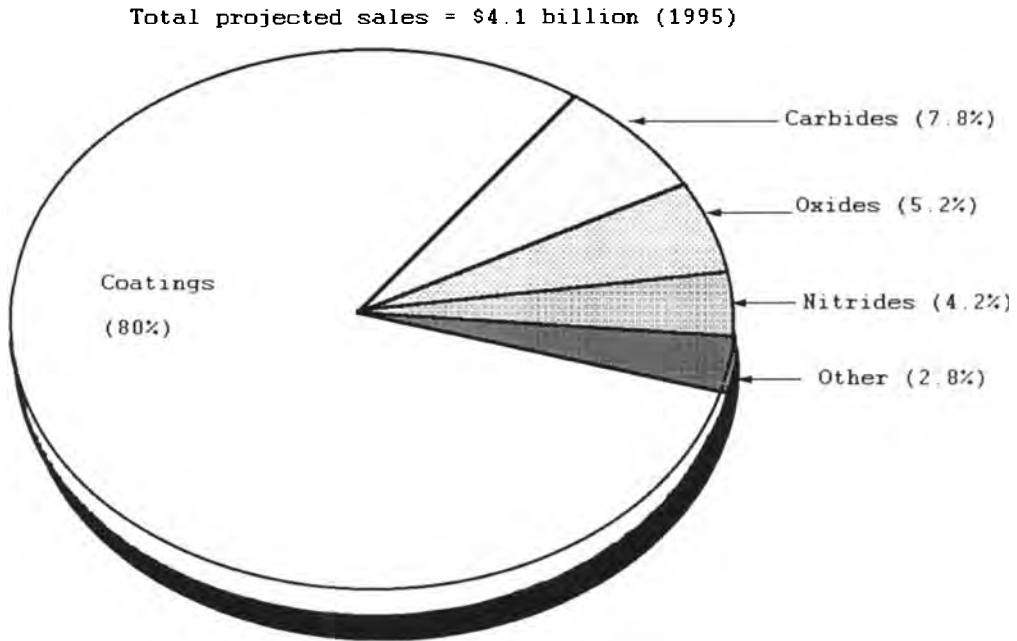


Figure 1-1. Forecast of worldwide sales in advanced structural ceramics and ceramic coatings [2].

ular, industries threatened by international competition, erosion of raw material prices, and shifts to new materials and technologies must radically improve operational efficiency, industrial diversification and environmental compatibility to survive. An important contribution in this struggle can be made by coatings that combat wear, erosion and corrosion found at all levels of operations in industry, that impart new functional properties, extend the service life of machinery, and contribute in general to sustainable development required by the increasingly environmentally conscious world of the decades to come.

The market development of ceramic coatings depends to a large extent on individual products that must, in terms of materials and technology alternatives, show better performance than competing materials. The field of application of the product appears to be less important. Figure 1-3 shows that the onset of substantial market penetration in automotive applications is considerably earlier for ceramic coatings than for monolithic ceramics and ceramic composites [6].

1.2 Surface Coating Techniques

Before providing details on plasma spray technology, and the wide field of applications of plasma spray-generated surface coatings, a short review will be given of

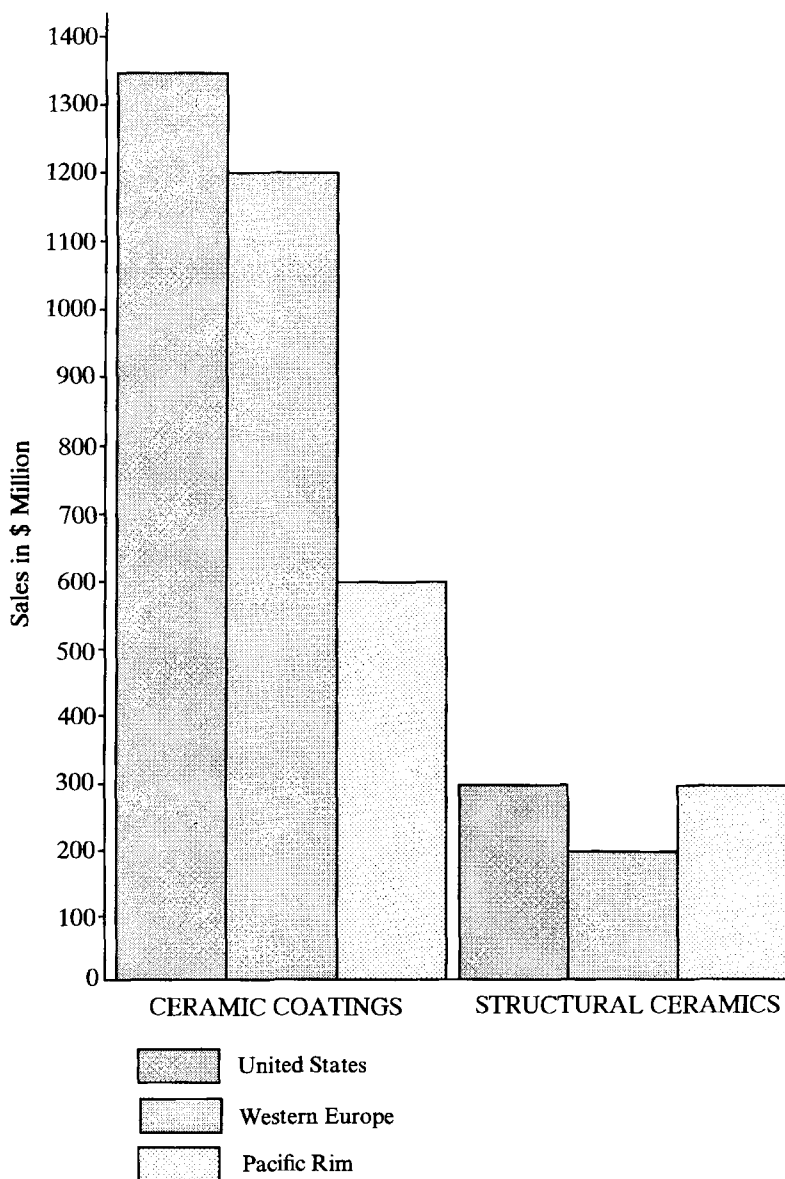


Figure 1-2. Forecast of worldwide sales of advanced structural ceramics and coatings by region [2].

various other surface coating techniques. More details can be found in the literature [7, 8].

The advantage of coating technology, in general, is that it marries two dissimilar materials to improve, in a synergistic way, the performance of the whole. Usually mechanical strength and fracture toughness are being provided by the substrate and

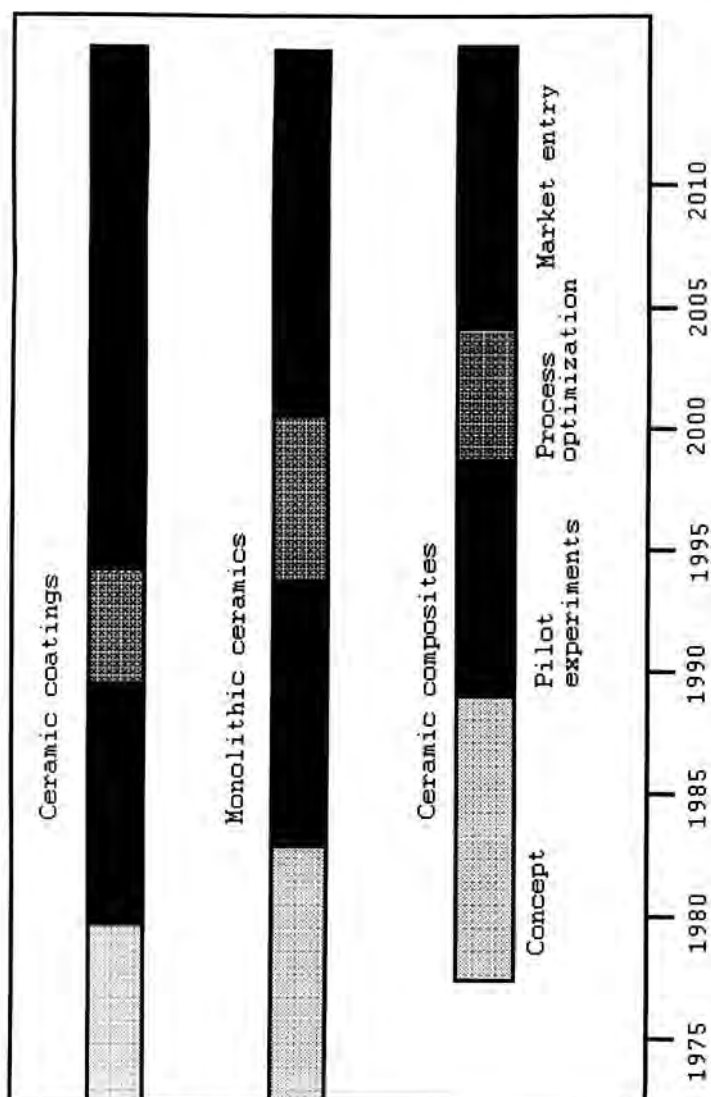


Figure 1-3. Development stages of ceramic engine parts [6].

the coating provides protection against environmental degradation processes including wear, corrosion, erosion, and biological and thermal attack.

Surface coating technologies have the following advantages.

- *Technical advantages.* Creation of new materials (composites) with synergistic property enhancement, or completely new functional properties, for example electronic conductivity, piezo- or ferroelectric properties etc.
- *Economic advantages.* Expensive bulk materials such as stainless steel or super-alloys can be replaced by relatively thin overlays of a different material. These savings are enhanced by longer life time of equipment and reduced downtime and shortened maintenance cycles.
- *Attitudinal advantages.* Materials engineers trained in metals handling need not be afraid to deal with new materials with unfamiliar properties, specifications and performance such as ceramics or polymeric composites. The ceramic coating just becomes a part of a familiar metal materials technology.

Coatings are, of course, not a new invention. For times immemorial, wood and metal have been painted with organic or inorganic pigments to improve their esthetic appearance and their environmental stability. Corrosion-, wear- and abrasion-resistance of the substrate materials were significantly improved by the paint coatings. These organic paint coatings, however, did not endure high temperatures and did not adhere well. The performance of traditional coatings has been improved by the use of chemically-cured paints in which components are mixed prior to application and polymerized by chemical interaction, i.e. cross-linking. Epoxy resins, polyurethanes and various polyester finishes show considerable resistance to alkalis and acids, and also to a wide range of oils, greases and solvents.

Traditional enamels are glass-based coatings of inorganic composition applied in one or more layers to protect steel, cast iron or aluminum surfaces from corrosion. This technology has been extended today to manufacture thick film electronics in which metals or metal oxides are added to a fusible glass base to generate a range of thick film conductors, capacitors and other electronic components.

Chemical coatings are frequently applied by electroplating of metals such as copper and nickel. Nickel, for example, forms a highly adherent film for wear applications by an electroless plating process, and thus is applied to manufacture aerospace composites. A related technology is the anodizing of aluminum by electrochemically induced growth of aluminium oxide in a bath of sulphuric or phosphoric acids. *Spray pyrolysis* involves chemical reactions at the surface of a heated substrate. Increasingly transparent conducting coatings of tin oxide or indium tin oxide are used to coat glass windows for static control, radio frequency shielding and environmental temperature control.

Sol-gel coatings based on the pyrolysis of organometallic precursors such as metal alkoxides are used today. The process was originally developed for aluminum and zirconium oxide but is now extending to a wide range of glasses including silicates and phosphates, and has recently been applied to complex ferroelectrics such as PZT (lead zirconate titanate) and PLZT (lead lanthanum zirconium titanate). Sol-gel coatings enjoy a high compositional flexibility and ease of preparation at generally

ambient temperature but because of the frequently expensive precursor materials their application is limited to high-value added devices, in particular in electronics.

Thin coatings produced by CVD are widely employed in the semiconductor industry for large band-gap materials such as gallium arsenide, indium phosphide and other compound semiconductor materials. The technology uses vapor phase transport to grow epitaxial and highly structured thin films including insulating oxide films on single crystal silicon substrates. A related technology is the growth of thin crystalline diamond films by decomposition of methane or other hydrocarbons in a hydrogen(>95%)–argon(<5%) plasma. Much activity is currently devoted in Japan and the USA to the improvement of the thickness and the crystallographic perfection of diamond thin films. Major potential industrial applications of such films can be found for protective coatings on compact discs, optical lenses, in particular such carried by low-earth orbit space craft, and substrates for ULSI (ultra large scale integration) devices.

Physical Vapor Deposition (PVD) technologies using evaporation, sputtering, laser ablation, and ion bombardment are a mainstay of present-day surface engineering technology.

Evaporation is the most simple vacuum technique. The materials to be deposited on a substrate are melted and vaporized either on a resistively heated tungsten or molybdenum boat, or by an electron beam. The method is suitable for many metals, some alloys, and compounds with a high thermal stability such as silica, yttria and calcium fluoride. While films deposited by evaporation are inferior to other vacuum techniques in terms of adhesion to the substrate, the excellent process control generating optical films with well-defined thicknesses and indices of refraction has made this technique popular.

Sputtering methods deposit material by causing atoms to separate from a target by bombardment with highly energetic ions from a gas plasma or a separately excited ion beam, and depositing them on a substrate. Magnetron sputtering uses confinement of the exiting plasma by a strong magnetic field that results in high deposition rates and good reproducibility. Large area sources are used to coat plastic foils and ceramic substrates for packaging materials in the food industry, as well as for metallizing plastic ornaments and automotive components such as bumpers, for architectural glass, and for multilayer holographic coatings on identification and credit cards to prevent forgeries.

Laser ablation is a modern technology that has been developed in particular for high temperature superconducting ceramics. A focused laser beam is used to vaporize the target material. Since this material comes from a highly localized region the ion flux reproduces the target composition faithfully. Even though the cost of the lasers is still high and the deposition rates are quite low, future developments may lead to much wider application of this technique if reproducible process control can be achieved.

The PVD methods mentioned so far all rely on a coating deposited on an existing substrate surface with given composition. However, *ion implantation* modifies the properties of the substrate itself. A beam of high energy ions can be created in an accelerator and brought in contact with a substrate surface. Thus corrosion and wear performance can be improved dramatically. For example, implantation of 18%

chromium into a steel results in an *in-situ* stainless steel with high corrosion resistance, the use of boron and phosphorus produces a glassy surface layer inhibiting pitting corrosion, and the implantation of titanium and subsequent carbon ions creates hard-phase titanium carbide precipitates. Likewise implantation of nitrogen produces order of magnitude improvement of the wear resistance of steel, vanadium alloys, and even ceramics.

Modern high performance machinery, subject to extremes of temperature and mechanical stress, needs surface protection against high temperature corrosive media, and mechanical wear and tear. For such coatings a highly versatile, low cost technique must be applied that can be performed with a minimum of equipment investment and does not require sophisticated training procedures for the operator. Such a technique has been found in thermal spraying. It uses partially or complete melting of a wire, rod or powder as it passes through a high temperature regime generated electrically by a gas plasma or by a combustion gas flame. The molten droplets impinge on the substrate and form the coating layer by layer. This technique is being used widely to repair and resurface metallic parts and also, in recent years, to build up wear-, chemical- and thermal barrier coatings based on alumina or zirconia, in particular for applications in the aerospace and automotive industries. High temperature-erosion protection of boiler tubes and fire chambers of coal-fired power plants, corrosion protection of special concrete parts, and of bio-ceramic coatings for orthopedic and dental prosthetic implants are just a short list of ever increasing fields of service of thermally sprayed coatings.

For all these reasons, advanced materials, i.e. ceramics or polymer coatings, become more and more popular among materials engineers. The equipment, ease of application of coatings to complex surfaces, and the availability of tailored materials makes novel surface coatings increasingly attractive. Thus it has been said that coatings technology will be the materials technology of the 21st century.

1.3 Brief History of Thermal Spraying

After several patents in 1882 and 1899, in 1911 M. U. Schoop in Switzerland started to apply tin and lead coatings to metal surfaces by flame spraying to enhance corrosion performance [9]. The field developed quickly, and in 1926 a comprehensive book was published by T. H. Turner and N. F. Budgen called *Metal Spraying*. A new edition was published in 1963 with the title *Metal Spraying and the Flame Deposition of Ceramics and Plastics* to reflect the shift from metals to other materials.

Figure 1-4 gives an impression of the pace of development of thermal spray technology [10]. It illustrates those applications that have been either motivated or made possible by the technological progress (see, for example [11]) and shows advances being led by entrepreneurs or companies. The curve follows a typical life-cycle curve: slow at first after inception by Schoop in 1911, and then increasing at a modest rate until the late 1950s. At this time the appearance of a variety of then-modern plasmatrons boosted the development considerably. In particular, the D-gun coatings

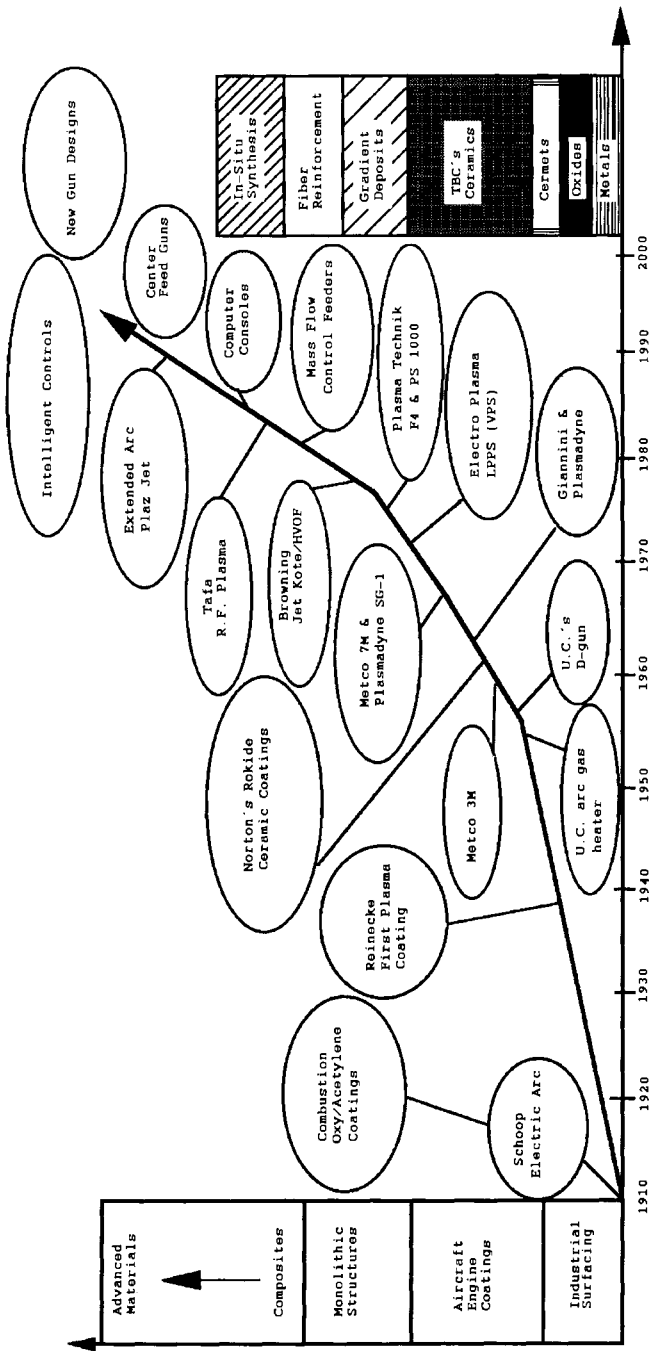


Figure 1-4. Thermal spray technology growth: summary and milestones [10]: UC = Union Carbide Co.

(Praxair Surface Technology, Inc., Indianapolis, IN, USA) applied by the Union Carbide Corporation found a receptive market in the aerospace industry, and a large proportion of the subsequent technological growth was due to plasma-sprayed thermal barrier coatings based on stabilized zirconia. The second growth spurt shown in the figure occurred in the 1980s with the invention of the vacuum plasma spraying/low pressure plasma spraying (VPS/LPPS) and the Jet Kote/hypervelocity oxyfuel gun (HVOF) techniques and the high temperature-coatings for aerospace gas turbine associated therewith shown in Fig. 1-5, [12]. (Jet Kote is manufactured by Browning Engineering, Enfield, NH, USA.) Future developments, undoubtedly highlighted by a further increase in the rate of technological innovation, will probably include improved on-line real-time feedback control, intelligent SPC, design of new equipment and spray powders as well as 3D-process modeling and improved understanding of the complex nonlinear physics underlying the plasma spray process.

In the last two decades there has been increasing interest in coatings from the military and commercial sectors, leading to a wealth of information. Journals totally dedicated to thermal spraying exist, for example the *Journal of Thermal Spray Technology* (ASM), and biennial national and triennial international conferences present ongoing worldwide university and industry research and development efforts in a wide variety of thermal spray processes. Figure 1-6 illustrates these trends by showing the exponential growth of papers published between 1967 and 1991; Fig. 1-7 shows the number of papers presented and the number of attendees at the seven International Metal Spray Conferences (1956 to 1973) and seven International Thermal Spray Conferences (1976 to 1995) held so far [13]. Again, the number of papers, Y , follows an exponential growth law, $Y = 19.7 \exp(0.05X)$ with a correlation coefficient $r = 0.96$, where X is the year measured from the inception of the international conferences.

Activities are well underway to develop expert systems that integrate exhaustive databases with expert knowledge and practical experiences. For example, powerful software has been developed that allows the engineer to determine the best coatings for a given part or application, as well as information on how and where the coatings are being used. This database provides detailed information on over 1300 thermal spray applications and contains a listing of international suppliers. The materials covered are categorized into 12 groups including iron-based materials, nickel-based materials, cobalt-based materials and non-ferrous metallic-based materials [14]. Process simulation plays an increasingly important role in estimating the interdependence of spraying parameters and desired coating properties [15].

The main activities today center around:

- improving powder feedstocks, spray application equipment, and process control through SDE, SPC, and quality function deployment (QFD) techniques,
- designing new control devices, real-time feedback looping, mass flow controllers, powder metering equipment, manipulators and robots [16],
- effective innovation and technology transfer from research organizations to small and medium-sized enterprises (SMEs) [17] and
- development of data bases and expert systems [18].

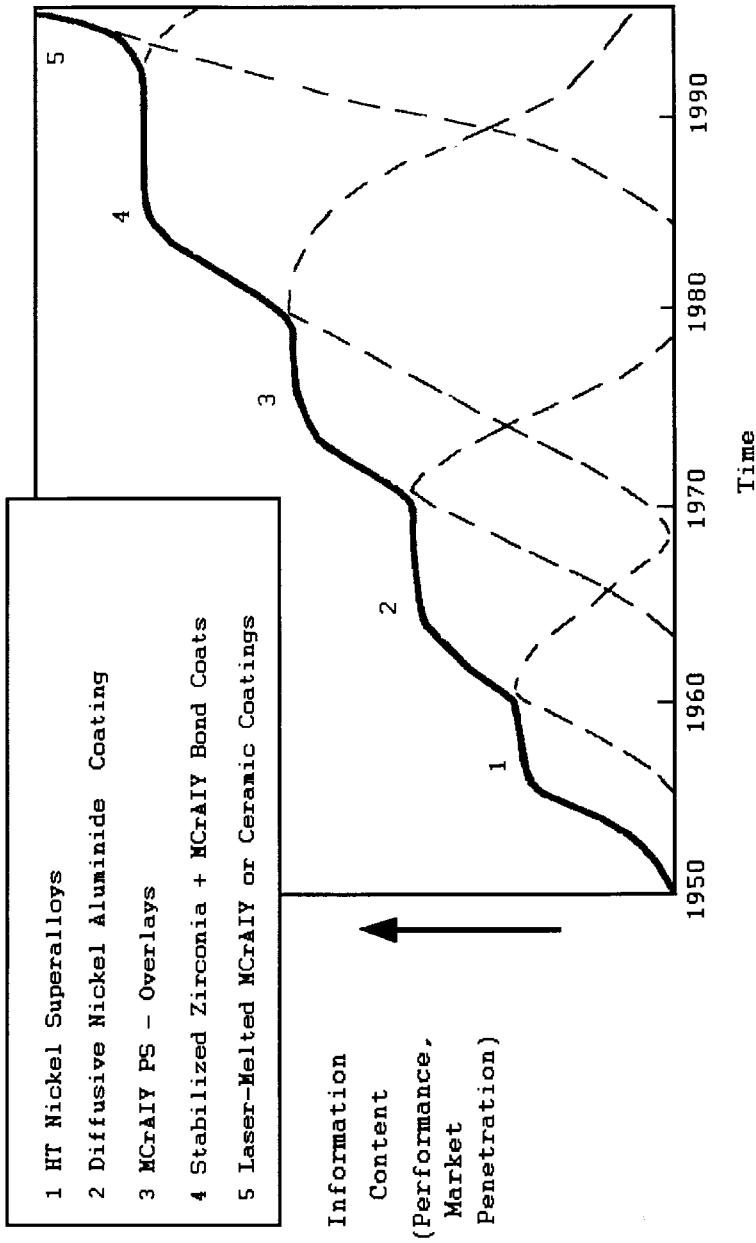


Figure 1-5. Evolution of high temperature coatings for gas turbines [12]: HT = high temperature, PS = plasma spray.

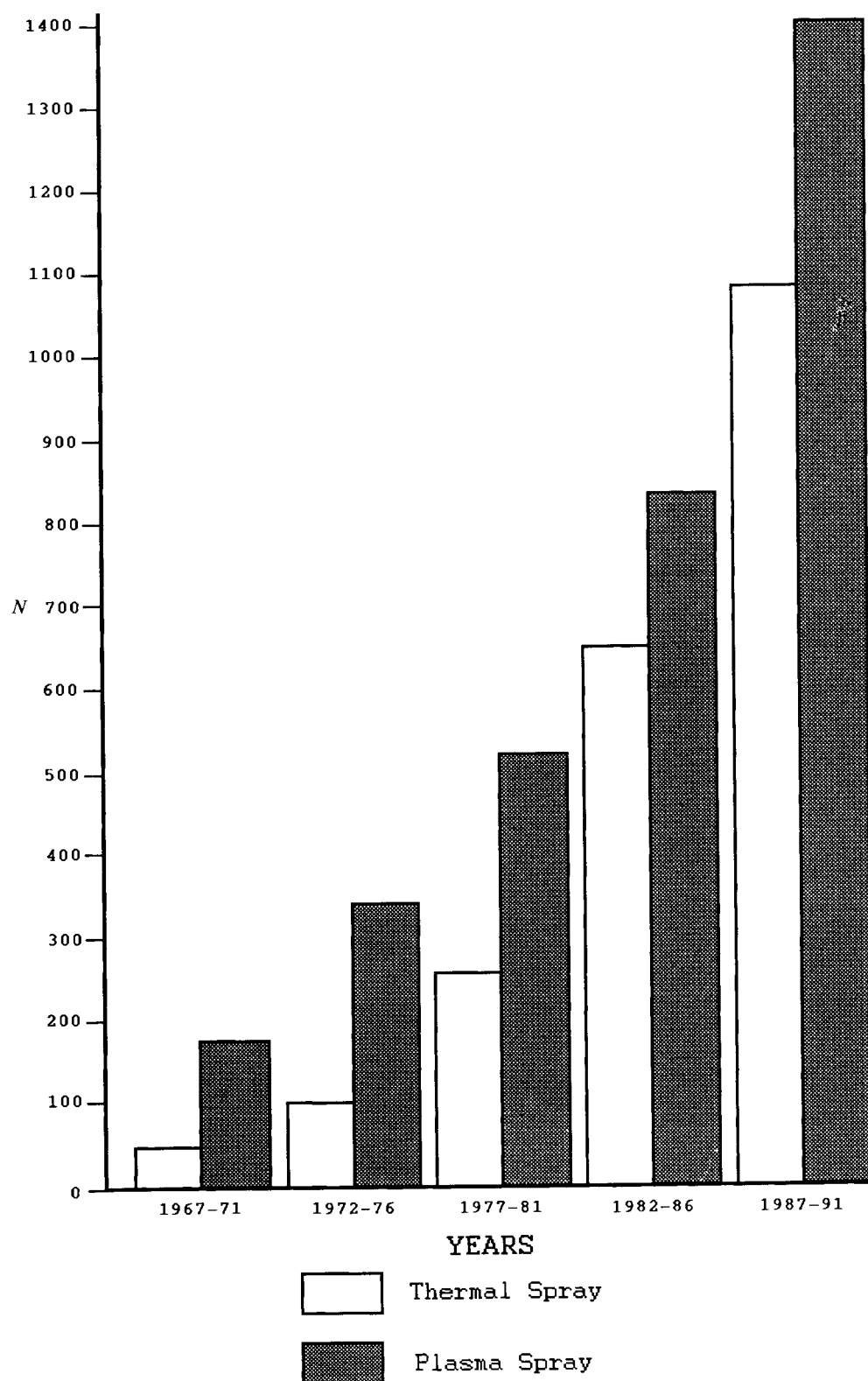


Figure 1-6. Exponential growth of research papers on thermal spray technology (1967-1991).

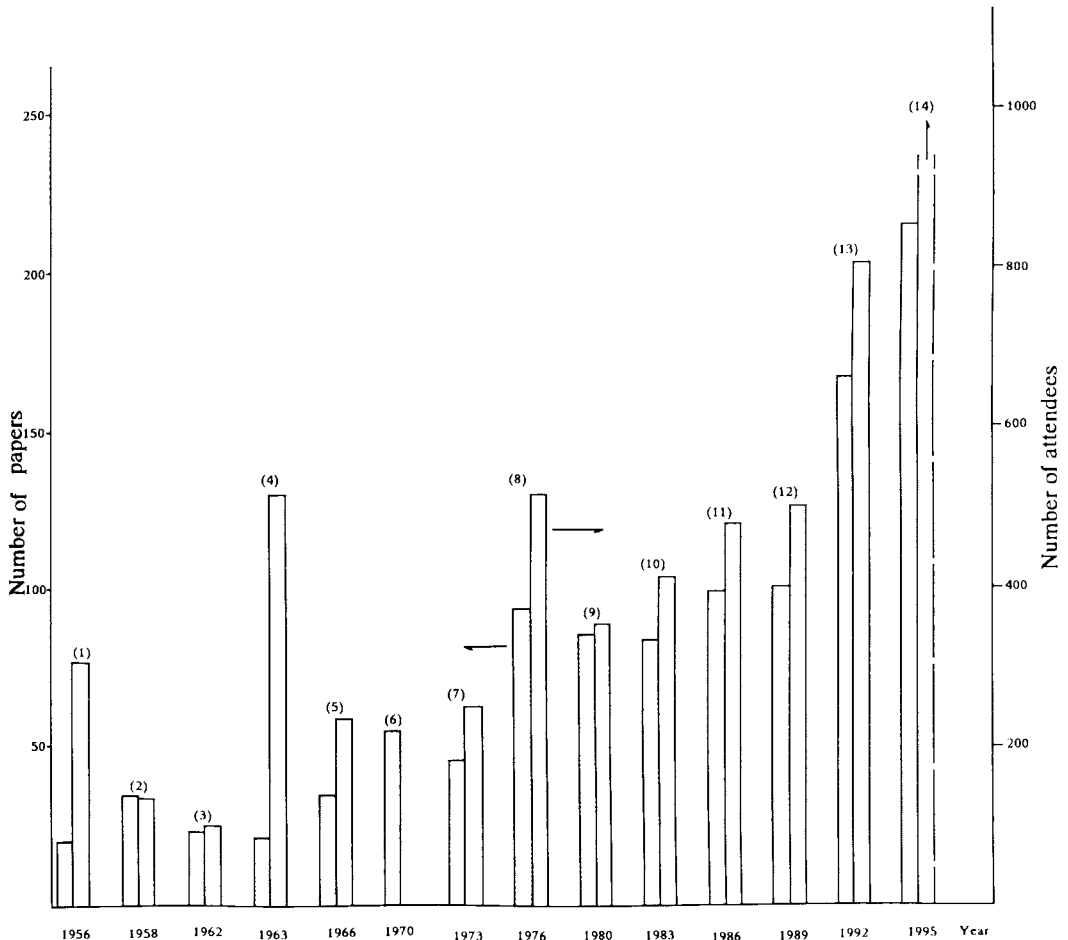


Figure 1-7. Exponential growth of papers presented (left bar) at International Metal Spray Conferences (1956–1973) and International Thermal Spray Conferences (1976–1995), and number of attendees (right bar) [13].

1.4 Synergistic Nature of Coatings

A metal substrate/ceramic coating system combines the mechanical strength of a metal with the environmental stability of a ceramic material. Typical metal properties exploited are:

- creep strength,
- fatigue strength,
- flexural strength,
- ductility,

- high fracture toughness,
- high coefficient of thermal expansion,
- high heat conductivity, and
- low porosity.

Typical ceramic properties are:

- high thermal stability,
- chemical stability,
- high hardness,
- low fracture toughness,
- low coefficient of thermal expansion,
- low heat conductivity, and
- medium to high porosity.

The combination of these properties yields a superior composite material. However, several aspects have to be carefully controlled such as the difference between coefficients of thermal expansion of metal and ceramic which leads to undesirable stresses at the substrate–coating interface. Also, the generally high porosity of plasma-sprayed ceramics has to be dealt with by either infiltrating the coating with another material, hot isostatically pressing, or by laser densification or other techniques. The low fracture toughness of the ceramic is also of concern. Intense research is ongoing worldwide to develop ceramics with improved fracture toughness. For example, research is being pursued to thermally spray fiber-reinforced ceramics, such as silicon carbide–alumina composite coatings.

1.5 Applications of Thermally Sprayed Coatings

There is an ever increasing number of technical applications of plasma-sprayed metal and ceramic coatings. Many of such applications have resulted from the demand from the users of machinery and equipment to protect their investment from wear, corrosion, erosion, and thermal and chemical attack. Others result from the desire to impart new functional properties to conventional materials, such as high-temperature superconducting coatings, bioceramic coatings, diamond coatings, and electrocatalytic coatings for solid oxide fuel cells (SOFCs). It is not possible to cover here all applications of thermally sprayed coatings. The list below shows but a few industrial areas where coatings have been successfully used to solve performance problems. Practical solutions to a specific problem frequently follow a well-established sequence of events [19]:

- problem identification,
- specification of coating properties,
- proposed solution including selection of materials to be sprayed, equipment and technique used etc.,

- application of coating, and
- evaluation of results in terms of technical performance and economic viability.

Typical applications of metallic and ceramic coatings are:

- wear and erosion control of machinery parts and turbine vanes, shrouds and blades in coal-fired power generating stations;
- particle erosion control in boiler tubes and superheaters of coal-fired power plants;
- chemical barrier coatings for ethane steam cracking furnace tubes for coking and erosion protection;
- wear control and improvement of friction properties in a variety of machine parts, including pump plungers, valves, bearings, and calender and printing rolls;
- metal coatings for corrosion protection of engineering structures such as steel and concrete bridges in coastal regions;
- corrosion protection against liquid metals in extrusion dies, ladles and tundishes;
- corrosion protection of equipment for petrochemical and chemical plants, and high-temperature corrosion in internal combustion engines;
- thermal and chemical barrier coatings for pistons and valves in adiabatic diesel engines and related machinery, as well as for aerospace gas turbine blades and combustor cans;
- resurfacing of worn equipment, for example in railway applications, ship building and maintenance, and mining tools and equipment;
- superalloys for aerospace gas turbine vanes and shrouds to prevent hot gas erosion and corrosion;
- ceramic membranes for osmotic filtering and ultrafiltration;
- biomedical coatings for orthopedic and dental prostheses with biocompatible properties based on hydroxyapatite and tricalcium phosphate;
- stabilized zirconia electrolyte and electrocatalytic active compound coatings for SOFCs;
- high-temperature superconducting coatings for electromagnetic interference (EMI) shielding;
- abradable coatings and seals for clearance control in gas turbines;
- coatings to protect concrete floors from corrosive action of fruit juices and other agricultural products;
- sealing of concrete floors in dairy industrial operations;
- thick metal overlays for PVD sputter targets; and
- diamond-like coatings for wear applications and for heat sinks in high-power electronic chips.

Some of these applications are dealt with in more detail in Chapter 6.

References

- [1] L. S. Alf, *Quality Improvement Using Statistical Process Control*, HBJ Publishers, NY, **1988**.
- [2] Gorham Advanced Materials Institute, *Thermal Spray Coatings*, Gorham, ME, USA, **1990**.

- [3] K. Chan, J. B. Wachtman, *Ceram. Ind.* **1987**, 129, 24.
- [4] L. L. Hench, *J. Am. Ceram. Soc.* **1991**, 74, 1487.
- [5] R. B. Heimann, *Proc. Adv. Mater.* **1991**, 1, 181.
- [6] H. R. Maier (Ed.) *Technische Keramik als Innovations-grundlage für die Produkt- und Technologie-Entwicklung in NRW*. Ministerium für Wirtschaft, Mittelstand und Technologie des Landes Nordrhein–Westfalen, December **1991**, p. 108.
- [7] M. Sayer, *Can. Ceram. Q.* **1990**, 59, 21.
- [8] R. F. Bunshah, *Deposition Technologies for Thin Films and Coatings*, Noyes Publications, Park Ridge, NJ, USA, **1982**.
- [9] M. U. Schoop, H. Guenther, *Das Schoopsche Metallspritz-Verfahren*, Franckh Verlag, Stuttgart, Germany, **1917**.
- [10] R. W. Smith, R. Novak, *Powder Metallurgy Int.* **1991**, 23(3), 14.
- [11] R. B. Heimann, *Am. Ceram. Soc. Bull.* **1991**, 70, 1120.
- [12] R. Sivakumar, B. L. Mordike, *Surf. Coat. Technol.* **1989**, 37, 139.
- [13] A. Omori, Introduction, *Proc. 14th ITSC'95*, Kobe, Japan 22–26 May, **1995**.
- [14] F. H. Longo, H. Herman, K. Kowalski, *The Thermal Spray Source Program*, MS Card, CRC Press, London, **1994**.
- [15] O. Knotek, U. Schnaut, *Proc. TS'93*, Aachen, Germany, **1993**, DVS 152, 138.
- [16] K. D. Borbeck, *Proc. 10th ITSC*, Essen, Germany, **1983**, DVS 80, 99.
- [17] H. Riesenhuber, *Vak. Techn.* **1989**, 38(5/6), 119.
- [18] H. Kern, M. Fathi-Torbaghan, M. Stracke, *Proc. TS'90*, Essen, Germany, **1990**, DVS 130, 247.
- [19] L. Pawlowski, *The Science and Engineering of Thermal Spray Coatings*. Wiley, Chichester **1995**, p. 327.

Plasma- Spray Coating

by. Robert B. Heimann

Copyright© VCH Verlagsgesellschaft mbH. 1996

2 Principles of Thermal Spraying

Thermal spraying requires a device that creates a high temperature flame or plasma jet. In the case of a plasma, such a device is called a *plasmatron*¹, i.e. a plasma generator powered by an arc or a high frequency discharge whose plasma is superposed by streaming gas. A metal, ceramic or even polymer powder is being injected into the fluid medium, melted during the very short residence time in the flame or plasma jet, and propelled towards a target where it solidifies and builds up a solid coating. Any material can be sprayed as long as it has a well-defined melting point, and does not decompose or sublime during melting.

Figure 2-1 shows the organization of thermal spraying methods [1] divided into the two principal energy sources, *chemical energy* of the combusting gases that power the flame spray torches, and *electric currents* providing energy for the plasmatrons. The plasma spray methods are shown in Figure 2-2. The different techniques are distinguished here by the *surrounding atmosphere*, i.e. air for conventional air plasma spraying (APS) and high power plasma spraying (HPPS), as well as APS with an inert gas shroud to prevent oxidation of oxygen-sensitive powders (SPS), and plasma spray methods relying on special atmospheres, most importantly inert gas plasma spraying (IGPS), vacuum, i.e. low pressure plasma spraying (VPS and LPPS, respectively), and controlled atmosphere plasma spraying (CAPS).

The principal difference between flame spraying and plasma spraying is given by the maximum temperatures achievable. In flame spraying the temperature is limited by the internal heat of combustion of the plasma gases (acetylene, propane, butane). Conventional oxyacetylene torches reach temperatures of around 3 000 K; special devices such as Union Carbide Corporations's (now Praxair Surface Technology, Inc.) D-Gun and Jet Kote System are limited to about 3 500 K, whereas the present limit of the Hypervelocity Oxyfuel Gun (HVOF) seems to be below 3 200 K [1]. The advantage of the latter techniques lies in the exceptionally dense structure of the coatings.

Using electric energy as the source to create the plasma provides for theoretically

¹ The terms plasma burner, plasma torch, plasma arc torch etc. should be avoided since they convey the inaccurate notion of something burning. Also, the term plasma gun should not be used for obvious reasons.

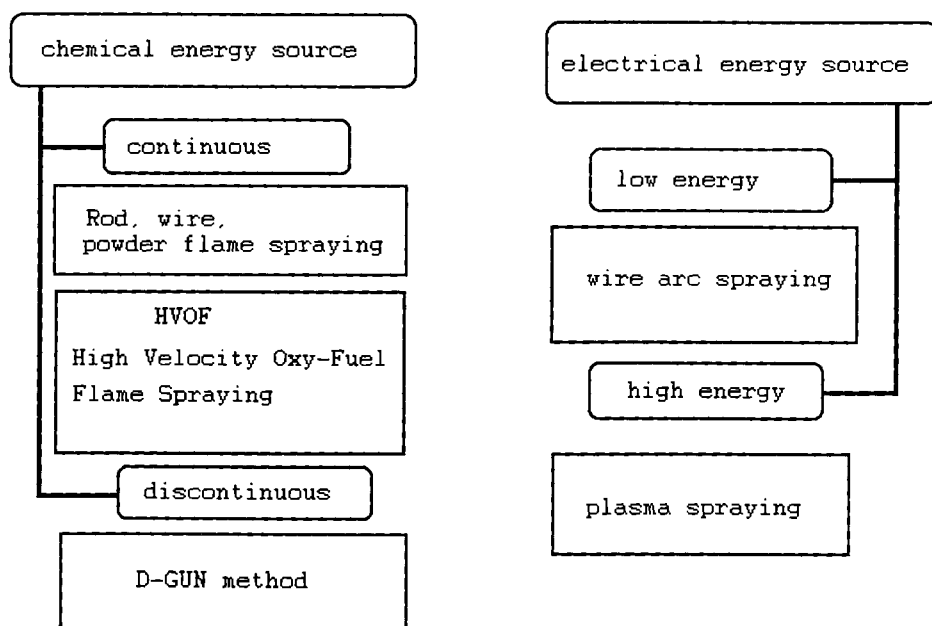


Figure 2-1. Thermal spray techniques divided by their principal energy sources (according to [1]).

The plasma spray methods

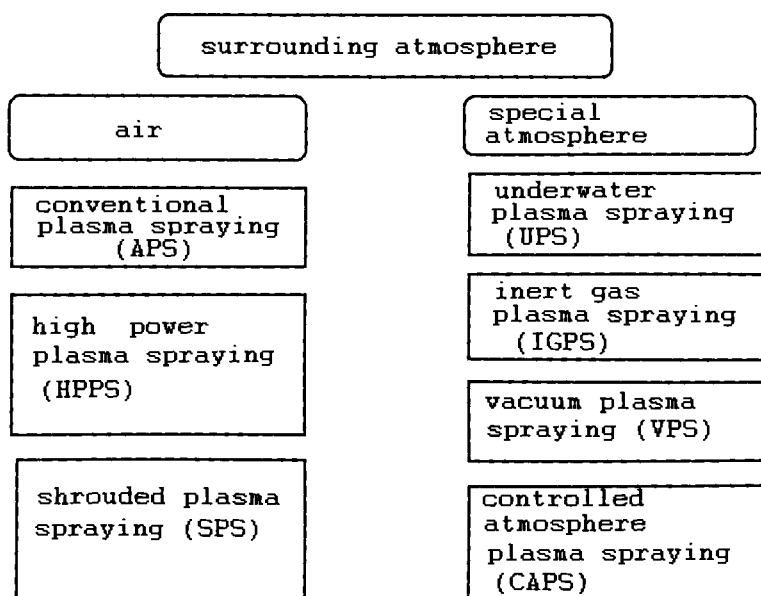


Figure 2-2. Plasma spray techniques divided by their surrounding atmospheres (according to [1]).

unlimited temperatures that are controlled by the energy input. The maximum power supplied to the plasmatron depends on the cross-sectional area of the power leads between a d.c. or a.c. transformer and the device. Electric arc wire-spraying reaches arc temperatures of close to 6 000 K. APS temperatures are typically around 15 000 K depending on the type of the plasma gas used (argon, nitrogen, auxiliary hydrogen) and the powder input. Similar temperatures can be obtained by inductively-coupled radiofrequency plasmatrons and LPPS devices.

Thermal spraying is emerging as an active area of research and development. These worldwide activities include the development of new techniques and associated devices. Modern applications include underwater plasma spraying (UPS) [2] and laser spraying (LS) [3, 4]. A concise review of state-of-the-art spraying technology including a to-the-point description of flame torches and plasmatrons has been given recently [5].

Modern equipment is so versatile that a polymeric substrate can be coated with metal, or a metal substrate with plastic, just by changing the plasma or flamespray parameters. As simple as this sounds there are highly sophisticated requirements for selecting and controlling numerous intrinsic and extrinsic plasma spray parameters. Some researchers say that there are many hundreds of parameters which can potentially influence the properties of the coatings.

For economic (time requirements) and theoretical reasons (interdependence of parameters) it is not possible to control all possible parameter variations. In fact, only eight to twelve parameters are routinely controlled at pre-set levels, using principles of SDE and SPC (see Chapter 8). The most common control parameters are:

- power input,
- arc gas pressure,
- auxiliary gas pressure (helium, hydrogen, nitrogen),
- powder gas pressure,
- powder feed rate,
- grain size/shape,
- injection angle (orthogonal, downstream, upstream),
- surface roughness,
- substrate heating,
- spray distance,
- spray divergence, and
- spray atmosphere.

These parameters can control a variety of secondary parameters such as quench rate, residence time of particles in jet, gas composition of plasma jet, heat content etc. Some of the more important parameters are shown in Fig. 2-3 [6]. For economical reasons, one of the most important secondary parameter is the deposition efficiency. Figure 2-4 illustrates schematically the way in which specific variables affect deposition efficiency. Variables that can greatly influence efficiency include power input, arc gas flow, and spray (stand-off) distance. Variables with moderate effects are the powder feed rate and the powder gas flow rate within limits. Finally, changes in the traverse rate have little or no effect on deposition efficiency and coating density [7].

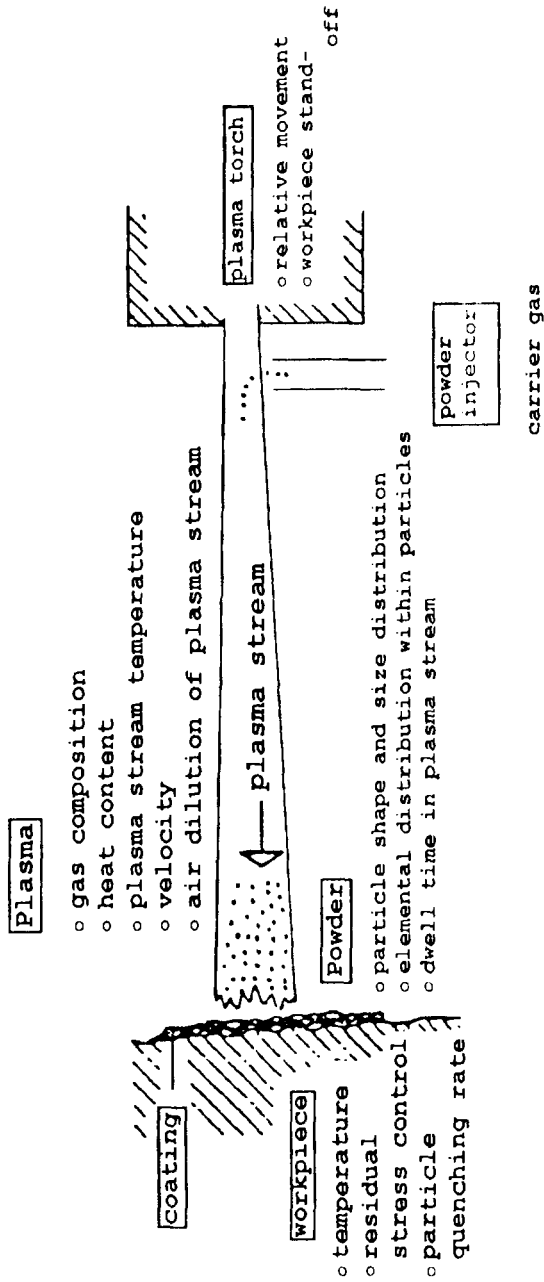


Figure 2-3. Main plasma spray parameters controlled at preset levels [6].

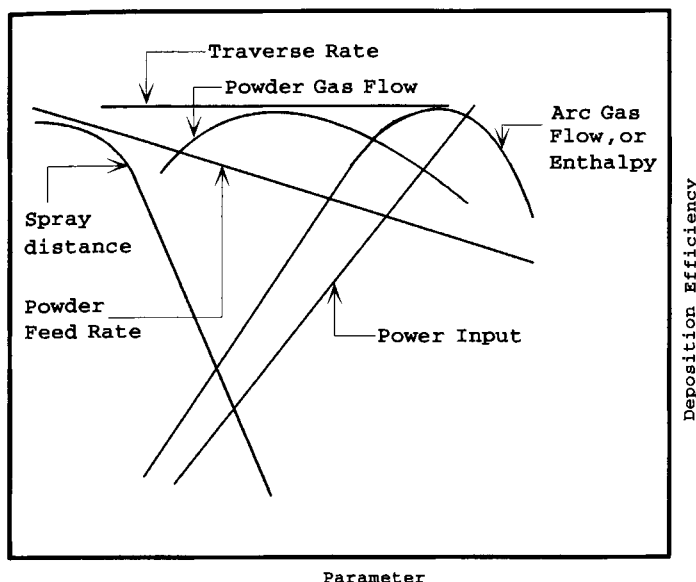


Figure 2-4. Dependence of deposition efficiency on various plasma spray parameters [7].

2.1 Characterization of Flame versus Plasma Spraying

The main difference between these two techniques is that of the temperature of the powder melting. The temperature of a combustion flame is limited by the enthalpy of the chemical reaction that leads to the combustion of gases such as acetylene or propane in the presence of oxygen. While the flame velocity can be boosted in modern equipment (such as HVOF) to values near Mach 5, the temperatures achievable are limited to approximately 3 300 K. On the other hand, plasma jets have temperatures limited only by the amount of electrical energy supplied which in turn is a function of the cross-section of the power leads. Temperatures as high as 25 000 K can be easily generated. Thus, flame spray including HVOF systems are used mainly for the spraying of materials with lower melting points such as metals or metal-ceramic (cermets) composites, for example tungsten carbide-cobalt or chromium carbide-nickel-chromium composites. The high flame velocity of the HVOF system leads to dense, well-adhering coatings for a wide variety of applications in the resource and manufacturing industries. Thermal spraying of ceramics with high melting points, such as alumina (2 050 °C) or zirconia (2 680 °C) is the domain of plasma spray systems.

Figure 2-5 shows a comparison of various flame and plasma arc spray techniques with maximum temperatures indicated. Table 1.1 shows a comparison of combustion flame systems, HVOF (D-Gun, Jet Kote), air plasma spray (APS), inductive plasma spray (IPS), vacuum plasma spray (VPS) and radio-frequency (RF) spray in terms of gas temperatures, particle velocity, flame length, and particle injection mode [8].

Flame spraying(Temperature (T) limited by internal heat of gasses.)

Oxyacetylene torch	($T = 2700\text{ }^{\circ}\text{C}$)
Detonation gun (D-gun)	($T = 3200\text{ }^{\circ}\text{C}$)
Jet Kote system	($T = 3000\text{ }^{\circ}\text{C}$)
Hypervelocity oxyfuel gun	($T = 3000\text{ }^{\circ}\text{C}$)

Arc spraying(Temperature (T) unlimited, controlled by energy input)

Electric arc wire-spraying	
Air plasma spraying (APS)	($T = 15000\text{ }^{\circ}\text{C}$)
Inductive plasma (IPS)	($T > 15000\text{ }^{\circ}\text{C}$)
Reduced pressure ('vacuum')	
plasma spraying	($T > 15000\text{ }^{\circ}\text{C}$)
RF-Plasma spraying	($T > 15000\text{ }^{\circ}\text{C}$)
Low pressure laser spraying (LPLS)	($T = 10000\text{ }^{\circ}\text{C}$)

Figure 2-5. Comparison of various flame and plasma arc spray techniques.**2.2 Concept of Energy Transfer Processes**

The plasma spraying process can be conveniently described as a connected energy transfer process, starting with the transfer of electrical energy from an electrical potential field to the plasma gas (ionization and thus plasma heating), proceeding with the transfer of thermal energy and impulse (heat and momentum transfer) from the plasma to the injected powder particles, and concluding with the transfer of thermal and kinetic energy from the particles to the substrate to be coated. Figure 2-6 shows the three stages of this connected energy transfer process together with fundamental constituent parts of the plasma spray system [9].

2.3 Unique Features of the Plasma Spray Process

The plasma spray process is characterized by a set of unique features. These are listed below [10].

1. With the process a wide range of materials, from metal to ceramics to polymers, and any combination of them can be deposited.

Table 1-1. Comparison of different spraying processes.

	Flame	D-Gun	Jet Kote	APS	IPS	VPS	RFS
Gas Temp. (°C)							
$p = 1 \text{ atm}$	2700	3200	3000	14000	14000	—	—
$p = 0.25 \text{ atm}$	—	—	—	—	—	10000	8000
$p = 0.07 \text{ atm}$	—	—	—	—	—	5000	—
Particle velocity (m s^{-1})							
$\text{Al}_2\text{O}_3\text{-}30 \mu\text{m}$							
$p = 1 \text{ atm}$	70	500	350	230	250	—	—
$p = 0.25 \text{ atm}$	—	—	—	—	—	380	30
$p = 0.07 \text{ atm}$	—	—	—	—	—	300	—
Flame length (cm)							
$p = 1 \text{ atm}$	<10	—	<20	<7	<10	—	—
$p = 0.25 \text{ atm}$	—	—	—	—	—	<15	<15
$p = 0.07 \text{ atm}$	—	—	—	—	—	<50	—
Particle injection	axial	axial	axial	orthogonal to plasma jet downstream arc root			axial

APS: air plasma spraying. IPS: inductive plasma spraying. VPS vacuum plasma spraying. RFS radio frequency spraying.

- It is possible to deposit mixed ceramics and alloys containing components with widely differing vapor pressures without significant changes in coating composition.
- Homogeneous coatings with time invariant changes in composition, i.e. without compositional changes across the thickness can be produced.
- Microstructures with fine, equiaxed grain but without columnar defects can be deposited. This is in contrast to electron-beam deposition.
- Graded coatings can be produced with the same type of equipment whereby the coating composition can be changed from that of a pure metal to that of a pure ceramics via continuously changing metal–ceramic mixtures.
- High deposition rates of the order of mm s^{-1} can be achieved with only modest investment in capital equipment.
- Free-standing thick forms can be sprayed in near-net shape fashion of pure and mixed ceramics.
- The process can be carried out in any conceivable environment such as air, reduced pressure, inert gas, or underwater.

Despite these apparently simple and straightforward characteristics it must be emphasized that the underlying physical principles are complex and in many cases nonlinear. Achieving a coating with the desired mechanical or functional properties requires great care and stringent control of many plasma spray parameters that in a generally synergistic way influence the coating properties and thus performance.

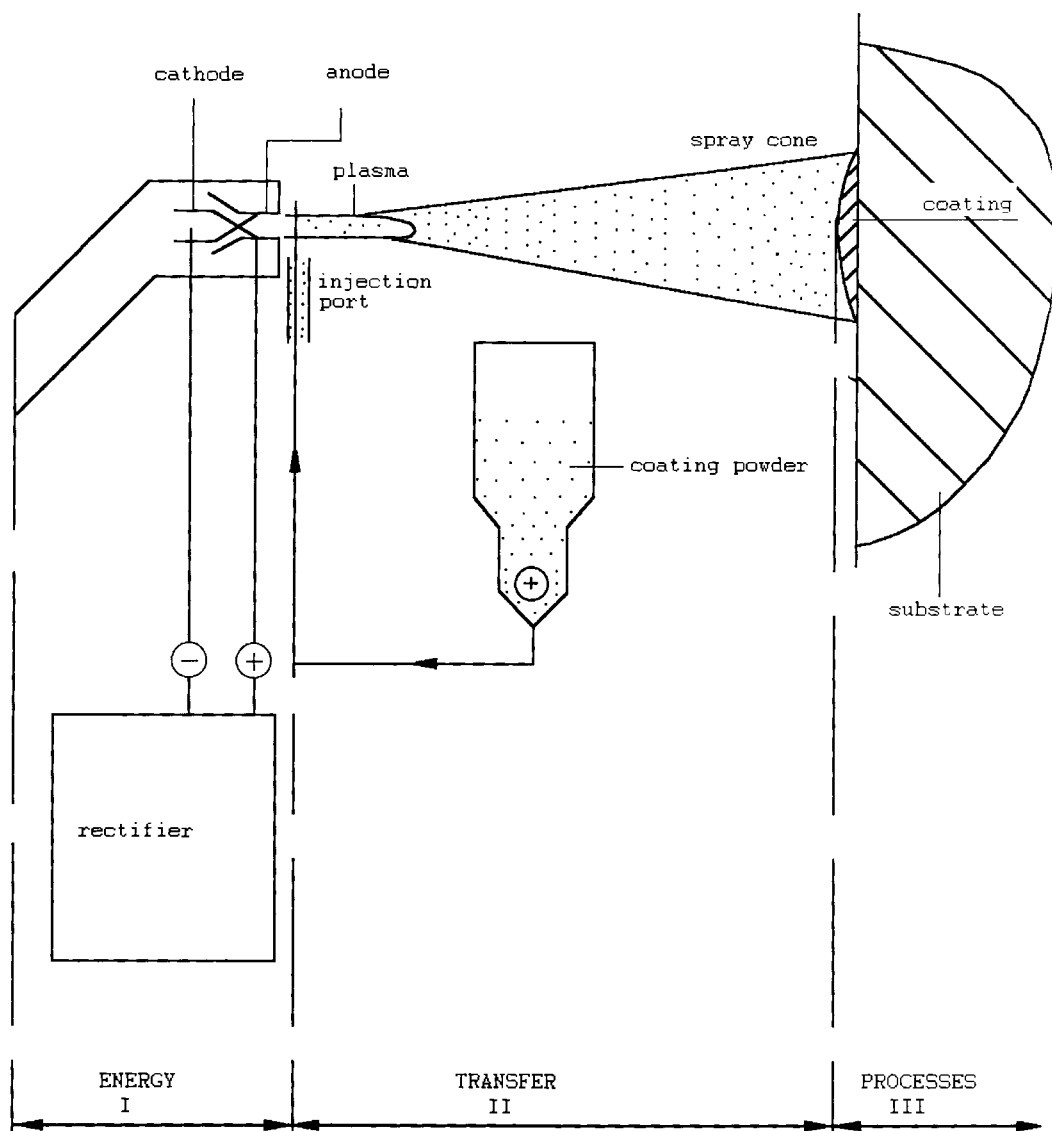


Figure 2-6. The three stages of the connected energy transfer process [9].

With automated technology such as robotics and adaptive statistical process control as well as the incipient development of on-line feedback control reproducibility and consistent coating quality can be achieved.

References

- [1] E. Lugscheider, *Technica*, **1992**, 9, 19.
- [2] E. Lugscheider, B. Bugsel, *Proc. 1st Plasma-Technik Symposium*, Lucerne, Switzerland, 18–20 May, **1988**, p. 55.
- [3] F. Uchiyama, *et al.*, *Proc. 13th ITSC*, Orlando, Florida, 28 May–5 June, **1992**, p. 27.
- [4] A. Petitbon, Guignot, U. Fischer, J.-M. Guillemot, *Mater. Sci. Eng.* **1989**, A121, 545.
- [5] L. Pawlowski, Chapter 3 in *The Science and Engineering of Thermal Spray Coatings*, Wiley, Chichester, New York, Brisbane, Toronto, Singapore, **1995**, 28–50.
- [6] A. R. Nicoll, *Thermal Spray* (CEI Course on High Temperature Materials and Coatings), Plasma-Technik AG, Wohlen, Switzerland, **1984**.
- [7] D. R. Mash, N. E. Weare, D. L. Walker, *J. Met.* **1961**, (July), 473.
- [8] M. I. Boulos, P. Fauchais, E. Pfender, *Fundamentals of Materials Processing Using Thermal Spray Technology* (CUICAC Short Course), Edmonton, Alberta, Canada, 17–18, October **1989**, p. 275.
- [9] J. M. Houben, Relation of the adhesion of plasma sprayed coatings to the process parameters size, velocity and heat content of the spray particles. PhD Thesis, Technical University Eindhoven, The Netherlands, **1988**.
- [10] H. Herman, C. C. Berndt, H. Wang, Chapter 5 in *Ceramic Films and Coatings* (Eds.: J. B. Wachtman, R. A. Haber), Noyes Publications, Park Ridge, NJ, USA, **1993**, p. 131–188.

3 The First Energy Transfer Process: Electron–Gas Interactions

3.1 The Plasma State

The interaction of an electric current with a gas leads to dissociation and ionization. A plasma consists of electrons, positively charged ions, and neutral gas atoms.

The definition of the plasma state is as follows [1].

‘Plasmas are quasi-neutral multiparticle systems characterized by gaseous or fluid mixtures of free electrons and ions, as well as neutral particles (atoms, molecules, radicals) with a high mean kinetic energy of electrons or all plasma components ($\langle \epsilon \rangle \approx 1 \text{ eV} - 2 \text{ MeV}$ per particle), and a considerable interaction of the charge carriers with the properties of the system’.

Since the states of matter can be defined by the mean kinetic energy $\langle \epsilon \rangle$ of the constituent particles there exists an energy threshold ϵ_n at the phase boundaries that marks the transition among states and can be treated as typical binding energies. A criterion of the existence of the n th state of matter is $\epsilon_{n-1} \leq \langle \epsilon \rangle \leq \epsilon_n$. With increasing $\langle \epsilon \rangle$, i.e. increasing temperature matter passes through the states $n = 1 \dots 3$ (solid, liquid, gaseous), and finally, through ionization of gas atoms, free electrical charge carriers appear that characterize the systems as the 4th state of matter. We have arrived at a plasma.

While the plasma is electrically conductive, its overall charge is neutral. This quasi-neutrality is being maintained by strong electric fields. The neutrality restoring electric field can be estimated as follows [2].

If a cubic centimeter of a plasma contains n^* electrons than the total charge contained in a sphere of radius r is $Q = -(4/3)\pi r^3 n^* e$ ($-e$ is the Millikan elementary electron charge $= 1.6 \times 10^{-19} \text{ C} = 4.8 \times 10^{-10} \text{ ESU}$ (electrostatic charge units)). Assuming a centrosymmetrical charge distribution the total charge Q is concentrated at the centerpoint of the sphere. This charge generates an electric field of strength $E = Q/r^2$ at a distance r from the centerpoint. If $r = 1 \text{ cm}$ and $n^* = 10^{15}$ (thermal or ‘hot’ plasma, see below) then $E = -6 \times 10^8 \text{ V cm}^{-1}$. One of the characteristics of the state of quasi-neutrality of a plasma is the fact that the number of positive and negative charge carriers per unit volume equals each other. If n_1 is the number and $+Ze$ the individual charge of the Z -times positively charged ions than the condition of quasi-neutrality is $n^* = Z \times n_1$ or $|n^* - Z \times n_1| \ll n^*$. Since the ions generate

a field $+6 \times 10^8 \text{ V cm}^{-1}$ the total electric field strength is zero in the state of quasi-neutrality. However, any slight deviation, for example by statistical density variations of a ratio $1:10^{-6}$ results in the occurrence of an electric field strength of $10^{-6} \times 6 \times 10^8 = 600 \text{ V cm}^{-1}$ that instantaneously restores the quasi-neutrality. Only the occurrence of oscillations of very high frequency, for example a displacement current, leads to a spacial separation of the centres of the positive and the negative charge clouds because the ions with their relatively high masses cannot follow the high frequency oscillations anymore.

3.1.1 Characteristic Plasma Parameters

Since the plasma state occupies an extremely wide range of densities, temperatures and magnetic field strengths it is convenient to define several characteristic plasma parameters. Hereby microscopic and macroscopic parameters can be distinguished. The former refer to interactions between individual particles in a plasma, the latter to specific plasma properties in a continuum that can be described by the basic magnetohydrodynamic (MHD) equations. As we will see, based on the magnitude of these microscopic parameters the electron density–temperature–magnetic field space can be subdivided. The most important microscopic parameters are the Langmuir plasma frequency, ω_{Pl} , the Debye screening length, λ_{D} , the Landau length, l_{L} , the mean free path length, λ (collision length), and the collision frequency, ν_{c} .

3.1.1.1 Langmuir Plasma Frequency

From the one dimensional radial equation of movement of electrons

$$m^*(d^2r/dt^2) = -(4/3)\pi n^* e^2 r \quad (3-1)$$

(m^* = mass of electron, n^* = number of electrons per cm^3) with the exponential relations $r(t) = r_0 \exp(i\omega t)$ it follows that the electrons in a plasma undergo harmonic oscillations with a frequency

$$\omega = [4\pi n^* e^2 / 3m^*]^{1/2}. \quad (3-2)$$

More accurate 3D-calculations (see for example [2]) lead to the equation for the Langmuir frequency

$$\omega_{\text{Pl}} = [4\pi n^* e^2 / m^*]^{1/2} \quad (3-3a)$$

or, in the SI system,

$$\omega_{\text{Pl}} = [n^* e^2 / m^* \epsilon_0]^{1/2}, \quad (3-3b)$$

where ϵ_0 = vacuum dielectric permittivity ($= 8.86 \times 10^{-12} \text{ A s V}^{-1} \text{ m}^{-1}$).

3.1.1.2 Debye Screening Length

To obtain characteristic plasma properties the electric space charge effects must exceed those of the thermal movement of the carriers. Only then collective interaction phenomena can occur that distinguish a plasma from a normal gas or a cloud of charged individual particles. Simplified one-dimensional calculations yield

$$\operatorname{div} \mathbf{E} = (\delta E_x / \delta x) = 4\pi\rho^*, \quad \rho^* = -n^*e \quad (3-4a)$$

($E_x = E$, $E_y = E_z = 0$), and after integration

$$E = -4\pi n^* e x. \quad (3-4b)$$

The displacement of an electron by a distance λ_D in the electric field generated by the n^* electrons per cm^3 leads to an increase in energy defined by

$$\int eE \, dx = 2\pi n^* e^2 \lambda_D^2. \quad (3-5)$$

This energy increase equals the mean thermal energy per degree of freedom, kT , and from $2\pi n^* e^2 \lambda_D^2 = kT/2$ it follows that

$$\lambda_D = [kT/4\pi e^2 n^*]^{1/2}. \quad (3-6)$$

This quantity is called the Debye screening length, and can further be expressed as

$$\lambda_D = 6.905 [T/n^*]^{1/2}. \quad (3-7)$$

Since λ_D can be defined as that distance from a point charge within which the potential of the charge decreases to the e th part as the result of space charge effects, it is also called the 'screening length' of the potential ($\phi(r) = r^{-1} \exp[-r/\lambda_D]$).

3.1.1.3 Landau Length

That distance from a point charge at which the vacuum electrostatic energy equals the kinetic energy kT is called 'critical distance' or Landau length: $l_L = e^2/kT$. The necessary condition preventing a recombination of ions and electrons is $a > l_L$, i.e. the mean distance a between plasma particles must exceed the Landau length. Since on the other hand the distance of the electrostatic interaction of plasma particles is the Debye length λ_D , the relation $a > \lambda_D$ means that there is no cooperative interaction between particles, i.e. there is no plasma.

Assuming spherical and continuous charge distribution, the volume of interaction, the so-called *Debye sphere* is given by $(4/3)\pi\lambda_D^3$. The Debye sphere contains thus $(4/3)\pi\lambda_D^3 n^*$ electrons. In order to apply continuity conditions there is the requirement $(4/3)\pi\lambda_D^3 > 1$ or $\Lambda = (n^*\lambda_D^3)^{-1} \ll 1$ or $(n^*)^{-1/3} \ll \lambda_D$. If the 'plasma parameter' $\Lambda \ll 1$ a true plasma exists!

3.1.1.4 Collision Path Length

In electrically neutral gases only van der Waals forces play a role with short interaction distances. Thus collisions among two or more particles are generally negligible. In a plasma, however, electric forces occur whose interaction distances (Debye length) exceed those of the intermolecular van der Waals forces. All charged particles are interacting constantly with a cloud (Debye sphere) of surrounding particles. For a minimum particle density an average ('smeared out') electric field can be assumed, and calculations can be performed as if a particle is being scattered only by this averaged field. Thus all elastic collisions among particles can be treated as binary collisions.

In general, plasma particles can collide inelastically and elastically. During *inelastic collisions* the total kinetic energy of a particle changes by transferring a portion of it to internal energy. Such inelastic collisions are responsible for excitation, ionization, recombination and charge transfer in plasmas. The hallmark of an *elastic collision* of particles is the conservation of its total kinetic energy. Such collisions occur predominantly in neutral gases at low temperatures.

The number of collisions per cm^3 and per second is determined by $\sigma(v)nF$, where $\sigma(v)$ is the collision cross-section, n is the number of scattering particles per cm^3 and F is the number of particles per cm^3 and per second that are being scattered. The mean free path length λ is the average path length traversed by a particle between two collisions. From the laws of kinetic gas theory it follows that $\lambda = [n\sigma(v)]^{-1} = kT/p\sigma(v)$, where p is the plasma pressure. For $p = 1 \text{ atm}$ and $T = 300 \text{ K}$, λ is about $0.4 \mu\text{m}$.

For elastic collisions the cross-section depends on the relative velocity ω of the particles and the scattering angle χ . However, assuming Coulomb forces limited by a finite value of λ_D , a mean free path length λ can be calculated independent of the scattering angle:

$$\lambda = [0.6 \times 10^6 T^2] / [n \ln(\lambda_D/l_L)] \approx (1.3 \times 10^4 T^2 / n). \quad (3-8)$$

The term $\ln(\lambda_D/l_L)$ is called the *Coulomb logarithm* Λ_c . The particle velocity can be expressed through the temperature for a Maxwell–Boltzmann distribution as $m^* u^2 = kT$. For a thermal plasma ($T_e = T_h$; see Fig. 3-1) it follows that $\lambda_{\text{Ion}}/\lambda_{\text{El}} = m_{\text{Ion}}/m^*$, and for a collision angle of 90° $\lambda_{90} = (4\pi l_L^2 n)^{-1}$. With $l_L = e^2/kT$ and $\lambda_D = (kT/4\pi e^2 n^*)^{1/2}$ we obtain

$$\lambda_D^2 = \lambda_{90} l_L. \quad (3-9)$$

Combination with the inequalities expressed above leads to the *definition of a plasma*:

$$l_L \ll \lambda_D, \quad (n^*)^{-1/3} \ll \lambda_D, \quad \lambda_D \ll \lambda_{90}. \quad (3-10)$$

Furthermore the condition $\Lambda \approx l_L/\lambda_D = \lambda_D/\lambda_{90} \ll 1$ must be fulfilled.

In addition to these conditions, another one has to be fulfilled. To treat a plasma as a continuous medium all statistical fluctuations must be alleviated to obtain a

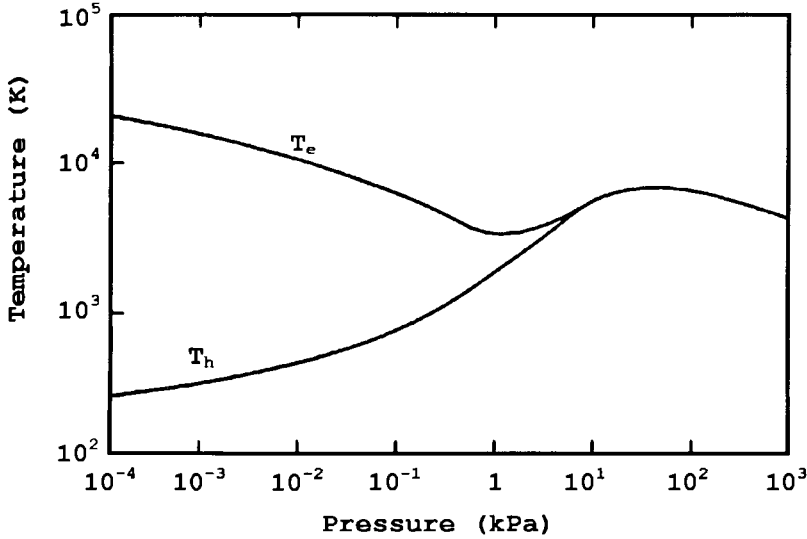


Figure 3-1. Electron (T_e) and heavy particle (T_h) temperatures as a function of pressure [3].

Maxwellian distribution of particle velocities. This requires frequent collisions of particles. The characteristic dimension of the plasma cloud, l , must be large compared to the collision length λ in order to guarantee many collisions: $\lambda \ll l$.

3.1.1.5 Collision Frequency

The velocity distribution of particles within a plasma is given, under equilibrium conditions, by a Maxwell distribution. The mean velocity \bar{u} is defined by the thermodynamic temperature

$$\bar{u} = (8 kT / \pi m)^{1/2}; \quad \bar{u}^2 = 3 kT / m. \quad (3-11)$$

Without applied strong magnetic fields a particle in a plasma moves between two collisions in a force-free fashion, i.e. with constant speed \bar{u} . The relaxation time τ between two collisions is $\tau = \lambda / \bar{u} \sim T \sqrt{T} / n$, and for the collision frequency ν_c we obtain $\nu_c = \tau^{-1} = \bar{u} / \lambda$, or in terms of the collision cross-section, $\nu_c = n \bar{u} \sigma(v)$. Introducing the plasma parameter $\Lambda \approx l_L / \lambda_D$, and using the expressions for the Langmuir frequency ω_{p1} , the Debye length λ_D and $kT \approx m \bar{u}^2$ it follows

$$\Lambda \approx \lambda_D / \lambda \approx \nu_c / \omega_{p1}. \quad (3-12)$$

3.1.2 Classification of Plasmas

Depending on the electron density, it is possible to distinguish low-pressure ‘cold’ (nonthermal) plasmas found in outer space with electron densities typically around

10^{-2} electrons per cm^3 , and high pressure ‘thermal’ plasmas with electron densities exceeding 10^{18} electrons per cm^3 (Fig. 3-2). Thermal plasmas have pressures high enough to facilitate energy exchanges among light, fast moving and therefore energetic electrons and heavy, slowly moving charged ions. This energy exchange leads to efficient transfer of energy, increasing the plasma temperature, and thus reaching equilibrium. In such plasmas the electron temperature T_e equals the heavy particle temperature T_h ; the plasma is in general or local thermodynamic equilibrium, and can be described according to the laws of thermodynamics (Fig. 3-1). The behavior of such a plasma is predictable. The energy extracted by the electrons from the electric field is transferred to enthalpy and, in turn, to an increase in temperature.

3.1.2.1 Low Density Plasmas

The variation of particle number per cm^3 (particle density) and temperature can be expressed by the plasma parameter Λ (see above). If $\Lambda \ll 1$, the plasma condition $\lambda \ll l$ is not guaranteed. In this case the number of collisions is low. If $\lambda > l$ than low density conditions prevail. Such a plasma is called a collision-free or Vlasov plasma (Fig. 3-3). Its relaxation time is $\tau = l(m/2kT)^{1/2}$.

3.1.2.2 Medium Density Plasmas

With increasing particle density the mean free collision paths decrease. If $\lambda \approx l$, medium density plasmas can be stabilized depending on the strength of the magnetic field. In a homogeneous static magnetic field an electrical charge describes a circular path around the field lines. The radius of this path is called the radius of gyration (Larmor radius) and given by

$$r_L = (muc/eB) \approx (8 kTm)^{1/2}/eB(\pi)^{1/2}, \quad (3-13)$$

where u = linear circular velocity perpendicular to \mathbf{B} , c = velocity of light, m = particle mass, B = magnetic field. For $M = m^*$, and with $m^*u^2 = kT$, the Larmor radius of an electron is

$$r_L^* = 3.7 \times 10^{-2}(\sqrt{T}/B). \quad (3-14)$$

The Larmor radius of a proton is $r_{L,\text{Prot}} = 1.6\sqrt{T}/B$. Assuming local thermal equilibrium, i.e. $T_e = T_h$, it follows that $r_{L,\text{Ion}} = r_L^*(m_{\text{Ion}}/m^*)^{1/2}$. Thus it is always true that $r_{L,\text{Ion}} > r_L^*$. The rotation frequency (cyclotron or Larmor frequency) is $\omega_L = eB/mc$.

For a low density plasma with $\lambda_D \ll \lambda$ or $l_L \ll \lambda_D$ (plasma condition) and $l \ll \lambda$ (low density condition), and in the presence of a weak magnetic field, r_L is relatively large but because of $l \ll \lambda$ always small compared to λ . With increasing field strength B , r_L decreases and fulfills even more the condition $r_L \ll \lambda$. This means that a charged particle undergoes many Larmor rotations before a collision occurs that knocks it off its cyclotron path. Collisions therefore influence a low density plasma at a high magnetic field only marginally.

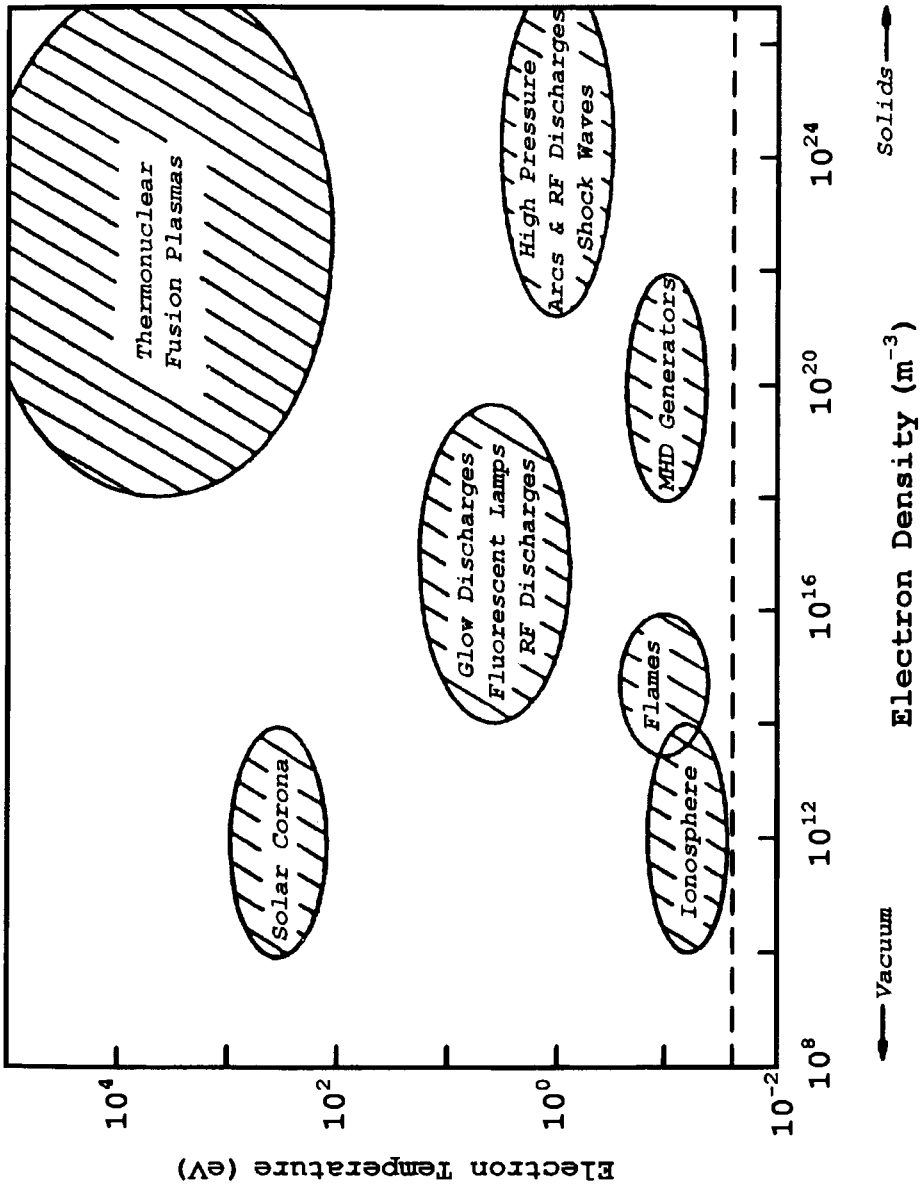


Figure 3-2. Classification of plasmas as a function of electron temperature and electron density [3].

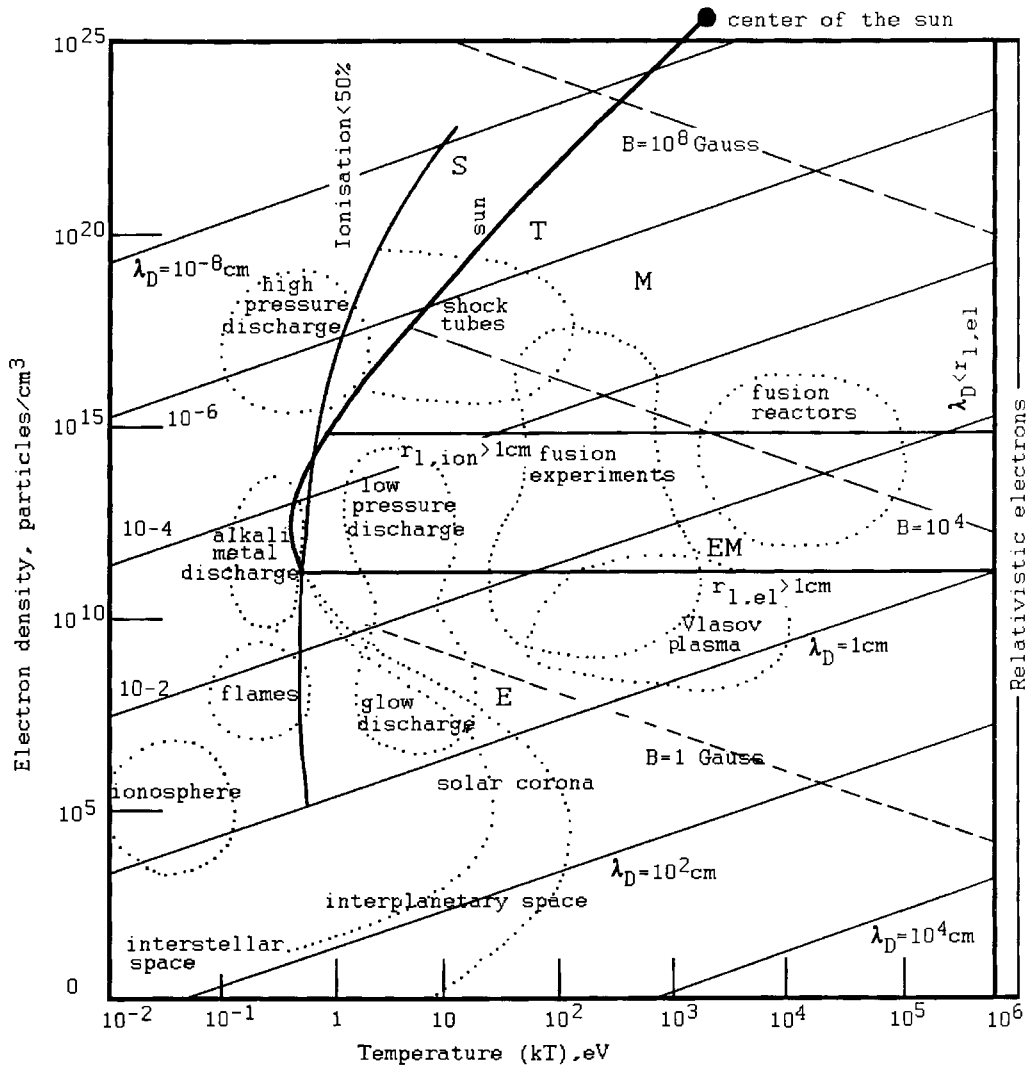


Figure 3-3. Possible states of a plasma [2].

A medium density plasma is characterized by $\lambda_D \ll \lambda$, $l_L \ll \lambda_D$ (plasma condition) and $l \gg \lambda$ (medium density condition). Depending on the strength of the magnetic field four plasma types can be distinguished: *electric* plasmas (E) ($l < r_L^*$ and $l < r_{L,ion}$), *electromagnetic* plasmas (EM) ($l > r_L^*$, $l < r_{L,ion}$), *magnetic* plasmas (M) ($l > r_L^*$, $l > r_{L,ion}$; $\lambda_{El} > r_L^*$, $\lambda_{ion} > r_{L,ion}$) and *tensorial* plasmas (T) ($\lambda_{El} \gg r_L^*$, $\lambda_{ion} < r_{L,ion}$). The ranges of existence of these plasma types are shown in Figure 3-3. For a more detailed description, see textbooks on plasma physics and magneto-hydrodynamics.

3.1.2.3 High Density Plasmas

If the density increases so that $\lambda_{\text{El}} \ll r_{\text{L}}^*$, $\lambda_{\text{Ion}} \ll r_{\text{L, Ion}}$ then collisions outdo all anisotropic effects. In contrast to a tensorial plasma mentioned above any direction-dependent properties will cease to exist, and a ‘scalar’ (isotropic) plasma (S) (see Fig. 3-3) evolves that can be described by the laws of fluid dynamics. Depending on the temperature, i.e. the degree of ionization ‘two-fluid’ (electrons and ions) or ‘three-fluid’ (electrons, ions and neutral particles) plasmas exist. In plasmas of extremely high densities ($n^* > 10^{19} \text{ cm}^{-3}$) squeezing of charges can lead either to *recombination*, i.e. formation of a neutral gas or to *condensation*, i.e. formation of a solid state plasma.

Table 3-1 shows the classification of plasmas according to the characteristic plasma parameters, the electron density, temperature, magnetic field and characteristic distance, l [2]. Figure 3-3 shows the state of a plasma in an electron density–temperature net. Also shown are straight lines of equal Debye lengths ($10^{-8} < \lambda_{\text{D}} < 10^4 \text{ cm}$) and magnetic field strengths ($1 < B < 10^8 \text{ Gauss}$). Relativistic effects (particle velocity $u > 0.9c$) can be neglected for $T < 10^8 \text{ K}$; quantum effects are negligible for $T_{\text{e}} > 6 \times 10^{-11} n^{2/3}$, $T_{\text{h}} > 3.2 \times 10^{-14} n^{2/3}$. The ranges of existence of the plasma types E, EM, M, T and S are also shown.

The plasma parameters, i.e. densities and temperatures of the charged species can be derived, in principle, by using an electric or Langmuir probe [4]. Such a probe consists of a single electrode whose voltage–current characteristics are measured when it is surrounded by plasma [5]. In practice, the measurement of the densities and temperatures of the charged species reduce to the bulk ionization density n_0 and the electron temperature T_{e} .

3.1.3 Equilibrium and Nonequilibrium Plasmas

Extremely low pressure plasmas occurring in the interstellar space ($10^{-2} \text{ e per cm}^3$) and low pressure ‘cold’ plasmas generated under moderate vacuum conditions are *nonequilibrium* or *two-temperature* plasmas. They are characterized by the fact that the electron temperature T_{e} is much greater than the heavy particle temperature T_{h} . The electron temperature is measured in eV where 1 eV is the energy gained by an electron when passing through a potential difference of 1 V. The kinetic temperature can be calculated from the mean particle energy $\langle \varepsilon \rangle$: $kT_{\text{K}} = (2/3)\langle \varepsilon \rangle$ (1 eV corresponds to 7 733 K or $1.6 \times 10^{-19} \text{ J}$). Frequently the kinetic temperature of a plasma is given in terms of the most probable particle velocity, c_{Pr} : $kT_{\text{K}} = (1/2) mc_{\text{Pr}}^2$ (1 eV corresponds to 11 600 K). The electron density of a low pressure plasma is typically $< 10^{14} \text{ per cm}^3$, the electron temperature between 10^{-1} and 10 eV.

At a soft vacuum or atmospheric pressure thermal or ‘hot’ plasmas can be generated the electron temperature of which is of the order of the heavy particle temperature. Therefore such plasmas are called *equilibrium plasmas*.

The application of both types of plasma in materials processing is as follows:

- Low pressure ‘cold’ plasmas:
 - plasma etching in semiconductor processing,
 - plasma-assisted vapor deposition (PAVD),
 - plasma surface modification.

Table 3-1. Characteristic plasma parameters (see Fig. 3-3): from reference [2].

Plasma type	Electron density (n) [cm ⁻³]	Temperature (T) [K]	Debye length (λ_D) [cm]	Collision length (λ) [cm]	Langmuir plasma frequency (ω_{pi}) [s ⁻¹]	Collision frequency (ν_c) [s ⁻¹]	Magnetic field (B) [Gauss]	Larmor radius (r_L) [cm]	Characteristic distance (l) [cm]	Type of plasma
Interstellar gas	$1 \dots 10^2$	10^4	10^3	1.3×10^{12}	5×10^4	10^{-4}	10^{-6}	3.7×10^6	10^{22}	Low to medium density M, EM
Interplanetary gas	10^2	10^5	10^2	1.3×10^{12}	5×10^5	10^{-3}	10^{-4}	10^5	10^{13}	Low to medium density M, EM
Ionosphere F-layer	10^6	10^3	10^{-1}	1.3×10^4	5×10^7	10^3	0.2	5	10^6	Medium density E, M, EM
Solarcorona	$10^6 \dots 10^8$	10^6	10	1.3×10^{10}	5×10^8	10^2	10^{-4}	3.7×10^5	10^{11}	Low density
Hot plasma, diluted	10^{12}	10^6	10^{-2}	1.3×10^4	5×10^{10}	10^5	10^3	3.7×10^{-2}	10^3	Low density
Gas discharge	10^{14}	10^4	10^{-4}	1.3×10^{-1}	5×10^{11}	10^8	10^3	3.7×10^{-3}	10^2	Medium density EM, T
Dense hot plasma	10^{16}	10^6	10^{-4}	1.3	5×10^{12}	10^9	10^4	3.7×10^{-3}	10^3	Medium density T
Fusion plasma	$10^{15} \dots 10^{17}$	10^8	10^{-3}	1.3×10^4	5×10^{12}	10^6	3×10^5	1.2×10^{-3}	10^3	Low to medium density EM
Air, standard conditions	10^{19} (atoms)	300	—	6×10^{-6a}	—	6×10^9	—	—	10^3	Ultrahigh density
Liquid mercury	10^{23}	10^2	10^{-10}	1.3×10^{-15}	10^{16}	10^{15}	10^3	3.7×10^{-4}	10	High density S
Interior of stars	$10^{22} \dots 10^{25}$	10^8	10^{-6}	1.3×10^{-2}	10^{16}	10^{12}	$10^4 \dots 10^8$	3.7×10^{-4}	10^{11}	Medium to high density M, T

^a In air the mean free path length is calculated from $16n\sigma\lambda = 3$ or $3\eta = \lambda\rho u$ where $\eta =$ viscosity, $n =$ electron density, $\sigma =$ collision cross-section, $\lambda =$ collision length, $\rho =$ density, $u =$ velocity.

- High pressure 'hot' plasmas:
plasma spraying,
plasma spheroidizing,
plasma chemical synthesis for ultrapure ceramic powder production.

3.1.4 Maxwellian Distribution of Plasma Energies

The electrons and the heavy particles will both establish a characteristic Maxwellian energy distribution. Under steady state (stationary) conditions the 'temperature' of a plasma is defined by the mean kinetic particle energy given by the equation $(3/2)kT = (m/2)u^2$ (see Eq. 3-11). Since the colliding particles change their velocities there is no universal particle velocity but only an averaged value $(\bar{u}^2)^{1/2}$.

A Maxwell distribution shows the fraction f of the plasma particles with a kinetic energy or velocity within the interval ϵ and $\epsilon + d\epsilon$ (or v and $v + dv$). Despite the continuous collisions this fraction is time invariant even though different particles will contribute to the overall distribution at any one time. Figure 3-4 shows the dependence of $f(\epsilon)$ on ϵ for various mean energies $\bar{\epsilon}$. The relationship between the velocity v and the kinetic energy ϵ is $\epsilon = (m/2)v^2$.

This velocity distribution (Maxwell distribution) is

$$f(v) dv = (2/\pi)^{1/2} (m/kT)^{3/2} v^2 \exp(-mv^2/2kT) dv, \quad (3-15)$$

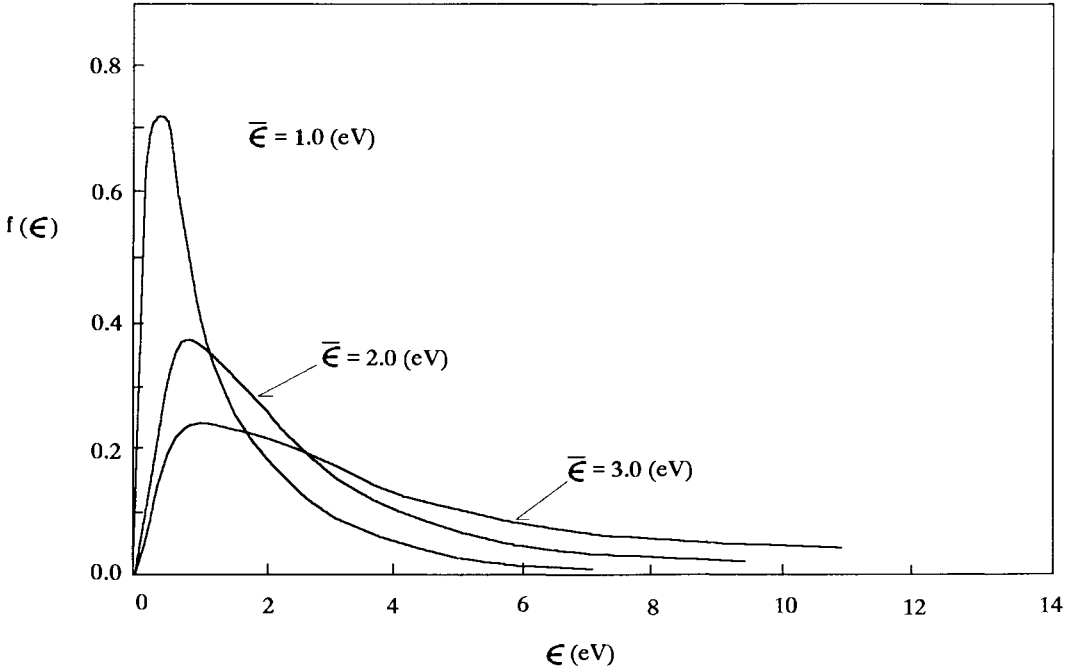


Figure 3-4. Maxwellian distribution of plasma particles.

or in terms of the kinetic energy ε ,

$$f(\varepsilon)d\varepsilon = 2/\sqrt{\pi} (kT)^{-3/2} \sqrt{\varepsilon} \exp(-\varepsilon/kT) d\varepsilon. \quad (3-16)$$

The Maxwell distribution of plasma particles determines how many electrons have sufficient velocity and energy, respectively to extract energy from the electric field that is being transferred to enthalpy. It also determines the probability of collisions.

3.1.5 Equilibrium Compositions of Plasma Gases (Phase Diagrams)

Ionization of plasma gases takes place by a variety of processes chiefly among which are high energy radiation such as neutron beams, X-rays and ultraviolet radiation, collision processes in electric discharges, and also collision processes in intensively heated gases.

The ionization products assume a specific distribution in a particle density (number density)–temperature plot thus resulting in a phase diagram of ionization. Figure 3-5 shows such equilibrium distributions at 1 atm pressure of argon and nitrogen plasmas [6].

Figure 3-6 shows the energy content of typical plasma gases as a function of the temperature. This relationship is essentially linear but deviations from linearity occur due to ionization and dissociation. Monoatomic gases such as argon and helium need only to be ionized to enter the plasma state. Bimolecular hydrogen and nitrogen must first be dissociated. They thus need larger energy input to enter the plasma state. This enhanced energy will create increased enthalpy of the plasma. Small quantities of hydrogen or helium added as an auxiliary gas to argon lead to increased plasma enthalpy and thus increased heat transfer rates from the plasma to the powder particles. As a result, the plasma is hotter, and particles melt easier and more complete. Figure 3-7 shows the specific heat of various plasma gases at constant pressure as a function of the temperature. It can be seen that the high specific heat of helium and, in particular hydrogen increases the heat transfer rate.

3.2 Plasma Generation

The different methods of plasma generation are applications of gas ionization. In principle, energy will be transferred to atoms or molecules in an elementary process that is sufficient to initiate ionization. There exist two basic mechanisms.

- Increase of the energy content of all internal degrees of freedom of the gas by application of heat. This application can be accomplished directly through the container walls, or indirectly through chemical processes, compression or an electrical current. Plasma is generated by collision ionization of the particles and photoionization of the electromagnetic radiation in the hot gas. Such plasmas are generally close to their thermodynamic equilibrium state (isothermal plasmas).
- Transfer of energy for effective ionization without substantial temperature in-

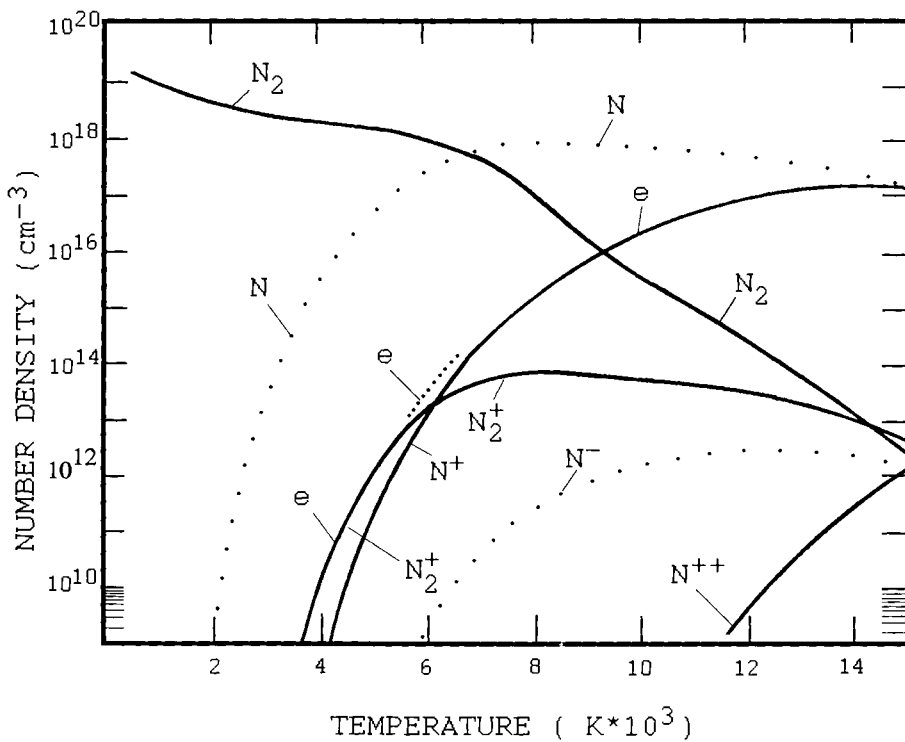
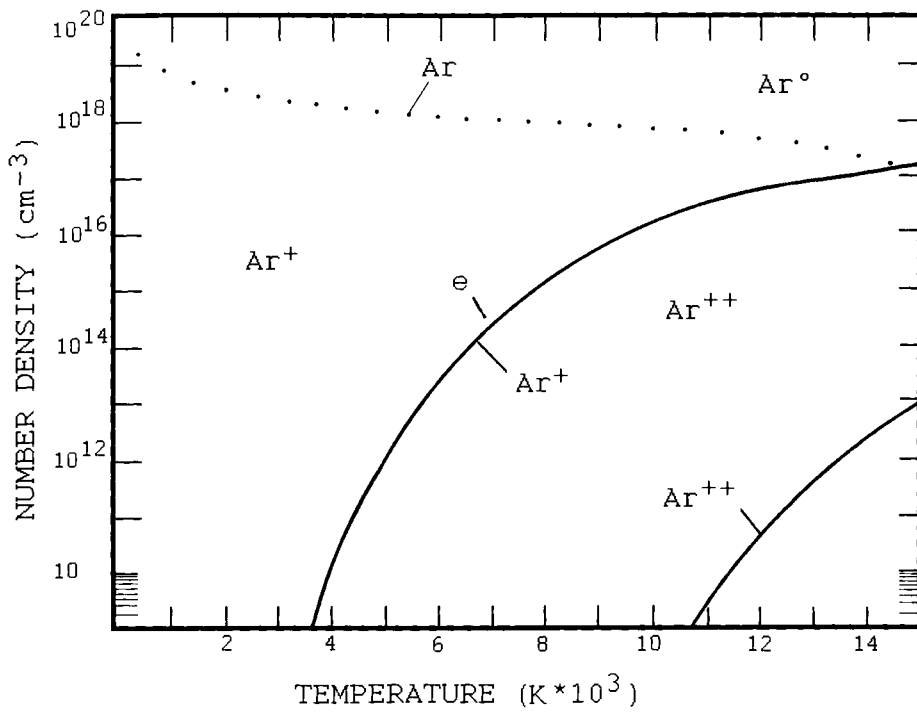


Figure 3-5. Equilibrium distribution (phase diagram) of argon (top) and nitrogen (bottom) plasmas [6].

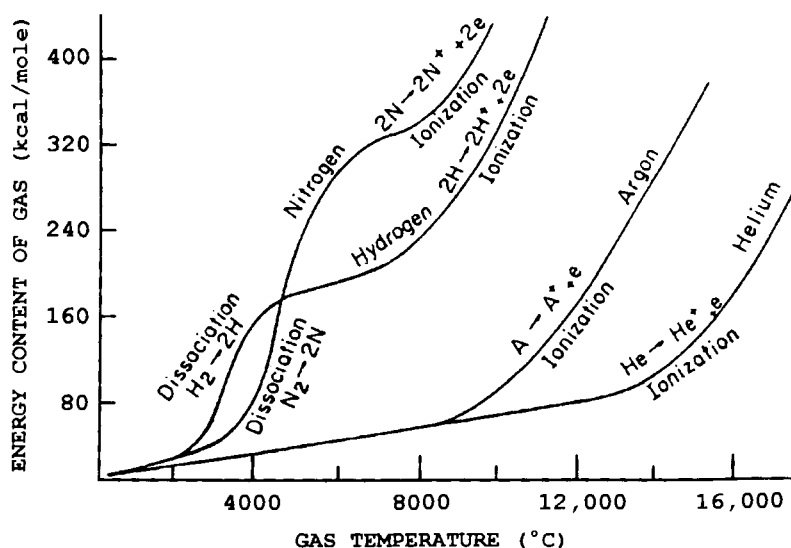


Figure 3-6. Energy content of typical plasma gases as a function of temperature [6].

crease of the gas through particle or electromagnetic radiation and electrical current, respectively. Such plasmas are nonequilibrium plasmas with a high electron temperature $T_e \gg T_{\text{gas}}$ (nonisothermal plasma).

Coupled mechanisms occur frequently during technical generation of plasmas.

3.2.1 Plasma Generation through Application of Heat

In a so-called *plasma furnace* (Fig. 3-8a) a gas is heated by temperature increase of the confining walls. A true thermal equilibrium plasma forms whose degree of ionization, x , is determined by

$$x^2/(1-x^2) = 2(2\pi m^*/h^3)^{3/2} (g_1 E_0^{5/2}/g_0 p) (kT/E_0)^{5/2} \exp(-E_0/kT) \quad (3-17)$$

(Saha-Eggert equation), where m^* = mass of the electron, E_0 = ionization energy, p = gas pressure, and g_1 and g_0 = statistical weights of the ionization and the ground states, respectively.

Since the highest temperatures achievable are around 3 500 K, the degree of ionization is only about 1%. Thus this methods is confined to generation of low-energy plasmas for fundamental laboratory investigations.

An increase of the degree of ionization is possible by utilization of the contact ionization that occurs when the ionization energy of the atoms colliding with the hot

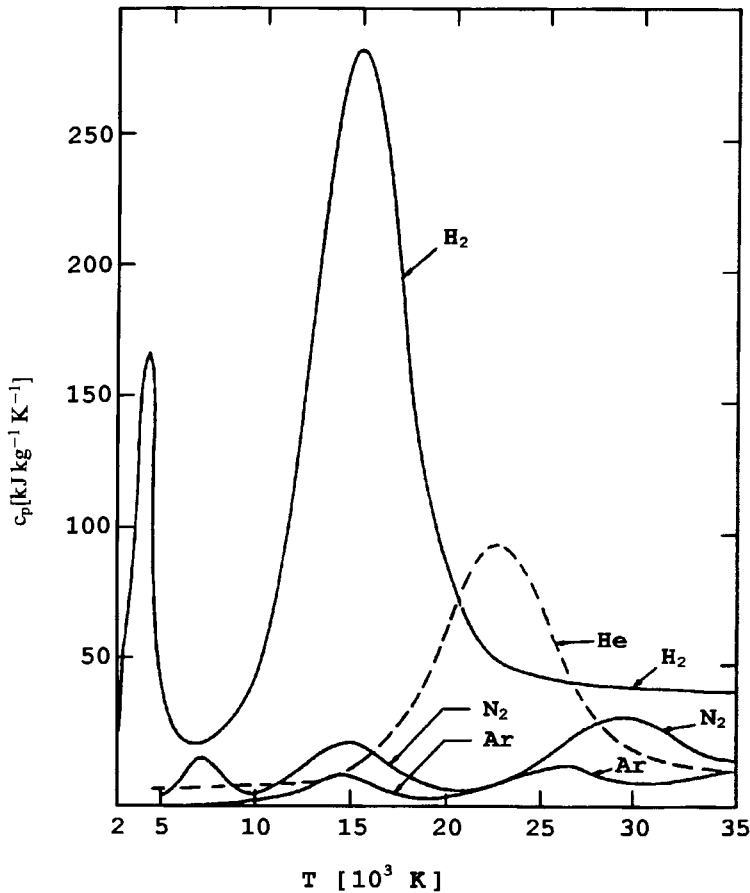


Figure 3-7. Specific heat of plasma gases at a constant pressure (1 atm) as a function of temperature [3, 6].

container walls is smaller than the work function, i.e. the thermionic electron emission energy of the wall material. For example, the ionization of cesium vapor atoms at heated tungsten plates leads to a noiseless ('quiet') plasma in which the reduction of the radial charge carrier losses of the plasma column is achieved through a longitudinal magnetic field (magnetic plasma confinement). The degree of ionization is up to 50%. Such a plasma generation device is called a 'Q-engine' (Q for quiet) (Fig. 3-8b).

Indirect heat transfer to a gas by exothermic chemical processes (flames, explosions) can yield stationary temperatures of up to 5000 K. However, dramatically higher temperatures can be achieved during short times, for example, a strategic nuclear fusion device (H-bomb) can be triggered by the explosion of a nuclear fission device (Pu-bomb). Chemical reaction heat plasmas are being utilized in the MHD generator.

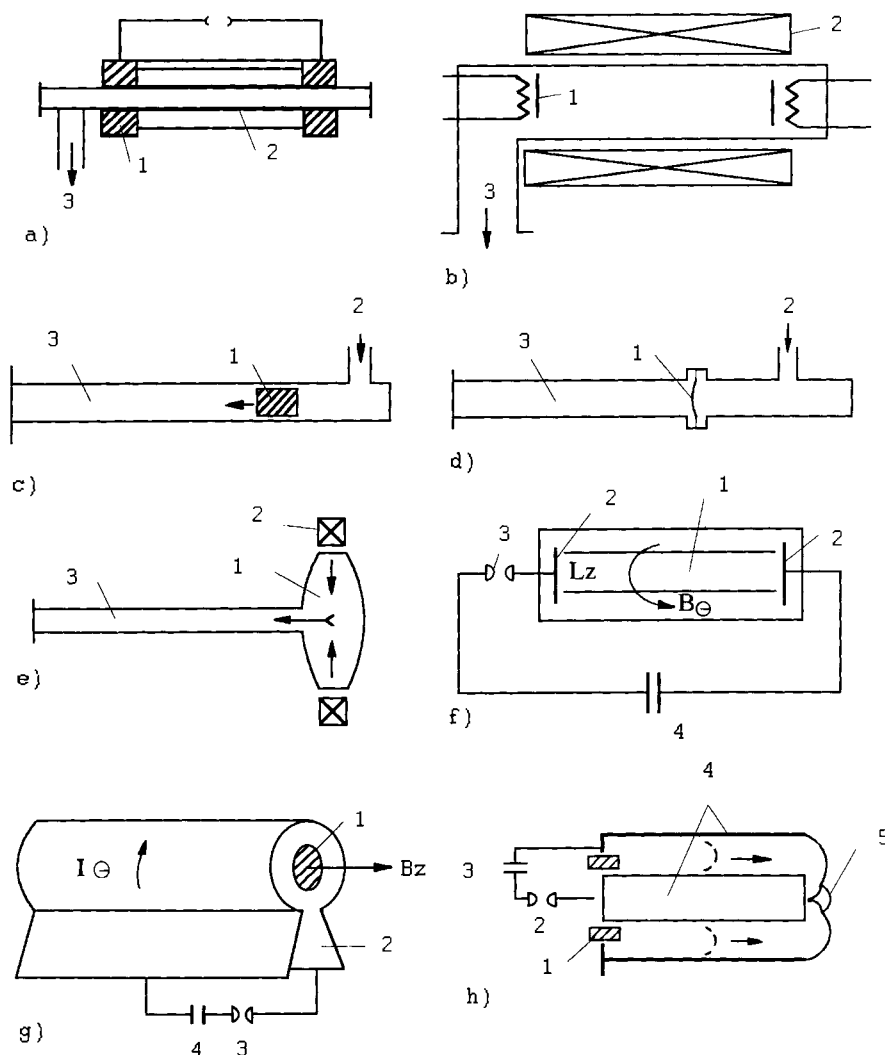


Figure 3-8. Principal ways of generating plasmas by heating (a,b) and compression of gases (c–h) [1]: (a) King's plasma furnace (1 electrodes, 2 graphite tube, 3 vacuum connection), (b) 'Q engine' (1 indirectly heated tungsten plates, 2 magnetic coil, 3 vacuum connection), (c) Ballistic compressor (1 sliding piston, 2 propellant gas inlet, 3 compression and observation section), (d) Mechanical shock tube (1 diaphragm, 2 high pressure gas inlet, 3 compression and observation section), (e) Inductive-hydrodynamic shock tube (1 discharge chamber, 2 shock coils for magnetic field, 3 compression and observation section). (f) z-pinch apparatus (1 plasma column, 2 electrodes, 3 arc gap, 4 capacitor battery), (g) Θ -pinch apparatus (1 plasma column, 2 one-turn coil, 3 arc gap, 4 capacitor battery), (h) Plasma focus (1 insulator, 2 arc gap, 3 capacitor battery, 4 electrodes, 5 focused plasma).

3.2.2 Plasma Generation through Compression

A ballistic compressor (Fig. 3-8c) consists of a tube a few meters long through which a piston of a few kilograms mass is accelerated by a burst of a propellant gas. The kinetic energy of the piston will be transformed to heat by adiabatic compression. Instead of the moving piston the compression can be achieved by a shock wave generated by bursting a membrane separating the high pressure from the low pressure region of the tube (Fig. 3-8d). For a short time temperatures of up to 5×10^4 K can occur.

In an electromagnetic shock tube (Fig. 3-8e) an oscillating magnetic field is used to generate ionization waves in a shallow chamber that propagate as a shock wave into the tube.

The so-called *pinch effect* refers to magnetic self-compression of a current-carrying plasma. In an impulse mode, temperatures up to 10^7 K can be generated in rapidly increasing magnetic fields. There are two principal configurations:

1. z-pinch (Fig. 3-8f).

Two planar electrodes conduct an axial current j_z . The compression of the plasma occurs in the resulting magnetic field B_θ by the inwardly directed Lorentz force, $F = (j \times B_\theta)$. In the regions of decreasing cross-section of the plasma column coupling of the Lorentz force and the pressure drop results in an axial force and consequently to the formation of a high velocity plasma jet. This mechanism is essential for the design of plasmatrons for plasma spraying machines.

2. Θ -pinch (Fig. 3-8g).

A current j_Θ flowing through a coil generates an axial magnetic field B_z that compresses a plasma formed by pre-ionization.

3. Plasma focus (Fig. 3-8h).

This is a special variant of the z-pinch configuration in which the discharge of a capacitor battery in a coaxial electrode system leads to an electrodynamic acceleration of the plasma along the electrodes and a subsequent compression by radially directed forces.

3.2.3 Plasma Generation by Radiation

Gases can be ionized by interaction with energy provided by either particle radiation such as electrons or protons, or by electromagnetic waves. This kind of ionization is found in astrophysical plasmas.

In an electron beam plasma generator an energetic electron beam (keV range) will be focused on a diluted gas to provide, by collisional ionization, a plasma. Interaction of the beam with the plasma can generate turbulent Langmuir oscillations. In

the field of these oscillations the electrons of the plasma can acquire energy to form a nonisothermal plasma with a high electron temperature.

Gases can also be ionized in the optical range by application of powerful laser radiation. A focused laser beam produces at a threshold intensity of about 10^5 MW cm^{-2} a plasma in the focal plane in an explosive fashion by extension of the high frequency discharge beyond the microwave region (optical discharges).

3.2.4 Plasma Generation by Electric Currents (Gas Discharges)

The oldest and most important method of generating plasmas is by the formation of an electric current in a gas. The conversion of electrical energy in the various energy forms of a plasma is facilitated by the acceleration of charge carriers in an electric field with subsequent energy transfer by collision. According to the temporal behavior of the current there are several options:

- d.c. discharge mode,
- a.c. discharge mode, or
- impulse mode.

In the a.c. discharge mode the frequencies used range from technical a.c. current to the high frequency range to microwaves and optical frequencies to X-ray and γ -ray frequencies. In the d.c. discharge mode the current is being supplied to the gas discharge region directly through metallic electrodes whereas in the a.c. mode the electrodes can be separated from the gas region by a solid insulating material.

In general, gases are good insulators and to start a discharge free charge carriers must be generated or injected into the gas. In many cases the gas creates those carriers by self discharge. In other cases a plasma is being ignited by a high frequency impulse, i.e. a spark that ionizes the gas and creates enough charge carriers to sustain the electric discharge.

The static discharge characteristic of a gas column is shown in Fig. 3-9 in an I – V plot [1]. At small voltages a very small current flows based on external sources of ionization such as space ionization. In this range Ohm's law is valid in good approximation, i.e. I is linearly proportional to U . At larger currents deviations from Ohm's law occur if the loss of charge carriers due to their movement towards the electrodes cannot be neglected anymore compared to the generation of carriers by external sources of ionization. Beyond the saturation current $I = I_s = \text{const.}$ the characteristic enters a region of increasing current in which due to collisional ionization of electrons additional carriers will be generated in an avalanche fashion. Along a distance x the number of electrons formed by ionization increases to $\exp(\alpha x)$. In particular the multiplication along the electrode distance d is $M = \exp(\alpha d)$, where α is the first Townsend coefficient that is determined by the ionization frequency ν_i and the drift velocity v_e of the electrons ($\alpha = \nu_i/v_e$).

As long as the current is still dependent on the existence of an external ionization source to sustain the discharge despite the multiplication effect of charge carriers, the gas remains in the state of a *dependent discharge*. The ignition of an *independent dis-*

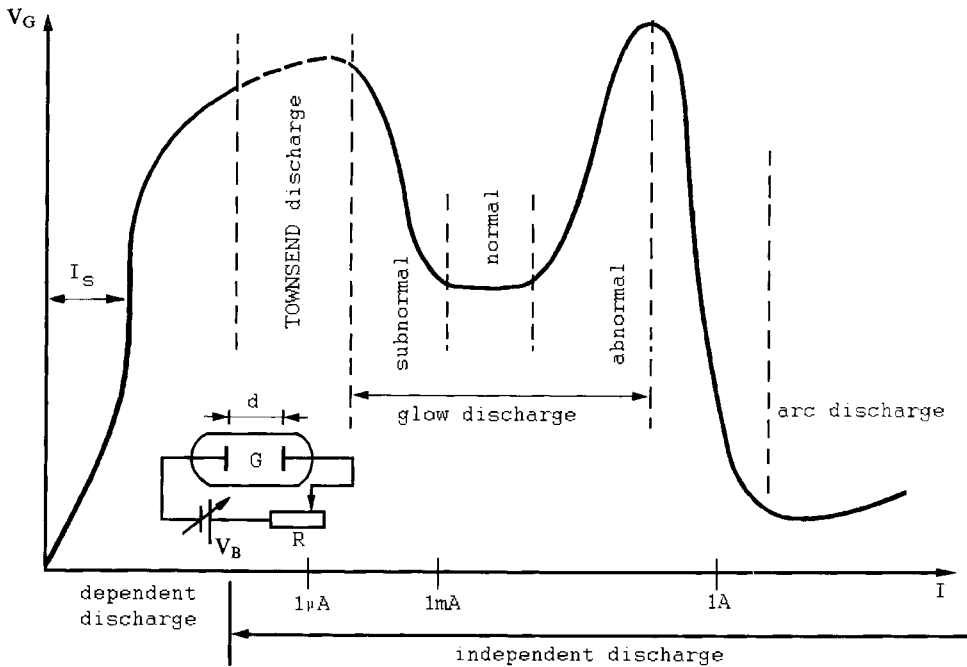


Figure 3-9. Complete static discharge characteristic of a gas [1].

charge is achieved by fulfilling the Townsend ignition condition, $\gamma[\exp(\alpha d) - 1] = 1$. The second Townsend coefficient γ considers all processes leading to the generation of secondary electrons, for example electron emission at the cathode by ion impact, photoelectrons, and the volume ionization by fast ions or photons.

In the range of small currents in the transitional range between the dependent and independent discharge there is the dark- or Townsend discharge (Fig. 3-9). It is characterized by lack of luminescence, small field displacement by space charges, and an almost horizontal I - U characteristic. With increasing current electrical space charge domains occur with a tendency to decrease the voltage. Dependent on the value of the current, two cathode mechanisms can be distinguished, the glow cathode with a small discharge current, and the arc cathode with a large discharge current.

3.2.4.1 Glow Discharges

Glow discharges occur in diluted gases ($p \approx 1$ – 10^4 Pa) at small currents ($I \approx 0.1$ – 100 mA). They lead to characteristic luminescent features between the electrodes that are divided into differently colored lighter and darker parts depending on the nature of the gas (cathode layer, Crooke's dark space, negative glow light, Faraday's dark space, positive column, anode glow light). In front of the glow cathode there is a strong space charge field called the *cathode fall*. In this region the electrons acquire the energy for ionization. The formation of the cathode fall at the transition from the

Townsend discharge to the glow discharge is associated with the decrease of the voltage (subnormal discharge, see Fig. 3-9). At higher currents the cathode fall obtains initially a minimum value independent on the current (normal cathode fall). The typical range of the normal cathode fall is between 100 and 300 V. When the cathode is being completely covered by the glow light, the cathode fall and the current density increase with increasing current again (abnormal cathode fall).

3.2.4.2 Arc Discharges

The glow discharge is of no consequence for the plasma spray process. At high current densities, however, the abnormal glow discharge is replaced by an *arc discharge*. The arc cathode acquires a high temperature that leads to thermal electron emission. Normally on the cathode a narrowly confined termination of the arc occurs as a bright and highly mobile spot with an extremely high current density up to 10^7 A cm^{-2} and a low cathode fall of typically 10 to 50 V. Ions impinging on the cathode are responsible for sustaining the cathode temperature and thus electron emission. Heating of the cathode (thermal arc) is complemented by a field emission of electrons (field arc) generated by the space charge field of ions flowing towards the cathode. Typical values for the current densities required for thermal emission and field emission are, respectively 10^3 – 10^4 A cm^{-2} and 10^6 – 10^8 A cm^{-2} with characteristic temperatures of $> 3\,500 \text{ K}$ (hot cathode with thermal emission) and $< 3\,000 \text{ K}$ (cold cathode with field emission). In general the production of secondary electrons by collective processes at the arc cathode is much more effective than the individual processes occurring at the glow cathode.

Recent investigations have shown that nonsteady state electron emissions from the arc cathode may also play an important role. Such a mechanism is characterized by extremely fast heating of microscopic asperities at the cathode surface by Joule heating and ion impingement. The asperities evaporate explosively as a dense plasma and release a large quantity of charge carriers.

Accordingly, the electrical processes occurring in different parts of the arc discharge are complex and despite a considerable amount of research in the past [7] still the subject of controversy.

The potential distribution in the arc is shown in Fig. 3-10a with the existence of three main arc regions, namely a positive column extending over the major portion on the arc path with a constant field strength, a cathode fall region with a voltage drop V_c close to the cathode of a typical thickness d_c of about 1 mm and supporting a voltage of approximately 10 V, and an anode fall region of similar size with a similar voltage drop of V_a . The layers d_c and d_a immediately adjacent to the surface of the cathode and anode, respectively are the thermal boundary layers or space charge zones with a typical thickness of 10^{-4} cm . They provide the greater part of the voltage drop. The remainder of the cathode and anode falls are also called the contraction zones. Figure 3-10b shows the extension of the space charge regions adjacent to the electrodes in the areas of the cathode and the anode falls. In general the gas pressure in arc discharges is much higher than in glow discharges (high pressure discharge, $p \geq 10^5 \text{ Pa}$). The requirement for the existence of the positive column is a sufficiently large electrode distance. The high gas pressure in the positive column

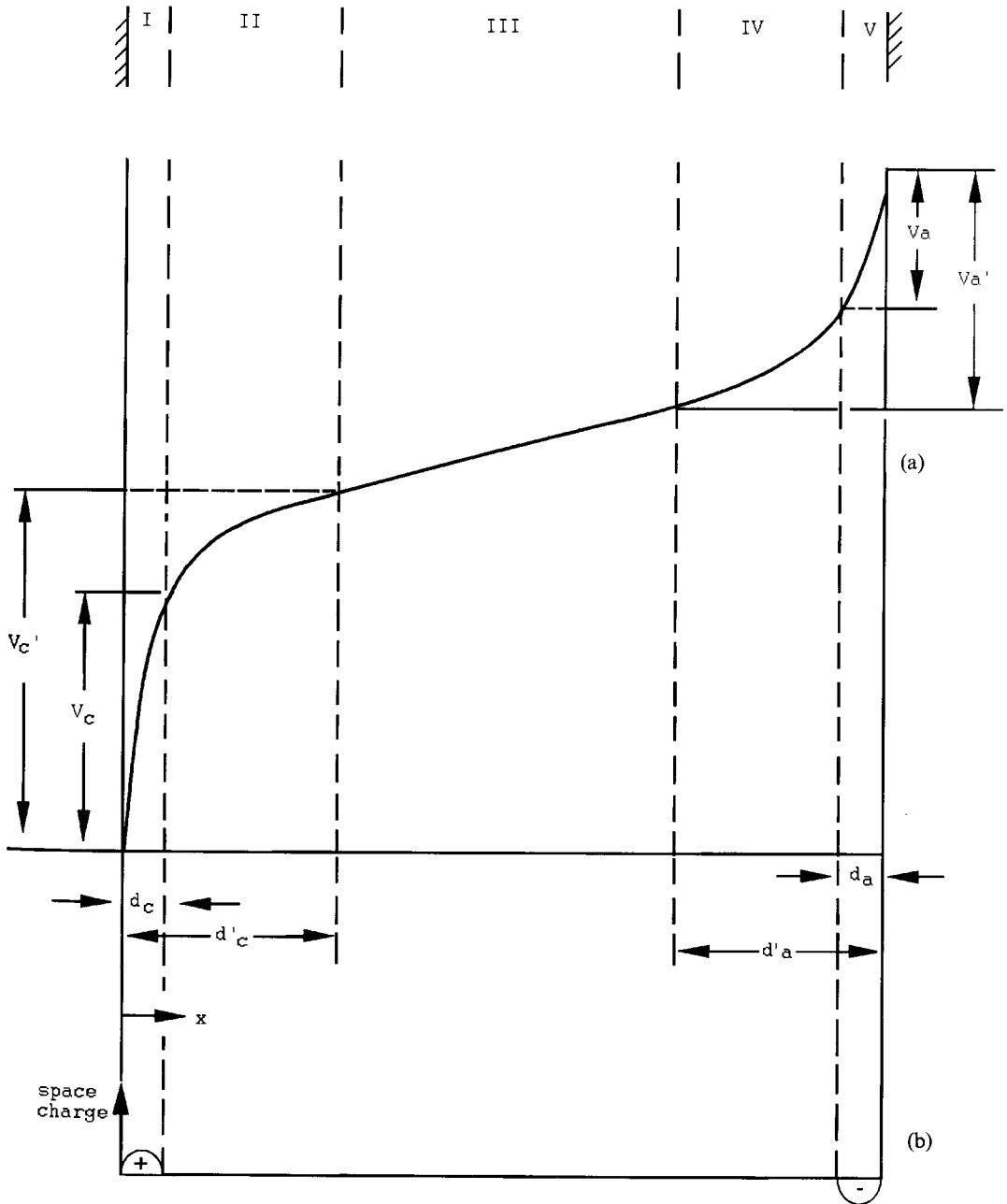


Figure 3-10. Potential distribution in an electric arc (a) and extension of the space charge region adjacent to the electrodes (b) (after [7]).

causes many collisions of ions that are responsible for an equalization of the electron and heavy particle temperatures (thermal plasma, see above).

3.2.4.3 Modeling of the Arc Column

In the case of a thermal equilibrium, the calculation of the characteristic plasma parameters can be performed assuming thermodynamic equilibrium conditions. In particular, rather simple modeling of the arc column was performed by Elenbaas [8] and Heller [9] already in the 1930s by equating the temperature gradient in the arc column with the generating electrical field:

$$\text{div}(-\lambda \text{grad } T) - \sigma E^2 = 0, \quad (3-18)$$

where λ is the thermal conductivity, σ is the electrical conductivity, and E is the electrical field. It should be particularly emphasized that the actual situation in an arc column is too complex to be solved through the conservation equations of mass, momentum and energy. In the Elenbaas–Heller approach thermal diffusion and effects of radiation have been neglected. Assuming rotational symmetry and introducing cylindrical coordinates the equation reads

$$(1/r) \text{d}/\text{d}r \{ r \lambda (\text{d}T/\text{d}r) \} + \sigma E_z^2 = 0. \quad (3-19)$$

With the definition of the heat flux potential, $S = \int \lambda \text{d}T$ it follows that

$$(1/r) \text{d}/\text{d}r \{ r (\text{d}S/\text{d}r) \} + \sigma E_z^2 = 0; S = S(\sigma). \quad (3-20)$$

With Ohm's law, $I = 2\pi E_z \int \sigma r \text{d}r$ we arrive, following Maecker [10], at the closed-form solutions

$$I = R f_1(S); E = (1/R) f_2(S), \quad \text{and also} \quad (3-21a)$$

$$IE = f_3(S) = f_4(T), \quad \text{from which follows} \quad (3-21b)$$

$$T_{\text{max}} = f(IE), \quad (3-21c)$$

i.e. the maximum temperature in an arc depends only on the power input per unit length. Thus in contrast to a flame torch with a maximum achievable temperature limited to that obtained from the internal enthalpy of the combustion gases, the maximum temperature of a plasmatron is basically unlimited. It only depends on the power input that itself is limited by the cross-section of the power leads. The modeling approach was taken from [3]. An experimental confirmation of the statement made above is shown in Fig. 3-11 that displays the almost linear dependence of the axial temperature of an hydrogen arc as a function of the power input in kW m^{-1} .

More involved modeling using the simultaneous solution of the conservation equations as well as species diffusion and the Maxwell equations can only be performed assuming:

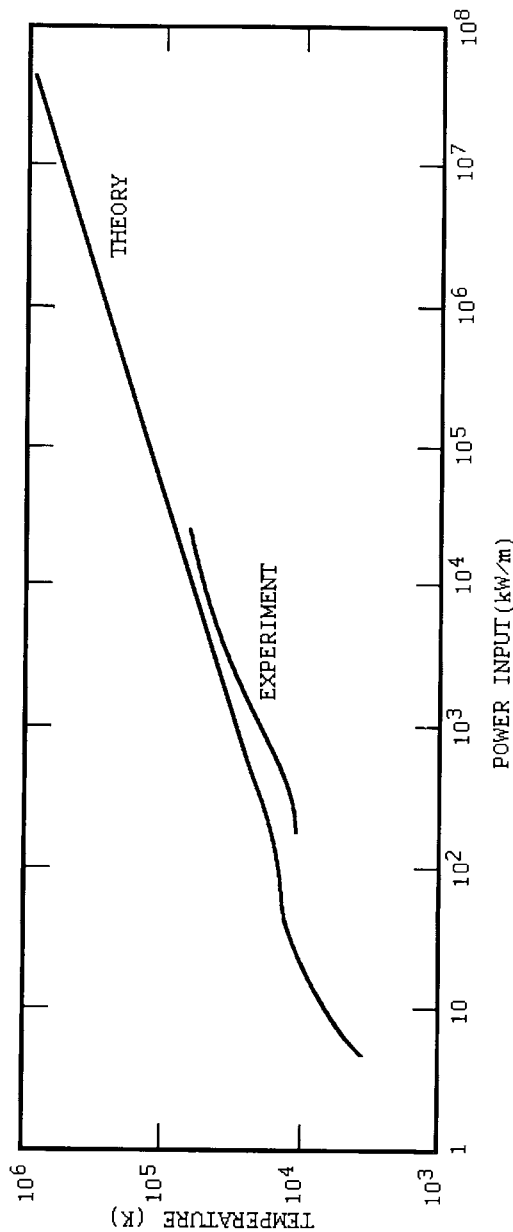


Figure 3-11. Maximum axial temperature in a hydrogen arc [10].

- 2D-rotational symmetry of the arc column,
- turbulent flow for d.c. plasmas,
- laminar flow, i.e. low Reynolds number Re for R.F. plasmas,
- optically thin arc,
- local thermal equilibrium, i.e. $T_e = T_h$,
- no viscous dissipation of the arc,
- negligible diffusion, and
- wall-stabilized arc conditions (see below).

Under these assumption it appears feasible to model the temperature and velocity profiles in a plasma arc column, and from this to predict particle trajectories, and heat and momentum transfer from the plasma to the particles (see Chapter 4). For details see, for example, Mostaghimi *et al.* [11] and Proulx *et al.* [12].

3.2.4.4 Structure of the Arc Column

Positive column

For a cylindrical symmetric column the field strength is constant and, according to Poisson's law the net space charge is zero (Fig. 3-10b). This indicates that the concentration of positive, n^+ , and negative n^- , charges must be equal. The positive column thus satisfies the condition for a plasma (see above). The current flowing through the column will have two components, an electron current J^- and a positive-ion current J^+ . The total current density is

$$\mathbf{J} = \mathbf{J}^- + \mathbf{J}^+ = e(n^- \mathbf{v}^- + n^+ \mathbf{v}^+) = ne(\mathbf{v}^- + \mathbf{v}^+), \quad (3-22)$$

where \mathbf{v}^- and \mathbf{v}^+ are the drift velocities produced by the electric field. The drift of the charged particles is impeded by collisions with neutral and other charge carriers. This represents a resistive phenomenon. Since $\mathbf{v}^- \gg \mathbf{v}^+$, the total current is carried predominantly by the electrons. Thus it follows that

$$\mathbf{J} \approx \mathbf{J}^- = n^- e \mathbf{v}^- = n^- e \mu \mathbf{E} = \sigma \mathbf{E}, \quad (3-23)$$

where μ is the electron mobility and σ the electrical conductivity.

The cathode fall region

To satisfy the continuity condition, the current flowing through the positive column must also make the transit from gas to metal at both electrodes. Hence in the cathode region conditions must exist that allow this transition. For refractory cathodes the mechanism is one of thermionic emission. There is a continuous and controllable transition from a glow discharge to an arc state depending upon the cathode temperature (Fig. 3-12, [13]). To lower the work function of the electrons, and to get an abundance of electron emissions to initiate and sustain the arc discharge, the cathode of a plasmatron is usually coated with thorium. Figure 3-13 shows the current char-

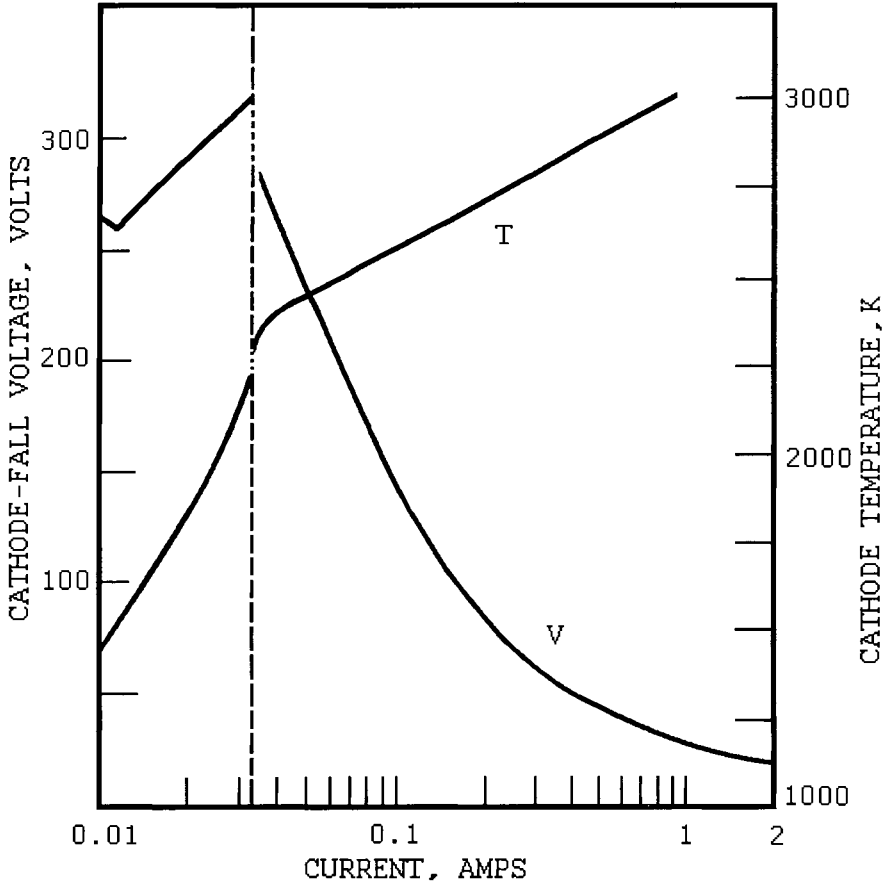


Figure 3-12. Variations of cathode-fall voltage and cathode temperature with the applied current during thermionic glow discharge-to-arc transition [13].

acteristic of thermionic electron emission in a vacuum diode. It can be described by the Richardson–Dushman equation

$$j_s = AT^2 \exp(-e\Phi_c/kT), \quad (3-24)$$

where A is the area of the electron emission and Φ_c is the electron work function. Because of the space charge region adjacent to the cathode the emission of electrons is impeded by the electric field on the cathode surface. Therefore the equation must be corrected. For high cathode temperature and moderate field strength the Schottky correction can be applied:

$$j_s = AT^2 \exp\{-[e\Phi_c - (e^3 E/4\pi\epsilon_0)^{1/2}]/kT\}. \quad (3-25)$$

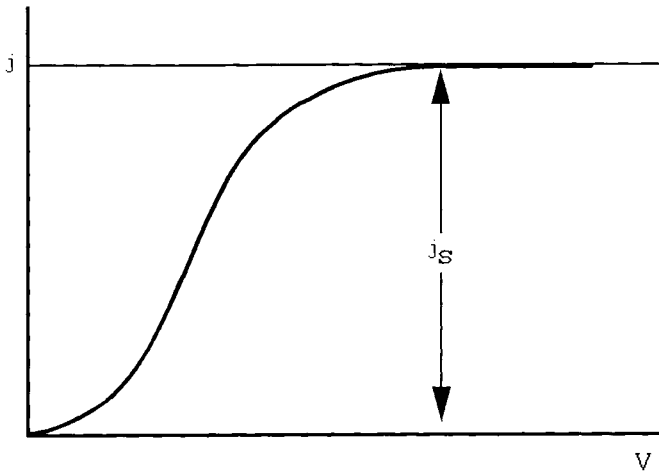


Figure 3-13. Current characteristic of thermionic electron emission in a vacuum diode.

The ability to emit electrons by thermionic emission differs among different metals. Figure 3-14 shows a plot of the thermionic work function Φ_c against the boiling temperature of the metal. Metals with particularly high work functions and thus thermionic emission are molybdenum, tungsten, tantalum and rhenium [14].

The net energy supplied to the cathode can be described by the balance between the current carried by the impinging ions and that caused by electron emission. The energy supplied to the cathode by impinging ions is

$$j_i(V_c + V_1 - \Phi_c + (5/2)kT_i/e, \quad (3-26a)$$

the energy removed by electron emission is

$$-j_e\Phi_c. \quad (3-26b)$$

This is, however, an idealization. The cathode also acquires energy from other sources such as neutralization energy transfer, condensation energy from the ions, heat conduction from the gas, radiation and possibly chemical reactions. The energy losses also encompass vaporization, loss of metal globules by thermal sputtering, radiation and heat conduction through both solid and surrounding gas.

The ratio j_i/j_e is between 0.15 and 0.5 depending on the cathode material and the electrical field strength.

As mentioned above, loss of material from the electrodes frequently occurs as do usually preferentially directed plasma arc jets. Such plasma jets may also be produced by constricting the diameter of a small section of the arc column. In this case the pressure gradient due to the pinch of the self-generated magnetic field increases with current density in the steady state. The constricting Lorentz force is directed inwardly and confines the plasma jet. This phenomenon will be discussed in detail later. Figure 3-15 shows the interaction of cathode and anode jets in an arc. The mode of attachment of the cathode arc jet at the surface of the cathode de-

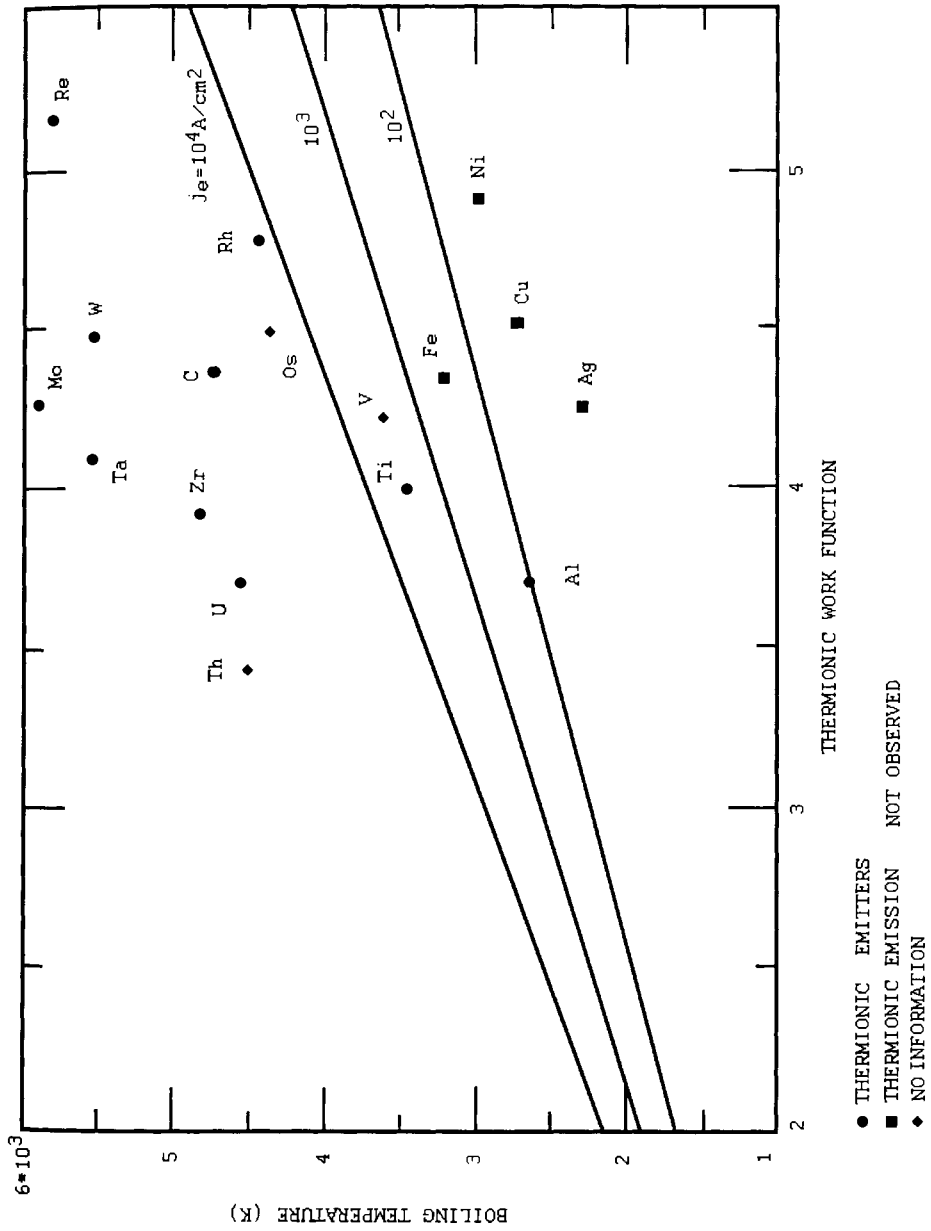


Figure 3-14. Thermionic work function, Φ_c , as a function of the boiling temperature of various metals [14].

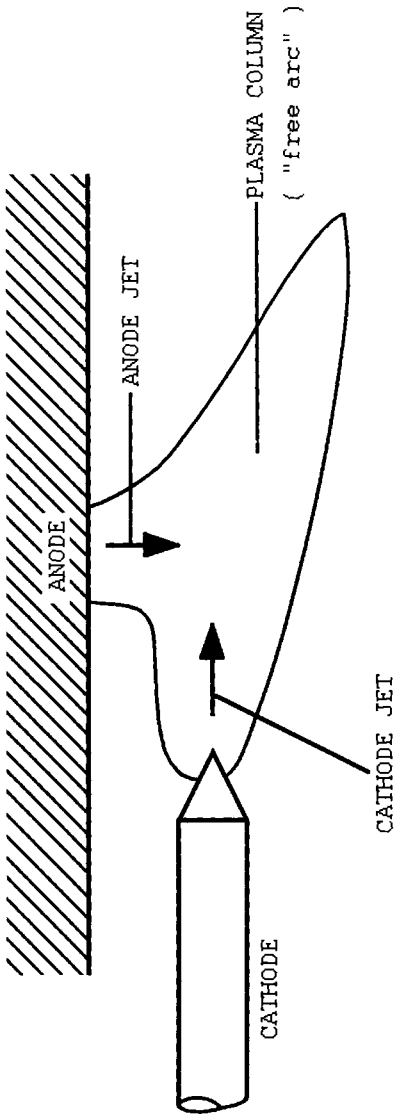


Figure 3-15. Interaction of cathode and anode jets in an arc [3].

depends on the current density. Diffuse attachment without localized spots occurs at 10^3 – 10^4 A cm $^{-2}$ whereas distinct spots are visible at higher current densities (10^6 – 10^8 A cm $^{-2}$). In case of the attachment of the anode arc jet, lower current densities of 10^2 – 10^3 A cm $^{-2}$ produce diffuse, higher ones (10^4 – 10^5 A cm $^{-2}$) constricted, i.e. spot-like attachment. Frequently the diffuse attachment of the anode arc jet is caused by the cathode jet impinging on the anode. This is known as the cathode jet-dominated (CJD) mode.

The anode region

Positive-ion emission from the anode can be neglected for most arc conditions. In this region current continuity is thus achieved by the total current being fed into the anode by electrons. This necessitates the production of extra electrons in the anode region. In many ways the anode region is similar to the cathode region even though the conditions are not so extreme. For example, the contraction zone is less sharp. The calculation of the energy balance at the anode is simpler than that at the cathode since a number of the coefficients involved are more definite. Most of the power is consumed in metal vaporization so that a high anode vapor pressure exists. This is then the source for the often observed anode vapor jets [8] (see Fig. 3-15) when the cathode arc jet impinging on the anode surface causes material to evaporate.

By introducing a diaphragm in front of the anode of a high-intensity argon arc the flow is interrupted thus resulting in the anode jet-dominated (AJD) mode. Temperature measurements based on line-emission coefficients and on absolute continuum-emission coefficients (see Sec. 3.4), and modeling by simultaneously solving the conservation equations under simplifying boundary conditions show reasonable agreement of the temperature distribution along the anode region (Fig. 3-16, [16]).

3.3 Design of Plasmatrons

Simplistically, one can visualize plasmatrons as resistance heaters in which familiar resistance elements such as nichrome, silicon carbide, tungsten etc. are replaced with a consumable, conductive and partially ionized gas. Thus the plasma column can be considered a 'consumable heating element' whose resistivity varies with operating conditions and type of gas used for ionization. The resistance range of a plasma in Ω cm is 0.01–0.5 for argon, 0.05–0.25 for nitrogen, and 0.25–0.0035 for hydrogen [17]. These values should be compared to the resistance ranges of solid materials such as iron (0.001–1.00), carbon (9×10^{-4} – 3.5×10^{-3}) and copper (5×10^{-7} – 9×10^{-8}).

An important design consideration for plasmatrons is the confinement of the plasma jet along the central channel of the torch by two phenomena, the thermal and the magnetic 'pinch'.

Thermal pinch occurs because at the cooled wall of the anode nozzle the conductivity of the gas is reduced thus increasing the current density at the centre. The

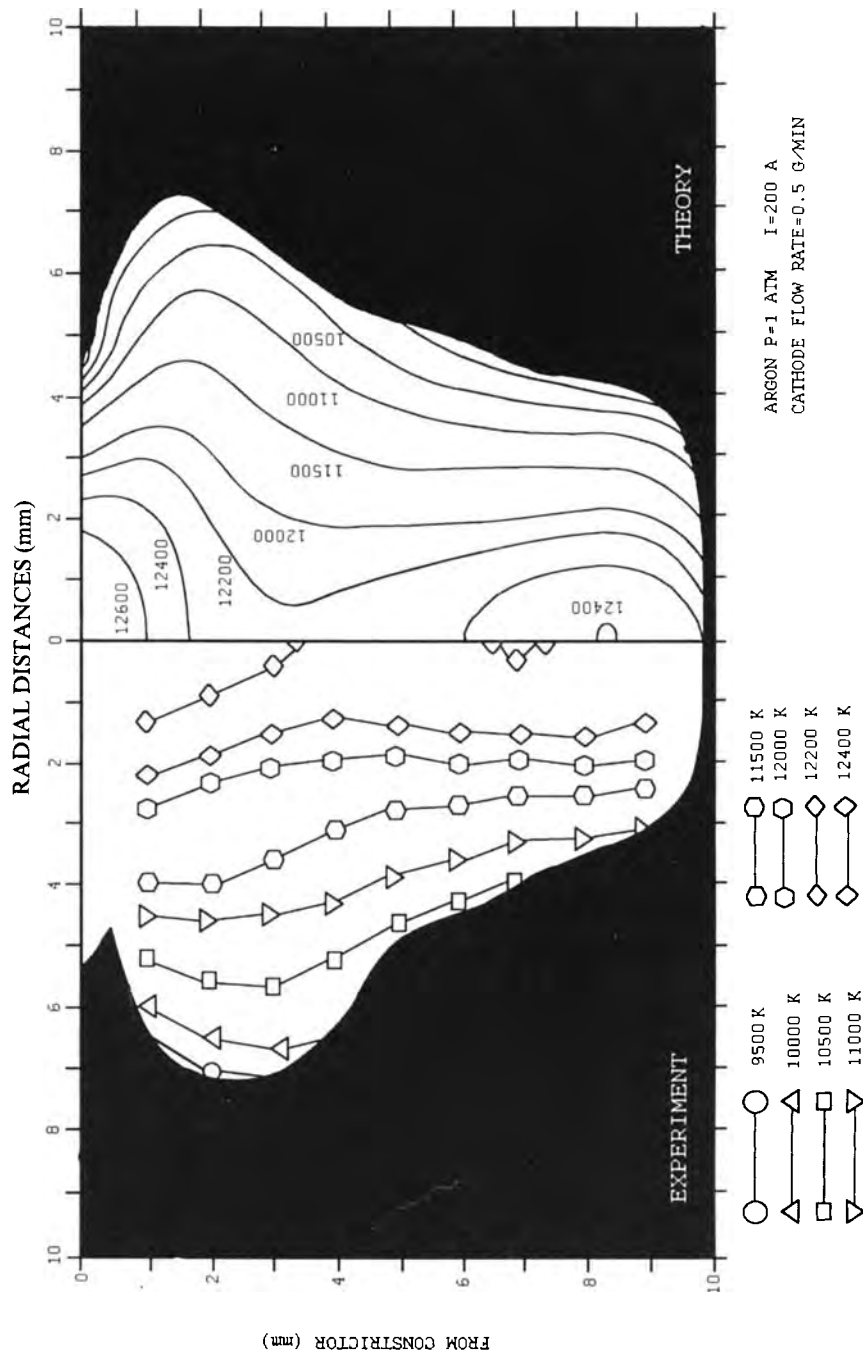


Figure 3-16. Anode region of a high intensity arc (after [16]).

charged plasma tends to concentrate along the torch axis thus confining the jet. Simply put, this means that the cold gas surrounding the arc absorbs a significant amount of energy from the arc in proportion to the energy required to ionize it.

Magnetic pinch is related to a magnetohydrodynamic Lorentz force created by the electrically conductive central region of the plasma jet. The moving charges induce a magnetic field. According to electrodynamics, the vector cross-product of the current and the magnetic field strength define the Lorentz force whose vector is mutually perpendicular to the former vectors. An inward moving force is created that constricts the jet even further. Its core pressure increases, and the jet is blown out of the front nozzle with supersonic speed.

Figure 3-17 shows schematically the direction of the Lorentz force $[\mathbf{j} \times \mathbf{B}]$ (longitudinal or *z*-pinch). The current flowing in the *z*-direction causes circular magnetic field lines B_θ that compress and thus confine the plasma.

From the momentum conservation equation the Euler flow equation

$$\rho(d\mathbf{v}/dt) \equiv \rho(d\mathbf{v}/dt + (\mathbf{v}\nabla)\mathbf{v}) = (1/c)[\mathbf{j} \times \mathbf{B}] - \nabla p \quad (3-27)$$

can be derived, where $\rho(z, t)$ is the particle density, $\mathbf{v}(z, t)$ is the (macroscopic) particle flow velocity, p is the plasma pressure and $\rho(\mathbf{c}; \mathbf{c})$ is the tension tensor [2]. This equation neglects the influence of gravity and other volume forces such as centrifugal and Coriolis forces³. This leads to the simplified Navier–Stokes equation for momentum conservation,

$$\rho(d\mathbf{v}/dt) + \nabla p = [\mathbf{j} \times \mathbf{B}]. \quad (3-28)$$

The first term on the left side of the equation describes the time-dependent mass flux, i.e. the particle acceleration, the second term is the outward directed plasma pressure gradient. Their sum is balanced by the vector cross-product of the current and the magnetic field, i.e. the inwardly directed Lorentz force. For very high currents the *z*-pinch effect increases the temperature by magnetic compression considerably. Its value can be calculated by applying the Bennett equation

$$J^2 = 8\pi k T n / \mu_0, \quad (3-29)$$

where n is the number of particles per unit length of the plasma cylinder, and μ_0 is the electron mobility. Plasma heating by magnetic compression is being utilized in nuclear fusion reactors.

3.3.1 Arc Discharge Generators and their Applications

There is a wide variety of approaches towards achieving high temperatures in a plasma jet heating device. Only a few basic principles will be considered here.

We can distinguish among three categories as shown in Table 3-2:

³ However, it can be shown that a self-confinement of a finite plasma is impossible in a gravity-free environment by its own magnetic field alone [2].

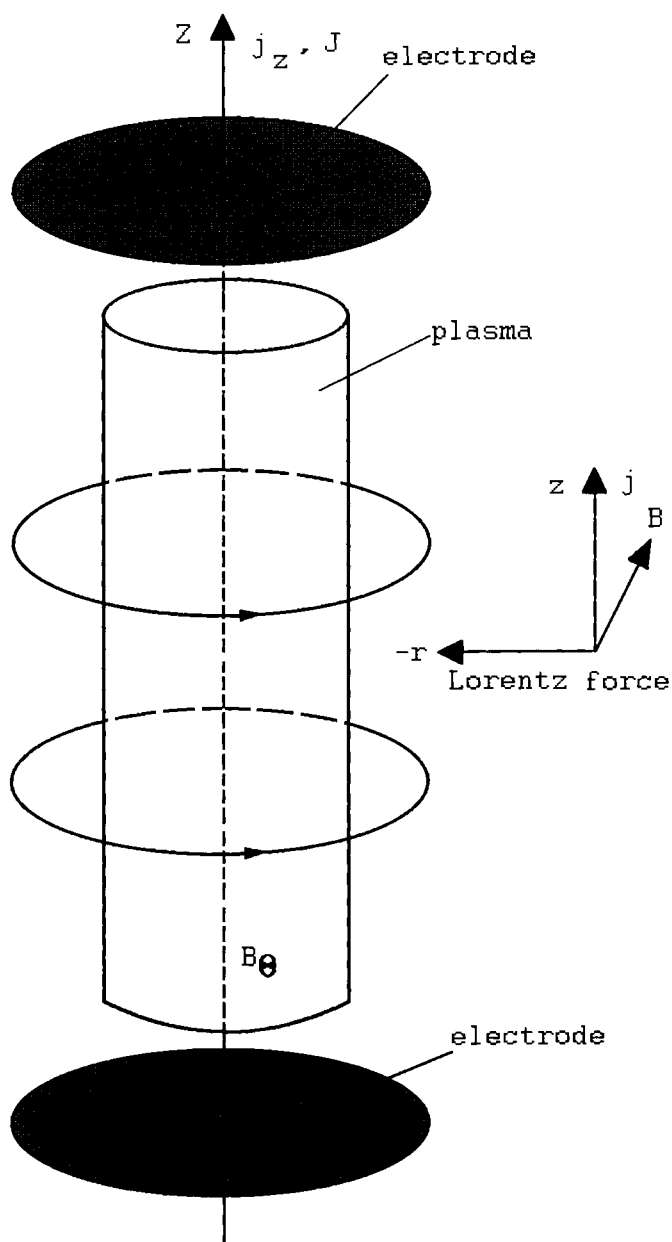


Figure 3-17. Direction of the Lorentz force (longitudinal or z-pinch).

Table 3-2. Arc discharge generators and uses: after reference [17].

Generators	Uses
Electrode plasmas (EPs)	
Nontransferred	
Low voltage	Spraying/particle heating Welding Melting Low velocity Gas heating
High voltage	High-pressure operation Hydrogen heating Spraying
Transferred	
Direct work heating	Welding Cutting Melting conductive materials Surfacing
Secondary Electrode (Water stabilized, metal/carbon, multiple ring)	Spraying/particle heating Gas heating
Electrodeless plasmas (ICPs)	
Low frequency	High power Gas heating Particle heating
High frequency	Low power Gas heating Particle heating Spraying High-resistivity gases High pressure
Hybrid	
ICPs superimposed on EPs	Particle heating Gas heating

d.c. types: wall/gas/magnetically stabilized, pin/hollow electrodes, fixed/movable electrodes, external field augmentation; a.c. types: single- and multiphase, fixed/movable electrodes, external magnetic field augmentation; electrodeless types: tandem inductive coupling, tandem capacitive coupling, inductive/capacitive coupling.

- electrode plasmas (EP) as either nontransferred or transferred plasmas,
- electrodeless plasmas (inductively coupled plasmas, ICP) operating at low or high frequencies, and
- hybrid devices where ICPs are superimposed on EPs [17].

3.3.1.1 Electrode-supported Plasmas

Nontransferred electrode plasmatrons (indirect plasmatrons) operate at comparatively low voltages between 20 and 150 V d.c. Figure 3-18 shows the cross-section of a typ-

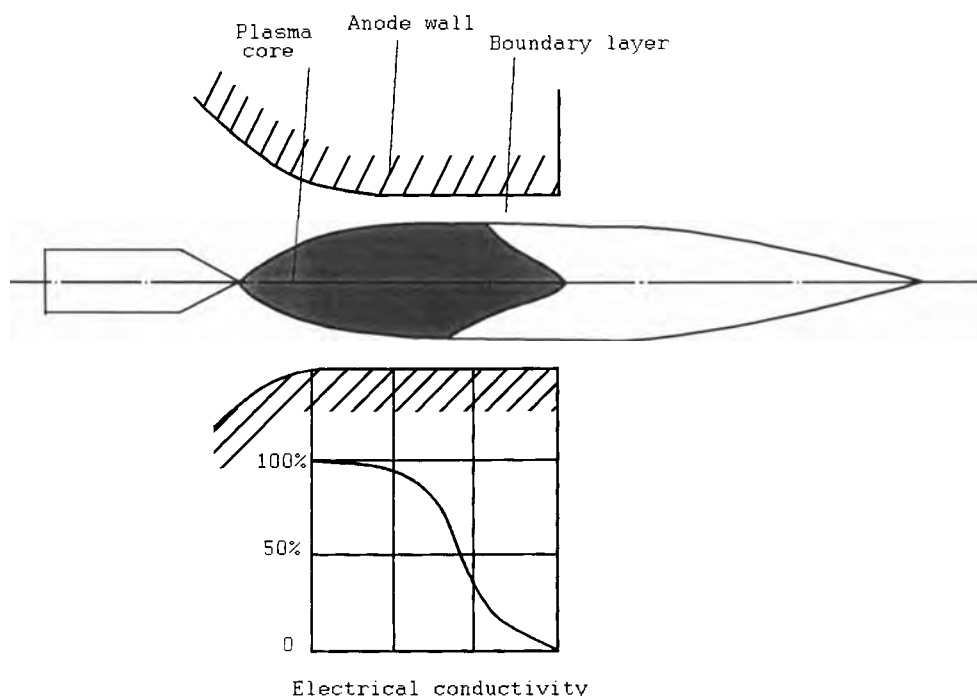


Figure 3-18. Cross-section of a typical nontransferred d.c. plasmatron.

ical nontransferred d.c. plasmatron. It consists of a stick- or bullet-shaped cathode made from tungsten, and a water-cooled copper anode which forms the front nozzle of the torch. The tungsten cathode is thoriated to lower the electron work function, and to get an abundance of electron emissions that initiate and sustain an electric arc between the tip of the cathode and the internal diameter of the positive anode nozzle. The plasma rapidly diminishes in charged particle density near the nozzle exit. This results in an exponential decrease in electrical conductivity as shown in the lower part of Fig. 3-18. The actual discharge is initiated by a high frequency pulse or a high voltage field emission discharge. The arc stretches down the cathode with a constant voltage field gradient and is attached to the anode by a voltage drop (anode fall). The flow through the torch is mildly turbulent with a minimum swirl content for devices operated at low voltages. High voltages between 150 and 1 000 V, however show a significant amount of highly turbulent swirl gas that produces a strong vortex with a low-pressure center core that must be traveled through by the arc.

The heat transfer rates are close to the heat flux failure limit of the anode, i.e. copper material [17]. Therefore, effective cooling by a constant stream of water is essential to keep the anode from evaporating. In this configuration the maximum cathode amperage is about 3 000 A. This sets a maximum achievable power. For example, at a voltage of 200 V the maximum electrical power input would be 600 kW. The workpiece to be coated remains relatively cool and rarely exceeds 200 °C.

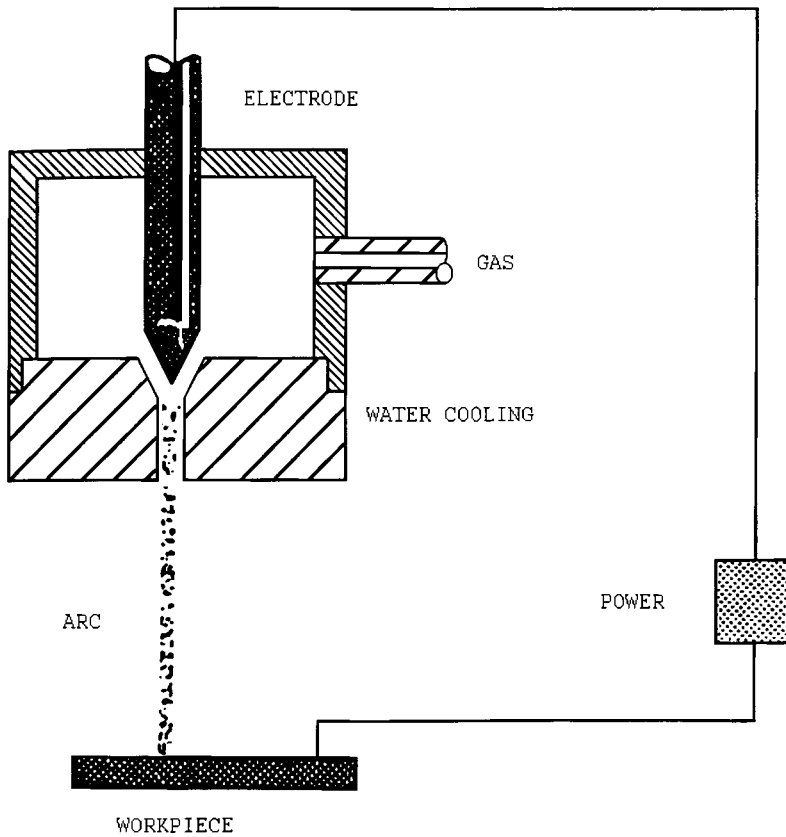


Figure 3-19. Working principle of a direct plasmatron (transferred electrode plasmatron).

Transferred electrode plasmatrons (direct plasmatrons) can be operated in two modes: transfer of energy to the workpiece that is electrically connected to the power source, and transfer of energy to an intermediate electrode.

In the first type (Fig. 3-19), the cathode is some distance (usually less than 15 cm) from the 'working' anode. An arc is struck between the two electrodes by either a capacitance or a high-frequency discharge with the direct current following the ionized path thus generated. The workpiece (substrate) is electrically connected to the power source, and the whole assembly actually constitutes an arc-welding configuration. This means that the substrate is heated to high temperatures. The heat losses by radiation or convection are high (20–40%). If the system is used for plasma spraying, care must be taken to inject the powder downstream of the arc root at the anode to avoid contamination of the electrodes. Also, the substrate may have to be cooled in order to avoid melting, warping or undesirable changes of the micro-structure.

Applications of a transferred arc include welding, cutting and melting operations of conductive materials. With severe constriction of the arc by an intermediate nozzle of small diameter, the heat flux and gas velocity are very high, and this device is

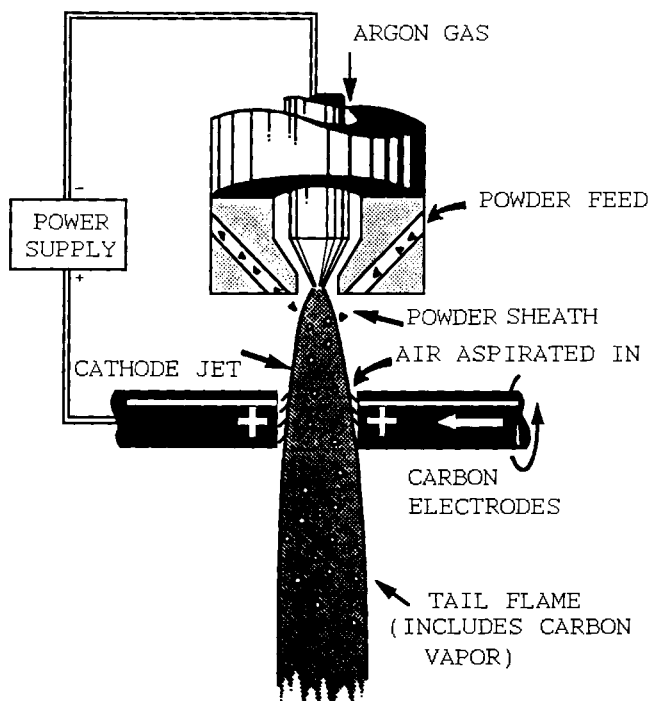


Figure 3-20. Working principle of a transferred arc terminated by an intermediate electrode [17].

therefore used for cutting metal. Less constricted arcs with larger intermediate nozzle size have lower gas velocities. Thus the arc is 'softer' and can be used for welding and melting operations.

In the second type (Fig. 3-20), the transferred arc is terminated by an intermediate electrode that produces a nontransferred free plasma jet. As shown in the figure, the secondary carbon anode is self-cleaning and slowly consumed. In the Ionarc (TAFA Inc., Concord, NH, USA) device shown there are three rotating carbon electrodes that are fed at a rate that replenishes the consumed material. Powder injected close to the cathode spot can be heated with high thermal efficiency. For example, the powder feed rate is as high as $0.9 \text{ kg h}^{-1} \text{ kW}^{-1}$ as opposed to $0.1 \text{ kg h}^{-1} \text{ kW}^{-1}$ for normal tail-flame injection type plasmatrons.

Today, transferred arcs are frequently used to clean the surface of the part to be coated by sputtering off oxide scale. This requires a polarity change, i.e. the working anode is made more negative for some time. This procedure is particularly important if highly oxygen-sensitive material is to be sprayed in a 'vacuum' environment, such as NiCrAlY for coating of gas turbine vanes and blades for aerospace applications.

Segmented anodes allow the arc to strike from the central cathode through one or more insulated and water-cooled metal rings to the terminating, also water-cooled anode rings (Fig. 3-21a). This is done to increase the arc voltage that permits higher power operation. Since the amperage is reduced at given power level electrode life is increased because erosion is decreased.

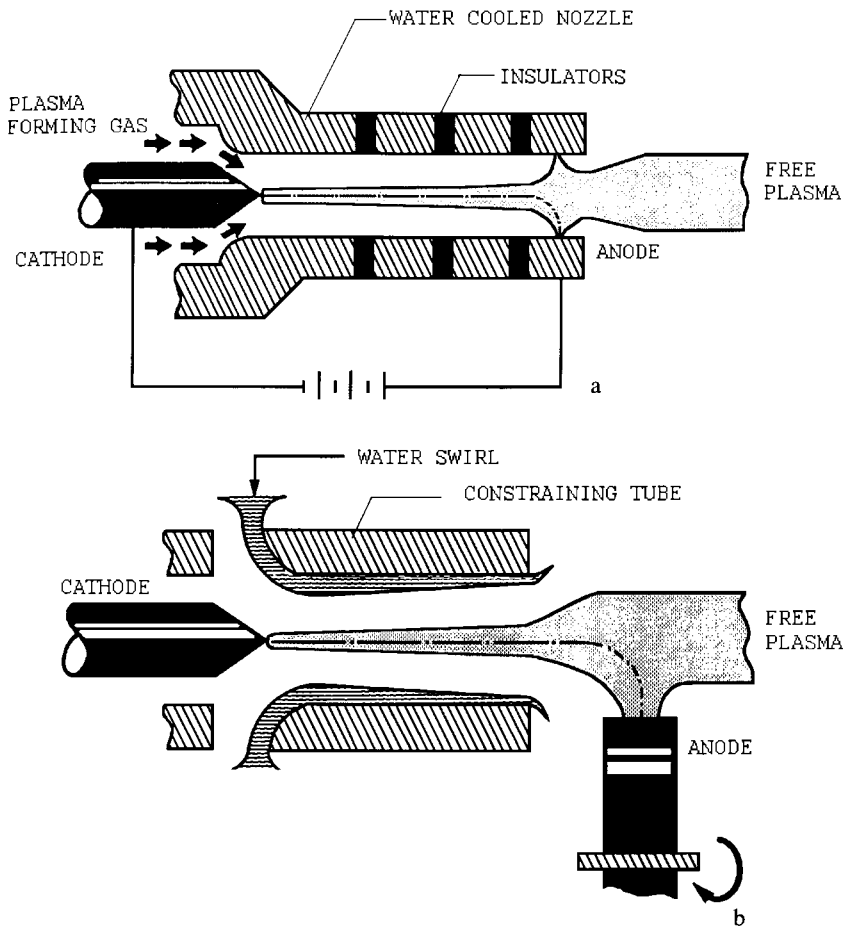


Figure 3-21. Segmented anode plasma (a) and water-stabilized arc (b) [17].

Figure 3-21b shows a water-stabilized arc (see Sec. 3.3.2.2). Water vortices in a tube section between consumable cathode and anode form a hollow passage and protect the walls from overheating. Very high power can be applied and temperatures can therefore reach 50 000 K (Gerdien arc, [18]). Transferred water-stabilized arcs are being used to spray alumina at powder feed rates as high as 34 kg h^{-1} compared with less than 10 kg h^{-1} for a conventional gas-stabilized nontransferred d.c. arc [17].

3.3.1.2 Electrodeless Plasmas

Radiofrequency (RF) inductively-coupled Plasma (ICP) devices were conceived by Reed in 1961 [19], and treated extensively theoretically, for example by Eckert [20] and Boulos [21]. They generally consist of a coil surrounding a water or gas-cooled refractory (often silica glass) tube through which the plasma-forming gas, the sheath-

gas for wall cooling, and the powder gas pass (Fig. 3-22). The devices operate in widely varying power (0.5 kW–1.0 MW) and frequency (9.6 kHz–40 MHz) ranges [21].

Energy coupling to the plasma is achieved through the electromagnetic field of an induction coil. The plasma gases do not come in contact with any electrode and therefore any contamination is largely excluded. Mostly argon is used because of its ease of ionization. The device, however, works also well with an air plasma.

The main attraction of the radio-frequency inductively coupled torch is in-flight melting of relatively large particles of refractory metals and ceramic powders at high throughputs.

Figure 3-22 shows schematically the temperature (left) and flow fields (right) in the discharge region of an inductively coupled torch [21, 22]. The maximum plasma temperature is off-axis because the energy dissipation is limited to the outer annular region of the discharge. The argon plasma (power level 3 kW, oscillator frequency 3 MHz) is confined in a water-cooled silica glass tube with several gaseous stream introduced. Q_1 ($=31 \text{ min}^{-1}$) is the axially injected powder gas that serves to introduce the material into the plasma, Q_2 is the intermediate gas that serves to stabilize the plasma and is kept constant at 31 min^{-1} ; it is often introduced with both axial and tangential velocity components. Q_3 is the sheath gas that serves to reduce the heat flux to the walls of the confinement tube, and thus protects it from damage due to overheating. In this example it had been adjusted in such a way that the total flow rate Q_0 is constant at 201 min^{-1} .

The flow field shows low velocities ($10\text{--}20 \text{ m s}^{-1}$) compared to a d.c. plasma arc torch ($100\text{--}400 \text{ m s}^{-1}$). There exists an recirculation eddy current in the coil region, caused by the electromagnetic pinch effect. In order to properly deliver the powder into the torch, it has either to be introduced at high velocity to overcome the back flow, or to be injected in the middle of the induction coil region, below the recirculation eddy current.

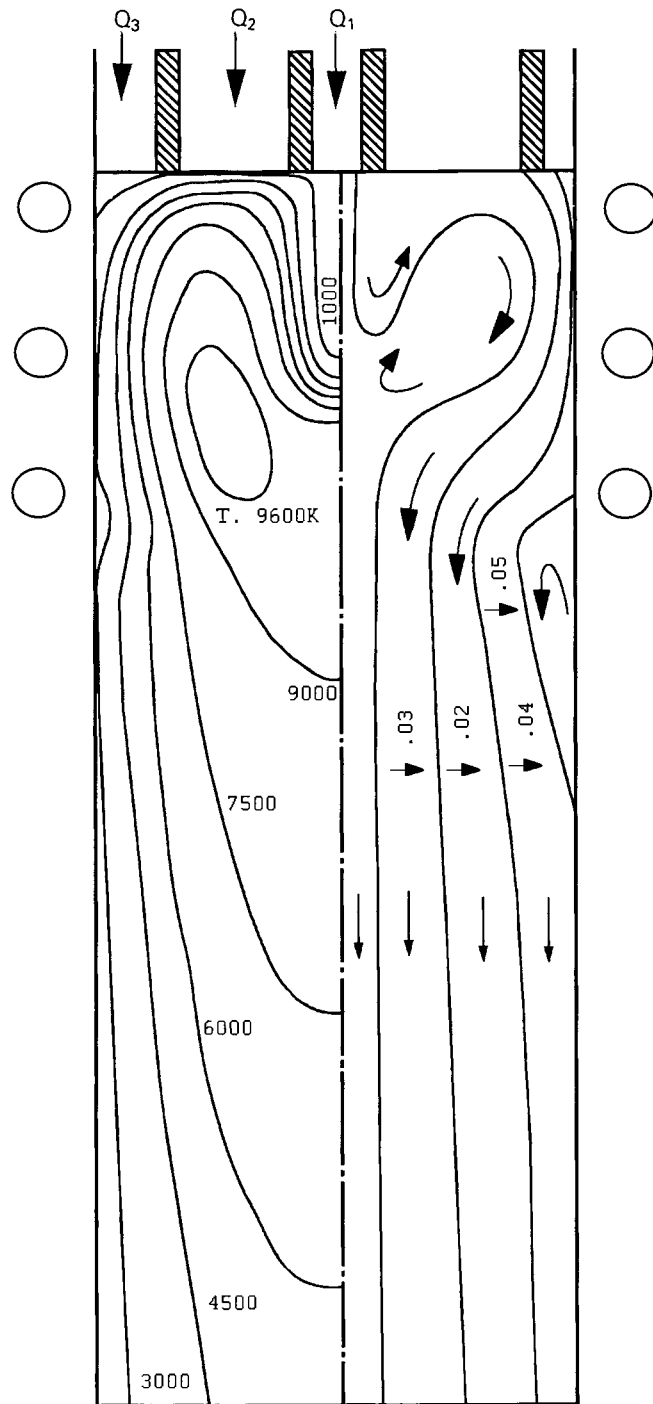
Advantages of this method include:

- no electrodes,
- any gas possible,
- no upper temperature limit,
- low velocity plasma,
- large diameter plasmas,
- quasi-laminar flow regime, i.e. low Reynolds numbers, and
- operational without gas flow because of arc stabilization by thermal pinch in the center of the tube.

Disadvantages include:

- high frequencies and voltages that lead to high transmission losses,
- low power densities, and thus lower maximum temperatures (usually below $10\,000 \text{ K}$),
- local cooling of plasma at point of powder injection, and
- complex geometry of device that makes fixation necessary.

Figure 3-22. Electrodeless radiofrequency inductively-coupled plasmatron. Left section: temperature distribution. Right section: flow field distribution [21].



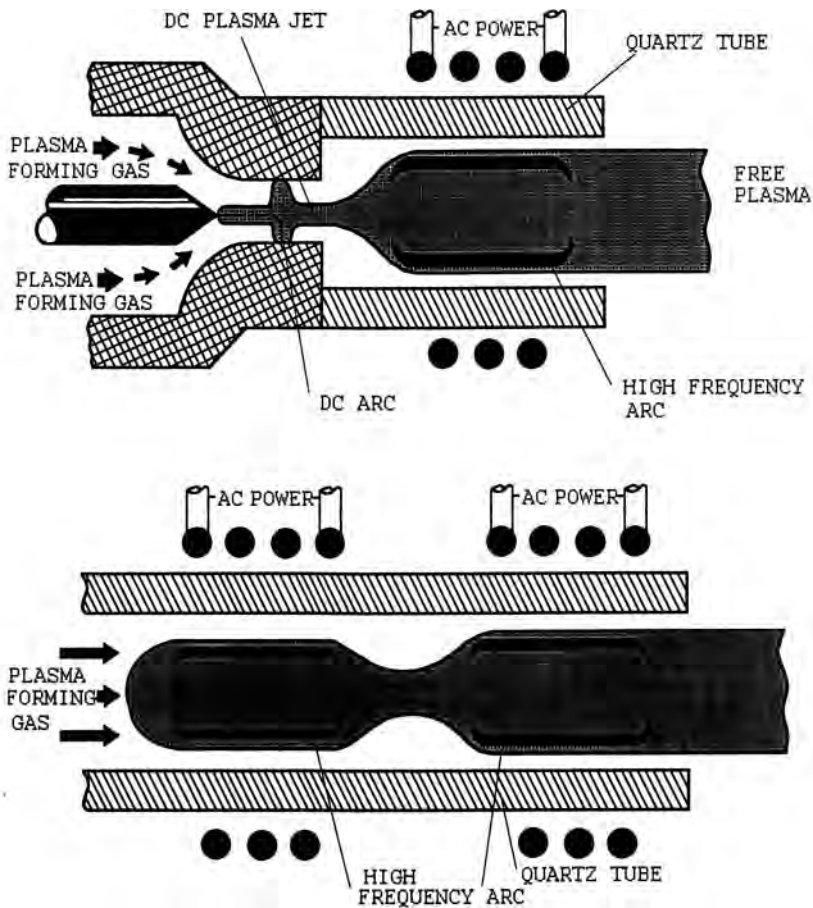


Figure 3-23. Inductively-coupled plasmatron (ICP) operated in tandem with another ICP (bottom) or a d.c. discharge (top) [17].

3.3.1.3 Hybrid Devices

It is feasible to operate the ICP in tandem with either another IPC (Fig. 3-23, bottom) or a d.c. discharge (Fig. 3-23, top). The d.c. plasma forms the center core of the plasma, acting as an ignition source, and the ICP adds additional heat downstream to maintain the temperature level. It also increases the diameter of the plasma, i.e. the volume of the plasma and its energy density so that more powder per unit time can be processed by the device. There are, however, problems with plasma contamination by the material evaporated from the d.c. plasmatron electrodes. The lengthening of the plasma zone by several hybrid devices is shown in Fig. 3-24. It provides the possibility to achieve higher particles residence time in the hot zone, and also adds design flexibility when chemical reaction times have to be increased, for example in reactive plasma processing [23]. Successful approaches to hybrid devices

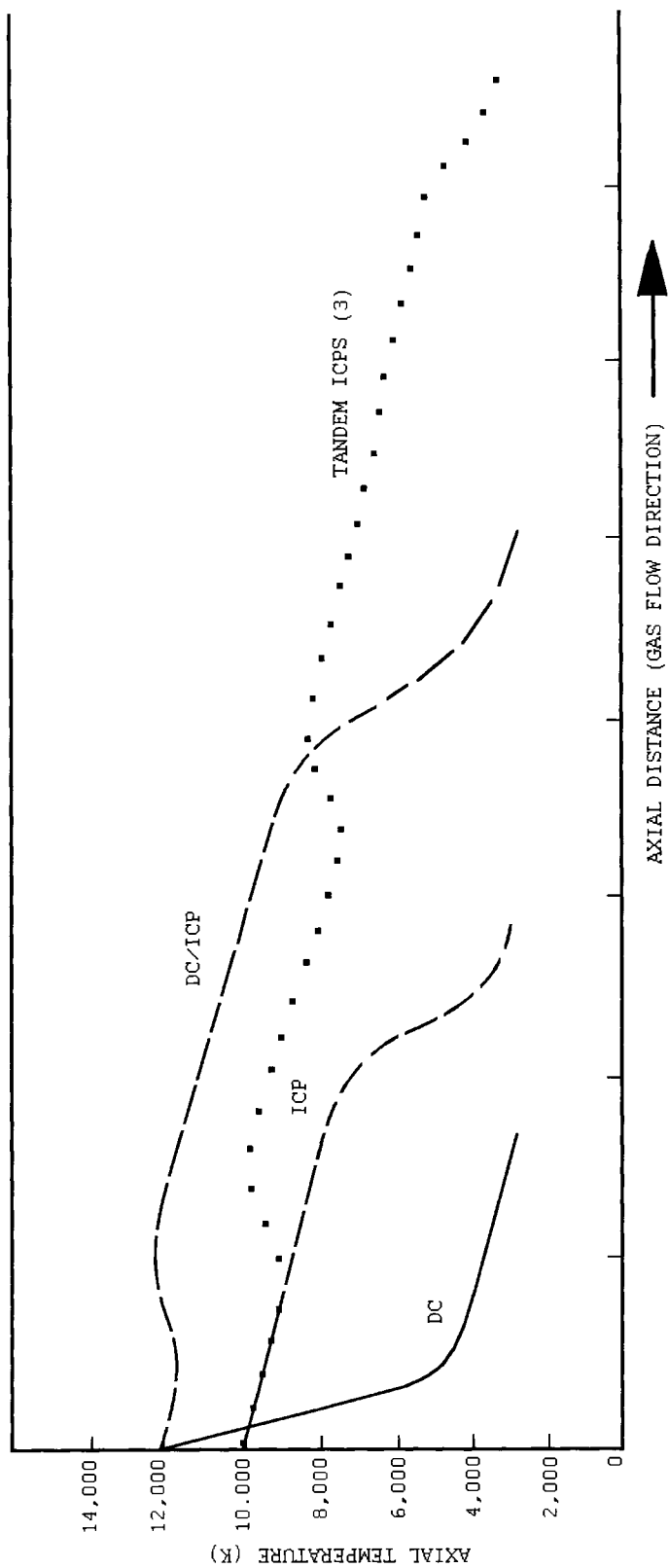


Figure 3-24. Axial temperature variations of d.c., ICP, and tandem-operated d.c./ICP and ICP/ICP plasmatrons [17].

were taken by Yoshida *et al.* [24] using a d.c. power of 4–5 kW, an RF plate power of 10–30 kW, and an oscillation frequency of 4 MHz, and by Takeyama and Fukuda [25] using an RF–RF two frequency hybrid plasma (pilot RF source with 2 kW and 27.12 MHz, and secondary RF source with 15 kW at 5 MHz).

3.3.2 Stabilization of Plasma Arcs

Since the power supply of the plasmatron normally has a negative characteristic ($R = dV/dI < 0$), it is inherently unstable. The voltage decreases with increasing current so that for steady-state conditions a resistance must be included in the circuit. The slope of the load line is given by $dv/di = -R$. The intersections of the characteristics (load line) of the current source and the plasmatron define the two stable working points A and B of the device. The Kaufman stability criterion of a plasmatron is $dv/di + R > 0$ or $R > |dv/di|$. Considering the capacitance and inductance of the arc, the criterion becomes $R < L/c|dv/di|$.

Electric stabilization can be achieved in several ways:

- power supply with a rectifier with a saturable core,
- thyristor-controlled silicon rectifier system and inductor to damp high frequency transient current variations leading to erratic movement of the arc root at the anode surface,
- additive stabilization resistance of the electric cables in the water-cooled circuits of the torch,
- several gas- or liquid-stabilized arc configurations.

3.3.2.1 Wall-stabilized Arcs

Wall-stabilized designs consist of a solid and a hollow electrode, and the plasma gas, instead of constricting the arc, becomes an integral part of it, filling the nozzle from wall to wall. Since for a cylindrical symmetric arc with fixed temperature boundary and therefore predominant thermal conduction losses the whole discharge is determined for a given current I , the field strength is determined almost entirely by R (thus $E \propto 1/R$), and the axial temperature T_0 increases with the input power per unit length, EI . Since with forced cooling the effective wall radius decreases, for a given current EI and T_0 increase. This explains the apparent anomaly that with enhanced cooling the temperature increases.

3.3.2.2 Convection-stabilized Arcs

In the wall-stabilized arc the discharge fills the major portion of the internal nozzle tube space, and for large nozzle diameters the arc can be wall-stabilized only if very high currents and arc temperatures exist. The large tube constitutes essentially the condition of a free-burning arc that requires no external stabilization at low currents.

Stabilization in this case is achieved by convective gas flow. The energy equation consists of a conductive and a convective term:

$$\sigma E^2 = \nabla(-k\nabla T) + \rho v_0(C_p \nabla T + \nabla \Phi), \quad (3-30)$$

where C_p is the specific heat at constant pressure, k is the thermal conductivity of the plasma gas, and v_0 is the volume of the tube space. The convective term makes it possible for arc stabilization to occur without the maintenance of thermal conduction to the wall boundaries. In the outer regions of a cylindrically symmetric arc the energy flow is constant and equals the total energy input, E , but the balance between the conductive and convective terms changes as the radius increases. Ultimately, before the wall boundaries are reached, the convective term predominates the conductive term, and the thermal conduction becomes negligible. The convective gas thus acts effectively as a boundary wall and the arc is convection-stabilized. From Eq. 3-30 it can be gathered that energy is transported by mass flow only when the flow has a component in the direction of the temperature or gravity gradient. In a *vertical arc* a steady-state is established between the forces of gravity and viscosity, and the gas moving upward flows into the lower arc portion thus cooling this region. When leaving the upper arc region, however, the flow heats the arc since the flow is against the temperature gradient. Thus convection tends to broaden a vertical arc at the top. In the case of a *horizontal arc* a similar process occurs where convection produces arc bowing [26].

In the *vortex stabilized arc*, the electrodes are made from tungsten, carbon or other materials, and may be water-cooled. Gas is fed tangentially into the chamber between the electrodes to produce an intense vortex within the hollow electrode, which usually is the cathode. Thus, the arc is forced to travel from the solid anode out of the nozzle and then strike back to the front face on the hollow cathode. Since the arc channel is imbedded in the vortex flow intense convective cooling of the arc fringes occurs. The media producing the vortex can be liquids (water; Gerdien arc [18]) or gases (high field-strength hydrogen arc). Modified arrangements of vortex-stabilized arcs rely on a rotating discharge vessel ('Wälzbogen') or a torus stabilized by a toroidal vortex [3]. In some plasma reactors to synthesize ultrafine particles an argon gas shroud is used to convection-stabilize the plasma arc [27].

3.3.2.3 Electrode-stabilized Arcs

When the electrode separation is small (1 mm) and the electrode mass is large, it is possible for the arc to be dominated and thus stabilized by the energy losses to the electrodes. In this case the electric field and current distribution may be symmetric about the midplane of the electrode system [26]. The arc contour is elliptic with the electrodes acting as focal points.

3.3.2.4 Other Stabilization Methods

The *gas-sheath stabilized plasma jet* is between a solid tungsten cathode and a hollow water-cooled copper anode. The arc remains within the nozzle and is prevented from

striking the wall by a gas sheath that is much thicker than the arc diameter. Vortex flow is not used, and the position of the arc is determined by the gas flow pattern and the turbulences.

In a *magnetically-stabilized jet*, the arc strikes radially from an inner to an outer electrode. Gas is blown axially through the annulus. The arc is rapidly rotated by a magnetic field, so that its position at various times resembles the spokes of a wheel. With this design, high pressure jets can be created without erosion of the electrodes. Since the external magnetic field interacts with the charged particles in the plasma the arc is magnetically stabilized in a cross-flow: the drag force acting on the arc is effectively compensated by the Lorentz force ($\mathbf{j} \times \mathbf{B} \propto C_D^2$), and the arc actually behaves similarly to a solid body with respect to its response to drag. The arc cross-section assumes the shape of an ellipse with its major axis perpendicular to the jet axis. Within this elliptic contour two symmetric vortices with opposite directions of rotation are formed. Magnetically-stabilized arcs are extensively used for applications in arc gas heaters including plasmatrons, circuit breakers, arc furnaces, arc welding devices, and plasma propulsion systems.

3.3.3 Temperature and Velocity Distribution in a Plasma Jet

3.3.3.1 Turbulent Jets

The complex magnetohydrodynamic interactions within a plasma jet affect profoundly the macroscopic plasma parameters temperature and velocity. There exist strong temperature and plasma velocity gradients in a plasma arc jet. Figure 3-25 shows the temperature (a) and the axial velocity v_z (b) of a typical d.c. argon/hydrogen arc along the direction of propagation of the plasma jet, z [28]. The isotherms show clearly that the maximum temperature exists in the core of the jet close to the nozzle exit ($z = 0$) and the center line ($r = 0$). This very hot region is followed by a transitional region in which the plasma temperature falls rapidly to less than 3 000 K at $z = 80$ mm. Eventually there is the fully developed region in which the gas temperature decreases rather gradually by mixing with entrained cold ambient air. The radial temperature profile is extremely steep in the core region with temperature gradients of more than 4 000 K over the distance $r = 1$ mm. It is this very steep temperature gradient that makes difficult the problem of complete heating of the powder particles (see Chap. 4) and thus necessitates close control of particle size distribution and injection conditions into the plasma jet. The extremely large radial and axial temperature gradients require that in order to properly melt them, the injected particles should travel close to the center line. Also, the axial velocity isopleths indicate a fast velocity decay away from the point of injection close to the nozzle exit. To measure the velocity of the plasma, small amounts of fine alumina particles (3 μm diameter) were injected as tracers under the assumption that they do not influence the flow conditions and the temperature field. The radial velocity distribution at $z = 5$ mm in an atmospheric argon jet is shown in Fig. 3-26 for an arc current of 286 A. Figure 3-27 shows the associated radial temperature distributions at $z = 5$ mm for different currents ranging from 147 to 268 A. The tracer particles were injected at a rate of 0.18 g s^{-1} . Figure 3-28 finally indicates the symmetric enthalpy distri-

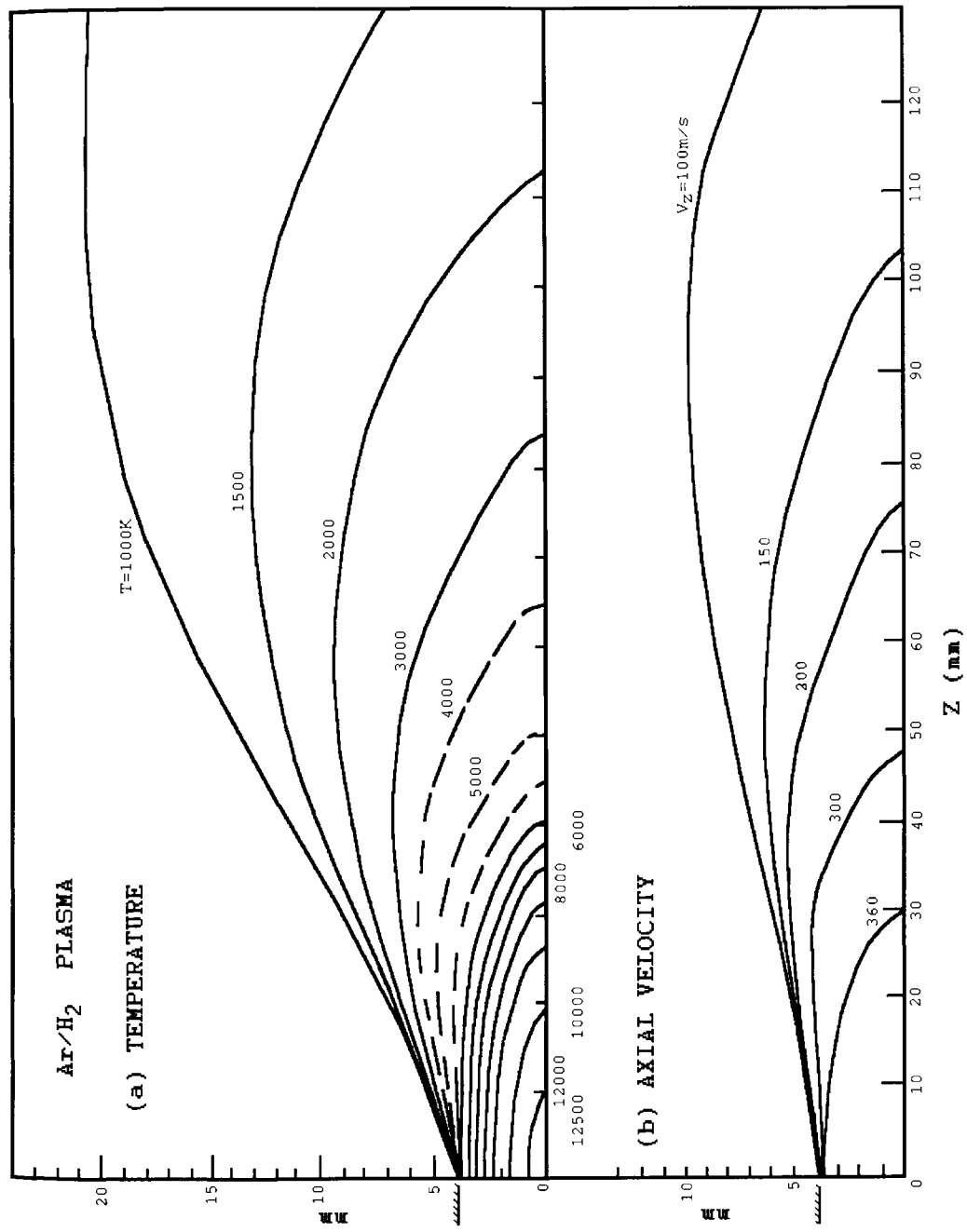


Figure 3-25. Temperature (a) and axial velocity (b) distribution of a typical d.c. argon/hydrogen plasma arc along the direction of propagation, z [28].

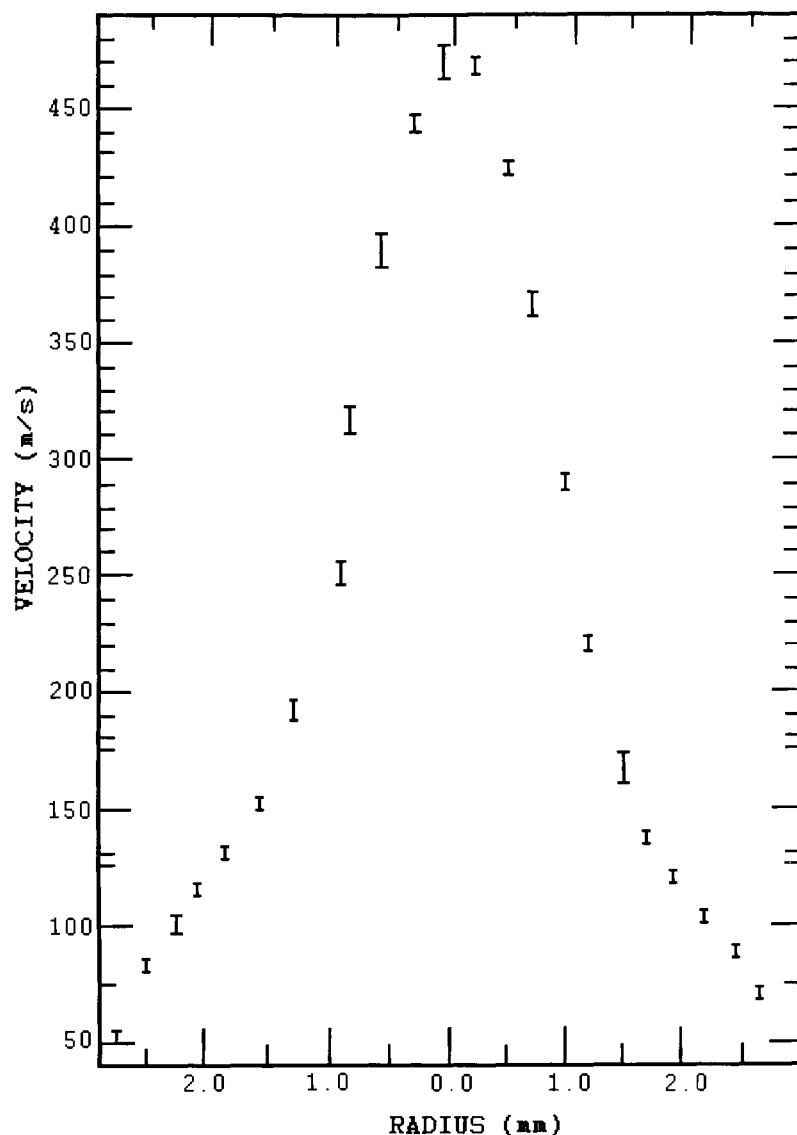


Figure 3-26. Radial velocity distribution at $z = 5$ mm in an atmospheric argon plasma jet at an arc current of 286 A [29].

bution in kJ kg^{-1} [29]. Temperatures, velocities and enthalpies can be measured with sophisticated probing techniques (for details see Sec. 3.4).

The symmetry of the distributions shown in Figs 3-25 to 3-28 suggests the picture of a quiet, undisturbed and essentially laminar flow within the plasma column. This, however, is far from reality. As the gas flow increases as required in energy-efficient high temperature plasmatrons, large scale flow structures evolve that are dominated by turbulences and entrained eddies of cold surrounding air. In particular, the large

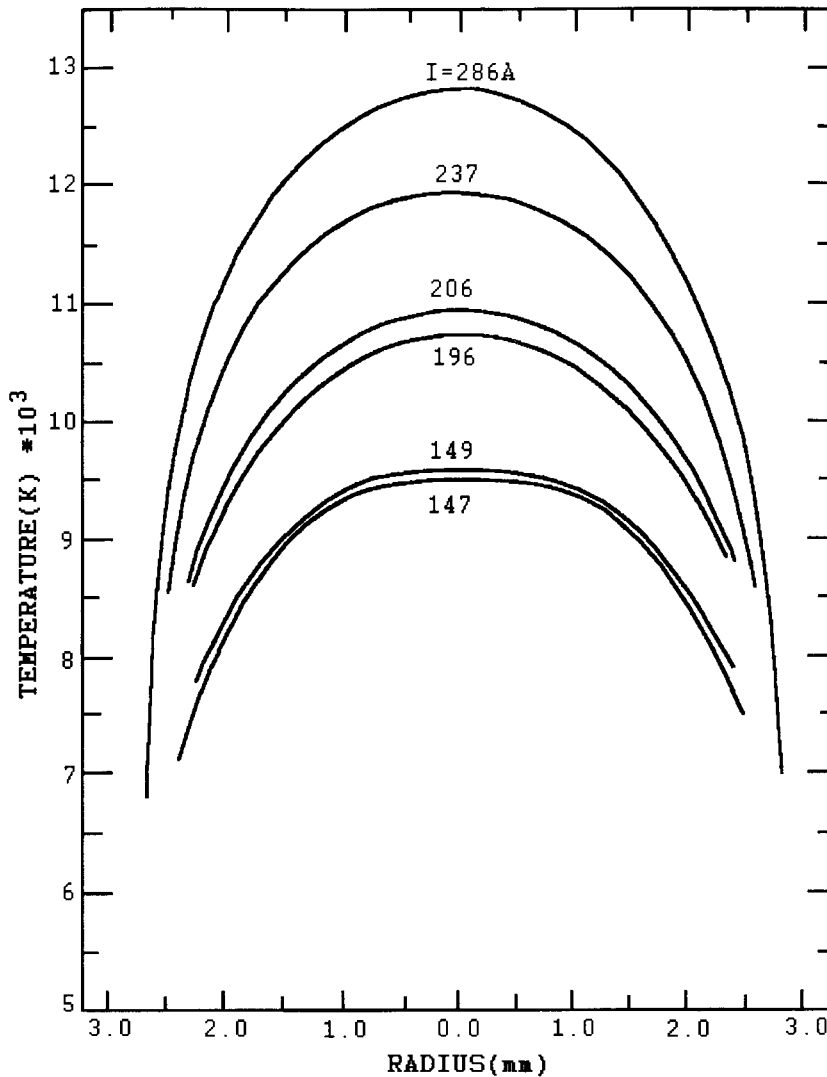


Figure 3-27. Radial temperature distribution at $z = 5$ mm in an atmospheric argon plasma jet at various currents [29].

difference in density of the plasma gas and the atmospheric air increases the degree of turbulence. Figure 3-29 shows the complex structure of a plasma jet approaching transition from a laminar to a fully turbulent flow regime. Following Pfender *et al.* [30], the plasma jet leaving the nozzle encounters a steep laminar shear at the jet's outer edge that causes a rolling-up of the flow around the nozzle into a ring vortex. This vortex is pulled downstream by the gas flow, and allows thus the process of ring vortex formation to continue. The subsequently formed rings have the tendency to coalesce forming larger vortices. Perturbations of the latter lead to wave instabilities.

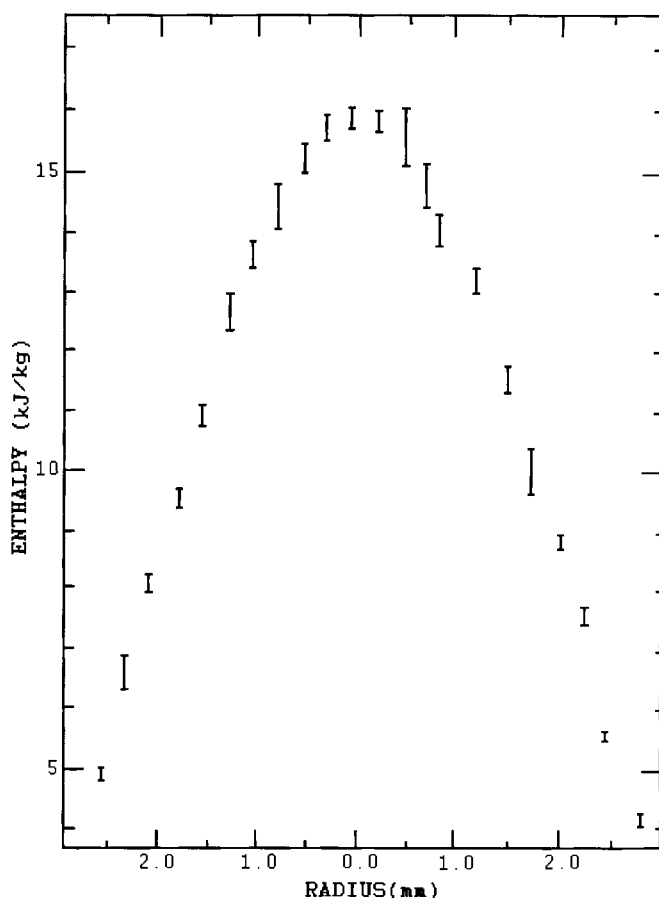


Figure 3.28. Enthalpy distribution at $z = 5$ mm in an argon plasma jet at 286 Å [29].

Finally, the vortex interactions result in a total breakdown of the vortex structure into large scale eddies and the onset of turbulent flow⁴. Since the entrained eddies of cold air have a density and inertia much higher than that of the high temperature plasma gas, the cool eddies are left behind when the hot plasma gas is accelerated around them. Thus initially little mixing occurs. With increasing distance from the nozzle exit, however, the larger eddies are breaking down into smaller and smaller ones, and mixing and diffusion at the eddy boundaries increase. Eventually the mixing process reaches the center line of the jet, and destroys the plasma core. At this point the jet undergoes the transition to a fully turbulent flow regime. As a result, both the temperature and the velocity of the jet decay. The consequences of this process for the melting behavior of injected powder particles will be explored in Chap. 4.

⁴This has been humorously described, in verse, by Lewis F. Richardson [31]: 'Big whorls have little whorls/Which feed on their velocity,/And little whorls have lesser whorls/An so on to viscosity'. This is a take-off on the well-known verse by Jonathan Swift: 'So, naturalists observe, a flea/Hath smaller fleas that on him prey;/And these have smaller fleas to bite 'em,/And so proceed *ad infinitum*.'

3.3.3.2 Quasi-laminar Jets

To modify the turbulent d.c. plasma jet towards quasi-laminar flow condition a so-called Laval nozzle is attached to the front of the anode (Fig. 3-30). The powder is injected within this nozzle at different ports whose positions depend on the melting

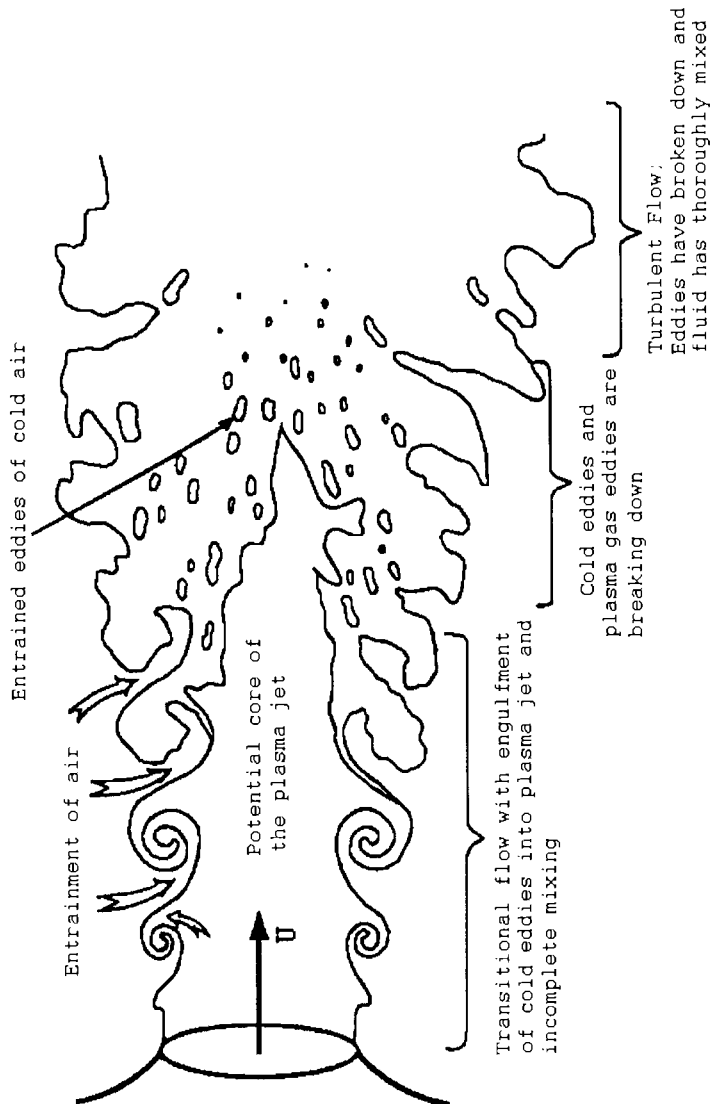


Figure 3-29. Complex structure of a plasma jet approaching transition from laminar to fully turbulent flow regime [30].

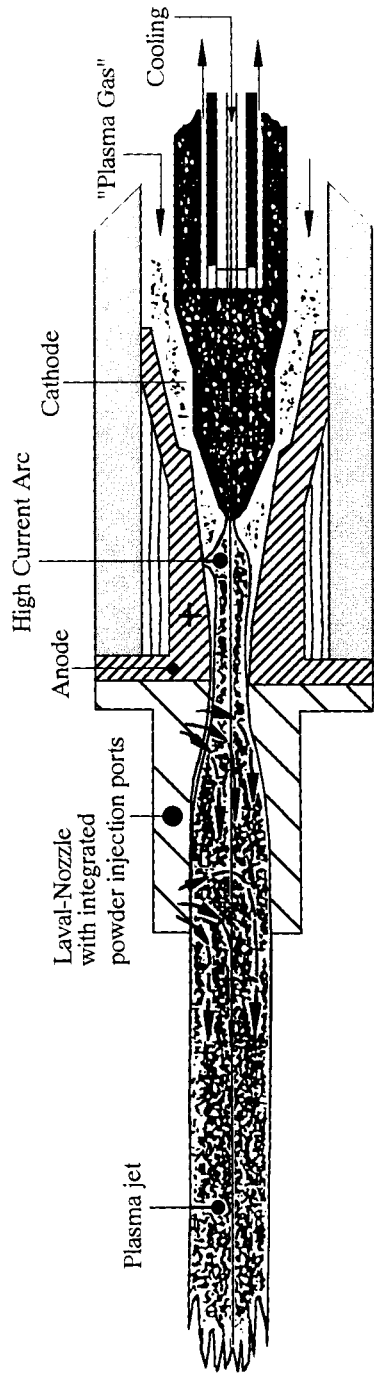


Figure 3-30. Principle of the DLR-VPS plasmatron with attached Laval nozzle and integrated injection ports (DLR: Deutsche Forschungsgesellschaft für Luft- und Raumfahrt) [32].

temperature of the material to be plasma-sprayed. One port is located close to the nozzle root where dense, hot and relatively slow plasma conditions prevail that aid in effective melting of materials with high melting temperatures. The other port is close to the nozzle exit [32]. Owing to the special layout of the inner nozzle contour [33] a long quasi-laminar plasma jet is produced that reduces the reaction between spray powder and surrounding residual oxygen by essentially two mechanisms. First, the residence time of the particles in the jet is strongly reduced (< 1 ms for alumina particles $-22 + 5.6 \mu\text{m}$) since the plasma jet acquires a velocity of $> 800 \text{ m s}^{-1}$ (50 mbar chamber pressure, 600 A, 6 V, Ar/H₂ @ 60/5 SLMP (Standard liter per minute)) [32]. Second, because of the laminar characteristics of the plasma jet the powder particles are carried close to the central jet axis so that their divergence is low. Consequently, the particles have a lesser chance of reacting with residual oxygen surrounding the jet and being entrained by the remaining turbulent eddies. Thus the level of impurities within the deposited coating can be better controlled. This low divergence ($> 60\%$ of the particles are deposited within a circle of 20 mm diameter at a stand-off distance of 300 mm) leads naturally to an improved deposition efficiency and thus to a more economical operation of the plasmatron.

3.4 Plasma Diagnostics: Temperature, Enthalpy and Velocity Measurements

Vardelle *et al.* [34] developed a highly sophisticated system to measure, simultaneously, plasma temperature field, plasma velocity field, particle number flux, particle velocity distribution, and particle temperature distribution. Figure 3-31 shows the equipment. Before discussing the details of the results of these measurements, the physical background of the diagnostic methods will be briefly reviewed. In this chapter, only plasma diagnostics, i.e. plasma temperature and velocity field measurements will be covered. Particle diagnostics will be treated in Chap. 4.

3.4.1 Temperature Measurements

3.4.1.1 Spectroscopic Methods

In the plasma jet with temperatures approaching 15 000 K conventional temperature measuring techniques are unsuccessful. Plasma temperatures can be measured assuming local thermodynamic equilibrium (LTE) using atomic or molecular spectroscopy. These methods have the advantage of high spatial resolution but can be applied only if the temperatures exceed about 6000 K. The plasma temperature field can be approximately deduced from the volumetric emission coefficient $\varepsilon_L(r)$ of suitable atomic emission lines, such as NI (746.8 nm) for a nitrogen plasma, and Ar I (763.5 nm) or Ar II (480.6 nm) for an argon plasma. The local emissivity ε_L is

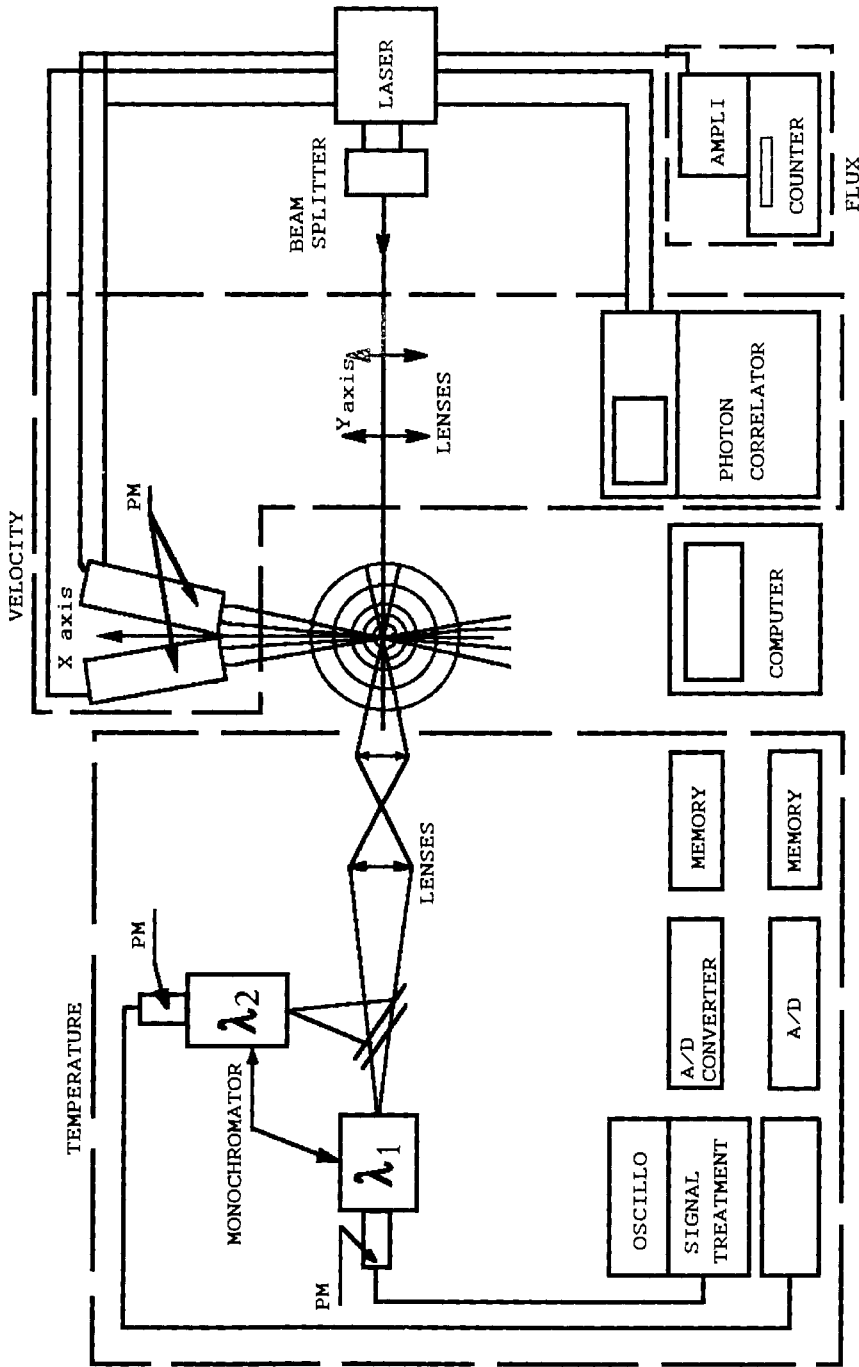


Figure 3-31. System for measuring simultaneously plasma temperature field, plasma velocity field, particle number flux, particle velocity distribution, and particle temperature distribution [34].

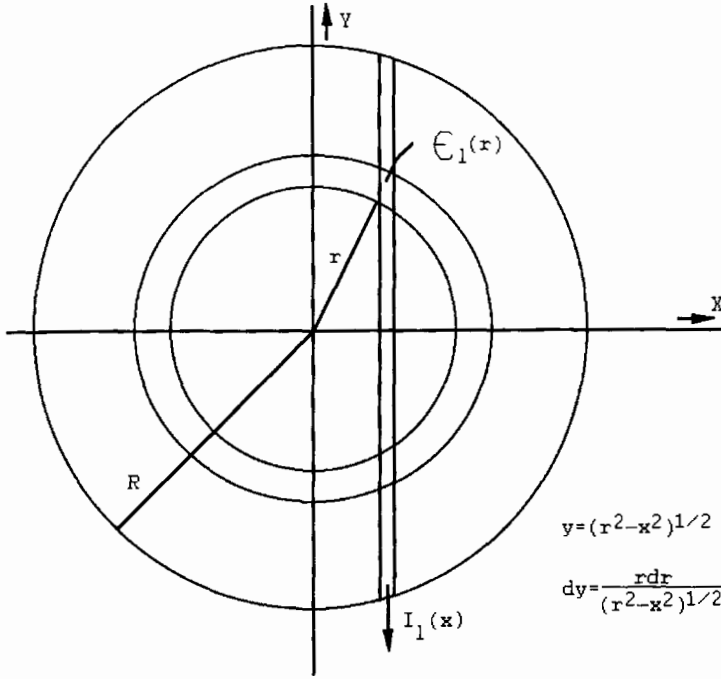


Figure 3-32. Geometric relationship of a plasma volume element used to measure local plasma emissivities ϵ_l by Abel's inversion [3].

obtained from the observed side-on intensity $I_L(x)$ (Eq. 3-31) by Abel's inversion (Eq. 3-32) according to [3]:

$$I_L(x) = 2 \int \epsilon_L(r) dy = 2 \int \epsilon_L(r) r dr / (r^2 - x^2)^{1/2} \quad (3-31)$$

$$\epsilon_L(r) = -(1/\pi) \int [I_L(x)/(x^2 - r^2)^{1/2}] dx. \quad (3-32)$$

Figure 3-32 shows the geometric relationships of a plasma volume element of dimensions dx and $dy = r dr / (r^2 - x^2)^{1/2}$.

If oxygen is present in the plasma, the temperature can be measured using the rotational states of oxygen molecules and measuring the intensity of the rotation bands (Schumann–Runge bands) in the 336–351 nm range.

Using monochromators equipped with holographic gratings, and x - y stepping-motors to control the displacement of the plasma jet the precision of the measurement is within 5% [35]. Using the temperature determined from the local (relative) emission coefficient, the absolute emission coefficient $\epsilon_{L,abs}$ can be obtained as

$$\epsilon_{L,abs} \propto \exp(-E_s/kT) h\nu. \quad (3-33)$$

From the ratio of the absolute emissivities of two spectral lines, $\varepsilon_{L1}/\varepsilon_{L2} \propto \exp[(-E_{s1} - E_{s2})/kT]$, the relative error of the temperature measurement can be estimated as

$$\Delta T/T = \Delta(E_{s1} - E_{s2})/E_{s1} - E_{s2}. \quad (3-34)$$

With temperature measurements of this type the temperature distribution shown in Fig. 3-25 was measured [28].

3.4.1.2 Two-wavelengths Pyrometry

The temperature of a plasma can also be measured by two-color pyrometry at two wavelengths [34, 36]. While the spectroscopic methods to measure the plasma temperature can be performed in an ‘empty’ plasma, i.e. without the presence of radiating particles, the two-color (wavelength) pyrometry requires seeding particles such as alumina particles of small diameter (3 μm). Figure 3-31 shows the equipment used by Vardelle *et al.* [34] to measure plasma temperatures. The light scattered by the moving particles was observed off-axis by two photomultipliers directed at angles of 81° and 99° to the optical axis of the laser beam. Measurements were made of the in-flight particle emission at two wavelength, 680 and 837 nm. A monochromator placed in front of each of the photomultipliers was used to define the wavelength of the particle emission by filtering out the background plasma radiation. It is crucial to select wavelengths that are unaffected by neighboring gas emission lines and also to assume that the emissivity of the particles does not change with the wavelength, i.e. that conditions of a grey body radiation prevail. In this case the color temperature of the particles corresponds to their true surface temperature, and the assumption is thus satisfied that the tracer particle temperature reflects faithfully the plasma temperature. By calibration using a tungsten lamp the statistical information provided by the particle emission at the two selected wavelengths can be converted into statistical information about the particle surface, and thus the plasma temperature distribution. It should be emphasized that these assumptions are only satisfied under low-loading conditions, i.e. if local cooling of the plasma due to the presence of particles can be neglected (see Sec. 4.4.1).

Under other simplifying assumption, for example uniform emissivity of the ideally spherical particles over their entire surface area and constant surface temperature along the entire path of observation, the particle temperature can be calculated from

$$T_P = \{C(\lambda_1 - \lambda_2)/\lambda_1\lambda_2\} / [\ln(I_{\lambda 1}/I_{\lambda 2}) + 5 \ln(\lambda_1/\lambda_2)], \quad (3-35)$$

where λ_i denote the wavelengths, $I_{\lambda i}$ the measured spectral intensities, and C is a constant. While this technique shows a vast improvement over the spectroscopic methods based on line emissions of gas atoms, there are three principal limitations [34]. The first relates to the presence of background plasma radiation, in particular close to the core of the plasma jet. Therefore no measurements can be made on particles whose trajectories are close to the central axis of the jet. The second limitation results from the rapid decrease of the emission intensity with decreasing surface

temperature. As a consequence the lower temperature limit for successful measurements is around 1 800 K. Finally, the third limitation is due to the long field of depth that requires extremely low particle loading conditions in order to avoid saturating the photoelectric system.

3.4.2 Velocity Measurements

The plasma velocity can be measured with either a Pitot tube probe technique [37, 38] or with a time-of-flight two-point laser anemometer [39, 40]. The first method relies on rather stringent simplifying assumptions made about the local Reynolds numbers, plasma densities and plasma viscosities, the second one is limited by laser beam diffraction, statistical bias towards high velocity particles, inhomogeneous seeding across zones of steep velocity and temperature gradients, and slip between the particle and the plasma velocities which, however, can be reduced by reduced particle size. Despite these limitations both methods are frequently used to estimate plasma jet velocities in order to optimize plasma spray conditions and coating properties.

3.4.2.1 Enthalpy Probe and Pitot Tube Techniques

A water-cooled so-called enthalpy or Grey probe is immersed in a plasma jet to extract a sample of gas. In order to minimize the disturbance of the plasma jet the dimensions of the probe should be as small as possible. Today probes with a diameter as small as 1.5 mm can be used. A tare measurement is required to account for the external heat transfer to the probe [41]. This is accomplished by interrupting the gas stream (no-flow regime) through the Grey probe and measuring the increase of the temperature of the cooling water due to heat transfer from the surrounding plasma. The 'tare' measurement yields

$$\Delta Q_{\text{nf}} = (dm_c/dt)c\Delta T_{\text{nf}}, \quad (3-36)$$

with ΔQ_{nf} = difference in heat content at no-flow condition, dm_c/dt = mass flow rate of the coolant, c = specific heat, and ΔT_{nf} = temperature rise at no-flow conditions. After opening the sampling valve of the probe, the amount of heat acquired by the probe increases to

$$\Delta Q = (dm_g/dt)(h_1 - h_2) + \Delta Q_{\text{nf}} = (dm_c/dt)c\Delta T, \quad (3-37)$$

with dm_g/dt = mass flow rate of the plasma gas, h_1 = enthalpy of the gas at the inlet temperature, and h_2 = enthalpy of the gas at standard conditions (room temperature). From Eq. 3-37 follows the expression for the stagnation enthalpy:

$$h_1 = h_2 + [(dm_c/dt)c]/(dm_g/dt)(\Delta T - \Delta T_{\text{nf}}). \quad (3-38)$$

The temperatures are measured with thermocouples, the cooling water mass flow rate with a rotameter or a similar device, and the gas mass flow rate with either a

sonic orifice or a mass flow meter. In the case of a sonic orifice the mass flow rate of the gas is, according to [41]

$$dm_g/dt = C_A \left(p_0/T_0^{1/2} \right) \left[(M/R)\gamma(2/\gamma + 1)^{(\gamma+1)/(\gamma-1)} \right]^{1/2}, \quad (3-39)$$

where C_A = effective cross-sectional area of the orifice, p_0 and T_0 = pressure and temperature immediately upstream of the orifice, and γ = adiabatic exponent ($= c_p/c_v$).

The Grey probe cannot be operated continuously but can be used during the no-flow regime as a Pitot probe to measure the stagnation pressure, p_{st} and according to Bernoulli's theorem, the free-stream velocity of the plasma jet:

$$v = [2(p_{st} - p_{atm})/\rho]^{1/2}, \quad (3-40)$$

where the plasma gas density ρ must be determined from thermodynamic tables using the plasma temperature determined by the methods described in Sect. 3.4.1. In more detail, for an argon plasma the gas density ρ can be approximated by $\rho = X_{Ar}\rho_{Ar} + X_{Air}\rho_{Air}$. X_{Air} can be determined with a lambda-type oxygen sensor probe based on stabilized zirconia, and ρ_{Ar} and ρ_{Air} from thermodynamic tables. As a check for the validity of the plasma velocity measurement the total mass flow rate of argon can be used according to [3]

$$dm_{Ar}/dt = 2\pi \int (X_{Ar}\rho_{Ar}v)r dr \quad (3-41)$$

integrated between the boundaries 0 and r_0 that define the radius of the plasma jet. The energy flux through a given cross-section of such a jet can be expressed by

$$Q = 2\pi \int \rho(r)h(r)v(r)r dr, \quad (3-42)$$

where $\rho(r)$, $h(r)$ and $v(r)$ are, respectively the radial density, enthalpy and velocity profiles of the plasma jet within the boundaries 0 to r_0 . Figure 3-33 shows the decay of the axial plasma velocity for the currents of 450 and 600 A, and various argon flow rates between 23.6 and 47.2 l min⁻¹. For arc currents around 450 A the change in flow rate has only a small effect on the plasma velocity and its axial decay. An explanation for this may be found by assuming two opposing effects that affect the flow velocity with increasing argon flow rate [41]. Increasing gas flow rates require an increase of the plasma velocity in order to satisfy the continuity equation of mass. This can be achieved only if the plasma temperature remains constant. Higher gas flow rates, however, reduce the temperature thus leading to higher plasma gas densities, and consequently to lower plasma velocities at constant cross-section of the plasma jet. These two opposing phenomena appear to compensate each other at lower arc currents. At higher currents the length of the jet varies considerably with varying gas flow rates, and compensation cannot be achieved anymore. For details on the mea-

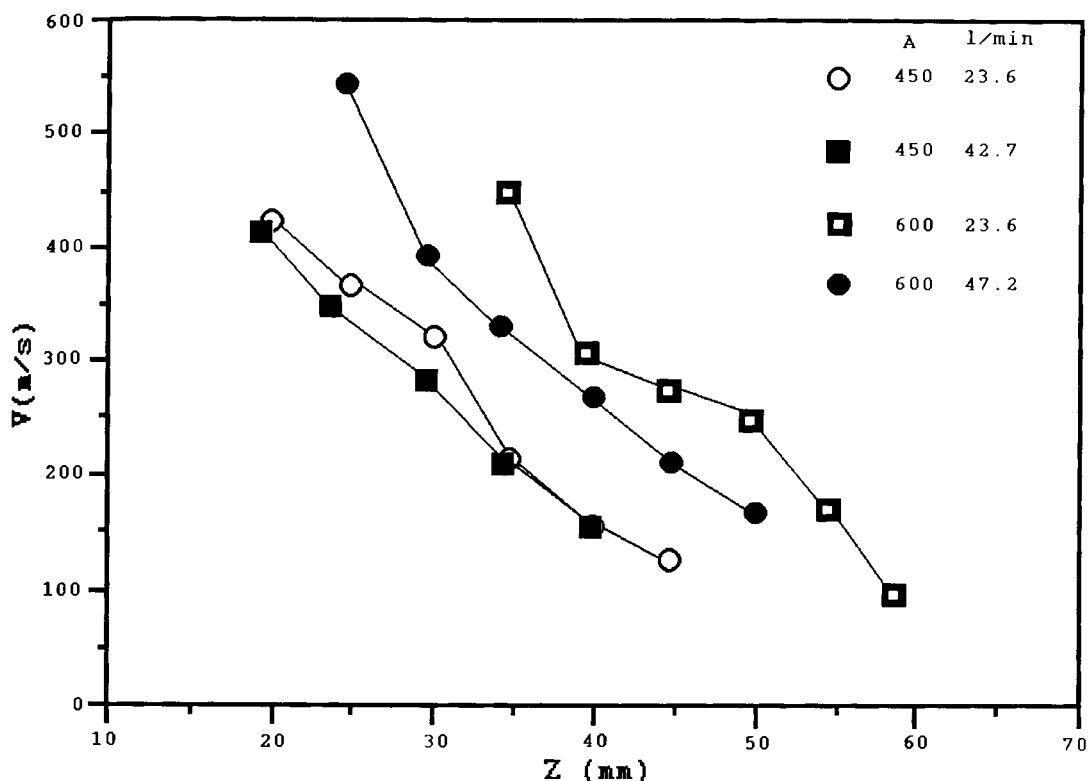


Figure 3-33. Axial velocity decay of an argon plasma measured by an enthalpy probe [41].

surement techniques and typical results the reader is referred to the paper by Capetti and Pfender [41].

3.4.2.2 Laser Doppler Anemometry (LDA)

One of the standard plasma velocity measurement techniques, LDA has emerged as a powerful method of plasma diagnostics. Since it is an optical method it does not interfere with the flow of the plasma. However, the plasma jet must be seeded with very fine powder particles, usually alumina or zirconia [42], carbon or silicon [43] or silicon nitride [44]. Also, a laser pulse of 15 ns duration that produced a plasma drop of high intensity has been used as a tracer [45]. The LDA technique can be used in two modes: *fringe* and *two-point measurement modes*. While the former is mostly used for velocity measurements of larger powder particles in the plasma jet (see Sect. 4.5.1) the latter is being used to measure the supposedly undisturbed plasma velocity via the observation of very small tracer particles [46]. It is essential that the particles must be small enough as not to interfere with the plasma flow but large enough as to not evaporate during their residence time in the hot plasma jet. Also, the method of

seeding is of importance. Adding very fine powder through the powder injection port of a d.c. plasmatron leads to incomplete particle distribution and failure of the particles to penetrate the hot core of the jet. This can be avoided by passing a part of the plasma gas through a fluidized bed consisting of a mixture of very fine and coarse powders [42]. The passing gas extracts selectively the fines and carries them over into the jet.

In the *two-point LDA* measurements [47] the laser beam, after passing through a beam splitter, is focused using a lens of a focal length of 16 mm to form two coherent light beams of 50 μm diameter and 400 μm apart. Those two beams are projected in the plasma jet by a second lens of a focal length of 50 mm (Fig. 3-34). Furthermore each beam is focused onto the entrance slit of two photomultipliers equipped with a narrow-band interference filter (514.5 nm, $\Delta\lambda = 0.25$ nm). By cross-correlating the electrical output of the photomultipliers via a photon correlator, the particle (= plasma) velocity can be determined. When a particle crosses the two beams in the cylindrical measuring volume of 0.6×1.1 mm, it produces two successive light bursts. Their time delay can be used to calculate the velocity.

In the *fringe mode* measurements the two laser beams produced by the beam splitter are focused and allowed to interfere thus forming an interference fringe pattern in the flow region. The interfringe spacing is

$$\delta = \lambda / [2 \sin(\phi/2)], \quad (3-43)$$

where λ = wavelength of the incident laser beam and ϕ = angle of interception of the two laser beams.

When a particle traverses the point of intersection of the two beams a light burst is being produced modulated at a frequency that is a function of its velocity and the fringe spacing δ . The signal output of the photomultiplier is being used to determine the time required for the particle to pass a given number of fringes. After acquisition of a sufficient number of measurements, statistical analysis is carried out giving the minimum velocity, maximum velocity, mean velocity and standard deviation of the particle velocities. From this the probability distribution function is obtained by dividing the velocity window into a number of segments and then counting the number of particles falling into each segment. Eventually the normalized probability distribution function can be calculated from

$$\text{Pr}(v_j) = (m_j/v_j) / \sum (m_j/v_j), \quad (3-44)$$

where m_j = number of particles with a velocity between v_j and v_{j+1} .

Figure 3-35 shows the profiles of the axial plasma velocity (bottom) and the intensity of turbulence in axial and radial directions (top) along the centerline of an Ar/N₂ plasma jet (80 vol% Ar, $dm_g/dt = 23.6 \text{ l min}^{-1}$, $I = 400 \text{ A}$, $U = 38 \text{ V}$, $E = 15.2 \text{ kW}$) [42]. The centerline plasma velocity is 250 m s^{-1} and shows a rapid drop with increasing distance z from the nozzle. Contrary to this, the intensity of turbulence, defined as v'/v , i.e. the ratio of the standard deviation of the velocity to the mean velocity (Fig. 3-35, top) first increases with increasing distance from the nozzle to about 40% at $z = 40 \text{ mm}$, and then decreases gradually. This is consistent

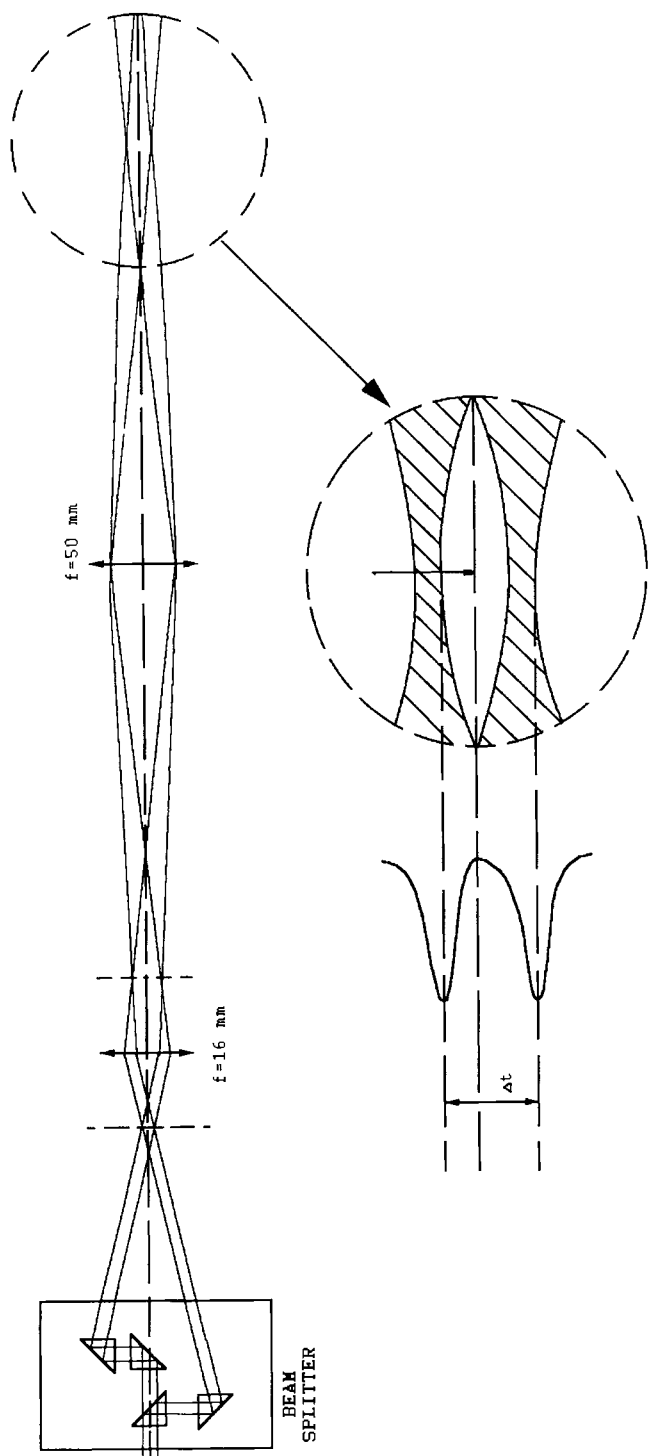


Figure 3-34. Experimental setup of a two-point laser Doppler anemometer (LDA) according to [28].

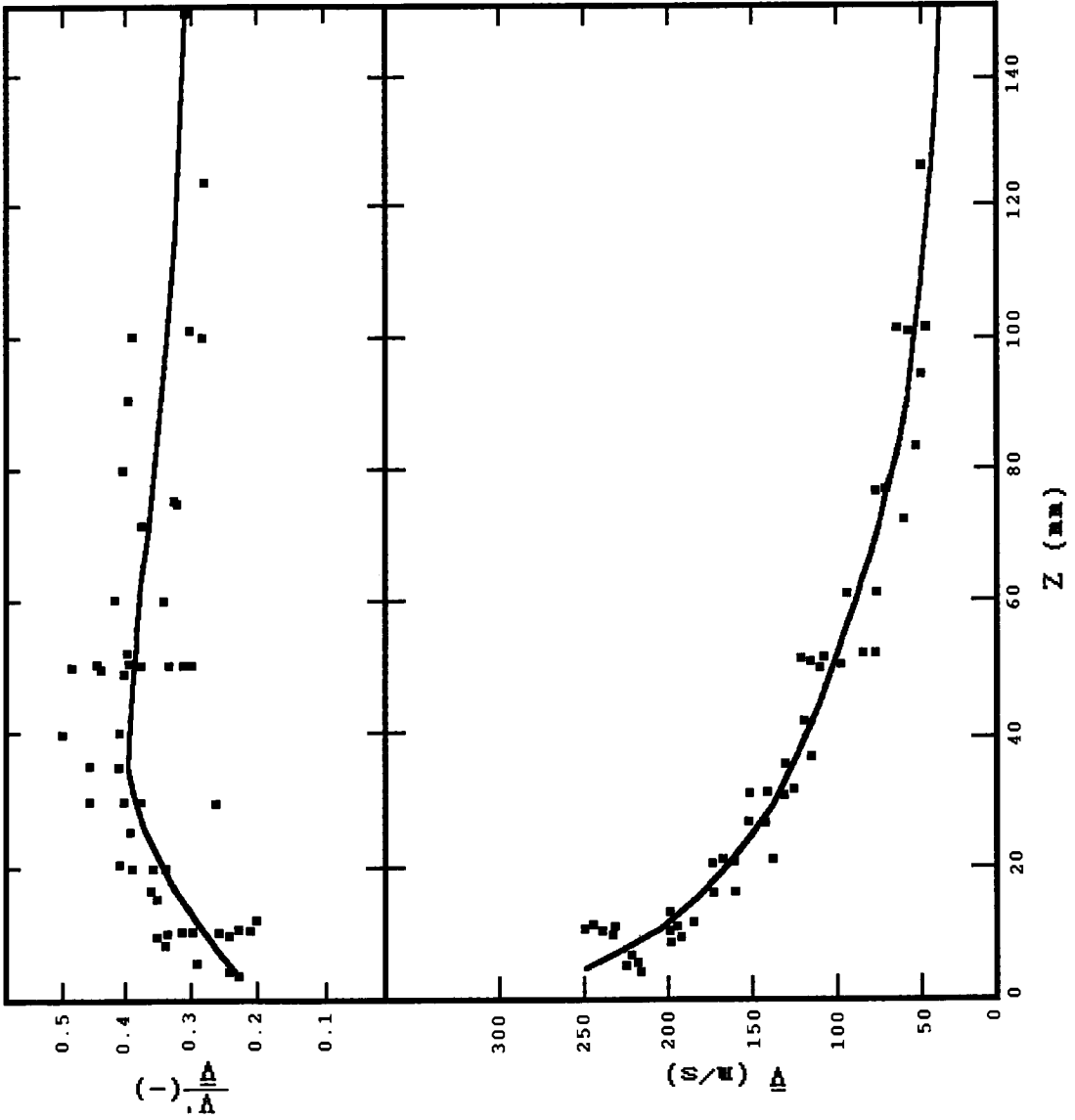


Figure 3-35. Plasma and particle velocities (bottom) and intensity of turbulence (top) along the centerline of an argon/nitrogen (80 vol% argon) plasma jet [42].

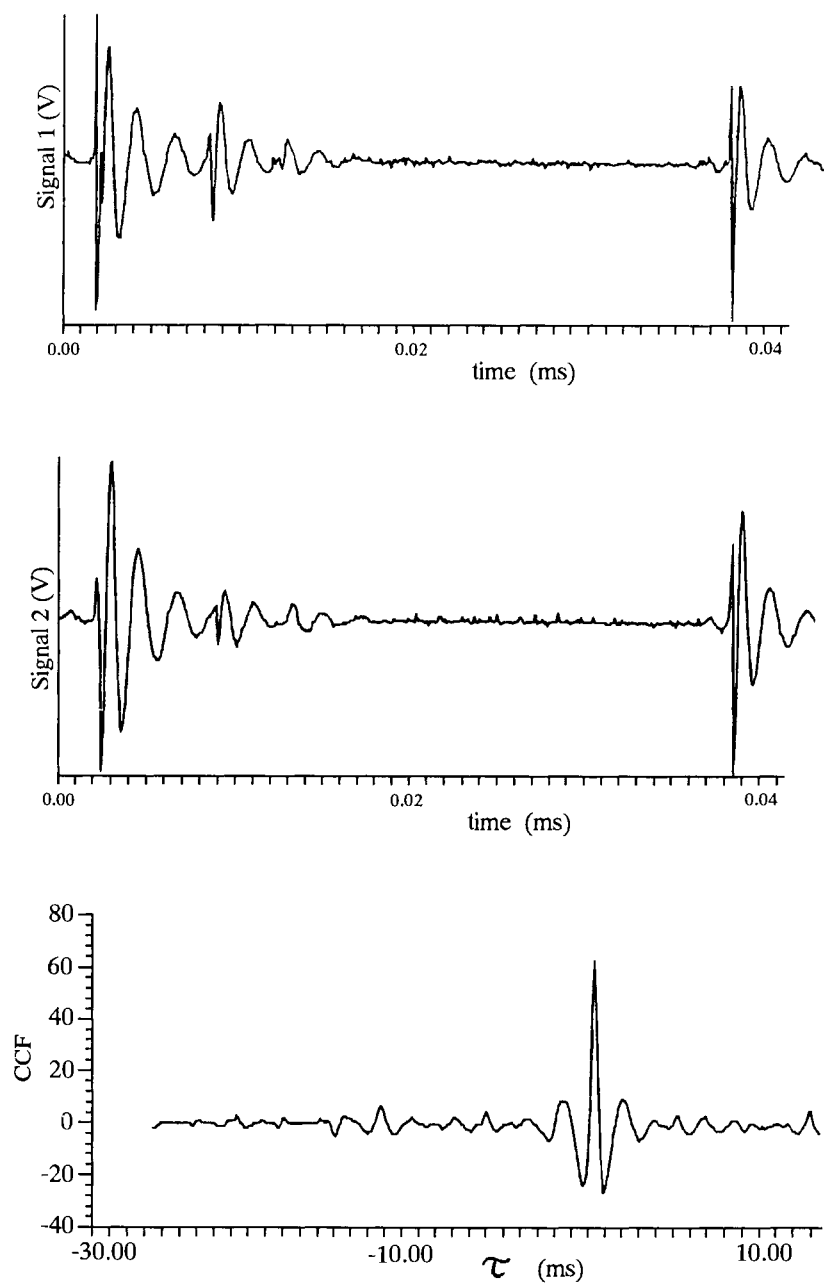


Figure 3-36. Schematic of the cross-correlation method to measure particle velocities [48].

with other findings [28] of the formation of vortices immediately at the exit point of the plasma from the nozzle. This fact has led to approaches to reduce the turbulences in a plasma jet by appropriately formed nozzles such as axially symmetric Laval nozzles that produce parallel and uniform flow, and thus prevent entrainment of cold surrounding gas [33] (see Sect. 3.3.3.2).

3.4.2.3 Other Methods

A different approach to velocity measurements requiring less sophisticated equipment is the *cross-correlation method* [48]. It is based on the measurement of the travel time, t , of powder particles between two observation points in the particle flow direction separated by the distance s . The light emitted from the two observation points will be recorded by two photodiodes. To suppress the plasma light the electrical signals will be filtered through a band pass filter. Figure 3-36 shows two typical signals 1 and 2. Shifting the signals $s_1(t)$ and $s_2(t)$ against each other by a variable time difference τ yields a maximum similarity for $\tau = \tau_{\max} = t$. A quantitative expression of this similarity is the cross-correlation function $\text{CCF}(\tau)$:

$$\text{CCF}(\tau) = \phi_{s(1),s(2)}(\tau) = \int s_1(t) \times s_2(t + \tau) dt. \quad (3-45)$$

The position of the maximum of the CCF (Fig. 3-36, bottom) finally yields the velocity of the streaming plasma, $v = s/t$.

Kuroda *et al.* [49] developed a technique to measure particle velocities *in situ* using a spatial filter without the need of complex optical settings. The technique allows measuring the average particle velocity at dense particle loading. The spatial filter consists of five parallel flat plates at equal intervals, d . A parallel beam passing through the filter is focused into an optical fiber. The filter can be moved horizontally and vertically through a sliding table. When a particle radiating light traverses in front of the filter assembly, four peaks of light intensity are being detected by a photomultiplier placed at the end of the optical fiber. Analysis of the time interval of the peaks, t yields the particle velocity according to $v = d/t$, where d = known interval of the slits. Also, analysis of the power spectrum of the radiated light by an a fast Fourier transform (FFT) analyzer allows calculation of particle velocities by the relationship $f = v/d$, where f = peak frequency.

References

- [1] A. Rutscher, *Plasmatechnik. Grundlagen und Anwendungen. Eine Einführung*. Carl Hanser-Verlag, München, Wien, **1982**.
- [2] F. Cap, *Einführung in die Plasmaphysik I, Wiss. Taschenbücher*, Bd. 72. Akademie-Verlag Berlin, Pergamon Press Oxford, Vieweg + Sohn Braunschweig, **1970**.
- [3] M. I. Boulos, P. Fauchais, E. Pfender, *Fundamentals of Materials Processing using Thermal Plasma Technology*. Canadian University–Industry Council on Advanced Ceramic (CUICAC) Short Course, Edmonton, Alberta, Canada, 17–18 October, **1989**.

- [4] P. R. Smy, *Adv. Phys.* **1976**, 25(5), 517.
- [5] I. Langmuir, M. Mott-Smith, *Phys. Rev.* **1926**, 28, 727.
- [6] K. S. Drellishak, Ph.D. Thesis, Northwestern University, Evanstown, IL, **1963** (after [3.3])
- [7] H. Edels, *IEEE*, Vol. 108A, Paper No. 3498, **1961**.
- [8] W. Elenbaas, *Physica* **1934**, 1, 673.
- [9] G. Heller, *Physics* **1935**, 6, 389.
- [10] H. Maecker, *Z. Phys.* **1959**, 157, 1.
- [11] J. Mostaghimi, *Trans. 17th Workshop CUIAC* (Ed. R. B. Heimann), Quebec, Canada, 2 October, **1991**.
- [12] P. Proulx, J. Mostaghimi, M. I. Boulos, *Proc. ISPC-8*, Tokyo, Japan, **1987**, 1, 13.
- [13] M. Wehrli, *Helv. Phys. Acta* **1928**, 1, 323.
- [14] A. E. Guile, *IEEE Rev.* **1971**, 118, 1131.
- [15] J. D. Cobine, E. E. Burger, *J. Appl. Phys.* **1955**, 27, 895.
- [16] N. Sanders, K. C. Etermadi, E. Pfender, *J. Appl. Phys.* **1982**, 53(6), 4136.
- [17] M. Thorpe, *Chem. Eng. Prog.* **1989**, July, 43.
- [18] H. Gerdien, A. Lotz, *Wiss. Veröff. Siemens Werke* **1922**, 2, 489.
- [19] T. B. Reed, *J. Appl. Phys.* **1961**, 32, 821.
- [20] H. U. Eckert, *High Temp. Sci.* **1974**, 6, 99.
- [21] M. I. Boulos, M. I. *Pure Appl. Chem.* **1985**, 57(9), 1321.
- [22] J. Mostaghimi, P. Proulx, M. I. Boulos, *J. Plasma Chem. Plasma Proc.* **1984**, 4, 129.
- [23] R. W. Smith, Z. Z. Mutasim, *J. Therm Spray Technol.* **1992**, 1(1), 57.
- [24] T. Yoshida, T. Tani, H. Nishimura, K. Akashi, *J. Appl. Phys.* **1983**, 54, 640.
- [25] T. Takeyama, K. Fukuda, *Development of an all-solid state r.f.-r.f. thermal plasma reactor*, National Chemical Laboratory for Industry, Internal Report, AIST/MITI, Tsukuba, Japan, **1986**, 21(4).
- [26] W. Weizel, R. Rompe, *Theorie elektrischer Lichtbogen und Funken*, Barth, Leipzig, **1949**.
- [27] Y. Chang, R. M. Young, E. Pfender, *J. Plasma Chem. Plasma Proc.* **1989**, 9, 272.
- [28] M. Vardelle, A. Vardelle, P. Fauchais, M. I. Boulos, *AIChE J.* **1983**, 29, 236.
- [29] C. V. Boffa, E. Pfender, *Enthalpy probe and spectrometric studies in argon plasma jets*, HTL Tech. Rep. No.73, University of Minnesota, MN, USA, **1968**.
- [30] E. Pfender, W. L. T. Chan, R. Spores, *Proc. 3rd NTSC*, Long Beach, CA, USA, 20- 25 May **1990**, 1.
- [31] J. Gleick, *Chaos. Making a New Science*. Penguin Books, New York, NY, USA, **1988**.
- [32] R. Henne, M. v. Bradke, G. Schiller, W. Schurnberger, W. Weber, *Proc. 12th ITSC*, London, 4-9 June, **1989**, P112, 175.
- [33] K. Foelsch, *J. Aeronaut. Sci.* **1949**, March, 161.
- [34] M. Vardelle, A. Vardelle, P. Fauchais, M. Boulos, *AIChE J.* **1988**, 34, 567.
- [35] A. Vardelle, M. Vardelle, P. Fauchais, *J. Plasma Chem. Plasma Proc.* **1982**, 3, 255.
- [36] J. Mishin, M. Vardelle, J. Lesinski, P. Fauchais, *J. Phys. E.: Sci. Instrum.* **1987**, 20, 620.
- [37] J. Grey, P. F. Jacob, M. P. Sherman, *Rev. Sci. Instrum.* **1962**, 33(7), 738.
- [38] J. B. Cox, F. J. Weinberg, *J. Phys. D.: Appl. Phys.* **1971**, 4, 877.
- [39] G. Gouesbet, *Plasma Chem. Plasma Proc.* **1985**, 5, 91.
- [40] L. E. Drain, *The Laser Doppler Technique*, Wiley, New York, **1980**.
- [41] A. Capetti, E. Pfender, *Plasma Chem. Plasma Proc.* **1989**, 9, 329.
- [42] J. Lesinski, M. I. Boulos, *Plasma Chem. Plasma Proc.* **1988**, 8, 113.
- [43] J. Lesinski, M. I. Boulos, *Plasma Chem. Plasma Proc.* **1988**, 8, 133.
- [44] T. Yoshida, T. Tani, H. Nishimura, K. Akashi, *J. Appl. Phys.* **1983**, 54, 640.
- [45] C. J. Chen, *J. Appl. Phys.* **1966**, 37, 3092.
- [46] B. Richards (ed.), *Measurements of Unsteady Fluid Dynamic Phenomena*, McGraw Hill, New York, **1977**.
- [47] M. Vardelle, A. Vardelle, P. Fauchais, M. I. Boulos, *AIChE J.* **1982**, 29, 236.
- [48] M. Kloke, *Proc. 3rd Workshop 'Plasma Technology'*, Ilmenau, Germany, 22-23 June, **1995**.
- [49] S. Kuroda, T. Fukushima, S. Kitahara, H. Fujimori, Y. Tomita, T. Horiuchi, *Proc. 12th ITSC*, London, 4-9 June, **1989**, P27-1.

4 The Second Energy Transfer Process: Plasma–Particle Interactions

4.1 Injection of Powders

There are several ways to inject powder particles into the plasma jet. Figure 4-1 shows injection perpendicular to the jet at the point of exit of the jet from the anode nozzle (position 1), ‘upstream’ or ‘downstream’ injection at an angle to the jet axis (position 2), or injection directly into the nozzle (position 3). Upstream injection is used when increased residence time of the particles in the jet is required, for example to melt high refractory materials with high melting points. Downstream injection protects the powder material from excessive vaporization. Experiments with molybdenum and alumina coatings showed that the cohesion of coatings and their tensile strengths increase with oblique injection [1].

Also, experiments have been conducted with coaxial powder injection where the powder enters through a bore in the cathode, and is swept along the total length of the plasma jet for maximum residence time (position 4). This configuration, however, tends to disturb the smooth plasma flow and thus creates turbulences and eddies that may damage the nozzle walls. Problems may also occur with clogging the plasma paths with excess powder. A somewhat different approach has been taken by Maruo *et al.* [2] by feeding powder axially into the space between three thoriated tungsten cathodes set at 120° around the plasmatron axis. As three individual anode spots are formed the thermal and erosion-damage of the anode nozzle was diminished.

4.2 Feed Materials Characteristics

Feed materials can be used in form of solid wires, rods, filled wires and powders (Table 4-1). One of the main materials requirement is that melting must occur without decomposition or sublimation.

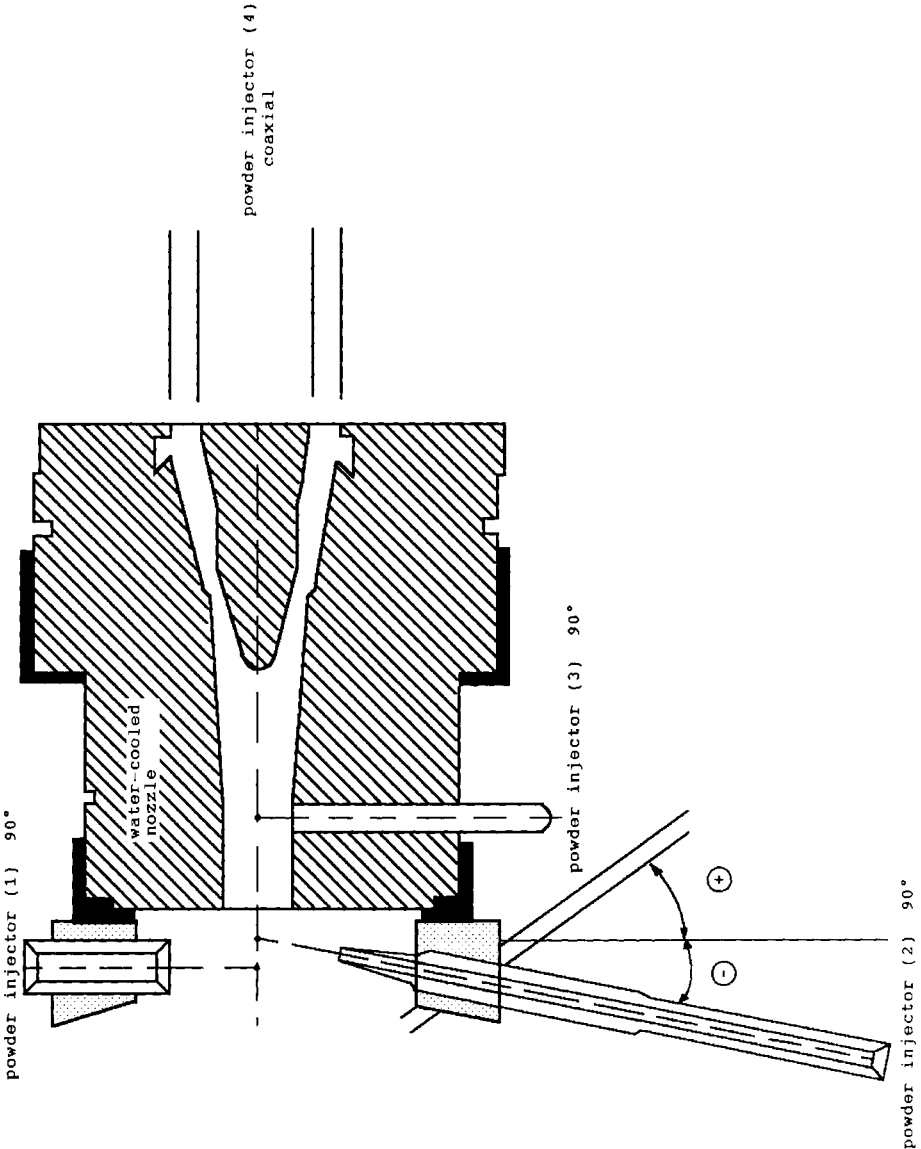


Figure 4-1. Powder injection options (see text).

Table 4-1. Spray coating materials and their standards (after reference [3]).

Parameter	Solid wires	Solid wires	Rods	Filled plastic tubes	Filled wires	Powders
German standard	8566	8566	8566	8566	-	32529
DIN	Part 1	Part 2	Part 3	Part 3	-	65097
Spraying process	flame spraying	electric arc spraying	flame spraying	flame spraying	electric arc spraying	flame and high-energy spraying
Diameter, mm	1.5-4.16	1.6-3.2	3.15, 4.75, 6.3	1.5-6.3	2 and 3.2	5-180 ^a
Length, mm		450 and 600				
Main materials	steels, nonferrous metals and alloys, molybdenum		oxides	metals, oxides	Fe-Cr-C carbides	complete range

^a Particle size, μm

4.2.1 Solid Wires, Rods and Filled Wires

Solid wires and rods as well as filled wires are mostly used in flame and electric arc spraying operations. Steel and nonferrous metals and alloys can be shaped into wires. A special technique (Bifilar system, OSU Oberflächentechnik KG, Bochum, Germany) allows the simultaneous spraying of two wires of different compositions to form a pseudo-alloy coating [3]. Rods of metal oxide compositions are being manufactured by the Rokide process by Norton Industrial Ceramics, Worcester, MA, USA. Filled wires are composed of hollow steel or nickel tubes filled with powder of tungsten, chromium carbide or compositions of the Fe–B system [4]. Also, an outer tube of polymeric material filled with metal oxide or metal powder can be used (Sfecord, Société de fabrication d'elements catalytiques, France).

4.2.2 Powders

Powder particle diameters are generally between 5 and 200 μm with a preferred range of 20–100 μm , and a median diameter of 50 μm for APS applications. Many materials can be made into powders by a variety of techniques to yield spray powders with a narrow grain size distribution, good flowability and optimum deposition efficiency for optimized spray parameter ranges. Powders utilized for flame spraying must have melting points not exceeding 2 500 K because of the rather low temperatures in the flame. Special conditions apply for HVOF and detonation gun techniques. Powders designed for plasma spraying operations must be able to withstand the high mechanical and thermal stresses exerted on them by the hot, high speed plasma jet. Thus powders manufactured by agglomeration of finer particles must be thoroughly sintered to guarantee mechanical stability. Very fine reactive plasma spray powders with an extremely narrow grain size distribution range for vacuum spraying (LPPS) operations demand the highest quality specifications and thus very strict quality control procedures.

To produce spray powders, precursor materials must be melted or sintered with subsequent size reduction by crushing, grinding and attrition milling. Mixing of powders and classification are also important process steps. Specialized powders for a variety of industrial applications are being produced by spray drying, fluidized bed sintering, agglomeration, fusing/melting, plasma spheroidizing, atomizing, surface coatings and sol–gel processes. Figure 4-2 shows schematically different powder types, particle shapes and microstructures. Figure 4-3 relates the particle porosity to the structural fineness, i.e. the crystal size. Electronmicrographs shown in Figure 4-4 demonstrate the wide variability of thermal spray powders ranging from gas- and water-atomized (a,b) to fused and crushed (c), clad (d), sintered (e) or agglomerated (f) powders [5].

For nonstandard applications special powders must be designed and thoroughly characterized in terms of chemical composition, microstructure, physical properties, morphology and spraying behavior by a large spectrum of methods. Development of new spray powders is an extremely involved task that has to be controlled at all process stages by established methods of total quality management (TQM) including

Powder Type Manufacture	fused milled	sintered milled	agglomerated (sintered)	spheroidized	atomized
Particle Shape	blocky-angular	blocky-angular	spherical	spherical	spherical- irregular
Microstructure					
-Porosity	dense	dense-porous	porous	dense-hollow	porous-hollow
-Crystal size	coarse-fine	coarse-fine	medium-fine	medium-fine	fine
-Homogeneity	alloyed	alloyed	alloyed (heterogeneous)	alloyed (heterogeneous)	alloyed

Production Specific Powder Characteristics / Powder Types

Figure 4-2. Different powder types, particle shapes, and microstructures.

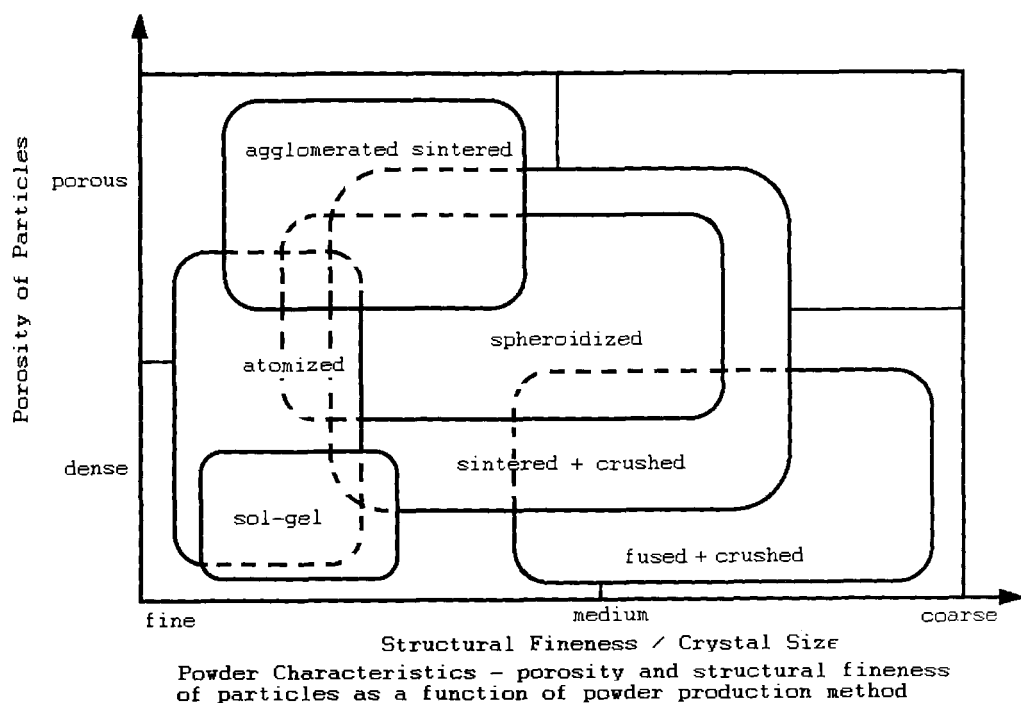


Figure 4-3. Relation of porosity and crystal size of powder particles as a function of the production method.

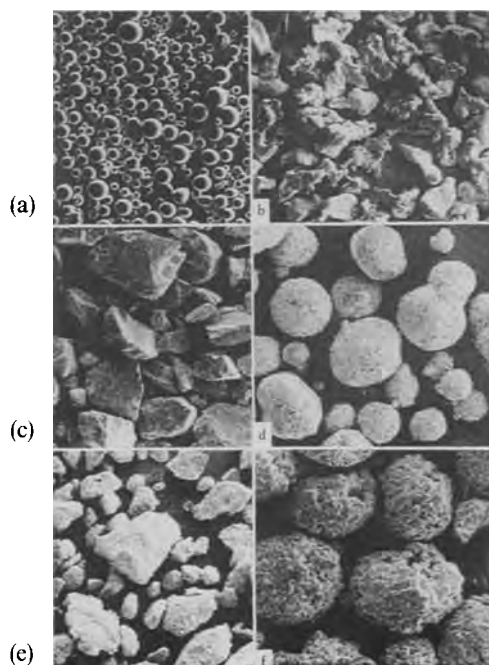


Figure 4-4. Powder morphology dependent on the production method: gas- and water-atomized (a,b), fused and crushed (c), clad (d), sintered (e) and agglomerated (f) powders [5].

SDE, SPC and QFD. Important morphological parameters are shape, surface properties, porosity, homogeneity and phase composition [6]. Figure 4-5 shows a compilation of testing procedures and quality control measures for plasma spray powders and coatings [3]. For more details on methods of powder production and characterization see [7].

The size of the particles is of critical importance. The size distribution is usually statistical, i.e. follows a Gaussian or log-normal distribution. While the median size for an average powder used in plasma spraying is around 40 μm , there are much smaller and much larger particles available. The small particles will evaporate rather quickly prior to impact at the surface, whereas the larger ones melt only incompletely, and may actually rebound from the surface or fall out of the jet owing to gravitational forces. In either case these small and large particles are lost from the flame or plasma jet and thus reduce the deposition efficiency. This deposition efficiency is defined as the ratio between the number of particles deposited at the surface to the number of particles sprayed. Evidently a high deposition efficiency is of overriding economical importance so that its optimization constitutes a crucial step in any coating development operation.

4.2.2.1 Atomization

This technique is frequently used to produce powders based on iron-, cobalt-, nickel- and aluminum alloys. The particles exhibit a distinct difference in shape depending on the method of quenching. Gas-atomized particles (Fig. 4-4a, Fig. 4-6a) are highly spherical whereas water-atomized particles (Fig. 4-4b) have a more angular shape. As a consequence, different coating characteristics are obtained when these two powder types are thermally sprayed at identical feed rates and plasma parameters even if comparable particle-size distributions are used. This also means that the parameters optimized for gas-atomized powder can not be uncritically transferred to water-atomized powders. In this case, clogging of the spray nozzle, discoloration, and/or cracking and spalling of the coating can result. On the other hand, spraying gas-atomized powders with parameters optimized for water-atomized powder will generally result in low deposition efficiency, increased coating porosity, and poor adhesion.

4.2.2.2 Fusion and Crushing

This technique of manufacturing is applied to ceramics and cermet (carbide) powders (Fig. 4-6b) as well as to brittle metals. Adjusting the solidification rate during fusion (casting) yields differences in the crystallinity. Subsequent crushing results in a wide range of particle shapes and consequently in apparent particle density. These variations in processing parameters lead to a variability in coating density, macrohardness and wear resistance, and also thermal-cycling fatigue of oxide thermal barrier coatings. Special techniques to manufacture yttria-stabilized zirconia powders for thermal barrier coatings include the arc-fuse/crush, hollow-spherical-powder (HOSP)/plasma-fuse, and arc-fuse/spray-dry processes [5]. In particular, *arc-fuse/crush powders* (Fig. 4-4c) are being produced by fusing, crushing and screening a premixed

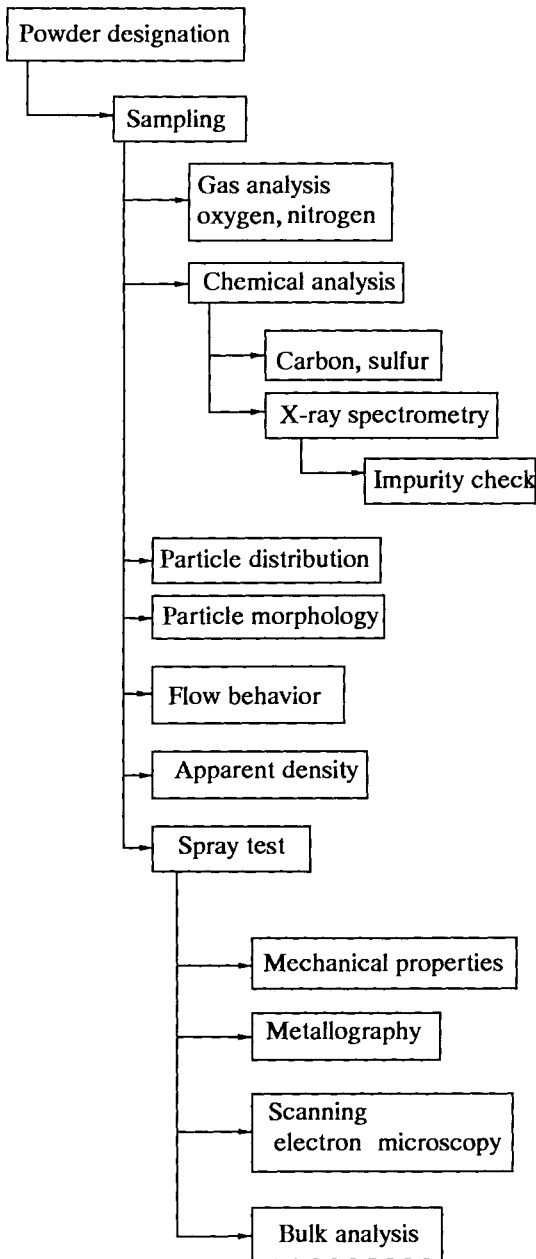
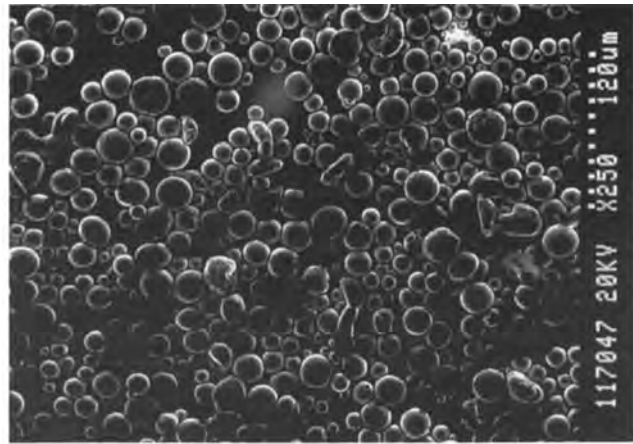
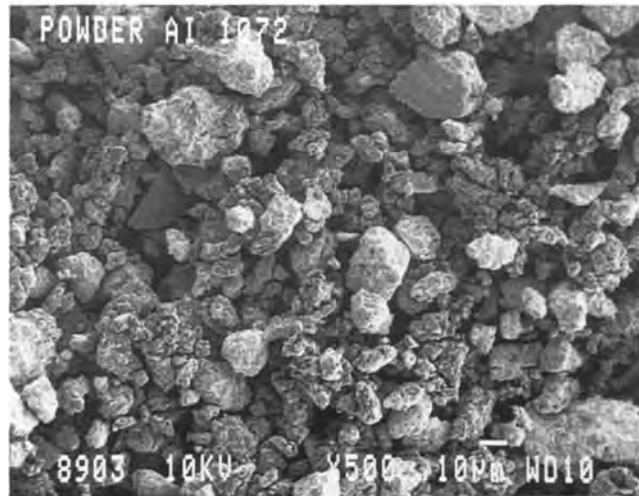


Figure 4-5. Testing procedures and quality control for plasma spray powders and coatings [3].

Figure 4-6. Water-atomized 85Fe15Si (a) and arc-fused/crushed 88WC12Co (b) powder particles [8].



(a)



(b)

powder of 7–8 mol % yttrium oxide and zirconia. The particles obtained are irregularly shaped and have a rather broad size distribution. Thus they flow not too well, and because of their angular shape can be difficult to melt in a non-optimized plasmatron configuration.

HOSP powders are produced by premixing, spray drying, fusing the product in a plasma jet, and screening. The hollow spherical particles thus produced show excellent flowability, and their low mass guarantees easy melting. However, the thin-shelled particles can be destroyed in the plasma jet by the large forces exerted on them. *Arc-fuse/spray-dry powders* combine micronizing and spray-drying with the arc-fuse/crush process. Even though the particles are often hollow their walls are porous in contrast to the walls of the HOSP powders. This results in a tenfold increase in surface area. Such powders are advantageous if very high coating porosities

are required as needed in effective thermal barrier and bioceramic coatings (see Secs. 6.2, 6.3).

4.2.2.3 Compositing

Combining two or more dissimilar materials is achieved by chemical cladding (Fig. 4-4d), organic bonding and/or sintering. Typically Ni-Al composite powders are produced by this method. Spatial variation of the ratios of the materials in the cladding, or loss of material due to preferential vaporization/evaporation may result in nonuniform chemical composition, hardness and fracture toughness of the coating. Clad-powder coatings frequently have exceptionally high adhesion strengths surpassing those of coatings produced from gas- or water-atomized powders.

Composite powders are the first stage of composite materials. At the Institute of Materials Science, Rheinisch-Westfälische Technische Hochschule (RWTH) Aachen, Germany, ceramics, metals and polymers can be combined into micropellets with one or more reinforcing material (fibers, particles) by spray drying [9]. The starting powders are distributed homogeneously in the micropellets that show an excellent flowability. Also, a special technique for coating powders of any morphology and from submicron up to several hundred micrometer size was developed using the so-called HYPREPOC (HYdrogen Pressure-REDucing POWder Coating) process. An inorganic or organic metal salt (sulfates, nitrates, acetates, carbonates, chlorides etc.) solution is reduced in an autoclave by hydrogen in the presence of a powder of the core material. The coatings so produced are smooth, dense and highly adherent to the core particles. Successive precipitation steps result in either very thick coatings or multilayer coatings of dissimilar materials. The advantage of the HYPREPOC process is that nearly any material can be used either as core material or as a coating. Core material can be coated regardless whether the particles are angular or spherical.

4.2.2.4 Agglomeration

The agglomeration process is carried out through a sequence of different steps including pelletizing, pressing or spray drying. Variation of the processing parameters leads to large differences in powder densities and surface areas (Fig. 4-4f). Powder particles with a low density and a high surface area behave like very fine particles and thus do not flow easily compared to dense particle of the same grain-size distribution. As a consequence the deposition efficiency is decreased and porous coatings are produced.

4.3 Momentum Transfer

4.3.1 Connected Energy Transmission

As mentioned above, plasma spraying can be described as a connected energy transmission process, starting with the transfer of energy from an electric potential field to

the plasma gas (plasma heating), proceeding with the transfer of energy (momentum and heat transfer) from the plasma to the powder particles, and concluding with the transfer of energy from the particles to the substrate.

In the following section, principles of momentum transfer and modeling will be discussed. Particles are being accelerated in the plasma jet. The process can be described by a two-phase fluid flow, but is much more complex because of the presence of charged particles, chemical reactions, and large temperature gradients. Particle velocities can be measured by time-of-flight LDA (see Sect. 3.4.2.2).

4.3.2 Modeling of Momentum Transfer

Figure 4-7 shows the velocities of differently sized alumina particles in an argon/hydrogen plasma jet [10]. The larger the particles the lower is the response to the gas velocity. The 3 μm particles are used as ‘tracers’ to measure the velocity of the gas alone in the absence of larger particles. The gas velocity decreases continuously on exiting from the nozzle. The 18 μm particles reach a maximum velocity of 220 m s^{-1} . If the target distance is 15 cm, then the particle velocity is around 170 m s^{-1} , i.e. one half of the velocity of sound at atmospheric pressure in air. Larger particles, like the 46 μm particles reach a maximum of only 140 m s^{-1} but this velocity does not decay quickly because of the high inertia of the large particles.

Momentum transfer from the plasma to the particles can be modeled with the following assumptions:

- the molten droplets are spherical,
- the molten droplets are carried in a gas stream with constant temperatures along its symmetry axis,
- the gas jet is not influenced by particles, i.e. operation is carried out in a diluted system as opposed to dense loading conditions (see Sect. 4.4.3), and
- continuum gas flow.

The governing equation applied to describe the impulse (momentum) transfer is the Basset–Boussinesq–Oseen equation of motion¹. This equation determines the time dependency of the particle velocity, dV_p/dt , considering only the viscous drag force, F_D and the velocity gradient, $V_g - V_p$:

$$dV_p/dt = V_p(\partial V_p/\partial x) = [3C_D\rho_g/4d_p\rho_p]|V_g - V_p|(V_g - V_p) \quad (4-1)$$

¹ The equation given here is a simplification. The complete equation of motion of a particle injected into a plasma jet can be described in a summary form by $F_p = F_D + F_{PG} + F_{AM} + F_H + F_E$, where F_p = mass–acceleration product, i.e. particle inertia, F_D = Stokesian drag force, F_{PG} = drag due to the plasma pressure gradient, F_{AM} = drag due to the added mass, F_H = Basset history term due to the nonsteady motion of the particle, and F_E = external potential forces such as gravity, electric or magnetic forces [11]. Since in a thermal plasma the density of the gas is rather low compared to that of the particle, all terms but the viscous drag force F_D and the history term F_H may be neglected. Thus the equation reduces to $F_p = F_D + F_H$. This applies essentially to pure Stokesian motion with low Reynolds numbers ($C_D = 24/\text{Re}$). According to Pfender [12] additional turbulence and thermophoretic effects must be considered.

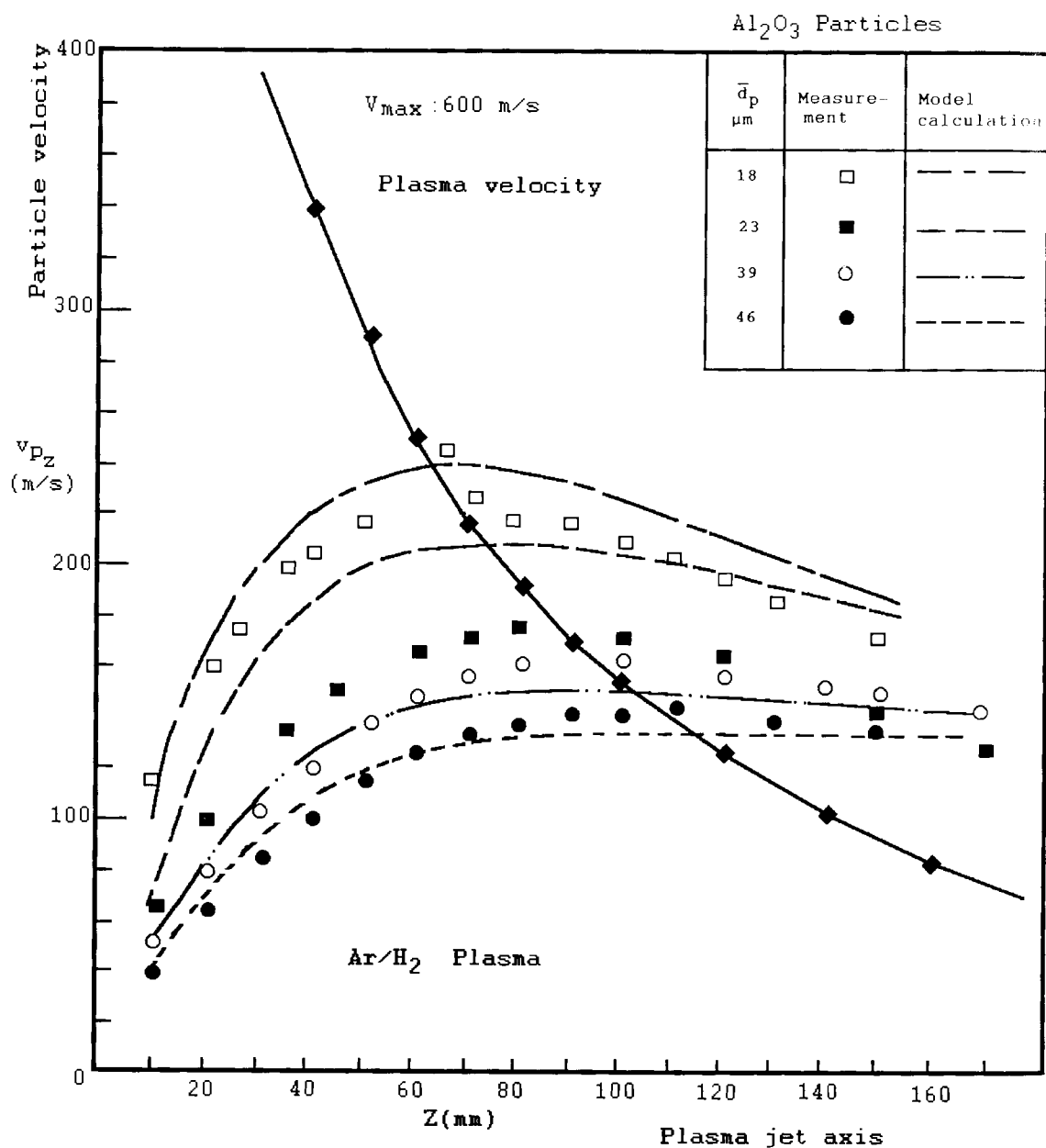


Figure 4-7. Transfer of plasma velocity to alumina particles of different sizes [10].

where

$$C_D = [F_D/A_p]/[1/2\rho_g u_R^2] \quad (4-2)$$

with d_p being the particle diameter and A_p the cross-sectional area of the particle. The velocity term $u_R = V_g - V_p$, i.e. the relative velocity of a particle with respect to the plasma gas can be more accurately described by considering the velocity components of the particle in axial (z) and radial (r) directions: $u_R = [(V_g^{(z)} - V_p^{(z)})^2 + (V_g^{(r)} - V_p^{(r)})^2]^{1/2}$.

The decay of the plasma velocity V_g with distance from the nozzle exit is inversely proportional to the distance x , and can hence be described by the simple relation

$$V_g = V_0/(c_1 + c_2 x), \quad (4-3)$$

where V_0 is the exit velocity, and c_1, c_2 are constants.

A semiempirical approach to the particle velocity in a plasma jet was developed by Nikolaev [13] for a Reynolds number $Re < 1$

$$V_p = V_g \{1 - \exp[18\nu\rho_g t/(d_p^2\rho_m)]\}, \quad (4-4a)$$

with ν = kinematic viscosity of the plasma, ρ_g = plasma gas density, ρ_m = particle density, and t = dwell time of the particle, and for $Re > 2$

$$V_p = (V_g t)/t^* + t; \quad t^* = 4d_p\nu/3C_D v_g \rho_m. \quad (4-4b)$$

4.3.3 Estimation of the Drag Coefficient

The viscous drag coefficient C_D has been evaluated for different Reynolds numbers ranging from $C_D = 24/Re$ for $0 < Re < 0.2$ (Stokesian motion) to $C_D = (24/Re)(1 + 0.189 Re^{0.63})$ for $21 \leq Re \leq 200$ [14]. An expression for higher turbulent plasmas ($0.15 \leq Re \leq 500$) was given as $C_D = (23.7/Re)[1 + 0.165 Re^{2/3} - 0.05 Re^{-0.1}]$ [15]. It should be noted that there are problems with modeling the forces acting on a particle in a plasma jet that require modification of the Basset–Boussinesq–Oseen approximation. These problems relate to (1) the large temperature gradient present, (2) the change of the particle diameter d_p and thus the projected surface area by surface ablation (see 4.3.4), thermal expansion, decomposition and vaporization, and (3) noncontinuum effects for small particles with $d_p < 10 \mu m$.

1. Corrections for temperature effects have been made by Lewis and Gauvin [11] who modified the drag coefficient assuming a local Reynolds number

$$C_D = C_{Df} [(\rho_\infty/\rho_f)(\nu_f/\nu_\infty)^{0.15}], \quad (4-5)$$

with C_{Df} = drag coefficient evaluated at the ‘mean film temperature’ ($T_f = (T_\infty - T_s)/2$), ρ_f = gas density at T_f , ρ_∞ = gas density at T_∞ , ν_f = kinematic vis-

cosity at T_f , and ν_∞ = kinematic viscosity at T_∞ . Another correction approach was reported by Lee *et al.* [16] with

$$C_D = C_{Df}[\rho_\infty \mu_\infty / \rho_s \mu_s]^{-0.45} = C_{Df}(\nu_\infty / \nu_s)^{-0.45} = C_{Df} f_1 \quad (4-6)$$

where the subscripts ∞ and s refer to the plasma temperature, T_∞ and the surface temperature of the particle, T_s , respectively.

2. The drag coefficient is according to Eq. 4-2 dependent on the projected surface area of the particle perpendicular to the flow, A_p . When the particle diameter decreases by ablation or evaporation, the surface area also decreases, and the drag coefficient and hence the drag force change accordingly.
3. Noncontinuum effects for small particles ($d_p < 10 \mu\text{m}$) can be accounted for through the Knudsen number, $\text{Kn} = (\lambda/d_p)$, where λ = molecular mean free path. In the slip flow regime $0.01 < \text{Kn} < 1$, a correction of the drag coefficient has been proposed [17] as

$$C_{D,\text{slip}} = C_{D,\text{cont}}[1/(1 + AB(4 \text{Kn}/\text{Pr}))]^{0.45} = C_{D,\text{cont}} f_2 \quad (4-7)$$

where $A = (2 - a)/a$ with a = thermal accommodation coefficient, $B = (\gamma/1 + \gamma)$ with $\gamma = c_p/c_v$, and Pr = Prandtl number. According to Pfender [12] the corrections expressed in Eqs. 4-6 and 4-7 can be combined and a general expression for the drag coefficient is obtained:

$$C_D = C_{Df} f_1 f_2. \quad (4-7a)$$

The acceleration of the particles caused by the viscous drag forces is proportional to the relative velocity of the particles, and inversely proportional to the density and the square of the diameter of the particle. The correction for noncontinuous effects is particularly important for low-pressure plasma spraying where the mean free path of the gas molecules, λ is close to the diameter of the particles, d_p .

Figure 4-8 shows the dependency of the viscous drag coefficient, C_D expressed in Eq. 4-2 as a function of the Reynolds number. It can be seen that the standard drag curve is limited by the Stokes equation for low Reynolds numbers, i.e. laminar flow regime, whereas it is limited by Newton's law at high Reynolds numbers, i.e. turbulent flow regime as present in most plasma arc jets. The turbulent flow causes a non-steady flow field around the immersed particles and thus a rapid change of the particle Reynolds number with time. According to Lewis and Gauvin [11] this results in an excess drag that was predicted to range from 20% for $30 \mu\text{m}$ particles to 100% for $150 \mu\text{m}$ particles. Together with the effect of the Basset history term the effect of excess drag must be considered in momentum transfer modeling.

4.3.4 Surface Ablation of Particles

For liquid or plastically deformable material a global approximation of the force balance on the side walls of the deforming particle is

$$(4\pi r^2)(C_D \rho_p v^2/4) \approx m(d^2 r/dt^2), \quad (4-8)$$

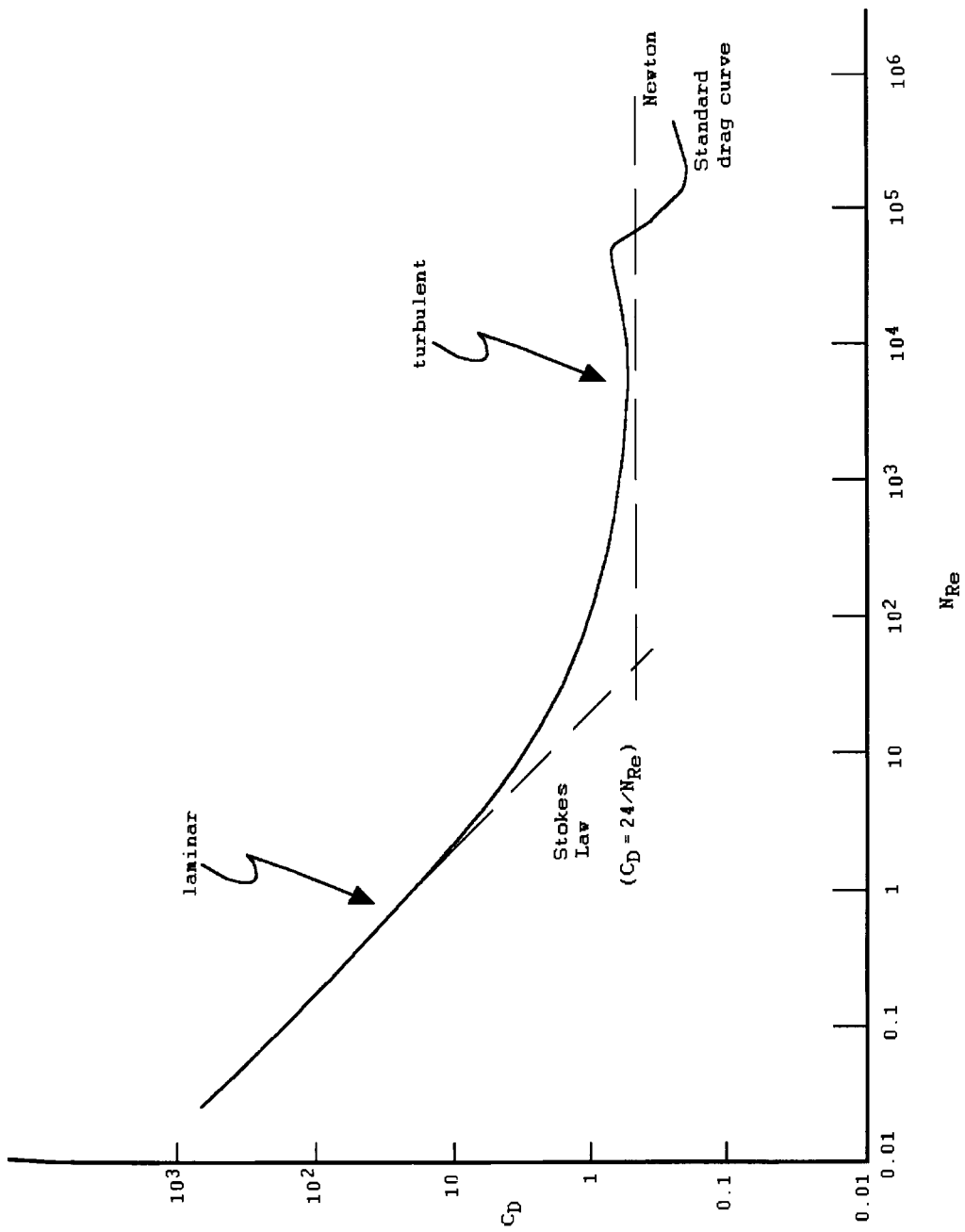


Figure 4-8. Dependence of the viscous drag coefficient C_D on the Reynolds number.

where C_D = drag coefficient, ρ_p = density of plasma gas, v = particle velocity, m = particle mass and r = particle radius.

Assuming the density of the material, ρ_m remains constant, the expression

$$r(d^2r/dt^2) = C_D\rho_p v^2/2\rho_m \quad (4-9)$$

can be derived. The surface of the sphere is heated by convection and it is shed by ablation. The resulting mass change is

$$Q_A(dm/dt) = -(1/2)h\rho_p A_p v^3, \quad (4-10)$$

where Q_A = heat of ablation, and h = heat transfer coefficient. It can be seen that the mass change is proportional to the third power of the particle velocity and thus the materials loss becomes significant at high velocities. Also, the maximum ablation rate can be determined [18] from

$$Q_A(dm/dt) \approx A\sigma T^4, \quad (4-11)$$

and finally

$$Q_A(dm/dt) = -A_p \min[(h/2)\rho_p v^3, \sigma T^4]. \quad (4-12)$$

4.4 Heat Transfer

4.4.1 Heat Transfer under Low Loading Conditions

If the mass of powder particles injected into a plasma jet is small enough not disturb the flow of the plasma and to cool it down by radiative losses, the heat transfer can be estimated under simplifying assumptions. In particular, the Navier-Stokes equations (see Sect. 4.4.3) for the flow around a sphere are highly nonlinear even under the simplifying assumptions made above, i.e. for constant physical property plasmas. Thus no completely exact solutions exist for these equations [19].

In many cases an analytical solution is not available, and only numerical models can be used successfully. As shown in Fig. 4-9, a particle in contact with a heated plasma jet acquires energy by convective (and conductive) processes, q_c and loses energy to the surroundings by radiation, q_r . The net energy contribution to the heating and melting of particles is the difference between these two values (Eq. 4-18).

The amount of heat gained by convective energy transfer from the plasma to the particle is

$$q_c = ha(T_\infty - T_s), \quad (4-13)$$

the amount of heat lost by radiative energy transfer to the surrounding is

$$q_r = \sigma \epsilon a(T_s^4 - T_a^4), \quad (4-14)$$

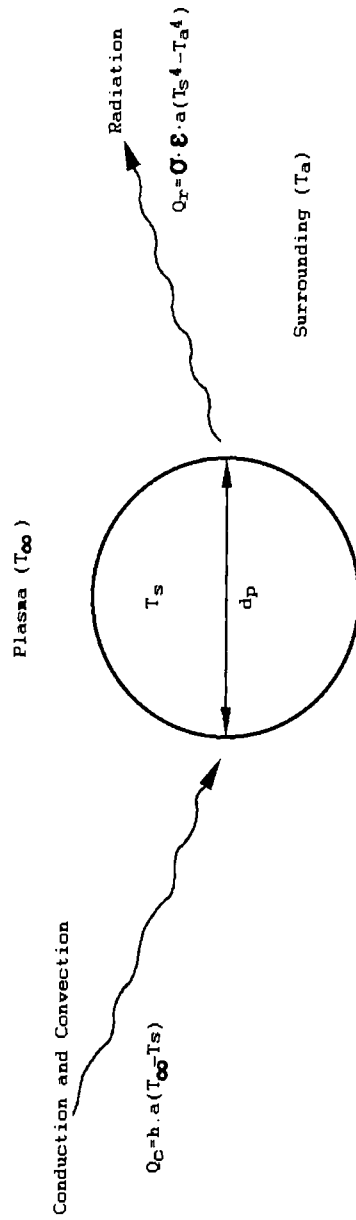


Figure 4-9. Heat transfer equilibrium of a powder particle in a plasma.

where h = plasma/particle convective heat transfer coefficient, a = surface area of the particle, T_∞ = free-stream plasma temperature, T_s = particle surface temperature, T_a = temperature of the surrounding, σ = Stefan-Boltzmann constant, and ε = particle emissivity.

The heat transfer coefficient can be expressed as

$$h = k_f \text{Nu}/d_p, \quad (4-15)$$

where $k_f = C_g \eta / \text{Pr}$, or $h = [C_g \eta / d_p][\text{Nu}/\text{Pr}]$ (see Appendix A).

The symbols Nu and Pr denote the Nusselt and Prantl numbers, and k_f is the thermal conductivity of the particles. C_g , d_p and η are, respectively the specific heat of the plasma gas, the particle diameter and the gas viscosity.

The choice of the numerical value of the Nusselt number is crucial for a realistic estimate of the heat transfer rates from the plasma to the particles in the same way the choice of the drag coefficient is important for the momentum transfer. For the heat transfer between a gas and a spherical particle the expression

$$\text{Nu} = 2.0 + b \text{Re}^m \text{Pr}^n \quad (4-16)$$

was given by Frösling [20], and Raithby and Eckert [21], and later used by Sayegh and Gauvin ($b = 0.473$, $m = 0.552$, $n = 0.78 \text{Re}^{-0.145}$) [19]² and Vardelle *et al.* ($b = 0.6$, $m = 0.6$, $n = 0.33$) [22]. Other more complex expressions for Nu were introduced by Fiszdon [15], Lee *et al.* [16] and Lewis and Gauvin [11]. Also, noncontinuum effects in heat transfer over the range of the Knudsen number $0.01 < \text{Kn} < 1.0$ have been proposed by Chen and Pfender [23] as

$$q_{\text{noncont}} = q_{\text{cont}}[1/\{1 + (2Z^*/d_p)\}], \quad (4-17)$$

with Z^* = temperature ‘jump’ distance. Because the particle size is of the same order of magnitude as the molecular mean free path length in the plasma gas, this ‘rarefaction effect’ [12] may exert a strong influence on the heat transfer.

The net energy acquired by a particle in a plasma is obtained from Eqs. 4-13 and 4-14 as

$$q_n = q_c - q_r \gg 0, \quad (4-18)$$

since q_r is generally small compared to q_c because of the small value of the Stefan-Boltzmann constant $\sigma = 5.67 \times 10^{-8} \text{ W m}^{-2} \text{ K}^{-4}$.

The requirement for an efficient energy economy during the plasma spray operation is that all particles melt completely during their very short residence time in the plasma jet. This means that the total energy received by the particles, q_n must be

² Actually, instead of the limiting Nusselt number of 2 an expression $2f_0 = \{2(1 - [T_w/T_\infty]^{1+x})/\{(1+x)/(1 - [T_w/T_\infty])(T_w/T_\infty)^x\}\}$ with $x = 0.8$ was used, where T_w is the surface temperature of the particle and T_∞ is the plasma temperature.

equal to or larger than the energy required to melt the particles. This energy quantity consists of two components: the energy needed to heat the particles from their initial temperature to their melting point and the latent heat of fusion.

$$\int_0^\tau q_n dt > \sum \{m_p c_p (T_m - T_0) + m_p H_m\}, \quad (4-19)$$

where m_p = mass of particle, c_p = specific heat of particle, T_m = melting point, T_0 = initial temperature, H_m = latent heat of fusion and τ = residence time of the particle in the plasma jet.

Normally, superheating is required to achieve sufficiently high temperatures of the particles, and to decrease the viscosity of the liquid droplet. The degree of superheating depends on the Biot number, which is the ratio of the thermal conductivity of the plasma gas, k_g to the thermal conductivity of the particles, k_p :

$$Bi = k_g/k_p. \quad (4-20)$$

The requirement of a uniform particle temperature implies that $Bi < 0.01$, i.e. the thermal conductivity of the particle material has to be much higher than that of the plasma gas. Thus the numerical value of the Biot number can be used to determine *a priori* whether large temperature differences may occur between the surface and the center of a (spherical) particle that may compromise the conjecture of a uniform temperature distribution and thus uniform melting behavior. According to Bourdin *et al.* [24], a characteristic temperature $T^* = \Delta T_s / (T_\infty - T_s) = f(Bi)$ can be defined. For $Bi < 0.02$, the temperature between the surface and the center of the particle becomes less than 5% of $(T_\infty - T_s)$.

Porous particles and particles with low thermal conductivity will develop large internal temperature gradients that can often exceed 1 000 K. Figure 4-10 shows the temperature history of alumina particles of 50 μm radius at a plasma temperature of 10 000 K in hydrogen, nitrogen and argon plasmas [24]. The left lines depict the particle surface temperature, the right lines the temperature at the center of the particles. The temperature difference depends strongly on the heat flux to the particle. For example, the temperature difference in a hydrogen plasma can be so high that the thermal stresses induced can lead to shattering of the particles. As is obvious from Fig. 4-10, the radial temperature differences across a particle are quite large for a hydrogen plasma, and decrease for a nitrogen and even more for an argon plasma. This is because of the large differences in the thermal conductivities, k_g of the plasma gas, being 4.6, 1.6 and 0.2 $\text{W m}^{-1} \text{K}^{-1}$ for hydrogen, nitrogen and argon, respectively. The value of the thermal conductivity influences the particle surface temperature because the solution of the equation

$$dT_s/dt = -12k_g(T_s - T_\infty)/\rho_s c_s d_p^2 \quad (4-21)$$

($Nu = 2$, i.e. only conductive heat transfer, $q_r = 0$, i.e. no radiative heat losses) is

$$(T_s - T_\infty)/(T_0 - T_\infty) = \exp[12k_g t / \rho_s c_s d_p^2], \quad (4-22)$$

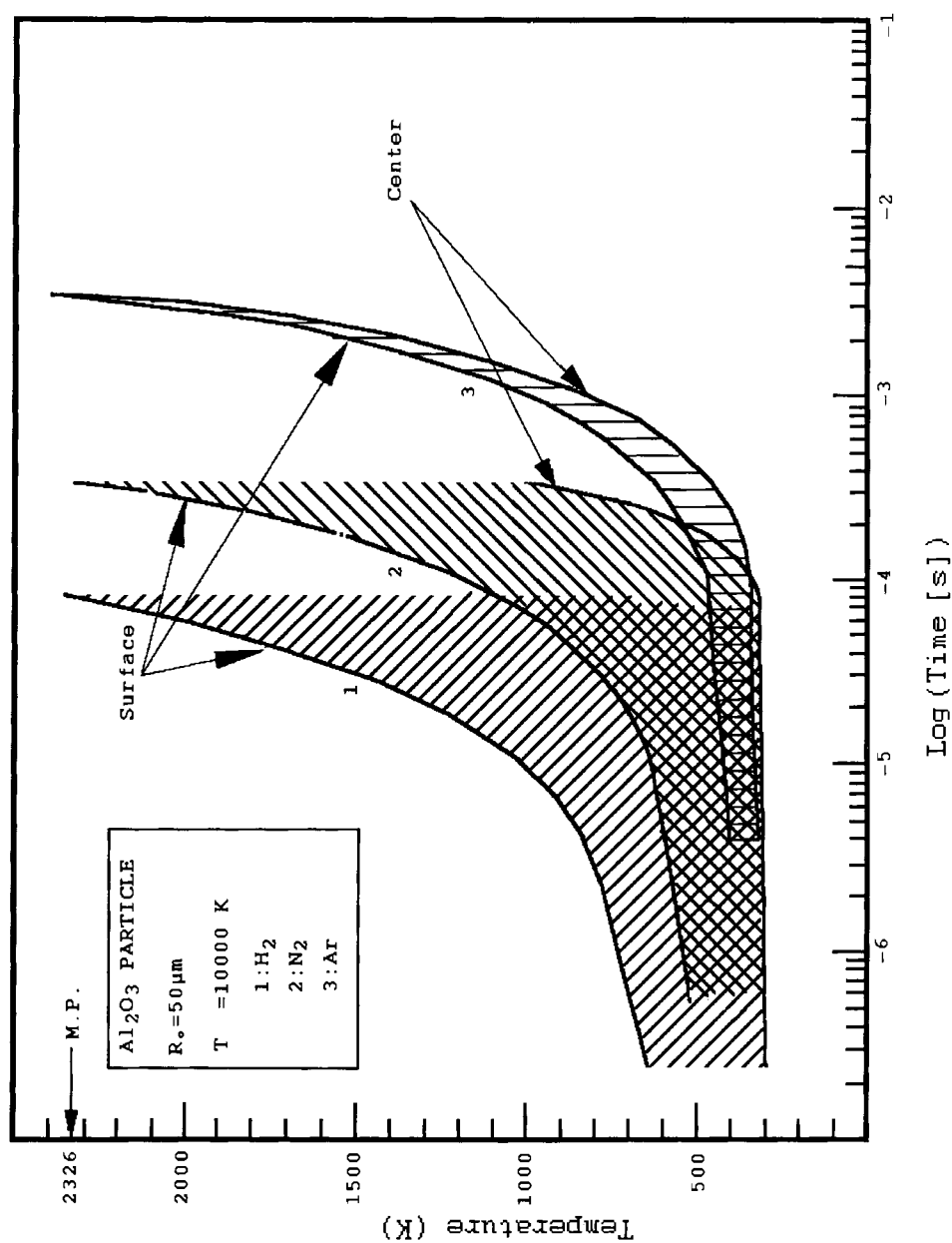


Figure 4-10. Temperature history of 50 μm -alumina particles at a temperature of 10 000 K in hydrogen (1), nitrogen (2) and argon (3) plasmas [24].

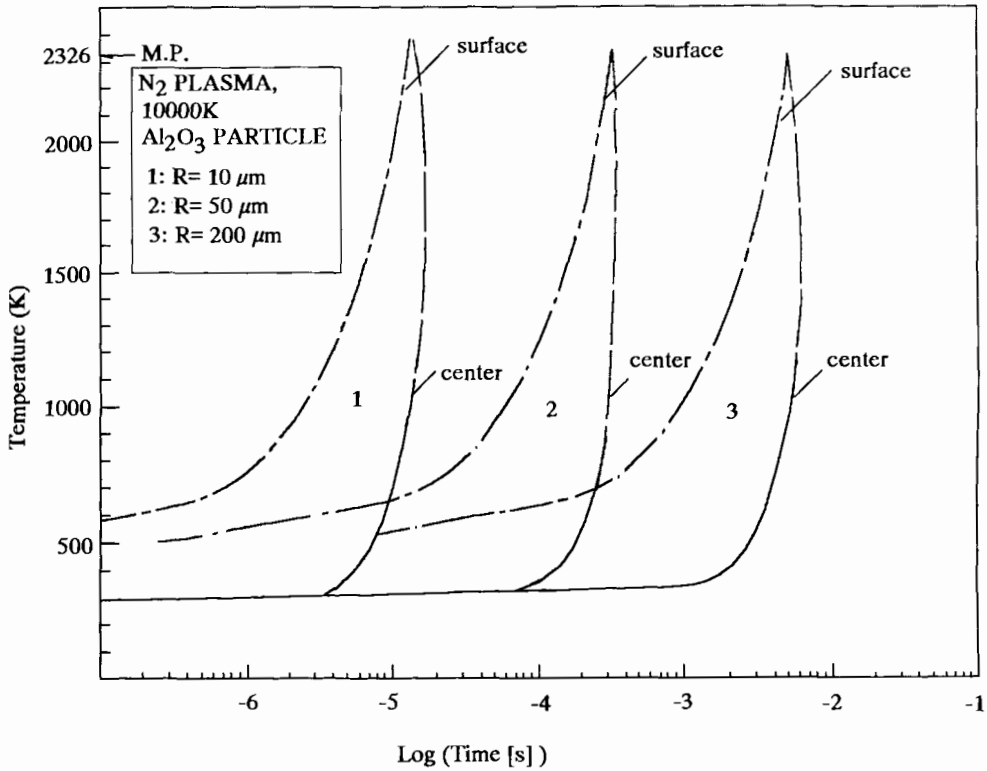


Figure 4-11. Temperature history of alumina particles of different radii suddenly immersed in a nitrogen plasma at 10000 K [24].

where ρ_s and c_s are the density and the specific heat, respectively of the particle, d_p the particle diameter, and T_0 and T_∞ the temperature of the surrounding and the plasma, respectively [24]. From Fig. 4-10 it can be seen that the time required to melt an alumina particle of 50 μm radius ranges from 80 μs (hydrogen plasma) to 0.3 ms (nitrogen plasma) to 4 ms (argon plasma).

Figure 4-11 shows the temperature history of alumina particles of different radii (10, 50 and 200 μm) suddenly immersed in a nitrogen plasma at 10000 K [24]. Again, the leading curves refer to the surface temperature of the particle, the trailing curves to the center of the particles. The radius of the particles has little influence on T_s .

A somewhat easier approach to make a qualitative estimate of the materials performance in terms of ease of plasma melting of particles is to consider the maximum particle diameter for complete melting, d_{max} . This is a useful parameter for comparing materials with widely differing densities and thermophysical properties.

Based on the equation of transient heat conduction in solid spheres (assumption: surface of particle is brought instantaneously to its melting point), the following expression can be evaluated [25]:

$$(T_m - T_R)/(T_m - T_I) = f(\text{Bi}, \text{Fo}) = f[hr/k, \alpha\Theta/r^2], \quad (4-23)$$

Table 4-2. Relative ease of plasma spraying for various oxide, carbide and metallic coatings [25].

Material	Thermal diffusivity, a [cm ² s ⁻¹]	$C_p(T_m - T_i)$ [cal g ⁻¹]	d_{\max}^a [μm]	Relative ease of plasma spraying
ZrO ₂	0.005	430	26	5
UO ₂	0.025	214	58	4
TiC	0.04	645	72	3
TaC	0.09	115	110	1
ZrC	0.05	525	82	3
TiN	0.07	556	96	2
B ₄ C	0.06	109	90	2
Steel 304	0.05	226	82	3
W	0.63	111	280	1

$$^a d_{\max} = 2[a\Theta/0.3]^{1/2} \text{ for } \Theta = 10^{-4} \text{ s}$$

Table 4-3. 'Ease of melting' parameter, Φ , according to Marynowski [27].

	Material	Φ	T_m (K)	ρ (g cm ⁻³)
Difficult	TiC	1.53	3.410	4.93
Carbides,	TiN	1.40	3.200	5.21
Nitrides	ZrC	1.58	3.840	6.73
Easier	ZrO ₂	1.38	2.700	4.40
	Al ₂ O ₃	1.26	2.318	3.97
Oxides	TaC	1.09	4.150	14.53
	SiO ₂	1.21	1.975	2.65
Easy	Ni	0.58	1.728	8.90
	Ta	0.80	3.270	16.60
Metal	W	0.83	3.650	19.30
	Mo	0.90	2.883	10.20

where T_m = melting point of material, $T_R = T$ at points along the radius of a sphere ($r = 0$ at center, $r = r_0$ at surface), T_i = initial temperature of particle, α = thermal diffusivity = $k_p/\rho c_p$, Θ = time, Bi = Biot number and Fo = Fourier number.

At the particle center ($r = 0$), the equation becomes approximately

$$1 - (T_0/T_m) = \Phi \{hr_0/k, \alpha\Theta/r_0^2\}. \quad (4-24)$$

A comparison of different materials in terms of the relative ease of plasma spraying is given in Table 4-2. Assuming constant time (100 μs), a center temperature of the particle $T_0 = 0.9T_m$, a Biot number of 10, and a Fourier number of 0.3, an ex-

pression can be obtained for the maximum diameter of a particle that completely melts in 100 μs :

$$d_{\max} = 2r_0 = 2[\alpha\Theta/0.3]^{1/2}. \quad (4-25)$$

For a qualitative comparison of the melting behavior of different materials Marynowski [26] introduced an ‘ease of melting’ parameter $\Phi = 10^{-3}T_m/\rho^{1/2}$. Easy to melt materials have $\Phi < 1.0$, difficult to melt materials $\Phi > 1.4$ (see Table 4-3). The parameter Φ is based on considerations by Engelke [27] involving equating the time required for the particle to traverse the plasma of length X to the time required to melt this particle completely. An expression can be evaluated that leads to

$$[X(k_p\Delta T)^2/V\mu] \geq [L^2D^2/16\rho], \quad (4-25a)$$

where k_p = mean boundary layer thermal conductivity, V = plasma velocity, μ = plasma viscosity, L = particle heat content, D = particle diameter, and ρ = particle density. Since the left hand side of Eq. 4-25a increases proportionally to the square of the plasma enthalpy it follows that the enthalpy should be proportional to $(LD/\rho^{1/2})$ [27].

4.4.2 Exact Solution of Heat Transfer Equations

According to Chen and Pfender [28] exact solutions for the heat transfer from a plasma to a particle under low-loading conditions can be obtained considering the following simplifying assumptions:

- particles are exposed to a uniform atmospheric pressure argon plasma,
- heat transfer process is steady,
- spherical particles,
- free convection neglected ($\text{Re} = 0$, $\text{Gr} \ll 1$),
- radiation from and to particle neglected ($\text{St} = 0$), and
- influence of vapor from evaporating particles neglected.

Two cases can be distinguished: heating of a particle without evaporation, and with evaporation. However, realistically a certain degree of vaporization of material below the boiling point has always to be taken into account. As the temperature of a particle in the plasma jet increases its vapor pressure also increases. Then the mass loss by vaporization [12] becomes

$$dm/dt = \rho h_m M \ln(p/p - p_v), \quad (4-26)$$

where h_m = mass transfer coefficient, M = molecular weight of the material, p = partial vapor pressure with respect to saturation, and p_v = partial vapor pressure with respect to the particle surface temperature. The mass transfer coefficient can be

expressed similarly to the Nusselt number (Eq. 4-15) by related dimensionless groups as

$$\text{Sh} = h_m d_p / D_{ij} = 2.0 + 0.6 \text{Re}^{0.5} \text{Sc}^{0.33}, \quad (4-27)$$

with Sh = Sherwood number, Re = Reynolds number, Sc = Schmidt number, d_p = particle diameter and D_{ij} = interdiffusion coefficient [12].

4.4.2.1 Particle Heating without Evaporation

The simplified heat transfer equation is

$$4\pi r^2 (k \, dh / c_p \, dr) = Q_0 \quad (4-28)$$

where k = thermal conductivity, c_p = specific heat, h = specific enthalpy of plasma and r = radial coordinate.

Introducing the ‘heat conduction potential’, S , as

$$S = \int_{T_0}^T k \, dT = \int_{h_0}^h (k / c_p) \, dh, \quad (4-29)$$

Eq. (4-28) can be rewritten as

$$Q_0 = 4\pi r_s^2 \, dS / dr \quad (4-28a)$$

and on integration

$$Q_0 = 4\pi r_s (S_\infty - S_s), \quad (4-30)$$

where S_∞ and S_s are the values of S at the surface and far away from the surface, and r_s is the particle radius.

The specific heat flux is $q_0 = Q_0 / 4\pi r_s^2$, and thus

$$q_0 = (S_\infty - S_s) / r_s. \quad (4-31)$$

It can be seen that the specific heat flux is inversely proportional to the particle radius.

The Nusselt number is defined as

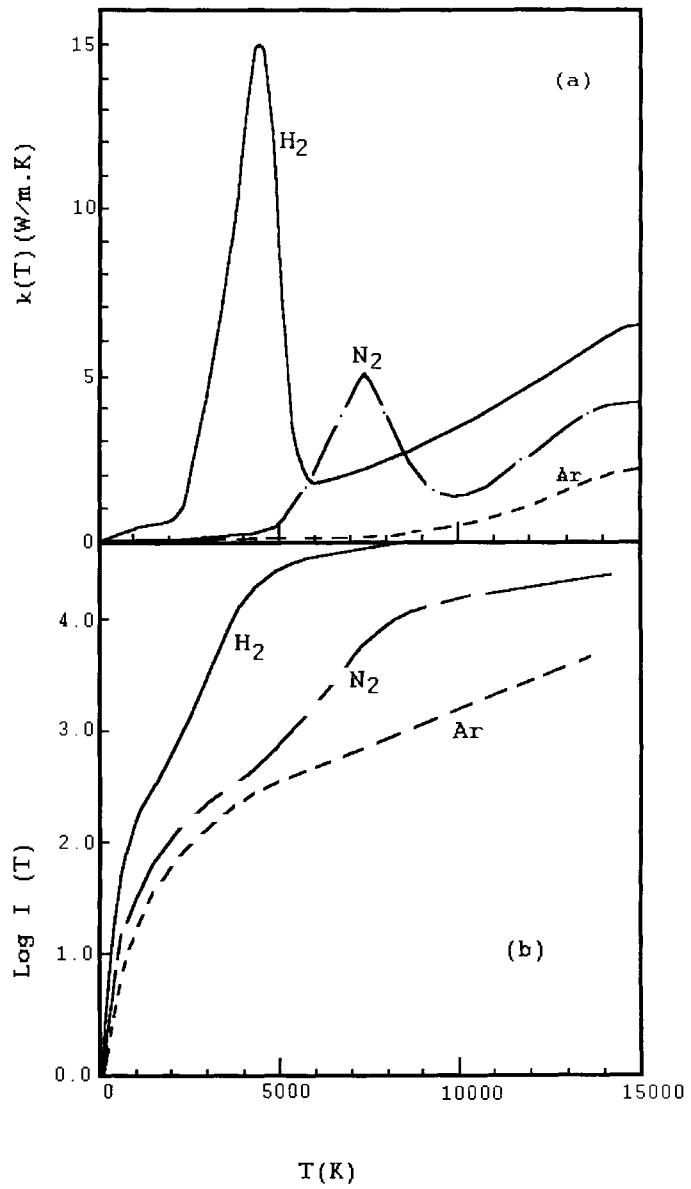
$$\text{Nu} = q_0 2r_s / (S_\infty - S_s) = (h d_p) / k_f \quad (4-32)$$

Under pure heat conduction condition ($\text{Re} = 0$), $\text{Nu} = 2$. For $\text{Re} \neq 0$ follows

$$\text{Nu} = q_0 2r_s / k(T_\infty - T_s) = q_0 2r_s / (k c_p)(h_\infty - h_s). \quad (4-32a)$$

From Eq. 4-29 it follows that S is only a function of the temperature for a given plasma gas and a given solid material. Figure 4-12 relates the thermal conductivities of the plasma gases argon, nitrogen and hydrogen and the heat conduction potentials as functions of the plasma temperature [24]. Figure 4-13 shows in addition the plot of the heat conduction potential, S , of an argon/hydrogen mixture as a function

Figure 4-12. Thermal conductivities $k(T)$ (a) and heat conduction potentials $I(T)$ (b) of some pure plasma gases [24].



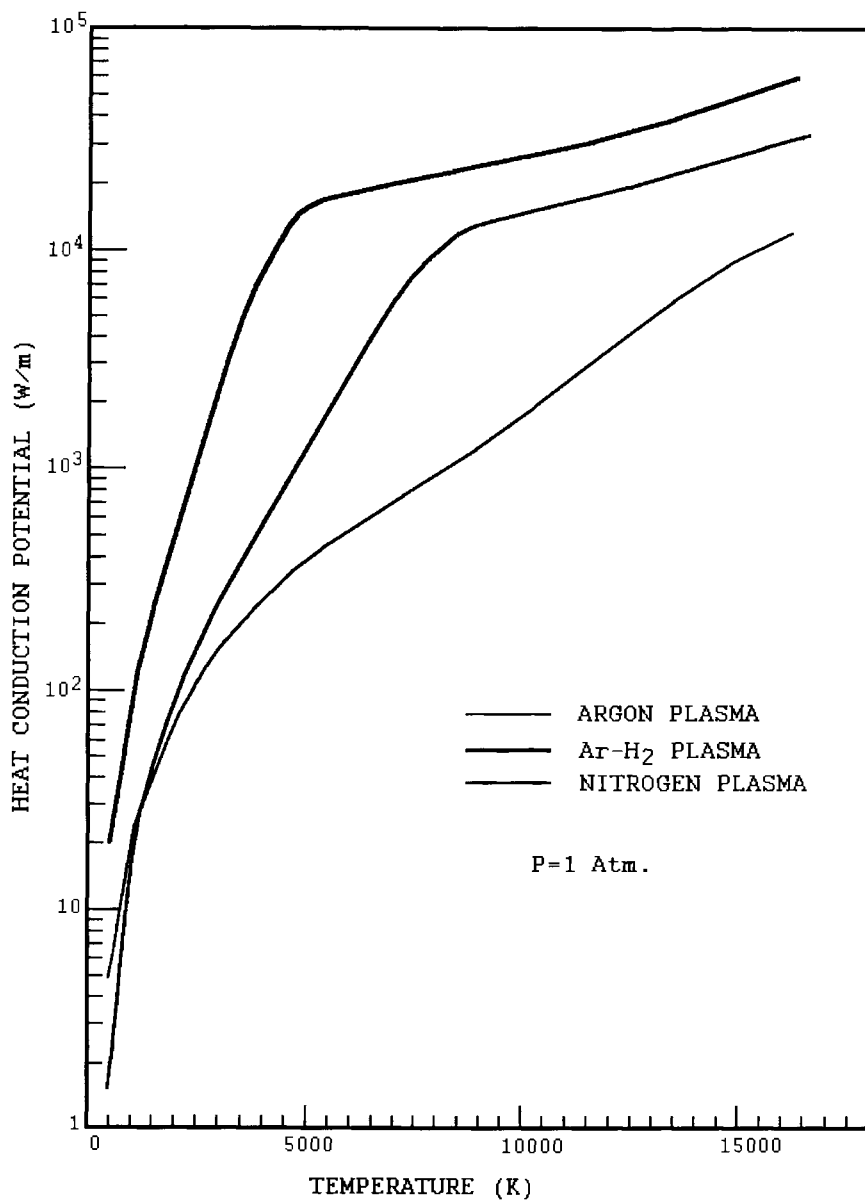


Figure 4.13. Heat conduction potentials of pure (argon, nitrogen) and mixed (argon/hydrogen) plasmas at atmospheric pressure [28].

of the plasma temperature. The high thermal conductivity of the added hydrogen leads to a substantially increased heat conduction potential of the mixture compared to pure argon. For this reason argon/hydrogen mixtures are frequently used as a plasma gas to improve the melting characteristics of powders with high melting points such as zirconia.

4.4.2.2 Particle Heating with Evaporation

The simplified convection–diffusion equation can be written as

$$-4\pi r^2 D \rho \, df/dr + Gf = G \quad (4-33)$$

or

$$4\pi r^2 D \rho \, df/dr = G(f - 1) \quad (4-33a)$$

where G = total mass flux due to evaporation, f = mass fraction of evaporated species, D = diffusion coefficient and ρ = gas density. Boundary conditions are $f = 0$ as $r \rightarrow \infty$.

The related energy equation is

$$4\pi r^2 (k/c_p) (dh/dr) = G(h - h_s + L), \quad (4-34)$$

where h = enthalpy corresponding to the surface of particle and L = latent heat of evaporation. Boundary conditions for solving Eq. 4-34 are

$$r = r_s \quad h = h_s$$

$$r \rightarrow \infty \quad h = h_\infty$$

The solution of Eq. 4-34 is

$$G = 4\pi r_s \int (k/c_p) (dh/h - h_s + L) = 4\pi r_s \int (k \, dT)/h - h_s + L. \quad (4-35)$$

The total mass flow rate is related to the total heat flux by

$$Q_1 = GL. \quad (4-36)$$

Therefore:

$$Q_1 = 4\pi r_s L \int (k \, dT)/h - h_s + L, \quad (4-37)$$

and, because $q = Q/4\pi r^2$, the specific heat flux becomes

$$q_1 = (L/r_s) \int (k \, dT)/h - h_s + L. \quad (4-37a)$$

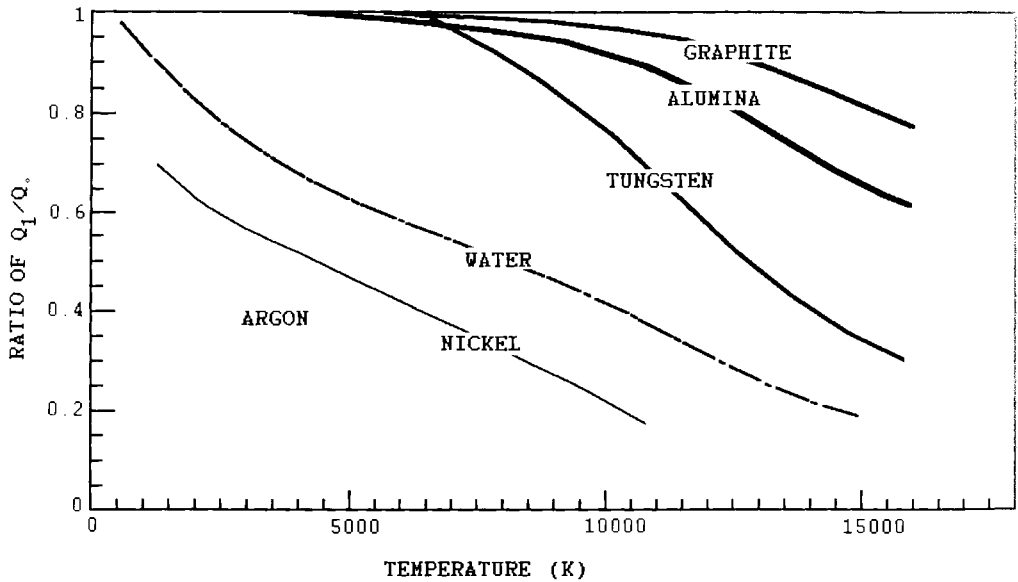


Figure 4-14. Heat flux ratios Q_1/Q_0 of different materials as a function of the argon plasma temperature [28].

Since the integral is only a function of T for a given plasma gas and a given material it can be replaced by the function

$$\int (k \, dT)/h - h_s + L = M(T_\infty, T_s, L). \quad (4-38)$$

From Eqs. 4-31 and 4-37a, the ratio of the heat flux with and without evaporation becomes

$$q_1/q_0 = (L/S_\infty - S_s)M(T_\infty, T_s, L). \quad (4-39)$$

Figure 4-14 shows a plot of q_1/q_0 as a function of the plasma temperature for different materials. It can be seen that evaporation has a strong effect if the plasma temperature is high, and if the material has a low latent heat of evaporation.

4.4.2.3 Evaporation Time of a Particle

For quasi-steady state evaporation it follows that

$$Q_1 = 4\pi r_s^2 (-dr_s/dt) \rho_c L \quad (4-40)$$

or

$$q_1 = -\rho_c L (dr_s/dt). \quad (4-40a)$$

With Eq. (4-40a), (4-37a) and (4-38) one obtains

$$q_1 = (L/r_s)M(T_\infty, T_s, L) = -\rho_c L(dr_s/dt) \quad (4-41)$$

or

$$-(dr_s^2/dt) = K \quad (4-42)$$

where $K = 2M(T_\infty, T_s, L)/\rho_c$ is the so-called *evaporation constant*. This constant is only a function of temperature, not a function of the radius of the particle. Figure 4-15 shows the evaporation constant K for several materials as a function of the plasma temperature.

The integration of Eq. (4-42) leads to

$$r_{s0}^2 - r_s^2 = Kt \quad (4-43)$$

where r_{s0} is the initial radius of the droplet at $t = 0$.

The time for complete evaporation of a droplet ($r_s = 0$) becomes then

$$t_V = r_{s0}^2/K. \quad (4-44)$$

This time does not include the time needed for initial heating and melting of the particle. From Fig. 4-15 we obtain for an alumina particle of a radius $r = 50 \mu\text{m}$, heated in an argon plasma of $T_\infty = 10\,000 \text{ K}$ the time for complete evaporation $t_V = (5.0 \times 10^{-5})^2/(3.0 \times 10^{-8}) = 80 \text{ ms}$. From this result it is obviously necessary to design the plasmatron nozzle and to set the spray parameters in such a way that the residence time of a $50 \mu\text{m}$ -alumina particle in the $10\,000 \text{ K}$ -zone of the plasma jet is much shorter than 80 ms to avoid substantial evaporation. On the other hand the dwell time must be substantially larger than the 4 ms required to completely melt an alumina particle of that size as shown in Figs 4-10 and 4-11.

The evaporation of particles in the plasma gas can drastically reduce the specific heat flux in the plasma (Eq. (4-39), Fig. 4-14). On the other hand, the heat transfer calculations by Chen and Pfender [28] assumed that no influence exists on the vapor from evaporating or sublimating particles on the thermophysical properties of the plasma.

There is, however, a noticeable effect on the temperature of the plasma under dense particle loading conditions (see, for example, Proulx *et al.* [29]). Local cooling of the plasma takes place owing to the presence of particles. This will be described in the following section.

4.4.3 Heat Transfer under Dense Loading Conditions

In dilute systems, i.e. systems at low-loading conditions, it has been tacitly assumed that particle movement, including momentum and heat transfer can be considered in a ballistic manner. This means that the stochastic single-particle trajectories calculations, as well as those of the continuum flow, temperature and concentration fields can be performed under the simplifying assumptions used above. However, under realistic conditions the mass of particles injected into a plasma jet is far from those

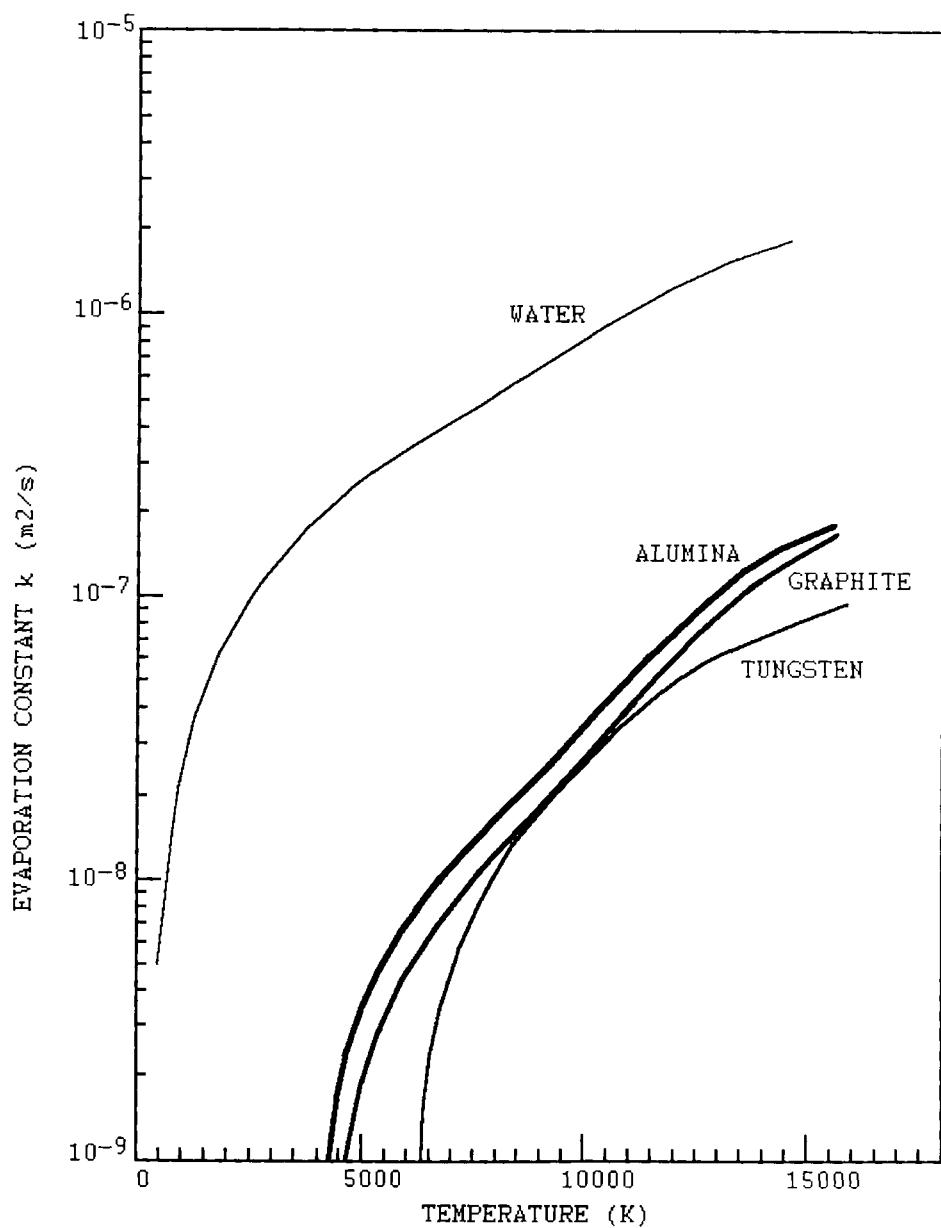


Figure 4-15. Evaporation constants for various materials in an argon plasma as a function of the plasma temperature [28].

idealized dilute systems. Indeed, in-flight processing of powders to produce plasma-sprayed coatings must be performed under high loading conditions in order to make efficient use of the thermal energy stored in the plasma. On exceeding a certain critical loading it is not warranted anymore to treat the individual impulse and thermal histories of the particles in a stochastic way. As a result particles interact with each other, and the momentum and temperature of the plasma jet will decrease with increasing mass of powder. The temperature decrease has three sources: 1. the heat extracted from the plasma to melt a larger mass of powder could cause substantial local cooling of the plasma, 2. the evaporated fraction of the powder (see Sect. 4.4.2.2) can drastically alter the thermophysical, thermodynamic and transport properties of the plasma gas, and 3. small powder particles with high optical emissivities evaporate easily, and radiate away plasma energy.

In order to arrive at an analytical solution for plasmas under dense loading conditions, the continuity, momentum, energy and species conservation equations, as well as the Maxwell electromagnetic field equations have to be solved simultaneously. This is beyond the scope of this text. Detailed descriptions of the numerical techniques employed to solve the plasma conservation equations and the electromagnetic field equations can be found in work by Mostaghimi *et al.* [30], Proulx *et al.* [29] and Crowe *et al.* [31].

4.4.3.1 Conservation Equations

To account for the particle interaction in a densely loaded plasma jet, the PSI (particle-source-in)-cell model by Crowe *et al.* [31] has been adopted by Proulx *et al.* [29]. Coupling of the stochastic single-particle trajectory calculation with those describing the continuum flow, temperature and concentration fields was obtained by introducing source–sink terms for mass, S_p^c , momentum, S_p^m (in r - and z -directions), and enthalpy, S_p^h .

The four plasma equations used to model the plasma–particle interactions under dense loading conditions [29] are

1. the continuity (mass conservation) equation

$$\text{div}(\rho u) = S_p^c, \quad (4-45)$$

with $S_p^c = \sum C(\Delta m_p/\tau)$ (C = particle concentration, Δm_p = amount of mass evaporated, τ = residence time), or, in cylindrical coordinates

$$(1/r)[\delta(r\rho v)/\delta r] + \delta(\rho u)/\delta z = S_p^c. \quad (4-45a)$$

2. the momentum conservation (Navier–Stokes) equation

$$\rho u(\text{grad } u) = -\text{grad } p + \text{div}(\eta \text{ grad } u) + \mathbf{j} \times \mathbf{B} + S_p^m, \quad (4-46)$$

with $S_p^m = \sum C[\Delta(mpv_{zp})/\tau]$ (axial direction, z) and $\sum C[\Delta(mpv_{rp})/\tau]$ (radial direction, r).

3. the energy conservation equation

$$\rho u(\text{grad } h) = -\text{grad}(k/c_p) \text{ grad } h + \sigma E_\theta^2 - q_r + S_p^h, \quad (4-47)$$

with $S_p^h = \sum C(q_p + q_v)$, where the expression in brackets is the energy balance between convective and radiative energy transfer (see above). The term σE_θ^2 describes the energy gain of the plasma by Ohmic heating, the term q_r the energy loss by radiation. The source-sink term, S , can be evaluated for the local cooling generated under dense loading conditions.

4. the species conservation equation

$$\rho u(\text{grad } Y_i) = \text{div}(D \text{ grad } Y_i) + S_p^c. \quad (4-48)$$

The general term Y_i refers to the concentration in different reference systems. In the barycentric (mass-centred) system, Y_i becomes W_i , i.e. the mass fraction of species i ; in the mole-centred system, Y_i is the mole fraction, X_i , and in the volume centred system, Y_i becomes $C_i v_i$, i.e. the product of the concentration of species i and its partial molar volume.

4.4.3.2 Results of Modeling under Dense Loading Conditions

Results shown below were obtained by Proulx *et al.* [29]. The authors injected copper particles of 70 μm diameter downwards through the central tube of an inductively coupled plasmatron. Copper evaporates easily, and the vapor changes the electrical and radiative properties of argon drastically. Figure 4-16 shows the isotherms and stream lines (left) and the isocontours of the concentration of copper vapor (right) for a feed rate of 5 g min^{-1} copper powder. Since the trajectories of the particles are very close to the axis of the jet, the plasma gas is significantly cooled down in this region as shown in Fig. 4-17. Even a feed rate of copper as small as 5 g min^{-1} leads to a temperature drop of about 2000 K. Higher feed rates lead to even lower plasma temperatures.

Table 4-4 gives numerical data of the feed rate m_p in grams per minute, the mass of copper evaporated, m_v , the heat absorbed by the solid particles, Q_p , and the heat absorbed by the copper vapor, Q_v . Q_v is generally much smaller than Q_p , and the ratio Q_v/Q_p changes from 29.6% at 1 g min^{-1} feed rate to 4.5% at 20 g min^{-1} feed rate. The total energy absorbed by the powder is between 3.1 and 17.8% of the plasma power input.

4.4.4 Heat Transfer Catastrophy

It is a puzzling but well known fact that the properties of plasma-sprayed coatings vary widely even though the spray parameters have supposedly been fixed within narrow ranges using sophisticated microprocessor-controlled metering devices, and stringent quality control measures have been applied using, for example, SPC and Taguchi analysis. In other words, infinitesimally small changes of the input param-

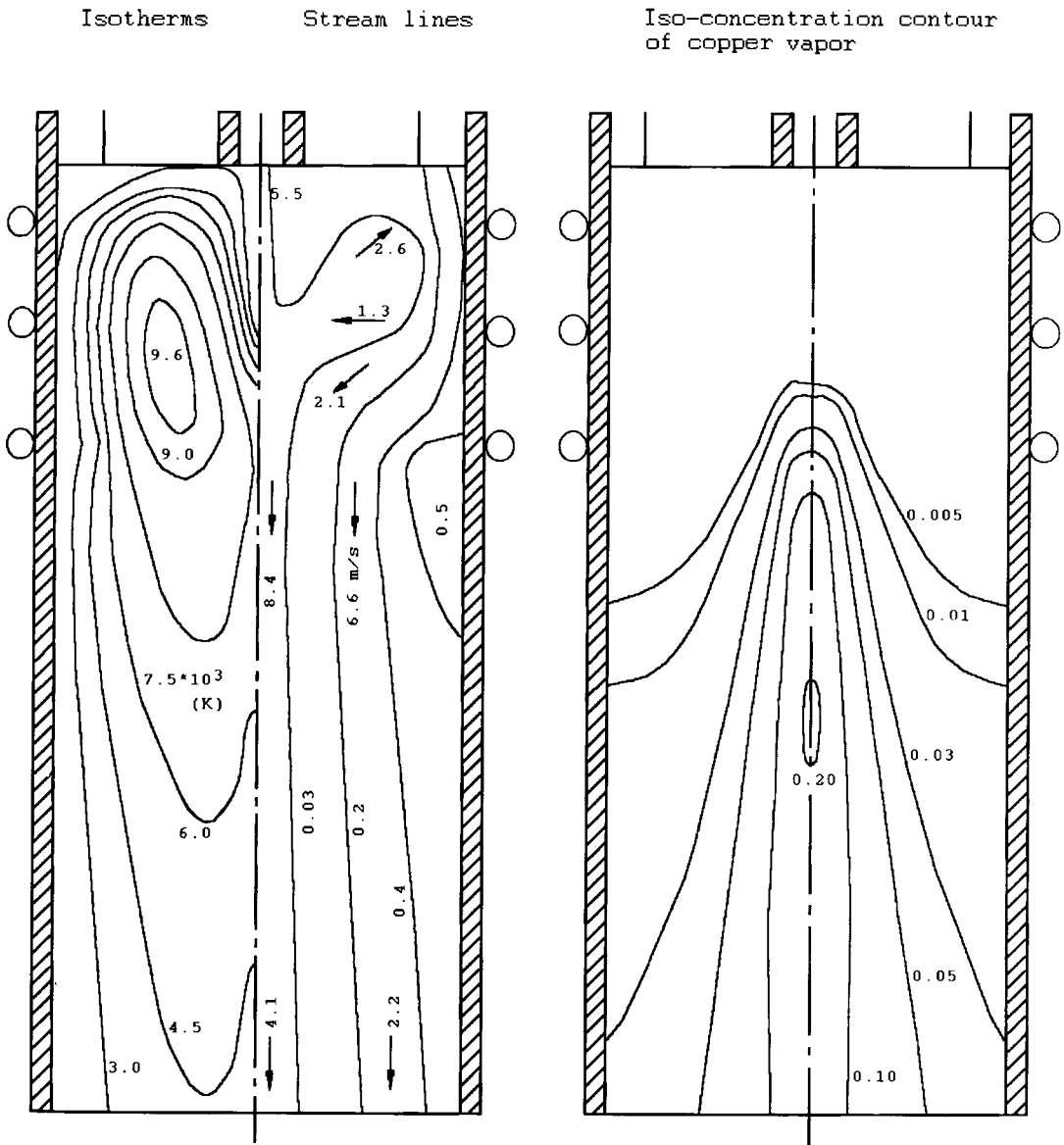


Figure 4-16. Cross-section of an inductively-coupled plasmatron after injection of copper powder (5 g min^{-1}). Left: isotherms and stream lines. Right: isopleths of concentration of copper vapor [29].

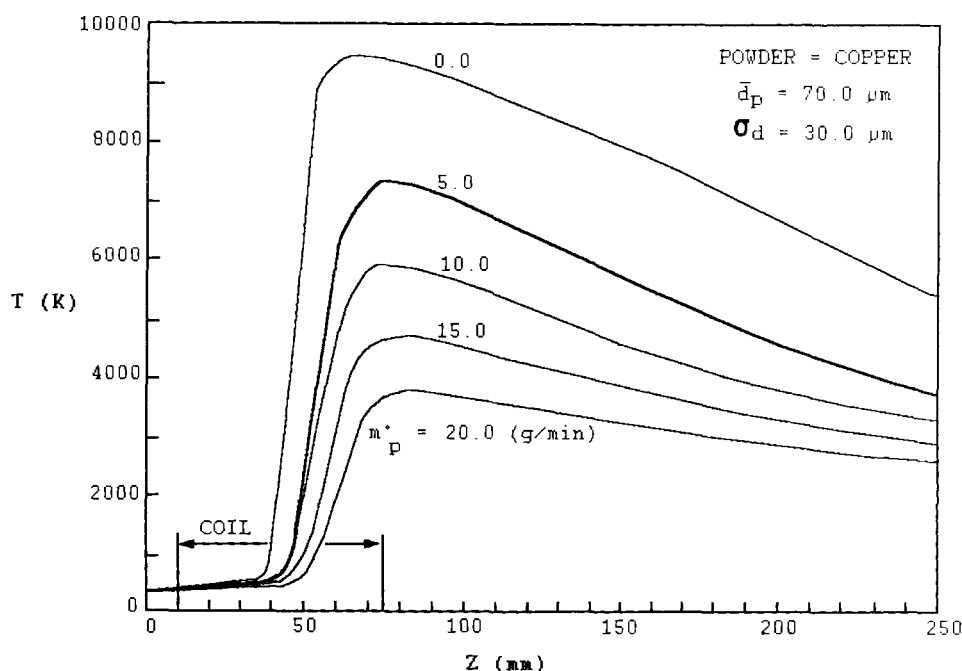


Figure 4-17. Cooling of a plasma under dense loading conditions of copper particles along the centerline of the plasma jet [29].

Table 4-4. Numerical data of plasma power absorbed by copper particles under dense loading conditions [29].

m_p (g min ⁻¹)	m_v (g min ⁻¹)	Q_p (W)	Q_v (W)	% of total energy absorbed
1.0	0.50	71.0	21.0	3.1
5.0	1.40	255.0	42.0	9.9
10.0	1.40	386.0	35.0	14.0
15.0	1.16	460.0	28.0	16.3
20.0	0.94	511.0	23.0	17.8

ters cause large, and generally nondeterministic changes in the output parameters, i.e. those parameters influencing the properties and hence the performance of the coatings. This is the hallmark of nonlinearity.

To search for the cause of nonlinear behavior of a collection of particles under dense loading conditions in a plasma jet, several approaches may be taken that all relate to very complex interactions within the plasma. It may suffice to outline in the context of this book only one possible chain of events leading to nonlinearity.

In a thermal plasma cooperative processes occur through numerous types of waves (transverse electromagnetic, longitudinal plasma-acoustic Langmuir, magnetohydrodynamic, and drift waves) that interact and cause stochastic fluctuations

in which the phases of the waves exhibit probabilistic distributions. Such nonequilibrium distributions can be roughly described, respectively as *electromagnetic and magnetohydrodynamic turbulences* (see Sec. 3.1.1). Since both of these turbulences affect the local magnetic field strength, \mathbf{B} , and the electrical current density, \mathbf{j} , their cross-product, the Lorentz force ($\mathbf{j} \times \mathbf{B}$) fluctuates rapidly and with it the plasma compression ('z-pinch'). The Lorentz force is being compensated for by the gas kinetic pressure gradient, $\text{grad } p$; consideration of the plasma velocity and viscosity yields the momentum (Navier–Stokes) conservation equation that is known to be nonlinear:

$$(\mathbf{j} \times \mathbf{B}) = \rho_m u (\text{grad } u) + \text{grad } p - \text{div}(\eta \text{ grad } u), \quad (4-49)$$

(see also Eq. (4-46)). Hence changes in the magnitude of the Lorentz force influence the plasma velocity, u , the pressure gradient, $\text{grad } p$, and the dynamic plasma viscosity, η . In particular, the fluctuations of the plasma-confining Lorentz force generate a plasma jet pulsating perpendicular to the jet axis with frequencies that are on the order of the residence time of the particles in the jet, i.e. tenths of microseconds. The rate with which turbulent eddies of cool air surrounding the plasma jet are entrained by the pumping action of the plasma changes accordingly. In this way a rapidly fluctuating temperature profile is obtained with likely rapidly changing heat transfer coefficients, h , of the plasma–particle system. As a consequence the degree of melting of the particles is affected because the relative proportion of heat transferred by convective and radiative processes is severely and instantaneously disturbed. Finally, the local thermal equilibrium breaks down on a scale that is small compared to the overall volume of the plasma jet. Then the system enters the realm of a '*heat transfer catastrophe*'. This phenomenon can be tentatively described in terms of stability theory by an elementary cusp catastrophe of codimension two (Riemann–Hugoniot catastrophe [32]). The order parameters X and Y on the control surface, and the parameter Z separating the control from the behavior surface can be selected in such a way that only dimensionless groups (see Appendix A) as real variables occur (Fig. 4-18). The first ordering parameter X is the heat flux that can be expressed as the product of the Grashof, Prandtl and Nusselt numbers, $\text{Gr} \times \text{Pr} \times \text{Nu}$. The second ordering parameter Y is the temperature difference, expressed through the thermal Rayleigh number, Ra . The two ordering parameters define a bifurcation set of local competition between two stable states of heat transfer: a convective heat transfer mode and a radiative heat transfer mode. On the control surface, curves A (radiative mode) and B (convective mode) meet at a temperature-dependent point C with the critical Rayleigh number, Ra_c and a critical heat flux, ξ , beyond which the bimodality ceases to exist. As the parameter defining the z-coordinate the Boltzmann number Bo can be chosen, given by $\text{Bo} = [\text{Re Pr/St}]/e^* = [\text{Pe/St}]/e^*$, where Re = Reynolds number, Pr = Prandtl number, Pe = Péclet number, and St = Stefan number, and e^* = surface emissivity of the particles.

The behavior surface shows the characteristic shape of the fold of a cusp catastrophe that outlines the region of inaccessibility: heat transfer from plasma to particles occurs either in the convective mode at lower temperature, or in the radiative mode at higher temperature. Consequently, the lower sheet of the behavior surface corresponds to the convective regime B, characterized by a large Boltzmann number

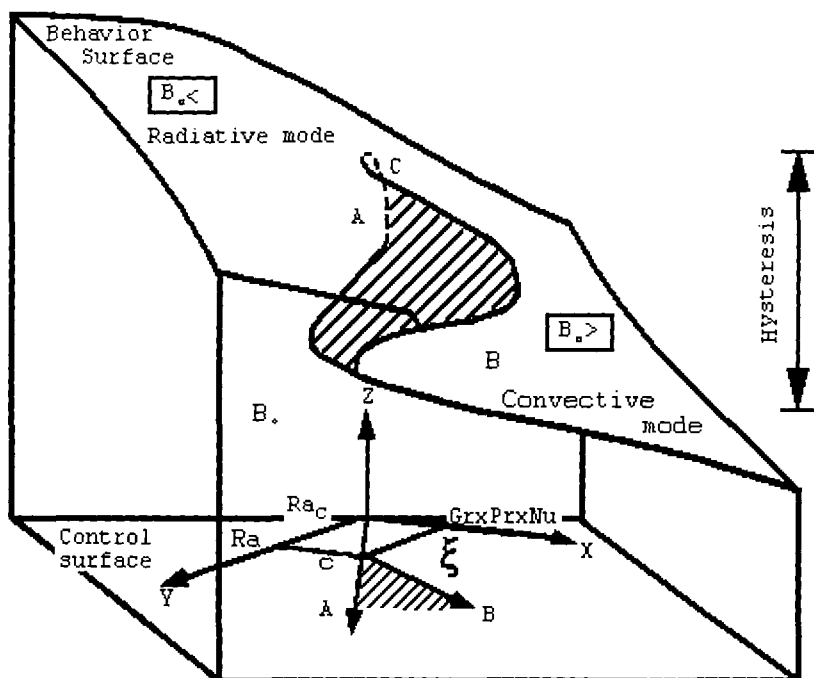


Figure 4-18. Control and behavior surfaces of a plasma undergoing a heat transfer catastrophe (see text).

Bo. The upper sheet corresponds to a radiative regime A with a small Boltzmann number³. The Boltzmann number defines the ratio of the bulk heat transport to the heat transported by radiation. For dense loading conditions the Bougue number ($B = 3C_B\lambda_r/4\rho_D r$, with C_B = mass ratio of particles to unit bed volume, λ_r = mean path of radiation, ρ_D = particle density, r = mean particle radius) must be used. This dimensionless group describes the radiant heat transfer to a particle-loaded plasma gas stream. The approach taken here to relate the nonlinear characteristics of a plasma to plasma turbulences with high frequencies and the ensuing heat transfer catastrophe is similar to that of the thermodiffusive mass transport in systems with rapidly changing chemical potential and temperature gradients [33].

4.4.5 Energy Economy

At this point it should be mentioned that only a small fraction of the energy supplied to the plasma gas is being stored in the particles. A macroscopic energy balance [34] shows:

³ The expression for the Boltzmann number is $Bo = \rho_m c_p v_s / e^* \sigma T^3$, with ρ_m = mass density, c_p = specific heat, v_s = plasma velocity, e^* = surface emissivity of the particles, σ = Stefan-Boltzmann coefficient of radiative heat transfer, and T = local plasma temperature.

Table 4-5. Comparison of process variables for welding and plasma spraying operations.

Variable	Unit	CO ₂ welding	Hand- welding	Plasma- spraying
Deposit mass flow rate	g min ⁻¹	42	40	40
Current	A	200	200	400
Voltage	V	25	25	40
Traverse speed	mm s ⁻¹	5.5	3.6	40
Weld/spray width	mm	11.5	10	25
Heat content of the spray particles	kJ kg ⁻¹	–	–	1 500
Energy efficiency	%	80	80	2.4

Energy supplied to the torch	42.0 kW
Cooling water losses (66%)	–27.7 kW
Losses due to convection and radiation to surroundings	–13.3 kW
Net energy stored in particles	1.0 kW

The energy efficiency is thus only 2.4%. This low number should be compared to a typical energy balance in welding using heat flow density data. Table 4-5 shows process variables for welding and plasma spraying operations. For a *welding process*, the heat flow density is $q_w = (\text{efficiency} \times \text{current} \times \text{voltage} \times \text{time}) / (\text{traverse speed} \times \text{weld width} \times \text{time})$. For the *plasma spraying process*, it is $q_p = (\text{deposit mass flow rate} \times \text{heat content of particles}) / (\text{traverse speed} \times \text{spray width} \times \text{time})$. With the data of Table 4-5 one obtains

$$q_w = (0.8 \times 200[\text{A}] \times 25[\text{V}] \times 1[\text{s}]) / (3.6[\text{mm s}^{-1}] \times 10[\text{mm}] \times 1[\text{s}]) \\ = 111 \text{ J mm}^{-2}$$

$$q_p = (40[\text{g min}^{-1}] / 60[\text{s}] \times 1500[\text{J g}^{-1}]) / (40[\text{mm s}^{-1}] \times 25[\text{mm}] \times 1[\text{s}]) \\ = 1 \text{ J mm}^{-2}$$

Consequently, the heat flow density during plasma spraying is only about 1% of that of the standard welding process. In conclusion this means that plasma spraying has a low energy efficiency and a low heat flow density compared with plasma welding.

Similarly low efficiencies have been calculated for plasma-arc wire-spraying operations [35]. Approximately 40% of the input energy is spent to heat the plasmatron and hence is removed by water-cooling whereas the majority of the energy is used to heat the plasma gas. Only 2–5% of this energy is available for melting the wire and accelerating the liquid droplets, and another 6–9% is used to heat the substrate.

The results of the modeling of the momentum and heat transfer could be used on-line for estimating the powder velocities and temperatures at the time of impact. Then a computer-assisted feedback loop could be installed to directly control the input parameters such as:

- power to the plasmatron,
- particle feed rate,
- plasma gas composition, and
- stand-off distance.

To verify the feedback parameters, time-of-flight LDA and multiwavelength pyrometry could be employed. This advanced concept of plasma spray process control, however, is still in the future. Areas of improvement and developments are [36]:

- internal particle heat transfer,
- 3D-models for d.c. plasma spraying,
- verification and control of drag and Nusselt correlations,
- modeling of particle impact on substrate, and
- low pressure, supersonic models for d.c. plasmas.

4.5 Particle Diagnostics: Velocity, Temperature, and Number Densities

The methods of measurement of plasma velocities and plasma temperature, and the equipment used for this purpose have been described in Chapter 3. In this section some typical results related to particle velocities and temperatures, and number densities will be described.

4.5.1 Particle Velocity Determination

As described in detail above, the highly accelerated plasma jet transfers momentum to the powder particles injected near the arc root. The resulting particle velocities have to be chosen in such a way that most particles travel in trajectories that assure optimum residence time in the hot zone of the jet. To obtain axial trajectories an optimum injection velocity is likewise required and thus the powder gas pressure has to be adjusted to the remaining selected plasma parameters. As the flow of the carrier gas controls the particle trajectory through the plasma jet a balance must be maintained between plasma gas and powder carrier gas velocities to correctly position the particles in the plasma for proper melting and acceleration. For a given powder there is an optimum value of powder feed rate that will produce maximum deposition efficiency.

Figure 4-19 shows that for experiments in an argon/hydrogen plasma at a power of 29 kW alumina particles with a mean diameter of $18 \pm 3 \mu\text{m}$ injected with a carrier gas (argon) flow rate of 5.51 min^{-1} move in a trajectory close to and grazing the plasma jet axis. On increasing the powder carrier gas flow rate to 101 min^{-1} , the particles completely cross the axis of the jet at a distance of approximately 8 mm from the point of injection [37]. Thus they enter the hotter region of the jet but are blown quickly out of it again so that their residence time in the jet actually decreases.

Figure 4-19. Dependence of the particle trajectories on the flow rate of the argon carrier gas (after [37]).

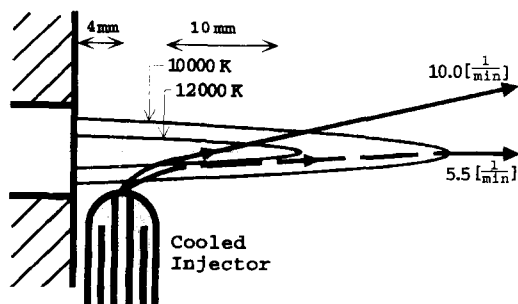


Figure 4-20. Alumina particle velocity profiles at an axial distance of $z = 75$ mm for different argon carrier gas flow rates [37].

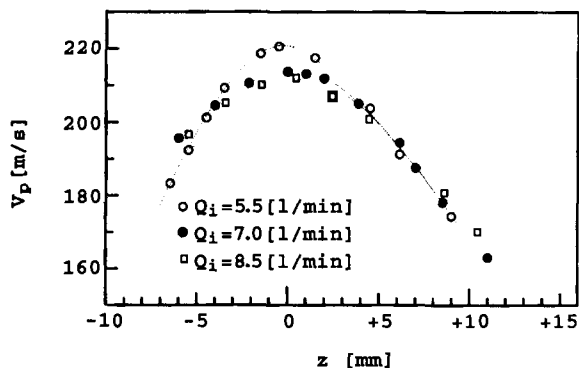


Figure 4-20 shows the particle velocity profiles at an axial distance of $z = 75$ mm for carrier gas flow rates between 5.5 and 8.5 l min^{-1} [37]. Maximum velocities were obtained with a low carrier gas flow rate (5.5 l min^{-1}). Under these conditions the majority of the powder particles did occupy trajectories close to the jet axis (see Fig. 4-19) where they acquired the highest momentum and temperature.

It should be noted, however, that the real trajectory of a particle may deviate considerably from the calculated one based on the momentum conservation equation. This has been explained by Vardelle *et al.* [10] by the influence of *thermophoretic forces*. Thermophoresis, however, is strongly dependent on the (free stream) temperature and the particle size [12]. Also, thermophoresis becomes comparable to viscous drag forces only for small relative velocities (around 1 m s^{-1}). Therefore this effect is only significant for very small particles ($< 10 \mu\text{m}$) that follow very quickly the flow field.

Particle injection can be described in two stages. In the first stage (penetration stage) the particles still maintain the velocities acquired by momentum transfer from the carrier gas. In addition they pick up momentum from the highly accelerated plasma gas. In this stage thermophoretic effects will be negligible since the particle velocities are relatively high even though the temperature gradients are on the order of 10^7 K m^{-1} . But during the following stage of deceleration (relaxation) thermophoretic effects may also be rather insignificant because the temperature gradient decreases rapidly; the displacement of particles will also be small during their short residence time of around 1 ms in the plasma jet [12].

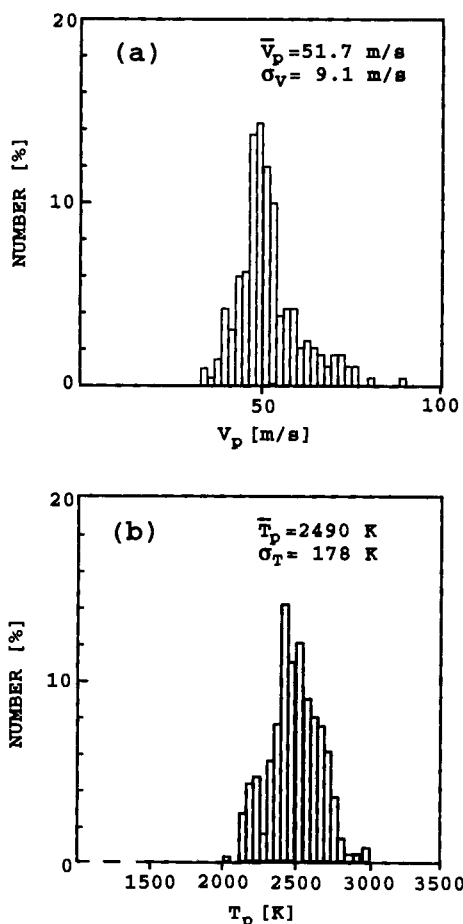


Figure 4-21. Histogram of the velocity (a) and temperature (b) of alumina particles ($79 \pm 18 \mu\text{m}$ diameter) injected with a feed rate of 1.2 g min^{-1} into an inductively-coupled RF argon plasma [38].

The particle velocity distribution assumes frequently a quasi-Gaussian distribution. Figure 4-21a shows a histogram of the velocity of alumina particles of a mean diameter of $79 \pm 18 \mu\text{m}$ injected with a feed rate of 1.2 g min^{-1} into an inductively coupled RF argon plasma operated under soft-vacuum conditions at a plate power of 15 kW [38]. The powder carrier gas was helium with a flow rate of 8 l min^{-1} . The velocities were measured in-flight simultaneously with particle temperatures (Fig. 4-21b) utilizing the analysis of the change in the time- and amplitude domains of the waveform of a He-Ne laser light pulse. A powder particle with a diameter d_p traverses the observation window of height H and width W . The half-width, t_w , of the laser light pulse corresponds to the time-of-flight of the particle through the slit height. Thus the particle velocity, V_p is:

$$V_p = H/(t_w R), \quad (4-50)$$

where R = image ratio determined by the optical setup.

Figure 4-22. Dependence of particle velocity on density and grain size of spray powders [40].

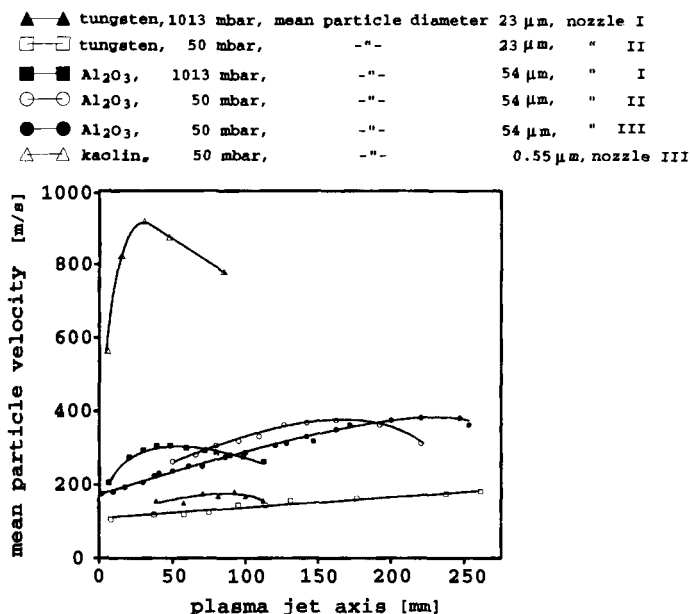
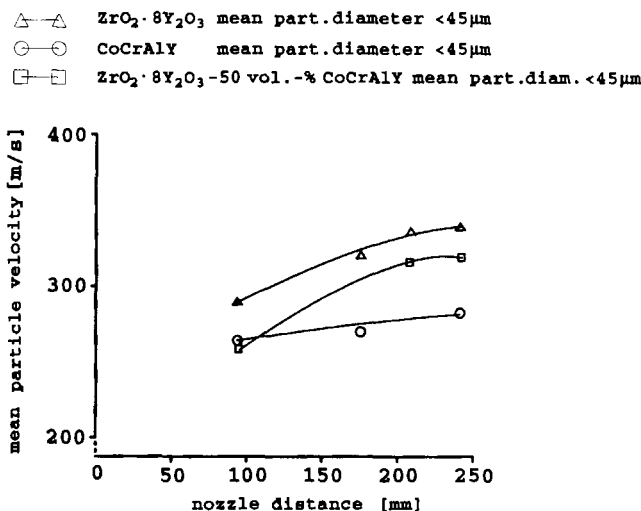


Figure 4-23. Dependence of particle velocity on density of powders utilized in spraying of thermal barrier coatings [40].



The rise time, t_r , and the fall time, t_f , of the trapezoidal profile of the light pulse correspond to the time elapsed between which the particle is entering or leaving the observation window:

$$t_r = t_f = d_p / V_p. \quad (4-51)$$

The pulse intensity, i.e. the amplitude, can give information on the surface temperature of the particle, T_p , as shown in Eq. (3-35).

The particle velocities in the plasma jet are also dependent on the residual chamber pressure. Work by Steffens *et al.* [39] showed that momentum and heat transfer between plasma and particles are reduced at low pressure compared to atmospheric pressure. Modeling of the particle velocity under low pressure ('vacuum') plasma spray conditions require noncontinuum assumptions about the flow conditions [40] (see also [12]). As shown in Figs 4-22 and 4-23 the particle velocities are strongly dependent on density and grain size of the powder materials used. Also, the acceleration of the particles in a low pressure-plasma jet is considerably less than under atmospheric pressure conditions. Figure 4-23, in particular, illustrates the problems associated with the production of graded ceramic/metal coatings as suggested for thermal barrier coatings on gas turbine blades for aerospace applications (see also Sec. 6.2).

4.5.2 Particle Temperature Determination

In principle, the analytical techniques applied to measure in-flight particle temperatures have already been reviewed in the preceding chapter (see Sec. 3.4.1). In order to measure the plasma temperature by two-color pyrometry, very small particles have to be introduced into the plasma jet as seeds that do not disturb the flow of the plasma (Sec. 3.4.1.2).

4.5.3 Particle Number Density Determination

It is of great interest to study simultaneously the velocity, temperature and number density of powder particles in a plasma jet. Any successful modeling requires input

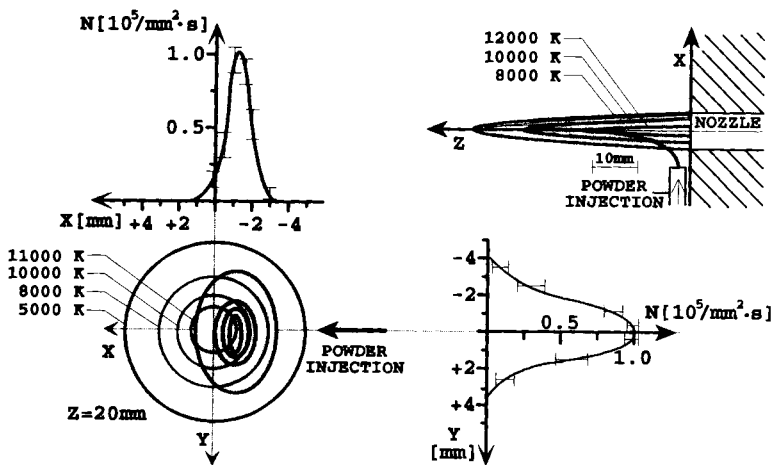


Figure 4-24. Determination of particle flux number densities N in axial and radial directions (alumina, $18 \pm 3 \mu\text{m}$ diameter) [37].

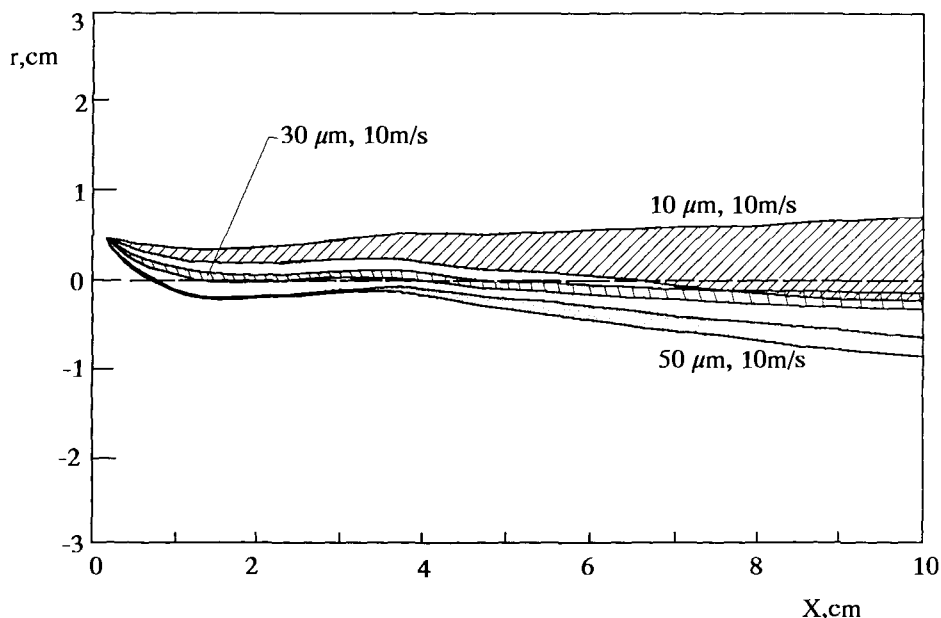


Figure 4-25. Dispersed particle trajectories of alumina particles of different sizes in a turbulent free plasma argon jet [12].

parameters that give reliable information on the numerous forces acting on the powder particles. Equipment has been developed to accomplish the difficult task of measuring simultaneously the three parameters mentioned above (see Fig. 3-31). Typical particle trajectory data and particle flux number density distributions obtained with this equipment are shown in Fig. 4-24. Alumina powder particles ($18 \pm 3 \mu\text{m}$ diameter) were injected with a powder gas flow rate of 5.5 l min^{-1} into an Ar/H₂ plasma (29 kW arc power) with a feed rate of 4 g min^{-1} . The tip of the non-cooled powder injection probe was 4 mm from the edge of the nozzle, i.e. 8 mm from the axis of the jet. The particles spread over a large region of the plasma (Fig. 4-24, left, bottom) as shown by the isopleths of the particle flux in the X - Y plane. The profiles of the particle flux number densities are shown in the orthogonal X - Z (top left) and Y - Z (bottom right) planes. There is a noticeable off-center asymmetry in the X - Z plane of injection, indicating the disturbance of the smooth plasma flow by the injected powder. Comparison of these results with those shown in Fig. 4-19 shows that by using a water-cooled injection probe and advancing the point of injection of the powder by only 4 mm towards the plasma jet axis, a substantial modification of the particle trajectories can be observed. As a consequence, in spite of identical carrier gas flow rates in this case the particles penetrate deeper into the jet that results in turn in an acquisition by the particles of larger momentum and higher temperatures.

In the preceding paragraphs the turbulent nature of the plasma jet was not explicitly considered. As the smooth and steady flow field of the plasma is disturbed by

turbulences, the particle trajectories also become dispersed, i.e. the plasma velocity field is locally modified by randomly oriented turbulent eddies [41]. For typical eddy sizes of 1 mm, Fig. 4-25 illustrates the dispersed particle trajectories of alumina particles with mean diameters of 10, 30 and 50 μm injected with a velocity of 10 m s^{-1} into a turbulent free plasma argon jet [12]. Obviously, smaller particles will be more dispersed than larger ones since the smaller particles are following more easily the turbulent motions within the eddies. Also, the dispersion becomes more prominent when moving downstream from the point of injection due to the accumulated 'random walk' influence. For sufficiently large particles the variable property corrections in the equation of motion (see Eq. (4-1)) may still exceed the turbulent dispersion term. Therefore, a correction for turbulent motion of the plasma can be neglected for larger particles.

References

- [1] A. Hasui, S. Kitahara, T. Fukushima, *Trans. NRI* **1970**, 12(1), 9.
- [2] H. Maruo, Y. Hirata, J. Kato, Y. Matsumoto, *Proc. Intern. Symp. Adv. Thermal Spraying Technol. and Allied Coatings (ATTAC'88)* **1988**, 153.
- [3] B. Elvers, S. Hawkins, G. Schulz (eds.), *Ullmann's Encyclopedia of Industrial Chemistry, 5th edition, Metals, Surface Treatment, Vol. A16*, VCH, Weinheim, **1990**, p. 433.
- [4] Y. Borisov, N. Voropaj, I. Netesa, V. Korzhyk, I. Kozyakov, *Proc. 14th ITSC'95*, Kobe, 22–26 May, **1995**, 1115.
- [5] E. J. Kubel, *Adv. Mater. Proc.* **1990**, 12, 24.
- [6] H. Eschnauer, *Die morphologische Struktur von pulverförmigen Spritzwerkstoffen. Habilitationsschrift*, RWTH Aachen, **1982**.
- [7] L. Pawlowski, *The Science and Engineering of Thermal Spray Coatings*, Wiley, Chichester, **1995**, pp. 1–20.
- [8] R. B. Heimann, *Development of Plasma-Sprayed Silicon Nitride-Based Coatings on Steel*. Research Report to NSERC and EAITC Canada, 15 December **1992**.
- [9] *Powder Technology, Product brochure*, Institute of Materials Science, RWTH Aachen, **1992**.
- [10] A. Vardelle, M. Vardelle, P. Fauchais, *Plasma Chem. Plasma Proc.* **1982**, 2, 255.
- [11] J. A. Lewis, W. H. Gauvin, *AIChE J.* **1973**, 19, 982.
- [12] E. Pfender, *Plasma Chem. Plasma Proc.* **1989**, 9, 167S.
- [13] A. V. Nikolaev, In: *Plasma Processing in Metallurgy and in Process Engineering of Non-Organic Materials*, Nauka, Moscow, **1973**.
- [14] K. V. Beard, H. R. Pruppacher, *J. Atmos. Sci.* **1969**, 26, 1066.
- [15] J. K. Fiszdon, *Int. J. Heat Mass Trans.* **1979**, 22, 749.
- [16] Y. C. Lee, K. C. Hsu, E. Pfender, *Proc. 5th Int. Symp. on Plasma Chemistry* **1981**, 2, 795.
- [17] X. Chen, E. Pfender, *Plasma Chem. Plasma Phys.* **1983**, 3, 351.
- [18] K. J. Zahnle, *J. Geophys. Res.* **1992**, 97(10), 243.
- [19] N. N. Sayegh, W. H. Gauvin, *AIChE J.* **1979**, 25, 522.
- [20] N. Frösling, *Göteborg. Beitr. Geophys.* **1938**, 52, 170.
- [21] G. D. Raithby, E. R. Eckert, *Int. J. Heat Mass Trans.* **1968**, 11, 1233.
- [22] M. Vardelle, A. Vardelle, P. Fauchais, M. I. Boulos, *AIChE J.* **1983**, 29, 236.
- [23] X. Chen, E. Pfender, *Plasma Chem. Plasma Phys.* **1983**, 3, 97.
- [24] E. Bourdin, P. Fauchais, M. I. Boulos, *Int. J. Heat Mass Trans.* **1983**, 26, 567.
- [25] D. R. Mash, N. E. Weare, D. L. Walker, *J. Met.* **1961**, July, 473.
- [26] C. W. Marynowski, F. A. Halden, E. P. Farley, *Electrochem. Technol.* **1965**, 3, 109.
- [27] J. L. Engelke, *Proc. AIChE Meeting*, Los Angeles, CA, 5 Feb, **1962**.

- [28] X. Chen, E. Pfender, *Plasma Chem. Plasma Proc.* **1982**, 2, 185.
- [29] P. Proulx, J. Mostaghimi, M. I. Boulos, *Int. J. Heat Mass Trans.* **1985**, 28, 1327.
- [30] J. Mostaghimi, P. Proulx, M. I. Boulos, *Int. J. Heat Mass Trans.* **1985**, 28, 187.
- [31] C. T. Crowe, M. P. Sharma, D. E. Stock, *J. Fluid Eng.* **1977**, 99, 325.
- [32] R. Thom, *Structural Stability and Morphogenesis*, Benjamin, New York, NY **1975**.
- [33] R. B. Heimann, *Appl. Geochem.* **1987**, 2, 639.
- [34] J. M. Houben, Relations of the Adhesion of Plasma Sprayed Coatings to the Process Parameters Size, Velocity and Heat Content of the Spray Particles. Ph.D. Thesis, Technical University Eindhoven, The Netherlands, **1988**.
- [35] N. N. Rykalin, V. V. Kudinov, *Pure Appl. Chem.* **1976**, 48, 229.
- [36] J. Mostaghimi, *Trans. 17th Workshop CUITAC*, (Ed. R. B. Heimann) 1–2 October, **1991**, Quebec, Canada.
- [37] M. Vardelle, A. Vardelle, P. Fauchais, M. I. Boulos, *AIChE J.* **1988**, 34(4), 567.
- [38] T. Sakuta, M. I. Boulos, *Proc. 8th Int. Symp. Plasma Chem. ISPC-8*, Tokyo, **1987**, paper BVII-02, p. 371.
- [39] H.-D. Steffens, K.-H. Busse, M. Schneider, *Adv. Therm. Spraying*, (Ed. N. F. Eaton) (Proc. 11th ITSC, Montreal, 8–12 Sept.) Pergamon Press, New York, **1986**, 49.
- [40] D. Wei, D. Apelian, M. Paliwal, S. M. Correa, *Proc. Symp. Mat. Res. Soc. Plasma Processing and Synthesis of Materials*, **1984**, 30, 197.
- [41] Y. C. Lee, E. Pfender, *Plasma Chem. Plasma Proc.* **1985**, 5, 3.

5 The Third Energy Transfer Process: Particle–Substrate Interactions

5.1 Basic Considerations

Coatings are built up particle by particle. The solidification time, t_{sol} , of a hot molten particle arriving at the cold substrate surface is orders of magnitude shorter than the intermission time, t_i , the time between the arrival of two particles flying in the same trajectory. Therefore, a particle does not encounter, on arrival, a permanent liquid melt pool as it would in welding processes. The cooling time from the freezing point down to ambient temperature is two to three orders of magnitude longer than the solidification time. This means that a limited degree of particle interaction by diffusion as well as some stress relief is still possible.

- The properties of the layered deposited material are determined by the:

- velocity and temperature of the particles on impact,
- relative movement of the plasmatron and the substrate, and
- substrate and coating cooling during spraying.

-

The wetting and flow properties of the liquid droplets are of great importance. They influence the:

-

- coating porosity,
- morphology of the coating/substrate interface,
- cohesive bonding among splats and successive layers, and
- adhesive bonding to the substrate.

These influences will be discussed briefly in Sec. 5.5.

Flow and solidification of molten droplets on impact are difficult to treat theoretically because of interaction between heat transfer and crystal growth kinetics [1–4]. It is also necessary to take into consideration the propagation of shock waves into the flattened particles and the substrate. The study of particle splats on glass or ceramic slides ('wipe test') [5] is a useful method to determine quickly the degree of superheating and thus the viscosity of the liquid particle droplets (see Sec. 5.5.1).

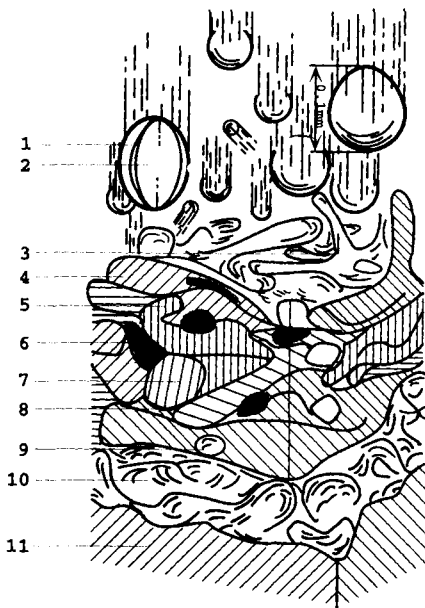


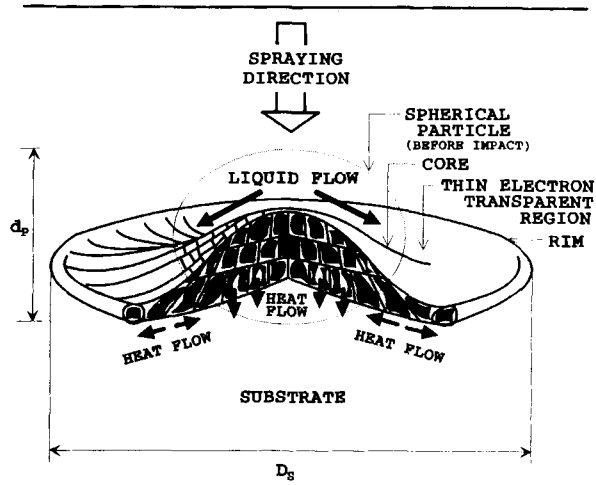
Figure 5-1. Schematic rendering of the chaotic structure of a plasma-sprayed coating layer 1: Thin molten shell; 2: unmelted core; 3: liquid splash; 4: 'pancake' splat; 5: interlocked splats; 6: oxidized particle; 7: unmelted particle; 8: pore; 9: void; 10: roughened substrate surface; 11: substrate [6].

Figure 5-1 shows an artistic rendering of the chaotic plasma spray process [6]. The molten droplets are thought to arrive one at a time, propagate along ballistic trajectories, and do not interfere with each other during flight ('ballistic model', see Sec. 5.5.1.3). A droplet with a diameter d_p impacts the solid substrate surface, and deforms to a so-called 'pancake' or 'Mexican hat' shape with a splat diameter D_s (Fig. 5-2). Entrained gases, unmelted and oxidized particles, and voids are mixed with the particle splats, and tend to degrade the coating properties because they provide points of stress concentration during in-service loading that will act as crack initiation centers. Particles with sizes substantially larger than the mean do not melt completely to their core and thus do not spread on impact. In their wake porosity can build up as well as trains of other only partially melted particles (Fig. 5-3). Thus it is extremely important to utilize spray powders with a narrow particle size distribution with a sufficiently small standard deviation.

5.2 Estimation of Particle Number Density

A quantitative estimation of the number of particles arriving at a defined surface area of the substrate in unit time, and the build-up of lamellae of the coating has been given by Houben [7] by considering spraying molybdenum powder (density $\rho_{Mo} = 10\,200 \text{ kg m}^{-3}$) of a mean particle size d_p of $50 \times 10^{-6} \text{ m}$ with a powder feed

Figure 5-2. Deformation of a plasma-sprayed particle [6].



rate of 40 g min^{-1} ($6.7 \times 10^{-4} \text{ kg s}^{-1}$) onto a steel substrate. Thus, the number of particles injected into the plasma jet, N_1 , is 10^6 particles per second¹.

The traverse speed of the plasmatron moving relative to the substrate is assumed to be $v = 4 \times 10^{-2} \text{ m s}^{-1}$, and the spray width, $w = 2.5 \times 10^{-2} \text{ m}$. The lamella diameter, D , of a single splat is $125 \times 10^{-6} \text{ m}$. With these parameters, the average number of lamellae on top of each other, N_2 , after one pass of the plasmatron can be calculated with the assumption that all particles, N_1 , injected will arrive at and stick to the substrate surface (deposition efficiency 100%) as follows.

The N_1 particles produce a total spray surface per unit time of

$$\begin{aligned} A_p &= N_1 (\pi/4) D^2 = 10^6 [\text{p s}^{-1}] (\pi/4) (125 \times 10^{-6})^2 [\text{m}^2] \\ &= 1.23 \times 10^{-2} \text{ m}^2 \text{ s}^{-1}. \end{aligned} \quad (5-1)$$

Because the plasma jet moves, the covered substrate area will be

$$A_s = vw = 1.0 \times 10^{-3} \text{ m}^2 \text{ s}^{-1}. \quad (5-2)$$

Then the average number of lamelle on top of each other is

$$N_2 = A_p / A_s = 12. \quad (5-3)$$

The deposition time, i.e. the time required to lay down the N_2 lamellae, is $t_{\text{dep}} = w/v = 0.625 \text{ s}$. The intensity of the bombardment of the surface is $n = N_1/w^2 =$

¹ Mass of single particle $m_p = V_p \rho_{\text{Mo}} = (4/3)\pi(d_p/2)^3 \rho_{\text{Mo}} [\text{kg m}^{-3}] = (\pi/6)(50 \times 10^{-6} [\text{m}])^3 10.2 \times 10^3 [\text{kg m}^{-3}] = 6.7 \times 10^{-10} \text{ kg}$. Powder feed rate $m = 6.7 \times 10^{-4} \text{ kg s}^{-1}$. Number of particles injected $N_1 = m/m_p = 10^6 \text{ s}^{-1}$.

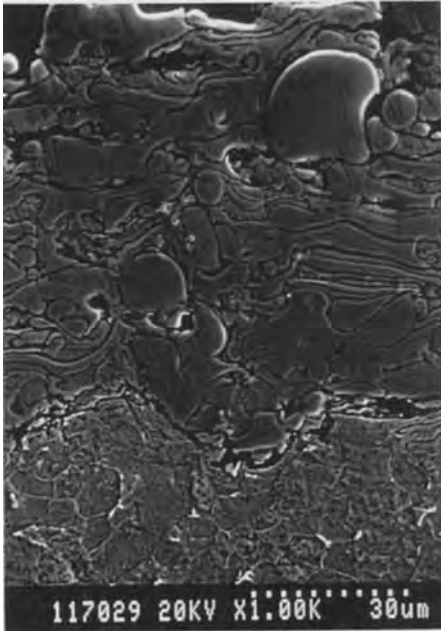


Figure 5-3. Development of porosity in the vicinity of large unmelted particles (85Fe15Si on low carbon steel, etched for 20 s in Nital).

1.6×10^9 particles per second per m^2 . The surface receives per unit area $N_2 = t_{\text{dep}} n = N_1/vw = N_1/A_s = 1.0 \times 10^9$ particles m^{-2} .

Furthermore, the time elapsed between the arrival of two particles belonging to the i th and $(i + 1)$ th lamella plane is defined as t_i or ‘intermission’ time. It follows that:

$$t_i = w/vN_2 = 0.052 \text{ s.} \quad (5-4)$$

The solidification time for a $50 \mu\text{m}$ Mo droplet can be calculated using an approximate solution of the heat diffusion equation at the interface solid substrate/liquid droplet:

$$t_{\text{sol}} = x^2/4p^2a, \quad (5-5)$$

where x = lamella thickness, p = constant², and a = thermal diffusivity.

Numerically, for a lamella thickness of $7 \mu\text{m}$,³ the solidification time becomes $t_{\text{sol}} = (7 \times 10^{-6}[\text{m}])^2/4(0.582)^2(5.61 \times 10^{-5}[\text{m}^2 \text{ s}^{-1}]) = 6.5 \times 10^{-7} \text{ s}$.

² According to Houben [7], p is the Neumann–Schwartz parameter that can be estimated as the fitting parameter from the solidification time versus layer thickness relationship (Fig. 5-11).

³ Assuming that the originally spherical droplet with a diameter $d = 50 \times 10^{-6} \text{ m}$ and a volume V_p of $65.4 \times 10^{-15} \text{ m}^3$ deforms on impact to a cylindrical disc of diameter $D = 125 \times 10^{-6} \text{ m}$ of a volume $V_c = h(\pi/4)D^2 = 65.4 \times 10^{-15} \text{ m}^3$, the height h of the disc, i.e. the lamella thickness is $5.3 \times 10^{-6} \text{ m}$. Accounting for the ‘Mexican hat’ shape of the splat the geometric factor of 1.3 [4] transforms this value to an actual thickness of $7 \times 10^{-6} \text{ m}$.

The ratio between intermission time and solidification time is $t_i/t_{\text{sol}} = 5.2 \times 10^{-2}[\text{s}]/6.5 \times 10^{-7}[\text{s}] = 80\,000!$ This means that the time between two consecutive collisions is much longer than the time needed to solidify the droplets. Thus the liquid droplets are not likely to encounter a liquid surface, i.e. a weld pool does not exist. This is consistent with the view of plasma spray technology as a rapid solidification technology with cooling rates exceeding 10^6 to 10^7 K s^{-1} . It should be emphasized that Eq. (5-5) is only a very rough zero-order solution of the heat transfer (Fourier) equation. An exact solution is presented in Sec. 5.4.1, and a numerical example will be given in Sec. 5.4.2 and Appendix B.

With similar simple assumptions [7] further insight can be gained into the particle 'economy' and distribution at the substrate surface. Questions to be answered include how far two particles, on average, are apart, i.e. what their flight distance along a common trajectory might be. This distance, z_s , can be calculated simply by multiplying the intermission time, t_i , by the flight velocity, u_p , of the particles. If the flight velocity is 50 m s^{-1} , then with the time of $t_i = 0.052 \text{ s}$ calculated above, the flight distance between two particles becomes $z_s = u_p t_i = 50[\text{m s}^{-1}][0.052[\text{s}]] = 2.60 \text{ m}$.

On the other hand, the required flight distance between two particles in the same trajectory in order to meet a liquid preceding particle can not be longer than $z_1 < u_p t_{\text{sol}} = 50[\text{m s}^{-1}][6.5 \times 10^{-7}[\text{s}]] = 3.25 \times 10^{-5} \text{ m}$. Again, it is not likely that a particle will meet another liquid one.

While one particle solidifies at the surface, the number of particles arriving will be

$$N_3 = t_{\text{sol}} N_1 = 6.5 \times 10^{-7}[\text{s}][10^6[\text{p s}^{-1}]] = 0.65 \text{ particles.} \quad (5-6)$$

These particles are distributed over the surface area $A_0 = (\pi/4)w^2 = 4.9 \times 10^{-4} \text{ m}^2$. Thus the number of particles arriving per unit area during solidification of one particle is

$$N_4 = N_3/A_0 = 0.65[\text{p}]/4.9 \times 10^{-4}[\text{m}^2] = 1326 \text{ particles m}^{-2}. \quad (5-7)$$

These N_4 particles will start to solidify simultaneously. Since they are very small but spread out over a large area, they will not interact with each other, i.e. the initial assumption of a ballistic deposition process is warranted. Experimental determination of the particle number density for model systems have been shown in Sec. 4.5.3.

5.3 Momentum Transfer from Particles to Substrate

Molten particle arrive with high velocities at the substrate surface, will be deformed, and as shown below, solidify partially due to the increase of the melting temperature with shock pressure. The flattening ratio D_s/d_p (D_s = splat diameter, d_p = original particle diameter; see Fig. 5-2) depends not only on intrinsic materials properties such as viscosity, μ , and density, ρ , of the liquid phase but also on the impact veloc-

ity, v_i , and the impact angle. A semiquantitative expression has been given by Madejski [2] for a particle impact at an angle of 90° on a flat substrate as follows:

$$D_s/d_p = 1.3(\rho(v_i/\mu))^{0.2}. \quad (5-8)$$

Since the Reynolds number is given by $Re = \rho v d / \mu$, an approximate relationship exists for the flattening ratio as

$$D_s/d_p \approx Re^{0.2} \quad (5-8a)$$

assuming an isothermal particle [8]. However, due to the pronounced thermal gradients across the particles this relationship cannot be taken for granted in reality [9]. Also, the flattening ratio increases with increasing starting particle radius.

With deviation of the spray angle from 90° the properties of the coatings change depending on the nature of the sprayed material. For example, in case of molybdenum the cohesion within the coating increases by a factor of two for an angle of 45° whereas for alumina coating the cohesion increases slightly and the adhesion is unaffected. The deposition efficiency decreases for both materials with increasing deviation of the spray angle from 90° [10].

Recently several attempts were made to study theoretically the time-dependent deformation and solidification of molten droplets according to the Madejski model [11–13]. For example, Maruo *et al.* [11] solved the conservation law of mechanical energy using the *marker and cell method* [14]. As heat from the molten droplet is transported by the high speed flow of the spreading, cooling and solidification occurs at a much higher rate compared to the Madejski model that operates with the assumption of pure heat conduction. Also, a substrate with higher thermal conductivity results in a lower deformation ratio of the droplets. The work by Solonenko *et al.* [13] showed that for particle sizes of $d_p = 0.31$ mm the theoretical solution of the heat transfer equations scales satisfactorily with experimental results without taking into account any empirical constants under the conditions of a main regime parameters (MRP) control prior to impact. Those parameters were the velocity, temperature, size, density, thermal conductivity, and latent heat of melting of the particles, as well as the substrate temperature. One of the important results of the study was that the parameter

$$F_{p,s} = (\rho_{pm} L_p) / (\rho_{sm} L_s), \quad (5-8b)$$

where the subscripts p and s refer to particle and substrate, respectively, and m refers to the melting point, affects in a profound way the dynamics of simultaneous solidification and particle flattening. The parameter c_ξ (dimension: length) characterizes the thickness, h_s , of the molten layer of the substrate according to $h_s = c_\xi (Fo)^{1/2}$, and can be computed from the equation

$$c_\xi = F_{p,s} [c_\zeta + 2(q_2 - q_1) / Ku_p], \quad (5-8c)$$

where q is the heat flux and $Ku = L_p / c_{pm} T_{pm}$ is the Stefan–Kutateladze dimen-

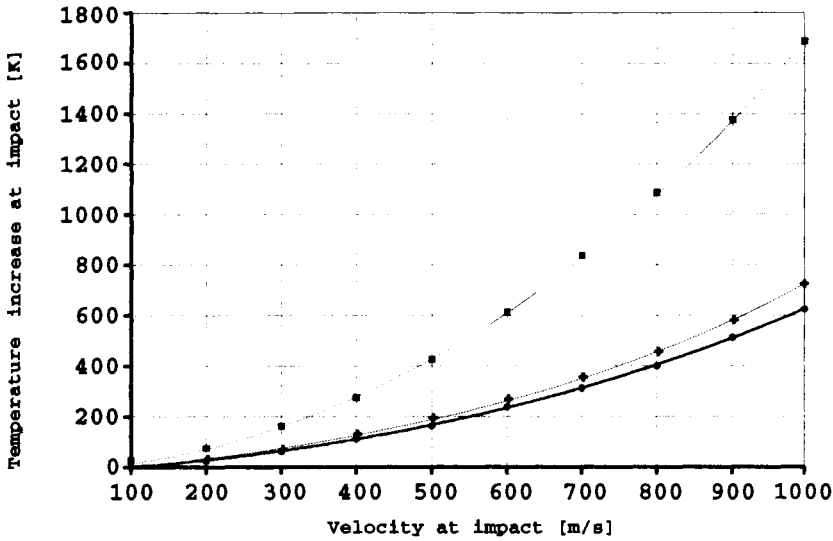


Figure 5-4. Dependence of the temperature increase due to particle impact on the particle velocity [16].

sionless group. If the heat flux into the melt, q_1 , and into the substrate, q_2 , are comparable than $F_{p,s} = c_\xi/c_\zeta$. The parameter c_ζ is a function of the Fourier number, Fo , and the Péclet number, Pe , and according to Eq. 5-8b it equals ρ_{sm}/L_s . It should be emphasized that the parameter $F_{p,s}$ is a criterion of the relative ease of melting (see Sec. 4.4.1). A second important finding of the study was that the theoretical as well as experimental results differ appreciably from those reported by Madejski [2] and Jones [15].

Particles traveling in a high velocity plasma as produced in a D-gun or under HVOF conditions acquire a high kinetic energy that on impact with a velocity v can be partially transformed adiabatically into heat according to

$$\Delta T = v^2/2c_p, \quad (5-9)$$

where c_p = specific heat at constant pressure. The temperature increase reaches appreciable values only for particle velocities exceeding about 400 m s^{-1} as shown in Fig. 5-4 [16]. The collision of particles with the substrate surface and with already deposited solidified particles, respectively, causes a deformation-induced melting within a thin surface layer thus generating a quasi-metallurgical bond at very high particle velocities [17]. Particle velocities of around 100 m s^{-1} lead to negligible temperature increase of only 5°C on deceleration to zero speed assuming $c_p = 1000 \text{ J kg}^{-1} \text{ K}^{-1}$.

Apart from the transformation of kinetic impact energy to heat by an adiabatic process there is, however, another process that can lead to substantial particle and

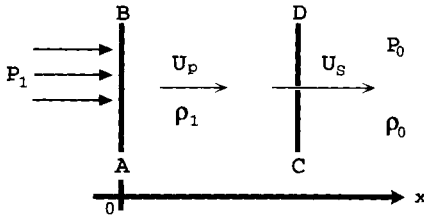


Figure 5-5. Shock wave front CD moving through a solid material (see text).

substrate heating by isentropic energy changes facilitated by planar shock waves⁴. These shock waves obey the conservation equations of mass, momentum, and energy (Rankine–Hugoniot equation of state).

The shock wave concept can be illustrated by the idealized situation of Fig. 5-5. A uniform pressure, P_1 , is suddenly applied to the thick slab of compressible material. This pressure is transmitted to the interior of the slab through a high-amplitude stress wave. If the material behaves normally in compression, i.e. if the compressibility decreases with increasing pressure, the wave front will essentially be a discontinuity in the stress and materials velocity fields, and in density and internal energy, and travels at supersonic speed with respect to the material ahead of the shock. This discontinuity is called a *shock wave*, characterized mathematically by a set of nonlinear hyperbolic differential equations. If P_1 remains time-invariant the state variables are constant between the boundary AB and the shock front CD. As shown in Fig. 5-5 the particle velocity is U_p and the shock wave front velocity is U_s . The mass flux density (in $\text{g cm}^{-2} \text{s}^{-1}$) into and out of the shock front is the product of the material density and the particle velocity relative to the shock front, $\rho_0(U_s - U_{p0})$ ahead of the shock and $\rho(U_s - U_p)$ behind the shock. Conservation of mass requires that

$$V/V_0 = \rho_0/\rho = (U_s - U_p)/(U_s - U_{p0}). \quad (5-10)$$

Momentum conservation is expressed through Newton's second law,

$$F = m(du/dt). \quad (5-11)$$

The force per unit area across the shock front is the pressure difference $P - P_0$, the mass flux per unit area is again $\rho_0(U_s - U_{p0})$, and the materials velocity change is $(U_p - U_{p0})$. Substituting into Eq. (5-11) the momentum conservation equation

$$P - P_0 = \rho_0(U_s - U_{p0})(U_p - U_{p0}) \quad (5-12)$$

results.

The conservation of energy across the shock front can be expressed by equating

⁴ According to Trapaga and Szekely [8] the shock approach is not fully legitimate since the Mach numbers in normal plasma spray jets appear to be rather low (<0.05). However, with supersonic particle velocities obtained in D-gun or HVOF processes the assumption of shock waves are valid.

the work done per unit area and time by the pressure forces, $(PU_p - P_0 U_{p0})$ to the sum of the kinetic energy change, $(1/2)\rho_0(U_s - U_{p0})(U_p^2 - U_{p0}^2)$ and the internal energy change $\rho_0(U_s - U_{p0})(E - E_0)$, i.e.

$$PU_p - P_0 U_{p0} = (1/2)\rho_0(U_s - U_{p0})(U_p^2 - U_{p0}^2) + \rho_0(U_s - U_{p0})(E - E_0). \quad (5-13)$$

It can be shown [18] that combining Eq. (5-13) with Eqs. (5-10) and (5-12) yields the common form of the energy conservation equation

$$\Delta E = (E - E_0) = (1/2)(P + P_0)(V_0 - V), \quad (5-14)$$

where P and P_0 are the pressures behind and ahead of the shock front, and E and E_0 are the internal energies of the substrate material behind and ahead of the shock. The conservation equation in the form of Eq. (5-14) is called the Rankine–Hugoniot equation.

From the conditions of conservation of mass, momentum and energy, assuming $U_{p0} = 0$, it follows that

$$U_s/U_s - U_p = V_0/V, \quad (5-15a)$$

$$U_s U_p / V_0 = P - P_0. \quad (5-15b)$$

The conservation equations have intuitive geometric interpretations. Assuming $P_0 = 0$ in Eqs. (5-15a) and (5-15b), two definitions of the shock front velocity, U_s , and the particle velocity, U_p , can be derived as

$$U_s^2 = V_0^2/(P/V_0 - V) \quad (5-16a)$$

$$U_p^2 = P(V_0 - V). \quad (5-16b)$$

Any set of values for U_s and U_p correspond in the P – V diagram (Fig. 5-6) to a straight line $U_s = \text{constant}$ and a hyperbola $U_p = \text{constant}$. The intersection of the curves fixes the state of the shock compression with parameters P_1 , V_1 in A through which the Hugoniot adiabat P_H passes. The shock wave with a pressure P_1 results in a decrease of the specific volume $V_1 < V_0$. The pressure P_1 is composed of two contributions P_c and P_t . P_c is the ‘cold’ pressure resulting from the strong repulsive force of the interatomic potential, and P_t is the ‘thermal’ pressure associated with the thermal motion of atoms and electrons due to the shear compression. Therefore, as follows from Eq. (5-14), the total increase in internal energy (ΔE) is equal to the area of the triangle OAB in Fig. 5-6. This energy increment consists of an elastic component, ΔE_c (curvilinear triangle OCB) which is a result of the elastic (cold) pressure developing in the material, and a thermal energy component, ΔE_t , represented by the similar curvilinear triangle OAC. The shock transition provides both kinetic and internal energy to the material through which the shock wave propagates. Moreover, irreversible work is done on the material as it passes through the shock front. It can be shown that the entropy increases monotonically with pressure along the

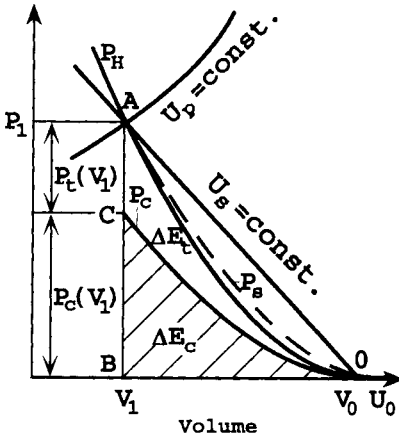


Figure 5-6. P - V diagram of the shock compression of a solid material. P_H is the Rankine-Hugoniot shock adiabat (see text).

Rankine-Hugoniot shock adiabetic that lies above the adiabetic passing through the initial state.

In as much as $\Delta E > \Delta E_c$, the shock-compression process is accompanied by heating of the substance and by an increase in its entropy which in turn leads to the appearance of the thermal pressure component P_t . It can be seen in Fig. 5-6 that the thermal energy and the thermal pressure increase progressively with increasing shock pressure. The shock temperature can be determined by the equation

$$T_A = T_C \exp[S_A/c_v], \quad (5-17)$$

where T_A = shock state temperature at state A (P_1, V_1) and T_C = adiabatic compression temperature at state C (P_c, V_1). On the other hand, during relaxation the heated material cools down, and the volume increases along the expansion isentrope P_s as shown by the dashed line in Fig. 5-6. The temperature after relaxation can be determined by

$$T_E = T_0 \exp[S_A/c_p], \quad (5-18)$$

where T_0 = temperature before the shock, and S_A = entropy in the shocked state.

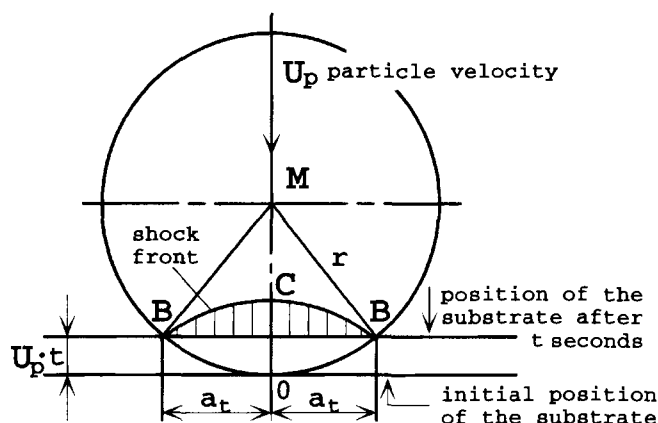
The mechanics of a spherical molten particle with radius r colliding with the flat surface of a substrate at a velocity U_p can be approximated by Fig. 5-7. The inward moving shock front defines that portion of the material initially within the volume BOB that has been compressed into the volume BCB at time t . The contact face perimeter, a_t , moves outward with a velocity \dot{a}_t . It can be simply calculated by

$$a_t^2 = 2rU_pt - [U_pt]^2 \quad (5-19)$$

and the time derivative, i.e. the velocity at which the perimeter of the contact area moves outwards can be expressed as

$$da_t/dt = \dot{a}_t = U_p[r - U_pt]/[2rU_pt - (U_pt)^2]^{1/2} = U_p[r - U_pt]/a_t. \quad (5-20)$$

Figure 5-7. Collision of a spherical molten particle with a flat surface [7].



The following conclusions can be drawn [7].

1. The perimeter velocity \dot{a}_t increases with decreasing contact area radius a_t . For larger particles \dot{a}_t may even exceed the shock velocity, U_s .
2. The initial collision phase, arbitrarily defined by a contact area radius of $1\text{ }\mu\text{m}$, lasts only 2×10^{-9} to 1.3×10^{-10} s for small ($5\text{ }\mu\text{m}$), and 5×10^{-10} to 3×10^{-11} s for larger ($25\text{ }\mu\text{m}$) particles.
3. The spreading velocity of the particles increases with size. The spreading process is about two orders of magnitude faster than the solidification time, t_{sol} .
4. During the process, adiabatic conditions prevail. Superheated particles will spread as a liquid from the start of the collision. This will provide good conditions for adherence of the coating to the substrate. Due to adiabatic shock heating the particle splats can spread more easily over the substrate surface. This improves adhesion by establishment of a thin diffusion layer, i.e. a metallurgical bond.

An important conclusion from the increase of the melting temperature of most substances with pressure (Clausius–Clapeyron’s equation) is that a completely molten particle arriving at the substrate surface can partially solidify during collision not by conductive heat loss to the cold substrate but through adiabatic processes. This was used by Houben [7] to develop a tractable model to explain the occurrence of different types of splats (pancake-, flower-, and exploded-type). Figure 5-8 shows how the generation of a shock wave on particle impact modifies the spreading pattern of this particle. In the (subcritical) phase I ($t < t_c$) compression but no flow occurs. This situation corresponds to the one shown in Fig. 5-7. The shock front moves inward thus increasing the pressure and leading to partial solidification because of the pressure dependence of the melting temperature expressed by the Clausius–Clapeyron equation. In the post-critical phase II ($t > t_c$) the shock wave front squeezes out solid material laterally forming the typical flower pattern often observed in the ‘wipe’ test (see Sec. 5.5.1). In phase III the rarefaction wave accompanying the shock pressure

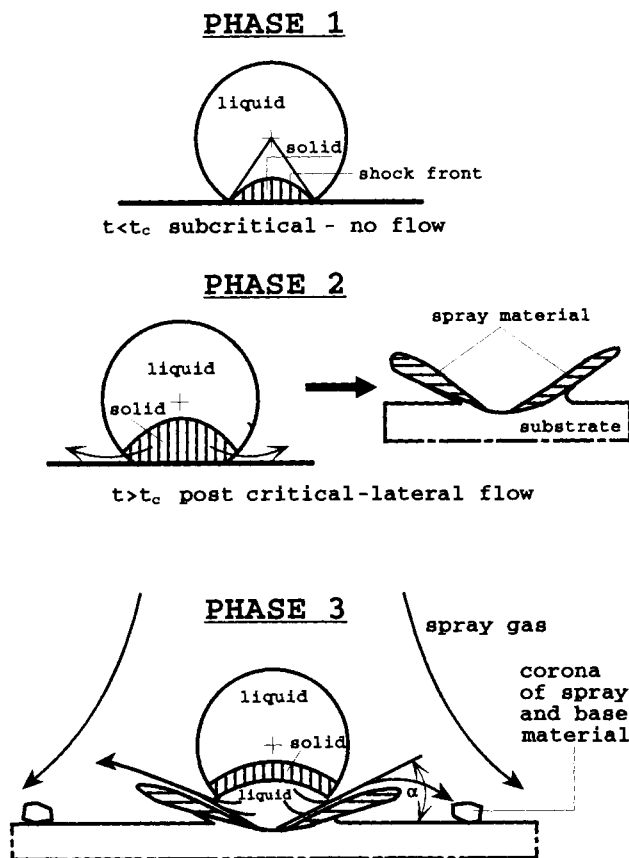
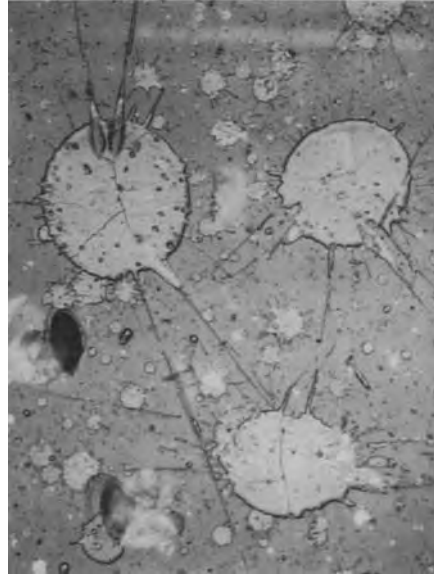


Figure 5-8. Spreading pattern of highly accelerated molten particles [7].

release moves in opposite direction towards the shock wave front. The compressed solid material of the droplet can relax and thus reliquify. This liquid materials now flows out sideways over the splat surface and forms a corona of spray material surrounding the splat. Depending on the critical radius of the outflow and the angle α , material tends to escape from the pressurized zone. The larger the critical radius the larger the potential energy stored in the pressurized zone. Instantaneous release of this pressure may lead to an explosive splat pattern that is detrimental to the coating cohesion as well as adhesion to the substrate.

Another type of pattern occurs during impact of highly superheated material presumably without the involvement of a partially solidified portion. Figure 5-9 shows frozen-in-time traces of superheated alumina splats with material ejected on impact through the shock process [19]. This ejected matter leaves behind voids that build up secondary microporosity in the plasma-sprayed layer. Very complex sequences of shock compression and rarefaction waves are being set up which generate non-equilibrium relaxation temperatures in 'hot spots'. These high local temperatures may delay solidification of the particle, and help to spread a liquid film across the surface of the substrate. In this way the adhesion of the coating to the substrate can

Figure 5-9. Frozen-in-time traces of superheated alumina splats with material ejected on impact [19].



be improved because the surface of the latter can melt partially to form a reaction boundary layer of intermediate composition [20].

Furthermore, the solidified part of an impacting particle on collision may undergo shattering by catastrophic fragmentation because of differential pressures across the particle. The leading face of the arriving particle is subjected to an average dynamic pressure

$$p_{\text{dyn}} \approx C_D \rho_p v^2 / 2, \quad (5-21)$$

with C_D = drag coefficient, ρ_p = plasma gas density and v = particle velocity. The pressure on the trailing face is much smaller. Integration of Eq. (5-21) over the surface of the spherical particle, $4\pi r^2$, yields the drag force

$$m (dv/dt) = -(1/2) C_D \rho_p A v^2 + (g/m) \sin \phi, \quad (5-22)$$

where m = particle mass, $A = \pi r^2$ = cross-sectional area, ϕ = angle between particle trajectory and plasma jet axis [21]. The second term in Eq. (5-22) can be neglected because of the short distance of travel of the particle. Fragmentation of the particle occurs when p_{dyn} in Eq. (5-21) exceeds the characteristic yield strength of the solid material.

5.4 Heat Transfer from Particles to Substrate

The Eq. (5-5) used above for the solidification time is only very approximate. It is the solution of the second-order differential equation of the thermal diffusivity (Fourier's

law) in exactly the same way that the expression $D = x^2/t$ is the approximate solution of the second-order differential equation of the chemical diffusivity (Fick's law).

Exact solutions require some mathematical 'inconveniences'. For the sake of completeness, and to show the elegance of the solution steps, the complete treatment will be given in Appendix B adopted from the work by Houben [7].

5.4.1 Generalized Heat Transfer Equation

The temperature at the substrate surface will be investigated by solving the heat transfer equations in a Cartesian coordinate system $[x, y, z]$. The temperature at the position x, y, z at the time t is $\Theta(x, y, z, t)$. The heat flux \mathbf{j} per unit time and unit area is

$$\mathbf{j} = -a \text{ grad } \Theta, \quad (5-23)$$

and for the change of temperature with time follows

$$\partial\Theta/\partial t = -\text{div } \mathbf{j}, \quad (5-24)$$

where a is the thermal diffusivity. Eliminating the flux \mathbf{j} from Eqs. (5-23) and (5-24) by forming the divergence on both sides of Eq. (5-23), $\text{div } \mathbf{j} = -a \text{ div grad } \Theta$, and inserting this expression into Eq. (5-24), one obtains

$$\begin{aligned} \partial\Theta/\partial t &= a \Delta\Theta \quad \text{or} \\ \Delta\Theta - (1/a)[\partial\Theta/\partial t] &= 0, \end{aligned} \quad (5-25)$$

where $\Delta a = \text{div grad } a = \partial^2 a/\partial x^2 + \partial^2 a/\partial y^2 + \partial^2 a/\partial z^2$ (Laplace operator).

Equation (5-25) is a partial differential equation of second order for the temperature Θ as a function of space and time. The starting condition is $\Theta(x, 0) = f(x) = \Theta_0 = T_{s0}$. The solution of Eq. (5-25) follows the Bernoulli method by anticipating $\Theta(x, t) = X(x)T(t)$ [22]. Introducing this assumption in Eq. (5-25) and dividing by XT , it follows that

$$X''/X - (1/a)[T'/T] = 0. \quad (5-26)$$

Equation (5-26) leads to two ordinary differential equations:

$$X''/X = k^2 \quad (5-27)$$

$$(1/a)[T'/T] = k^2, \quad (5-28)$$

where k^2 is a constant. The general solutions of those differential equations are

$$X = A_1 \exp(kx) + A_2 \exp(-kx) \quad (5-29a)$$

and

$$T = C_k \exp(ak^2t). \quad (5-29b)$$

While there are no boundary conditions required for a one-dimensionally unlimited space, physically meaningful solutions must assure that the temperature Θ will not be infinite at $x = +\infty$ and $x = -\infty$. This would be fulfilled if Eq. (5-29a) did not contain an exponential function but only trigonometric functions. The term k^2 must therefore be negative, and consequently k must be imaginary. With $k^2 = -\kappa^2$, one obtains for the partial integral

$$(a_\kappa \exp(i\kappa x) + a_{-\kappa} \exp(-i\kappa x)) \exp(-\kappa^2 at). \quad (5-30)$$

From this expression a coefficient a_κ can be evaluated so that the starting condition $\Theta(x, 0) = \Theta_0$ is fulfilled:

$$a_\kappa = (1/2\pi) \int f(\xi \exp(-i\kappa \xi) d\xi. \quad (5-31)$$

Integration over κ , pulling out (at) , and quadratic addition in the exponent of Eq. (5-30) eventually leads to

$$\begin{aligned} \Theta(x, t) &= (1/2(\pi at)^{1/2}) \int \delta(\xi - x_0) \exp(-[x - \xi]^2/4at) d\xi \\ &= (1/2(\pi at)^{1/2}) \exp[-x^2/4at], \end{aligned} \quad (5-32)$$

with $\delta(\xi - x_0) = \Theta(x, 0)$ (Dirac delta function). Full details of the derivation of Eq. (5-32) may be found in the literature [22].

From Eq. (5-32) the solution for the temperature profile of the substrate and the coating, respectively can be derived as

$$\Theta(x, t) = \Theta(x, 0) + \beta \{1 + \operatorname{erf}[x/(4at)^{1/2}]\}, \quad (5-33)$$

where β = 'contact' thermal conductivity at the interfaces [7] and $\operatorname{erf}[x/(4at)^{1/2}] = (1/(\pi at)^{1/2}) \int \exp[-x^2/4at]$ (error function). These expressions will be used to calculate the temperature profile across a plasma-sprayed Mo coating on a steel substrate as shown in Sec. 5.4.2 and Appendix B.

5.4.2 Heat Transfer to Substrate

Figure 5-10 shows the coordinate system for the thermal diffusion from the particles into the substrate. The substrate surface is at $x = 0$, at $x = X(t)$ the interface between solid and liquid deposit. It will be assumed that for $x < 0$ the temperature approaches ambient conditions, i.e. $\Theta_0 = T_{s0}$ for $x \rightarrow -\infty$. The initial temperature condition of the particles in the plasma jet is $\Theta = T_3 > T_m$ for $x \gg 0$, where T_m is the

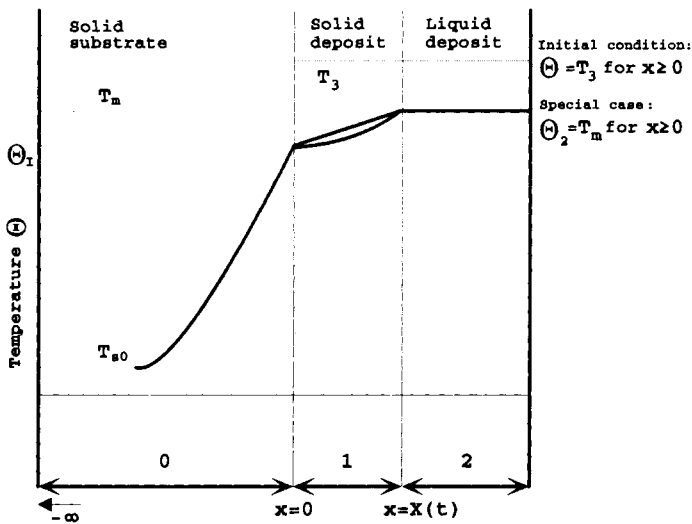


Figure 5-10. Coordinate system for solving the equations of heat transfer from the liquid/solid deposit into the substrate [7].

melting temperature of the particle. At the interface between liquid and solid deposit $\Theta = T_m$ for $x \geq 0$.

The heat transfer equations can be solved numerically with the following assumptions:

- heat transfer takes place only by conduction,
- thermophysical properties of materials are not temperature dependent,
- particle disks have uniform temperature (= melting temperature, T_m),
- supercooling or pressure dependent effects are absent in the contact area,
- melting of substrate does not take place⁵.

Initial conditions are that the region $x > 0$ is liquid at the uniform temperature T_3 , and the region $x < 0$ is solid at the uniform temperature T_{s0} . The treatment of the thermal diffusion (heat conduction) equations for the solid substrate (0), the interface substrate/solid deposit (1) and the interface solid deposit/liquid deposit (2) are given in Appendix B.

Table 5-1 summarizes the thermophysical quantities for Mo, low carbon steel and AISI-316 stainless steel [7].

The simplified solution of the thermal diffusion equations for the solidification time, $t_{\text{sol}} = x^2/4p^2a$ (Eq. (5-5)), are plotted in Fig. 5-11 against the thickness of the deposit of Mo and stainless steel AISI-316 on low carbon steel. Because of the much lower thermal conductivity of the stainless steel, the solidification time of a Mo droplet is considerably shorter than that of AISI-316 by $t_{\text{sol}}(\text{AISI-316})/t_{\text{sol}}(\text{Mo}) = 7.55$.

⁵ As we will see later this requirement has to be relaxed for the deposition of a coating of a materials with an extremely high melting point (molybdenum) on a steel substrate.

Table 5-1. Numerical values of thermophysical quantities for iron, molybdenum and AISI-316 stainless steel used to calculate temperature profiles across the coating/substrate interface as well as contact temperatures [7].

Quantity	Fe	Mo	AISI-316	Unit
λ	75	146	18	$\text{J s}^{-1} \text{m}^{-1} \text{K}^{-1}$
ρ	7870	10200	7670	kg m^{-3}
$C = C_p$	460	255	489	$\text{J kg}^{-1} \text{K}^{-1}$
a	2.07×10^{-5}	5.61×10^{-5}	4.8×10^{-6}	$\text{m}^2 \text{s}^{-1}$
T_m	1536	2610	1375–1400	$^{\circ}\text{C}$
L	272×10^3	288×10^3	297×10^3	J kg^{-1}
$(\lambda \rho c)^{1/2}$	16478	19478	8217	$\text{J m}^{-2} \text{K}^{-1} \text{s}^{-1/2}$
$\frac{C(T_m - T_{s0})}{L(\pi)^{1/2}}$ ^a	1.4464	1.2938	1.2707	—
T_{s0}	20			$^{\circ}\text{C}$
		Mo on Fe	AISI-316 on Fe	
B		1.1826	0.4987	—
$(B + \text{erf } p)pe^{p^2}$		1.2938	1.2703	—
p		0.5487	0.6835	—
pe^{p^2}		0.7415	1.0905	—
$\text{erf } p$		0.5622	0.6662	—
$(a_1/a_0)^{1/2}$		1.6463	0.4815	—

^a e.g. for Fe: $\frac{C(T_m - T_{s0})}{L(\pi)^{1/2}} = \frac{460(1536 + 273 - 293)}{272 \times 10^3(\pi)^{1/2}} = 1.4464$

Figure 5-12 shows the temperature profiles across the interface solid Mo deposit/steel substrate (top) and solid AISI-316 deposit/steel substrate (bottom). The data points were calculated using the procedure shown in Appendix B for a thin AISI-316 layer (profiles 5 and 7) and a thick Mo layer (profiles 2 and 4). From Fig. 5-12 it can be seen that the contact temperature between Mo and steel of 1775.5°C is high enough to melt a thin ($1\text{--}2\text{ }\mu\text{m}$) layer of substrate material thus likely improving adhesion because a solid solution of Mo in $\alpha\text{-Fe}$ can be assumed with a diffusion depth of approximately 20 nm [7].

5.5 Coating Diagnostics: Microstructure, Porosity, Adhesion, and Residual Stresses

5.5.1 Microstructure of Coatings

A few principles have to be considered that are important for assessment and control of the microstructure of ceramic coatings.

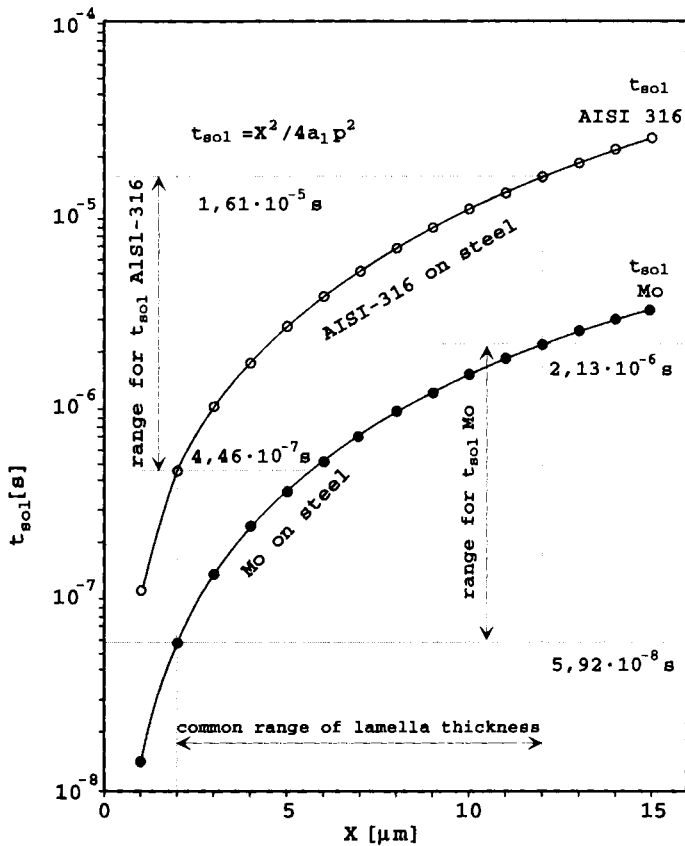


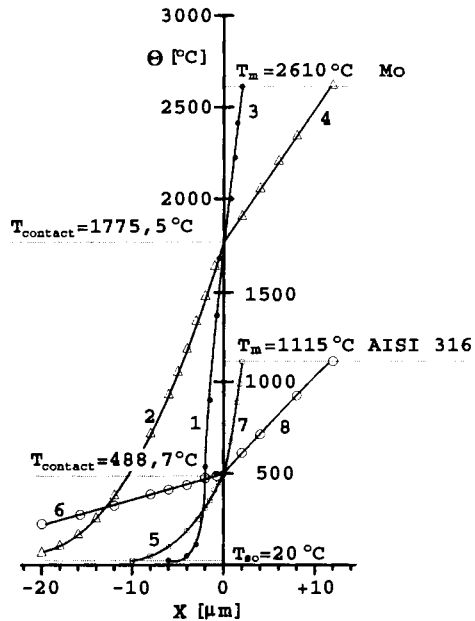
Figure 5-11. Solidification time of Mo particles, and AISI-316 stainless steel particles impacting on mild steel [7].

- Flow and solidification of the molten droplets upon impact is a very complex process.
- Solidification occurs in less than 1 μs .
- Complete cooling of an isolated particle of 50 μm diameter takes about 100 μs depending on the thermal conductivity of the material.
- The time between the arrival of two particles flying in the same trajectory is about 1 ms for a particle velocity of 100 m/s.
- Wetting and flow properties are very important.
- Coatings may possess fractal properties.

5.5.1.1 Splat Configuration

A rather good estimation of the flow characteristics of the molten particles can be obtained by applying the simple 'wipe' test [5]. A flat surface is quickly brought into the path of a molten particle trajectory with the intention of capturing only a

Figure 5-12. Calculated contact temperatures and temperature gradients at the interfaces Mo/mild steel and AISI-316/mild steel, respectively [7].



few particles. The solidified particle splats are investigated with optical or electron-microscopy. Figure 5-13 shows typical examples of hydroxyapatite particle splats obtained from an argon/hydrogen plasma jet under low-pressure conditions [23]. The plasma enthalpy, given here by the interaction of the plasma power and the stand-off distance, increases from Figs. 5-13a to 5-13d. In Fig. 5-13a (plasma power 45 kW, stand-off distance 26 mm) the enthalpy supplied to the particle is not sufficient to achieve melting. Figure 5-13b (plasma power 30 kW, stand-off distance 24 mm) shows a splat pattern of a particle whose outer rim has been melted but its core has remained highly viscous as exemplified by its porous microstructure. In Fig. 5-13c (plasma power 30 kW, stand-off distance 22 mm) a well-melted splat is shown whereas Fig. 5-13d shows the somewhat exploded splat (see Fig. 5-8) of a severely overheated particle (plasma power 45 kW, stand-off distance 22 mm).

Many modeling studies exist dealing with the behavior of particles impacting on a rigid substrate surface. Recently, Bertagnolli *et al.* [24] performed finite element calculations of the spreading process of ceramic liquid droplets on a flat cold surface and found that there is a correlation between the degree of flattening (Eq. (5-8)) and the initial process parameters. Since the mechanical performance of coatings depends crucially on the way particles flatten and establish intersplat bonding, such studies are very important to unravel the complex interaction of spray parameters and coating properties.

5.5.1.2 Surface Roughness of Coatings

Thermally sprayed coatings exhibit on mechanical treatment such as grinding, lapping and polishing very different surface structures compared with homogenous bulk

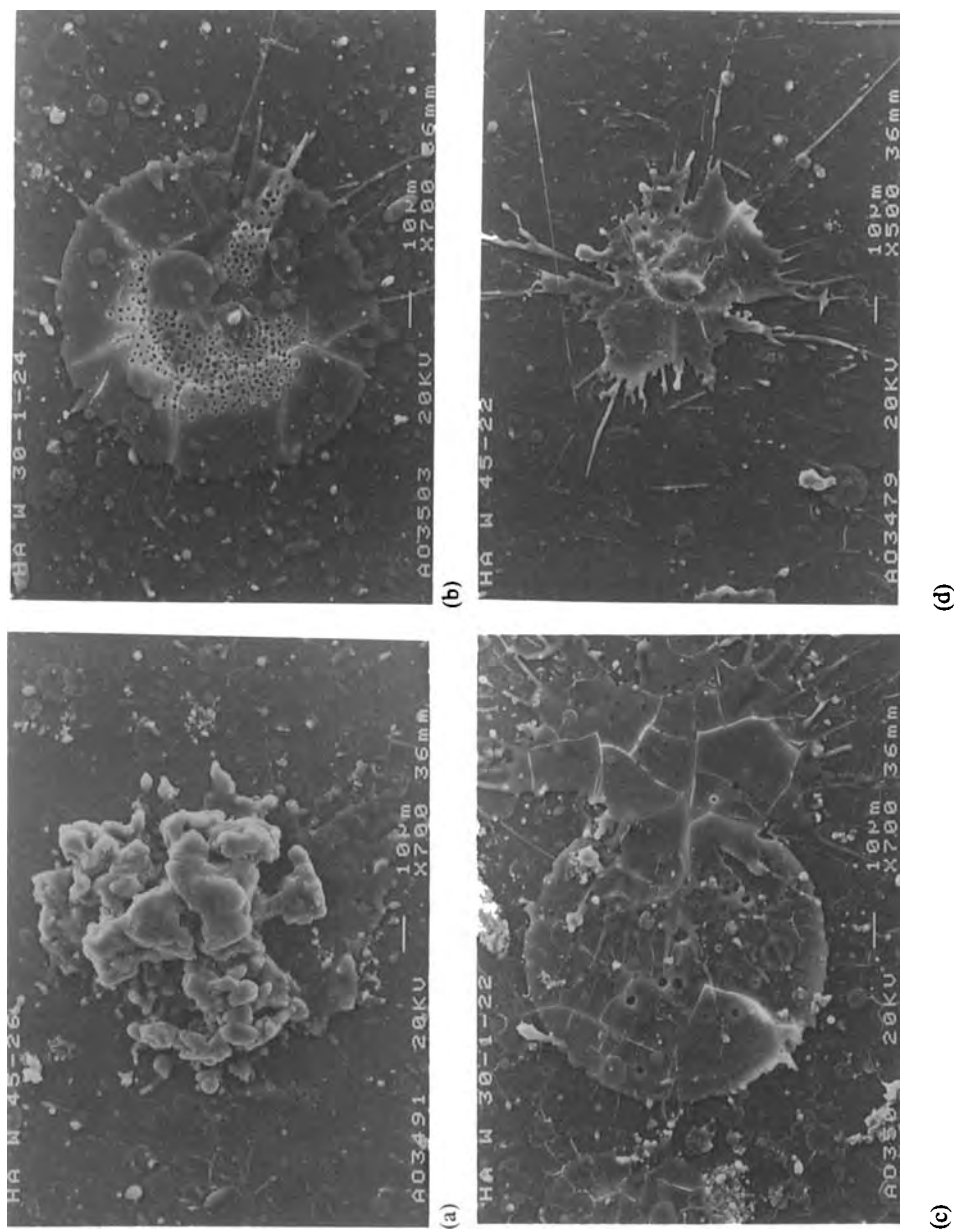


Figure 5-13. ‘Wipe’ test results on hydroxyapatite particles sprayed onto a glass slide (VPS argon plasma). For explanation see text [23].

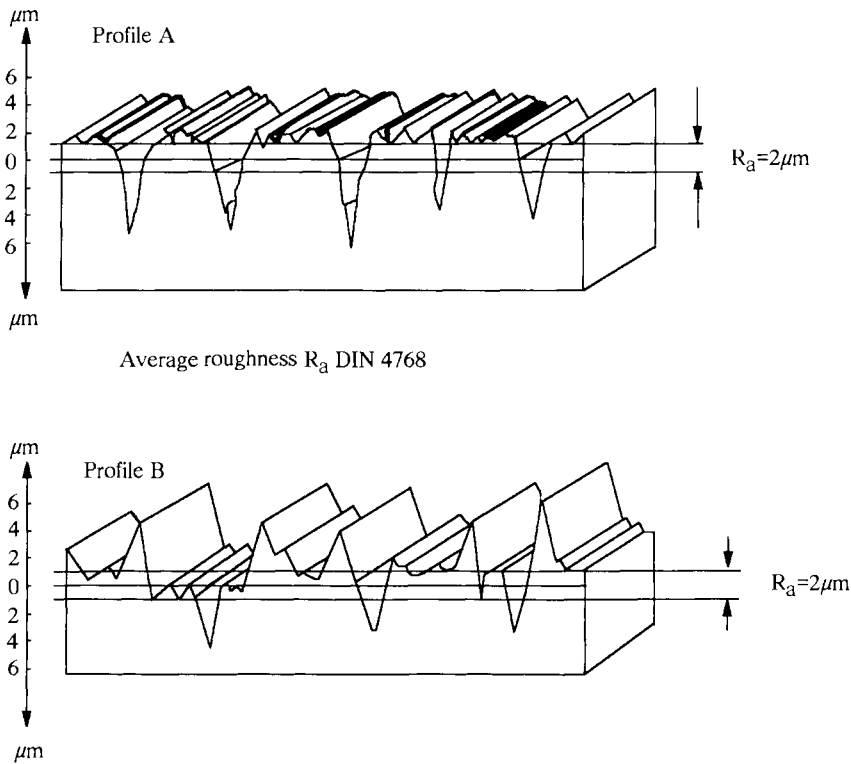


Figure 5-14. Surface roughness profiles of a plasma-sprayed coating. Despite identical average roughnesses two situations arise: a smooth plateau surface with depressions (profile A), and a strongly ragged surface with protrusions (profile B) [25].

materials. Homogeneous materials show after mechanical treatment a ploughed surface that is characterized by scratches; plasma-sprayed surfaces show an inhomogeneous profile given by the original splat structure, porosity and pulled-out and chipped-off areas. To describe such surfaces according to their functional behavior in service it is necessary to separate the undulation, i.e. the waviness of the surface (macroroughness) and the roughness *per se* (microroughness) that is responsible for the tribological behavior of the coating. Using a diamond-stylus surface roughness tester the profile obtained can be manipulated by electronic filtering methods so that a cut off-line is obtained that correspond to the long-wave surface profile [25]. Applying an RC high-pass filter (DIN 4768, ISO 3274) the information obtained from smooth surfaces with pores and pull-outs may be severely erroneous. This is shown in Fig. 5-14. The average roughness R_a (DIN 4768)⁶ is measured to be

⁶ The value R_a is the arithmetic mean of the deviation of the protrusions and depressions of the roughness profile from the average line, $R_a = (1/lm) \int |f(x)| dx$.

identical for the two very different surface roughness profiles (smooth plateau surface with depressions, or strongly ragged surface with protruding asperities). Similar results are obtained for a comparison of the maximum roughness R_{\max} and the median roughness R_z . Obviously, the first profile has a much larger ‘carrying’ surface, i.e. supports the countersurface of a bearing much more effectively than the second profile. The depressions of the first profile will also much more efficiently act as reservoirs for lubricating materials and thus promote the frictional properties of the coating. In order to describe the surface roughness more properly by determining the plateau-like amount of material, surface roughness should be measured by DIN 4776 [25]. Here the waviness of the surface can be determined by cutting-off the depressions, and application of digital phase-true filters to measure Abbot’s curve of the amount of material ‘carrying’ the profile (Fig. 5-15). For thermally sprayed coatings the Abbot curve always has an S-shaped character. Approximating this curve by three straight lines the roughness profile can be subdivided into three areas: the core area of the profile, the spike area of the profile, and the depression area of the profile. The *reduced spike height* characterizes the height of the spikes protruding from the core area, the *reduced depression depth* characterizes the depth of the depressions below the core area.

5.5.1.3 Fractal Properties of Surfaces

Fractal geometry is a natural description for disordered objects ranging from macromolecules to the earth’s surface [26]. These objects often display ‘dilatation symmetry’, meaning that they look geometrically self-similar under transformation of scale such as changing the magnification of a microscope. Many structures can be simply characterized by a single parameter D , the fractal dimension that is defined as the exponent that relates the mass M of an object to its size R [27]:

$$M \propto R^D. \quad (5-34)$$

This applies to Euclidian objects such as rods, discs, and spheres, for which the exponent D equals 1, 2, and 3 respectively consistent with the common notion of dimensionality (topological dimensions). However, for fractal objects the exponents need not be integral. While the objects described by Eq. (5-34) are called ‘mass fractals’ or polymers, ‘surface fractals’ are uniformly dense, i.e. colloidal, $D = 3$ as opposed to polymeric but have a rough surface. Such surface fractals share the self-similarity property⁷ in the sense that if the surface is magnified, its geometric features do not change. Mathematically, surface self-similarity can be expressed analogously to Eq. (5-34) by

$$S \propto R^{D(S)}, \quad (5-35)$$

where S is the surface area and $D(S)$ is the surface fractal dimension. For a smooth object, $D(S) = 2$. For fractally rough surfaces, however, $D(S)$ varies between 2 and

⁷ Note, however, that fractal sets are infinitely detailed but not necessarily self-similar.

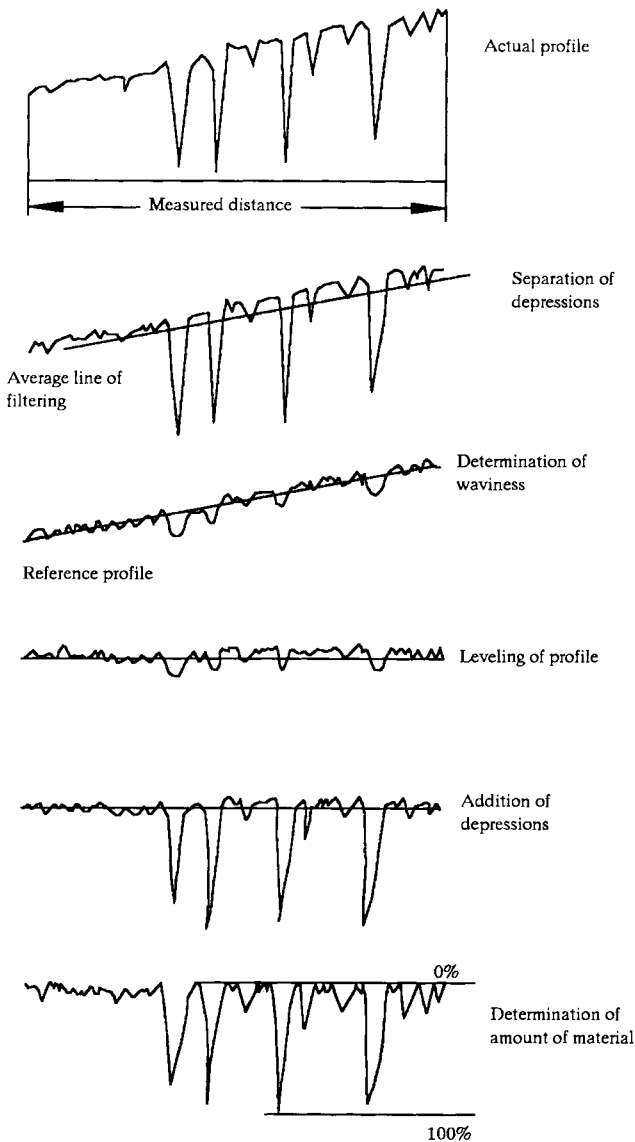


Figure 5-15. Determination of the waviness of a plasma-sprayed surface through Abbot's curve (see text) [25].

3, so that $D(S)$ is a measure of roughness [28, 29]. It should be emphasized here that fractals describe only the principle of ordering but do not give any information on the mechanism that leads to this ordering. A state-of-the-art treatise on fractals, in particular methods to determine fractal dimensions was provided recently by Stoyan and Stoyan [30].

A popular way to describe the deposition of coatings is a ballistic model. In this

model particles are added, one at a time, to the growing deposit through randomly selected linear or ballistic trajectories [31]. In the most simple of these models the particles stick to the surface at the position at which contact is first made, i.e. surface diffusion is excluded. Also, since the conditions in the direction perpendicular to the surface are very different from those parallel to the surface, we will deal essentially with *self-affine geometries* [32]. Self-affine fractals are structures that can be rescaled by a transformation that involves a different change in length of scales in different directions. For example, whereas the scaling factor perpendicular to a plasma-coated surface may be on the order of micrometers, the scaling factor along the coated surface will be measured in millimeters or even centimeters. For structures of rough surfaces such as plasma-sprayed ones the approaches developed for self-similar structures are not strictly valid anymore and must be modified to account for this self-affinity. Since a rough surface can be represented by a single-valued function $h(\mathbf{x})$ of the position \mathbf{x} in the lateral directions parallel to the surface, it is convenient to use the height difference correlation function $C_h(x)$ defined by

$$C_h(x) = \langle h(\mathbf{x}) - h(\mathbf{x}_0 + \mathbf{x}) \rangle_{|\mathbf{x}|=x}. \quad (5-36)$$

to characterize the surface. It is reasonable to expect that the surface roughness ξ_\perp will grow with some power of time according to

$$\xi_\perp \sim t^\beta, \quad (5-37)$$

assuming that the surface advances with a constant rate. The variance ξ^2 , i.e. the amplitude of the waviness (see Sec. 5.5.1.3) is defined by $\xi^2 = \langle h_i - h^2 \rangle$ and is often used as a quantitative measure of the surface 'thickness' or roughness. For a growing fractal plasma-sprayed surface layer there will also be a characteristic correlation length ξ_\parallel describing the lateral distance over which surface height fluctuations occur. This length is related to the former by

$$\xi_\perp \sim \xi_\parallel^\alpha, \quad (5-38)$$

and from Eqs. (5-37) and (5-38) it follows that

$$\xi_\parallel \sim t^{\beta/\alpha} \sim t^{1/z}. \quad (5-39)$$

Using these self-affinity scaling laws the height difference correlation function (Eq. (5-36)) can be expressed as

$$C_h(x, t) \sim t^\beta f(x/t^{\beta/\alpha}). \quad (5-40)$$

The theoretical values of α and β are 1/2 and 1/3, respectively [33]. However, the true value of β may be obtained from the time dependence of the surface thickness (Eq. (5-37)). Numerical simulations of the dependence of the surface roughness (ξ) on the deposited layer thickness, h may be obtained from the literature [31].

It is quite tempting to apply the fractal approach to other plasma-sprayed coating properties. Fractal dimensions should provide information that may be used to de-

scribe not only surface roughness [34] but also surface area [28], fracture toughness [35, 36], adhesion strength [34], hardness, porosity, thermal conductivity and frictional properties of wear-resistant coatings. There are, however, to date but a few papers available in the literature that attempt to apply the concept of fractal geometry to describe coating properties even though the fractal approach will provide very fundamental answers to questions about the microstructure of thin surface coatings. For example, Yehoda and Messier [37] discussed the nature of very thin CVD layers in terms of a fractal structure. Their criterion was that fractal films should be self-similar at least over three orders of magnitude. This was not observed, however, but the development of pores in the film showed a scaling similar to the percolative scaling found by Voss *et al.* [38] in thin evaporated gold films.

Fractal dimensions can be determined from a variety of relationships that are unique to systems conforming to fractal geometries. Five of these relationships will be described in more detail below.

Box counting method

This method is the most simple way to evaluate fractal dimensions. The interface line of a surface roughness profile of a coating is shown in Fig. 5-16a. It is covered with boxes of side length d . If the interface line is completely covered with N squares then according to the rules of fractal geometry it holds that

$$N(d) = \mu d^{-D} \quad (5-36)$$

$$\text{or } \log N(d) = -D \log d + \log \mu. \quad (5-37)$$

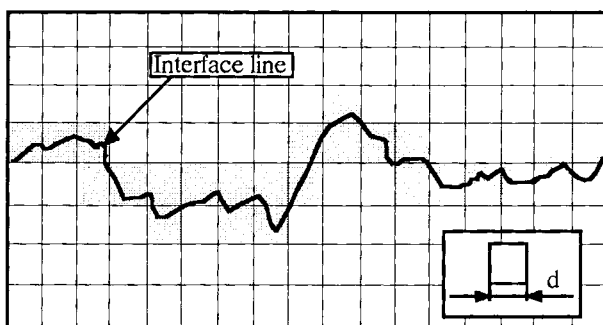
By continuously changing the size of the boxes d , i.e. the magnification scale, the number of squares $N(d)$ covering the interface line is counted. On plotting $\log N$ versus $\log d$ the slope $-D$ of the straight line obtained is the fractal dimension sought (Fig. 5-16b). Fractal geometry was used to investigate the dependence of the fractal dimension on the angle of grit blasting [34]. Even though the average roughness R_a did not change with blasting angle the fractal dimension was maximized at a blasting angle of 75° (Fig. 5-16c). This points to a more detailed rough surface with more undercuts and hook-like protrusions that will anchor a plasma-sprayed coating more strongly and thus improve coating adhesion by mechanical interlocking. The measurement and prediction of the fractal dimensions of grit-blasted surfaces will therefore be a very valuable tool to maximize coating adhesion. In particular, the R_a -values assessed normally will not give a true measure of the effective surface roughness as already pointed out in Sec. 5.5.1.2 but should be replaced by the fractal approach.

Density correlation function

The principle of this method is to find experimentally a density correlation function $C(r)$

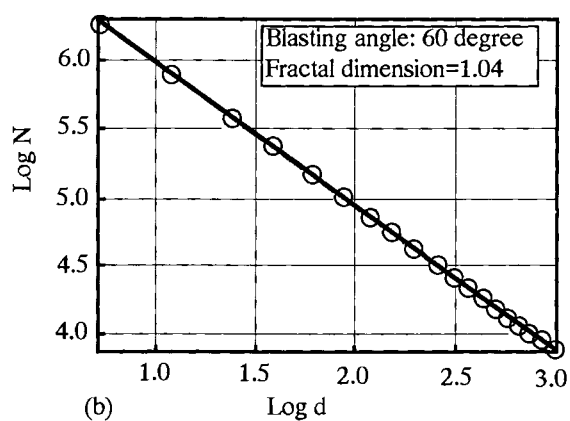
$$\langle C(r) \rangle \propto r^{-\alpha}, \quad (5-38)$$

$$C(r) = (1/N) \sum \rho(r_i) \rho(r_i + r), \quad (5-39)$$

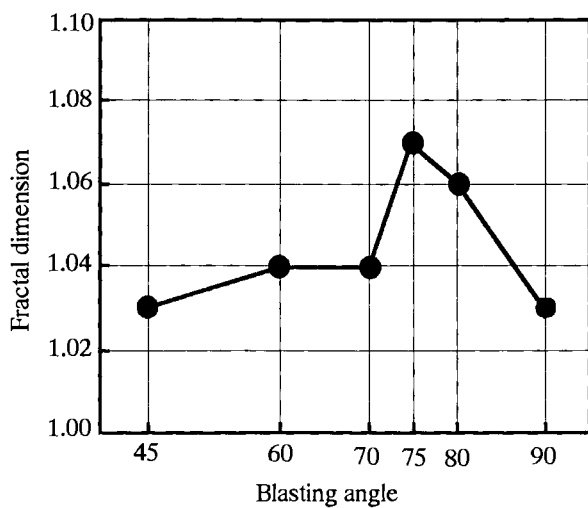


(a)

Figure 5-16. Box counting method to determine the fractal dimension of a plasma-sprayed coating [34].



(b)



(c)

where N is the number of splats, i is the observation point, $\rho(r_i)$ is the splat density at the observation point = 1, and $\rho(r_i + r)$ is the splat density at a point located a distance r from the observation point, and

$$-\alpha = D(\alpha) - d, \quad (5-40)$$

where $D(\alpha)$ is the fractal dimension, and d is the Euclidian dimension of the system [39]. In a 2D-section the density at the distance r is determined by the number of splats N divided by the area of a ring containing the N splats. For an inner ring of radius r and an outer ring of radius $(r + \Delta r)$ the density correlation function can be approximated by

$$\langle C(r) \rangle = \{N(r)\} / 2\pi r \Delta r. \quad (5-41)$$

Plotting $\ln \langle C(r) \rangle$ versus $\ln(r)$ results in a straight line of slope $-\alpha$ from which the fractal dimension $D(\alpha)$ can be calculated according to Eq. (5-40).

Mass Correlation Function

This method is very similar to the preceding one. Fractal dimensions can be obtained from the relation

$$\langle M(r) \rangle \propto r^{D(\beta)}, \quad (5-42)$$

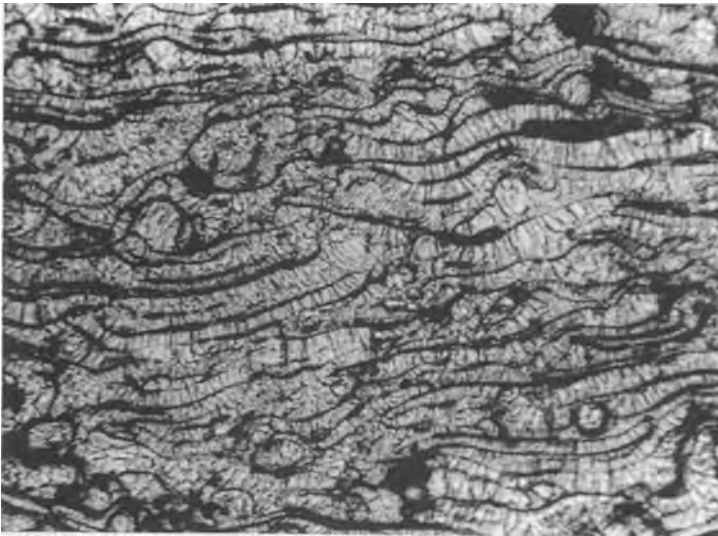
that may be obtained by integration of Eq. (5-41). M is the mass enclosed by some distance r . Assuming that each molten particle arriving at the substrate surface has equal mass, M can be replaced by the particle number $\langle N(r) \rangle$ contained within a sphere of radius r . Again, plotting $\ln \langle N(r) \rangle$ against $\ln(r)$ results in the slope $D(\beta)$. If $D(\alpha) \equiv D(\beta)$ then proof exists that the coating microstructure has fractal nature.

Slit island analysis (SIA)

This method is based on measuring the ratio perimeter/area of 'islands' that appear during successive removal of thin surface layers of a metal-coated fracture surface [40]. The surfaces obtained after each step are being investigated with modern image analysis software, and the perimeters P and areas F of newly appearing surface features recorded. Plotting of $\log P$ against $\log F$ of individual islands results in the slope $(D - 1)/2$ [36].

Fracture profile analysis (FPA)

Fracture profile analysis uses a Fourier analysis approach applied to a fracture surface to determine fractal dimensions [41]. Since the fracture profile can be considered a spectrum of microstructural information all signal-processing analytical tools developed for electric signals can be applied to fracture profiles. Many spectral details observed during analysis reflect the 'fundamental length', i.e. the correlation length (see above) of the microstructure and their related high-order harmonics. According to fractal hypothesis the integrated spectrum, i.e. the squared sum of the



-63+20 μm , 43 kW, 30 kPa, 23 g/min powder feed rate, 20 μm water cooling, 220 mm spray distance, porosity 2.8% etched

Figure 5-17. Microstructure of splats in an etched cross-section of a chromium coating on copper [66].

amplitudes takes the form $k^{-B'}$ where k is the wave number (inverse length) and $B' = B - 1 = 6 - 2D$ [36]. The fractal character of fractured coating surfaces can then be tested by plotting $\log(\text{amplitude})^2$ versus $\log k$ to obtain the slope B' from which the fractal dimension D can be calculated.

5.5.2 Porosity of Coatings

Whereas metallic coatings with nearly theoretical densities can be obtained by plasma spraying, the porosity of plasma-sprayed ceramic coatings is, in general, between 3 and 20%. While in some cases high porosity is advantageous, for example to reduce the thermal conductivity of thermal barrier coatings, to act as a retaining reservoir of lubricants in some wear-resistant coatings, or to enhance ingrowth of bone cells into bioceramic coatings, in most wear applications the wear resistance decreases dramatically with increasing porosity. Thus, porosity has to be tightly controlled in order to maximize coating performance.

Common causes of porosity are:

- shadow effects when splashing of a second particle over previously arrived ones may lead to a gap within one lamella layer (Fig. 5-3),
- narrow holes and/or gas inclusions between the i th and the $(i + 1)$ th lamella (Fig. 5-17),

- inclusion of unmelted, larger particles (Fig. 5-3), and
- exploded particles due to overheating, excessive particle velocities and thus occurrence of disruptive shock waves (Fig. 5-8, Fig. 5-13d).

Reduction of porosity includes the following measures:

- Preheating of substrate to increase the contact temperature and to reduce the viscosity of the impinging molten droplets.
- Use of low-pressure plasma spraying (LPPS) with increased particle velocities and thus increased kinetic impact energies.
- Post-spraying treatment such as
 - annealing of coatings to reduce microporosity by solid-state diffusion,
 - hot isostatic pressing (HIPping) of coatings [42],
 - laser surface densification [43–47], and
 - infiltration of coatings with polymers for low-temperature applications, Ni aluminides or other alloys for high-temperature uses [48], or by the sol–gel process [49].

Measurement of the porosity of plasma-sprayed coatings can be accomplished by a wide variety of methods that can be divided into those yielding as a result a simple number, the ‘porosity’ or pore volume related to the total volume of the coating in $\text{cm}^3 \text{g}^{-1}$, and those that yield a pore size distribution function. In many cases the former methods are sufficient to characterize the porosity of a coating. The following methods can be applied.

- Point-counting using optical microscopy [50, 51].
- Electron-optical microscopy in conjunction with discriminant analysis of optical density using automated image analysis.
- Mercury pressure porosimetry using stepwise filling of smaller and smaller pore sizes with increasing pressure [52].
- Bubble pressure method using stepwise squeezing out of liquid from a completely filled pore ensemble [53].
- Dynamic penetration followed by measuring the electrical conductivity of the porous coating [54].
- Determination of the distribution function of pores by X-ray small angle scattering [55].

5.5.2.1 Point Counting

This approach is based on the quantitative relationships between measurements on the two-dimensional plane of polish and the magnitudes of the microstructural features in three-dimensional materials. The determination of the volume of pores is based on Gauss’ principle that the spatial extension of a plane and a volume, respectively are determined by the number of hits that are obtained by randomly or regularly spatially distributed points in the various components of an aggregate. In modern point-counting techniques the points in space are points in a plane that are

counted optically or electronically. Thus the volume fraction occupied by a microstructural feature such as a void or pore, is equal to the point ratio of the selected feature as seen on random sections through the microstructure. Because point counting is tedious and special instruments for quantitative metallography are expensive, sometimes porosity is estimated by comparing the microstructures with standard photomicrographs. This method is simpler, faster, and quite suitable for control and quality acceptance purposes. Depending on their purpose, comparisons are usually based on micrographs taken at magnifications ranging from 50 to 500 times [56].

5.5.2.2 Mercury Pressure Porosimetry

The technique requires fully automated equipment for pore size distribution functions ranging from 10 μm to 10 nm. It is based on the Washburn equation [57] that relates the diameter of a pore, r , to the pressure, p , required to fill it with a liquid. Since the ability of a liquid with a contact angle, ϕ , exceeding 90° to fill a pore is limited by its surface tension, σ , the applied pressure must overcome this surface tension:

$$r[\text{\AA}] = 2\sigma \cos \phi / p, \quad (5-43)$$

where for mercury σ attains the value of 480 dyn cm^{-1} and $\phi = 140^\circ$. The disadvantage of this method is that Eq. (5-43) is strictly valid only for cylindrical pores. For noncylindrical pores correction factors must be applied. This is particularly true for ‘ink bottle’ pores. Also, on application of high mercury pressures pore walls can be destroyed and higher porosities will be suggested.

5.5.2.3 Archimedes’ Method

This is the classical method for determining the apparent density of a material and from this value the porosity. For plasma-sprayed metallic coatings a procedure has been suggested [58] involving the following steps:

1. Preparation of a solid cylindrical bar ($12.7 \times 2.2 \text{ cm}$).
2. Application of the coating approximately 2.8 mm thick for a length of about 6.4 cm.
3. Using the center holes, the bar is mounted on a lathe and the coated section is machined to a thickness of 2.54 mm.
4. Specimens of about 2.8 cm length are cut from both the coated and uncoated regions of the bar.
5. Both ends of the specimen are ground flat and perpendicular to the central axes.
6. Weighing of the specimens to an accuracy of 0.001 g.
7. Calculation of the volume.
8. Determination of the density of the coating using the following equation: $(\text{Weight of coated sample} - \text{weight of uncoated sample}) / (\text{Volume of coated sample} - \text{volume of uncoated sample})$. The volume fraction of porosity can be obtained

from 'measured' and 'true' density values by the equation: Pore volume fraction (%) = ('true' density – 'measured' density)/'true' density.

5.5.3 Adhesion of Coatings

Adhesion of coatings is controlled by three main mechanisms.

1. *Mechanical anchorage.* Surface roughness plays an overriding role. The particles must have sufficient plasticity, high impact velocity, low viscosity and good wettability. The adhesion strength of a ceramic coating is in many cases a linear function of the average surface roughness, R_a . However, as shown above the true influencing parameter appears to be the fractal dimension of the surface roughness.
2. *Physical adhesion.* This mechanism is controlled by diffusive bonding, where the diffusivity increases with increasing contact temperature according to Fick's law. This can be maximized by substrate preheating. Because of the small diffusion depth (produced by the rapid solidification), the diffusive adhesion generally plays only a minor role as an adhesion mechanism.
3. *Chemical adhesion.* Chemical adhesion can be engineered by adjusting the contact diffusivities. Thin reaction layers may be formed that improve the adhesion on a molecular scale by forming a true metallurgical bond.

In more detail, adhesion mechanisms can be classified as 'microbonding' and 'macrobonding' [59]. *Microbonding* refers to the bonding that takes place along very small surface areas the size of an individual particle of sprayed powder. *Macrobonding* refers to areas much larger by 10 to 100 times. Macrobonding relates to the macroroughness produced by threading and grooving methods or by extremely coarse grit blasting.

As indicated above, the microbonding between sprayed particles and the substrate, and between sprayed particles themselves, is never completely mechanical. There may be considerable bonding among particles at the microbond level, and no bond at all over a macroarea after a substantial coating has been built up. The reason for this is shrinkage. As each particle impinges at the substrate surface it flattens out, sticks to some extent, and then shrinks. An initial shrinkage occurs when the particle changes from a liquid, i.e. plastic to a solid, (rigid) state. In addition to this state-change shrink there is normal thermal shrinkage that continues as the particle cools down further. At the individual particle level shrinking may not cause much stress or at least not enough to rupture the microbond. A large body of evidence indicates a strong initial film adhesion between the sprayed particles and the substrate, and between neighboring particles. This microbonding mechanism is still not well understood. It is the same type of adhesion that occurs between an anodized coating and aluminum, or between chromium plate and steel. This adhesion has been variously referred to as 'film adhesion', 'solid-phase bond' or 'solid-state bond'. The bond may be very strong, nonmechanical, and occurring on a molecular level but is not usually referred to as 'metallurgical' or 'chemical bond'. Metallurgical bonds imply some alloying of the materials at the interface that normally is not observed in plasma-sprayed coatings. In the case of nickel aluminide coatings, however, the

exothermic reaction of this material causes alloying at the interface, and the result is a true metallurgical bond. Also, if very high contact temperatures occur at the interface as in the case of plasma-sprayed molybdenum on steel (see Sec. 5.4.2, Fig. 5-12), metallurgical bonding involving alloy formation is predominant.

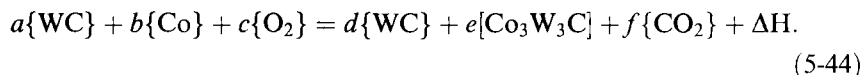
Various test methods for evaluating coating cohesion and adhesion will be described in Chapter 7.

5.5.4 Chemical Changes

Frequently, the molten droplets react with the plasma gas, or with air pumped by the plasma jet. In particular, oxidation or decomposition of carbides and nitrides takes place. For example, a WC/Co coating may encounter three connected chemical processes:

1. matrix alloying, i.e. solubility of WC in the Co metal matrix under formation of so-called ‘ η -carbides’ of the general composition $\text{Co}_n\text{W}_m\text{C}$,
2. decarburization, and
3. deoxidation [60].

The general equation for matrix alloying is



With increasing temperature and residence time in the hottest regions of the plasma jet decarburization reactions take place thought to occur in three stages [61, 62]:



As a consequence, HVOF spraying with lower temperature and shorter residence time considerably suppress tungsten and chromium carbide decomposition. Therefore, highly wear and corrosion-resistant coatings (see Sec. 6.1) are increasingly sprayed successfully with HVOF technique [63].

Figure 5-18 shows schematically the chemical and phase changes during thermal spraying of WC/Co(Ni) powder. It can be seen that the matrix of the coating consists in principle of an η -carbide with some residual WC, and a small degree of porosity [60].

A study by Brunet *et al.* [64] showed that during plasma spraying of TiC a severe carbon depletion occurs even when argon is used as a shroud gas to protect the

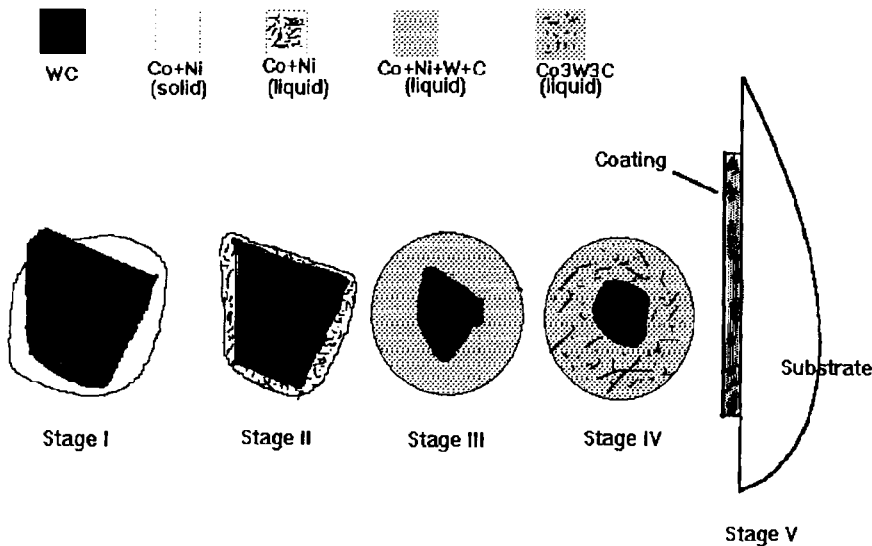


Figure 5-18. Schematics of chemical and phase changes during thermal spraying of WC/Co(Ni) powder [60].

sprayed TiC from oxidation. Plasma spraying in air results in the formation of crystalline oxides (Ti_3O_5 , TiO_2) and free titanium [65].

5.5.5 Residual Stresses

The stresses occurring in the coating can be divided into microscopic, mesoscopic and macroscopic stresses.

Microscopic stresses are found inside individual splats, and are generated by the gradient of the coefficient of thermal expansion between the hot particle and the cooler substrate. Figure 5-17 shows the etched cross-section of an RF inductively-sprayed chromium coating with stress-induced cracks in the individual particle splats perpendicular to the splat boundaries [66].

Mesoscopic stresses occur between particle splats inside a lamella, and are responsible for reduced coating cohesion. They result principally from frozen-in contraction of the rapidly quenched molten particles at the substrate interface (see below).

Macroscopic stresses occur between the coating as a whole and the substrate. They depend on the temperature gradients within the coating between passes of the torch which decrease when both the thickness of the lamella and the spray width are being decreased. Macroscopic stresses can be controlled by

- cooling with gas jets: compressed air or carbon dioxide [67],
- cooling with liquid gases such as argon or carbon dioxide,

- adjustment of the relative velocities of torch/substrate, or
- grooving of substrate.

Since residual coating stresses influence the quality and the service life of coatings, in particular their adhesion and wear performance, it is the goal of any coating development to minimize such stresses. The origin of residual stresses is twofold. First, rapid quenching of the molten particles at the substrate interface results in frozen-in particle contraction, and tensile forces between individual particles add up to residual stresses states of the first order ('macro' residual stresses) throughout the coating [68]. Second, the differing coefficients of thermal expansion of coating and substrate contribute to the total stress state of the system. If this stress state exceeds the adhesive or cohesive bonding forces of the coating crack formation or delamination occur [69]. Stresses at the coating/substrate interface can be determined approximately by the Dietzel equation [70, 71] that uses the differences in the coefficients of thermal expansion of coating and substrate, the temperature gradient, and the thickness ratio to calculate the coating stress:

$$\sigma_c = \{E_c(\alpha_c - \alpha_s)\Delta T\}/(1 - \nu_c) + [(1 - \nu_s)/E_s] d_c/d_s\}, \quad (5-46)$$

where α is the linear coefficient of thermal expansion, ν is the Poisson ratio, E is the modulus of elasticity, and d is the thickness. The subscripts c and s refer to coating and substrate, respectively. For $\alpha_c > \alpha_s$ compressive stresses develop in the coating and tensile ones in the substrate that can be minimized by maximizing the ratio d_s/d_c . Thus for given values of ν and E the coating stresses increase with increasing coating thickness (compare Fig. 5-20b).

Residual tensile stresses are particularly severe in ceramic–metal composite coatings because of the generally large difference in the coefficients of thermal expansion of ceramic and metal. Their states can be determined, in principle, by borehole (blind hole), and X-ray or neutron diffraction measurements.

5.5.5.1 Blind Hole Test

A hole is drilled into the coating and the measurement of the relaxation occurring allows estimation of the original stress state [72]. A strain gauge based either on a semiconductor circuit or a modified Wheatstone bridge and glued to the coating surface is employed to record the relaxation. The measuring principle is based on the expansion-resistance effect of metallic conductors according to Wheatstone and Thomson. The change of the resistance of a conductor subjected to tensile or compressive forces can be attributed to the deformation of the conductor as well as to the change of its specific resistance due to changes of the microstructure. The relaxation of the coating material on drilling of a borehole results in an expansion or contraction of a measuring grid of strain gauges that in turn is recorded as a change in resistance⁸. Since this method is affected in various ways by external parameters it

⁸ Actually the released surface strain measured with the strain gage rosette is converted to stress using a calibration curve and Hooke's law [75].

can only be used as a qualitative or at best semi-quantitative indicator of the stress state. Thus it has been suggested to use this method concurrently with other techniques such as X-ray diffraction measurement [73]. A more quantitative treatment of the method can be found by Bialucki *et al.* [74].

5.5.5.2 X-ray Diffraction Measurements ($\sin^2 \psi$ -Technique)

The determination of the stress state is based on the measurement of the lattice deformation of a polycrystalline materials subjected to stresses. This is accomplished by measuring the change of the D -values of the interplanar spacings of selected lattice planes $\{hkl\}$ relative to the stress-free state, D_0 :

$$dD = D - D_0. \quad (5-47)$$

Since the penetration of the radiation into the coating is quite limited (1–10 μm) only the stress state of the coating surface can be measured. To obtain a stress distribution profile the surfaces must be consecutively removed by polishing, sputtering or etching, and the measurement be repeated.

Differentiation of the Bragg equation $n\lambda = 2D \sin \theta$ yields the (relative) lattice deformation

$$\varepsilon^L = dD/D_0 = -\cot \theta_0 d\theta. \quad (5-48)$$

From Eq. (5-48) it follows that the change of the Bragg angle, $d\theta$ is maximized for a given ε^L when θ_0 is large. Therefore, interplanar spacings with the largest possible Bragg angles must be chosen. Also, $d\theta$ increases with increasing stress, σ , and decreasing Young's modulus, E . However, ceramic materials generally have large E values. Therefore, very small shifts of the interplanar spacings must be recorded with high accuracy. This requires highly sophisticated X-ray diffraction hardware and appropriate software [76].

Figure 5-19a shows the sample-based coordinate system used to deduce the basic equations for stress measurements. The lattice deformations $\varepsilon_{\phi, \psi}^L$ measured close to the surface obtained according to Eq. (5-48) in the directions ϕ , ψ are taken as the deformations $\varepsilon_{\phi, \psi}$ expected from the theory of elasticity. The angle ϕ is the azimuthal angle to the x -axis, and the angle ψ is the distance angle to the z -axis, i.e. the surface normal N of the sample. For a triaxial stress state $\{\sigma_1, \sigma_2, \sigma_3\}$ with σ_1 and σ_2 parallel to the surface the distribution of the deformation is given by

$$\begin{aligned} \varepsilon_{\phi, \psi} = \{ & (1 + \nu)/E \} [\sigma_1 \cos^2 \phi + \sigma_2 \sin^2 \phi - \sigma_3] \sin^2 \psi \\ & - (\nu/E) [\sigma_1 + \sigma_2] + \sigma_3/E, \end{aligned} \quad (5-49)$$

where ν = the Poisson ratio and E = Young's modulus. Owing to the uniaxial stress state of ceramic coatings [77], $\sigma_3 = 0$. With this the general equation for determination of the stress state is obtained as

$$\varepsilon_{\phi, \psi} = (s_2/2) \sigma_\phi \sin^2 \psi + s_1 (\sigma_1 + \sigma_2), \quad (5-50)$$

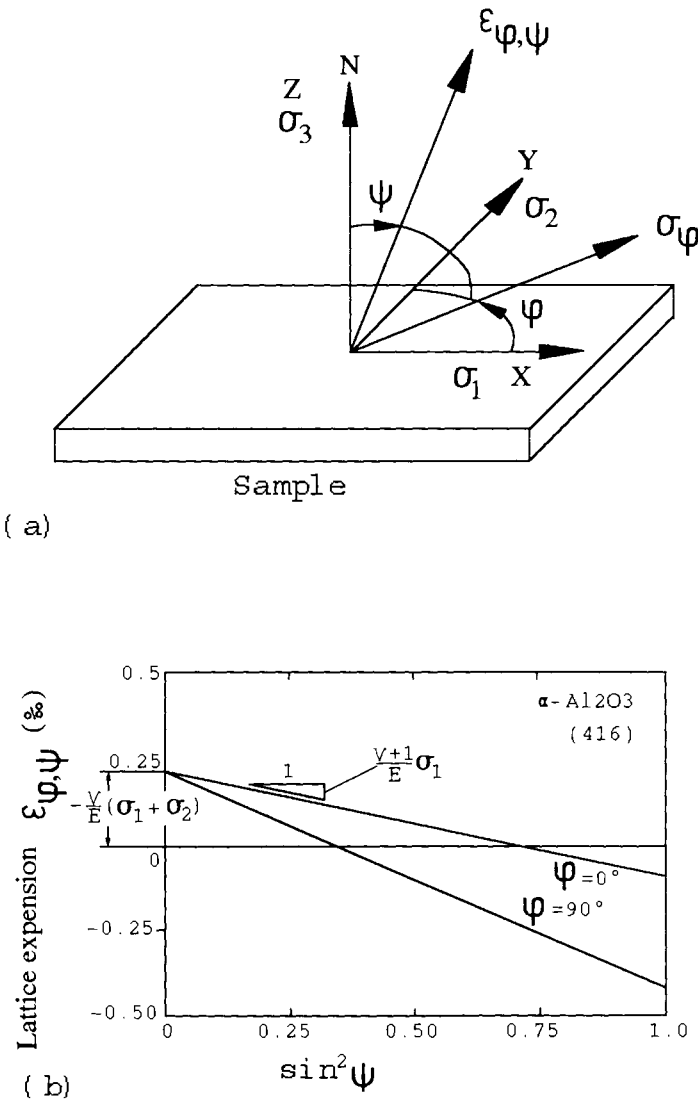


Figure 5-19. (a) Sample-based coordinate system for residual stress measurements, (b) lattice expansion against $\sin^2 \psi$ for (416) of alumina [76].

with $\sigma_1 \cos^2 \phi + \sigma_2 \sin^2 \phi = \sigma_\phi$ (see Fig. 5-19a) and $s_1 = -\nu/E$, $s_2/2 = (1 + \nu)/E$. Figure 5-19b shows an example of a plot of $\epsilon_{\phi, \psi}$ versus $\sin^2 \psi$ for the interplanar spacing (416) of alumina. From the slope of the lines the surface stress component σ_ϕ , and from the intersection with the ordinate axis ($\epsilon_{\phi, \psi} = 0$) the sum of the main stresses ($\sigma_1 = -100 \text{ N mm}^{-2}$, $\sigma_2 = -200 \text{ N mm}^{-2}$) can be obtained [76]. Figure 5-20a explains the often observed dependency of the residual stresses on the stand-off distance for a APS Al₂O₃/2.5% TiO₂ coating on St 37 steel using an NiAl bond

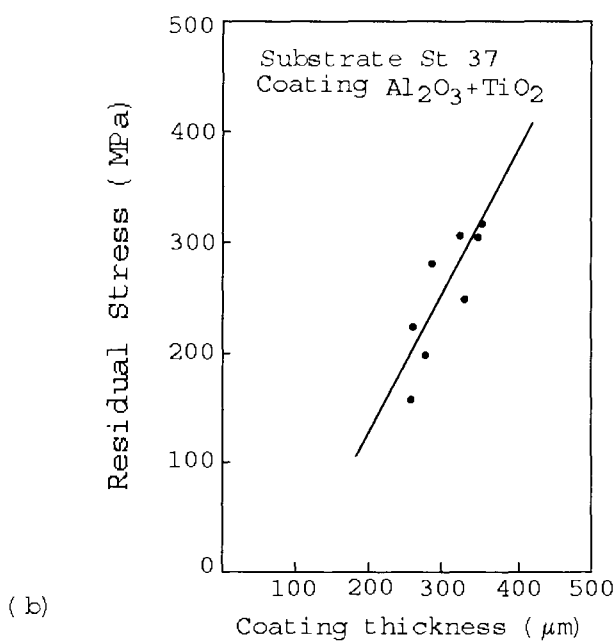
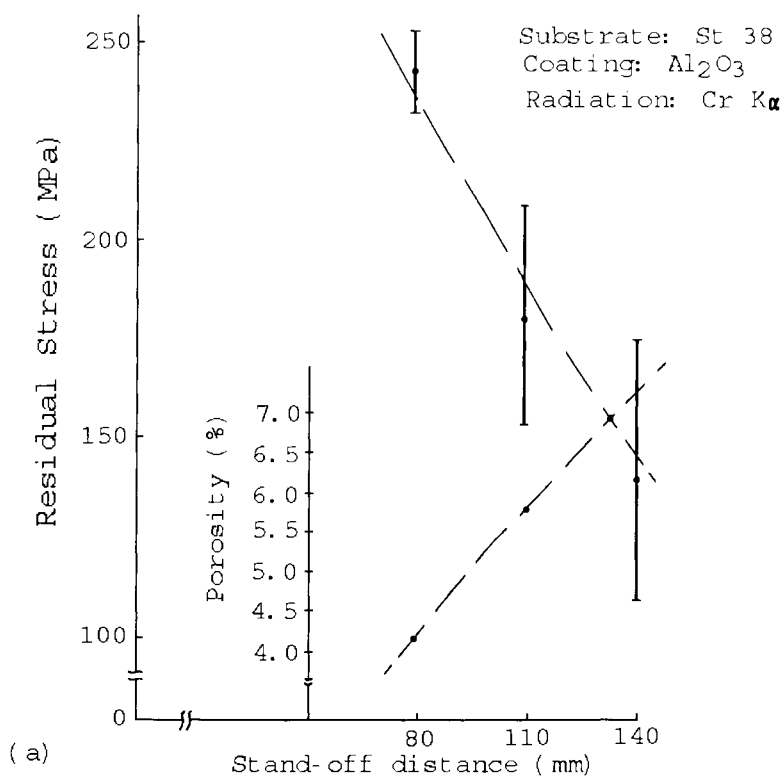


Figure 5-20. Dependence of the residual stress of an $\text{Al}_2\text{O}_3/2.5\% \text{TiO}_2$ coating on St 37 steel on (a) the stand-off distance and (b) the coating thickness [77].

coat [77]. As the stand-off distance increases the increasing coating porosity may cause the material to attain a quasi-elastic behavior that can compensate for differences in the coefficients of thermal expansion of the coating and the steel substrate. This has been confirmed by Berndt [78] who suggested that plasma-sprayed coatings have a high compliance since the bonding force between lamellae is low enough to permit some relative sliding. In Fig. 5-20b the linear increase of the residual coating stresses with the coating thickness is shown (see also Eq. (5-46)). It should be emphasized that the results shown in Fig. 5-20 do not consider the possibly different contributions of the alumina and the titania phases to the total stress pattern. Such different stress responses have been demonstrated for $t\text{-ZrO}_2/\alpha\text{-Al}_2\text{O}_3$ [76] and (Ti, Mo)C/NiCo [79] coatings. In particular, the former example has shown that a stress equilibrium exists between individual ceramic phases that can be described by a simple additive mixing rule [76].

A major problem exists in unequivocally describing the surface stress states by X-ray diffraction measurements. Since the deformation, ε , is dependent on material parameters such as the Poisson ratio, ν , and the modulus of elasticity, E , (see Eq. (5-38)), those quantities must be known with rather high accuracy. However, the bulk modulus of elasticity is certainly different from that of a coating owing, in particular, to the increased porosity of the latter [73]. Furthermore, free standing coatings have to be used to determine experimentally the value of E . This means that for every coating system the dependency of E on the porosity must be determined in parallel to the determination of the stress state for each plasma spray parameter set. As a consequence the method becomes extremely time-consuming and cannot be applied routinely in industrial practice. Also, the continuous removal of surface layers changes the stress state, and the surface roughness established by cutting or lapping may lead to scattering of the X-rays and thus to line broadening that influences the accuracy of the measurement. Furthermore, since the modulus of elasticity, E , is a sensitive function of the stresses present in the coating⁹ but the coating stress is attempted to be calculated using E as a determining parameter, conditions of non-linearity exist.

Another factor affecting the evaluation of the $\sin^2 \psi$ -plots is the often observed fact that severe internal residual stresses can result in a deviation from the true crystal symmetry. In titanium nitride [80] or hafnium nitride [81] coatings stresses in the coating plane cause densification and account for the distortion from cubic symmetry as evidenced in Nelson–Riley extrapolation function plots [80, 82].

5.5.5.3 Almen-type Test

To circumvent the drawbacks of the $\sin^2 \psi$ -technique described above including the problem of a nonlinear modulus of elasticity, attempts have been made to apply other tests to get an estimate of the residual stresses. The so-called Almen test for

⁹ The modulus at low stress levels or under conditions of the existence of a complex tension/compression stress pattern [84] is greater than that existing at pure tension and plastic flow of the material [78].

determination of the efficacy of shot peening applied to induce compressive stresses at the surface of metallic workpieces has been adapted to thermally sprayed thin coatings [68]. A thin test strip is mounted on a holder [83] and blasted with shot. This treatment leads to curving after removal from the fixture. The peened side of the curved strip will be convex. The degree of curving, measured with an appropriate gage, is a function of the residual compressive stresses developed in the strip. For estimation of residual stresses in thermally sprayed coatings a thin foil of the substrate material will be clamped to the Almen fixture and treated exactly in the same way as the substrate to be sprayed, i.e. grit blasting, ultrasonically cleaning, and spraying. After each working step the strip is being removed from the fixture and its stress state as displayed by the degree and direction of its curvature is determined. Fig. 5-21a shows the mounting block for the Almen test [83], Fig. 5-21b shows the thin foil before and after grit blasting. The induction of compressive stresses led to a convex curvature of the grit-blasted side of the foil that was reduced by the amount of the tensile stresses induced during coating. The reduction of the arc height, in this example 0.20 mm, can be directly related to the tensile residual stress state in the coating [63, 68].

5.5.5.4 Theoretical Analysis of Residual Stresses

Because of the complexity in terms of error possibilities, time and cost requirements of the X-ray diffraction-based measurements attempts have been made to solve the stress state determination in coatings by mathematical means. The mathematical models applied are subsequently validated by experiments. Thus the influence of individual parameters on the residual thermal stress state of the coatings can be studied, and the in-service behavior of the coating/substrate system predicted [85].

A model developed by Knotek *et al.* [86] is based on compartmentalization of the coating deposition process into time increments of 10^{-6} s. The coating thickness will be calculated for each time element and also the temperature distribution for the entire coating/substrate tandem from the difference of the amounts of heat introduced and dissipated. The thermal constraints are the convective heat losses at the surfaces, ideal contact between substrate and coating, and negligible radiation losses. Then the internal thermal strain state can be described by a two-stage model as follows.

In the first stage the total lateral expansion of the plate-shaped coated workpiece is found by numerical integration of the equation

$$\partial^2 x_i / \partial t^2 \sum m_i = x_i \sum E_i A_i / l_{0i} - \sum E_i A_i \alpha_i (\Theta_i - \Theta_{0i}), \quad (5-51)$$

where x = path coordinate along the substrate surface, m = mass of individual elements i , E = Young's modulus, A = cross-sectional area of individual elements i , α = temperature-dependent coefficient of thermal expansion, Θ_i = instantaneous temperature of individual elements i , l_{0i} = length of element in the unstressed state, and Θ_{0i} = maximum temperature of the $(i - 1)$ st coating lamella. Equation (5-51) is a special form of the fundamental Newton momentum equation. Each particle arriving at the surface is incorporated at the precise moment when the supporting $(i - 1)$ st lamella has reached its maximum temperature Θ_{0i} . Therefore the total lateral ex-

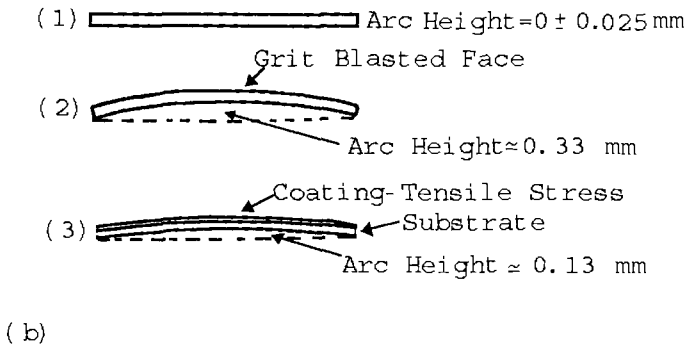
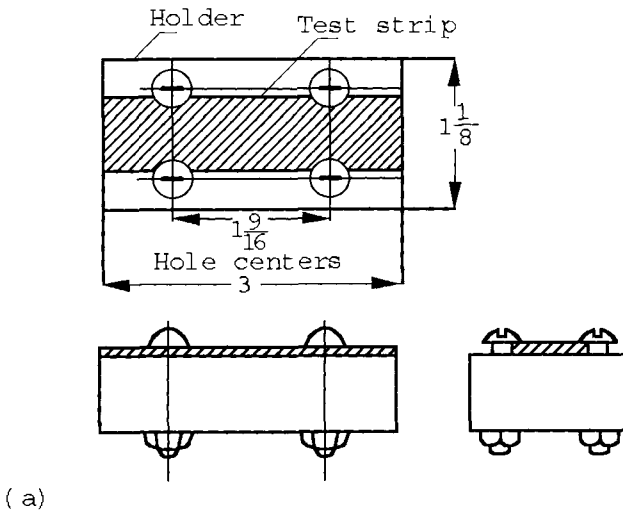


Figure 5-21. ALMEN test configuration, (a) mounting block, (b) a thin foil before (1) and after grit blasting (2). The convex curvature will be reduced by tensile stresses induced during coating (3). After [83].

pansion can be calculated from the instantaneous thermal expansion and the size of the substrate prior to deposition.

In the second state, after termination of the deposition process the length of the individual elements can be calculated by

$$l_i = l_{0i}[1 + \alpha_i(\Theta_i)(\Theta_i - \Theta_{0i})], \quad (5-52)$$

where l_i is the length that an element would attain at the temperature Θ if it could

adjust freely, i.e. unconstrained by the surrounding elements. The internal strain among individual elements can be calculated considering the bending moments and applying equations developed for bimetallic strips [86].

Verification of the model was done using experimental data obtained by depositing alumina (100 μm thick coatings) and stabilized zirconia (40 μm thick coatings) on ferritic and austenitic steel substrates. Internal strains were measured by the blind hole method (see Sec. 5.5.5.1). Even though the measured internal strain values were found to be lower than the calculated ones due to variations introduced by the drilling process, there is good agreement between the qualitative trend of the measured and the calculated internal strains.

Theoretical work has been performed at UKAEA's Harwell laboratory by Eckold *et al.* [87] on plasma-sprayed stabilized zirconia coatings deposited onto 304 stainless steel. The model considers transfer of heat to the substrate from the molten impinging particles as well as redistribution of heat radiatively and/or convectively to the surrounding atmosphere. The heat transfer model applied uses a number of constraints such as:

- continuity of the coating process,
- coating area is large compared to its thickness,
- heat loss can be described by standard convection and radiation heat loss equations,
- start of spraying approximates to a coating of infinitesimal thickness, and
- thermophysical and elastic properties are temperature-invariant.

The heat transfer model generates data that predict the thermal history of a coating during deposition. From this data the stress history of the coating is being calculated that aids in the prediction of the final residual stress state in the coating. Sensitivity analyses consider the influence of the following parameters on the stress state:

- deposition rate,
- plasma temperature (enthalpy),
- substrate temperature,
- final coating thickness,
- coating area,
- substrate area,
- thermal conductivity, specific heat and latent heat of coating,
- density, emissivity, Poisson ratio, Young's modulus and expansivity of the coating, and
- heat capacity and expansivity of the substrate.

The model produces a graphical output of the stress distribution within the coating dependent on a path coordinate x . It indicates that: the stress is everywhere compressive, the stress maximum occurs at the coating's free surface, and the magnitude of the stress (maximum values 25 MPa) is much lower than the operational stress in a diesel engine where such thermal barrier coatings (TBC) may be applied. As a first approximation it appears that the residual stresses occurring in such zirconia coatings

are not at all life limiting. However, because of the rather low Weibull modulus of ceramic coatings in general, failure probability is high. In particular, coating fracture stresses in ceramic coatings can be of the same order of magnitude as the residual stresses predicted by this model.

As pointed out by Steffens *et al.* [88] rather large errors will be introduced into thermal and residual stress calculations by neglecting the temperature dependence of the modulus of elasticity. Furthermore, since thermal barrier coatings are designed to be highly porous to minimize their thermal diffusivity, the strong dependence of the modulus on porosity must be considered. In the stress calculations performed [88] to determine the influence of residual and thermal stresses on the thermal shock resistance of yttria-stabilized zirconia TBCs, the following equation was used:

$$\sigma = [Ec(\alpha_s - \alpha_c)\Delta T]/(1 - \nu_c), \quad (5-53)$$

where the subscripts c and s refer to coating and substrate, respectively. This simplified equation does not consider the substrate rigidity E_s , Poisson ratio of the substrate and the coating thickness as done in the more comprehensive Dietzel equation discussed above (Eq. (5-46)). Since the residual stresses can be somewhat controlled by substrate preheating the normally occurring stress relaxation by micro- or even macrocracking of TBCs can be suppressed. Furthermore, the steep stress gradients at the interface coating/substrate where the stress state changes from tensile to compressive can be smoothed by inserting a soft compliant intermediate bond coat layer or a graded metal–ceramic coating [89].

References

- [1] D. Apelian in *Mat. Res. Soc. Symp. Proc.* (Eds. J. Szekely, D. Apelian) **1984**, Vol. 30.
- [2] J. Madjeski, *Int. J. Heat Mass Trans.* **1976**, 19, 1009.
- [3] R. McPherson, *J. Mat. Sci.* **1980**, 15, 3141.
- [4] J. M. Houben, *Proc. 2nd NTSC*, 31 Oct–2 Nov **1984**. Long Beach, CA, USA.
- [5] H. Gruner, *Thin Solid Films*, **1984**, 118, 409.
- [6] H. Herman, *Sci. Am.* **1988**, 112.
- [7] J. M. Houben, Relation of the adhesion of plasma sprayed coatings to the process parameters size, velocity and heat content of the sprayparticles. Ph.D. Thesis, Technical University Eindhoven, The Netherlands, **1988**.
- [8] G. Trapaga, J. Szekely, *Metall. Trans. B* **1991**, 22, 901; R. McPherson, *Surf. Coat. Technol.* **1989**, 39/40, 173.
- [9] S. Fantassi, M. Vardelle, A. Vardelle, M. F. Eichinger, P. Fauchais, *Proc. TS'93*, Aachen **1993**, DVS, Oberursel 152, 387.
- [10] A. Hasui, S. Kitahara, T. Fukushima, *Trans. Nat. Jpn. Res. Inst. Met.* **1970**, 12(1), 9.
- [11] H. Maruo, Y. Hirata, Y. Matsumoto, *Proc. 14th ITSC'95 Kobe* 22–26 May **1995**, 341.
- [12] M. Fukumoto, S. Kato, I. Okane, *Proc. 14th ITSC'95 Kobe* 22–26 May, **1995**, 353.
- [13] O. P. Solonenko, A. Ohmori, S. Matsuno, A. V. Smirnov, *Proc. 14th ITSC'95 Kobe* 22–26 May, **1995**, 359.
- [14] H. Harlow, J. E. Welch, *Phys. Fluid.* **1965**, 8, 12.
- [15] H. Jones, *J. Phys. D: Appl. Phys.* **1971**, 4, 1657.

- [16] L. Pawlowski, *The Science and Engineering of Thermal Spray Coatings*, Wiley, New York, USA, **1995**.
- [17] H. Kreye, D. Fandrich, H. H. Müller, G. Reiners, in *Advances in Thermal Spraying*, (Ed. N. F. Eaton) (Proc. 11th ITSC, Montreal, 8–12 Sept.) 1986, Welding Inst. of Canada, **1986**, p. 121.
- [18] M. H. Rice, R. G. McQueen, J. M. Walsh, in *Solid State Physics, VI* (Eds. F. Seitz and D. Turnbull), Academic Press, New York, USA, **1958**.
- [19] R. B. Heimann, *Proc. Adv. Mater.* **1991**, 1, 181.
- [20] S. Kitahara, A. Hasui, *J. Vac. Sci. Technol.* **1974**, 11, 747.
- [21] C. F. Chyba, P. J. Thomas, K. J. Zahnle, *Nature* **1993**, 361, 40.
- [22] H. G. Zachmann, *Mathematik für Chemiker, 4. Auflage*, VCH, Weinheim **1991**.
- [23] R. B. Heimann, T. A. Vu, M. L. Wayman, *Eur. J. Mineral*, submitted.
- [24] M. Bertagnolli, M. Marchese, G. Jacucci, *J. Thermal Spray Technol.* **1995**, 4(1), 41.
- [25] H. Kühn, O. Stitz, R. Letzner, *Proc. Thermal Spray Conf., TS 90* (DTV 130) Essen, 29–31, August, **1990**, p. 38.
- [26] B. B. Mandelbrot, *The Fractal Geometry of Nature*, Freeman, San Francisco, USA, **1982**.
- [27] D. W. Schaefer, *Science* **1989**, 243, 1023.
- [28] D. Avnir, D. Farin, P. Pfeifer, *J. Coll. Interface Sci.* **1985**, 103(1), 112.
- [29] E. E. Underwood, K. Banerji, *Mater. Sci. Eng.* **1986**, 80, 1.
- [30] D. Stoyan, H. Stoyan, *Fractals, Random Shapes and Point Fields. Methods of Geometrical Statistics*. Wiley, New York, USA, **1995**; D. Stoyan, H. Stoyan, *Fraktale, Formen, Punktfelder. Methoden der Geometrie-Statistik*, Akademie Verlag GmbH, Berlin, **1992**.
- [31] P. Meakin, *J. Mater. Educ.* **1989**, 11, 105.
- [32] B. B. Mandelbrot, *Physica Scripta*, **1985**, 32, 257.
- [33] M. Kardar, G. Parisi, Y.-C. Zhang, *Phys. Rev. Lett.* **1986**, 56, 889.
- [34] S. Amada, T. Hirose, K. Tomoyasu, *Proc. 14th ITSC'95*, Kobe, 22–26 May, **1995**, 885.
- [35] Y. Fahmy, J. C. Russ, C. C. Koch, *J. Mater. Res.* **1991**, 6(9), 1856.
- [36] J. J. Mecholsky, D. E. Passoja, K. S. Feinberg-Ringel, *J. Am. Ceram. Soc.* **1989**, 72(1), 60.
- [37] J. E. Yehoda, R. Messier, *Appl. Surf. Sci.* **1985**, 22/23, 590.
- [38] R. F. Voss, R. B. Laibowitz, E. I. Alessandrini, In, *Scaling Phenomena in Disordered Solids* (Eds. R. Pynn, A. Skjeltorp), Plenum Press, New York, **1985**, 279.
- [39] J. L. LaRosa, J. D. Cawley, *J. Am. Ceram. Soc.* **1992**, 75(7), 1981.
- [40] B. B. Mandelbrot, D. E. Passoja, A. J. Paullay, *Nature* **1984**, 308, 721.
- [41] D. E. Passoja, D. J. Amborski, *Microstruct. Sci.* **1978**, 6, 143.
- [42] M. Inada, T. Maeda, T. Shikata, *Proc. ATTAC'88, Adv. Thermal Spraying Technology and Allied Coatings*, Osaka, May **1988**, p. 211.
- [43] A. S. Khanna, A. K. Patniak, K. Wissenbach, *Proc. 14th ITSC'95*, Kobe, 22–26 May, **1995**, p. 993.
- [44] N. Takasaki, M. Kumagawa, K. Yairo, A. Ohmori, *Proc. 14th ITSC'95*, Kobe, 22–26 May, **1995**, p. 987.
- [45] R. B. Heimann, D. Lamy, V. E. Merchant, *Trans. 17th Workshop CUICAC* (Ed. R. B. Heimann), Québec City, Québec, Canada, 2 October **1991**.
- [46] R. Sivakumar, B. L. Mordike, *Surf. Engineering*, **1988**, 4, 127.
- [47] I. Zaplatynsky, The effect of laser glazing on life of ZrO₂ TBSs in cyclic burner tests. NASA Techn. Memorandum 88821, August **1986**.
- [48] A. Ohmori, Z. Zhou, K. Inue, K. Murakami, T. Sasaki, *Proc. 14th ITSC'95*, Kobe, 22–26 May, **1995**, p. 549.
- [49] K. Moriya, W. Zhao, A. Ohmori, *Proc. 14th ITSC'95*, Kobe, 22–26 May, **1995**, p. 1017.
- [50] A. A. Glagolev, *Trans. Inst. Econ. Min. Moscow*, **1933**, 59.
- [51] F. Chayes, *J. Geol. USA* **1954**, 62.
- [52] G. C. Ulmer, W. J. Smothers, *Am. Ceram. Soc. Bull.* **1967**, 46, 649.
- [53] L. Zagar, *Arch. Eisenhüttenwesen* **1955**, 26, 561.
- [54] A. Dietzel, H. Saalfeld, *Ber. DKG* **1957**, 34, 363.
- [55] H. L. Ritter, L. C. Erich, *Anal. Chem.* **1948**, 26, 665.
- [56] *A Plasma Flame Spray Handbook* (Ed. T. J. Roseberry, F. W. Boulger). Final Report No. MT-043 (March 1977) to Naval Sea Systems Command, Naval Ordnance Station, Louisville, KY, USA, **1977**.

- [57] E. W. Washburn, *Proc. Natl. Acad. Sci. USA* **1921**, 7, 115.
- [58] *Evaluation Methods and Equipment for Flame-Sprayed Coatings*, Metco Inc., **1963**, 15 pp. Quoted after [33].
- [59] *Plasma Jet Technology*, Technology Survey, NASA SP-5033 (Eds. P. R. Dennis, C. R. Smith, D. W. Gates, J. B. Bond), NASA, Washington, DC, USA, October **1965**, p. 42.
- [60] K. Hajmrle, M. Dorfman, *Mod. Dev. Powder Metall.* **1985**, 15/17, 609.
- [61] B. Bouaifi, U. Draugelates, I. Grimberg, K. Soifer, B. Z. Weiss, *Proc. 14th ITSC'95*, Kobe, 22–26 May **1995**, 627.
- [62] M. E. Vinajo, F. Kassabji, J. Guyonnet, P. Fauchais, *J. Vac. Sci. Technol.* **1985**, A3, 2483.
- [63] O. Brandt, *Proc. 14th ITSC'95*, Kobe, 22–26 May **1995**, p. 639.
- [64] C. Brunet, S. Dallaire, I. G. Sproule, *Proc. 14th ITSC'95*, Kobe, 22–26 May **1995**, p. 129.
- [65] S. Morozumi, M. Kikuchi, S. Kanazawa, *J. Nucl. Mater.* **1981**, 103/104, 279.
- [66] M. Müller, F. Gitzhofer, R. B. Heimann, M. I. Boulous, *Proc. NTSC'95*, Houston, TX, USA, 11–15 Sept. **1995**.
- [67] H.-D. Steffens, H.-M. Höhle, E. Ertürk, *Schweissen Schneiden*, **1981**, 33, 159.
- [68] R. Knight, R. W. Smith, *Proc. 5th NTSC* **1993**, Anaheim, CA, USA, p. 607.
- [69] J. Drozak, *Haftung und Schichtaufbau von Spritzschichten. Moderne Beschichtungsverfahren*. DGM-Verlag, Düsseldorf **1992**.
- [70] H. Salmang, H. Scholze, *Keramik, Teil I*, Springer, Berlin **1982**, p. 237.
- [71] S. R. Levine, R. A. Miller, M. A. Gedwill, *Proc. 2nd Conf. on Advanced Mat. for Alternative Fuel-Capable Heat Engines*, Monterey, CA, USA, **1981**.
- [72] J. Mathar, *Arch. Eisenhüttenwesen* **1932**, 6, 277.
- [73] A. Noutomi, *Weld. Int.*, **1989**, 11, 947.
- [74] P. Bialucki, W. Kaczmar, J. Gladysz, *Advances in Thermal Spraying* (Ed. N. F. Eaton), Welding Institute of Canada, Pergamon Press, **1986**, p. 837.
- [75] L. C. Cox, *Surf. Coat. Technol.* **1988**, 36, 807.
- [76] B. Eigenmann, B. Scholtes, E. Macherauch, *Mat.-wiss. u. Werkstofftech.* **1989**, 20, 314.
- [77] H.-D. Tietz, B. Mack, L. Pfeiffer, *Proc. TS'93, Aachen* **1993**, DVS 152, p. 205.
- [78] C. C. Berndt, *Advances in Thermal Spraying* (Ed. N. F. Eaton), Welding Institute of Canada, Pergamon Press, **1986**, p. 149.
- [79] S. Thiele, *Mikrohärte, Mikrostruktur und Haftung vakuumplasmagespritzter TiC/Mo₂C/Ni, Co-Verbundschichten*. Unpublished diploma thesis. Freiberg University of Mining and Technology, June **1994**.
- [80] D. S. Rickerby, *J. Vac. Sci. Technol.* **1986**, 4, 2809.
- [81] W. D. Sproul, *Thin Solid Films* **1984**, 118, 279.
- [82] C. S. Barrett, T. B. Massalski, *Structure of Metals, 3rd edn*, McGraw-Hill: New York, USA, **1966**, p. 465.
- [83] *Test Strip, Holder and Gage for Shot Peening*, SAE Standard J 442, SAE Handbook, Part I, SAE Inc., Warrendale, PA, USA **1977**, 9.05–9.06.
- [84] P. A. Siemers, W. B. Hillig, *Thermal barrier-coated turbine blade study*, Final report, NASA CR-165351, **1981**, p. 123.
- [85] R. Elsing, O. Knotek, U. Balting, *Surf. Coat. Technol.* **1990**, 43/44, 416.
- [86] O. Knotek, R. Elsing, U. Balting, *Surf. Coat. Technol.* **1988**, 36, 99.
- [87] G. Eckold, I. M. Buckley-Golder, K. T. Scott, *Proc. 2nd Conf. Surf. Eng.*, Stratford-on-Avon, UK, 16–18 June **1987**, p. 433.
- [88] H.-D. Steffens, Z. Babiak, U. Fischer, *Proc. 2nd Conf. Surf. Eng.*, Stratford-on-Avon, UK, 16–18 June, **1987**, p. 471.
- [89] R. Kaczmarek, W. Robert, J. Jurewicz, M. I. Boulous, S. Dallaire, *Proc. Symp. Mater. Res. Soc.* Boston, MA, USA **1983**.

6 The Technology Transfer Process: Solutions to Industrial Problems

This chapter will give some basic information on structural and functional coatings widely applied to solve mechanical and frictional performance and maintenance problems in industry as well as to impart new functional properties to materials surfaces. The material covered here is by no means exhaustive but should elucidate some fundamental trends in coating design as well as illustrate various physical processes occurring during plasma spraying of wear- and corrosion-resistant coatings, thermal and chemical barrier coatings, bioceramic coatings and various functional coatings.

6.1 Wear- and Corrosion-resistant Coatings

These coatings are most frequently based on transition metal carbides (WC, TiC, Mo₂C, TaC, NbC, Cr₃C₂) and also some hard oxides (Al₂O₃, TiO₂, Cr₂O₃), metals (W, Mo, Ti, Ta) and alloys (NiCoCrAlY), and diamond. Since the melting temperatures of the carbides are extremely high, and oxidation/decarburization generally occurs at such high temperatures, pure carbide powders cannot be properly melted and deposited even in high enthalpy plasma jets. Instead, carbide particles are embedded into easily melted binder metals such as Ni, Co, Cr, and their mixtures and alloys, respectively. There are, however, restrictions to the use of binder metals. For example, B₄C VPS-coatings on graphite, and carbon fiber composites CFC or steel tiles were tested for walls of nuclear fusion reactors without the use of binder metals that would be activated by the high neutron flux [1].

6.1.1 Pure Carbides

Carbides with simple structures are considered interstitial compounds characterized by a strong interaction of metal to carbon: the small carbon atom is located in either an octahedral interstitial site or at the center of a trigonal prism within the close-packed transition metal atoms.

The crystal structures of the carbides under discussion are determined by the radius ratio $r = r_X/r_T$, where X = carbon and T = transition metal [2]. If $r < 0.59$, the metal atoms form very simple structures with close-packed cubic or hexagonal arrangement. The carbon atoms are situated at interstitial sites. Those interstitial sites must be somewhat smaller than the carbon atom because otherwise there will be insufficient bonding resulting in an essentially unstable structure [3]. The following monocarbides crystallize in the cubic B1 (NaCl) structure: TiC, ZrC, HfC, VC, NbC, TaC, WC. Although molybdenum carbide has an r -value of 0.556 its cubic phase is non-stoichiometric MoC_{1-x} with a low temperature α -form and a high temperature β -form. The more stable structure with higher hardness and wear resistance is Mo_2C that crystallizes in the hexagonal T_2C structure in which only half of the interstitial sites are occupied by carbon. The same structure type is found for W_2C .

Although *titanium carbide* crystallizes only in the cubic B1 structure it has an extraordinarily wide compositional range, and is thus stable between $\text{TiC}_{0.97}$ and $\text{TiC}_{0.50}$. The melting point is 3067 °C near a composition $\text{TiC}_{0.80}$. *Tungsten carbide* is stable at room temperature as cubic α -WC that melts at 2867 °C. The hexagonal W_2C -phase melts at a slightly lower temperature of 2750 °C. As mentioned above, WC loses carbon at appreciable rate above 2200 °C and will form a surface layer of W_2C .

If $r > 0.59$, more complicated structures arise in which the transition metal atoms do not form a close-packed arrangement anymore. An example is chromium carbide whose complicated phase relationships include a peritectically melting cubic Cr_{23}C_6 high temperature phase, a hexagonal Cr_7C_3 phase, and a peritectically melting orthorhombic low temperature Cr_3C_2 phase ($T_P = 1810$ °C). All three phases show a narrow range of homogeneity. Precipitation-strengthening of Cr_3C_2 by formation of Cr_7C_3 due to decarburization may be the reason for the exceptional solid-particle erosion resistance of those coatings (see Sec. 6.1.2.3).

6.1.2 Cemented Carbides

Cemented carbides are composite materials of pure carbides with a binder metal of low melting point and high ductility. The principal use of these materials is to produce cutting tools, but plasma-sprayed coatings of cemented carbides enjoy wide applications as surface layers to protect an extraordinarily wide range of machinery and tools from wear, erosion and corrosion. The term refers to a carbide of group 4b–6b elements of the periodic table together in a metal matrix such as cobalt or nickel. Mixtures of these metals, also together with chromium are often utilized. The selection of the binder metal depends to a large extent on its ability to wet the surface of the carbide particles to ensure secure coating cohesion. Addition of TiC, TaC and NbC to WC/Co-cemented carbide causes important property changes in terms of surface reactivity and/or melting behavior. Such multicarbide materials may contain TiC–TaC–NbC solid solutions¹ that improve the oxidation resistance at high tem-

¹ In the American engineering literature on cemented carbide coatings the name columbium (symbol: Cb) instead of niobium is still used.

peratures as well as hardness and hot strength. Often such a modification of the hard phase content of the composite is augmented by incorporating chromium into the carbide mix or by modifying the binder phase, e.g. cobalt–chromium or chromium–nickel–cobalt alloys. Like the hardness the transverse rupture-strength of a coating can be strongly influenced by the binder metal content that can be varied by the degree of dispersion of the carbide and binder metal phase. It is evident that the starting spray powder must be highly homogeneous in the first place to avoid layering of the coating and thus introduction of potential weak zones. The corrosion resistance of cemented carbide coatings is determined by both the corrosion resistance of the carbide(s) and the binder metals. The latter are generally soluble in acids so that their corrosion performance limits the application of such coatings in operations where highly acidic solutions or gases occur. In such cases the design engineer often resorts to oxide ceramic coatings such as alumina. But although alumina is highly corrosion-resistant its low fracture toughness and compliance pose problems (see Sec. 6.1.3.1).

In addition to mixed carbides and carbide solid solutions, ternary complex carbides have been developed [4]. These hexagonal carbides T_2MC (T = group 3b–6b elements of the periodic table; M = group 2b, 3a–6a elements) are called H-phases. Their crystal structure has been determined for Cr_2AlC [5] and Ti_2AlC [6]. The latter was used as hard phase in a pseudo-alloy matrix together with a hard Ni–Cr–10B–Si alloy [7] to flame- and plasma-spray wear-resistant coatings onto steel [4]. Such tribological coatings show improved wear resistance.

6.1.2.1 Tungsten Carbide/Cobalt Coatings

These materials are widely applied in industry as wear-resistant coatings because of their high hardness and excellent abrasion resistance. Owing to the complex interactions of the spray powder with the plasma jet, the environment and the substrate material, the coating process requires careful control of the powder characteristics and the plasma parameters [8, 9]. The coating techniques applied comprise conventional flame spraying, HVOF techniques (D-Gun, Gator Gard, Jet Cote), arc spraying and plasma spraying including conventional APS, LPPS and VPS, respectively, reactive plasma spraying, UPS and more. Recent developments indicate that HVOF flame spraying yields coatings highly optimized in terms of density, hardness, adhesion strength and phase purity compared to APS or VPS methods [10, 11]. However, for the development of ‘designer coatings’ under exclusion of oxygen that may lead to coating degradation VPS is also being considered [12, 23].

The coatings deposited must be rather thin so as not to compromise given tolerances of the machined parts and tools. While for wear applications a high coating density is desired, sometimes this requirement must be relaxed. The surfaces of plungers and barrels of reciprocating and centrifugal pumps, for example, must be somewhat porous so that the lubricants can adhere [13]. Cobalt-based tungsten carbide coatings are most useful for achieving high sliding-wear resistance and better friction properties [14]. They can be used to prevent general wear, cavitation erosion, and also chemical corrosion of a variety of oil field equipment including protection against severe particle erosion of choke nozzles of tungsten carbide alloy that are

used to control high-velocity flow of heavy oil contaminated with sand [15]. This requires secure bonding of a thin layer ($<10\text{ }\mu\text{m}$) of compatible tungsten carbide-based material to the nozzle substrate [13]. As the nozzle is supposed to rotate within a steel sleeve, problems of clearance control must also be addressed. How sophisticated the present technology has become to protect these choke nozzles from failure due to severe erosion, corrosion and scaling caused by hot, corrosive fluids and sand is illustrated by a study performed by ESSO Resources Canada Limited [15] that concluded that the massive tungsten carbide/cobalt substrate is best protected by a system of a CVD titanium nitride coating of $10\text{ }\mu\text{m}$ thickness followed by a $7\text{ }\mu\text{m}$ alumina and then a boron diffusion coating. It is very obvious that a single conventional 'off the shelf' coating is not sufficient anymore to protect machinery from nonlinear effects of corrabrasion, i.e. the synergistic interaction of corrosive and abrasive destruction of the material. Also, while it is still common practice to develop coatings by establishing a set of spray parameters adapted to different substrates by making only minor modifications to parameter sets information obtained from the widespread literature on this subject, there is an increasing need to design coating/substrate systems as a single entity [16]. Since this requires optimization of coating properties, statistical multifactorial experimental designs should be applied (see Chap. 8).

Since proper adhesion of the WC/Co coatings requires an optimized D/d ratio (see Eq. (5-8)) and therefore optimized particle viscosity and velocity, the plasma enthalpy and thus the plasma temperature become the determining factors. The plasma jet temperature must be substantially higher than the melting point of cobalt ($1495\text{ }^{\circ}\text{C}$) but not so high that the tungsten carbide undergoes decomposition [17] or η -carbide ($\text{Co}_n\text{W}_m\text{C}$) formation [18]. The changes a stoichiometric WC/Co powder is subjected to during thermal exposure in the plasma spray process is illustrated in Fig. 6-1 that shows the low carbon portion of the ternary phase diagram W-C-Co. The WC phase reacts with the Co melt (see Fig. 5-18) and loses carbon by reaction with oxygen in the flame. The composition of the coating matrix is close to the η -carbide phase $\text{Co}_3\text{W}_3\text{C}$. This phase presumably leads to a deterioration of the mechanical strength due to its brittleness. Furthermore, W_2C formed by decarburization of WC tends to embrittle the coating. Even though under VPS conditions due to the absence of oxygen the formation of W_2C can be completely suppressed [8, 17], carbon can evaporate and form mixed tungsten carbides [12]. Figure 6-2 shows how, with increasing spray distance and the associated increase of the residence time of the particles in the flame, the carbon loss and the oxygen pick-up increased and the Rockwell hardness, HRC, substantially decreased [18].

Suppression of the decomposition of tungsten carbide by selecting high plasma gas flow rates at reduced hydrogen content has been attempted [19]. However, even under those conditions trace amounts of oxygen contained in the plasma gas (up to 50 p.p.m.) or in voids of the spray powder can lead to oxidative processes under formation of CoWO_4 [17]. Decrease of decomposition of tungsten carbide with increasing gas volumes at the same energy level because of reduced dwell time has also been confirmed by Chandler and Nicoll [9]. They also found that the use of an argon/hydrogen plasma reduced dramatically the amount of remaining WC and a concurrent increase in M_6C ($\text{Co}_3\text{W}_3\text{C}$) and M_{12}C_4 ($\text{Co}_3\text{W}_9\text{C}_4$) phases. Such an in-

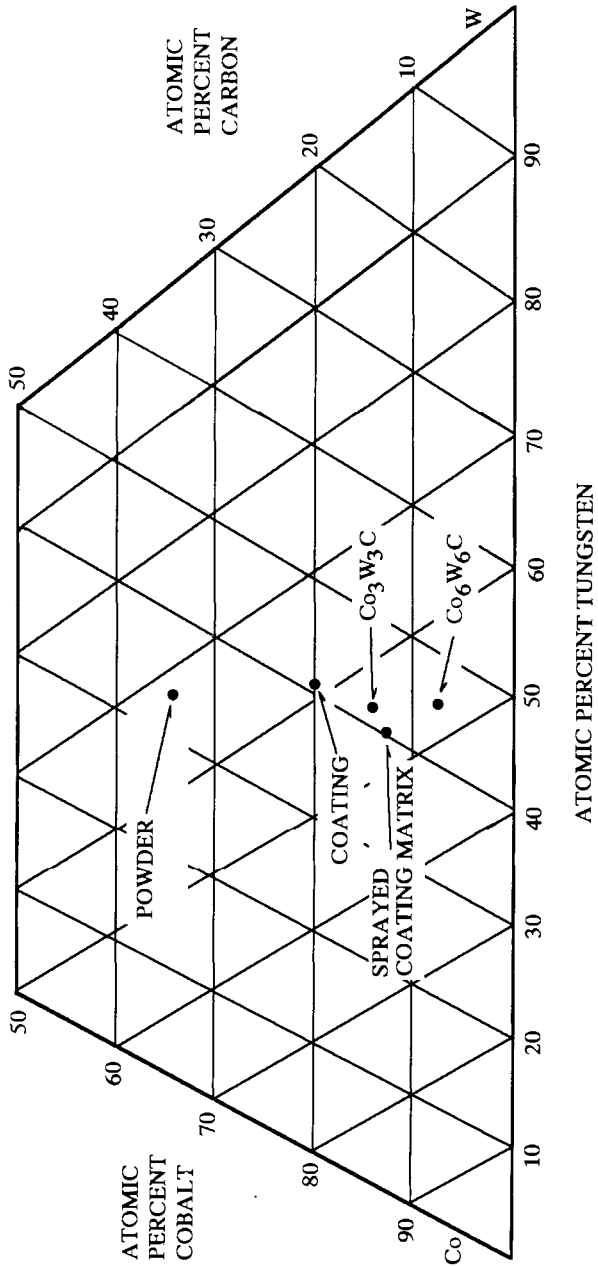


Figure 6-1. Low carbon portion of the ternary phase diagram W-C-Co showing the shift of the chemical composition of the starting powder towards the η -carbide phase $\text{Co}_3\text{W}_3\text{C}$ during spraying [18].

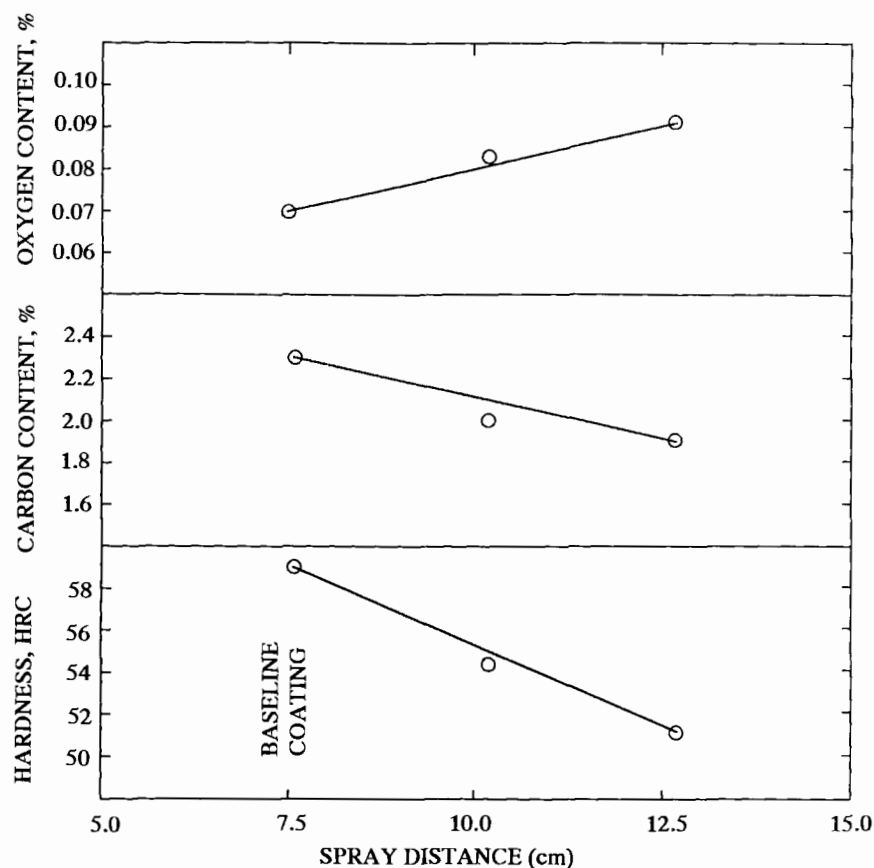


Figure 6-2. Oxygen pick-up, and carbon loss and decrease of the Rockwell hardness of WC-Co(Ni) coatings with increasing spray distance [18].

crease has been also observed with negative, i.e. upstream injection that has been found to disappear using positive, i.e. downstream injection. Again, the reduction of dwell time reduces decomposition.

Another way to suppress degradation of coating performance due to matrix-alloying is to inject separately the 88WC12Co phase and a Ni-based alloy (73Ni15Cr4Si4Fe3B1C) into a d.c. plasmatron with two injection ports [20]. The resulting composite coating deposited onto AISI 5150 steel is very dense and the carbide phase composition is close to that of the initial spray powder. In particular, decarburization products such as brittle W_2C and η -carbides are absent. The reason for this may be that with dual injection, the heat input to the carbide and the matrix metal can be independently tailored for optimum results by adjustment of the injection angles and locations as well as the plasmatron operating parameters.

The results of conventional co-spraying of a mechanical blend of 50WC50'A' ($A = 73\text{Ni}15\text{Cr}4\text{Si}4\text{Fe}3\text{B}1\text{C}$) onto very fine-grained powder-metallurgically densified tungsten carbide (88WC12NiCo) are shown in Figs 6-3 and 6-4. Figures 6-3a-c show cross-sections of the interfaces between the WC/NiCo substrate (left) and the 50WC50'A' coating (right) with X-ray line scans of tungsten (a), cobalt (b) and nickel (c). Figures 6-4a and b show the cracking behavior of the substrate/coating system subjected to a Charpy impact test. The main crack is situated within the fine-grained substrate (Fig. 6-4a) with a second crack running close to the interface but always within the substrate material. Figure 6-4b shows an enlarged view of the central area of Fig. 6-4a. In Fig. 6-4c a back-scattered image of the polished coating is shown illustrating the coarse-grained WC grains within the 'A' matrix [21]. Such tungsten carbide composite coatings were developed to combat severe solid-particle erosion (SPE) problems of choke nozzles in heavy crude oil production in the oil fields of Northern Alberta, Canada [15].

It has been mentioned above (see Sec. 6.1.2) that the modification of tungsten carbide by addition of highly refractory and extremely hard carbides such as TiC and TaC yields coatings with clearly improved wear resistance, frictional properties, and fracture toughness [22]. At low frictional velocities the wear resistance is rather low but increases with increasing velocities and therefore also temperatures [23]. This can be attributed to surface oxidation that decreases friction. In TiC-reinforced WC/Co coatings the TiC particles tend to collect near the surface of the coating owing to their low specific gravity thus creating a top layer that has an extremely good abrasion resistance.

The addition of TaC leads to three-phase alloys with improved high temperature properties in terms of oxidation and diffusion resistance against ferrous substrate materials [24].

Chemical degradation of the WC phase by oxidation, decarburization and matrix-alloying, as discussed above, yields coatings with noticeably decreased performance in terms of abrasion resistance. Coating microhardness may be, under simplified assumptions, indicative of abrasion resistance even though a proportionality between microhardness, and sliding and abrasive wear, respectively is rarely observed [25]. Much more important is the interaction of wear mode and microstructure of the coating. Spraying of WC/Co powder at high velocities in an inert atmosphere should considerably minimize the degradation of the WC/Co system. Indeed, experiments by Mutasim *et al.* [26] using a high velocity plasma spray process, modified with a plasmatron extension operating in a low pressure chamber (Fig. 6-5) pointed to a substantial decrease of the amounts of W_2C and $\text{Co}_3\text{W}_3\text{C}$ and thus to an increase in microhardness approaching that of the powder-metallurgically densified 88WC12Co material (Fig. 6-6). It was concluded that the higher amounts of WC retained contributed to the observed increase in microhardness. Figure 6-7 shows a cross-section of a dense, well-adhering 88WC12Co wear coating (right) on a mild steel substrate (left) produced by APS with careful parameter optimization [13].

The hardness of the WC/Co composite depends strongly on the ratio WC to Co as well as, for monolithic materials, its grain size (Fig. 6-8). Therefore, different areas of application emerge.

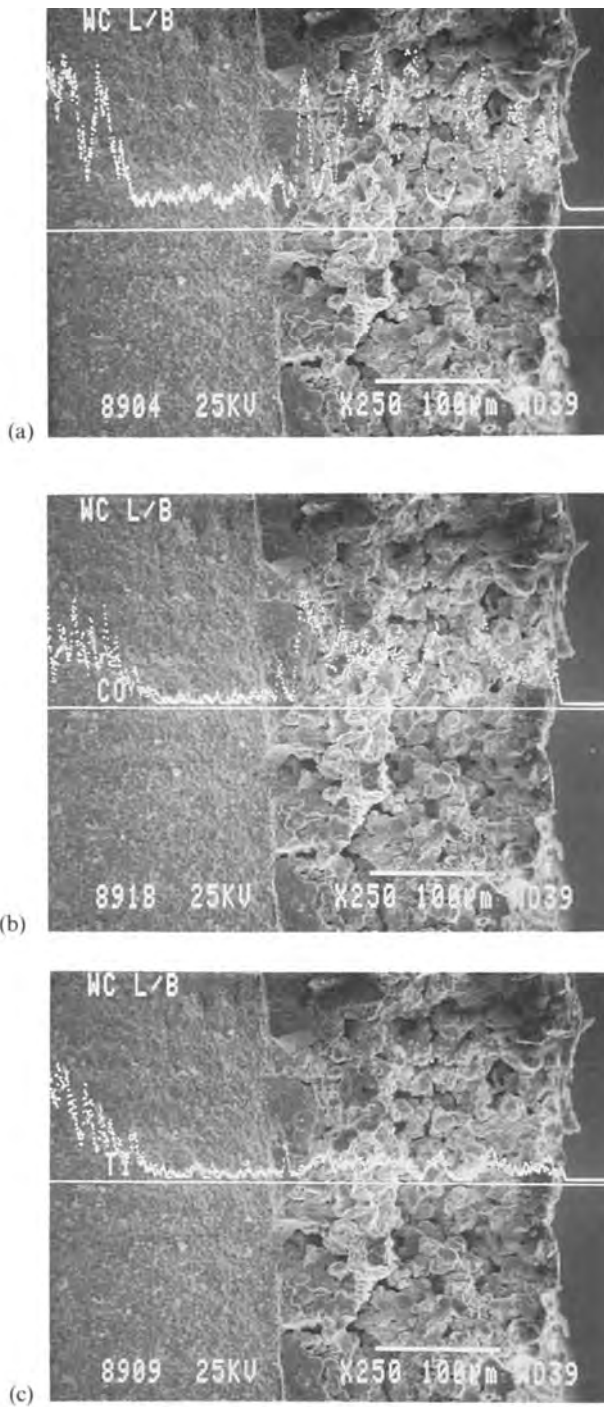
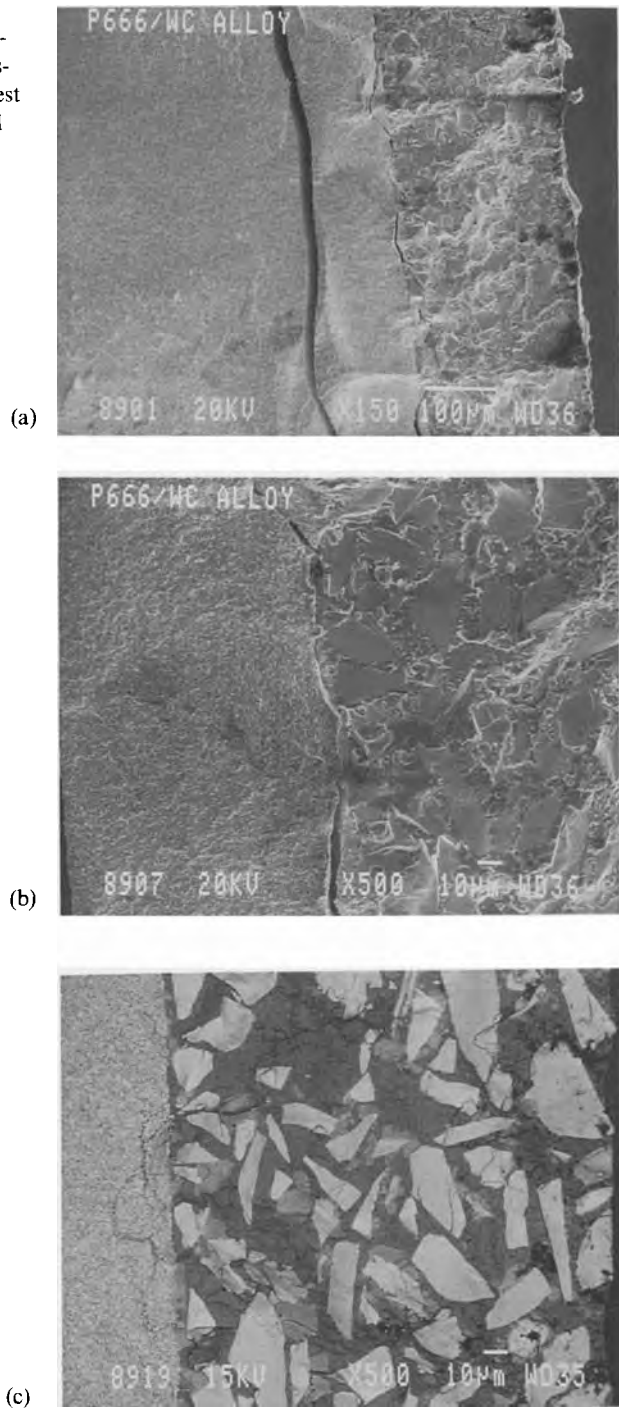


Figure 6-3. Tungsten carbide-based coating (right) on a fine-grained 88WC12NiCo substrate (left) with X-ray line scans of W(a), Co(b) and Ni(c).

Figure 6-4. Crack behavior of a tungsten carbide-based coating/fine-grained 88WC12NiCo substrate system subjected to a Charpy impact test (a,b) and an electron back-scattered image of the coating (c).



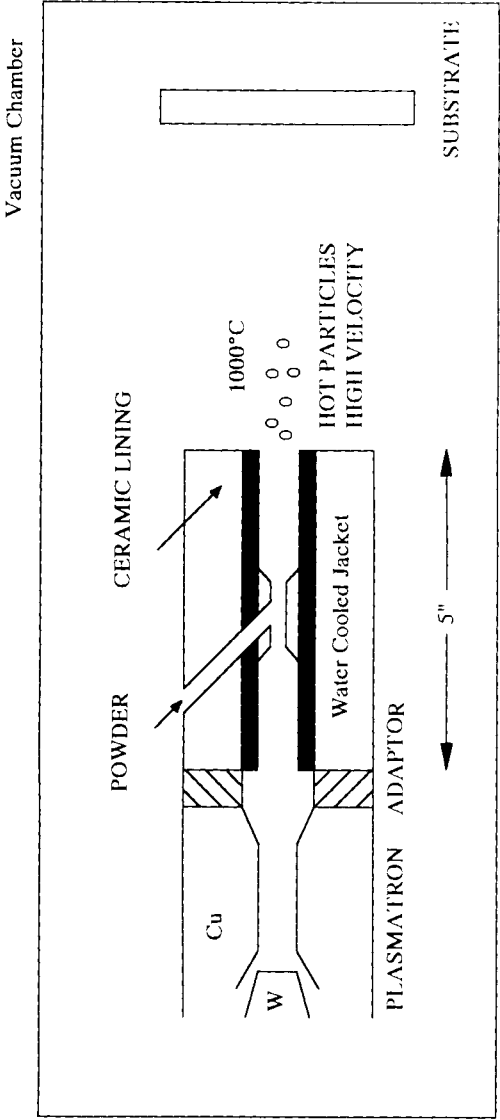


Figure 6-5. Modified plasmatron to reduce decarburization of WC-Co coatings (see text) [26].

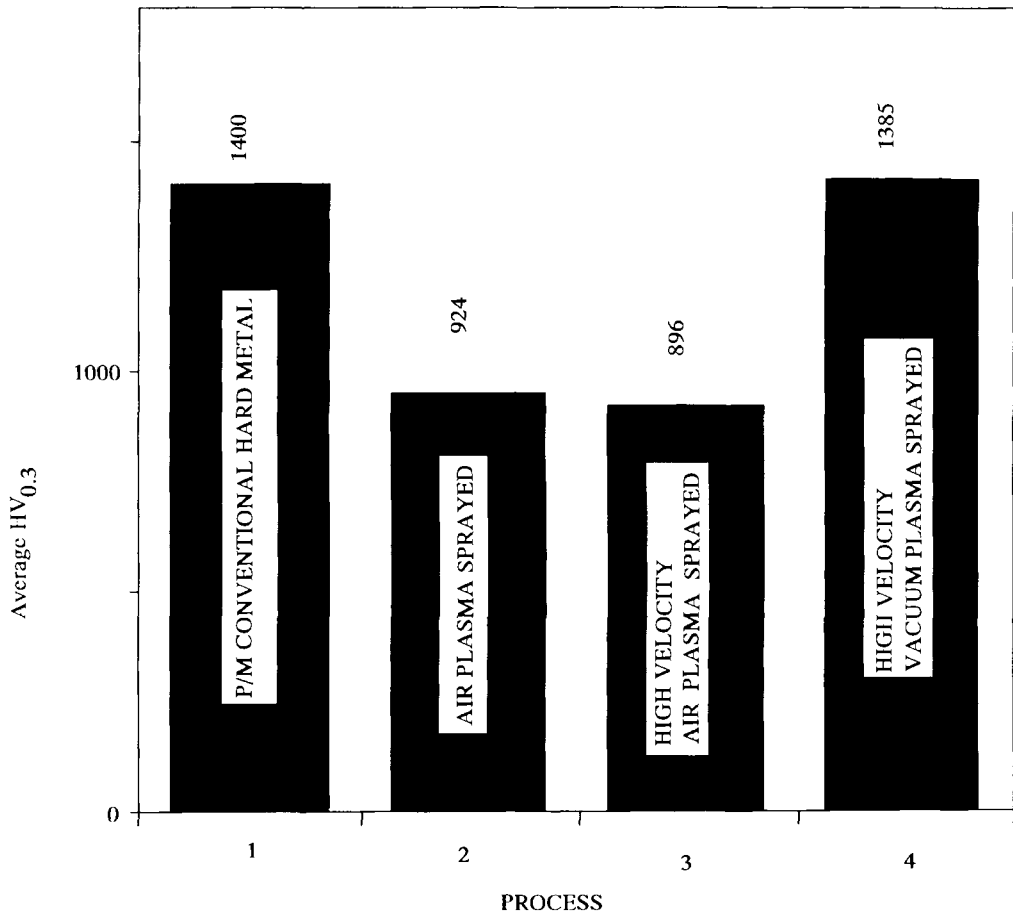


Figure 6-6. Comparison of the microhardness (HV_{0.3}) of differently processed 88WC12Co powder (2–4) and powder-metallurgically densified material (1) [26].

6.1.2.2 Titanium Carbide-based Coatings

Under conditions of simultaneous mechanical stress and chemical corrosion, in particular in a steam environment, commercially available WC–Co coatings frequently do not perform well at high working temperatures.

For example, the quest for an increased energy output of power plants and various kinds of heat engines necessitates an increase in the working temperature. In these cases, TiC–Ni is an alternative system [27] that because of higher temperature stability, lower coefficient of thermal expansion, higher hardness and lower specific gravity may outperform other coating systems. If the TiC phase is stable, and well bonded and dispersed in the matrix, a hard, low-friction surface is produced. WC or Cr_xC_y phases tend to decompose at high temperatures thus losing their friction properties.

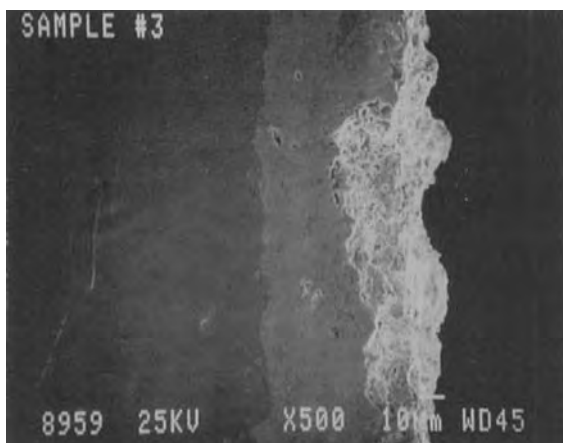


Figure 6-7. Cross-section of a 88WC12Co coating (right) on mild steel (left) [13].

Problems exist, however, in plasma spray operations that result in decarburization of TiC towards TiC_{1-x} . Therefore, TiC has been processed as ‘cermet coating clad’ in a metal system [28]. In order to suppress decarburization of TiC, a reduction of the dwell time of Ni-plated TiC particles (50TiC50Ni to 30TiC70Ni) utilizing VPS or HVOF techniques led to coatings on mild steel with low porosity ($<2\%$), high microhardness (900–1 000 $\text{HV}_{0.2}$ (the subscript refers to the applied load, 0.2 kp)) and high blast erosion resistance ($<0.1 \text{ mm}^3 \text{ g}^{-1}$ at a blast angle of 90° ; alumina grit 60 mesh, air pressure 490 kPa) [27]. The VPS coatings outperformed the HVOF coatings also in a reciprocating plane wear test.

The wear properties of TiC-based coatings are a strong function of the powder preparation method. Studies by Mutasim *et al.* [29] showed that a 40% TiC + Ni20Cr powder produced by the PMRS (plasma melted rapidly solidified) method and sprayed with VPS produced a coating with a wear resistance ten times that of a coating of the same composition whose starting powder was produced by physical blending. Similar results were obtained in an earlier study [30]. In this study, a comparison was made of the sliding wear performance of five different hard coatings (TiC reinforced alloys: Resistive CS-40 (45 vol% TiC, stainless steel matrix); Resistive CM (45 vol% TiC, tool steel/Fe,Cr,Mo matrix); Resistive HT-6A (40 vol% TiC, Ni20Cr matrix); 88WC12Co composite powder, and Stellite 6 ($\text{Co}_{28}\text{Cr}_{4.5}\text{W}_{3.5}\text{Fe}_{3}\text{Ni}_{1.5}\text{Si}_{1}\text{Mo}_{1}\text{Mn}_{1.15}\text{C}$) sprayed with APS onto steel. The TiC reinforced composite coatings had bond strengths exceeding 58 MPa and sliding wear resistances from 20% higher than the WC/Co coatings, and up to 100% higher than Stellite 6 coatings, depending on the deposit matrix of the TiC reinforced materials (Fig. 6-9a). Also, the type of auxiliary plasma gas (helium or hydrogen) played an important role for the wear resistance of WC/Co and Stellite 6 but did not influence that of the TiC-based coatings. The kinetic coefficient of friction during the sliding wear test was minimized for CS-40 (Fig. 6-9b).

A different way to circumvent the risk of thermal decarburization of TiC under high temperature conditions in a plasma jet is *reactive plasma spraying*. TiC is formed from titanium particles during their flight along the plasma jet. A reactor is

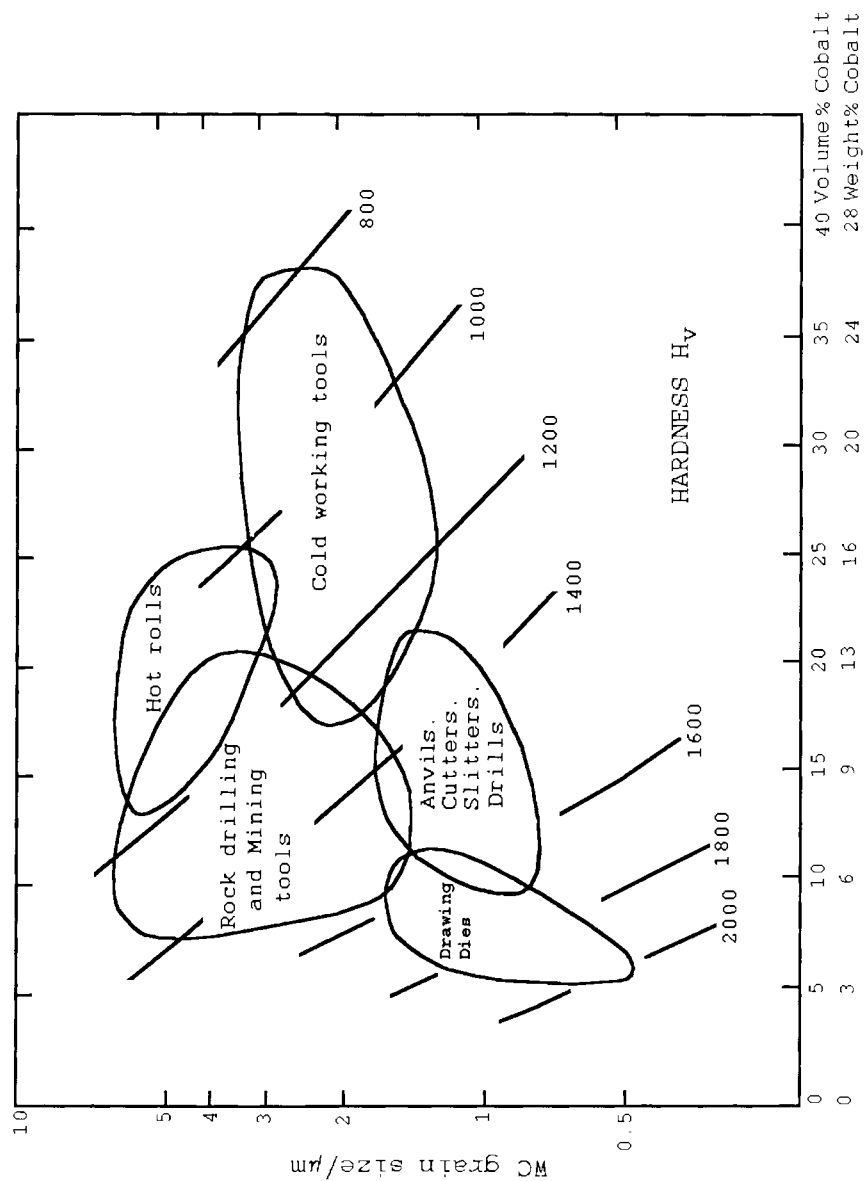
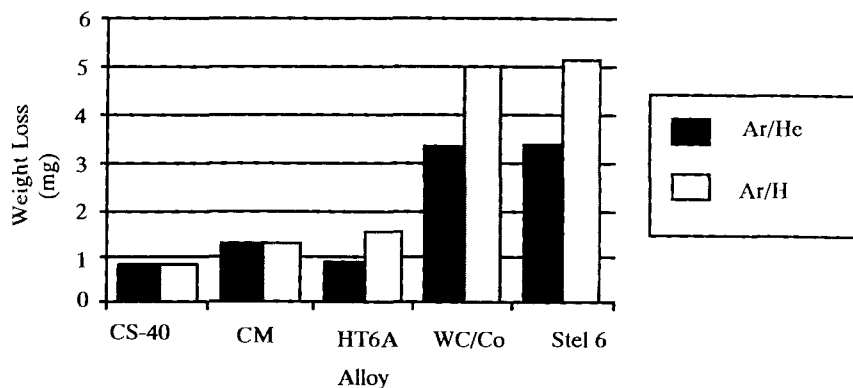
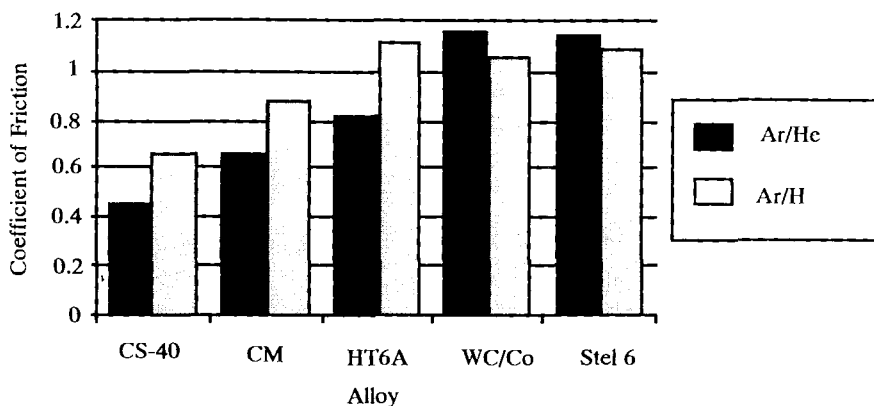


Figure 6-8. Hardness of WC-Co cemented carbide as a function of the WC grain size and the volume content of cobalt. Several application areas are indicated.



(a)



(b)

Figure 6-9. Weight loss (a) and coefficient of friction (b) during sliding wear resistance tests of TiC-metal matrix coatings (CS-40, CM, HT6A alloy). Values for WC/Co and Stellite 6 are given for comparison [30].

added to a conventional d.c. plasmatron into which carbon-containing precursor gases (methane, ethane, propane, acetylene, etc.) are fed (Fig. 6-10). Into the plasmatron titanium powder will be introduced in the conventional manner. Shroud gas (Ar, N₂) led into the reactor tube is thought to prevent build up on the reactor walls of Ti/TiC materials and carbon produced by thermal cracking of the hydrocarbon precursor gases. The modified plasmatron was operated in a controlled, sub-

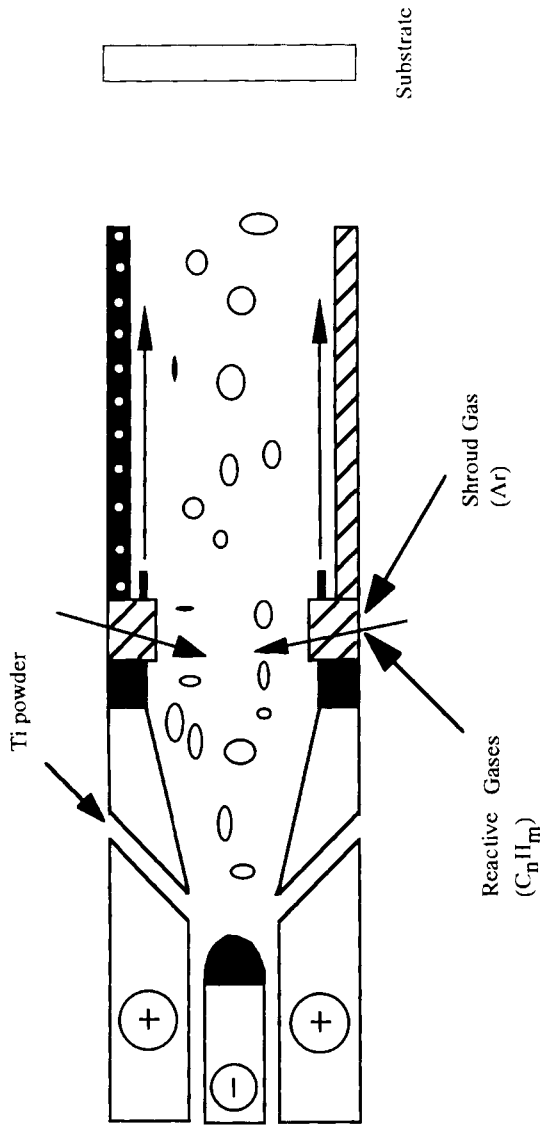


Figure 6-10. Reactive plasma spraying of Ti in a hydrocarbon environment to obtain TiC-containing hard coatings [31].

atmospheric pressure environment. The amount of TiC formed and retained in the coating is a function of several parameters such as substrate temperature, chamber pressure, type of reactive gas, flow rate of the reactive gas, and the method of introduction of the reactive gas [31, 32]. The hard TiC phases were observed predominantly in the intersplat region. The formation and distribution of the hard phases in the coatings suggest a two-stage mechanism illustrated in Fig. 6-11. In these experiments the content of the hard phase is still very low (around 8 vol%) and must be considerably improved by process optimization until reactive plasma spraying of TiC will become an economically competitive technology. A more promising way seems to be to reactively spray Ti/Ni20Cr powder with propylene as a precursor gas [32]. In the coatings, the hard phases Cr_7C_3 and TiC were deposited in very small crystals ($<1\text{ }\mu\text{m}$). From these results it was concluded that reactively plasma-sprayed prealloyed NiCr/TiC powders would show improved wear resistance owing to the better carbide/matrix cohesion of the *in situ* formed carbides Cr_xC_y . Indeed, the reactively sprayed NiCr/TiC material displayed harder coatings (840 $\text{VH}_{0.3}$) than nonreactively sprayed prealloyed coatings that showed a microhardness of only 700 $\text{VH}_{0.3}$ [33].

Several other papers on TiC-based coatings may be consulted to obtain information on applications and performance optimization [34–37]. The properties of the simple TiC/Ni system can be improved by alloying with other elements, such as molybdenum in the carbide, and cobalt in the binder phase. Preliminary investigations on such (Ti, Mo)C–NiCo coatings sprayed by APS and D-Gun techniques [38] as well as VPS [39] indicate that with proper parameter optimization very hard, highly wear resistant coatings can be produced for a variety of high temperature applications including high temperature erosion protection. It was demonstrated that the typical microstructure of the powders, produced by agglomeration and subsequent sintering, in particular the core (nearly pure TiC)–rim (Ti, Mo) C_{1-x} structure (Fig. 6-12) can be transferred to the coating without significant changes.

6.1.2.3 Chromium Carbide-based Coatings

Although chromium carbide is somewhat softer than tungsten carbide at room temperature (HRC 52 versus HRC 62) it shows excellent sliding-wear resistance [40] as well as superior oxidation and high temperature SPE resistance [41] in a steam environment. It thus offers promising opportunities for protecting steam path surfaces and turbine components from corrosion and erosion [42]. Several attempts have been made in the past to combat corrosion damage, stress corrosion cracking and corrosion fatigue in steam turbines [43] as well as SPE in boilers, tubing and steam lines including superheaters [42]. These attempts include the development of boride diffusion coatings and plasma-sprayed chromium carbide coatings.

The advantage of the *boride diffusion coatings* is that they do not have a line-of-sight limitation (as do plasma spray coatings) but this is more than compensated for by the negative fact that boride coatings can result in a fatigue loss in the ferritic base metal of boiler tubes of as much as 50% [44]. This fatigue loss originates from a combination of lack of coating ductility and the fact that the coating forms a metallurgical bond with the base metal. Strain damage occurs in cyclical thermal loading

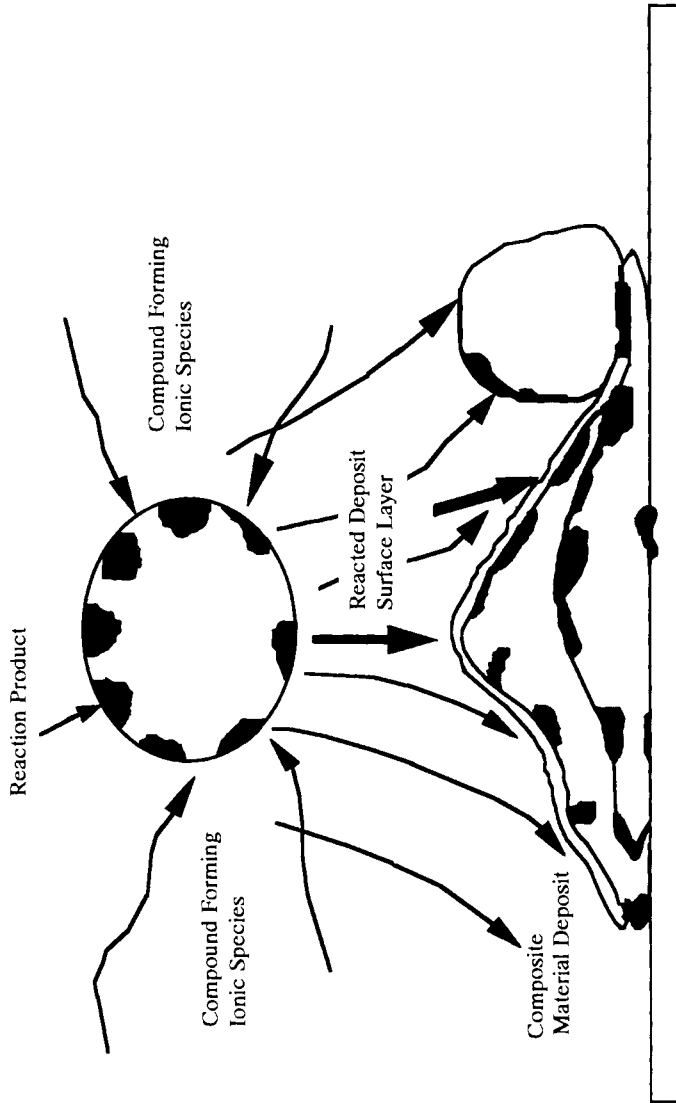


Figure 6-11. Model of TiC formation during reactive plasma spraying of Ti metal powder [31].

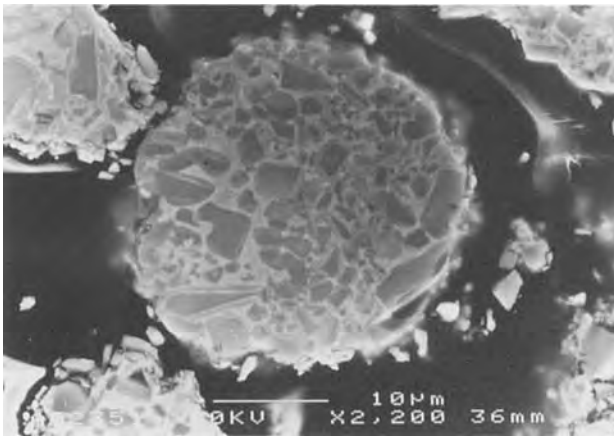


Figure 6-12. Dense as-sintered (Ti, Mo)C-NiCo alloy granule with a typical core (nearly pure TiC)-rim (Ti, Mo)C_{1-x} structure [39].

since the higher Young's modulus of the coating causes it to be put under tension that will be amplified in service and leads finally to cracks perpendicular to the stress direction.

Plasma-sprayed *chromium carbide coatings* can reduce considerably the steam path erosion rate. Comparative erosion tests on chromium carbide sprayed with a D-Gun technique and chromium boride/iron boride diffusion coatings on AISI 403 and AISI 422 martensitic stainless steels showed that at 538 °C the former are clearly superior in terms of SPE with chromite particles (75 μm, 152 m s⁻¹, 30 min) at impingement angles of 30° whereas the latter show higher SPE resistance at impingement angles of 90° [45]. During deposition of plasma-sprayed coatings the heat input into the ferritic base metal is much lower than for boride diffusion coatings. Therefore boride diffusion coatings require a post-coating treatment to restore the strength and ductility to the coated component [42]. The austenitic phase formed at the high diffusion temperature creates internal stresses in the base metal that result in distortion and thus the need for time-consuming post-coating machining or grinding operations to restore flatness or critical clearances.

Tungsten carbide coatings for the protection against SPE of steam turbine buckets were introduced in the early 1960s by the General Electric company, but it was subsequently found that such coatings have not been consistently effective in preventing erosion damage. Thus new solutions were sought and chromium carbide-NiCr cermet coatings on 12Cr martensitic stainless steel (AISI 422 cast) were developed and tested by the General Electric Turbine Technology Laboratory in a fully-ducted, dynamic burner rig heated by natural gas [46].

The Holdgren practice [42] used for protection of steam path surfaces is similar to coating practices specified by General Electric, and the Pratt & Whitney company for rotating aircraft components. An exothermic nickel aluminide bond coat, consisting of spherical aluminum powder particles overcoated with shells of nickel, is applied to the base metal. During spraying the two elements react to form a nickel aluminide intermetallic compound. Since this reaction results in the evolution of heat

that under optimum spraying conditions continues after impact and coating formation, microdiffusion may occur between base metal and bond coat thereby enhancing the adhesion strength by a factor of two compared to NiCr bond coats.

The reason for the outstanding erosion resistance of chromium carbide coatings seems to be based on precipitation-strengthening of Cr_3C_2 by the formation of Cr_7C_3 due to decarburization (oxidation) of the former (secondary carbide precipitation) [47]. The as-sprayed, carbon-deficient Cr_3C_2 transforms in service to Cr_7C_3 , thereby more than doubling the hardness and greatly enhancing the SPE resistance [48]. Since this precipitation-strengthening mechanism requires an air atmosphere, good erosion resistance is promoted by APS rather than VPS. Also, fine chromium carbide powders and pre-aging to optimum hardness further increases SPE resistance, as does the replacement of the NiCr or NiCrMo matrix by FeCrAlY or CoCrNiW [48]. Alloys such as FeCrAlY have also been tested in their own right as a barrier layer to high temperature erosion on coal combustion and conversion processes including fireside erosion, erosion of steam turbines and corrosion-assisted wear in flue gas desulfurization equipment [49]. The protection mechanism is based on the formation of Al_2O_3 scale [50].

Another widespread and yet unsolved problem exists in the petrochemical industry. High temperature steam cracking of ethane to produce ethylene causes several deleterious effects in the steel tubing in the convectively and radiantly heated sections of a typical cracking furnace. These effects include external oxidation and internal oxidation/deposition of coke that is thought to be formed under the catalytic action of nickel oxide. This oxide is formed from oxidation of nickel as an alloying element for steel (AISI 304, AISI 410) or nickel superalloys (Inconel 800, Hastelloy X) added to impart high temperature resistance. The coke deposited on the internal surfaces of tubing tends to form carbides with other alloying metals in the steel that can migrate into the metal. As a result, blistering and cracking of the steel can occur. Also, reduction of the heat conduction capability of the tubing may lead to local overheating in the convection section of an ethylene steam cracker. Since the surface roughness of the internal tubing walls seem to promote the rate of coke deposition [51, 52] mechanical polishing or application of a smooth coating can reduce the coke layer formed. Also, introduction of trace amounts of sulfur compounds or antifoulants into the process gas stream inhibits the catalytic effect of the metal surface and may offer some moderate measure of protection [53]. Finally, metallurgical remedies tested were either related to higher alloyed steels to reduce the carbon gradient or to the introduction into the metal of carbide-stabilizing additions such as W, Mo, Nb, or V. Unfortunately, these metal additions have adverse effects on the high temperature oxidation resistance and their oxides may form low melting eutectics with nickel or chromium oxide.

In order to reconcile the material requirements with the severity of the environmental attack, functional chemical barrier coatings (CBC) must be developed with the following properties:

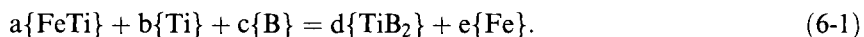
- high temperature resistance,
- high corrosion resistance,

- chemical inertness,
- high hardness,
- high wear, abrasion and erosion resistance,
- creep resistance,
- good adhesion,
- high fracture toughness,
- good thermal conductivity,
- thermal shock resistance,
- smooth surface/low porosity, and
- thermal fatigue cracking resistance.

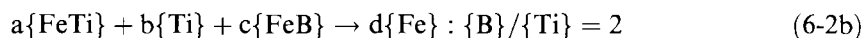
The first five criteria are best met by ceramic coatings, the remaining seven by metal or alloy coatings. To develop a coating material that would meet all requirements, ideally a type of coating should be selected that combines synergistically the advantages of both material classes. This, however, is extremely difficult to achieve since many of the desired properties listed above are noncompatible or even mutually exclusive. For example, partially stabilized zirconia (PSZ) would have all the advantages of ceramic coatings including good adhesion but would fail to meet the important criteria of good thermal conductivity and low porosity. In general, the most difficult problem is to match the coefficients of thermal expansion and the thermal conductivities of the coating and the metal substrate. Therefore, the composite coating performance will always have to be compromised. Attempts have been made to plasma-spray composite chromium carbide-based coatings such as $62\text{Cr}_3\text{C}_225\text{W}_2\text{C5TiC4Ni3Mo1Cr}$ that show excellent erosion resistance in a high temperature steam environment. While there seems to be controversy about the role chromium is playing as a possible catalyst for coke formation, there also exists evidence that increasing the chromium content and decreasing the nickel content of the alloy metal reduces the coke deposition rate [54]. There is, however, no general solution available yet to the problem of coke deposition, and chromium carbide coatings may be but a small step towards such an approach.

6.1.2.4 Boride-based Coatings

Although the borides and diborides of the transition metals of the fourth to sixth group of the periodic table have a metallic character (Fig. 8-1), extreme hardness, high melting points and high chemical stability they are difficult to process in plasma spray operations [55]. Early attempts to develop boride coatings used the deposition of CrB_2 from a Cr-B-Si-Ni alloy by a welding torch [56]. Modern approaches rely on the so-called 'auxiliary metal bath process' (Menstruum process) [55, 57] that promotes the reaction of elements by dissolving them in a liquid metal. To deposit TiB_2 , a ferrotitanium alloy is reacted with elemental boron in an iron bath according to:



Also, the synthesis route can start with melting ferrotitanium and ferroboron mixtures in an iron auxiliary bath [58] according to:



Obviously, the synthesized product depends on the $\{\text{B}\}/\{\text{Ti}\}$ atomic ratio and on the temperature. In the case of Eq. (6-2a) the reaction product contains Fe and FeTi compounds, in the case of Eq. (6-2c), Fe and Fe_2B occur. Only when the $\{\text{B}\}/\{\text{Ti}\}$ ratio is 2, the reaction product consists of titanium diboride in an iron matrix. Thus it is possible to produce such coatings by plasma spraying micropellets of ferrotitanium and ferroboron. These micropellets may act as 'microbath' in which the TiB_2 synthesis takes place. It should be emphasized that this technique mimics the commercial electrolytic production of borides in a bath of fused borax with highly concentrated boron depositing along the cathode at 900°C . With additional metal oxides present in the bath, metal borides are deposited in well crystallized agglomerates by reaction of the boron with the reduced metals (Eq. (6-1)) [3].

6.1.3 Oxide Coatings

As frequently pointed out in the preceding sections, cemented carbides do not stand up well to chemical degradation at high temperature, in particular a steam environment, due to decarburization, oxidation and matrix-alloying under formation of η -carbides. In these cases the material of choice may be an oxide ceramic coating, most frequently alumina and chromia, and their modifications and composite materials. However, the advantage of considerable increase in chemical and thermal resistance is counterbalanced by the disadvantage of generally low values of the coefficient of thermal expansions, thermal conductivity, mechanical strength, and fracture toughness. Also, the adhesion of such oxide coatings to a metallic substrate is compromised by the non-metallic bonding character of oxides. Indeed, their high proportion of ionic bonds (see Fig. 8-1) prevent the formation of compatible lattice planes at the interface. In such a case, thin mediating transition layers, for example TiC (see Fig. 8-2) may be useful. As will be shown later (Sec. 6.2), thermal barrier coatings of stabilized zirconia require metallic alloy bond coats to alleviate the gradient in the coefficients of thermal expansion between metal substrate and ceramic oxide coating. On exceeding a limiting coating thickness the residual tensile stresses built up in the coating layer will exceed the yield strength of the ceramic material, and delamination and catastrophic cracking will occur (see Sec. 5.5.5, Fig. 5-20b). Therefore, careful control of the residual tensile stresses in ceramic coatings by application of an appropriate bond coat, well-designed temperature schedule including substrate preheating, or reinforcing measures by addition of other oxides [59] is mandatory for

oxide coatings that are supposed to stand up to the severe in-service conditions in a high-temperature corrosive environment.

6.1.3.1 Alumina-based Coatings

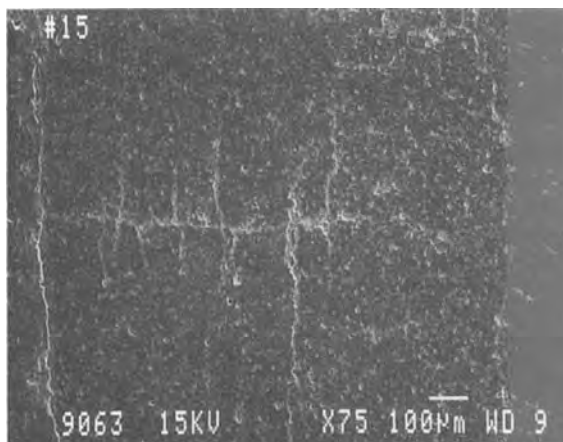
During plasma spraying, alumina transforms from its α -modification, stable at room temperature, to the γ -modification with a defect spinel lattice. Thus plasma-sprayed alumina coatings contain substantial amounts of the essentially metastable γ -phase. The ratio α/γ can be used to characterize the degree of melting of the starting powder with the assumption that high amounts of residual α -phase signal incomplete melting. Also, high amounts of γ -phase seem to lower the wear resistance of alumina coatings even though the microhardness is apparently little affected [21].

Due to its hardness and good electrical insulation, plasma-sprayed alumina coatings are being used as top coats for insulated metal substrates in automotive applications as about 50 μm -thick coatings for aluminum heat-sinks. On these top coats electronic circuitry is then built up. A basic requirement for this application is a maximum dielectric breakdown strength in the range of several hundred volts per 25 μm [60]. This, however, is compromised by the formation of the γ -phase that tends to absorb water [61] that will have a significant effect on the dielectric properties of the coating.

In many cases alumina is used in conjunction with titania: increasing TiO_2 content increases coating fracture toughness but reduces hardness and friction coefficient thus leading to decreased wear resistance. A compromise is to use a ceramic material that contains only a small amount of titania. Alumina/titania (97/3) coatings (called 'grey alumina') are used, for example, to prevent wear, cavitation erosion, and chemical corrosion of plungers from reciprocating and centrifugal pumps [62]. Such coatings are known to be very dense, and produce the smoothest surface of any as-sprayed ceramic coatings. This reduces the amount of post-spray grinding and polishing treatment required. The coatings must be thin to conform to available clearances between plunger and barrel of the pump. On the other hand, they should be hard (70–80 HRC) and show high adhesion strength (>50 MPa). Figure 6-13 shows the cross-section of a thick alumina/titania (97/3) APS coating on a commercial-grade, hot-rolled sheet steel (A 569). The coating appears to be very dense since the apparent porosity is mostly related to grain plug-out during preparation of microscopic samples. Two systems of cracks appear that are due to, first, residual tensile stresses owing to the exceptionally thick (0.9 mm) coating (horizontal cracks) and, second, delamination (vertical cracks). The microhardness of such coatings depends on the thickness and obeys a linear law, $\text{HV}_{0.3} = ad + b$ [MPa] with $a = 12$ MPa, d = coating thickness in mm, and $b = 97.4$. Abrasion wear test mass losses (ASTM G65) of the coatings show an inverse proportionality to the thickness ($\Delta m = c/d$ [mg], with $c = 45.3 \text{ mg mm}^{-1}$ and d = coating thickness in mm) and to the microhardness ($\Delta m = A \text{HV}_{0.3}^{-B}$ [kg], with $A = 4.3 \times 10^{24}$, $\text{HV}_{0.3}$ = microhardness in kg mm^{-2} , and $B = 9.5$ (Fig. 8-15). Similarly dense coatings with SPE-resistance approaching that of bulk alumina were produced by Kingswell *et al.* [63] and Chon *et al.* [64].

To further reduce porosity of alumina-based coatings to below about 5%, laser-

Figure 6-13. Dense $\text{Al}_2\text{O}_3/\text{TiO}_2$ (97/3) APS coating on A 569 steel (left) [62].



glazing can be used to densify to topmost layer of the coating and thus to seal it against penetration of corrosive agents. Inevitably the ceramic layer shows creasing or even severe cracking due to the induced thermal stresses when subjected to a high-power laser beam. These cracks frequently not only propagate through the laser-melted top layer but further extend into the underlying material. A solution to the severe cracking problem may be to introduce into the laser beam ceramic compositions with lower melting points that would develop smaller solidification stresses and less differential strains with respect to the unheated alumina material. Such attempts have been made by selecting $\text{Al}_2\text{O}_3/\text{TiO}_2$ (60/40) that transforms on laser-melting to a mixture of Al_2TiO_5 , TiO_2 and $\alpha\text{-Al}_2\text{O}_3$ [65], and $\text{Al}_2\text{O}_3/\text{ZrO}_2$ [66]. In both cases the cracking could be considerably reduced.

An instructive example is the optimization of WC/Co-tipped saw teeth for rip-sawing wood in the unseasoned state as performed in sawmilling operations. These saw tips were CVD-coated with $\text{Al}_2\text{O}_3\text{-TiO}_2$ to obtain self-sharpening characteristics of the tool [67]. This requires that the abrasive and erosive/corrosive wear resistance of the coating be synchronized with the wear resistance and microstructure of the substrate so that a cutting edge can be produced that maintains a sharply pointed profile, i.e. that is self-sharpening. As shown in Fig. 6-14 this is achieved by coating 60WC40Co tips (E) with alumina/titania on the rake face (rake angle 30° , clearance angle 7°). This materials system maintains a reasonable cutting edge during most of the cutting period for up to 60 km of cutting path since the wear-induced retreat of the surface of the coating and that of the substrate roughly coincide. The species cut was unseasoned Western Red Cedar (*Thuja plicata* Donn) of British Columbia, Canada, and the numbers next to the wear profiles indicate km of cutting path. At this point, a self-sharpening behavior up to 60 km is not sufficient for industrial application that require a minimum cutting path of 200 km between mechanical sharpening operations. This approach will become economically competitive to current technology only if a modified substrate material could be designed that ensures such high cutting paths.

Recently, alumina and alumina/zirconia (4:1) coatings have been used for oxida-

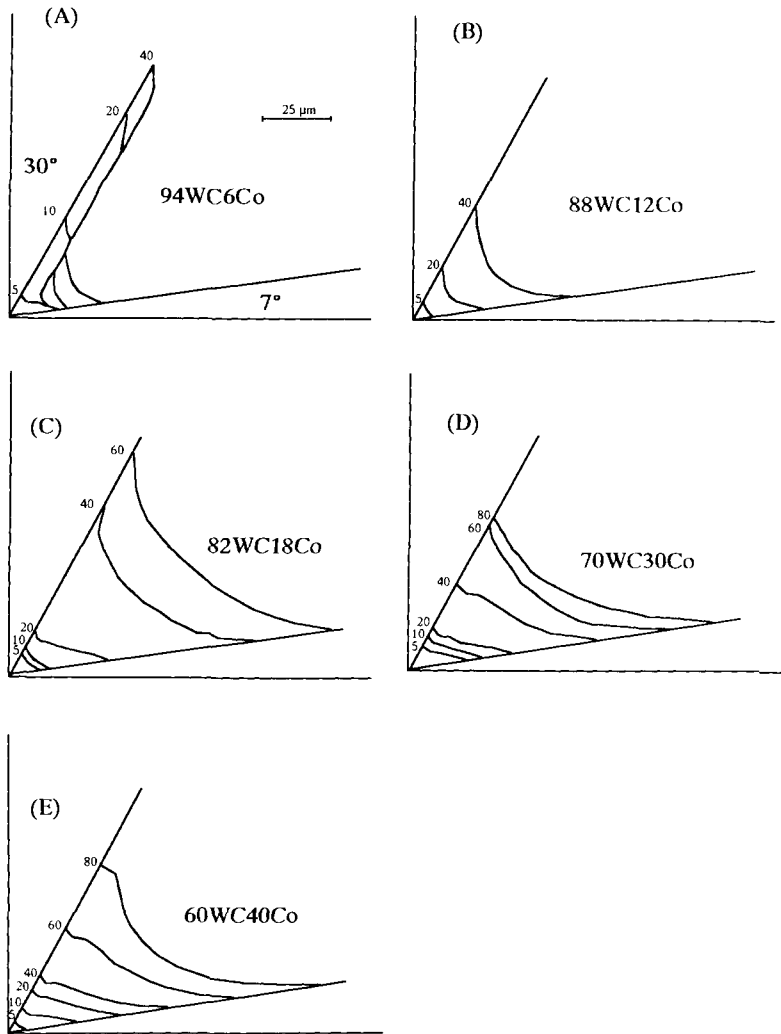


Figure 6-14. Self-sharpening wear behavior of WC-Co-tipped saw teeth coated with alumina/titania. The numbers refer to kilometers of cutting path [67].

tion protection of RSiC kiln aids used in fast firing of China ware. Vacuum plasma-sprayed alumina/zirconia coatings of 400 μm thickness performed best: the RSiC material showed an SiO₂ content of less than 2% after exposure to an O₂/N₂ (1:1) gas mixture for 2 500 h [68].

6.1.3.2 Chromia-based Coatings

Chromia coatings are being applied when corrosion resistance is required in addition to abrasion resistance, i.e. in the case of strongly synergistic corrabrasion. Such

coatings adhere very well to most metal substrate surfaces and show exceptional hardness of 2 300 HV_{0.05} [69]. Applications abound in chemical industry as coatings of joints in movable parts, in water pumps, steel rollers for ore classification, and smooth top coats for printing rolls [70]. Chromia coatings are also gas tight as shown by the occurrence of protective oxide films against sulfidation and carburization on high chromium steel and alloys at high temperatures [71]. While during APS operations only the di-trigonal α -modification (corundum structure) occurs, at reduced pressure Cr₂O₃ decomposes forming metallic chromium as well as a metastable Cr₃O₄ phase [69].

Chromia coatings perform particularly well in ship and stationary diesel engines where a corrosive environment is created by the use of less expensive but lower quality diesel fuel [72]. Serious corrosion occurs through the impurities of the fuel such as sulfur, vanadium, sodium, etc. Erosion is also of concern because catalytic cracking of fuel precursors introduces Al₂O₃-SiO₂ particles into the diesel fuel. Thus chromia coatings are required, for example to protect valve stems of diesel engines from wear and corrosion. Such coatings must be optimized for good adherence (>40 MPa) and maximum fracture toughness. Better coating quality can be obtained by HVOF spraying [73]. Here microhardnesses can be routinely achieved exceeding 2000 HV and a porosity of less than 1%.

Friction coatings on braking units of transportation machines have been suggested that consist of plasma-sprayed 60%Cr₂O₃ + 40%TiO₂ coatings with a very high friction coefficient of 0.8 and a porosity <3.5% [74].

6.1.4 Metallic Coatings

Metallic coatings are, in general, easy to apply to other base metal surfaces by a variety of thermal spray techniques, usually flame- and HVOF-spraying. However, refractory metals with very high melting points such as W, Mo, Ti, Cr, Nb, or Ta, and superalloys such as Inconel, Hastelloy and NiCoCrAlY-type alloys require APS- or VPS-plasma spray techniques.

6.1.4.1 Refractory Metal Coatings

Problems with Mo and W wear- and corrosion-resistant coatings occur because of the pronounced tendency of the molten metals to absorb gases during the spraying process [58]. For example, liquid molybdenum exposed to air at about 2730 °C absorbs approximately 13 wt.% oxygen [75]. Oxygen will be entrained from the surrounding air into a turbulent argon plasma jet and will react with the molten Mo particles forming MoO₂ that segregates during solidification along the grain boundaries of the splats. Thus VPS technology has been used to deposit Mo and W coatings [76–80]. Mo coatings show very good adhesion to steel substrates presumably due to the formation of a thin metallurgically bonded Fe–Mo alloy at very high contact temperatures [81]. However, with proper spray parameter optimization using statistical experimental design methodology it appears to be feasible to use APS technology [82] (see Sec. 8.4.2).

Nb/Hf and Ta plasma-sprayed coatings are being applied by VPS technology to the interior surface of advanced gun barrels because of their high temperature strength, creep resistance and toughness [83]. Addition of 15 vol% TiC increased the ultimate tensile strength (UTS) of 89Nb10Hf1Ti alloy from 469 MPa for the nonreinforced material to 523 MPa at room temperature. However, addition of 45 vol% TiC to 90Ta10W reduced the UTS from 606 MPa for the nonreinforced material to 284 MPa at room temperature. The UTS values at 1093 °C (2000 °F) were 209 MPa (89Nb10Hf1Ti) and 197 MPa (89Nb10Hf1Ti + 15 vol% TiC) and 191 MPa (90Ta10W) and 156 MPa (90Ta10W + 45 vol% TiC), respectively.

Ti and Ta plasma-sprayed coatings require VPS technology since at high temperatures considerable amounts of oxygen and nitrogen can be interstitially absorbed that compromise the properties of the coatings [84, 85]. With VPS, dense (<1% porosity), well adhering (72 MPa for 92.5Ti5Al2.5Fe) titanium coatings could be produced [85].

Cr- and Cr-based coatings are used to protect waterwall tubes in boilers in paper, power, and chemical process industries. Plasma-sprayed high chromium–nickel–titanium alloy (TAFALLOY 45CT) coatings were developed to combat degradation by chemical corrosion and erosion of unprotected waterwall tubes made from carbon steel in steam generating boilers [86]. Thick Cr coatings on copper substrates were developed as PVD sputter targets [87].

6.1.4.2 Superalloy Coatings

So-called superalloys are nickel-based γ' -phase precipitation hardened alloys of nickel aluminide, 'NiCoCrAlY' alloys and even more complex high-nickel alloys with additions of Cr, Co, Mo, W, Ti, Nb, B, Zr, and C [88]. They show excellent high temperature-corrosion resistance, and are predominantly applied to gas turbine engine blades and vanes. One of the main advantages of such overlay coatings is their inherent compositional flexibility that permits tailoring of the coating composition for both oxidation resistance and coating substrate compatibility [89]. This compositional flexibility allows the addition of active elements such as yttrium that improves the adherence of the oxide scale during in-service thermal cycling [90]. Currently, two competing techniques are used for applying NiCoCrAlY overlay coatings: electron-beam physical vapor deposition (EB-PVD) and low-pressure plasma spraying (LPPS, VPS). Increasingly, plasma-spraying becomes economically more attractive owing to advantages such as lower cost, tighter compositional control, and greater process flexibility.

One of the most important properties to be optimized is the low cycle fatigue (LCF) [91], and stress rupture and creep [92] behavior of plasma-sprayed NiCoCrAlY coatings. The coatings can significantly affect the mechanical superalloy component, for example oriented single-crystalline PWA 1460. The higher ductility of the coating compared to the diffusion aluminide coatings (see Fig. 1-5) is beneficial to the thermomechanical fatigue life of the coated superalloy component. However, at higher temperature the coatings are significantly weaker than the superalloy substrate and are thus considered to be non-load-bearing [92]. The LCF and creep

behavior is essentially connected with the complex microstructure of plasma-sprayed overlay coatings. The fine grained two-phase microstructure consists of a NiAl-phase (β) and a Ni-rich solid solution (γ). This γ -phase contains extremely fine-grained Ni_3Al (γ') precipitates [93]. A recent study [94] dealt with the precipitation and transformation kinetics of the structurally reinforcing γ' -phase. According to this transmission electron microscopy work, in an as-sprayed coating γ' - and β -phase were detected whereby the spherical γ' -phase was surrounded by β -phase. It was therefore concluded that the γ' -phase crystallized primarily from the liquid, and subsequently the β -phase during solidification of the plasma-sprayed splats. During heat treatment at 1273 K for 4 h to homogenize the coating, most of the γ' -phase was transformed into γ -phase by solid state diffusion of Co and Cr from the β - to the γ' -phase. This results in a decrease in microhardness and low cycle fatigue strength. In aged coatings at 873 and 973 K the γ' -phase was reformed and α -Co precipitates were observed in the β -phase. The reverse diffusion of Co to the β -phase from the γ -phase might contribute to ordering transition from the γ -phase to the γ' -phase. This is accompanied by a hardening process of the aged coating. In conclusion, to retain the hardness, and LCF and creep resistance of the NiCoCrAlY coatings in service, elements should be added that stabilize the γ' -phase such as Ti, V, W, Ta, or Mo. This sequence explains the observations by Gayda *et al.* [91] that NiCoCrAlY coatings show significant softening in LCF runs at 650 °C but show improved fatigue life and cyclic hardening at 1050 °C that may be related to a slower transgranular crack growth rate due to precipitation-hardening by the reformed γ' -phase.

In addition to LCF- and creep-resistant coatings NiCoCrAlY is also being used extensively as a bond coat or graded intermediate layer for partially-stabilized zirconia (PSZ) thermal barrier top coatings (TBCs) (see 6.2). In these applications it has a two-fold function. First, it provides a gradient of the coefficient of thermal expansion (CTE), i.e. it bridges the gap between the CTE of the Inconel or Hastelloy superalloy structure and that of the PSZ. Secondly, it protects the superalloy from hot corrosive gases penetrating the porous PSZ coating.

6.1.5 Diamond Coatings

The overwhelming majority of industrial thin diamond films and coatings is being produced by CVD, plasma-assisted CVD (PA-CVD), ion beam deposition, and excimer laser ablation techniques [95, 96]. Work in this area is directed towards electronic high-temperature devices, high-power switches, blue light-emitting diodes, radiation-hardened electronics, and ultra-wear-resistant overlays. While qualitatively superior diamond films could be grown with these well-established techniques, their pitifully low deposition rates of the order of only a few μm per h precluded any large scale industrial applications. This changed with the invention of a d.c. plasma jet process (DIA-JET) by Fujitsu Laboratories [97]. The method relies on argon as a plasma gas, and a reactive mixture of 5–20 l min^{-1} of hydrogen and 0.01–0.2 l min^{-1} of methane. Deposition rates were as high as 0.25 mm h^{-1} , and values exceeding 1 mm h^{-1} have been reported [96]. The short distance between nozzle and substrate

(<20 mm) requires very effective cooling of the substrate since temperatures exceeding 1300 °C lead to graphite deposition. Here lies one of the major shortcomings of the technique: the high substrate temperature does not allow for the use of steel since instead of diamond carbides will be deposited. This limitation can be somewhat overcome by an intermediate inert molybdenum or tungsten bond coat. However, diamond films on tungsten-coated steel show rather weak adhesion strength [98]. While silicon, alumina and vitreous silica substrate have been coated in the past [99], modern work was concerned with developing ultra wear-resistant coatings for WC/Co [98, 100, 101] and silicon nitride cutting tools [101] and silicon carbide ceramics [102].

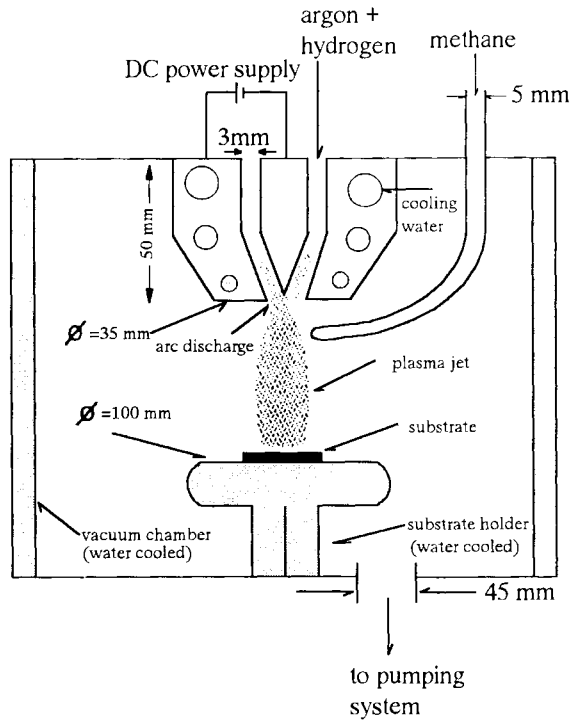
At relatively high methane concentrations the polycrystalline diamond coatings show cube-shaped crystals whereas low methane concentrations show octahedral crystals. The crystal morphology is also a function of the deposition temperature: {111} morphology is typical for low substrate temperatures (700 °C), {100} morphology appears at higher temperatures (1100 °C) [103].

The mechanism behind the process is still somewhat elusive. It is thought that the source gas dissociates in the high temperature plasma jet and forms activated atoms, ions and radicals such as H, CH, C₂H*, CH₃⁺, or CH₃*. Thermodynamic self-cooling occurs in the plasma jet when it exits the nozzle at very high speed. This process is augmented by entrainment of eddies of external cold gas that break up the potential core of the plasma jet, thereby shifting the initially laminar into a turbulent flow regime (Fig. 3-29). This will further reduce the mean temperature and, to a certain extent, the velocity of the jet. Thus the plasma enters a nonequilibrium state with an abundance of activated radicals remaining in the jet which transports them quickly to the substrate surface before they can recombine.

Figure 6-15 shows a typical setup of a d.c. plasma jet-CVD process [98]. With such an apparatus optimized fine-grained diamond coatings could be produced with a high deposition rate at a substrate temperature of about 1000 °C, chamber pressure of 300 mbar, CH₄/H₂ ratios of less than 5%, and stand-off distance of 70 mm. Best results in terms of coating density were reached with surface roughness values of 0.25 μm [100].

Quick and easy production of medium quality diamond films has been reported using a simple oxyacetylene welding torch [104, 105] in which acetylene provides both the carbon source and a high hydrogen flux. Calculations of the sticking probability of various species occurring in a thermal plasma, fed by methane and hydrogen, showed that gas-phase precursors to diamond are acetylene or acetylene-like radicals [106]. A sticking probability of 10⁻³ for acetylene gives calculated growth rates that compare favorably with experimental growth rates found by Kurihara *et al.* [97] and Matsumoto [103]. Acetylene-like radicals provide for much increased diamond growth rates in d.c. plasma jet deposition but for poorer quality films [107] compared with CH₃ radicals whose gas phase concentration is thought to be the rate-determining step in a typical slow CVD process. On the other hand there is a suggestion that the high growth rates in a d.c. plasma jet are related to high gas phase temperatures. Diamond growth species, whatever their nature might be, may be very effectively produced in 'hot spots', and subsequently rapidly quenched to temperatures below 1 000 °C on the substrate.

Figure 6-15. Typical setup of a d.c. plasma jet-CVD reactor to deposit diamond films [98].



6.2 Thermal and Chemical Barrier Coatings

6.2.1 Yttria-Partially Stabilized Zirconia Coatings (Y-PSZ)

Development and improvement of thermal barrier coatings based on partially-stabilized zirconia (PSZ) are carried on in two main areas.

The first area relates to the aerospace industry and is concerned with coating of austenitic superalloy blades and vanes of gas turbine engines, combustor cans and turbine shrouds. These efforts provide an excellent example of the sophistication now reached by ceramic coatings. Such coatings increase the lifetime of components subjected to a variety of degrading processes. As shown in Fig. 6-16, the lifetime of an uncoated superalloy turbine component part is limited by mechanical fatigue at temperatures below 800 °C, by hot corrosion between 800 and 900 °C, and by thermal fatigue between 900 and 1 050 °C. Above that temperature, oxidation and creep are life controlling [108]. Thermal barrier coatings fulfill a vital function by increasing turbine blade cooling efficiency, and in conjunction with MCrAlY (M = Ni, Co, Fe) (see Sec. 6.1.4.2) bond coats, prevent hot corrosion of the superalloy by molten salts and corrosive gases. It is thus said that a modern jetliner would not make a single transatlantic flight, but for the coatings [109].

The second area of application is as a potential material for inclusion in recip-

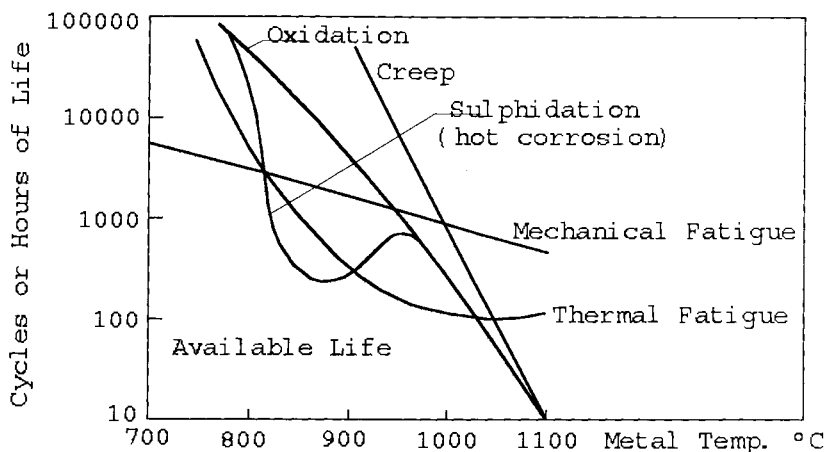
Factors Influencing Turbine Component Life

Figure 6-16. Factors influencing the lifetime of gas turbine components [108].

roccating internal combustion engines, principally diesel engines. The goals are to insulate components such as pistons, valves, intake and exhaust ports, and to protect moving parts from wear and corrosion. The quest for increasing fuel economy and decreasing levels of hydrocarbons in exhaust gases necessitates an increase in combustion temperatures. Recently, a joint venture between Adiabatic Inc. and the USA army has been carried out to develop thick TBCs and other ceramic wear coatings for a military adiabatic diesel engine. The thick (0.75 mm) zirconia-based TBC (called 'TTBC') was applied to the recess in the combustion face, to the intake and exhaust ports, and to the piston combustion bowl. The intermediate piston rings were coated with alumina-titania wear ceramic, and the cylinder liner with a proprietary tribological coating. Fuel economy improved from 16 to 37%, and the engine has survived a 400 h durability test with very low lubricating oil consumption.

Currently 90% of produced zirconia precursor powders are used for gas turbine applications, but this market segment is estimated to decrease to 40% by the year 2000, whereas diesel engine applications will increase from today's 2% to 40% at the turn of the century [99]. Figure 6-17 shows a NASA scenario of development trends in in-service temperatures of gas turbines for aerospace applications. The first step in the development cycle has been already reached by increasing the turbine blade surface temperatures to 1 100 °C. The second, visionary step, requires the development of completely new ceramic structural materials and systems that can withstand surface temperatures of up to 1 400 °C required to burn the fuel with considerably higher efficiency with concurrent reduction in polluting gases. Bridging these two steps is the current coating technology that reaches its temperature limit at approximately 1 200 °C [110].

Thick thermal barrier coatings (TTBCs) satisfy requirements of thermal efficiency

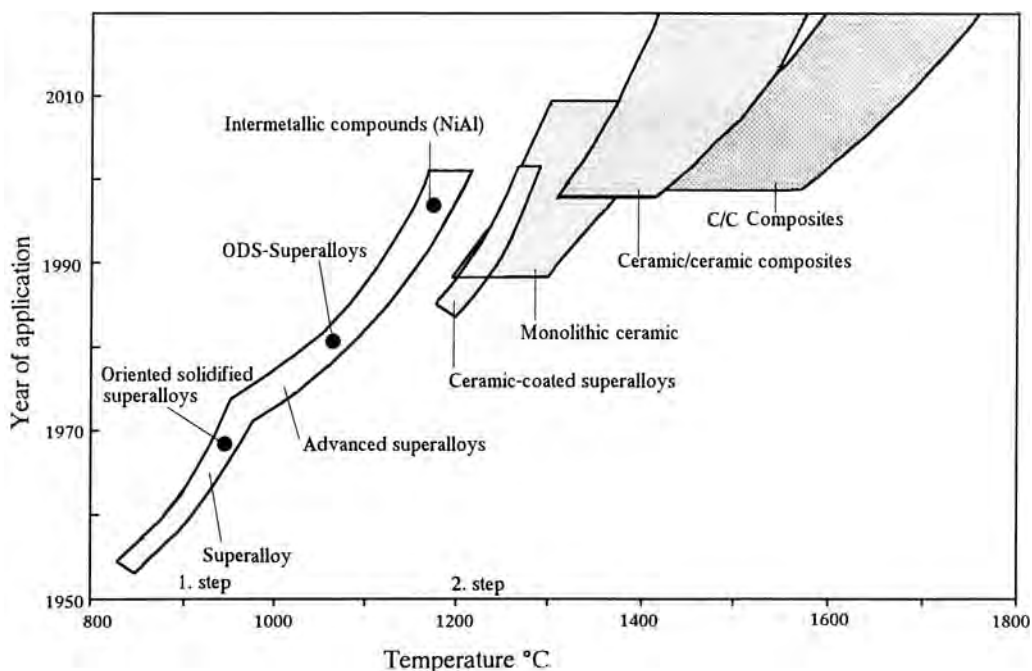


Figure 6-17. NASA scenario of development trends in in-service temperatures of aerospace gas turbines [110].

but pose problems with residual stresses that are maximized in such thick coatings (Fig. 6-18). Therefore, optimization of the ceramic material has been performed in two areas: *chemical modifications* and *microstructural modifications* [111].

As a result of *chemical modification*, the lifetime of a TBC has been maximized by varying the yttria content in zirconia. An yttria concentration of 6–8 wt. % coincides with the maximum amount of a nonequilibrium ‘non-transformable’ tetragonal zirconia polymorph (t'-zirconia).

State-of-the-art technology consists of applying zirconia coatings, partially stabilized with 7–8 wt. % yttria, over a metallic bond coat of Ni- or CoCrAlY alloy. The bond coat must be applied by VPS technology to prevent formation of alumina scale that is thought to reduce adhesion strength to the superalloy substrate. The PSZ top layer is generally being sprayed in the APS mode since VPS experiments have shown that in this case the PSZ layer develops Young's moduli three times larger than those observed in APS coatings [112]. Because of this larger modulus thermal stresses are expected to be generated in VPS-PSZ coatings. Figure 6-19 shows the phase relationships of the binary system $\text{ZrO}_2\text{-Y}_2\text{O}_3$ with several compositions whose grain sizes of the t-phase, bending strengths and fracture toughnesses are displayed. In general, fracture toughness increases with decreasing amount of yttria, whereas the thermal stability increases with increasing yttria content. This requires trade-offs depending on the application of the material. For 8 wt. % (2.65 mol %) yttria the phase

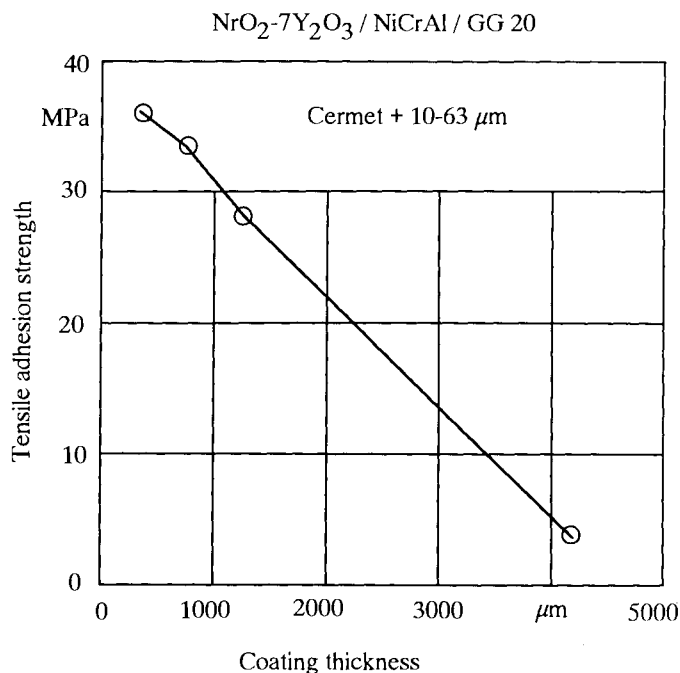


Figure 6-18. Dependence of the adhesion strength of an Y-PSZ-TBC coating on the coating thickness [132].

assembly at ambient temperature should consist of a mixture of cubic and monoclinic zirconia (Fig. 6-19). However, extensive X-ray diffraction work on as-sprayed coatings have shown a tetragonal phase and only a small amount of monoclinic phase [113–116]. This tetragonal (t') phase does not transform to the monoclinic (m) phase because of the rapid splat cooling during plasma spraying. It is a tetragonal solid solution with high yttria content that on annealing at high temperatures (1300 °C) transforms slowly by a diffusion-controlled mechanism to equilibrium tetragonal (t) zirconia with low yttria content, and cubic (c) zirconia [117].

A second aspect of chemical modification concerns the replacement of the stabilizing yttria by other elements. Work in this area has been rather scarce. Using ceria instead of yttria, the microhardness and crack resistance could be markedly improved for a PSZ stabilized with 15 mol % CeO_2 [118].

The *microstructural modifications* relate to porosity control. Porosity and microcrack distribution impart to the material a tolerance to thermal and residual stresses. Thus the lifetime of a TBC is sensitive to density variations that can be controlled by proper adjustment of the plasma spray parameters by statistical experimental design methodology.

Not surprisingly, most modern developments in the field of TBCs are carried out by manufacturers of aerospace gas turbine engines, i.e. Rolls-Royce [119, 120], General Electric [121, 122], NASA [123–126] and Pratt & Whitney [127] but also by plasma spray equipment manufacturers [128, 129] and superalloy suppliers [130].

The future performance profile of TBCs will include improved thermal barrier function, oxidation resistance as well as corrosion- and erosion resistance. With im-

Improved thermal stability
by a Y_2O_3 -rich coating

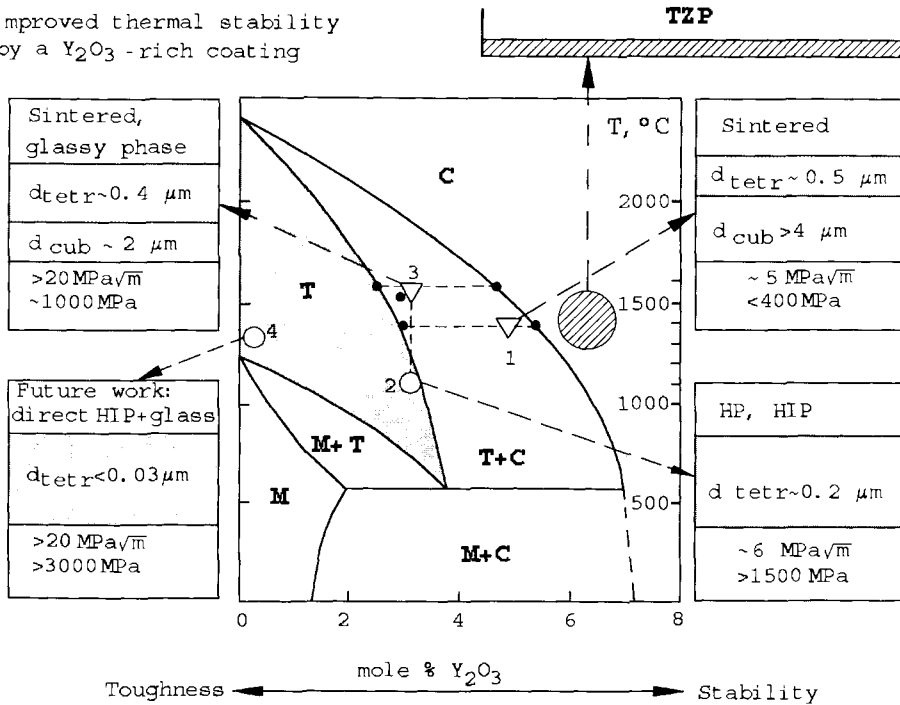


Figure 6-19. Phase relationship of the binary system ZrO_2 - Y_2O_3 . Different compositions for different applications are indicated (TZP: tetragonal zirconia polycrystal).

proved TBCs, economic and environmental requirements will be addressed such as higher combustion temperatures resulting in better fuel efficiency, lower cooling air requirements and hence higher compressor effectivity, and lower thermal stresses on materials that result in longer service life and maintenance cycles. There are, however, problems with TBCs that manifest themselves in increased spalling and chipping at higher operational temperatures and times. This is caused by higher residual stresses in the coatings, bond coat oxidation as well as volume changes induced by phase transformations. Here improvements are urgently needed to attain performance levels anticipated by NASA [110] for airborne gas turbines (10 000 h at turbine blade surface temperatures up to 1 400 °C), stationary gas turbines (25 000 h at up to 1 000 °C) and large stationary diesel engines (5 000 h at cycling loads).

6.2.1.1 Stress Control and Modeling

Since coated turbine section parts are subject to steep temperature gradients, high thermal shock resistance of the metallic bond coat/ceramic top coat is generally required. However, residual stresses in the as-sprayed PSZ coating arising from the difference in the CTE between the Inconel 617 substrate (CTE = 16 p.p.m. at 850 °C) and the 7% yttria-PSZ coating (CTE = 10 p.p.m. at 850 °C) decrease the thermal

Distribution of Residual Stresses In a Zirconia Coating

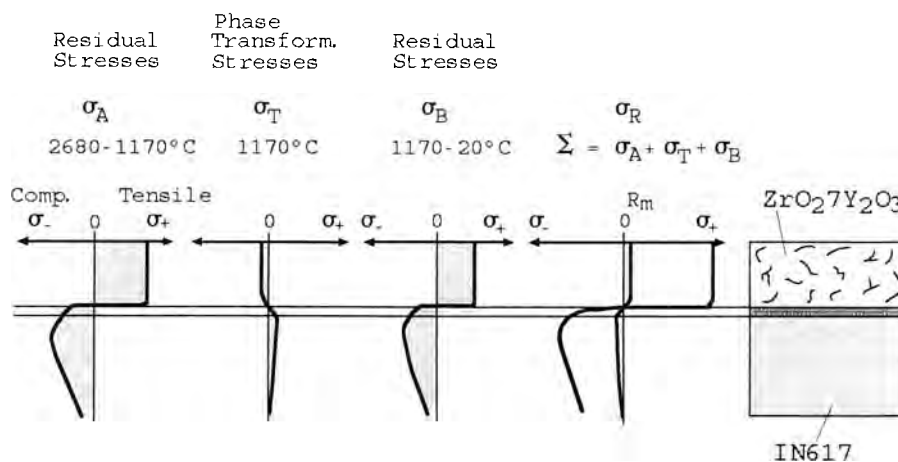


Figure 6-20. Modeling of the distribution of residual stresses in an Y-PSZ coating [131].

shock resistance, and thus the life expectancy of the TBC. Figure 6-20 shows how, in PSZ, strong shrinkage by cooling from the melting temperature at 2680 °C to the temperature of the martensitic tetragonal–monoclinic phase transition at 1170 °C introduces large tensile stresses in the coating [131]. The phase transition in PSZ with approximately 8% of monoclinic phase increases the volume only slightly, and thus adds some compressive component that, however, is too small to offset the strong tensile stresses introduced. Further temperature decrease to room temperature again introduces shrinkage, i.e. tensile stresses in the ceramics. Since the added-up tensile stresses exceed the yield strength of the material many times over, stress relief occurs through microcracking and/or delamination.

The NiCrAlY bond coat provides a good mechanical bond between the substrate and the ceramic coating, and also oxidation and hot corrosion (sulfidation) resistance for the substrate. Due to the routinely applied grit-blasting procedure before plasma spraying, the interface between the metal substrate and the coating is rough, and can be modeled as a quasi-sinusoidal surface. Finite element analyses [124] have shown that compressive axial and hoop stresses are located in the valleys of the quasi-sinusoidal surfaces but tensile radial stresses at the peaks of the asperities (Fig. 6-21(i)). Thus, a microcrack originating at the point of maximum tensile loading (Fig. 6-21(ii)) will be arrested once it enters a region of compression.

It has been amply confirmed that the key failure mechanism of TBCs is bond coat oxidation [111]. If the NiCoCrAlY bond coat is oxidized by penetration through the porous PSZ layer of hot corrosive gases, the signs of the axial and radial stresses are reversed (Fig. 6-22(iii)). As a result, crack extension can occur from the region of the peaks, now under compression, into the region of the valley, now under ten-

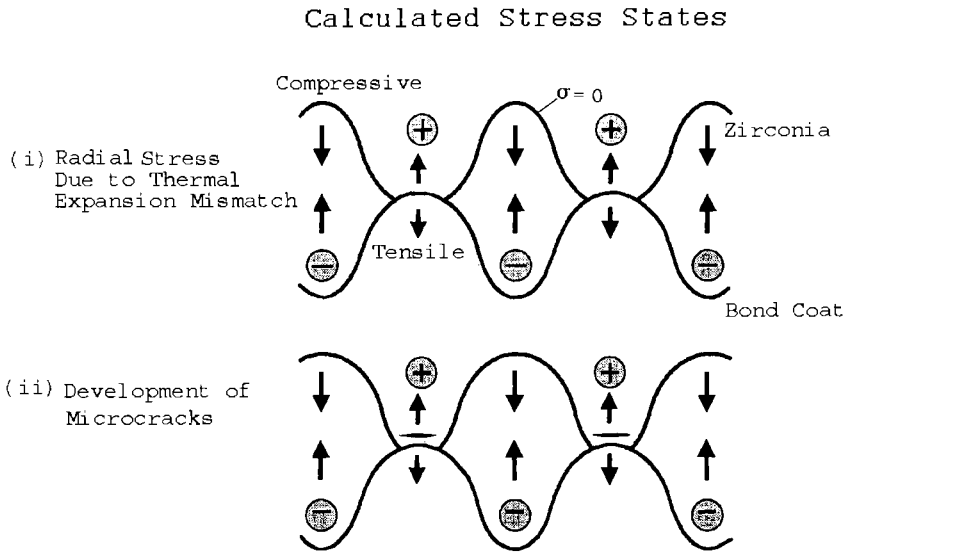


Figure 6-21. Calculated stress states in a PSZ-bond coat system with sinusoidally modeled interface [124].

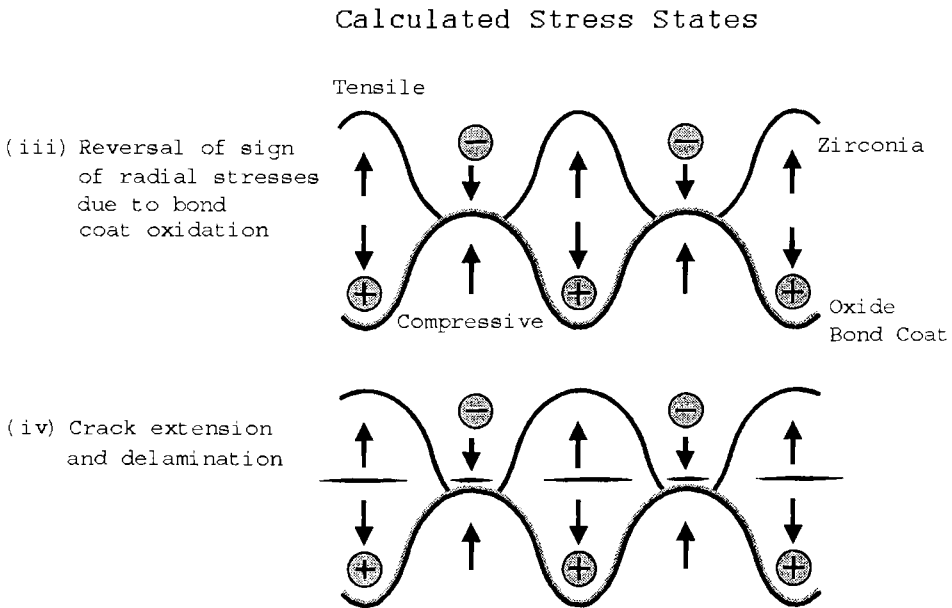


Figure 6-22. As Fig. 6-21 but with stress sign reversal due to bond coat oxidation [124].

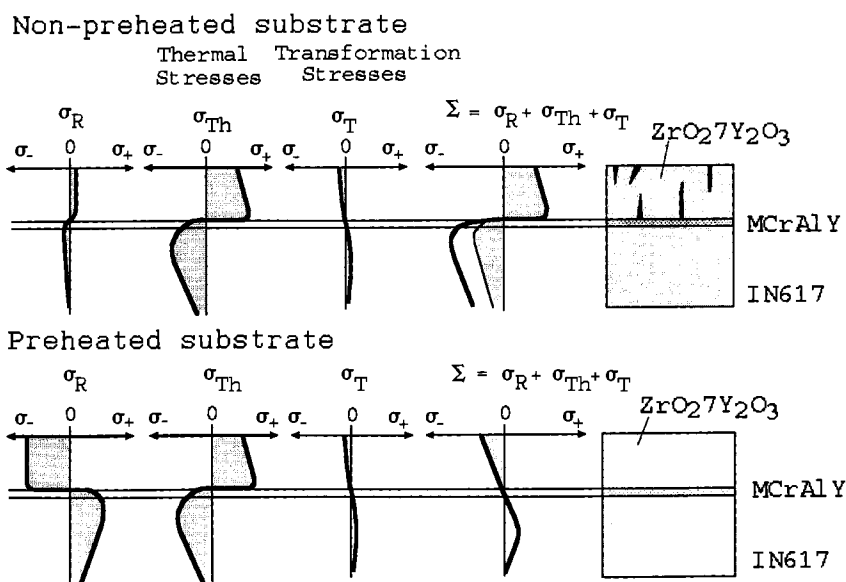


Figure 6-23. Distribution of residual stresses in Y-PSZ coatings on nonpreheated and preheated substrates [131].

sion. Hence, complete delamination or exfoliation will eventually take place (Fig. 6-22(iv)) [124].

Tackling the problem of cracking involves two aspects: Controlling the residual tensile stresses in the coating, and preventing bond coat oxidation. The first task involves the, at least theoretical, possibility of reversing the stresses in the ceramic layer on an Inconel 617 substrate from tensile to compressive by substrate preheating. Figure 6-23 shows the stress distribution during thermal shock testing of non-preheated (top) and preheated (bottom) substrates [131]. The preheating of the IN 617 substrate induces large compressive stresses in the coating that should offset the tensile stresses occurring during cooling. As a result, a slight compressive stress component remains at room temperature thus producing a crack-free coating. However, coatings cannot be treated as a continuum bulk ceramics but are built up layer by layer in several traverses of the plasma jet. Thus every new layer acts as a heat treatment for the previously deposited one, and heat flow from the substrate decreases. It should be emphasized that this dynamic scheme of *in situ* annealing leads to a degrading of the coating, and thus largely foils any attempt to model its complete thermal history by finite element analysis. Work in this area [124] was based on the assumption of homogeneous, isotropic and linearly elastic behavior of the PSZ layer, the bond coat, and the substrate. The modulus of elasticity was assumed to be constant and time-invariant, whereas in reality it is a strong function of the porosity of the coating (Fig. 6-24, [132]). The porosity of the coatings will also affect the value of the thermal conductivity: a small change from 1.00 to $0.75 \text{ W m}^{-1} \text{ }^{\circ}\text{C}^{-1}$ can shift the residual stress from overall compressive to overall tensile [133].

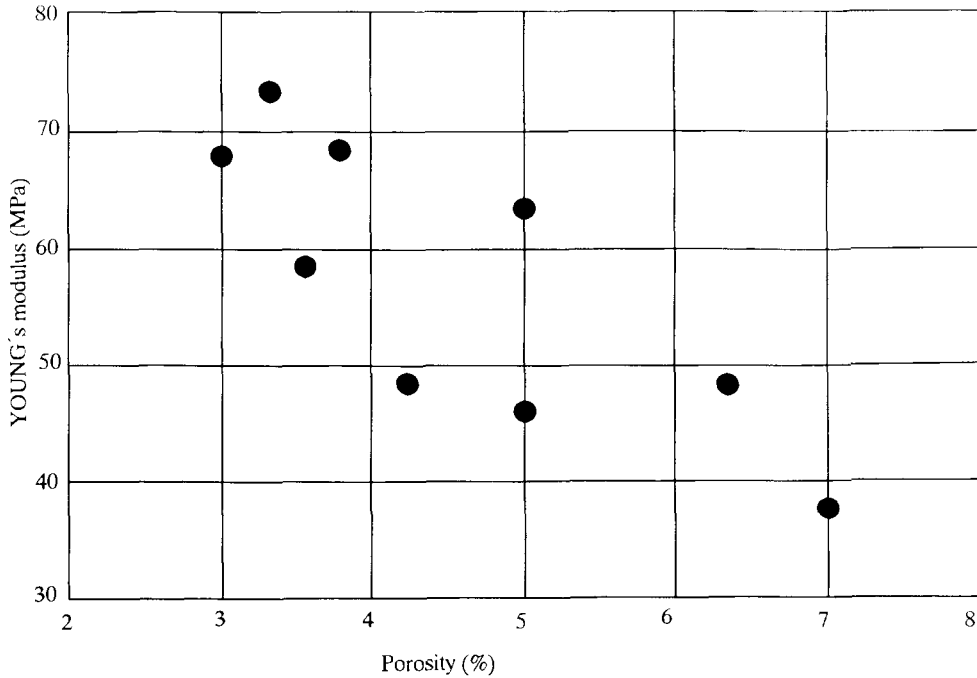


Figure 6-24. Modulus of elasticity as a function of coating porosity in Y-PSZ coatings [132].

A rough estimation of the preheating temperature required to alleviate residual tensile coating stresses can be obtained from Eq. (5-53) that determines the critical temperature difference ΔT_c between the lowest temperature of plastic flow and the preheating temperature:

$$\Delta T_c = \sigma(1 - \nu)/E\alpha \quad (6-3)$$

with $\sigma = 600$ MPa, $\nu = 0.26$, $E = 200$ GPa, and $\alpha = 10^{-5} \text{ mm}^{-1} \text{ }^\circ\text{C}^{-1}$. With these values, $\Delta T_c = 533$ K, i.e. if the critical temperature difference between the lowest temperature of plastic flow (Nabarro–Herring creep) and the preheating temperature is less than 260°C , then there is no microcracking. The Nabarro–Herring creep limit is approximately $0.6 T_m = 0.6 \times 3133 \text{ K} = 1880 \text{ K}$. Thus the minimum preheating temperature becomes $T_p = 1880 - 533 = 1347 \text{ K}$! For a finite quench rate, the Biot modulus is $\text{Bi} = dh/k$, where d = thickness of the ceramic layer, $h = c_p \times a \times \rho/d = 3.3 \times 10^4 \text{ J s}^{-1} \text{ m}^{-2} \text{ K}^{-1}$, and $k = 1.0 \text{ J s}^{-1} \text{ m}^{-1} \text{ K}^{-1}$. Thus $\text{Bi} = 1.16$, $\Delta T_c = 533[\text{K}] \times 1.16 = 618 \text{ K}$; $T_p = 1262 \text{ K}$! Therefore, the minimum preheating temperature required to alleviate microcracking is close to the range of the melting temperature of the Ni-based superalloy. This is to be expected since stress relief in ceramic coatings generally requires very high temperatures owing to the non dislocation-type mechanism of lattice rearrangement.

6.2.1.2 Sealing of As-sprayed Surfaces

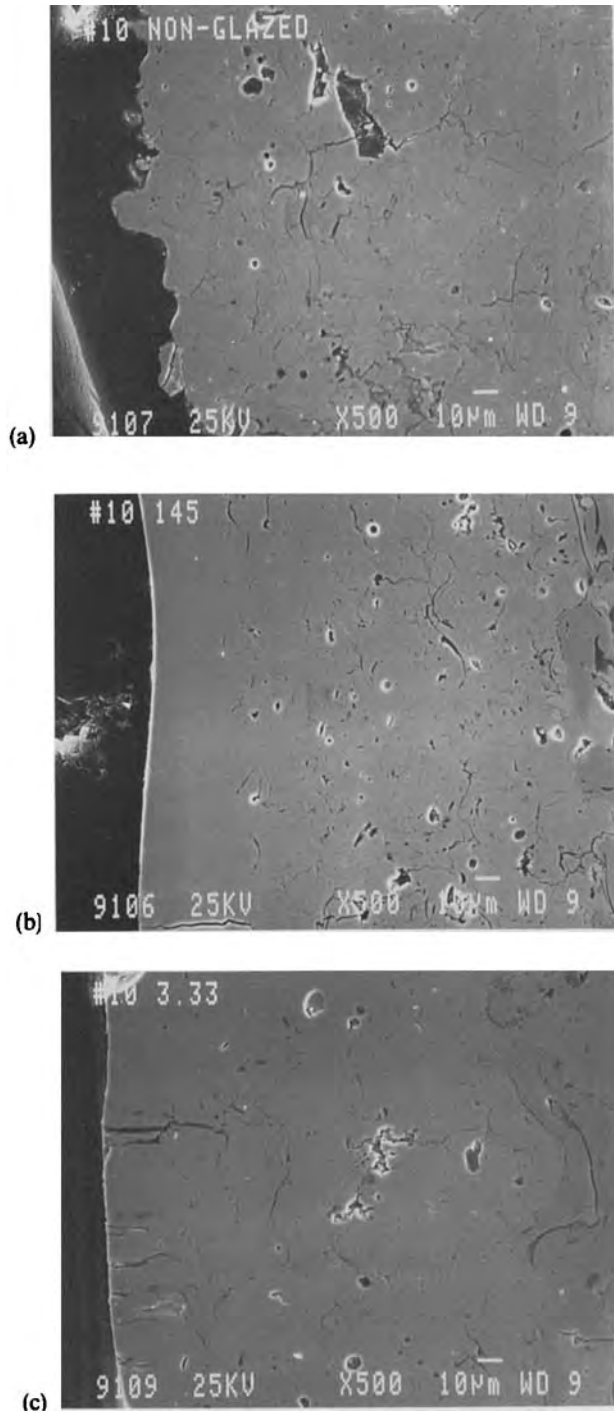
To prevent bond coat oxidation, sealing the surface of the porous PSZ coating can be performed in several ways.

- Spraying of the bond coat under vacuum or low-pressure inert gas conditions prevents *a priori* oxidation, and thus increases drastically the number of cycles-to-failure as compared with air plasma spraying.
- Through infiltration of the PSZ coating with hot corrosion-resistant material such as nickel aluminide or CVD-SiC, effective sealing can be achieved.
- Reduction of surface porosity by plasma-spraying a final top layer of very fine zirconia.
- Treatment of plasma-sprayed PSZ with a 0.1 mm slurry layer that is subsequently densified by a heat treatment.
- Control of porosity with adjusted powder morphology.
- Addition of Si to the MCrAlY bond coat to improve its oxidation/corrosion resistance.
- Plasma-spraying of low yttria PSZ whose expansion during the martensitic t-m transition offsets the thermal contraction.
- Laser surface remelting ('laser glazing').
- Reactive laser treatment with alumina and silica to produce dense, low melting eutectic compositions.
- Hot isostatic pressing.

6.2.1.3 Laser Surface Remelting of Y-PSZ Coatings

Laser glazing provides a smooth, dense top layer but tends to introduce cracks owing to nonuniform cooling after the point-like introduction of heat through the focused laser beam. Figure 6-25a–c shows scanning electron micrographs of plasma-sprayed Y-PSZ (Plasmalloy grade AI-1075)/NiCoCrAlY (Plasmalloy grade AI-1065-2; right border) 'tandem' plasma-sprayed with an argon/helium plasma jet at an arc current of 800 A (NiCoCrAlY) and 900 A (Y-PSZ), respectively. Figure 6-25a shows the as-sprayed TBC with a typically rough and detailed surface, large pores close to the surface as well as a network of radial (transverse) and layer-parallel (longitudinal) microcracks. Laser treatment was performed with a Mitsubishi CO₂-CW laser with a power of 1 kW, a beam diameter of 3 mm, and a wavelength of 10.6 μm [134]. Figure 6-25b shows the result of laser glazing using a laser beam scanning speed of 23 cm s^{-1} that translates to a laser irradiance (energy density) of 1.45 J mm^{-2} . The surface is smooth and essentially free of pores down to a depth of 30–40 μm . Increasing the laser energy density to 3.33 J mm^{-2} (Fig. 6-25c) results in pronounced cracking. This, however, is not necessarily deleterious to the performance of the TBC since laser-induced *radial cracks* may increase the mechanical stability and the fracture toughness, respectively by a crack arresting mechanism thus leading to a strain-tolerant toughened ceramics. They also constitute sinks for thermal stresses introduced by the differences in the coefficients of thermal expansion. On the other hand, transverse cracks are oriented parallel to the heat flux,

Figure 6-25. SEM micrographs of as-sprayed (a) and laser-remelted (b: laser irradiance: 1.45 J mm^{-2} ; c: laser irradiance: 3.33 J mm^{-2}) Y-PSZ coatings [134].



and this results in a maximum value of the thermal diffusivity. Effective thermal diffusivity values a_{eff} are

$$a_{\text{eff}} = a_0(1 + 8Nb^3/3)^{-1} \text{ for cracks perpendicular to the heat flux} \quad (6-4a)$$

$$a_{\text{eff}} = a_0(1 + 8Nb^3/9)^{-1} \text{ for randomly oriented cracks} \quad (6-4b)$$

$$a_{\text{eff}} = a_0 \text{ for cracks parallel to the heat flux,} \quad (6-4c)$$

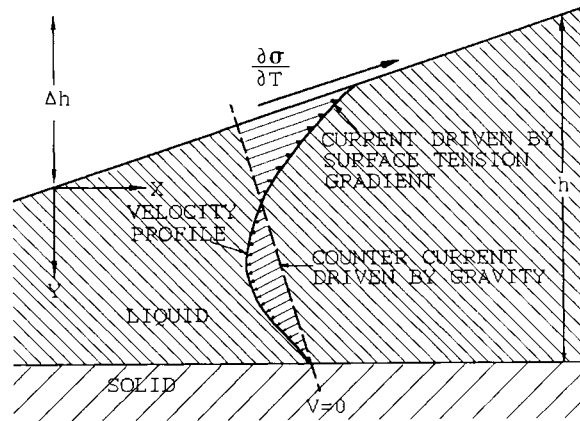
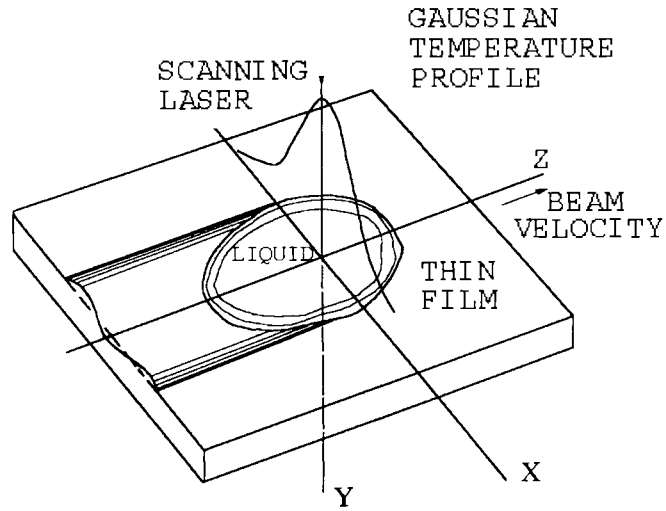
where a_0 = bulk thermal diffusivity, N = number of cracks, and b = f (crack radius). With increasing layer thickness, both radial and longitudinal cracks will be formed. Longitudinal cracks appear to delineate splat boundaries and are thus undesirable since they tend to increase the risk of delamination and exfoliation of the coatings. On the other hand, they also limit the transverse crack propagation. It was found that despite such cracking the lifetime of laser-densified coatings in corrosive thermally cycled burner rig tests can increase by a factor of three to ten, depending on the coating thickness [135]. A problem, however, exists since the surface cracks are known to act as nuclei for subsequent cavitation erosion damage [136].

It should be noted that the specific laser energy density required to melt a ceramic material is much lower than that needed to melt a metal. This can be related to the lower reflectivity and the lower thermal conductivity of ceramics compared to a typical metal. The Cline–Anthony model for a moving Gaussian laser beam to calculate the depth of the melt pool is not applicable [137] since the high scanning rate (15 to 30 cm s^{-1}) of the laser beam renders the temperature distribution asymmetric in the direction of the beam traverse. Figure 6-26 (top) shows the temperature profile that can be approximated by a Gaussian distribution, $T = T_0 \exp(-x^2/2R^2)$, where R = radius of the laser beam. Due to the low thermal conductivity of the material, the molten ceramic pool does not cool instantaneously, and a pronounced asymmetry develops. The figure shows also the onset of surface rippling associated with surface-tension gradients [138]. Also, in the ceramic layer under the center of the laser beam depressions develop (Fig. 6-27b). Their origin is related to such surface-tension gradients induced by a temperature difference between the center of the beam and the regions further away from it. In the center, the temperature of the melt is at its maximum and thus the surface tension at a minimum. As the temperature decreases away from the center, the surface tension increases. This pulls away the melt from the center thereby depressing the surface under the beam and raise the melt level at the periphery of the melt pool (surface ‘rippling’, Fig. 6-26, top). As the height difference increases, a pressure head develops that will eventually induce a gravity-driven counterflow (Fig. 6-26, bottom). At steady state, the liquid flow away from the beam center, driven by the surface-tension gradient, will be exactly balanced by the gravity-driven counterflow towards the beam center².

Increase of the laser irradiance from 0.34 (Fig. 6-27a) to 1.45 (Fig. 6-27b) to 3.33 J mm^{-2} (Fig. 6-27c) leads to more pronounced cracking. Also, as shown in Fig.

² This mechanism is identical to the mechanism responsible for the formation of wine ‘tears’ where a surface-tension gradient, produced by evaporation of alcohol, exerts a shear stress on the surface of the liquid that drags it up the sides of the wine glass.

Figure 6-26. Temperature profile of a scanning laser beam (top) and explanation of the onset of surface 'rippling' due to a strong gradient in surface tension (bottom) [138].



6-27b the depths of the laser-induced depressions increase with decreasing scanning speed (top to bottom). It is therefore mandatory to optimize the specific laser energy for sealing of coatings. Experiments have shown [139] that at high laser irradiance two solidification fronts exist in the laser-melted coating, one originating at the melt/substrate interface and one at the melt/air interface. The former is related to conductive heat losses, the latter to radiative heat losses. Which front will overtake the other depends on the laser power. Also, the appearance of the remelted layers are

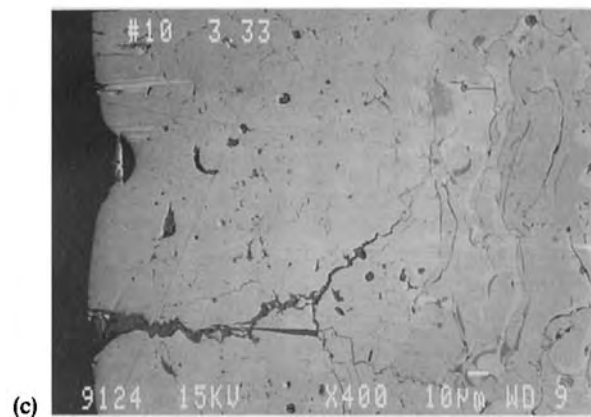
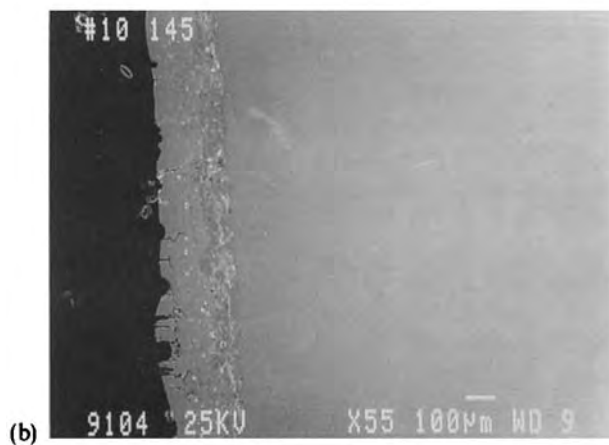
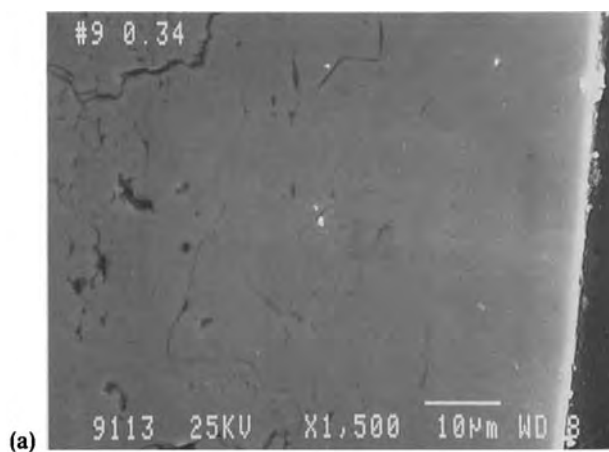


Figure 6-27. Increase of radial cracking with increasing laser irradiance (a: 0.34 J mm^{-2} , b: 1.45 J mm^{-2} , c: 3.33 J mm^{-2}) [134].

different: equiaxed grains in case of radiative heat loss, columnar grains in case of conductive heat loss.

Two other treatments have been explored with the objective to reduce coating cracking: pulsed laser sealing and reactive laser treatment. Experiments with *pulsed lasers* [140] revealed that although microcracking could be only slightly reduced the resulting coatings showed less depressions, smoother surfaces, and improved thermal shock resistance, particularly when laser-glazing was preceded by sample preheating. The extremely rapid solidification stabilizes the nontransformable tetragonal zirconia (t') phase [141]. The amount of the cubic equilibrium phase decreases. Non-transformable tetragonal zirconia contains a high amount of yttria in solid solution, and during laser remelting there is not enough time available to redistribute yttria by diffusion to form the equilibrium t -phase with low yttria content. On annealing such a laser remelted coating, the t' -phase transform indeed to $(t + c)$ phase. The maximum rate of transformation has been found to occur at 1400 °C as represented in a time–temperature–transformation- (TTT) diagram [116].

A promising *reactive laser sealing* approach was put forward by Petitbon *et al.* [66] by feeding alumina powder directly into a laser beam through a modified nozzle of a 3 kW CO₂ laser. A eutectic alumina–zirconia top layer was formed that produced a smooth, dense and very hard (20 GPa) surface layer with reduced microcracks that shows greatly improved wear- and erosion resistance and may thus be applied to improve coatings for turbine airfoils and diesel engine valves.

In conclusion, laser surface-engineering of plasma-sprayed thermal barrier coating systems is necessary to improve their performance in terms of high-temperature corrosion, wear- and thermoshock resistance for demanding applications including those in the aerospace and automotive industries. Laser surface remelting and reactive laser treatment are modern techniques that need more work and, in particular, the synergistic interaction of various scientific and engineering disciplines. Since laser equipment is predominantly operated by physicists, materials scientists must become more conversant in laser physics, and *vice versa*, physicists must better understand the specifics of ceramic engineering. Only then can the tremendous challenges be overcome that are being posed today by ceramic thermal barrier coatings.

6.2.2 Other Thermal Barrier Coatings

The search for other ceramic materials to be used as thermal barrier coatings was triggered by the still large difference in the coefficients of thermal expansion between base metal and ceramic coating that tend to introduce large thermal and residual stresses. Coatings consisting of dicalcium silicate (C₂S) over a NiCrAlY bond coat on stainless steel (SUS-304) revealed a higher coefficient of thermal expansion compared to PSZ (13 p.p.m. *versus* 9 p.p.m.), good thermal shock resistance, excellent hot corrosion resistance against V₂O₅ and Na₂SO₄ as well as a small thermal conductivity comparable or even less than PSZ [142].

A second line of investigation deals with the ternary system CaO–SiO₂–ZrO₂, i.e. C₂S–CZ. The high temperature oxidation behavior up to 1100 °C of these coatings is characterized by a lack of exfoliation and severe cracking that has been observed in

PSZ TBCs under comparable conditions. Instead, a reaction layer develops, presumably by involvement of Al and/or Cr from the bond coat underneath. In hot corrosion tests involving molten salts, the new coating behaved quite poorly, and showed high reactivity at temperatures around 1000 °C [143].

6.3 Bioceramic Coatings

Research and development on bioceramic materials have reached a level of involvement and sophistication comparable only to electronic ceramics. The reason is clear: large proportions of an aging population rely increasingly on bone replacement ranging from alveolar ridge augmentation to hip endoprostheses. Ceramics based on calcium phosphates such as $C_{10}P_3H$ (hydroxyapatite, HAp) or C_3P^3 are prime candidates for both replacement of bone subjected to low loading conditions and osseointegrative coatings of the femoral shafts of hip prostheses and dental root replacement parts [144].

Bioactive ceramics, for example calcium phosphates and bioactive glasses, not only interact with the body by stimulating osseointegration but will sometimes also be resorbed and transformed to calcified osseous tissue. The dominating biorelevant mechanism is bonding osteogenesis characterized by a chemical bond between implant and bone. Bioinert materials such as alumina, zirconia, carbon and also some metals like titanium or tantalum react to the host bone by contact osteogenesis characterized by a direct contact between implant and bone. Biotolerant materials such as bone cement (polymethylmethacrylate, PMMA) and also stainless steel and Co–Cr alloys will be accepted by the body and develop an implant interface characterized by a layer of connective tissue between implant and bone thus resulting in a distance osteogenesis.

The application of bioactive calcium phosphate ceramics is generally restricted to non-load-bearing areas because of their low fracture toughness and limited modulus of elasticity. To counteract this drawback calcium phosphate coatings are being applied to load-bearing metallic parts thus creating a synergistic composite of a tough and strong metallic substrate providing strength, and a porous bioactive HAp coating providing osseointegration function. In fact, many *in vivo* investigations have shown that a coated implant is readily accepted by the body and develops within a few weeks a type of bonding osteogenesis with the surrounding bone. Uncoated implants react by a distance osteogenetic mechanisms developing a connective tissue layer at the interface [145, 146]. Films of a few μm thickness have only a limited application for stimulating bone in-growth but may be beneficial for their self repair function in contact with aggressive body fluids. Thick plasma-sprayed HAp coatings [147] are now being applied routinely to the shafts of hip endoprosthetic devices and

³ Here the cement chemistry notation will be used: A = Al_2O_3 , C = CaO, P = P_2O_5 , S = SiO_2 , H = H_2O , T = TiO_2 etc.

to dental root implants. Their preparation, however, requires a high degree of skill, and general principles of total quality management must be adhered to. Important factors of HAp coating performance include chemical composition, i.e. purity (HAp content > 98%, heavy metal content < 50 p.p.m. [148]), Ca/P molar ratio (> 1.67), crystallinity of the deposit, phase purity, microstructure, i.e. density, adhesive strength to the metal substrate, and coating thickness. Optimization of these factors are required to assure that the long-term *in vivo* performance of the coatings will not be compromised.

The positive behavior of HAp-coated metallic implants has triggered intense research into the development of appropriate coating techniques. Because of the vital importance of such bioceramic thin and thick coatings, a brief review of other than plasma-spray techniques will follow [155].

6.3.1 Thin Film Techniques for HAp Coatings

6.3.1.1 Ion Beam Dynamic Mixing

This technique has been used to produce amorphous HAp layers on a titanium substrate [149]. The layers transform during short tempering (1 h) in air at 873 K to a crystalline structure. Advantages of such layers include high adhesive strength and self repair function. Photoelectron spectroscopic investigations of a pristine and a HAp-coated titanium surface both treated for 30 days with a simulated body fluid (Hank's solution) showed that even though the thin ($\sim 1 \mu\text{m}$) HAp coating has been completely dissolved within one day an extremely thin well-adhering Ca-P-Ti-OH layer remained at the surface [149].

6.3.1.2 RF Sputtering

Glassy sputter targets with varying Ca/P ratios were used to deposit thin amorphous calcium phosphate layers onto titanium substrates [150]. Dependent on the C/P ratio and the water vapor partial pressure, stoichiometric HAp or defect apatites with both Ca and OH vacancies were formed. At a C/P ratio below 0.4 no HAp forms, not even in an atmosphere containing large amount of water vapor.

6.3.1.3 Liquid Immersion Techniques

Thin dense and homogeneous HAp layers grow on a metallic (titanium) or ceramic (alumina) substrate in contact with a C-S glass submerged in a simulated body fluid containing phosphate [151]. While the technique allows growth of HAp coatings on any substrate the process is quite slow so that rather long times are required to deposit coatings of appreciable thicknesses.

6.3.1.4 Electrophoretic Deposition

The deposition is performed in a calcium phosphate suspension [152]. Once deposited the layer is being heat treated in vacuum to enhance the adhesion to the tita-

niun substrate. During this process hydroxyl groups are partly lost from the structure and a mixture of hydroxyapatite, $\text{Ca}_{10}[(\text{OH})_2(\text{PO}_4)_6]$, oxyhydroxyapatite, $\text{Ca}_{10}[\text{O}(\text{PO}_4)_6]$ and tetracalcium phosphate, $\text{Ca}_4[\text{O}(\text{PO}_4)_2]$ forms. This was documented by Fourier transformed infrared spectra of a HAp with Ca deficit after sintering for 2 h in vacuum as well as after an electrophoretic deposition and sintering in vacuum. In both cases the phonon spectra did not show the infrared bands characteristic of the OH group at 3571 and 633 cm^{-1} but showed instead bands in the range of $550\text{--}610\text{ cm}^{-1}$ attributed to oxyhydroxyapatite [153].

6.3.2 Thick HAp Coatings

Thick coatings can be applied to titanium alloy substrates by essentially three methods: powder sintering, powder adhesion by glueing, and plasma spraying. In this context only plasma-spraying will be considered.

6.3.2.1 Plasma Sprayed HAp Coatings

This process constitutes the state-of-the-art procedure to improve the biological integration of implants into the body. Techniques applied include atmospheric plasma spraying (APS), flame spraying, high velocity oxyfuel flame (HVOF) spraying [154], and occasionally, vacuum plasma spraying (VPS) [155]. Both hydroxyapatite (HAp) and fluorapatite (FAp) can potentially be deposited by plasma spray techniques. FAp in particular does not decompose in the plasma jet compared to HAp that tends to form C_3P or C_4P by thermal decomposition (see below). Also, plasma spray-deposited FAp coatings show a high degree of crystallinity [156]. Histologic and histomorphometric investigations of coatings implanted in animals show, however, that in contrast to HAp the FAp coatings are intensely attacked by soft tissue [157]. In addition, the in-growth of bone cells into the porous FAp coatings is much suppressed [158]. Obviously, fluoride ions released from the coatings cause a cytotoxic response and thus hamper implant integration. This excludes FAp from the list of biocompatible ceramics. It should be mentioned that in the vicinity of uncoated titanium implants significant titanium ion concentrations were measured because of the extremely aggressive body environment. Even though at this time this accumulation of titanium ions is being considered nontoxic, an implant coated with HAp seems to provide a more benign environment in which only Ca and P ions concentrate [148].

Spraying of HAp is performed worldwide under widely varying conditions [154, 155, 159–162] resulting in coatings differing in their phase purity, adhesion strength and crystallinity. The control of these coating properties is crucial: HAp shows during *in vitro* as well as *in vivo* tests a significantly higher stability than C_3P and C_4P . Since also the resistance to resorption increases with increasing crystallinity, and proper adhesion of the coating to the metal implant prevents the invasion of acellular connective tissue leading potentially to a loosening of the bond to the bone, optimization of the three responses is vital.

Vacuum plasma spraying of highly crystalline, phase-pure HAp coatings with maximum adhesion to Ti6Al4V substrates led to new insight into the deposition

mechanism [155]. Research is also in progress to design biocompatible bond coats to increase the adhesion of the HAp coating to the substrate, prevent release of Ti ions, prevent direct contact of the HAp with the Ti alloy that appears to promote decomposition of HAp, and reduce the fast removal of heat and thus prevents the formation of a rapidly quenched amorphous contact layer immediately at the titanium interface [155].

Parametric study of HAp coating properties

The high temperature of the plasma jet promotes, even during the very short residence time of the HAp powder particles in its hot zone, a noticeable decomposition towards C_3P and C_4P or even CaO . The calcium phosphate phases occurring in the sprayed samples are compatible with the phase diagram shown in Figure 6-28 that indicates decomposition of HAp above 1360°C [163]. The stability of HAp is also a function of the water vapor partial pressure, $p_{\text{H}_2\text{O}}$ of the surrounding atmosphere (Fig. 6-28). The temperature representing the equilibrium $\text{HAp} + \text{CaO} \rightarrow \text{HAp} + \text{C}_4\text{P} + \text{H}_2\text{O}$ increases with increasing water vapor partial pressure, i.e. at a given temperature and a higher $p_{\text{H}_2\text{O}}$ is the phase assembly $\text{HAp} + \text{CaO}$ more stable than $\text{HAp} + \text{C}_4\text{P}$.

The powder feed rate, m , influences the heat transfer from the plasma to the powder particles, i.e. at the same plasma energy, η , the thermal decomposition of the HAp decreases with increasing powder feed rate. By the same token HAp decomposition is minimized at low substrate temperature, T_s , increasing chamber pressure, P , and increasing stand-off distance, X . On the other hand, optimizing the coating adhesion requires a reduction of residual stresses, σ , in the coating. This can be achieved at low plasma energies, η , high substrate temperature, T_s , and low stand-off distance, X .

The high substrate temperature promotes diffusion of Ti into the coating and leads to an increase in thickness of the reaction layer found to consist of CT (perovskite) [147] and/or CT_2 [164]. This thicker reaction layer in turn reduces the thermal decomposition of subsequently deposited HAp layers [152, 165]. Under these conditions the sprayed HAp layer attains a brown color thus supporting the ideas of an increased Ti diffusion. The brown color disappears after heat treatment at 800°C in air for 2 h possibly by oxidation of Ti^{3+} originally formed in the reducing argon/hydrogen plasma [155].

Increasing the chamber pressure, P , produces a shorter plasma jet so that at a constant stand-off distance, X , lower surface temperatures occur. This in turn suppresses the thermal decomposition of HAp.

Parametric VPS experiments performed on HAp powder with different plasma energies, η , powder feed rates, m , stand-off distances, X , chamber pressures, P , and substrate preheating, T_s , revealed the following coating optimization strategies.

- To suppress thermal decomposition of HAp the enthalpy supplied to the powder and the coating, respectively must be reduced. This can be done effectively by minimizing the plasma power, η , and the substrate temperature, T_s , but maximizing the powder feed rate, m , the stand-off distance, X , and the chamber pressure, P .

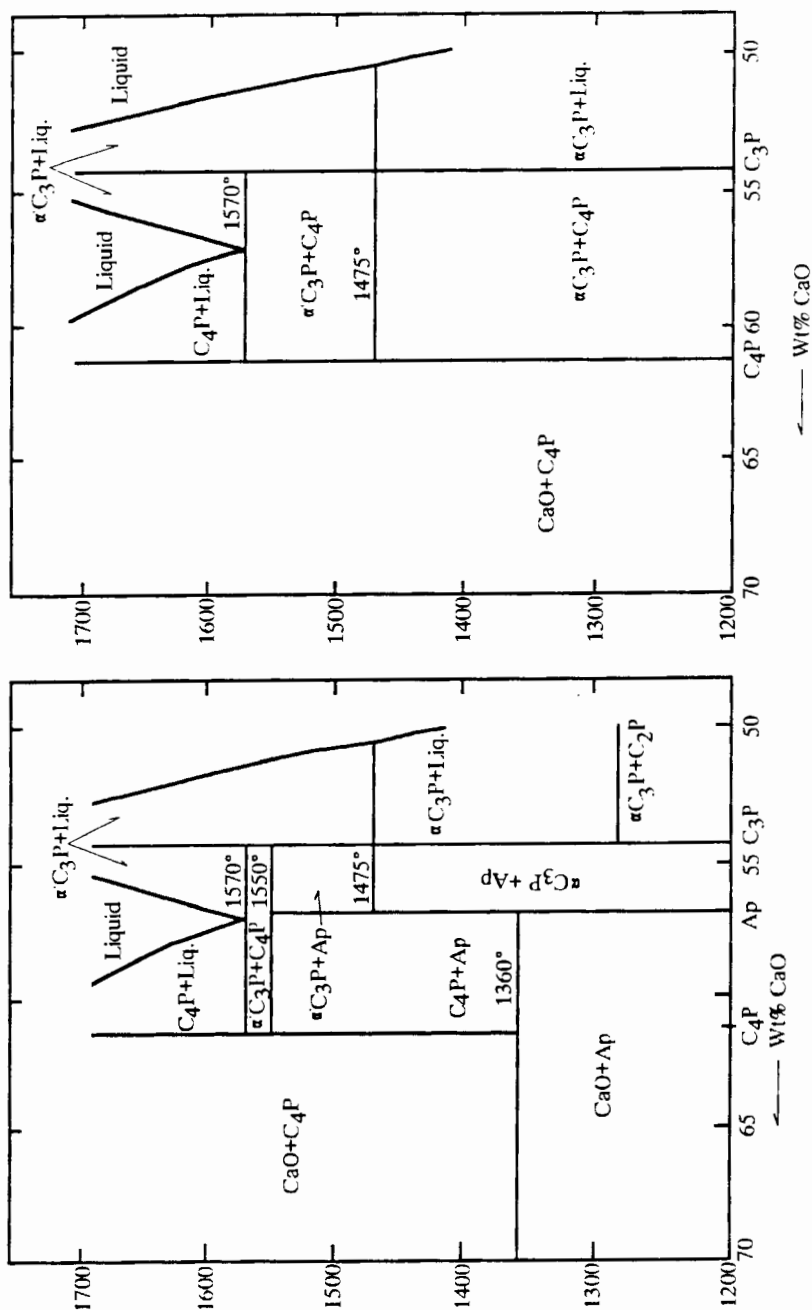


Figure 6-28. Central portion of the phase diagram $\text{CaO}-\text{P}_2\text{O}_5$ in air (right) and with a water vapor partial pressure of 0.67 atm (left) [163].

- To reduce the coating porosity but retain its biological functionality the enthalpy supplied to the powder must be increased by both increasing the plasma power, η , and the substrate temperature, T_s , but minimizing the stand-off distance, X .
- Finally, to optimize the coating adhesion both the plasma power, η , and the stand-off distance, X , should be minimized but the substrate should be preheated to alleviate the gradient of the coefficients of thermal expansion between coating and substrate, and hence the residual stresses introduced during cooling.

As it turns out, the simultaneous fulfillment of these three conditions is clearly impossible and the production of HAp coatings on Ti6Al4V implants optimized in terms of phase purity, porosity and adhesion requires a parameter and property trade-off.

Optimization studies

Based on the parametric studies reported above, attempts were made to optimize the coating properties with regard to minimizing the thermal decomposition and maximizing the coating adhesion [155]. The strategy selected was to reduce the plasma power η to 29 kW thus avoiding decomposition of HAp, and to reduce the stand-off distance X to 150 mm and 190 mm, respectively to retain a sufficient particle plasticity. Figure 6-29a shows the dense although cracked microstructure of such a coating that should be compared to that of a sample obtained with a plasma power of 42 kW (Figs. 6-29b and c). The former, however, contains only traces of C₄P whereas the latter has substantially decomposed forming large amounts of C₃P and C₄P (Fig. 6-30).

Adhesion strengths tests (ASTM C 633-79) using Araldite AV 118 as an adhesive of the optimized samples give values of 60–70 MPa, much higher than those of the samples sprayed with high plasma power that show values generally <20 MPa. The adhesion strength results for HAp coatings produced at comparable deposition conditions and reported in the literature span a wide range from 10 to 70 MPa [159–162, 166]. The deviations have been explained by the application of varying test procedures [145] as well as utilization of different adhesives [161]. There exist two contradictory opinions. First, penetration of the adhesive into the open pores of the HAp coatings will increase the adhesion so that the lower range of 10 to 20 MPa should be assumed a realistic estimate of the true adhesion strength [161]. Second, the low viscosity adhesive entering the open pores will create stresses during curing and thus weakens the microstructure of the coating, resulting in a decrease of the adhesion strength. Thus the high range of measured strength values around 70 MPa should be considered realistic [160]. If the latter is true than an adhesion strength of 70 MPa approaches the limit of bending strength (100 MPa) of HIPed high-density HAp ceramics. Push-out tests of HAp-coated implants after 3 months implantation yielded intermediate values. For example, Klein *et al.* [145, 167] reported values of around 34.5 MPa pointing to a rather strong bonding between coating and substrate, respectively and osseous hard tissue. In conclusion, a standardized test for *in vitro* and *in vivo* measurements of the coating adhesion strength is urgently needed to arrive at comparable data.

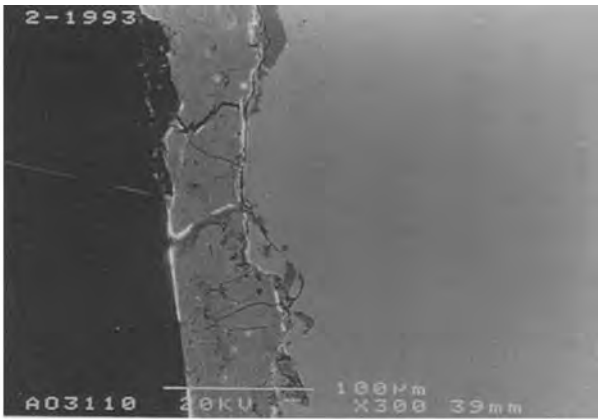
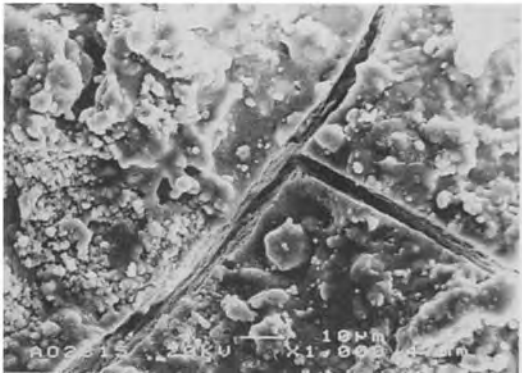
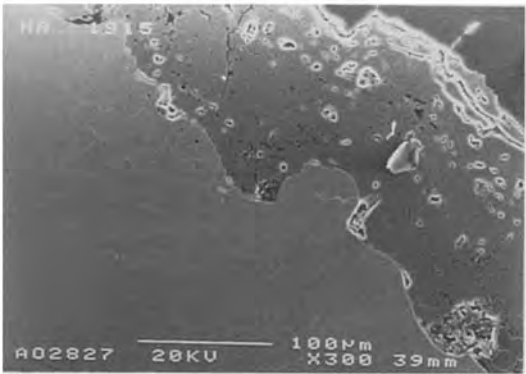


Figure 6-29. Hydroxyapatite coatings sprayed with low plasma power of 29 kW (a) and higher plasma power of 42 kW (b,c) [155].



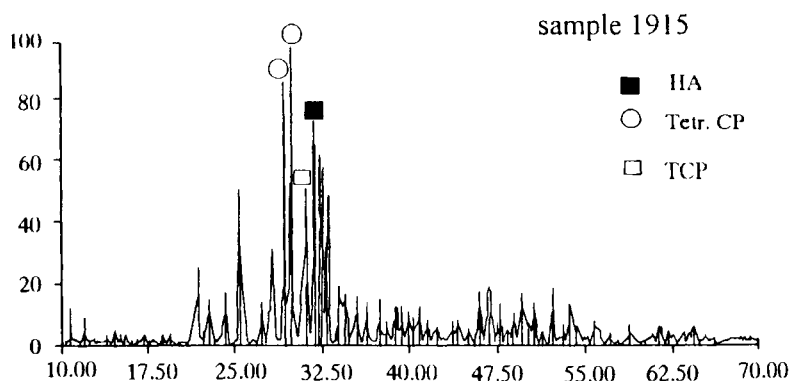


Figure 6-30. X-ray diffraction diagram of hydroxyapatite deposited by VPS at 42 kW shows pronounced decomposition into C_3P and C_4P [155].

Laser Raman spectra of selected optimized HAp coatings show a strong Raman shift of 961 cm^{-1} and weak intratetragonal bands at 430 , 600 and 1050 cm^{-1} all attributed to crystalline hydroxyapatite, and a shoulder at 949 cm^{-1} thought to originate from amorphous hydroxyapatite [153].

Other coating techniques

Despite some attempts to improve the HAp-coatings by selecting HVOF [168, 154] and RF ICP techniques [169] the results were not very convincing. HVOF thermal spraying reduces powder losses in the flame because of the short residence time, and produces coatings with high crystallinity but leads to rather low adhesion ($<18\text{ MPa}$) and some decomposition as shown by the presence of C_3P and C_4P in the coatings. Inductively coupled-plasmas avoid contamination of the coating by W and Cu used as electrode materials in the d.c. plasmatrons but lead even at low plasma powers between 3 and 12 kW to pronounced decomposition of HAp owing to the long residence time of the particles in the plasma with free-stream velocities typically around $10\text{--}30\text{ m s}^{-1}$. The long residence times of the powder compared to a d.c. plasma or HVOF system leads to intense particle heating and thus decomposition. Also, a low adhesion strength of only $5\text{--}14\text{ MPa}$ may be attributed to the low plasma velocities that impart only low momentum to the particles.

Future development trends

From the parametric studies of the dependence of the coating properties on the levels of the five parameters varied in the tests the following conclusions can be drawn.

1. Thermal decomposition of hydroxylapatite (HAp) starts in air above 1360°C .
2. At identical plasma powers η an increase of the powder feed rate m causes a decrease of the thermal decomposition of HAp.
3. At identical plasma powers η and chamber pressures P an increase of the stand-off distance X causes a decrease of the thermal decomposition of HAp.

4. At identical plasma powers η , powder feed rates, m , and stand-off distances, X , a decrease of the chamber pressure, P , causes a decrease of the thermal decomposition of HAp.
5. At identical plasma powers η , powder feed rates, m , stand-off distances, X , and chamber pressures P a preheating of the substrate with the plasma jet causes increased thermal decomposition of HAp.
6. At identical stand-off distances, X , chamber pressures, P , and powder feed rates m an increase of the plasma power η causes increased thermal decomposition of HAp.

From this a catalogue of future research and development requirements can be deduced. This includes the following.

1. Minimizing thermal decomposition of plasma-sprayed HAp.
2. Minimizing coating porosity with concurrent maintenance of their biofunctional properties.
3. Maximizing crystallinity of the coatings and thus *in vivo* stability and resorption resistance.
4. Maximizing fracture toughness of coatings.
5. Maximizing coating adhesion by proper parameter optimization and/or appropriate bond coats.

6.4 Functional Plasma-sprayed Coatings

6.4.1 HT-superconducting (HTSC) Coatings

Plasma-sprayed HTSC coatings were developed with a variety of materials, among them Y–Ba–Cu–oxide [170, 171] and Bi–Sr–Ca–Cu–oxide [172]. One of the first attempts were undertaken by IBM's Yorktown Heights Laboratory to use thermal spraying to create simple integrated circuits [170]. The technique involved ionizing a jet of a powdered mixture of the starting oxides in an electric arc close to the substrate surface. Spraying through a mask or template resulted in thin strips of HTSC ceramics that were supposed to provide loss-free links between chips in computers cooled with liquid nitrogen. Major problems to overcome included stringent oxygen control to assure compositional integrity, and dimensional control to prevent overspraying and to guarantee the accuracy of the sprayed pattern.

Oxygen control indeed is one of the major weak points in plasma-spraying HTSC coatings. Precursor Y–Ba–Cu–oxide material of nominal composition $\text{YBa}_{2.06}\text{Cu}_{4.13}\text{O}_x$ ($6.6 < x < 7$) resulted in oxygen deficient coatings with a bulk composition of cubic $\text{YBa}_{2.04}\text{Cu}_{2.98}\text{O}_{5.6}$ [172] pointing to a considerable loss of Cu_2O during plasma-spraying. Heat treatment in oxygen at 875 °C for 20 h led to the formation of superconducting orthorhombic $\text{YBa}_2\text{Cu}_3\text{O}_x$ ($x = 7 \pm 0.1$) with a very fine-grained, relatively dense microstructure. a.c. susceptibility data for this sample showed an

onset of superconductivity at 90.4 K and a critical current density (shielding current) j_c at 77 K of 460 A cm^{-2} . This low value is expected since the splat structure of a plasma-sprayed coating provides for many weak links. Moreover, it is surmised that the splats are far from being uniformly conductive throughout their granular structure but that only a rather thin shell of a few micrometer thickness around each 20–50 μm splat is superconducting.

A somewhat easier way to produce HTSC coatings with the required stoichiometry and oxygen deficiency to ensure higher critical current densities may be to use liquid precursors fed into the reaction chamber of an RF inductively-coupled plasma system [173–176].

6.4.2 Coatings for Solid Oxide Fuel Cells (SOFCs)

Fuel cells convert chemical energy stored in the fuel directly to electrical energy through an electrochemical reaction and are thus considered by many one of the most advantageous energy conversion systems of the future. They combine high energy conversion efficiency (>60% for SOFCs with bottoming cycle), flexibility in fuel use, and cogeneration capability with very low chemical and acoustic pollution of the environment.

An SOFC consists of several layers with specific functions. Figure 6-31 shows the working principle. The anode (fuel electrode) consists of Ni or a Ni–Al₂O₃ or NiAl–ZrO₂ composite material. It is separated from the cathode (air electrode), made from Sr-doped lanthanum composite oxide (LaMnO₃, LaCoO₃, LaSrMnO₃) with perovskite structure, by the Y-stabilized zirconia electrolyte. The arrangement of these three layers ('PEN', Positive electrode–Electrolyte–Negative electrode) can be tubular, monolithic or in a flat plate configuration (Fig. 6-32). The PENs are

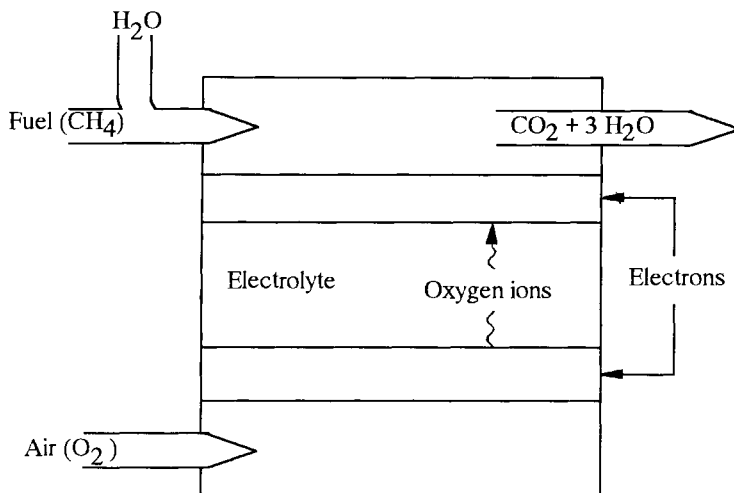


Figure 6-31. Working principle of a solid oxide fuel cell (SOFC).

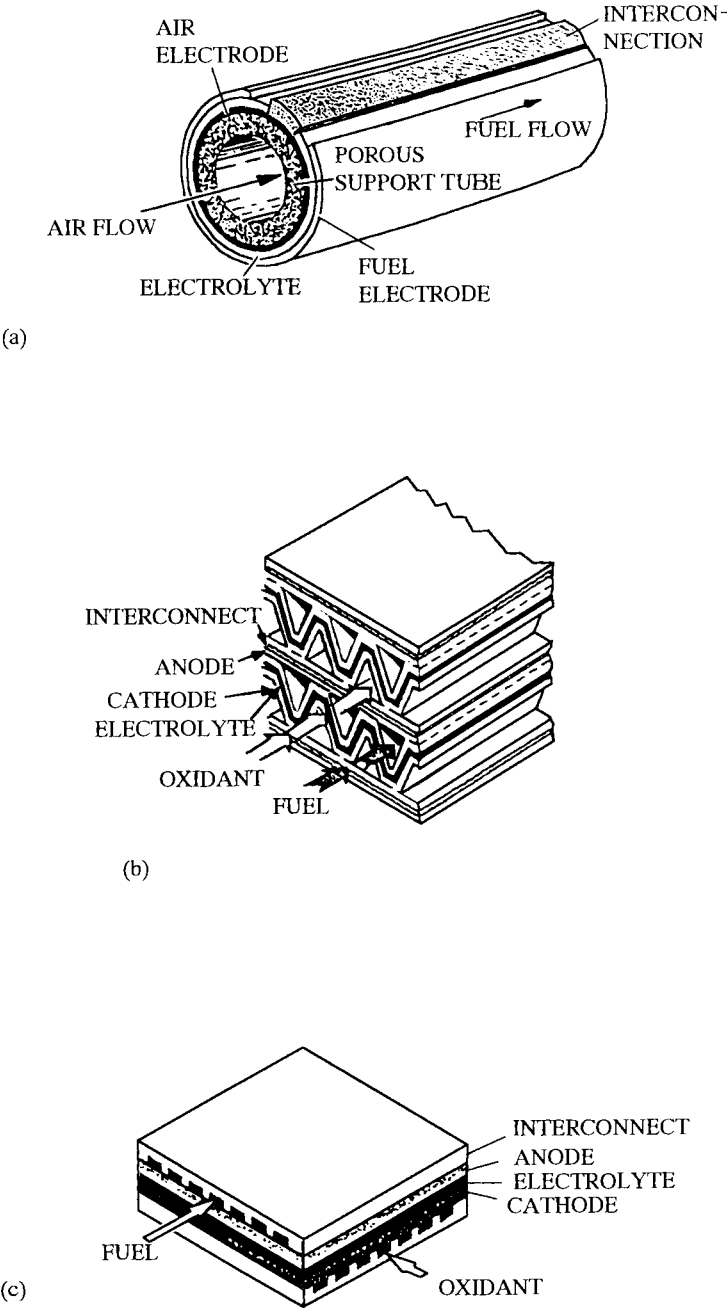


Figure 6-32. Tubular (a), monolithic (b) and flat plate (c) geometries of SOFCs.

separated by grooved bipolar plates or interconnects composed of Ni alloy– Al_2O_3 , Ni alloy–CSZ (completely stabilized zirconia), or LaCrO_3 [177] that transport the fuel gas and the air, respectively as well as heat and current.

At the air electrode (cathode), oxygen combines with electrons, and the negatively charged oxygen ions are transported through the electrolyte via oxygen vacancies in the stabilized zirconia. To obtain reasonable transport rates, the temperature of the electrolyte must be at least 950°C . At the fuel electrode (anode) a mixture of hydrocarbons and water reacts to hydrogen and carbon monoxide by internal reforming. The oxygen ions carried through the electrolyte oxidize the hydrogen and carbon monoxide to carbon dioxide and water releasing electrons that are transported back via an external circuit to the cathode (Fig. 6-31).

From this working principle of an SOFC it follows that the electrodes must have a high proportion of open porosity that will ensure fast and effective gas transport. On the other hand, the electrolyte transports only charged species, i.e. electrons and must thus be gastight. Increasingly work has been concentrated on producing the intricate shapes and compositions required for the PEN by plasma spraying technology. This includes the PSZ electrolyte [178–180], the cathodes [181, 182], cathodes and anodes [183] as well as the total PEN structure [184–187]. The interconnects of the planar SOFC, i.e. the bipolar plates, up to now hot pressed and rolled to a thickness of 3 mm and machined by ECM (electrochemical machining), can also be plasma-sprayed. Preliminary experiments were conducted with RF inductively-coupled plasma-sprayed $94\text{Cr}5\text{Fe}1\text{Y}_2\text{O}_3$ powders. The major challenge of economically producing bipolar plates by plasma spraying is concerned with producing a system of orthogonal grooves to carry the natural fuel/water mixture and air, respectively. Orthogonality is required to ensure effective cooling and a uniform temperature distribution that would considerably reduce thermal stresses across the PEN. A second problem is poisoning of the active cathode with nickel or chromium diffusing from the bipolar plate at the working temperature of 950°C . To prevent this, a protective layer of $(\text{La}, \text{Sr})\text{CrO}_3$ could be sprayed onto the cathode by VPS.

The functions of this protective ceramic layer include:

- electrical insulation of the bipolar plates,
- decrease of the thickness of the soldering gap between the ZrO_2 electrolyte and the bipolar plates,
- prevention of chromium oxide formation, and
- a barrier function against solid state diffusion of chromium oxide into the active internal cell volume.

These engineering challenges are not trivial and are compounded in monolithic SOFCs owing to the trapeziform gas channels (Fig. 6-32). For these reasons the tubular geometry of SOFCs is somewhat easier to realize and is thus closer to mass production [188]. A modern prototype of a tubular SOFC produced entirely by APS/VPS technology was recently developed in Japan [177]. Figure 6-33 shows a schematic illustration of the transaxial section of this tubular SOFC. On the surface of the outer support tube multiple cells are arranged: the anode consisting of Ni alloy/PSZ, followed by the Y–PSZ electrolyte, and on top the cathode consisting of a

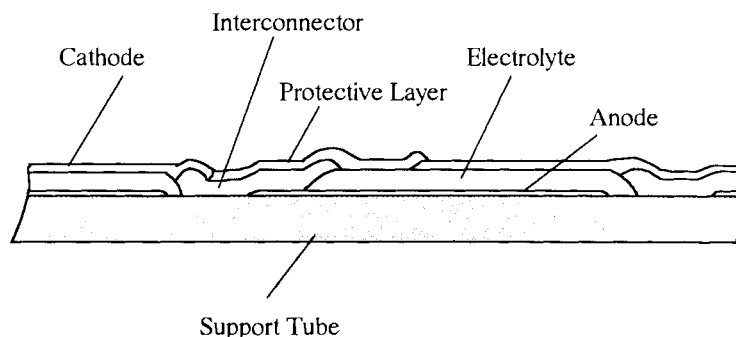


Figure 6-33. Prototype of an entirely plasma-sprayed tubular SOFC [177].

thanum composite oxide with perovskite structure, for example LaCoO_3 . Integrated in this design are the interconnects of Ni alloy/ Al_2O_3 coated by an Al_2O_3 protective coating to prevent oxidation of the Ni alloy. The electrodes and the interconnects were sprayed by APS, the very dense electrolyte by VPS. The support tube consisted of CSZ. This design has a very high fuel utilization of 87% and a high powder generation efficiency of 38%. A 1 kW prototype module, composed of 48 individual cells of the type shown in Fig. 6-33, was successfully operated for 3000 h.

Plasma-sprayed oxide electrocatalytic materials with spinel or perovskite structure are also being used as anode materials for water electrolyzers. Here an enormously important energy technology is being addressed as the production of hydrogen gas by electrolysis of water will be one of the mainstays of primary energy technology of the future. Electrocatalytic materials must conform to a complex set of stringent requirements [189]:

- chemical and electrochemical stability under operating conditions in alkaline water electrolysis,
- resistance to atomic oxygen,
- resistance to concentrated electrolyte solutions,
- resistance to working temperatures up to 150 °C,
- availability, and
- processability as layer or coating on metal electrodes.

Typical perovskites sprayed by VPS are $(\text{La}, \text{Sr})(\text{Ni}, \text{Co})\text{O}_3$ and, using an optimized Laval nozzle of low Mach number to generate a long laminar plasma jet, also the very attractive but highly parameter-sensitive Co_3O_4 [189, 190]. Using magnetite ore concentrates, magnetite– Co_3O_4 mixtures, and cobalt oxide, electrocatalytically active coatings for electrodes utilized in installations for water and sewage disinfection were produced by plasma spraying [191]. Even though the current efficiency is lower by 25–30% than for oxide–ruthenium–titanium anodes (ORTA), newly developed oxide–cobalt–titanium anodes (OCTA) have a higher chemical stability and an 8–12% higher productivity.

Prototype HT-SOFCs produced by Siemens in Germany operate between 800 and 1000 °C, and use as cathode gases oxygen or air, as anode gases hydrogen, H₂/CO/CO₂ or H₂/CO/CH₄ gas mixtures. The planar fuel cells are gathered together in stacks reaching an electrical power output of 1 MW m⁻³ installed stack. Present problems to be addressed include:

- requirement of varying coating thicknesses on one bipolar plate,
- control of tolerances,
- solderability of the layers to obtain a stack,
- corrosion protection to 1100 °C,
- chemical resistance against the soldering material (CaO–SiO₂–B₂O₃ based), and
- high thermal shock resistance.

The market potential for SOFCs appears to be huge: 300–800 MW per annum in Europe, 1800 MW per annum in the USA, and 1100 MW per annum in Asia including Japan.

References

- [1] W. Malléner, D. Stöver, *Proc. TS '90*, Essen **1990**, DVS 152, 3.
- [2] G. Hägg, *Z. Phys. Chem.* **1929**, 6, 221; **1931**, 12, 33.
- [3] W. Baumgart, Hard materials, in: *Process Mineralogy of Ceramic Materials* (eds. W. Baumgart, A. C. Dunham, G. C. Amstutz), Enke, Stuttgart, **1984**, p. 177.
- [4] E. Lugscheider, M. Kuelkens, D. Hofmann, *Proc. 2nd Int. Conf. on Surface Eng.*, Stratford-on-Avon, UK, 16–18 June, **1987**, p. 423.
- [5] E. Lugscheider, M. Kuelkens, *Advances in Thermal Spraying, Proc. ITSC*, Montreal, 8–12 Sept 1986 Canada **1986**, Welding Institute of Canada, p. 137.
- [6] W. Jeitschko, H. Nowotny, F. Benesovsky, *Mh. Chem.* **1964**, 94, 672.
- [7] O. Knotek, E. Lugscheider, H. Reimann, *J. Vac. Sci. Technol.* **1975**, 12(4), 75.
- [8] S. Rangaswamy, H. Herman, *Advances in Thermal Spraying, Proc. 11th ITSC*, Montreal, Canada, 8–12 Sept **1986**, Welding Inst. of Canada 1986, p. 101.
- [9] P. E. Chandler, A. R. Nicoll, *Proc. 2nd Int. Conf. on Surface Eng.*, Stratford-on-Avon, UK, 16–18 June, **1987**, 403.
- [10] R. W. Smith, R. Novak, *PMI*, **1991**, 23(3), 147.
- [11] H. Kreye, D. Fandrich, H. H. Müller, G. Reiners, *Advances in Thermal Spraying, Proc. ITSC 1986*, Welding Inst. of Canada, p. 121.
- [12] D. Tu, S. Chang, C. Chao, C. Lin, *J. Vac. Sci. Technol.* **1985**, A3(6), 2479.
- [13] R. B. Heimann, D. Lamy, T. Sopkow, *J. Can. Ceram. Soc.* **1990**, 59(3), 49.
- [14] C. D'Angelo, H. El Joundi, *Adv. Mat. Proc.* **1988**, 12, 41.
- [15] A. Wozniowski, *Proc. Int. Conf. Metallurg. Coatings*, ICMC, San Diego, 1–6 April, **1990**.
- [16] R. Sivakumar, B. L. Mordike, *Surf. Coat. Technol.* **1989**, 37, 139.
- [17] M. E. Vinayo, F. Kassabji, J. Guyonnet, P. Fauchais, *J. Vac. Sci. Technol.* **1985**, A3(6), 2483.
- [18] K. Hajmrle, M. Dorfman, *Mod. Dev. Powder Metall.* **1985**, 15/15, 609.
- [19] K. Kirner, *Schweißen Schneiden*, **1989**, 41, 11.
- [20] W. J. Lenling, M. F. Smith, J. A. Henfling, *Proc. 3rd NTSC, Thermal Spray Research and Applications*, Long Beach, CA, 20–25 May, **1990**, p. 451.
- [21] K. Kamachi, S. Goda, S. Oki, M. Magome, K. Ueno, S. Sodeoka, G. Ueno, T. Yosioka, *Proc. 3rd NTSC, Thermal Spray Research and Applications*, Long Beach, CA 20–25 May, **1990**, p. 497.

- [22] R. W. Smith, R. Novak, *PMI*, **1991**, 23(4), 231.
- [23] S. Shimizu, K. Nagai, *Weld. Int.* **1991**, 5, 12.
- [24] H. Kolaska, K. Dreyer, *DIMA*, **1989**, 11.
- [25] A. Sandt, *Schweißen Schneiden*, **1986**, 38, 4.
- [26] Z. Z. Mutasim, R. W. Smith, L. Sokol, *Thermal Spray Research and Applications, Proc. 3rd NTSC, Long Beach, CA*, 20–25 May, **1990**, p. 165.
- [27] S. Fujii, T. Tajiri, A. Ohmori, *Proc. 14th ITSC '95, Kobe*, 22–26 May, **1995**, p. 839.
- [28] C. Brunet, S. Dallaire, J. G. Sproule, *Advances in Thermal Spraying, Proc. ITSC 1986*, Welding Inst. of Canada, p. 129.
- [29] Z. Z. Mutasim, R. W. Smith, M. Mohanty, Drexel University, Personal Communication.
- [30] R. W. Smith, D. Gentner, E. Harzenski, T. Robisch, *Thermal Spray Technology: New Ideas and Processes. Proc. NTSC '88, Cincinnati, OH*, 24–27 October, **1988**, p. 299.
- [31] R. W. Smith, E. Lugscheider, P. Jokiel, U. Müller, J. Merz, M. Wilbert, *Proc. 5th NTSC, Anaheim, CA*, June **1993**.
- [32] R. W. Smith, Z. Z. Mutasim, *J. Thermal Spray Technol.* **1992**, 1(1), 57.
- [33] R. W. Smith, M. R. Jackson, J. R. Rairden, J. S. Smith, *J. Met.* **1981**, 33, 23.
- [34] R. W. Smith, E. Harzenski, T. Robisch, *Proc. 12th ITSC, London, UK*, June **1989**.
- [35] G. Veilleux, R. G. Saint-Jacques, S. Dallaire, *Thin Solid Films* **1987**, 154, 91.
- [36] H. Jungklaus, E. Lugscheider, R. Limbach, R. W. Smith, *Proc. 13th ITSC '92, Orlando, FL*, **1992**, p. 679.
- [37] S. G. Cliche, S. Dallaire, *Thermal Spray Research and Applications, Proc. 3rd NTSC, Long Beach, CA*, 20–25 May, **1990**, p. 761.
- [38] P. Vuoristo, K. Niemi, B. Jouve, T. Stenberg, T. Mäntylä, L.-M. Berger, M. Nebelung, W. Hermel, *Proc. 14th ITSC '95, Kobe*, 2–26 May, **1995**, 699.
- [39] S. Thiele, R. B. Heimann, L.-M. Berger, M. Nebelung, K. Schwarz, *J. Mater. Sci. Lett.* **1996**, 15(8), 683.
- [40] K. S. Fessenden, C. V. Cooper, L. H. Favrow, A. P. Matarese, T. P. Slavin, *Proc. 3rd NTSC, Thermal Spray Research and Applications, Long Beach, CA*, 20–25 May, **1990**, 611.
- [41] H. E. Hintermann, *J. Vac. Sci. Technol.* **1984**, 2, 816.
- [42] E. R. Buchanan, *Turbomachinery Int.* **1987**, 28(1), 25.
- [43] R. J. Ortolano, *Turbomachinery Int.* **1983**, April, 19.
- [44] *Development of low-pressure coatings resistant to steam-borne corrosives*, EPRI Project CS-3139, Vol. 1, June, **1983**.
- [45] J. Qureshi, A. Levy, B. Wang, *J. Vac. Sci. Technol.* **1986**, A4(6), 2638.
- [46] W. J. Sumner, J. H. Vogan, R. J. Lindinger, *Proc. Am. Power Conf.*, 22–24 April, **1985**, p. 196.
- [47] U. Menne, A. Mohr, M. Bammer, C. Verpoort, K. Ebert, R. Baumann, *Proc. TS '93, Aachen* **1993**, DVS 152, 280.
- [48] S. T. Wlodek, *EPRI Workshop on Solid Particle Erosion of Steam Turbines*, Chattanooga, TN, USA, **1985**.
- [49] I. G. Wright, *Mater. Sci. Eng.* **1987**, 88, 261.
- [50] I. G. Wright, V. Nagarajan, J. Stringer, *Oxid. Met.* **1986**, 25(3/4), 175.
- [51] L. F. Albright, C. F. McConnell, K. Welther, *Proc. ACS 175th National Meeting, Anaheim, CA, USA*, 12–17 March, **1978**, p. 175.
- [52] L. F. Albright, C. F. McConnell, *Proc. ACS 175th National Meeting, Anaheim, CA, USA*, 12–17 March, **1978**, p. 205.
- [53] G. L. Swales, in: *Behaviour of High temperature Alloys in Agressive Environments* (Eds. I. Kirman, J. B. Marriott, M. Merz), The Metals Society, London, **1980**, p. 45.
- [54] S. M. Brown, L. F. Albright, Chapter 17 in: *Industrial and Laboratory Pyrolysis* (Eds. L. F. Albright, B. L. Crynes), American Chemical Society, Washington, **1976**, 175.
- [55] S. Dallaire, B. Champagne, in: *Modern Development in Powder Metallurgy* (Eds. E. N. Aqua, Ch. I. Whitman), **1985**, 17, 589.
- [56] P. Schwarzkopf, F. W. Glaser, *Z. Metall.* **1953**, 44, 353.
- [57] B. Champagne, S. Dallaire, *J. Vac. Sci. Technol.* **1985**, A3(6), 2373.
- [58] T. W. Kuijpers, J. H. Zaat, *Metals Technol. March* **1974**, 142.
- [59] E. Lugscheider, H. Jungklaus, P. Remer, J. Knuuttila, *Proc. 14th ITSC, Kobe*, 22–26 May, **1995**, p. 833.

- [60] H. Herman, C. C. Berndt, H. Wang, Plasma Sprayed Ceramic Coatings, Chapter 5 in: *Ceramic Films and Coatings* (Eds. J. B. Wachtman, R. A. Haber), Noyes: Park Ridge, NJ, USA, **1993**, p. 131.
- [61] L. Brown, H. Herman, R. K. MacCrone, *Advances in Thermal Spraying*, Pergamon, Toronto, **1986**, p. 507.
- [62] R. B. Heimann, D. Lamy, T. N. Sopkow, *Proc. 3rd NTSC, Thermal Spray Research and Applications*, Long Beach, CA, USA, 20–25 May, **1990**, p. 491.
- [63] R. Kingswell, D. S. Rickerby, K. T. Scott, S. J. Bull, *Proc. 3rd NTSC, Thermal Spray Research and Applications*, Long Beach, CA, USA, 20–25 May, **1990**, p. 179.
- [64] T. Chon, G. A. Bancke, H. Herman, H. Gruner, *Thermal Spray-Advances in Coatings Technology*, ASM International, Cleveland, OH, USA, **1988**, p. 329.
- [65] H. Hannotiau, J. Leunen, J. Sleurs, S. Heusdains, H. Tas, *1st Int. Conf. Plasma Surface Eng.*, Garmisch-Partenkirchen, Germany, 19–23 September, **1988**.
- [66] A. Petitbon, D. Guignot, U. Fischer, J.-M. Guillemot, *Mater. Sci. Eng.* **1989**, A121, 545.
- [67] E. D. Kirbach, M. Stacey, Personal communication, Forintek Canada Corp., Western Laboratory, Vancouver, BC, Canada, **1989**.
- [68] H. Rump, W. Möhler, *Keram. Z.* **1995**, 47(4), 284.
- [69] T. Gößmann, H. G. Schütz, D. Stöver, H. P. Buchkremer, D. Jäger, *Proc. 3rd NTSC, Thermal Spray Research and Applications*, Long Beach, CA, USA, 20–25 May, **1990**, p. 503.
- [70] J. Beczkowiak, K. Munding, *Proc. 13th ITSC*, London, UK, **1989**, p. 94.
- [71] I. G. Wright, V. Nagarajan, J. Stringer, *Oxid. Met.* **1986**, 25(3/4), 175.
- [72] I. Kvernes, E. Lugscheider, *PMI*, **1992**, 24(1), 7.
- [73] D. Gansert, E. Lugscheider, U. Müller, *Proc. 3rd NTSC, Thermal Spray Research and Applications*, Long Beach, CA, USA, 20–25 May, **1990**, p. 517.
- [74] N. F. Seliverstov, V. A. Ryabin, M. Ya. Berezhneva, A. B. Chudinov, Yu. S. Borisov, *Proc. TS '93*, Aachen **1993**, DVS 152, 442.
- [75] L. N. Kozina, Yu. P. Revyakin, *Izvest. AN SSSR, Metall.* **1970**, 56.
- [76] D. J. Varacalle, M. G. Jacox, L. B. Lundberg, J. R. Hartenstine, H. Herman, G. A. Bancke, W. Riggs, *J. Surf. Coat. Technol.* **1993**, December.
- [77] D. J. Varacalle, R. A. Neiser, M. F. Smith, *Proc. 13th ITSC, Thermal Spray: International Advances in Coatings Technology*, Orlando, FL, USA, May **1992**.
- [78] E. R. Buchanan, A. Sickinger, *Proc. 1994 NTSC*, Boston, MA, USA, 20–24 June, **1994**.
- [79] T. McKechnie *et al.* *Proc. 1993 NTSC*, Orlando, FL, USA, 7–11 June, **1993**.
- [80] W. Cai, H. Liu, A. Sickinger, E. Muehlberger, D. Bailey, E. J. Lavernia, *J. Thermal Spray Technol.* **1994**, 3(2), 135.
- [81] J. M. Houben, Relation of the adhesion of plasma sprayed coatings to the process parameters size, velocity and heat content of the spray particles. Ph.D. Thesis, Technical University Eindhoven, The Netherlands, **1988**.
- [82] D. J. Varacalle, L. B. Lundberg, B. G. Miller, W. L. Riggs, *Proc. 14th ITSC*, Kobe, Japan, 22–26 May, **1995**, p. 377.
- [83] P. D. Prichard, R. L. McCormick, Z. Z. Mutasim, R. W. Smith, *Proc. Composite Forming Symp., AIME Winter Meeting*, Anaheim, CA, USA, February **1990**.
- [84] H.-D. Steffens, H.-M. Höhle, E. Ertürk, *Thin Solid Films* **1980**, 73, 19.
- [85] E. Lugscheider, P. Lu, B. Hauser, D. Jäger, *J. Surf. Coat. Technol.* **1987**, 32, 215.
- [86] M. L. Thorpe, R. H. Unger, *Advances in Thermal Spraying, Proc. ITSC 1986*, Welding Inst. of Canada, p. 3.
- [87] M. Müller, F. Gitzhofer, R. B. Heimann, M. I. Boulos, *Proc. NTSC '95*, Houston, TX, USA, 11–15 Sept, **1995**, p. 567.
- [88] R. Rairden, M. R. Jackson, M. F. Henry, *Proc. 10th ITSC, Essen* **1983**, DVS 80, 205.
- [89] M. G. Hebsur, R. V. Miner, *Mater. Sci. Eng.* **1986**, 83, 239.
- [90] C. A. Barrett, C. E. Lowell, *Oxid. Met.* **1977**, 11, 199.
- [91] J. Gayda, T. P. Gabb, R. V. Miner, *J. Fatigue* **1986**, 8(4), 217.
- [92] M. G. Hebsur, R. V. Miner, *Thin Solid Films* **1987**, 147, 143.
- [93] S. M. Merchant, M. R. Notis, *Mater. Sci. Eng.* **1984**, 66, 47.
- [94] K. Noguchi, M. Nishida, A. Chiba, J. Takeuchi, Y. Harada, *Proc. 14th ITSC*, Kobe, Japan, 22–26 May, **1995**, p. 459.

- [95] K. E. Spear, *J. Am. Ceram. Soc.* **1989**, 72, 171.
- [96] P. K. Bachmann, D. Leers, H. Lydtin, *Diamond Relat. Mat.* **1991**, 1, 1.
- [97] K. Kurihara, K. Sasaki, M. Kawarada, N. Koshino, *Appl. Phys. Lett.* **1988**, 52, 437; also *Fujiitsu Sci. Technol. J.* **1989**, 25, 44.
- [98] E. Lugscheider, U. Müller, F. Deuerler, W. Schlump, *Proc. TS '93, Aachen* **1993**, DVS 152, p. 19.
- [99] R. B. Heimann, *Proc. Adv. Mater.* **1991**, 1, 181.
- [100] E. Lugscheider, U. Müller, F. Deuerler, W. Schlump, P. Jokiel, P. Remer, *Proc. 13th Intern. Plansee Seminar*, Reutte, Germany **1993**, 3, p. 287.
- [101] E. Lugscheider, U. Müller, *Ingenieur-Werkstoffe*, **1992**, 4(7/8), 42.
- [102] F. Matsumoto, S. Kato, Y. Tomii, *Proc. 14th ITSC*, Kobe, Japan, 20–26 May, **1995**, 821.
- [103] S. Matsumoto, *Mater. Res. Soc. Symp. Proc.* **1988**, EA-15, 119.
- [104] M. Murakawa, S. Takeuchi, Y. Hirose, *Mater. Res. Soc. Symp. Proc.* **1989**, EA-19, 63.
- [105] K. A. Snail, *Inside R&D*, **1991**, 10(23), 1.
- [106] D. G. Goodwin, *Mater. Res. Soc. Symp. Proc.* **1989**, EA-19, 153.
- [107] W. A. Weimer, F. M. Cerio, C. E. Johnson, *J. Mater. Res.* **1991**, 6, 2134.
- [108] D. A. Spera, S. J. Grisaffe, *NASA Technical Memorandum TMX-2664*. National Technical Information Service, Springfield, VA, USA, **1973**.
- [109] R. Sivakumar, B. L. Mordike, *Surf. Coat. Technol.* **1988**, 37, 139.
- [110] *Neue Materialien für Schlüsseltechnologien des 21. Jahrhunderts*, MaTech, Bundesmin. für Forschung und Technologie, Bonn, August **1994**.
- [111] R. A. Miller, *Surf. Coat. Technol.* **1987**, 30, 1.
- [112] H. Yajima, Y. Kimura, T. Yoshioka, *Proc. 14th ITSC, Kobe*, Japan 22–26 May, **1995**, p. 621.
- [113] P. E. Hodge, R. A. Miller, M. A. Gedwill, *Thin Solid Films*, **1980**, 73, 447.
- [114] E. P. Butler, *Mater. Sci. Technol.* **1985**, 1(6), 417.
- [115] H. G. Scott, *J. Mater. Sci.* **1975**, 10(9), 1527.
- [116] K. M. Jasim, R. D. Rawlings, D. R. F. West, *Mater. Sci. Technol.* **1992**, 8(1), 83.
- [117] B. C. Wu, E. Chang, S. E. Chang, D. Tu, *J. Am. Ceram. Soc.* **1989**, 72(2), 212.
- [118] N. Iwamoto, N. Umesaki, M. Kamai, G. Ueno, *Proc. TS '90, Essen* **1990**, DVS 130, 99.
- [119] J. E. Restall, *Proc. 5th Intern. Symp. on Superalloys*, Champion, PA, USA, 7–11 Oct, **1984**, p. 721.
- [120] T. N. Rhys-Jones, *Corrosion Science* **1989**, 29(6), 623.
- [121] D. M. Comassar, *Metal Finishing* **1991**, March, 39.
- [122] R. W. Smith, W. F. Schilling, H. M. Fox, *Trans. ASME* **1981**, 103, 146.
- [123] S. Stecura, *Ceram. Bull.* **1982**, 61(2), 256.
- [124] G. C. Chang, W. Phucharoen, R. A. Miller, *Surf. Coat. Technol.* **1987**, 30, 13.
- [125] R. A. Miller, *NASA Technical Memorandum TM 100283*, **1988**.
- [126] R. A. Miller, *J. Am. Ceram. Soc.* **1984**, 67, 517.
- [127] D. L. Ruckle, *Thin Solid Films* **1980**, 73, 455.
- [128] A. Feuerstein, W. Dietrich, E. Muehlberger, Ph. Meyer, *Proc. Conf. High Temp. Alloys for Gas Turbines and Other Applic.*, Liege, Belgium, 6–9 Oct, **1986**, p. 1227.
- [129] F. N. Longo, H. Florant, *Proc. 8th ITSC*, Miami, FL, USA, Sept **1976**.
- [130] K. Cushnie, J. A. E. Bell, G. D. Smith, *Proc. 3rd NTSC, Thermal Spray Research and Applications*, Long Beach, CA, USA, 20–25 May, **1990**, 539.
- [131] H.-D. Steffens, Z. Babiak, U. Fischer, *Proc. 2nd Intern. Conf. on Surface Eng.*, Stratford-upon-Avon, UK, 16–18 June, **1987**, p. 471.
- [132] M. Gramlich, H.-D. Steffens, *Working Group Session 'Ceramic Coatings'*, German Ceramic Society (DKG), Heilbronn, Germany, 8–9 June, **1994**.
- [133] G. Eckold, I. M. Buckley-Golder, K. T. Scott, *Proc. 2nd Intern. Conf. Surface Eng.*, Stratford-upon-Avon, UK, 16–18 June, **1987**, p. 433.
- [134] R. B. Heimann, D. Lamy, V. E. Merchant, *Trans. 17th CUIAC Workshop*, (Ed. R. B. Heimann), Laval University, Québec City, Québec, Canada, 2 Oct, **1991**.
- [135] I. Zaplatynsky, *NASA Technical Memorandum 82830, Proc. Int. Conf. Metall. Coatings and Process Technology*, San Diego, CA, USA, 5–8 April, **1982**.
- [136] A. Adamski, R. McPherson, *Advances in Thermal Spraying, Proc. ITSC 1986*, Welding Inst. of Canada, p. 555.

- [137] T. R. Anthony, H. E. Cline, *J. Appl. Phys.* **1977**, 48(9), 3888.
- [138] H. E. Cline, *J. Appl. Phys.* **1981**, 52(1), 443.
- [139] J.-H. Shieh, S.-T. Wu, *Appl. Phys. Lett.* **1991**, 59(12), 1512.
- [140] K. M. Jasim, R. D. Rawlings, D. R. F. West, *J. Mater. Sci.* **1992**, 27, 3903.
- [141] K. M. Jasim, D. R. F. West, W. M. Steen, R. D. Rawlings, *Proc. 7th Intern. Congr. on Applic. Lasers and Electrooptics (ICALEO '88)* (ed. G. Bruck), Springer, Berlin, **1988**, p. 17.
- [142] H. Uchikawa, H. Hagiwara, M. Shirasaka, H. Yamane, *Proc. Surf. Eng. Intern. Conf.*, Tokyo, Japan, 18–22 Oct, **1988**, p. 45.
- [143] M. Yoshida, K. Abe, T. Aranami, Y. Harada, *Proc. 14th ITSC*, Kobe, Japan, 22–26 May, **1995**, p. 785.
- [144] K. Søballe, Hydroxyapatite ceramics coating for bone implant fixation. Mechanical und histological studies in dogs. *Acta Orthop. Scand.* **1993**, 64, 58.
- [145] C. P. A. T. Klein, P. Patka, H. B. M. vanderLubbe, J. G. C. Wolke, K. deGroot, *J. Biomed. Mater. Res.* **1991**, 25, 53.
- [146] D. P. Rivero, J. Fox, A. K. Skipor, R. M. Urban, J. O. Galante, *J. Biomed. Mater. Res.* **1988**, 22, 191.
- [147] K. deGroot, R. T. G. Geesink, C. P. A. T. Klein, P. Serekian, P., *J. Biomed. Mater. Res.* **1987**, 21, 1375.
- [148] B. Simons, in: *PLATIN-Seminar, Innovative Anwendungen von Plasma-Technologien in der Medizintechnik*, Wuppertal, Germany, 14. September **1995**.
- [149] O. Ohtsuka, M. Matsuura, N. Chida, M. Yoshinari, T. Sumii, T. Dérand, *Surf. Coat. Technol.* **1994**, 65, 224.
- [150] K. Yamashita, T. Arashi, K. Kitagaki, S. Yamada, T. Umegaki, K. Ogawa, *J. Am. Ceram. Soc.* **1994**, 77, 2401.
- [151] T. Kokubo *et al.* in: *Bioceramics Vol. 4* (Proceedings of the 4th International Symposium on Ceramics in Medicine, London, UK, September 1991) (ed. W. Bonfield, G. W. Hasting, K. E. Tanner) Butterworth-Heinemann, Oxford, UK, **1991**, p. 113.
- [152] P. Ducheyne, S. Radin, M. Heughebaert, J. C. Heughebaert, *Biomaterials* **1990**, 11, 244.
- [153] M. Weinlaender, J. Beumer, E. B. Kenney, P. K. Moy, F. Adar, *J. Mater. Sci.: Mater. Med.* **1992**, 3, 397.
- [154] A. J. Sturgeon, M. D. F. Harvey, M. D. F., *Proc. 14th ITSC '95*, Kobe, Japan, 22–26 May, **1995**, 933.
- [155] T. A. Vu, R. B. Heimann, *Eur. J. Mine.* in press.
- [156] K. de Groot, *J. Ceram. Soc. Jpn.: Int. Ed.* **1991**, 99, 917.
- [157] Ch. Zimmermann, Histologische und histomorphometrische Untersuchungen am Interface Apatit-beschichteter Titan-Implantate, Dissertation University of Heidelberg **1992**.
- [158] E. Lugscheider, M. Knepper, B. Heimberg, A. Dekker, C. J. Kirkpatrick, *J. Mater. Sci.: Mater. Med.* **1994**, 5, 371.
- [159] E. Lugscheider, M. Knepper, *Proc. TS '93*, Aachen **1993**, DVS 152, 82.
- [160] J. G. C. Wolke, J. M. deBlicke-Hogervorst, W. J. A. Dhert, C. P. A. T. Klein, K. deGroot, *J. Thermal Spray Technol.* **1992**, 1, 75.
- [161] M. J. Filiaggi, N. A. Coombs, R. M. Pilliar, *J. Biomed. Mater. Res.* **1991**, 25, 1211.
- [162] J. H. C. Lin, M. L. Liu, C. P. Ju, *J. Mater. Sci.: Mater. Med.* **1994**, 5, 279.
- [163] K. de Groot, *Ann. NY Acad. Sci.* **1988**, 523, 227.
- [164] H. Ji, C. B. Ponton, P. M. Marquis, *J. Mater. Sci.: Mater. Med.* **1992**, 3, 283.
- [165] J. Weng, *J. Mater. Sci. Lett.* **1994**, 13, 159.
- [166] D. M. Liu, H. M. Chou, J. D. Wu, *J. Mater. Sci.: Mater. Med.* **1994**, 5, 147.
- [167] C. P. A. T. Klein, P. Patka, J. G. C. Wolke, J. M. A. deBlicke-Hogervorst, K. de Groot, *Biomaterials* **1994**, 15, 146.
- [168] H. Ogushi, K. Ishikawa, S. Ojima, Y. Hirayama, K. Seto, G. Eguchi, *Biomaterials* **1992**, 13, 471.
- [169] T. Kameyama, M. Ueda, A. Motoe, K. Ohsaki, H. Tanizaki, K. Iwasaki, *Proc. 1st Intern. Conf. on Processing Materials for Properties*, (ed. H. Henein, T. Oki), The Minerals, Metals and Materials Soc. **1993**, p. 1097.
- [170] D. O. Welch, V. J. Enery, D. E. Cox, *Nature*, **1987**, 327, 278.
- [171] L. Pawlowski, A. Hill, R. McPherson, D. Garvie, Z. Przelozny, T. Finlayson, *Proc. 3rd*

- NTSC, Thermal Spray Research and Applications, Long Beach, CA, USA, 20–25 May, **1990**, p. 641.
- [172] E. Lugscheider, T. Weber, *Proc. 3rd NTSC, Thermal Spray Research and Applications*, Long Beach, CA, USA, 20–25 May, **1990**, p. 635.
- [173] A. Shah, S. Patel, E. Narumi, D. T. Shaw, *Appl. Phys. Lett.* **1990**, 57(14), 1452.
- [174] H. Zhu, Y. C. Lau, E. Pfender, *Proc. 9th Int. Symp. Plasma Chem.*, Pugnouchiuso **1989**, 876, 1497.
- [175] H. Zhu, Y. C. Lau, E. Pfender, *J. Appl. Phys.* **1991**, 69(5), 3404.
- [176] A. Shah, T. Haugan, S. Witanachi, S. Patel, T. Shaw, *Proc. Mat. Res. Soc. Symp.*, Boston, MA, USA, **1989**, p. 747.
- [177] A. Notomi, H. Hisatome, *Proc. 14th ITSC*, Kobe, Japan, 22–26 May, **1995**, p. 79.
- [178] M. Scagliotti, F. Parmigiani, G. Samoggia, G. Lanzi, D. Richon, *J. Mater. Sci.* **1988**, 23, 3764.
- [179] C. L. Curtis, D. T. Gawne, N. Priestnall, *Proc. 1993 NTSC*, Anaheim, CA, USA, June **1993**, p. 519.
- [180] A. R. Nicoll, G. Barbezat, A. Salito, *SOFC-Seminar*, Yokohama, Japan, Feb **1992**.
- [181] Z. Li, W. Mallener, L. Fuerst, D. Stöver, F.-D. Scherberich, *Proc. 1993 NTSC*, Anaheim, CA, USA, June **1993**, p. 343.
- [182] L.-W. Tai, P. A. Lessing, *J. Am. Ceram. Soc.* **1991**, 74(3), 501.
- [183] R. Okiai, S. Yoshida, I. Kaji, *1st Int. Symp. on SOFC*, Nagoya, Japan, 13–14 Nov, **1989**, p. 191.
- [184] I. Kaji, S. Yoshida, N. Nagata, T. Nakajima, Y. Seino, *2nd Int. Symp. on SOFC*, Nagoya, Japan, **1991**, p. 221.
- [185] R. Henne, G. Schiller, *Forschungsverbund Sonnenenergie, 'Themen 94/95'*, **1994**, 89.
- [186] R. Henne, E. Fendler, M. Lang, *Proc. 1st Europ. Solid Oxide Fuel Cell Forum*, Lucerne, Switzerland, 3–7 Oct, **1994**, 2, 617.
- [187] W. Mallener, K. Wippermann, H. Jansen, Z. Li, D. Stöver, *Proc. ITSC '92*, Orlando, FL, USA, 28 May–5 June, **1992**, p. 835.
- [188] K. Minazawa, K. Toda, S. Kaneko, N. Murakami, A. Notomi, *MHI Technical Bulletin*, **1991**, 28(1), 41.
- [189] R. Henne, M. v. Bradke, G. Schiller, W. Schnurnberger, W. Weber, *Proc. 12th ITSC '89*, London, UK, 4–9 June, **1989**, 175.
- [190] G. Schiller, R. Henne, V. Borck, *J. Thermal Spray Technol.* **1995**, 4(2), 185.
- [191] Yu. Borisov, A. Murashov, A. Iliencko, V. Balakin, V. Slipchenko, A. Slipchenko, V. Maksimov, *Proc. 14th ITSC*, Kobe, Japan, 22–26 May, **1995**, p. 141.

7 Quality Control and Assurance Procedures

7.1 Quality Implementation

An important aspect of the plasma spray technique is the development and implementation of stringent quality control and assurance procedures to ensure consistency in the properties of the coatings. Because a multitude of spray parameters can potentially influence the coating properties, parameter optimization involves statistical experimental design procedures. Such procedures provide a maximum of information on the behavior of a system with a minimum number of experiments. Thus there is generally a very favorable experimental economy that can save time and resources, and hence money. Principles of multifactorial analyses and several case studies will be dealt with in Chapter 8.

7.1.1 Total Quality Management

Total quality management, TQM, is a complex system of several innovative and interacting disciplines including management ('Achieving success through others'), philosophy, psychology, stochastics, engineering and scientific expertise. It involves the concept of continuous improvement (Japanese: Keizen), and can be divided into three groups and classified as *quality tools*, *quality philosophy*, and *management style*. To successfully implement TQM it is mandatory that all three units are linked, and interact smoothly. It is generally not sufficient to improve only one or two of these pillars of TQM. Even though some advantages will be gained the final product will not be optimized. Thus TQM is more than just a 'quality' evolution but a system of continuous improvement of the process and the product. The impressive success of Japanese industry in the past decades had its roots in rigorous TQM procedures [1, 2].

7.1.1.1 Quality Tools

Statistical design of experiments (SDE) is the backbone 'quality tool' of TQM. Using SDE many of the factors can be screened out that vitally control the process

and/or the product performance. Closely associated with SDE is statistical experimental strategy (SES) that attempts to answer crucially important questions at the start of a research program such as the number of experiments needed, the number and ranges of the parameters to be selected, the costs of the program, the equipment and manpower needed, the duration¹ etc. Likewise important is the initial selection of the quality characteristics that the experimental program is supposed to satisfy, i.e. the customer expectation. This will allow confident declaration of what, exactly, the analyses of the experimental data will teach the experimenter about the system under investigation. Linking SDE with SES will establish the only way to plan and execute experiments at conditions that will result in valid and statistically accurate and precise conclusions.

Several other quality tools also mostly based on statistics join in. These are statistical quality assurance (SQA) [3], statistical quality control (SQC) [4], Pareto and other distributions [5], cause-effect diagrams, benchmarking [6], the just-in-time (JIT) concept [7] and more. The most widely applied methods are *statistical process control* (SPC) [8] and *quality function deployment* (QFD) [9].

After factor screening by SDE/SES and determination of those factors that significantly influence the plasma spraying process and the coating properties, statistical process control is used to control the process so that despite the existence of internal and external variations the deposited coating is always within design specification. However, if information about the ranking of the controlling factors, i.e. their importance, is lacking the experimenter risks assuming that he/she is in control of a good process with SPC when in reality a nonoptimized process is being controlled (i.e. a local instead of a global extremum of the response surface), or worse, nonimportant factors [10].

An important element of TQM is quality function deployment. The customer of the deposited coating defines its 'quality', i.e. a set of properties that must be adhered to. This information supplied by the customer is analysed by the research team and transformed into engineering design and specification requirements. If this is done properly the final coating will have the predefined 'quality' even if the customer as a nonexpert cannot explain this desired 'quality' in engineering terms.

7.1.1.2 Quality Philosophy

With QFD entering the picture the dichotomy between nonexpert customer and expert designer/engineer can be resolved. In general, the two sources of quality are the research/engineering/technical staff of the coating developer, and the customers that define the term 'quality of the coating'. Since the most important asset of any organization is its staff, empowerment of that staff will be a natural part of any TQM implementation. This means that as much information about the process and the product must flow up and down the hierarchical structures of the company as needed

¹ This is not a trivial task. Starting a research program is rather easy but it takes guts and confidence to stop a program if it does not yield the desired results, i.e. if the program is not on time and within the allocated budget. Managers be aware: 'Self-perpetuating' programs usually waste resources and block the execution of other potentially more promising projects!

by the staff to understand the customers' needs. This informational empowerment encourages staff participation at all levels of the organization with the result of the creation of a considerable degree of initiative, commitment and motivation: a static and routine custodial organization is being transformed to a dynamic and flexible intra- and entrepreneurial one [10]. Because the process and the product quality requirements are fully understood by staff, it will be possible to anticipate, conform to, and also exceed the customers requirements. Only then 'total quality' can be achieved: doing the right things right, the first time, any time!

7.1.1.3 Management Style

The quality philosophy expounded above can only succeed if the style of management matches the quality philosophy's quest for motivation and challenge. This means that no philosophy can work unless it is applied, and it cannot be applied unless it is encouraged [10]. Products not conforming to quality are being subjected to a detailed 'failure/success analysis' or 'design/process monitoring'. The result of such types of analyses is to decide what needs to be done so that the root causes of the unreliability can be controlled. This is the hallmark of a successful TQM: to control the process, not the staff. Staff will feel encouraged to strive for continuous improvement that will create a high degree of autonomy of the teams and an increased level of responsiveness. While working under such conditions of 'enlightened participatory management' team members build trust and respect, share vital information and acquire common values. Hence a code of conduct is created that helps to resolve conflicts effectively and rapidly. In the end productivity as well as quality will be maximized. Several theories describe the productivity improvement operations such as 'Theory Z' [11], Juran's Quality Trilogy [12], Deming's Principles [13] and Crosby's 14 Steps [14].

To conclude the TQM approach involves a chain of events that should be implemented in order to arrive at a high quality process that will result in a high quality product, in this case a superior plasma-sprayed coating that meets the customers demand and expectations. The quality tools of this chain link research, development and product: SDE/SES identify those plasma spray parameters that significantly influence coating performance, process-based SPC ensures consistency in the industrial production of coating through Taguchi-type control designs, and QFD translates consumer demands into technical reality, i.e. engineering factors.

An excellent example how to introduce a quality management system based on the ISO 9001 [15] into a thermal spray company was recently given by Ebert and Verpoort [16]. The ISO 9001 standard is a model for quality assurance in design and development, production and servicing. It contains 20 quality management elements that were described in detail for a company developing new coatings and application areas.

7.1.2 Qualification Procedures

Qualification procedures of equipment, spray powders, process design and implementation, and operators are a mandatory part of TQM.

The success of plasma-sprayed coatings depends on the skill of the operator, the condition of the equipment, and the selection and optimization of the internal and external process variables. Thus it is logical that qualification tests be part of any quality assurance and TQM programs implemented by an organization required to produce components for severe service. The major purchasers of plasma-sprayed components for aircraft engines, for example, require potential suppliers to demonstrate their capabilities before being approved as vendors. The qualification procedures are intended to establish that the vendor has operators, equipment, and processes capable of producing plasma-sprayed coatings of acceptable quality and service life.

As far as plasma-spray system operators are concerned, qualification procedures should demonstrate skill and knowledge, the ability to follow process instructions, and eventually to produce acceptable products. As in the widely used welding qualification procedures, a combination of the following exercises is deemed appropriate [17].

- The operator should take and pass a short written test covering questions pertinent to cleaning, surface preparation and masking procedures, and the general principles of the plasma-spraying equipment and procedures.
- The operator should demonstrate familiarity with appropriate equipment by connecting, setting up, and operating plasma-arc spraying equipment safely according to manuals supplied by the manufacturers.
- The operator should demonstrate capability by depositing an acceptable coating to a specified thickness on an appropriate test specimen. The quality of the test coating should be judged by suitable methods such as bond strength.

The qualification of plasma-spray equipment required by purchasers of critical components is usually directed towards two quality control objectives. First, using a qualified operator, the equipment must be shown to be capable of producing coatings that meet the acceptance quality agreed upon by the vendor and the purchaser. Second, all of the control and metering devices governing deposition variables must be shown to be properly calibrated and checked at regular intervals but at least every 30 days [17].

The purchaser of high quality plasma-spray coated parts normally requires that the deposition process proposed for production be qualified by experiments, in general using methods and principles of SDE. In the qualification tests, the coatings are deposited on strips or samples of standard size representing the material and surface characteristics of those to be used in the spray shop. The coatings are deposited to a specified thickness by qualified operators using written process sheets and qualified, calibrated equipment. Then the coatings will be evaluated by test methods mutually agreed upon.

7.1.3 Powder Characterization

The suppliers of spray powders, and shot and grit used to roughen the surface of the parts to be coated normally provide chemical analyses and information about the particle size of the material. When chemical compositions are to be checked, standard analytical methods are employed. When analyzing metals optical emission

spectroscopy, X-ray fluorescence spectroscopy or ICP spectrometry will be used. Gas contents such as oxygen and nitrogen of metal powders, coatings and substrates are determined by vacuum fusion.

The particle size distribution of spray powders can be determined by a variety of methods and described by different designations. For particle sizes larger than 45 μm the range is characterized by the minimum and maximum cumulative percentages, by mass, that will pass through or be retained by sieves with different designations (ISO designation: mm and μm , respectively; ASTM designation: mesh size). In general, sieving is done with a set of standard sieves, for example ASTM E11-70 [18] and B214-66 [19], assembled in suitable order by nesting in a mechanical shaker. The mass of powder retained at the appropriate sieves is weighed with a balance to a sensitivity of 0.01 g. The recommended sample masses for sieve analyses are 100 g and 50 g for materials having apparent densities, respectively, above or below 1 500 Mg m^{-3} . Data obtained from a sieve analysis of a plasma-spray powder should identify the specific mass fractions passing a particular size opening and retained on screens with smaller openings. The classification should be in size steps small enough to be useful for characterizing the material.

Particle sizes smaller than 45 μm are used to produce coatings with a very smooth finish. Their size distributions are normally determined by the elutriation method described in ASTM specification D293-60 [20]. The method is based on the velocity of particles falling in a countercurrent of air or gas. The results are not strictly accurate for porous particles. Better accuracies can be obtained by applying the Coulter Counter that measures the change in electrical resistivity across an orifice as particles suspended in an electrolyte are passed through the orifice. This change in resistivity is related to the volume of the particles. The effective size range of this instrument is 1.0 to 500 μm . Sedimentation techniques, for example the MSA (Mining Safety Appliance) apparatus extend the particle range to be measured to the submicron range (0.1–80 μm). Modern laser-operated particle analyzers allow for an automated measuring protocol.

'True' particle and coating densities can be determined by Archimedes' technique by dividing the mass of the sample by the volume of water it displaces. If the powder is representative of the material in the coating after plasma spraying, the density determination can be used to compute the porosity of the sprayed coating. More exact densities can be obtained with a helium–air pycnometer.

Useful information on flow rates and apparent densities of powders can be obtained with the Hall Flow Funnel. Data give information on the ease of handling of the powder during processing as well as the densities to expect when powder is placed in the powder feeding device.

7.2 Characterization and Test Procedures

To test and qualify coatings, a limited set of procedures are applied to evaluate *mechanical* (cohesive and adhesive bond strength, shear strength, macro- and micro-hardness, fracture toughness), *tribological* (wear, mechanical fatigue) and *chemical* (corrosion, oxidation) properties.

7.2.1 Mechanical Properties

7.2.1.1 Bond Strength

The quality of a thermally sprayed coating is, to a large extent, determined by the quality of its adhesion to the substrate. While it is generally assumed that the main contribution to the adhesion is a mechanical interlocking of the particle splats with asperities of the grit-blasted substrate surface, increasingly chemisorptive and epitaxial processes are considered important contributors to coating adhesion [21]. This assumption is partly based on the experimental evidence that the presence of intermediate bond coats, preheating of the substrate and high particle temperatures generated by increased plasma enthalpy and/or the residence time translate into thermally activated bonding mechanisms.

Recent results by Gawne *et al.* [22a] indicate that mechanical interlocking may only play a secondary role in coating adhesion. Surface roughening by grit-blasting is then considered only a vehicle to promote disc-shaped particle splats and consequently to suppress exploded splash-type splats. The latter result in voids at the coating–substrate interface because the spaces between individual splashes may be too small for the second lamella to penetrate. Secondly, the flattening on impact of the splash-type splats is more extensive than for the disc-shaped splats. Consequently the lamellae are thinner, cool more rapidly and thus decrease the time available for chemical bonding. Thirdly, during splashing the particles break up into smaller droplets resulting in a loss of continuity of the flowing melt and thus decreased bonding to the substrate.

The requirement of a roughened substrate surface can apparently be relaxed by the application of an initial thin layer (about 25 μm) of ceramic on a smooth metal surface by low-pressure plasma spraying (LPPS) followed by the application of a thermal barrier coating (TBC) by APS technique [22b]. The smooth surface can be an uncoated oxidation-resistant alloy, a metallic diffusion coating, or a plasma-sprayed metallic bond coat ground smooth or even lapped. The LPPS ceramic layer adheres well to the smooth metallic surface but its top surface is sufficiently rough to accommodate the normal thick TBC.

Over the years a large variety of different tests have been devised to measure bond strengths in an accurate and reproducible way. Despite those efforts, however, there is, to date, no reliable method available that can be generally applied to any kind of coating on any kind of substrate. An older review by Davies and Whittaker [23] identified the ultracentrifuge and various ultrasonic techniques as those that could presumably successfully meet the requirements of routine quality control. However, the tensile pull test is still most widely used to determine bond strength [24] even though there is a rather urgent call to interpret tensile adhesion tests in terms of a more appropriate design philosophy [25].

Tensile tests with adhesive

The strength of the bond between a plasma-sprayed coating and the substrate is extremely important for most coating applications. For this reason, tensile testing is most commonly applied to evaluate the cohesive and/or adhesive strength as de-

scribed by the ASTM Specification C633-79 [26] or DIN 50 160 [27]. The main differences between these tests concern the sample dimensions. The method is limited to rather thick coatings exceeding 380 μm (ASTM C633-79) and 150 μm (DIN 50 160), respectively.

As pointed out by Milewski [28] the tensile test methods can be subdivided into, first, tests in which the coatings are pulled off from the substrate with the help of a counter-fixture glued or soldered to the coating, and, second, tests in which the coatings are pulled off from an appropriately formed auxilliary fixture without an adhesive (Sharivker/Ollard test, see below).

Because of the properties of the organic adhesives used application of the test is at or near room temperature. The method is recommended for qualification, quality control, and component or process acceptance testing. It also is applied frequently to compare the adhesive or cohesive strengths of different coatings or different methods of substrate preparation. However, because of complicating factors such as the penetration of the adhesive into a porous coating, the strength data obtained are not suitable for design purposes. Figure 7-1 shows the fixtures for aligning the test specimens [26]. A test specimen consists of a substrate fixture to which the sprayed coating is applied, and a loading fixture. Both fixtures should be round solid cylinders not substantially shorter than their diameters that should be between 23 and 25 mm. The fixtures should be preferably made from the same material that will be used for the production substrates. The material used for adhesive bonding the loading fixture to the substrate fixture must have a tensile strength at least as high as the adhesive and cohesive strengths of the coating. The adhesive should be sufficiently viscous not to penetrate through the coating.

The bonding strength or the cohesive strength of the coating is determined by the quotient of the maximum load F in N required to separate the two fixtures subjected to the tensile test, and the cross-sectional area A in mm^2 : $\text{Strength} = F/A [\text{N mm}^{-2}]$. If the failure occurs entirely at the coating-substrate interface, the value is reported as *adhesion strength*. If the failure occurs entirely in the coating, the measured strength is considered the *cohesive strength* of the coating. Failure in the adhesive can be considered a satisfactory result if the strength value exceeds requirements for quality assurance or qualification tests (Fig. 7-2).

This qualitative distinction between adhesive and cohesive failure modes of a coating can be quantified by a modified ASTM C633-79 tensile test jig developed by Berndt [29] that is able to measure the extension of the specimen during loading. Since already slight misalignments of the specimen with respect to the pulling axis cause inappropriate errors in determining the failure load, any deviations were taken into account by using clip gages positioned on opposite sides of the jig. For tensile experiments using this modified test set-up on ZrO_2 -8wt% Y_2O_3 -NiCrAlY 'tandem' coatings it was found that the stress/strain data approximately fitted a straight line, i.e. the slope of the stress/strain plot is directly proportional to Young's modulus. The probability plot of the stress/strain gradients (Fig. 7-3) reveals a bimodal distribution: large gradients, i.e. large moduli correspond to adhesive failure, small gradients, i.e. low moduli correspond to cohesive failure. Mixed-mode failures are distributed over the entire gradient range.

The German specification DIN 50 160/10.90, analogous to ASTM C633, has been

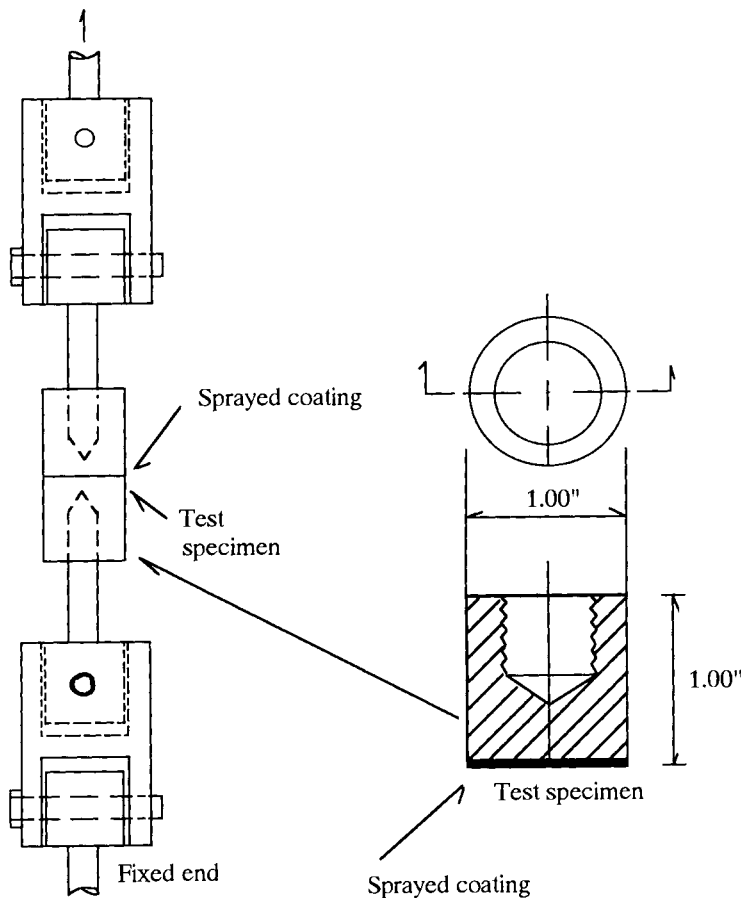


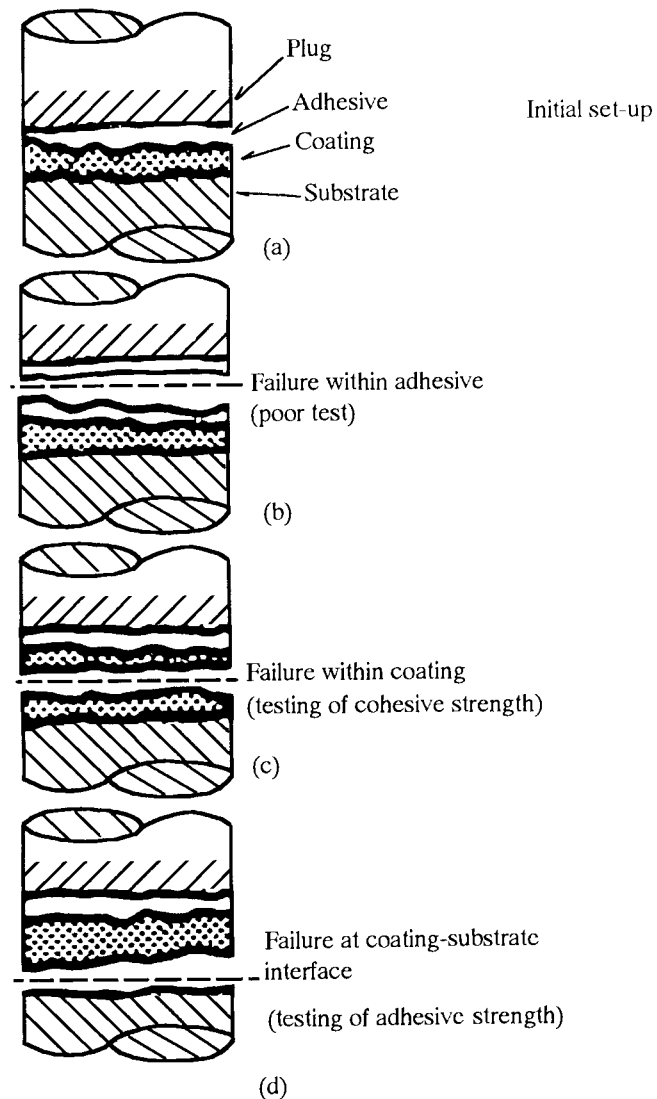
Figure 7-1. Loading fixture used to align the test specimens according to ASTM Designation C633-79 [26].

recently replaced by the European Standard EN 582:1993 [107]. This specification prescribes loading and coated substrate fixtures (configuration A) that allow for torsion- and momentum-free fixation by using ball- and socket-joints. Also, there is provision for having a coated disk of 25 or 40 mm diameter glued between two loading fixtures (configuration B).

Tensile tests without adhesive

Tensile tests without using an adhesive avoid the problem of the adhesive penetrating into open porosity of the coatings thus compromising the accuracy of the measurement. Also, interpretative problems related to the influence of the coating thickness on the measured strength values could presumably be alleviated. The Ollard-Sharivker test [30, 31] uses a special jig (Fig. 7-4a) consisting of a base and a smoothly fitting washer supported on the shoulder of the base. This device is grit-

Figure 7-2. Failure surfaces of loading and substrate fixtures.



blasted and inserted into a plasma spray apparatus through which the top face is coated as shown in the figure. The adhesion strength is determined by tearing away the base from the coating. Since the adhesion strength appears to be a function of the coating thickness, it seems feasible to determine the value of adhesion strength unaffected by internal stresses by extrapolating the adhesion strength vs. coating thickness curve to zero thickness as shown in Fig. 7-4b. When a certain critical coating thickness, δ_c , is reached, spontaneous peeling of the coating from the substrate is observed. With decreasing thickness the strength of adhesion increases linearly. Failure takes place in an adhesion-type stripping mode along the coating/substrate

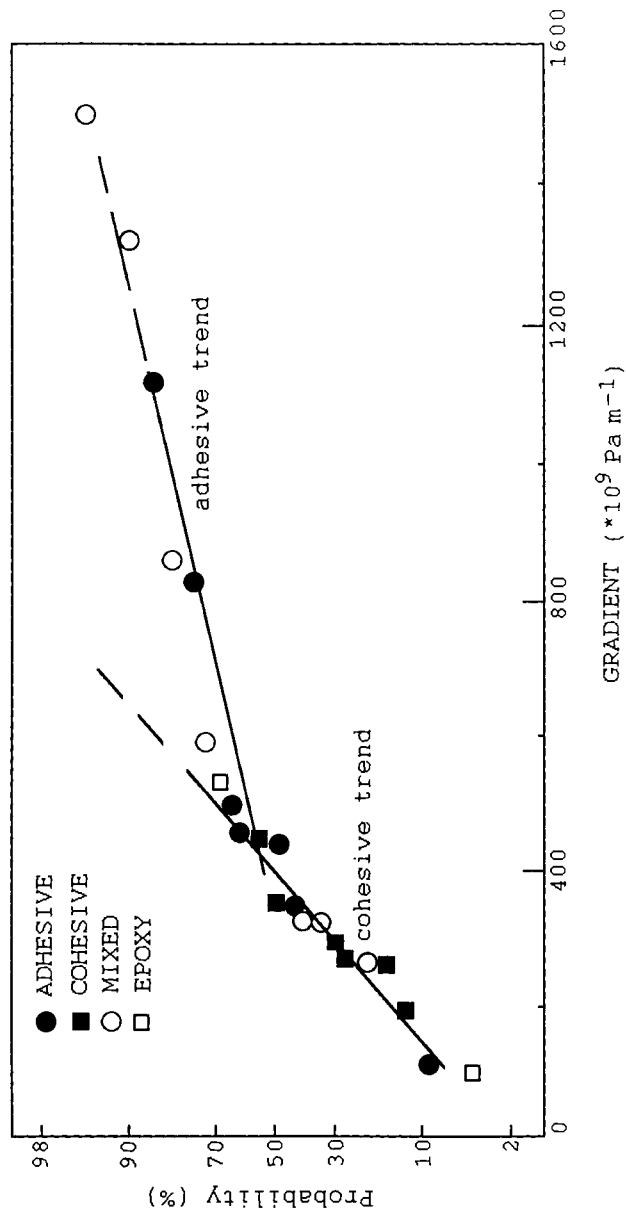


Figure 7-3. Probability plot of stress/strain gradients for a modified ASTM C633-79 test on ZrO_2 -8 wt % Y_2O_3 /NiCrAlY TBC [29].

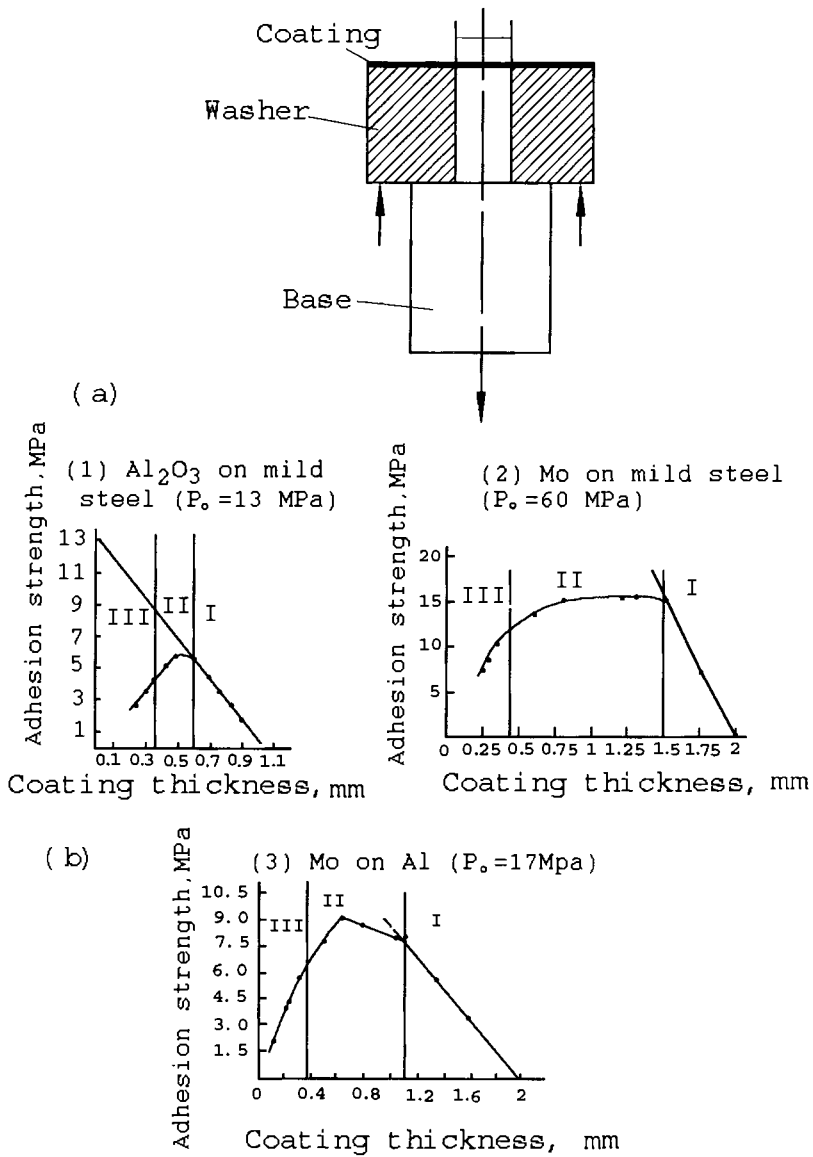


Figure 7-4. Test jig for the Ollard-Sharivker test (a), and adhesion strength versus coating thickness curves (b) for several coating/substrate combinations extrapolated to zero thickness [31].

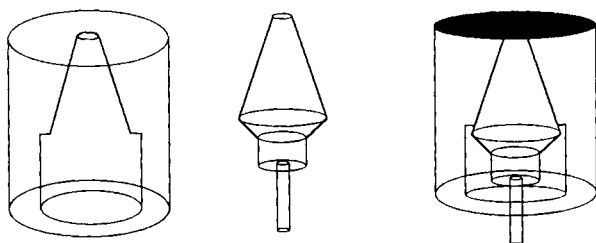


Figure 7-5. 'Pin-hole' test arrangement [36].

interface (zone I). With further decrease of the thickness a transition to cohesion-type stripping occurs (zone II), and finally coating rupture is observed (zone III). For example, the adhesion strength at 'zero' thickness (P_0) is extrapolated for an alumina coating on a steel substrate (coating conditions: 220 A, 85–95 V, argon/hydrogen plasma, argon flow rate 35 l min^{-1} , hydrogen flow rate 4.5 l min^{-1} , stand-off distance 75–100 mm) to be 13 MPa (Fig. 7-4b, 1). This value is comparable to that of a Mo coating on an Al substrate but much lower than that of a Mo coating on steel (Fig. 7-4b, 2 and 3). The geometry of the jig shown in Fig. 7-4a may not be optimal since there is a risk that separation occurs not by tensile forces but by bending or shearing. To account for this the original Ollard test was modified by Roehl [32], Hothersall and Leadbetter [33], Bullough and Gardam [34] and Williams and Hammond [35] (see also Milewski [28]).

A variant of the Ollard test is the 'pin-hole' test (Fig. 7-5). A pin with a diameter of 2 mm is fitted into a massive disc so that the end faces form a planar surface onto which a coating can be deposited [36]. The pin is then pulled off the disc, and the bond strength can be determined by the force at which it detaches from the coating.

Shear tests

These tests are based on the generation of stresses that act tangentially to the coating/substrate interface. It is quite difficult to localize the stresses exactly in the contact plane when the coated workpiece had undergone a preliminary milling or threading treatment. But even after customary surface preparation by grit blasting the shear forces occur predominantly in the coating itself and not at the contact plane coating/substrate [37]. Variants of the experimental realization of testing devices have been shown by Milewski [28]. Figure 7-6 shows a device suggested earlier by Metco Inc. [38]. The test is performed on a half-inch wide coating band deposited at the grit-blasted surface of a solid round cylinder. The former is subjected to an axial pressure to shear off the coating from the cylinder. After assembling the two sleeves and the round cylinder, grit-blasting, cleaning and depositing the coating, the set screws will be loosened and the cylinder will be pushed in the direction of the arrow to shear off the coating. The accurately measured load is used to calculate the shear force, and thus the shear strength of the coating. Friable or porous coatings should be given a top coat of stainless steel or Ni–Cr alloy to improve the distribution of the shear stress over the test section. A drawback of this technique is that shrinkage stresses induced into the coating during cooling after spraying will affect the mea-

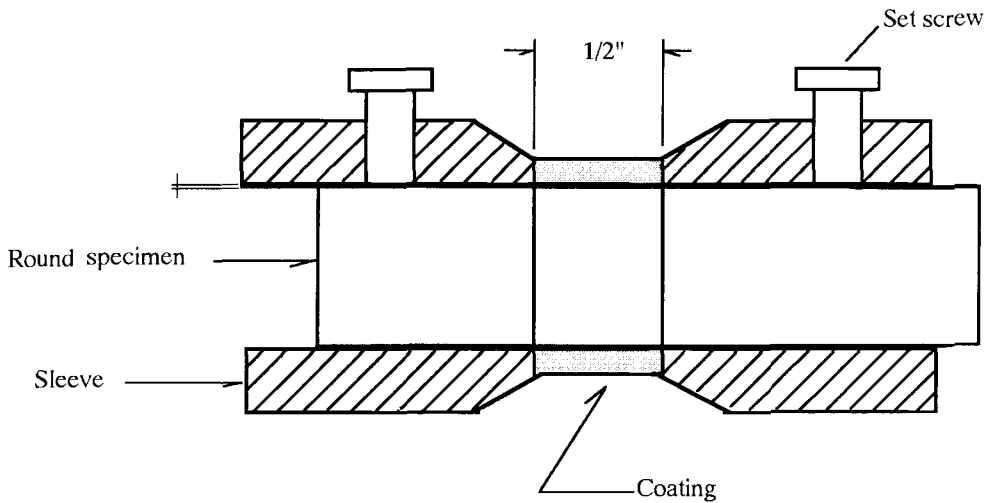


Figure 7-6. Device for measuring the shear strength of coatings (according to Metco Inc. [38]).

sured shear strength to a considerable extent. A shear test devised by Grützner and Weiss [39] attempts to circumvent this problem.

Peel test

Recently a modified ASTM D-3167 peel test was introduced by Sexsmith and Troczynski [40]. A coating is deposited onto a metal foil soldered to a massive copper block that provides mechanical support and acts as a heat sink. The block, foil and coating assembly is glued to a stiff aluminum plate and the copper block is then removed. Peeling off the foil from the coating (Fig. 7-7) causes a crack to propagate precisely along the coating/foil interface in a controllable manner because the sample geometry forces the crack tip to move along the interface [41] where it encounters the local least energy path. Although more work is required to fully characterize and evaluate the potential of this adhesion test, its highly controlled crack tip behavior opens up a new way of coating quality testing.

Scratch test

This method uses a Rockwell diamond pressed with increasing load into the coating surface and subsequent pulling away the sample. The ultrasonic signals from breaking of the coating and the interface, respectively as well as the increasing tangential force are measured during loading. Changes in the slope of this force indicate changes of the coating properties, changing in the ultrasonic signal point to coating failure through chipping and spalling as well as loss of adhesion. After the test the trace of the scratch can be evaluated microscopically. Figure 7-8 shows the recorded tangential force of a VPS (Ti, Mo)C–NiCo coating [42] tested in the range 100–200 N with a CSEM Revetest Automatic Scratch Tester. The coating thickness was 70 μm . The slope of the tangential force versus distance (time) shows a noticeable

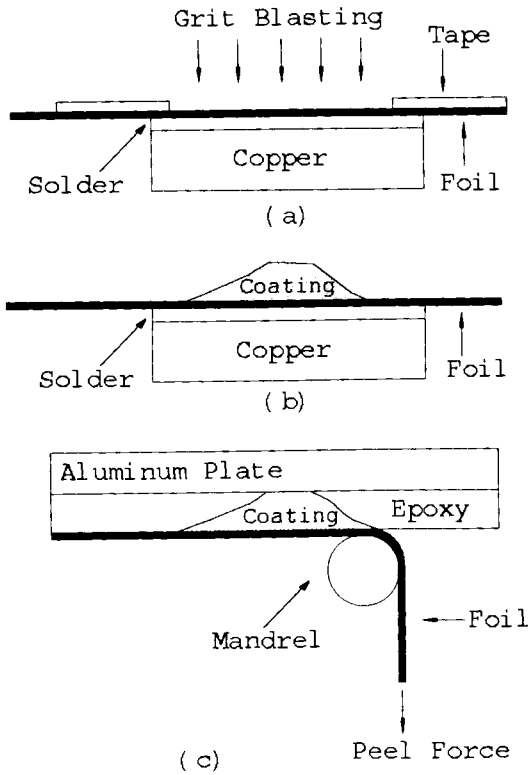


Figure 7-7. Peel test after [40] (a) schematic cross-section of the sample block before spraying, (b) sample block ready to be soldered to Al plate, (c) sample sandwich ready for peel test.

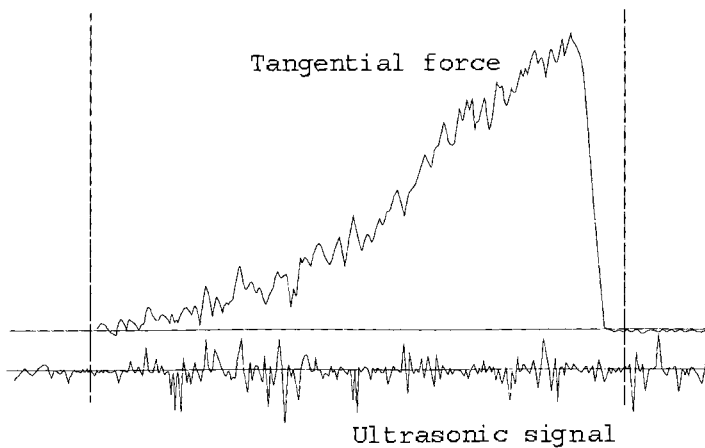


Figure 7-8. Recorded tangential force of a VPS (Ti, Mo)C-NiCo coating and ultrasonic signal obtained with a CSEM Revetest Automatic Scratch Tester [42].

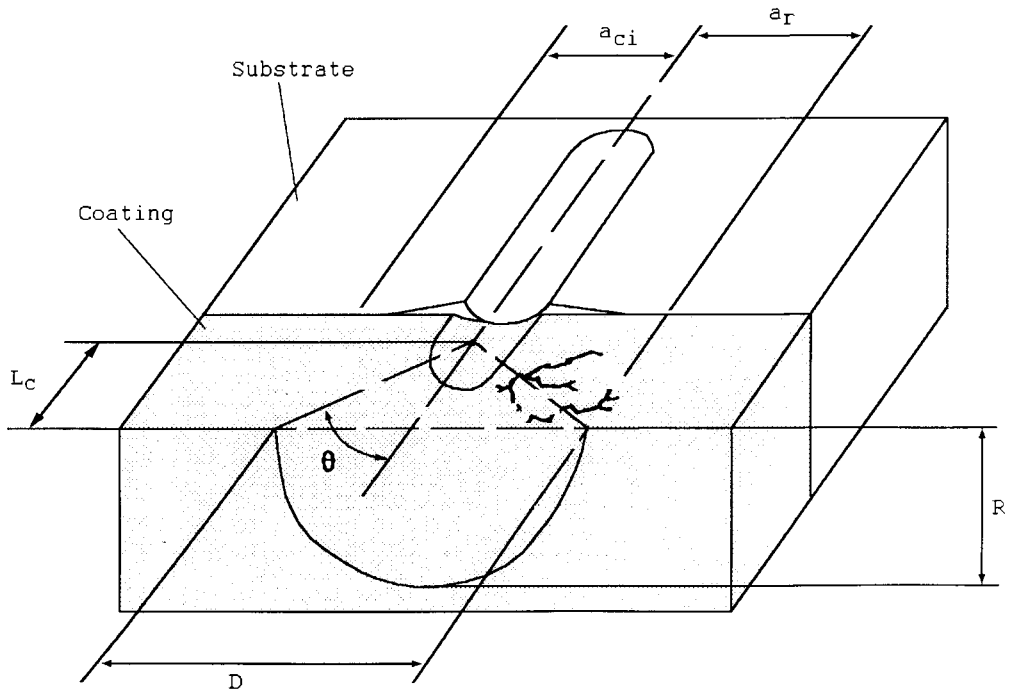


Figure 7-9. Interfacial fracture processes occurring during a scratch test [43].

change. Since the very hard and extremely well-adhering coating did not fail, this change in slope may be attributed to heterogeneities in the coating or even the influence of the substrate because of the rather thin coating. The noisy curve is due to the high surface roughness of $R_a = 30 \mu\text{m}$. The lower wiggly line in Fig. 7-8 is a recording of the ultrasonic signal that also shows no indication of a coating failure but remains within the range of the instrumental noise.

A similar test involves traversing a Rockwell C diamond under a fixed load across a polished cross-section of a coated substrate. Figure 7-9 shows schematically the interfacial fracture processes occurring [43]. At a critical distance (cone depth), L_c , the cracks formed in the coating propagate to the free surface and form a half cone-shaped chip whose depth R is a function of the applied indenter load and seems to be a measure of the coating cohesion. According to Belzung *et al.* [44] the cone depth L_c is related to the indentation load by $F_N = AL_c^{3/2}$ where A is proportional to the fracture toughness, K_c . However, the relationship for APS tungsten coatings was found to be linear by Gudge *et al.* [43].

Ultrasonic tests

With high-frequency ultrasonic waves defects at the coating–substrate interface can be detected and qualitatively related to the coating adhesion. In the second technique, low-frequency ultrasound induces stresses at the interface sufficiently high to

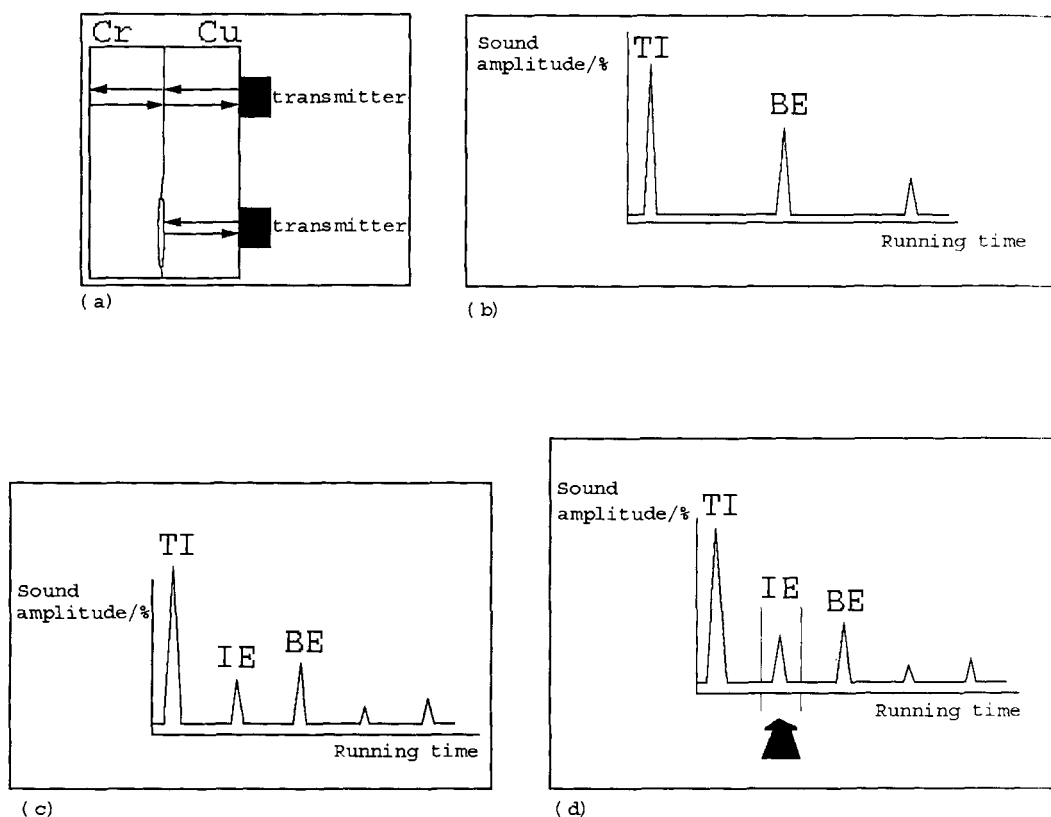


Figure 7-10. High frequency-ultrasonic adhesion test. (a) Geometry of the measuring device, (b) a-scan diagram of a well-adhering chromium coating on a copper substrate, (c) a-scan diagram indicating a coating failure by the presence of an interface echo, and (d) setup for obtaining a c-scan diagram by filtering out the interface echo [46].

detach the coating. The third technique is a combination of the first two, low-frequency ultrasonic energy being used to produce interfacial stresses, and a simultaneously applied high-frequency signal to detect any defects generated by the stressing [23]. Holographic imaging of ultrasonic waves allows imaging of the defects and determination of their size, geometric form, and position. The best sensitivity is obtained if the penetration depth of the induced surface waves is about eight times larger than the coating thickness [45]. Figure 7-10a shows the geometry of the measuring device. As long as there is good bonding between substrate (copper) and coating (chromium) the transmitted signal passes through the interface almost undisturbed. It is first reflected at the back wall and then detected at the copper surface (top). Coating failure is depicted in the bottom part of Fig. 7-10a: the sound waves will be totally reflected at the Cu/Cr interface. Figure 7-10b shows the so-called a-scan diagram of the first case with the transmitted impulse (TI) and the first back wall echo (BE) with its much weaker repetition after twice the original running time. In Fig. 7-10c the situation is shown when a small failure in

adhesion occurs. The waves will be partially reflected at the interface (IE) and only later at the back wall (BE), again with their weaker repetitions. Since only the amplitude of the interface echo is indicative of a good adhesion it is being filtered out of the total spectrum by a narrow strip-shaped window (Fig. 7-10d) and processed separately. Within the bounds of the set window the transmitter is being scanned across the sample and the so-called c-scan diagram is obtained. A useful scanning row distance and step width of 0.5 mm each results in a pixel area of 0.25 mm². The best signal resolution in the case of thick VPS-sprayed chromium coatings on copper was achieved using a sound wave frequency of 5 MHz [46]. A specific color can be assigned to each detected amplitude value. Figure 7-11 shows such a color-coded c-scan map of a thick VPS-sprayed chromium coating on an 8 mm thick copper plate. Dark red colors were assigned to 0% coating failure, i.e. maximum adhesion strength, dark purple colors to 100% coating failure, i.e. no adhesion. It can be deduced from the color map that a broad band with decreased adhesion exists passing through the center of the electrosark-machined sample [46, 48].

To quantify the results a combination of the signal amplitude of the interfacial echo (IE) in a c-scan, expressed through the color code, and the adhesion strength obtained destructively by an ASTM C633-79 tensile test can be used. In several cases a good correlation was found [47, 48]. Figure 7-12 shows representative results of the correlation between the mean amplitude of the interfacial echo in percentage calibrated against a coating with no bonding (100%) and the adhesion strength measured by an ASTM C633-79 tensile test [48]. Figure 7-12a is the correlation for an 8 mm thick substrate, Fig. 7-12b for a 5 mm substrate.

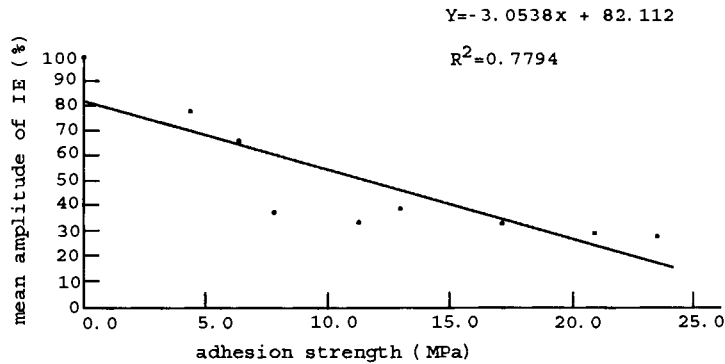
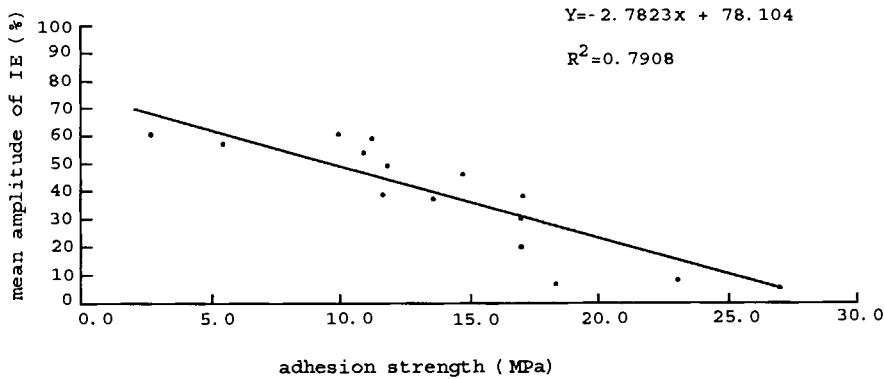
To extend the application of ultrasonic testing to samples with complex geometric shapes, recently a robot with five axes was constructed that can change the angle between sample surface and ultrasonic beam automatically [49]. Echo-impulse techniques with an auxiliary reflector, for example by using water as an immersion medium, allow reliable measurement of the adhesion of very thin coatings since the resolution of the reflected signal is much improved. Also, the coupling of the signal head is more uniform [25, 50].

Thermal wave ND scanning

Nonbonded areas perturb the heat flow through the coating into the substrate and thus affect the transient surface temperature [51a]. Bonding defects as small as 300 μm in size can be reliably localized, and such of 150 μm can be detected. Although the test results are affected by scores of parameters the operation does not require a high degree of knowledge of the emissivity of the materials. Thus thermal wave scanning has proved to be a valuable quality assurance tool for thermally sprayed coatings.

Heat is applied to the coating surface by an air-operated heating nozzle. The stream of hot air (500 to 600 °C) is switched between the nozzle and a bypass tube. A computerized infrared radiometer is used to record and store the surface temperature that is affected by the density of bonding defects. Figure 7-13 illustrates a scan of a plasma-sprayed NiCrAlMo bond coat–Al₂O₃/TiO₂ top coat duplex system on a valve stem that failed in service.

With time-resolved infrared radiometry (TRIR) thickness variations and debonding of zirconia thermal barrier coatings have been studied [51b]. In this case the



(b)

Figure 7-12. Representative results of the linear correlation between the mean amplitude of the interface echo (see Fig. 7-10d) and the adhesion strength measured by ASTM C633-79 for chromium coatings on an 8 mm thick (a) and a 5 mm thick (b) copper substrate [46, 48].

sample is pulse-heated as opposed to the continuous wave photothermal radiometry (CW-PTR) where a continuous modulated heating from a laser source is used. Mathematical modeling of thermal wave NDT of TBCs using numerical finite differences has been attempted by Georgiou *et al.* [52].

7.2.1.2 Macro- and Microhardness Tests

Coating hardness values are often reported to compare the performance of coatings in service as well as the effects of spray variables. These hardness values should gen-

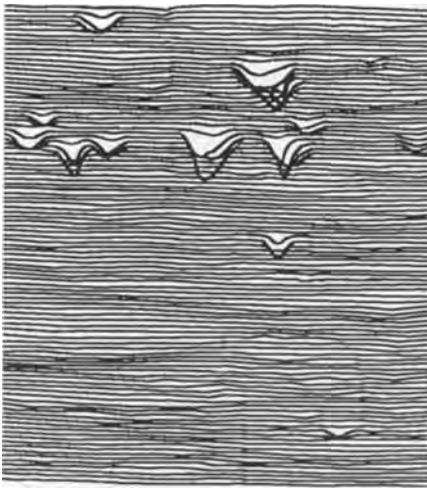


Figure 7-13. Thermal wave ND scan of a NiCrAlMo/ Al₂O₃-TiO₂ duplex coating showing bonding defects [51a].

erally not be considered as a measure of the actual coating strength. For thin and porous coatings with a low cohesion strength macrohardness tests are not applicable. Microhardness tests require careful determination and interpretation so that frequently Rockwell superficial hardness tests are being applied that are simpler to conduct than the standard Vickers or Knoop indentation tests (see below).

Rockwell hardness tests

Procedures for Rockwell superficial hardness tests are laid down in ASTM standard E18-74 [53]. In contrast to a normal Rockwell test this procedure employs smaller loads. The superficial hardness apparatus measures the difference in depth of indentation caused by a minor load (3 kgf) applied first and a major load (15–50 kgf). One unit on the superficial hardness scale represents a penetrator movement of 1 μm between minor and major loads. Most commonly used are the diamond penetrator (N scale) and the ball (T scale). There is no reliable general method of converting hardness numbers from one Rockwell scale to another, or to tensile strengths. The choice of an appropriate scale to use for measuring superficial hardness depends on the hardness and thickness of the coating.

The requirements of the plasma-sprayed coatings to be tested are surface cleanliness and absence of gross imperfections. The impressions of the penetrator should be spaced at least three impression-diameters from each other and from a free edge. Five determinations are normally sufficient to obtain reliable results. A surface finish of 1 μm is recommended for using the 15 N (15 kgf, diamond penetrator) scale. While flat specimens are preferred testing of curved specimens requires correction factors.

Microhardness testing

The standard methods of determining microhardness by indentation of a diamond pyramid are described in ASTM standard E384-73 [54]. Depending on the shape

of the indenter, Knoop and Vickers-type diamonds can be distinguished. In both systems, the hardness number in N mm^{-2} is the force exerted on the specimen by the diamond indenter used to produce the impression. In principle, both systems are less affected by porosity than scratch tests based on measuring the indenter travel caused by a specific increase in load. Microhardness tests are usually made transverse to the coating surface, even though loads occurring in service are usually normal to the surface and hardness may vary because of the anisotropy of the microstructure. It is often convenient to make microhardness indentations on specimens prepared for metallographic studies of coatings.

Even though it appears to be relatively easy to perform the measurements the microhardness can be affected by very many parameters including residual stresses, grain size, grain orientation, and the presence of pores and microvoids [55]. Therefore, microhardness is not an intrinsic quantity independent of operating conditions but characterized by the fact that the measured value depends on the applied load. The usual formula used for determining the Vickers hardness is

$$H_V = 1.8544(P/d^2), \quad (7-1)$$

where P is the load in kgf or Newton, and d the diagonal of the indent in mm. In this equation, however, the influence of the load P on H_V is not considered even though it is often observed experimentally that the measured hardness increases as the pyramid load decreases. This nonlinear behavior has been found for SiC [56], TiO_2 [57], Cr_7C_3 [58] and VC [59]. In order to account for the load dependence of the hardness two approaches are usually taken:

$$(i) \text{ Meyer's approach [60]: } P = a_m d^n, \quad (7-2)$$

where n represents the load–hardness dependence. If $n = 2$, then the hardness is independent of the load. Also, a relation was given by Burnett and Page [61] to describe the hardness in the regime of small loads as $H = qd^{m-2}$, where q is a constant and m the ISE index (indentation size effect).

$$(ii) \text{ Thomas' approach [62]: } H = H_0 + (b/d). \quad (7-3)$$

These relations, however, cannot be directly applied to thin films or coatings unless their thicknesses are several times (typically ten times [63]) greater than the indentation depth so that the subsurface deformation beneath the indenter is not influenced by the proximity of interfaces or free surfaces [63, 64]. Those interfaces can be considered for a stratified coating using Bückle's proposal [65] that the hardness should be expressed as a weighted sum of the hardnesses of the different layers. In this spirit a coating/substrate tandem could be considered a two-layer material whose composite hardness is then

$$H_C = \alpha H_F + \beta H_S = H_S + \alpha(H_F - H_S), \quad (7-4)$$

with $\alpha + \beta = 1$, and where H_F = coating hardness and H_S = substrate hardness. The correlation factor α varies from 1 (coating hardness is not dependent on the sub-

strate, i.e. the coating thickness t is at least ten times the indentation depth D) to 0 (coating thickness t is negligible compared to the indentation depth D).

The geometric approach by Jönsson and Hogmark [66] separates coating and substrate contributions to the measured composite hardness by applying a simple 'area law of mixtures':

$$H_C = (A_F/A)H_F + (A_S/A)H_S, \quad (7-5)$$

where A_F = area of indentation within the coating and A_S = area of indentation within the substrate ($A = A_F + A_S$). Figure 7-14a shows the geometry used by Jönsson and Hogmark for their model, and the definitions of A_F and A_S . From geometric considerations an equation can be derived that describes the composite hardness as a function of the ratio t/d using a constant C that takes the value $C = 2 \sin^2(11^\circ)$ for hard coatings on very soft substrates or $C = \sin^2(22^\circ)$ for coatings whose hardness is comparable to that of the substrate:

$$H_C = H_S + \{2Ct/d - C^2(t/d)^2\}(H_F - H_S). \quad (7-6)$$

In Eq. (7-6) the parameter t is the thickness of coatings and d is the diameter of the indent ($d \approx 7D$).

Comparison with Eq. (7-4) shows that Jönsson and Hogmark's model is identical to Bückle's when $\alpha = A_F/A = 2Ct/d - C^2(t/d)^2$. Figure 7-14b shows experimental data for thick Cr_3C_2 -25% NiCr coatings [67] and the predictions obtained from Bückle's and Jönsson-Hogmark's relations when the fitting parameter α is plotted against the ratio t/d . While Bückle's model fits the data quite well even for thick coatings the Jönsson-Hogmark model does not. However, modifying the original Jönsson-Hogmark model [67] by assuming that the C -value is not constant but varies continuously with t/d according to

$$C = (t/d)^n, \quad (7-7)$$

then the parameter α may be written as

$$\alpha = 2(t/d)^{n+1} - (t/d)^{2(n+1)}. \quad (7-8)$$

Fitting the experimentally measured hardness values to the modified Jönsson-Hogmark model satisfactory results are obtained for a value of $n = 3/4$ (Fig. 7-14c). This value, however, is purely arbitrary and there is no physical confirmation of its validity yet.

A different way to account for the load dependence of the measured hardness is to apply a correction factor to the measured diagonal of the indent (d_{cor}) to obtain a constant absolute hardness [68]. Combining Eqs. (7-1) and (7-3) one obtains

$$\begin{aligned} H &= 1.8544(P/d^2) = H_0 + (b/d) \\ H_{\text{cor}} &= 1.8544(P/d_{\text{cor}}^2) = H_0 \\ d_{\text{cor}}^2 &= d^2 + (b/H_0)d. \end{aligned} \quad (7-9)$$

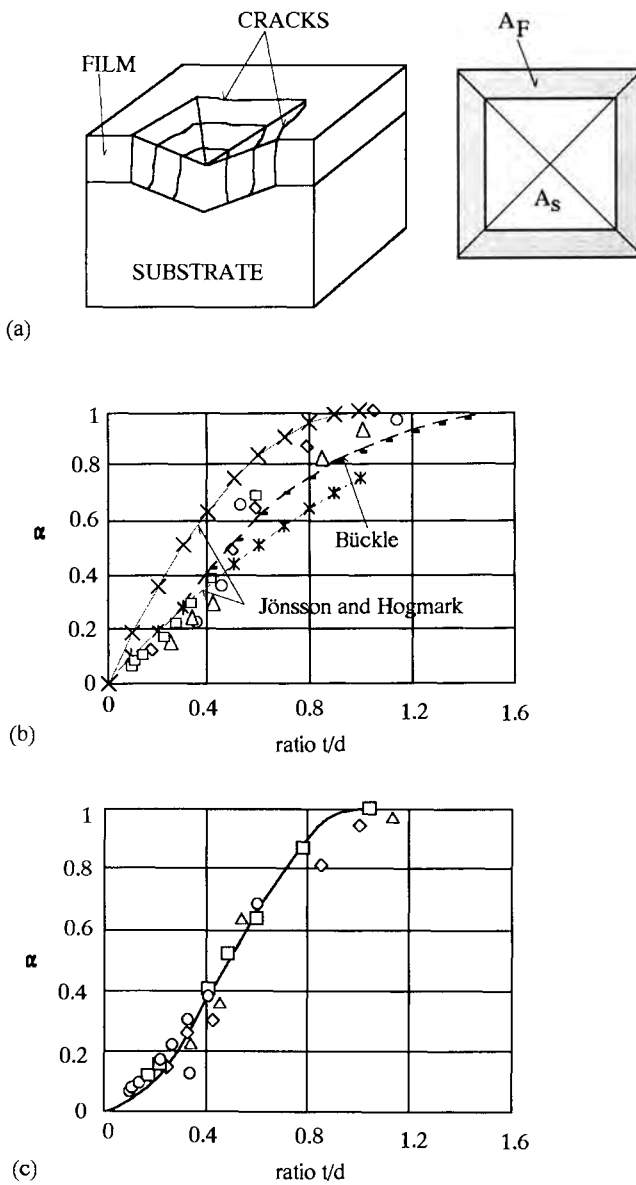


Figure 7-14. Jönsson-Hogmark 'area law of mixture' model (see text). (a) Geometry and definitions, (b) experimental data for thick Cr_3C_2 -25% NiCr coatings fitted to Bückle's [65] and Jönsson-Hogmark's [66] model, (c) experimental data fitted to Jönsson-Hogmark's modified model [67].

Introducing this expression into Jönsson and Hogmark's original equation the following equation is obtained [67]

$$H_C = H_{0,S}[1 - (t/d_{\text{cor}})^{n+1}]^2 + H_{0,F}(t/d_{\text{cor}})^{n+1}[2 - (t/d_{\text{cor}})^{n+1}], \quad (7-10)$$

with the limiting conditions

$$\text{if } t/d_{\text{cor}} = 0 \quad \text{than} \quad H_C = H_{0,S}$$

$$\text{if } t/d_{\text{cor}} = 1 \quad \text{than} \quad H_C = H_{0,F}.$$

The hardness of a material is related to the plastic work done in creating an indentation. Based on this concept, Burnett and Rickerby [63] developed a model that took into account the relative plastic zone size and the related amount of plastic work. Spherical cavity analysis (Marsh's relation [69]) done on the indentation that creates a hemispherical plastic zone showed that the size of the latter varies with the size of the Vickers indentation according to [70]

$$b/a = c(E/H)^{1/2} \cot^{1/3} \phi, \quad (7-11)$$

where a = indentation semidiagonal, b = radius of plastic zone, c = constant close to unity, and ϕ = indenter semiangle (74°). With this relation a nonlinear 'volume law of mixture' model was suggested by Burnett and Rickerby [63] that incorporated the so-called ISE term (indentation size effect), i.e. the dependence of hardness on load at small indentations as well as the plastic zone size term to yield

$$H_C = (V_F/V)H_F + (V_S/V)\chi^3 H_S \quad \text{for } H_S < H_F \quad (7-12a)$$

$$H_C = (V_S/V)H_S + (V_F/V)\chi^3 H_F \quad \text{for } H_F < H_S, \quad (7-12b)$$

where V_F and V_S are deforming volumes to be calculated using (7-11), and χ is an 'interface parameter':

$$\chi \propto (E_F H_S' / E_S H_F')^{n/2}, \quad (7-13)$$

where E_F and E_S = modulus of elasticity of coating and substrate, respectively and H_F' and H_S' = characteristic hardness values. The interface parameter is a strong function of the mismatch between the radii of the plastic zone predicted from Eq. (7-11) and also includes deviations from the ideal geometry of the indent. Its value is strongly dependent on the ability of an interface to accommodate the shear stress arising from this mismatch. It may therefore be regarded as a measure of the rigidity of the interface, i.e. the coating/substrate adhesion governing the transmission of shear stresses from a deformed layer to an initially undeformed substrate.

7.2.1.3 Fracture Toughness

It is questionable whether toughness measurements on ceramic coatings actually tell much about the material. Data are often inconsistent, and strength and toughness do

not always respond in the same manner to changes in microstructure of the coating or their interfacial properties. These inconsistencies arise from the sensitivity of the measurements to specimen preparation, i.e. precracking, getting a crack to grow properly in a double-torsion test, and specimen alignment. These problems have been well worked out over the years in more forgiving metals. For example, the fracture toughnesses K_{Ic} of bulk materials measured with the double torsion technique are around $50 \text{ MPa m}^{1/2}$ for medium-strength steel, $13 \text{ MPa m}^{1/2}$ for Co-bonded tungsten carbide, and $7 \text{ MPa m}^{1/2}$ for Ca-stabilized zirconia (double cantilever beam test).

A four-point bending test can provide at least some information on the toughness of plasma-sprayed coatings [71]. The test consists of placing a coated beam in pure four-point bending with the coating in tension and recording cracks by acoustic emission (AE) with a piezoelectric transducer attached to the surface of the coating. Simultaneously the coating strain is monitored by strain gages, and the test results are presented as strain to fracture (STF). It was found that for WC/Co coatings the STF (toughness) depends strongly on the residual stresses present (see Sec. 5.5.5) but neither appreciably on the microhardness nor the metal content of the coating. The acoustic signals picked up by the transducer occur at four different amplitudes thus suggesting different cracking mechanisms. Early in the test, low amplitude events around 50 dB took place that were related to pre-cracking or microcracking. On release of the bend stress no visible damage in the test specimen could be discerned. The second type of noise at greater 100 dB amplitude are true coating cracks as confirmed by a close to one-to-one correlation between high amplitude events and the number of macrocracks in the coating following testing. During macrocracking the number of low amplitude events increase strongly. They are considered reflections of the stress wave developed at the crack front and thus are not related to changes in the material. The last type of AE events around 80 dB may be related to cracks that propagate through fewer lamella than the cracks causing the 100 dB events.

Bend tests can also be used to determine the probability of rupture of ceramic coatings using Weibull analysis [72]. Free standing samples of PSZ with a length L and thickness d were subjected to a three-point bend test, and the modulus of elasticity, E and the mechanical strength, σ were determined from the moment of inertia, I :

$$E = FL^3/48fI, \quad (7-14)$$

where F = force, f = displacement of the center point, and

$$\sigma = FLd/8I. \quad (7-15)$$

The probability of rupture Pr of the zirconia ceramic is given by

$$Pr = \exp[-(\sigma/\sigma_0)^m], \quad (7-16)$$

where σ is the applied stress, σ_0 the normalized stress below which 63% of the sam-

ples fail, and m the Weibull modulus. Eq. (7-16) can be written in the following form

$$\ln[\ln(1/1 - Pr^i)] = m \ln(\sigma_r^i) + \ln(1/\sigma_0^m), \quad (7-17)$$

where i refers to the experiment number i when all experiments are classified starting from the lowest values σ_r to the highest, and where Pr^i is estimated by

$$Pr^i = (i - 0.5)/n \quad (7-18)$$

with n = total number of experiments. By plotting the left-hand term of Eq. 7-17 against $\ln(\sigma)$, the slope of the resulting straight line determines the Weibull modulus m , and the intersection with the $\ln(\sigma)$ -axis results in σ_r .

Using the scratch test described above and data obtained for the coating fracture toughness from the half-cone fracture shown in Fig. 7-9, Lopez *et al.* [73] estimated the coating cohesion for plasma-sprayed alumina, alumina-titania, chromium oxide, chromium carbide-NiCr, and WC-Co coatings.

7.2.2 Tribological Properties

There are three primary types of wear: adhesive, abrasive, and erosive. Other composite types of wear include surface fatigue, fretting and cavitation erosion. Since there is no universal type of wear, there is also no universal method or machine for testing wear. Laboratory tests are aimed at simulating service conditions and consider the position of the fixed or loose abrasive, the size, shape and hardness of the dominant abrasive, the direction and speed of relative motion during abrasion, and the contact pressures or loads in the system.

A rubber-wheel test (ASTM G 65) simulates low-stress or scratching abrasion with loose abrasive. Gouging abrasion is tested in a jaw-crusher (ASTM G 81). Sliding wear tests (ASTM G 77, ASTM G 83) and erosive wear tests (ASTM G 73, ASTM G 76) are generally applied to metals and plastics. Tests to evaluate the wear in ceramics are based on the pin-on-disc (POD) concept. In the microwear pin-on-disc apparatus, a diamond pin with a predetermined applied load rides on the rotating specimen (coating). In the macrowear tester, two freely rotating wheels (Taber apparatus) ride of the rotating specimen assembly that consists of twelve trapezoidal-shape sections held together by a circular ring on the outside edge and a disc in the center. A general discussion of tribological properties of thin films and coatings, thick coatings, and hardfacing has been presented by Kelley *et al.* [74].

Since the wear behavior of coatings is strongly influenced by composition, microstructure, residual stresses and surface conditions, tribological properties of coatings must be evaluated under conditions that match as closely as possible the actual in-service conditions [75]. As this is generally not possible, wear model tests are applied that simulate the very complex wear processes in technical tribosystems under simplifying conditions at ambient conditions [76]. As a consequence, application of the results of such wear model tests to the real world is generally unsuccessful.

To illustrate the degree of complexity, Fig. 7-15 shows the methodology of wear tests for tribomaterials [76]. Wear mechanism maps are particularly useful to reveal the relationships between interaction parameters and dominant wear mechanism [75].

7.2.2.1 Simulation of Basic Wear Mechanisms

These quality assurance procedures involve testing for adhesive and abrasive wear as well as for long-term fatigue and erosive wear. The tests permit to investigate the local behavior of the coating/substrate tandem system subjected only to those basic wear mechanisms. Evaluation of existing models for abrasive wear and impact erosion was performed by Dimond *et al.* [77] to reconcile the results of laboratory wear tests and theoretical models to the true wear performance of a material in service.

Adhesive wear

Friction is generated by local adhesion and subsequent separation of the contact faces of a tribological couple. The contact of the two surfaces does not occur along the entire geometrical surface area A_0 but only with the fraction

$$A/A_0 = (\sigma/H)R, \quad (7-19)$$

where A is the effective contact area. This ratio increases with increasing compressive stress $\sigma = F/A_0$ and surface roughness R , and decreasing hardness H of the materials. The friction coefficient μ is given by $\mu = F_R/F$, where F_R = frictional force = $(d\gamma/dx)A$ and F = compressive load. The energy dissipation γ per glide distance x , i.e. $d\gamma/dx$ in the effective contact area A is the actual physical reason for dry friction [78].

The test of adhesive wear uses the adhesion tendencies of tribocouples to determine an 'adhesion number' $\mu_{v,ad}$ that is numerically different from the friction coefficient defined above [76]. The adhesion number is determined as the ratio of the tangential force F_T to the normal force F_N of a tribosystem consisting of a counterbody attached to a torque rod transferring the torsional momentum to the coating surface that is pressed against the counterbody with the normal force F_N . The torsional momentum is only maintained by adhesive forces, and when the normal force F_N is being relaxed the counterbody slides back to its starting position. From the displacement diagram both F_T and F_N and therefore $\mu_{v,ad}$ as a measure of the adhesive tendency of the tribocouple can be determined.

Abrasive wear

Using the scratch tester mentioned above information on the abrasive wear properties of coatings subjected to the indentation load of a Vickers diamond pyramid can be obtained. The indenter is pressed against the surface of the coating with the normal force F_N and at the same time the sample is being moved relative to the indenter for a distance L_R with a velocity v_R . The measured tangential force F_T is related to

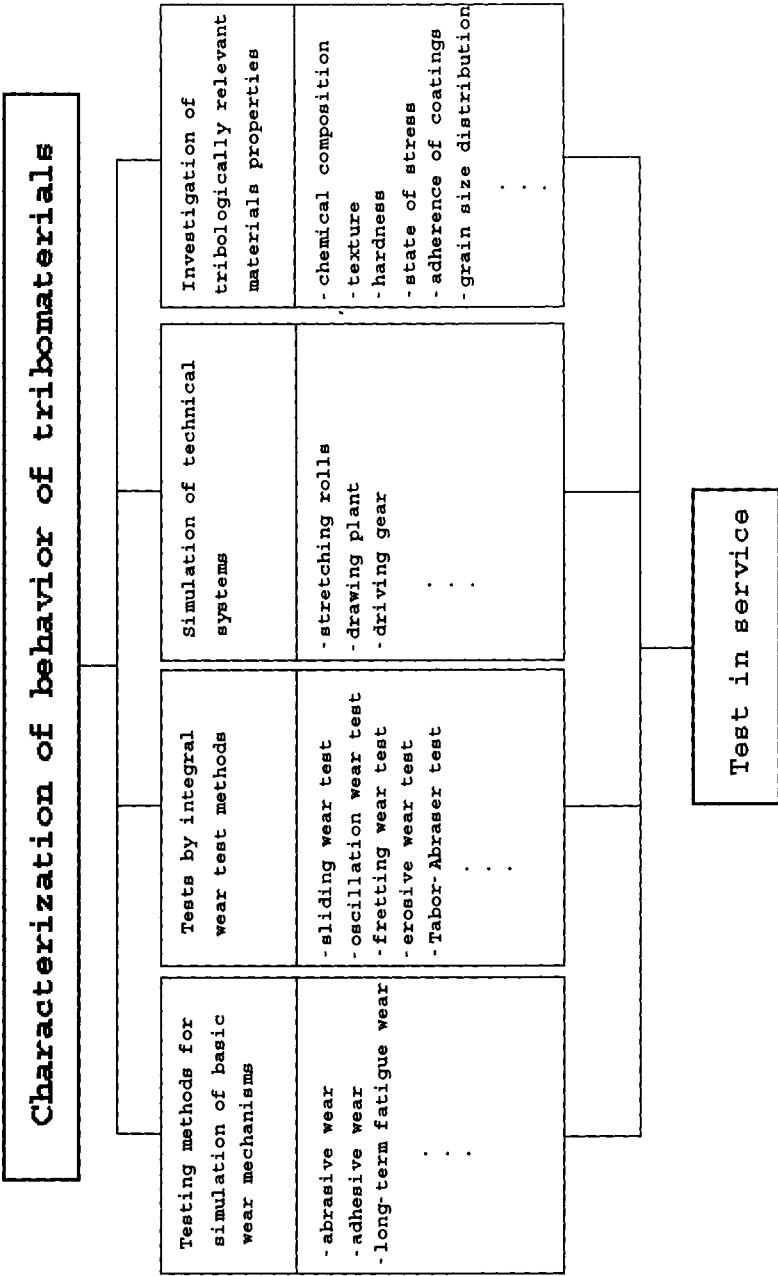


Figure 7-15. Methodology of wear tests for tribomaterials [76].

the volume of the produced scratch that can be determined by laser beam tracing and the scratch energy density W_R is obtained in J mm^{-3} :

$$W_R = (F_T L_R) / (A_R L_R), \quad (7-20)$$

where A_R is the so-called scratch square, i.e. the cross-section of the scratch. Note that the expression in the denominator of Eq. 7-20 is the volume of the material removed by the scratching operation.

Frequently problems occur due to microploughing, microcutting and -chipping and particle pull-out that tend to obscure the scratch traces. Figure 7-16 shows a scratch produced in a (Ti, Mo)C–NiCo coating on a mild steel substrate and its laser-generated profile. The scratch energy density was calculated to be 5.2 J mm^{-3} [42].

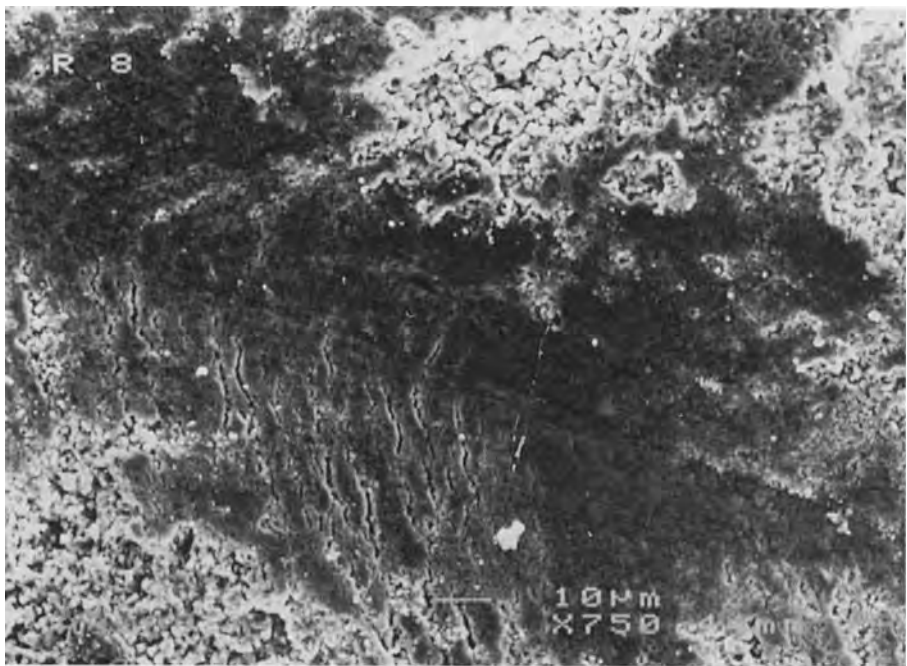
The most frequently applied abrasive wear test is the dry sand–rubber wheel abrasion test according to ASTM G65 [79]. This simple test measures material losses occurring when a coated sample surface is being pressed with a defined force against a steel wheel whose circumference is lined with rubber. Into the gap between the sample and the wheel sand (Ottawa sand) or other abrasive materials are being fed from a hopper reservoir with a constant flow rate (Fig. 7-17). After 2000 revolutions of the wheel the sample is removed and weighed. The loss of material is a measure of the abrasive resistance of the coating.

Long-term fatigue wear

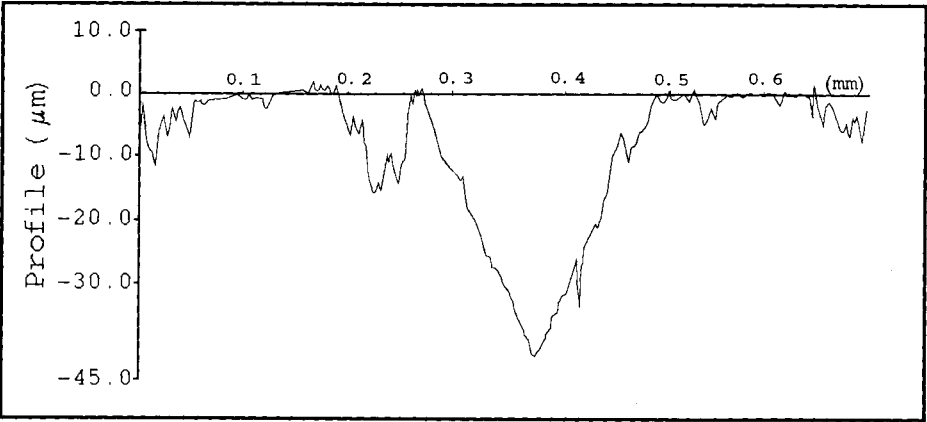
In this test the cylindrical sample to be tested is pressed against a curved counterbody disc whose diameter is ten times that of the cylindrical sample (Fig. 7-18). The curvature of the rotating disc is different in two perpendicular directions in order to minimize the contact surface between disc and cylindrical sample. The load m_A applied generates the normal force F_N . The critical number of load reversals as well as scratch and pit formation are evaluated. This test is still in the development phase [76].

Erosive wear

A widely applied test for erosive wear of ceramics and ceramic coatings is the impact abrasion/solid particle erosion test based on depth of penetration produced by a standard sand or grit blast (ASTM G76-83). Erosion is a mechanism of wear resulting from the impact of abrasive particles on a target material [80, 81]. The erosion rate of a plasma-sprayed coating is a complex function of many variables including the size, shape, velocity, flux and angle of impact of the impinging particles and such coating properties as hardness, grain size diameter (Orowan–Petch relation), porosity (Ryshkevich–Duckworth equation), ductility or fracture toughness. Figure 7-19 is a diagram of the erosion test apparatus according to ASTM G76-83. A screw-feed type metering system releases controlled amounts of an erodent (sand, glass beads, crushed alumina, carborundum etc.) into a flowing gas stream. Particles delivered are picked up in the stream and accelerated through a tungsten carbide nozzle before being directed at the coating surface. Figure 7-20 shows the schematic sequence of



(a)



(b)

Figure 7-16. Scratch produced with a diamond indenter in a (Ni, Mo)C-NiCo coating (a) and its laser-generated profile (b) [42].

Figure 7-17. Dry sand-rubber wheel abrasion test device according to ASTM Designation G65 [79].

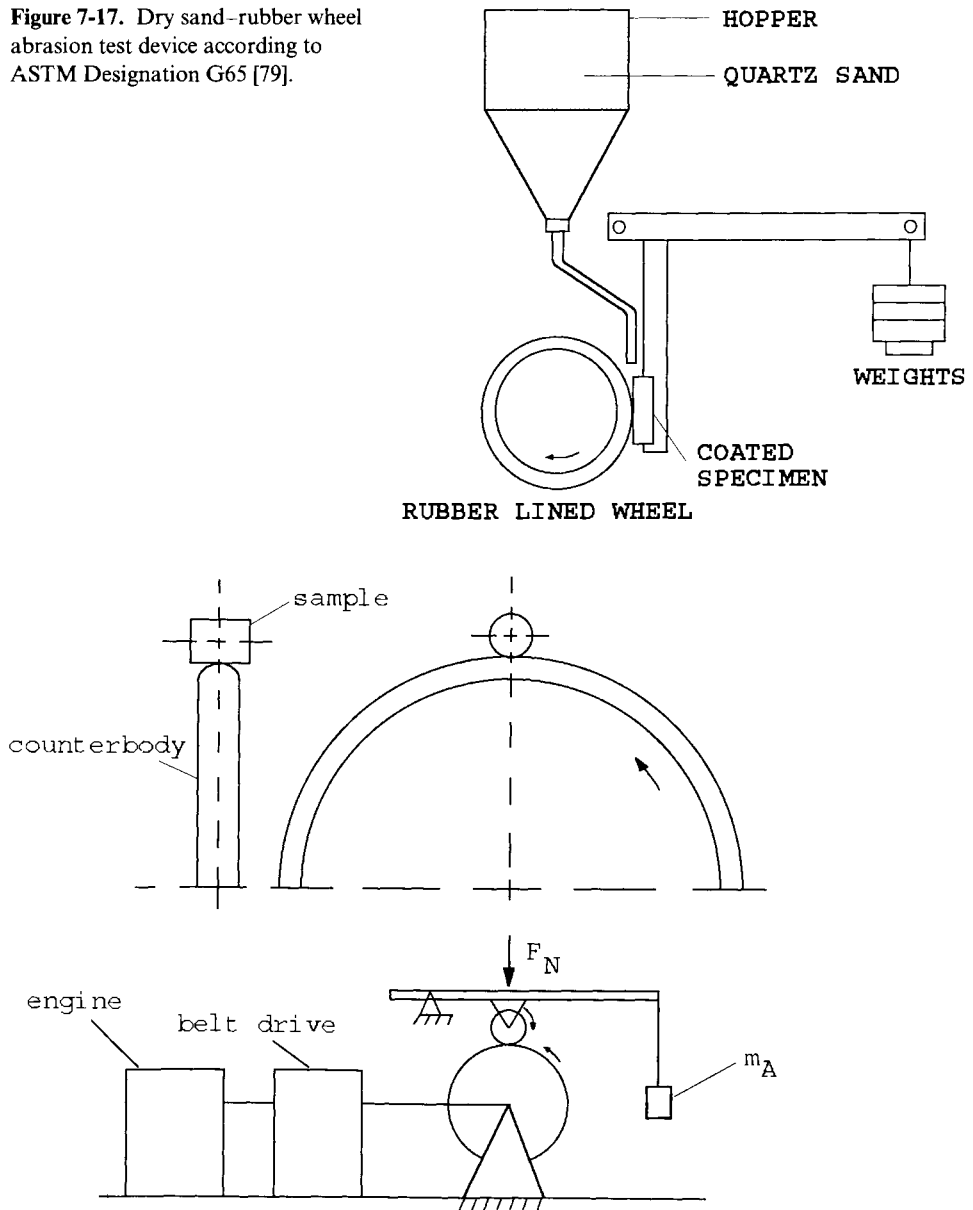


Figure 7-18. Long-term fatigue wear test device [76].

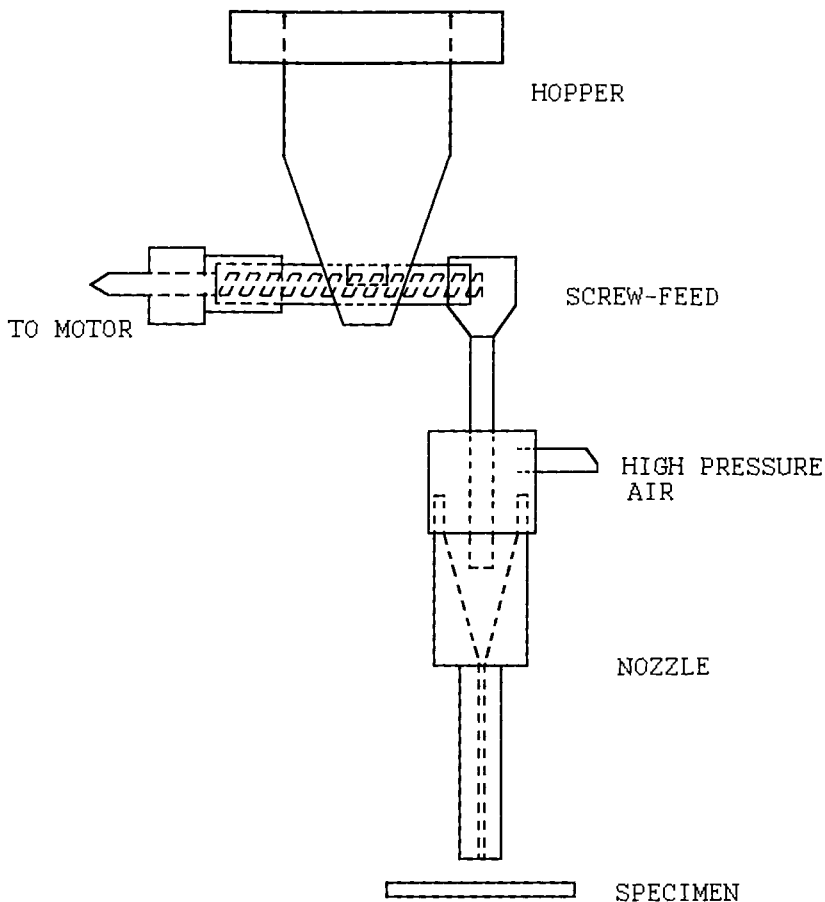


Figure 7-19. Solid particle erosion (SPE) test device according to ASTM Designation G76-83.

events for impact of a high-energy erodent particle [82]. The highly accelerated particles are able to penetrate the coating completely and to deform the metallic substrate underneath in a ductile manner by cutting and ploughing. Release of the deformation energy results in a chipping mechanism that removes parts of the coating and thus exposes the substrate to environmental attack by corrosion or abrasive wear. Maximum loss of coating would be expected at shallow impact angles in the 15–30° range (Fig. 7-21, [83]) and the velocity dependence exponent of erosive wear would be about 2.0 to 2.5 [82].

It should be pointed out that this is an important mechanism of the erosion of high-pressure turbine blades and valve components of fossil-fuel fired power plants [84, 85]. Hard particles of magnetite scale formed at elevated temperature by reaction of steam with ferritic alloy boiler tube material can exfoliate from the interior surfaces of the boiler tubes during boiler transients (startup and cooldown cycles).

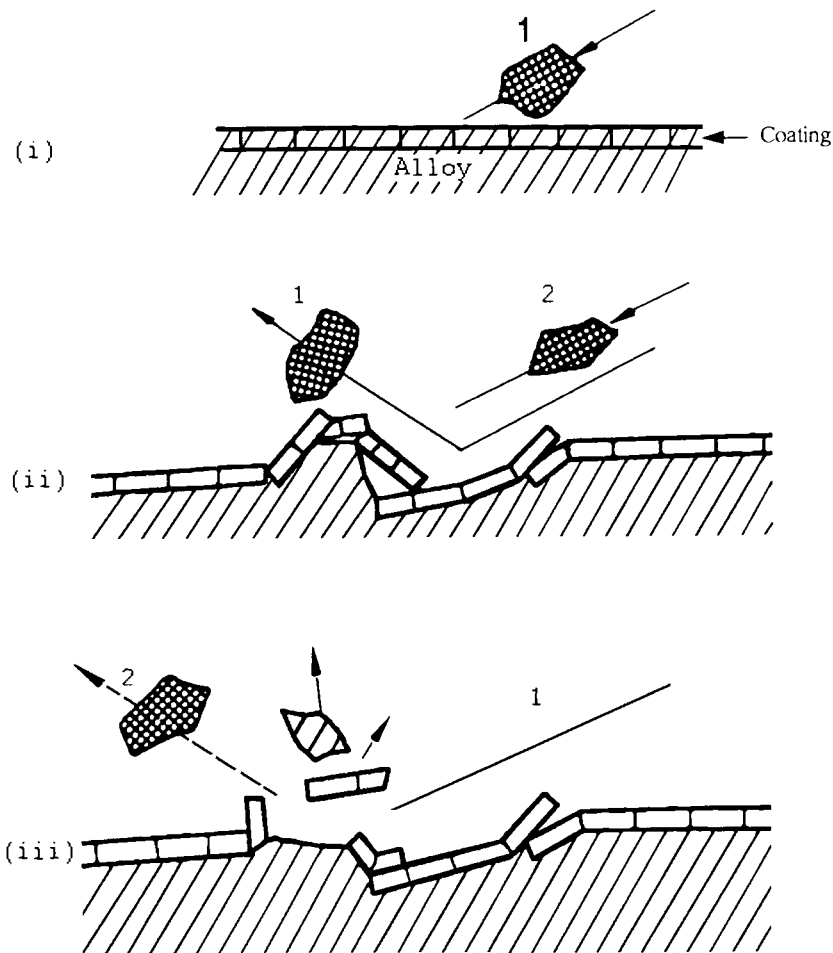


Figure 7-20. Schematic sequence of events occurring during the impact of a high-energy erodent particle onto a plasma-sprayed coating [82].

This solid particle erosion attacks the blade airfoil at various impingement angles when passing through the turbine and also erodes any other component of the steam path. By this mechanism protective coatings along the steam path such as plasma-sprayed $80\text{Cr}_3\text{C}_2/20(\text{NiCrMo})$ coatings [86] can be completely destroyed.

7.2.3 Chemical Properties

Performance specifications of coatings for high-temperature applications, for example gas turbine blades, combustor cans, ladles and tundishes for metal casting etc. require quality testing that must be able to simulate the severe service conditions at

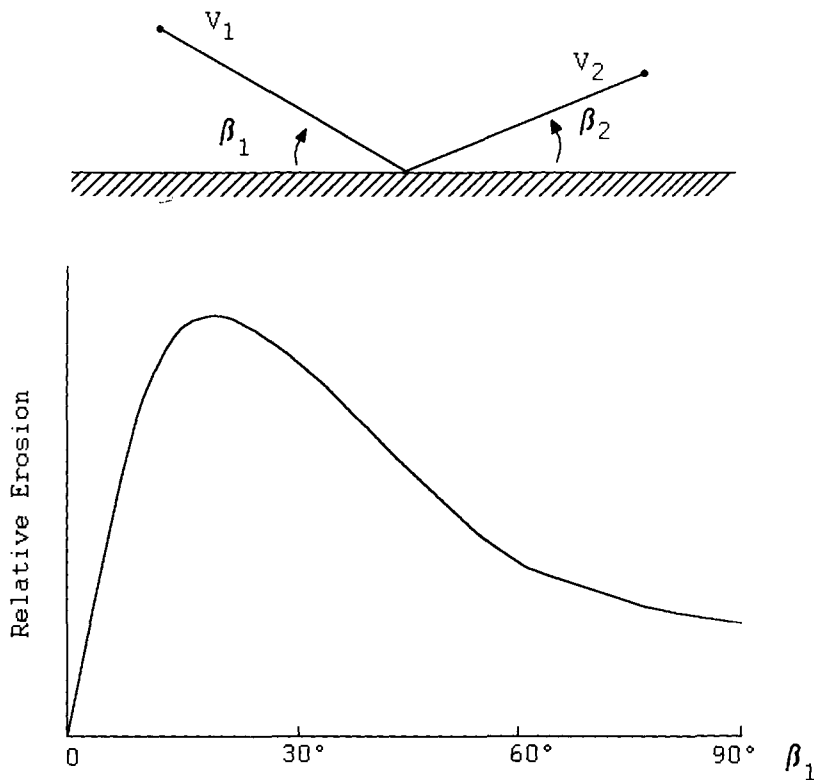


Figure 7-21. Dependence of relative erosion rate on the impact angle [83].

which the coated parts are supposed to function. A comprehensive review of production and performance evaluation of high-temperature coatings has been given by Nicoll [87]. Since the coatings are subjected to synergistic effects of mechanical stresses, temperature and corrosive environment small coating failures can lead to catastrophic destruction of components of engineering systems. Environmental test considerations include the gas temperature, composition, pressure, velocity and temperature cycling. Also, contaminants such as sulfates and vanadates as well as particulate matter can lead to deposition and corrosion, and also destructive erosion effects. Figure 7-22 shows several of such degradation mechanisms that can affect plasma-sprayed stabilized zirconia–NiCrAlY duplex coatings [88, 89]. While in combustion environment hot corrosion of ceramic components such as SiC, Si₃N₄, and SiAlON occurs in a manner similar to dry oxidation, i.e. under formation of a protective SiO₂ surface layer, impurity gaseous species such as Na₂SO₄ and NaCl can condense at the surface of engine components at temperatures as high as 1100 °C and lead to severe corrosion, pitting, and strength reduction [90, 91].

To select a proper protective coating system for high-temperature applications, three main factors must be considered: the applications, the structural alloys to be

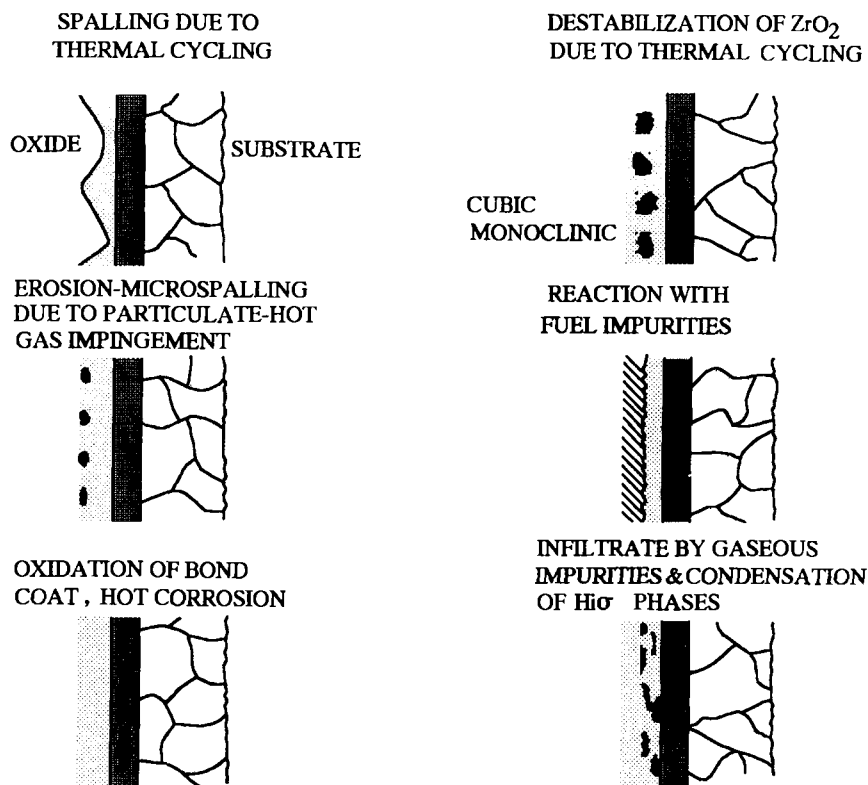


Figure 7-22. Degradation mechanisms of stabilized $ZrO_2/NiCrAlY$ thermal barrier coatings (TBC) [88].

protected, and the coatings themselves. Figure 7-23 show schematically the interactions of mechanical properties, coating processes, and the environmental attack the system is subjected to. The design of the component determines the service stresses, maximum operation temperatures, and service environment. Alloy properties are controlled by chemistry, processing and the resulting microstructure that can also control the high temperature stability [87]. Environmental considerations include the gas temperature, composition, pressure stream velocity, and temperature cycling. Since materials at high temperatures are subject to corrosion phenomena, e.g. oxidation, hot corrosion/erosion or carburization tests to evaluate high temperature performance of coating systems have to account for these interactions. Degradation of coatings also involve creep [92, 93], and low-cycle [94] and thermal fatigue [95].

All evaluation tests at various stages of the development of a high temperature protection coating system can be grouped according to their cost, number of tests required and their extrapolation risk. Thus *screening tests* require many samples at comparatively low cost performed as crucible tests at isothermal exposure. *Bench-scale tests* such as creep testing need fewer samples but the costs are increased. *Com-*

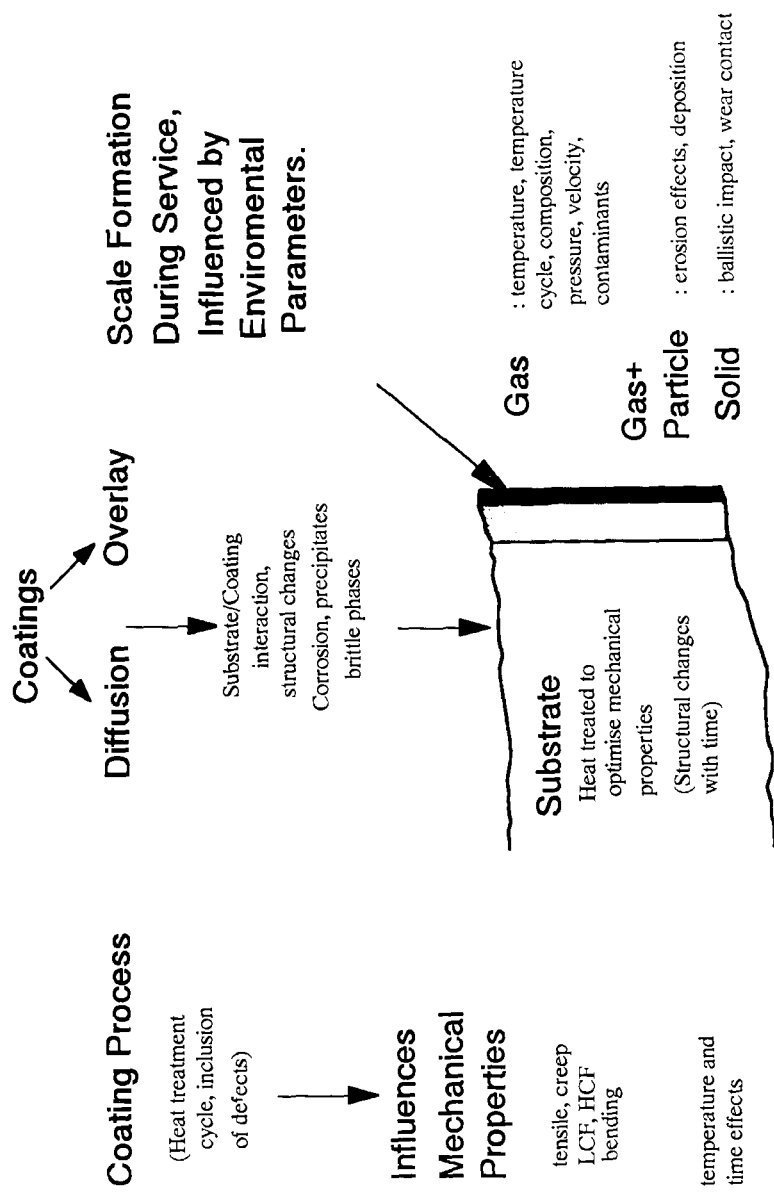


Figure 7-23. Interaction of mechanical properties, coating processes, and environmental attack for high temperature-resistant coatings [87].

ponent tests use a simulated service environment such as burner rig testing for gas turbine blades. Finally, tests designed to provide *service life prediction and systems verification* are most expensive, require but a few samples, and are performed in a pilot plant or for 5000 h in a stationary gas turbine. Figure 7-24 shows a typical coating evaluation program for the evaluation of new coating systems for industrial gas turbines [96] that includes a combination of short-term complex environmental exposure, mechanical tests and long-term laboratory test for structural stability (up to 10 000 h).

7.2.3.1 Chemical Corrosion Evaluation Tests

The short-term chemical corrosion tests in their required complexity are shown in Fig. 7-25 [97]. Since corrosion resistance of a coatings depends to a large extent on the rate of formation of a protective scale, the simplest method is to expose the coating isothermally to either air or oxygen, to atmospheres containing hydrogen sulfide, sulfur dioxide or trioxide, or to 'coal' atmospheres (methane). The weight change of the sample will be measured, and the nature of the scale formed be determined by X-ray diffraction analysis. Cyclic modes of testing are utilized to introduce thermal strain between coating and substrate, and coating and scale. Abrupt weight changes measured with a thermal balance may indicate spalling and chipping of the scale. Addition of impurities to the corrosive environment accounts for the presence of chlorides, sulfates and vanadates in the combustion gases. Such tests are usually performed as immersion tests where the coated sample will be immersed in an appropriate salt melt. The extent of attack can be determined from thickness changes on the metallographic cross-section or from weight loss after descaling [98]. Frequently the attack during such a crucible test would appear to be more severe than that encountered during normal service conditions of the coating. The reasons for this are manifold. For example, the salt composition is often unrealistic, the oxidation potential is low, and the test is static. To overcome these problems other test schedules were devised such as the salt-shower test [99], the synthetic slag test [100], and the modified Dean test [101].

7.2.3.2 Burner Rig Test

This test simulates reasonably well the severe conditions at which a coating has to function in a gas turbine [102]. Such a test rig consists of a combustion chamber taken from a small turbine into which fuel and compressed air is fed in the usual manner. Contaminants are supplied either to the fuel or to the air, or can be sprayed directly into the combustion chamber onto specimen coupons to be tested. These coupons are either stationary or rotate. Variables to be tested include coating temperature, gas pressure, velocity, dwell time, contaminant concentration and composition, and also the fuel-to-air ratio [87]. The samples are investigated after the test by measuring weight loss and/or penetration depth of the corrosive gases. To increase the realistic evaluation of coating systems the burner rig test can be cycled [103].

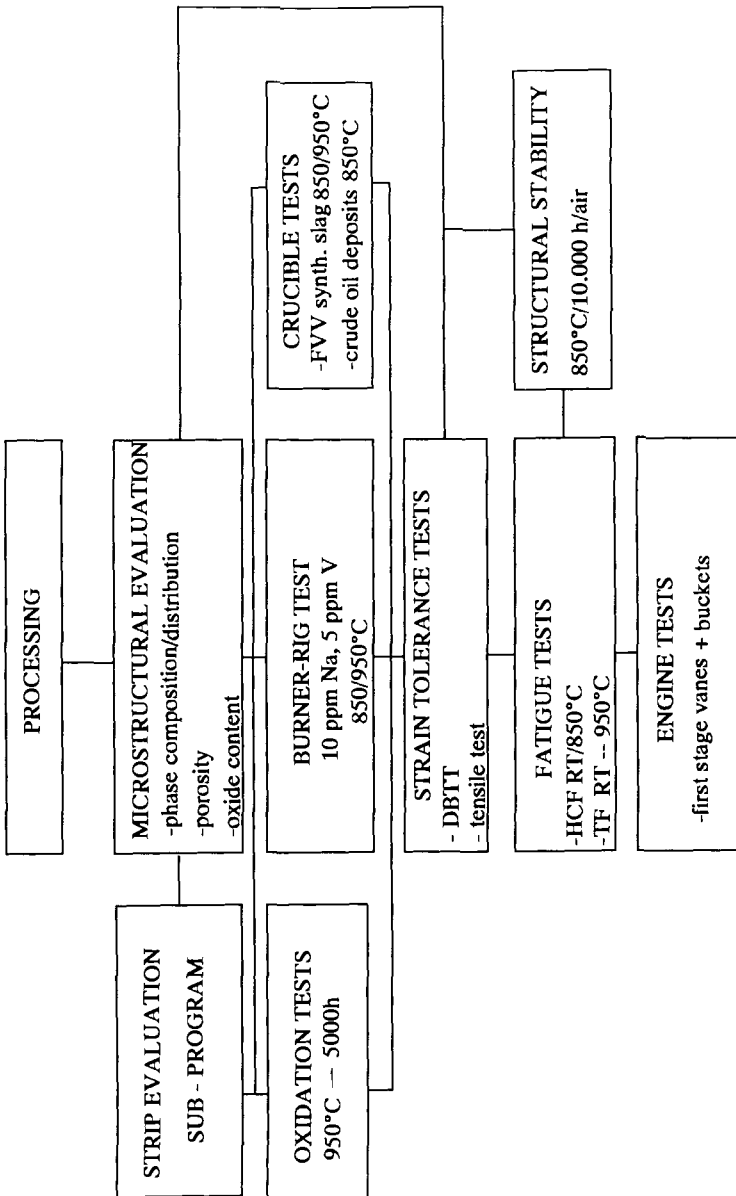


Figure 7-24. Typical coating evaluation program for coatings applied to stationary gas turbines [96].

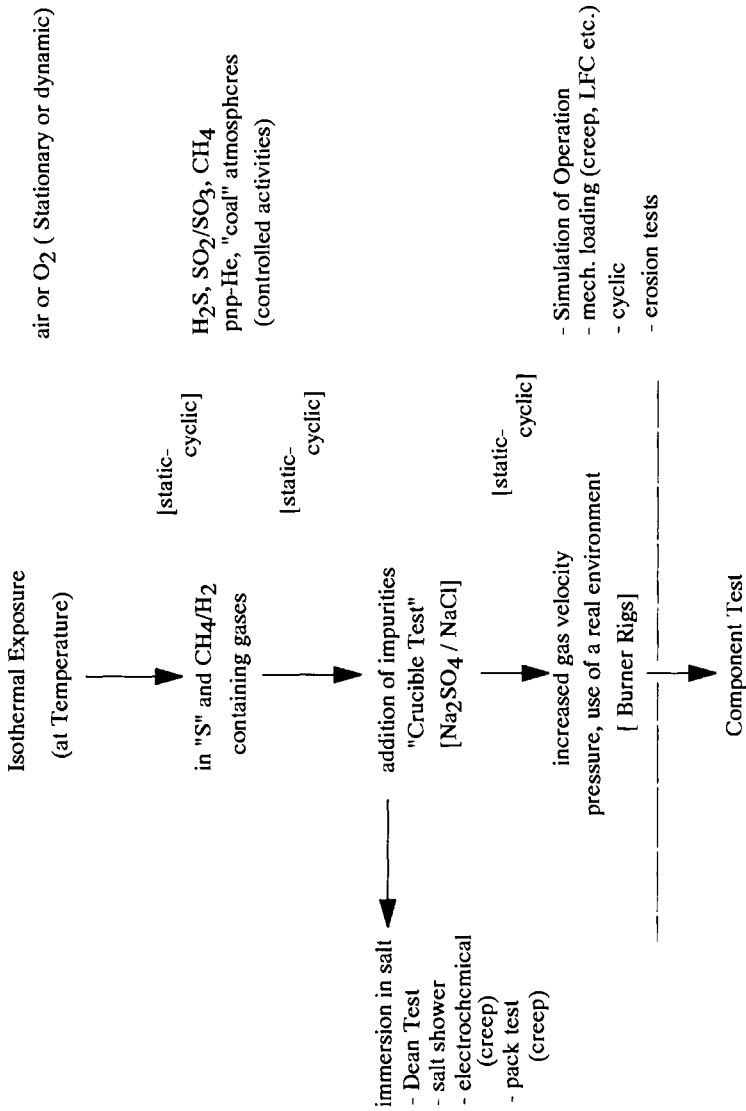


Figure 7-25. Complexity of short-term chemical corrosion tests [97].

References

- [1] B. Keys, T. Miller, *Acad. Managem. Rev.* **1984**, 9, 342.
- [2] J. Fakuda, *J. Gen. Managem.* **1986**, 11, 16.
- [3] H. M. Wadsworth, K. E. Stephens, A. B. Godfrey, *Modern Methods for Quality Control and Improvement*, Wiley, NY, USA, **1991**.
- [4] D. C. Montgomery, *Introduction to Statistical Quality Control*, Wiley, NY, USA, **1991**.
- [5] J. M. Juran, *Planning for Quality*, The Free Press, NY, USA, **1988**.
- [6] R. C. Camp, *Benchmarking: The Search for Industry Best Practices that Lead to Superior Performance*, Quality Press and UNIPUB/Quality Resources, **1989**.
- [7] E. J. Hay, J. Zonderman, *Just in Time Manufacturing: How the JIT System Can Decrease Costs, Increase Productivity and Enhance Quality*, Wiley, NY, USA, **1988**.
- [8] M. Owen, *SPC and Continuous Improvement*, Springer-Verlag, UK, **1989**.
- [9] J. R. Hauser, D. Clausing, *The House of Quality*, Harvard Business Review, May-June, **1988**.
- [10] G. Pouskouleli, T. A. Wheat, in: *Ceramic Coatings – A Solution Towards Reducing Wear and Corrosion* (ed. R. B. Heimann), *Trans. 17th CUICAC Workshop*, Quebec City, 2 October, **1991**.
- [11] W. Ouchi, *Theory Z*, Addison-Wesley, MA, USA, **1981**.
- [12] J. M. Juran, *Juran's Quality Control Handbook*, McGraw-Hill, NY, USA, **1988**.
- [13] W. E. Deming, *Out of the Crisis*, MIT Press, Cambridge, MA, USA, **1986**.
- [14] P. B. Crosby, *Quality is Free*, McGraw-Hill, NY, USA, **1979**.
- [15] ISO 9001, *Quality systems-model for quality assurance in design/development, production, installation and servicing*, **1994**.
- [16] K. Ebert, C. M. Verpoort, *Proc. 14th ISTC '95*, Kobe, Japan, 22–26 May, **1995**, p. 1191.
- [17] *A Plasma Flame Spray Handbook* (ed. T. J. Roseberry, F. W. Boulger). *Final Report No. MT-043* (March 1977) to Naval Sea Systems Command, Naval Ordnance Station, Louisville, KY, USA, **1977**.
- [18] *Standard Specification for Wire-Cloth Sieves for Testing Purposes*, ASTM Designation E11-70. (Feb. 15. 1973).
- [19] *Standard Test Method for Sieve Analysis of Granular Metal Powders*, ASTM Designation B214-66, 1966 (reapproved **1970**).
- [20] *Standard Method for Subsieve Analysis of Granular Metal Powders by Air Classification*, ASTM Designation B293-60 (reapproved **1970**).
- [21] H.-D. Steffens, K.-N. Müller, *Adhäsion* **1972**, 2, 34.
- [22] (a) D. T. Gawne, B. J. Griffith, G. Dong, *Proc. 14th ITSC '95*, Kobe, Japan, 22–26 May **1995**, p. 779; (b) R. A. Miller, W. J. Brindley, C. J. Rouge, G. Leissler, *NASA Tech. Briefs*, **1993**, 17, 56.
- [23] D. Davies, J. A. Whittaker, *Metall. Rev.* **1967**, 12, 15.
- [24] L. Pawlowski, *The Science and Engineering of Thermal Spray Coatings*, Wiley, Chichester, **1995**.
- [25] R. Frielinghaus, G. Schmitz, U. Wielpütz, *Proc. TS '90*, Essen, **1990**, DVS 130, p. 147.
- [26] *Standard Test Method for Adhesion or Cohesive Strength of Flame-Sprayed Coatings*, ASTM Designation C633-79. Annual Book of ASTM Standards, Part 17, ASTM, Philadelphia, PA, USA, **1982**, p. 636.
- [27] German DIN Standard DIN 50160: *Ermittlung der Haftzugfestigkeit im Stirnversuch*, **1981**.
- [28] W. Milewski, *Proc. TS '93*, Aachen **1993**, DVS 152, 258.
- [29] C. C. Berndt, *Advances in Thermal Spraying*, *Proc. ITSC 1986*, Welding Inst. of Canada, p. 149.
- [30] E. A. Ollard, *Trans. Faraday Soc.* **1925**, 21, 81.
- [31] S. Yu. Sharivker, *Poroshk. Metall.* **1967**, 6(54), 70; *Sov. Powder Met. Metal Ceram.* **1967**, 483.
- [32] E. J. Roehl, *Iron Age*, **1940**, 146, 17, 30.
- [33] A. W. Hotherhall, C. J. Leadbetter, *J. Electrodepos. Tech. Soc.* **1938**, 14, 207.
- [34] W. Bullough, G. E. Gardam, *J. Electrodepos. Tech. Soc.* **1947**, 22, 169.
- [35] C. Williams, R. A. F. Hammond, *Trans. Inst. Metal Finishing* **1954**, 31, 124.

- [36] Y. M. Rhyim, C. G. Park, S. B. Kim, M. C. Kim, *Proc. 14th ITSC '95*, Kobe, Japan, 22–26 May, **1995**, 773.
- [37] H.-D. Steffens, *Haftung und Schichtaufbau beim Lichtbogen- und Flammsspritzen*, Ph.D. Dissertation, Hannover, **1963**.
- [38] *Evaluation Methods and Equipment for Flame-Sprayed Coatings*, Metco Inc., Westbury, NY, USA, **1963**, 15 pp.
- [39] H. Grützner, H. Weiss, *Surf. Coat. Technol.* **1991**, 45, 317.
- [40] M. Sexsmith, T. Troczynski, *Proc. 14th ISTC '95*, Kobe, Japan, 22–26 May, **1995**, p. 897.
- [41] A. Crocombe, R. Adams, *J. Adhes.* **1981**, 12, 127.
- [42] S. Thiele, Mikrohärt, Mikrostruktur und Haftung vakuumplasmagespritzter TiC–Mo₂C–Ni, Co-Verbundschichten, Unpublished Master's thesis, Freiberg University of Mining and Technology, June **1994**, p. 66.
- [43] M. Gudge, D. S. Rickerby, R. Kingswell, K. T. Scott, *Proc. 3rd NTSC*, Thermal Spray Research and Applications, Long Beach, CA, USA, 20–25 May, **1990**, p. 331.
- [44] E. Lopez, F. Belzung, G. Zambelli, *J. Mater. Sci. Lett.* **1989**, 8, 346.
- [45] E.-H. Meyer, K.-J. Pohl, in: *Moderne Beschichtungsverfahren* (ed. H.-D. Steffens, W. Brandl), DGM Oberursel, **1992**.
- [46] M. Müller, *Haftungsuntersuchungen an vakuumplasmagespritzten Chromschichten*, Unpublished Master's thesis, Freiberg University of Mining and Technology, June **1994**.
- [47] Y. Suga, H. Makaba, K. Makabe, *Proc. TS'93*, Aachen, Germany 1993, DVS 152, 201.
- [48] R. B. Heimann, M. Müller, *Proc. 4th Intern. Seminar/Course on Coatings for Aerospace Industry* (CAI-4), Toronto, 26–27 Oct, **1995**; TS'96, Essen, Germany, DVS 175.
- [49] D. Lian, Y. Suga, S. Kurihara, *Proc. 14th ISCT '95*, Kobe, Japan, 22–26 May, **1995**, p. 879.
- [50] Y. Suga, D. Lian, S. Kurihara, *Proc. 14th ISTC '95*, Kobe, Japan, 22–26 May, **1995**, p. 961.
- [51] (a) R. Travis, C. Ginther, C. Zanis, *Advances in Thermal Spraying*, *Proc. ITSC 1986*, Welding Inst. of Canada, p. 309; (b) J. W. MacLachlan Spicer, W. D. Kerns, L. C. Aamodt, J. C. Murphy, *Rev. Prog. in Quant. Nondestruct. Eval.* **1990**, 9, 1169.
- [52] G. A. Georgiou, M. B. Saintey, A. M. Lank, D. P. Almond, *Proc. 14th ITSC '95*, Kobe, Japan, 22–26 May, **1995**, p. 1047.
- [53] *Standard Test Method for Rockwell Hardness and Rockwell Superficial Hardness of Metallic Materials*, ASTM Designation E18-74. American National Standard Z115.6, ANSI. **1974**.
- [54] *Standard Test Method for Microhardness of Materials*, ASTM Designation E384-73. American National Standard Z30.12-1973, ANSI.
- [55] J. E. Sundgen, H. T. G. Hentzell, *J. Vac. Sci. Technol. A* **1986**, 4, 2259.
- [56] P. M. Sargent, T. F. Page, *Proc. Br. Ceram. Soc.* **1978**, 26, 209.
- [57] A. J. Perry, H. K. Pulker, *Thin Solid Films*, **1985**, 124, 323.
- [58] A. J. Perry, E. Horvath, *J. Mater. Sci.* **1978**, 13, 1303.
- [59] E. Horvath, A. J. Perry, *Thin Solid Films* **1980**, 65, 309.
- [60] E. Meyer, *Phys. Z.* **1908**, 9, 66.
- [61] P. J. Burnett, T. P. Page, *J. Mater. Sci.* **1984**, 19, 845.
- [62] A. Thomas, *Surf. Eng.* **1987**, 3, 117.
- [63] P. J. Burnett, D. S. Rickerby, *Thin Solid Films* **1987**, 148, 41.
- [64] E. A. Almond, *Vacuum* **1984**, 35, 835.
- [65] H. Bückle, in: *The Science of Hardness Testing and its Research Applications* (eds. J. W. Westbrook, H. Conrad), ASM, Metals Park, OH, USA, **1971**, p. 453.
- [66] B. Jönsson, S. Hogmark, *Thin Solid Films* **1984**, 114, 257.
- [67] J. Lesage, D. Chicot, *Proc. 14th ITSC '95*, Kobe, Japan, 22–26 May, **1995**, p. 951.
- [68] A. Iost, J. Aryani-Boufette, J. Foct, *Mém. Et. Sci.: Rev. Mét.* **1992**, 11, 681.
- [69] D. M. Marsh, *Proc. R. Soc. Lond. A* **1964**, 279, 420.
- [70] B. R. Lawn, A. G. Evans, D. B. Marshall, *J. Am. Ceram. Soc.* **1980**, 63, 574.
- [71] L. C. Cox, *Surface Coat. Technol.* **1988**, 36, 807.
- [72] E. Rigal, T. Priem, E. Vray, *Proc. 14th ITSC '95*, Kobe, Japan, 22–26 May, **1995**, p. 851.
- [73] E. Lopez, G. Zambelli, A. R. Nicoll, *Proc. TS '90*, Essen **1990**, DVS 130, 241.
- [74] J. E. Kelley, J. J. Stiglich Jr., G. L. Sheldon, in: *Surface Modification Technologies* (eds. T. S. Sudarshan, D. G. Bhat), *Proc. 1st Int. Conf. Surf. Modification*, Phoenix, AZ, USA, 25–28 January, **1988**, The Metallurgical Society, p. 169.

- [75] M. O. Borel, R. K. Smith, A. R. Nicoll, *Proc. TS '90*, Essen **1990**, DVS 130, 68.
- [76] S. Steinhäuser, B. Wielage, *Proc. 14th ITSC '95*, Kobe, Japan, 22–26 May, **1995**, p. 693.
- [77] C. R. Dimond, J. N. Kirk, J. Briggs, *Wear of Materials*, **1983**, April, 333.
- [78] E. Hornbogen, *Werkstoffe*. Springer Berlin **1991**, p. 202.
- [79] *Standard Test Method for Measuring Abrasion Using the Dry Sand/Rubber Wheel Apparatus*, ASTM Designation G65-91, **1991**.
- [80] A. W. Ruff, S. M. Wiederhorn, *Treat. Mater. Sci. Technol.* **1983**, 16, 69.
- [81] S. M. Wiederhorn, B. J. Hockey, *J. Mater. Sci.* **1983**, 18, 766.
- [82] I. G. Wright, V. Nagarajan, J. Stringer, *Oxid. Metals* **1986**, 25(3/4), 175.
- [83] W. J. Sumner, J. H. Vogan, R. J. Lindinger, *Proc. Am. Power Conf.* 22–24 April, **1985**, 196.
- [84] J. Qureshi, A. Levy, B. Wang, *J. Vac. Sci. Technol.* **1986**, A4(6), 2638.
- [85] E. R. Buchanan, *Turbomachinery Int.* **1987**, 28(1), 25–27, 31.
- [86] S. T. Wlodek, *EPRI 1885-2, Phase II*, Final Report, **1986**.
- [87] A. R. Nicoll, Chapter 13 in: *Coatings and Surface Treatment for Corrosion and Wear Resistance* (eds. K. N. Strafford, P. K. Datta, C. G. Googan), Ellis Horwood, Chichester, UK, **1983**, p. 180.
- [88] I. Kvernes, S. Forseth, *Mater. Sci. Eng.* **1987**, 88, 61.
- [89] S. Levine, P. E. Hodge, R. A. Miller, *Proc. 1st Conf. on Advanced Fuel Capable Directly Fired Heat Engines*, Maine Maritime Academy, Castine, ME, USA, 31 July–3 August, 1979; DOE, Washington, DC, USA, **1979**.
- [90] N. S. Jacobson, J. L. Smialek, *J. Am. Ceram. Soc.* **1985**, 68, 432.
- [91] G. B. Davies, T. M. Holmes, O. J. Gregory, *Adv. Ceram. Mater.* **1986**, 3, 542.
- [92] M. G. Hebsur, R. V. Miner, *Mater. Sci. Eng.* **1986**, 83, 239.
- [93] M. G. Hebsur, R. V. Miner, *Thin Solid Films*, **1987**, 147, 143.
- [94] J. Gayda, T. P. Gabb, R. V. Miner, *Int. J. Fatigue* **1986**, 8(4), 217.
- [95] C. C. Berndt, *J. Mater. Sci.* **1989**, 24, 3511.
- [96] R. Bauer, Brown, Boveri & Cie, Mannheim, Germany. After [87].
- [97] A. R. Nicoll, in: *Coatings for High Temperature Applications*, (Ed. E. Lang), Applied Science Publishers, London, **1983**.
- [98] H. Lewis, R. A. Smith, *Proc. 1st Int. Congr. Met. Corr.* **1965**, p. 202. After [87].
- [99] S. W. K. Shaw, M. S. Starkey, M. T. Cunningham, High Temperature Corrosion in a Salt Shower Test and Oxidation of a Range of Superalloys, Materials for Gas Turbines: Cost 50, Final Report, March **1979**.
- [100] R. Bauer, K. Schneider, H. W. Grünling, *Proc. DOE Conf. on Adv. Mat. for Alternate Fuel Capable Directly Fired Heat Engines*, Castine, ME, USA, **1979**.
- [101] A. V. Dean, *Investigation into the Resistance of Various Nickel and Cobalt Base Alloys to Sea Salt Corrosion at Elevated Temperature*, NGTE Report, January **1964**. After [87].
- [102] B. Janke, A. R. Nicoll, *Proc. Conf. on Frontiers of High Temperature Materials II*, London, **1983**. After [87].
- [103] D. L. Ruckle, *Thin Solid Films*, **1980**, 73, 455.

8 Design of Novel Coatings

8.1 Coating Requirements

Thermally sprayed and PVD/CVD coatings must be carefully designed to obtain maximum performance for the required application. An initial example will be given based on the concept of advanced layered coatings for cutting tools [1]. Even though it relates predominantly to thin PVD or CVD coatings the strategy can also be applied, in principle, to thick thermally sprayed coatings [2].

- Coatings for cutting tools can:
 - improve service life of the tool, i.e. reduce the frequency of tool changes,
 - provide more favorable operating conditions, i.e. higher speed and feed rates and thus improve the economy of the cutting and milling operations,
 - provide higher product quality, i.e. better surface finish and tighter tolerances,
 - open up new areas of applications, i.e. machining of difficult to handle non-metallic materials such as wood, plastic and composites, and
 - achieve resource conservation, i.e. reduced materials losses and machining of more economical materials.

There are, however, conflicting basic requirements for coating performances. The hard coating materials in question are frequently oxide ceramics such as Al_2O_3 and Cr_2O_3 , or nonoxide ceramics such as transition metal carbides (TiC , TaC , WC , Mo_2C), nitrides (TiN , Si_3N_4 , SiAlONs) and borides (TiB_2). There are three problems.

1. Ceramic coatings must have good adhesion to the metallic substrate, but little tendency to react with the material of the metal chip removed by the tool from the workpiece. This is particularly important when at high cutting speeds and therefore high frictional temperatures the material of the coating dissolves in the chip.
2. The ceramic constitutes of a hard layer with a high melting point, but there should be little crack propagation, i.e. high fracture toughness of the coating is required.
3. The ceramic layer must be hard and high melting, but good adhesion is needed under widely changing temperature conditions imposed by friction and intense shear forces at the worked interface, and the associated high thermal stresses and high thermal expansion [1].

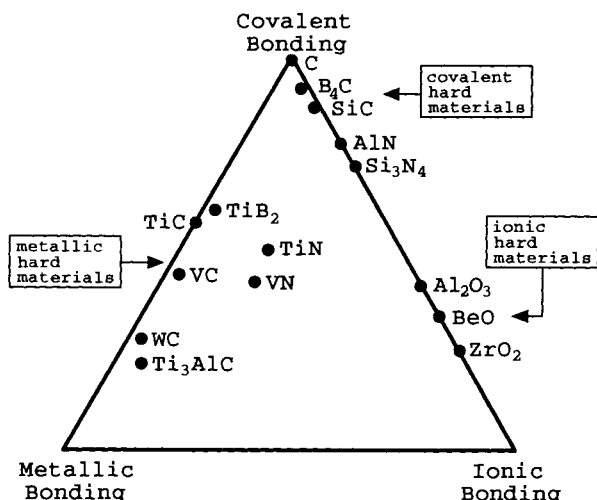


Figure 8-1. Chemical bonding types of different hard ceramic materials [1].

A way to look at the compatibility of different ceramic materials is through their differing chemical bonding type (Fig. 8-1). Metallic hard materials, such as WC, TiC or TiB₂ are characterized by their high proportion of metal–metal bonds in the f.c.c. closed-packed arrangement of metal atoms, whereas the small carbon or boron atoms occupy the octahedral interstitial sites. On the other hand, covalent ceramic materials have a high proportion of highly directional covalent bonds, and hetero-polar (ionic) ceramic materials possess simple sublattices of large close-packed oxygen anions with the small metal atoms at interstitial sites, opposite to the metal bonding structure.

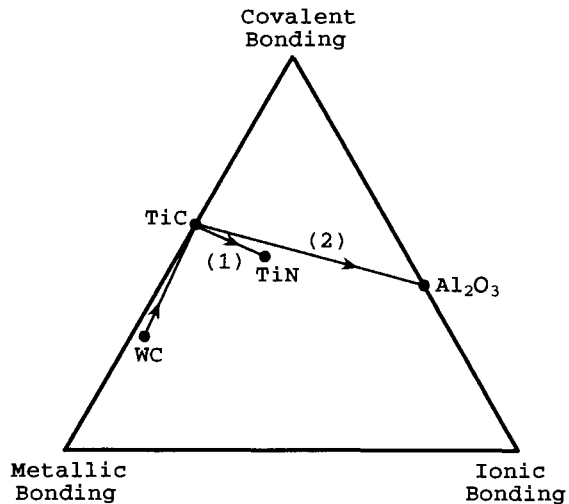
In general, all materials used for protective layers are characterized by mixed bonding types. Their properties change with the position of the material in the bonding triangle (Fig. 8-1). TiN close to the centre of the triangle has a particularly favorable combination of metallic, covalent and ionic bonding types. Carbide, nitrides and borides of the transition metals (Ti, V, W) crystallize in simple, densely packed lattices of large metal atoms with the non-metallic atoms joined to the metal lattice by covalent or mixed covalent/ionic bonds. If metallic and ionic structures are combined, i.e. TiC–Al₂O₃, there are no corresponding metal planes at the interface but the Ti-planes of TiC will match the oxygen planes of Al₂O₃ in positioning and size. Because the covalent structures have highly directional, saturated bonds, there is only a small tendency to interact with other materials at the interface.

8.2 Design of Novel Advanced Layered Coatings

The concept of ‘advanced layers’ includes the design [1] of:

- gradient layers [2],
- layer materials in thermodynamic equilibrium,

Figure 8-2. Possible designs of gradient-layer coatings WC–TiC–TiN (1) and WC–TiC–Al₂O₃ (2) [1].



- extended solid solution, and
- multilayers.

8.2.1 Gradient Layers

Functional gradient materials (FGMs) display continuously (or discontinuously) varying compositions or microstructures over definable geometric distances [2].

Very thin layers can be deposited by PVD techniques. Such coatings are designed so that to the substrate is first added an adhesive layer with a large fraction of metal bonds. These bonds tend to form a stable external layer with little tendency to interact. Examples are given in Fig. 8-2 of a gradient layer combination WC–TiC–TiN (1) and WC–TiC–Al₂O₃ (2). Such gradient layer coatings for cutting tools will exhibit superior flank wear resistance. In fact, the wear depth of uncoated WC during interrupted cutting is reduced by using a PVD TiC–TiN gradient coating from > 160 μm to a minimum wear depth of 20 μm [1]. These data were obtained from interrupted cutting conditions of CK 45 (speed: 125 m min⁻¹, feed: 0.2 mm per revolution, depth of cut: 2 mm, cutting time: 5 min; corresponding to 3500 impacts).

Plasma-spray processing offers an alternative way to deposit FGMs in a flexible and economical manner. It is possible to deposit multiple constituents simultaneously, for example to produce thermal barrier graded layers with enhanced survivability for gas turbines and diesel engines. Gradient layers are primarily employed to reduce discontinuities in the coefficients of thermal expansion to avoid mismatch-related failure in service. Such discontinuities frequently result in fatal cracks and spallation at the sharp interface between the substrate and a thermal barrier coating. FGMs are capable of spreading out this mismatch stress and thus reduce crack initiation. Equipment to deposit FGMs can be classified as: single plasmatron–multiple powder feeders with blended or composite powders; multiple plasmatron–independent feeding systems for each components; and process combinations–wire/powder feed systems combinations. Using a single plasmatron–dual feeder combination, a

graded NiCrAl/Y-PSZ coating has been produced with an almost linear increase of Y-PSZ as a function of the distance from the interface to the substrate. The microstructure of this 2 mm thick gradient coating was composed of 70 μm -thick discrete layers of varying compositions [2]. Likewise, the elastic modulus of such a gradient coating decreased nearly linearly with increasing Y-PSZ content, i.e. away from the interface [3]. Despite these advances the benefits of grading for stress relaxation need to be studied in detail in the context of other coating characteristics such as environmental stability and manufacturing complexity.

8.2.2 Layered Materials in Thermodynamic Equilibrium

In the structurally compatible systems TiC/TiN or TiC/VN (see Fig. 8-1), extended formation of solid solution takes place that can either lead to a single phase solid solution, or, at lower temperature, to the decomposition of this single phase into two phases with added particle strengthening due to mechanical reinforcement.

8.2.3 Extended Solid Solution

In structurally noncompatible ceramics (TiN/AlN, TiC/SiC) with different bonding types an equilibrium solid solution is not possible for metastable layer materials composed of a metallic and a covalent hard material. Rapid solidification may lead to extended metastable solid solution over the entire compositional range.

8.2.4 Multilayers

Fine-grained multiphase structures with many phase boundaries frequently produce structures with increased toughness. Limited crack propagation takes place in the modulated layer structure because of deflection and arrest of cracks at the interfaces due to many oscillations between tensile and compressive stresses. PVD methods are ideally suited to produce TiC/TiB₂, TiC/TiN or TiN/TiB₂ composite coatings with up to 500 individual layers with a total layer thickness not exceeding 5 μm . The advantage of the multilayer concept lies in the reduction of grain growth, the introduction of many interfaces, and the formation of modulated layer material that changes the mechanical properties, and leads to effective stopping of crack propagation. The application of various coating technologies to the design of novel coatings are shown in Table 8-1.

8.3 Principles of Statistical Design of Experiments

8.3.1 The Experimental Environment and its Evolution

A brief survey of the techniques of statistical design of experiments (SDE) most frequently applied to thermally sprayed coatings has been given by Bisgaard [4] and

Table 8-1. Design of surface coatings.

Layer materials concept	Coating technology
Solid solution coatings	PS, LPPS, CVD, PACVD, PVD
Gradient coatings	PS, LPPS, CVD, PACVD, PVD
Multilayers	PVD, CVD, (PACVD)
Metastable layer materials	PVD, (PACVD)
Multiphase layer materials	PVD, (CVD, PACVD, PS, LPPS)

PS = plasma spraying; LPPS = low-pressure plasma spraying; CVD = chemical vapor deposition; PACVD = plasma-assisted chemical vapor deposition; PVD = physical vapor deposition (magnetron sputtering, ion plating, arc evaporation).

Heimann [5]. Two-level factorial analysis applied to plasma spraying was reviewed by Lugscheider and Knepper [6]. The design methodologies are based on the ideas of Plackett and Burman [7], Box [8, 9], Deming [10] and Taguchi [11]. Software is available to perform the statistical calculations required with ease [12].

According to Tukey [13], industrial experiments can be classified according to their depths of intellectual investment as: confirmation experiments; exploration experiments; and fundamental or 'stroke-of-genius' experiments. A second method of classification is based on the distance of their objective from the real world, i.e. from the market [14]. Finally, the continuity of factors provides a third classification scheme. If the factors (parameters, variables) are continuous and controllable at preset levels, then the response surface methodology is the method of choice. If, however, some factors are orderable but not measurable, i.e. at discrete levels, the response surface analysis becomes less useful and should be replaced by nested or split-plot designs [15]. At a lower level of predicting power, screening designs like Plackett–Burman designs [7] that can handle mixtures of continuous and discrete factors are particularly important as a statistical experimental design for the optimization of plasma sprayed coatings (see Secs. 8.3.2, 8.4.1).

Every experiment attempts to approximate the 'real world' in some ways but must avoid, by a set of simplifying assumptions, the complex interactions occurring in real systems. There are, in principle, two ways to accomplish this: the '*classical*' *experimental strategy* that varies one parameter at a time but attempts to keep all others constant, and the *statistical strategy* that varies factors simultaneously to obtain a maximum of information with a minimum number of experiments. Thus the experimental economy becomes the overriding principle of the strategy. The classical experimental strategy yields accurate results but requires many experiments, and may give misleading conclusions to problems that have synergistic factor interactions, and also fails to elucidate the 'structure' of a system. Table 8-2 compares these two strategies [16].

8.3.1.1 Screening Designs

The evolution of the experimental environment usually starts with a screening design, for example a Plackett–Burman [7] or Taguchi design [11] with many indepen-

Table 8-2. Two viewpoints of the ‘real world’ [16].

	Classical	Statistical
Number of runs	many	few
Type of response	complex	simple
Synergism	absent	present
Error	small	large
Strategy	one-factor-at-a-time	factorial
Thought pattern	vertical	lateral [17]

dent (up to 40) variables. It yields a rather crude prediction of the relative magnitude and sign of the parameters and thus the ranking of importance of parameters through a first-order polynomial model. The experimenters should list and investigate carefully all possible parameters they can think of but should refrain from skipping some because of ‘folklore’, laboratory gossip, or preferences and hunches. The penalty for the tremendous reduction in the number of required experiments, however, will be the failure to detect synergistic interactions between parameters. On the other hand, an advantage of the screening designs is that they can accommodate a mix of continuous and discrete parameters. Plackett–Burman designs are *saturated*, i.e. they contain as many experimental runs as there are coefficients to determine in the first-order polynomial model. If the number of potential influencing factors is very large, *supersaturated* designs can be selected that contain less runs than coefficients to be estimated [18]. An even more reduced design plan can be obtained using the principle of chance balance [18, 19]. More modern approaches consider evolutionary algorithms combined with fuzzy logic that allow estimation of the behavior of a complex system with but a few randomly chosen tests.

8.3.1.2 Response Surface Designs

With the independent parameters (up to eight) identified by screening designs to significantly influence the response of the dependent parameter(s), a ‘limited response surface’ experiment should be run such as a full two-level factorial, 2^p or even a fractional three-level factorial (Box–Behnken) design [8] that yields higher quality predictions by allowing interpolation within the experimental space by a second-order polynomial model. Such a model determines nonlinear behavior, i.e. the curvature of the response surface and thus permits the estimation of synergistic parameter interactions.

8.3.1.3 Theoretical Models

The polynomial models approximate the ‘true’ response surface only in the necessarily narrow region of the investigated parameter space. Thus, any extrapolation beyond the proven validity of the predictions is dangerous and may lead to useless or even nonsensical results. To avoid this, eventually theoretical models have to be built

Figure 8-3. Saturated Plackett–Burman design for estimation of 11 parameters with 12 runs.

Run	x_1	x_2	x_3	x_4	x_5	x_6	x_7	x_8	x_9	x_{10}	x_{11}
1	+	-	+	-	-	-	+	+	+	-	+
2	+	+	-	+	-	-	-	+	+	+	-
3	-	+	+	-	+	-	-	-	+	+	+
4	+	-	+	+	-	+	-	-	-	+	+
5	+	+	-	+	+	-	+	-	-	-	+
6	+	+	+	-	+	+	-	+	-	-	-
7	-	+	+	+	-	+	+	-	+	-	-
8	-	-	+	+	+	-	+	+	-	+	-
9	-	-	-	+	+	+	-	+	+	-	+
10	+	-	-	-	+	+	+	-	+	+	-
11	-	+	-	-	-	+	+	+	-	+	+
12	-	-	-	-	-	-	-	-	-	-	-

[9, 20] that yield the exact mathematical response surface, usually by the application of first-order differential equations.

8.3.2 Screening Designs

In a real experimental program the screening designs, in particular Plackett–Burman designs are the starting point for any investigation of a completely unknown system. They are designed to screen out the few really important variables from a large number of possible ones with a minimum of test runs. Plackett–Burman designs are fractions of an $N = 2^p$ factorial for which N is a multiple of 4. Although they allow a tremendous reduction in experimentation there is no estimate of synergistic non-linear parameter interactions. In fact, only estimates of main effects clear of each other can be obtained. A saturated Plackett–Burman design useful for optimization of 11 plasma spray parameters in only 12 runs is shown in Fig. 8-3. The ‘+’-signs are assigned to the parameters x_i at their maximum levels, the ‘-’-signs to their minimum levels. The factor effects are calculated by adding in each column the ‘+’-responses ($\sum +$) and subtracting the sum of the ‘-’-responses ($\sum -$). The value $\Delta = (\sum +) - (\sum -)$, divided by the number of ‘+’-(or ‘-’)-signs in the columns with assigned factors is the factor effect for the parameter x_i . For the extra columns to which no factors have been assigned this ‘factor effect’ is an estimate of the experimental error. For example, assignment of only six variables, x_1 to x_6 leaves five degrees of freedom, i.e. unassigned factor effects x_7 to x_{11} that can be used to estimate the standard deviation of the factor effects, $\sigma_{FE} = \{(1/q) \sum x_{iq}^2\}^{1/2} = \{(1/n) \sum E_i^2\}^{1/2}$.

To determine which factors x_i are statistically significant the calculated factor effects are being compared with the minimum factor significance, {min}. The minimum significant factor effect is

$$\{\min\} = t_v^\alpha \sigma_{FE}, \quad (8-1)$$

with t_v^α = Student's t for v degrees of freedom, and α level of confidence for a double-sided t -distribution. All factors whose effects are larger than the (absolute) value of $\{\min\}$ are considered statistically significant. An example for the application of a Plackett–Burman screening test is given in Sec. 8.4.1. Although Plackett–Burman designs are available for nearly any multiple of four trials, the most useful ones are for 12, 20 or 28 trial runs. Such designs handle nominally 11, 19 and 27 factors, respectively. It is good practice to conduct an operability review after having selected any p columns for factors. For increased precision of prediction, a larger design could be used and/or a reflected design could be added [7]. By using the next larger design partial replication is obtained. For example, with 6 factors, the recommended design has 12 runs. This leaves 5 degrees of freedom for estimation of the experimental error. Alternatively, the 6 factors can be run in a 20 trial design, hence leaving 13 degrees of freedom for estimation of the experimental error. Reflected designs are able to estimate main effects (almost) clear of two-factor interactions, and thus approach the predicting power of fractional factorial designs (see below).

The selection of the level of significance, α , requires some discussion. When there is only a relatively small number of degrees of freedom, i.e. when a low number of runs has been performed, it is preferable to select a significance level lower than 0.95. In this case, the ‘power of test’ is greater, i.e. the likelihood of detecting a significant factor effect if it exists. As a rule of thumb, for degrees of freedom ≤ 5 , 5 to 30, and ≥ 30 , respectively, significance levels of 0.90, 0.95, and 0.99, respectively should be picked.

If two-factor interactions are present, Plackett–Burman designs have the desirable property that significant factor effects stand out over a pool of background noise containing both experimental error and interactions when present. In the absence of interactions, the *precision ratio* achieved is

$$\sigma_{FE}/\sigma = 2/n^{1/2}, \quad (8-2)$$

where σ_{FE} = standard deviation of a factor effect, σ = standard deviation of a single observation, and n = total number of observations (runs) in the selected design. The value of n , i.e. the number of experimental runs should be large enough to have a high probability of separating the significant signal from experimental noise, but small enough to optimize time and costs. The size of the factor effect to be detected is Ω , and the desired probability that a significant parameter can be detected when it has a true effect of size Ω , is $(1 - \beta) \geq 0.90$. This is satisfied if $\sigma_{FE} = \Omega/4$. From (8-2) it follows that

$$n = (8\sigma/\Omega)^2 = [8/(\Omega/\sigma)]^2, \quad (8-3)$$

with Ω/σ = signal-to-noise ratio.

Eq. (8-3) is called Wheeler's test. To detect effects twice as large as the experimental error ($\Omega = 2\sigma$), n must be 12 to 16. To detect effects the same size as the error ($\Omega = \sigma$), n becomes four times as large, i.e. 48 to 64. Weak factor effects thus require a large number of experiments.

8.3.3 Factorial Designs

8.3.3.1 Full Factorial Designs

Factorial designs permit the estimation of the main (linear) effects of several factors, x_i simultaneously and clear of two-factor interactions, $\{x_i x_j\}$. The total number of experiments, N is obtained by running experiments at all combinations of the p factors with l levels per factor, i.e. $N = l^p$ for a full factorial design. In particular, two-level factorial designs ($l = 2$) are highly useful for a wide variety of problems. They are easy to plan and to analyse, and readily adaptable to both continuous and discrete factors. Such designs provide adequate prediction models for responses without a strong nonlinear behavior in the experimental region. However, for best results the responses Y should be continuous, and have uniform and independent errors. This means that: the experimental error must have approximately the same magnitude at all experimental points; and the size and sign of error at any one experimental point must not be affected by the sizes and signs of errors that occur at other experimental points. If the first requirement cannot be guaranteed a logarithmic transformation of the responses Y is often advisable. With factor coding as discussed above, using the so-called Yates order [21] and randomization of the experimental trials, factor effects for each main effect and two-factor interaction are calculated similarly to the procedure mentioned in Sec. 8.3.2. The computation of factor effects and residuals can also be quickly and accurately accomplished using the inverse Yates algorithm, [22]. The test of significance can be derived from an appropriate t -test:

$$\{\min\}_{\text{lin}} = t_v^\alpha \sigma_{\text{FE}}(2/mk)^{1/2}, \quad (8-4a)$$

$$\{\min\}_c = t_v^\alpha \sigma_{\text{FE}}(1/mk + 1/c)^{1/2}, \quad (8-4b)$$

where $\{\min\}_{\text{lin}}$, $\{\min\}_c$ are the minimum significant factor effects for linear effects and curvature, respectively, and $m = 2^{p-1}$ for factor effects and 2^p for the average, k = number of replicates, and c = number of center points. If a computed factor effect is larger (in absolute value) than $\{\min\}_{\text{lin}}$ than it can be safely concluded that the true effect Ω is nonzero. Also, when the curvature effect is larger than $\{\min\}_c$ then at least one factor has nonzero curvature associated with it. Applications of full factorial designs 2^3 to the design of (Ti, Mo)C–NiCo– and 88WC12Co–coatings on mild steel, and a 2^5 design applied to a self-fluxing NiCr coating on steel will be dealt with in Sec. 8.4.2.

8.3.2.2 Fractional Factorial Designs

If the number of parameters p to be estimated becomes larger than, say 5 a full factorial may not be appropriate anymore for reasons of experimental economy. Then fractions of a full factorial can be run, i.e. $N = 2^{p-q}$. In particular, half-fraction of full factorials, $N = 2^{p-1}$ estimate main effects and two-factor interactions clear of each other.

Fractional factorial designs are useful in the following situations [23]:

1. when some interactions can be reasonably assumed nonexistent from prior knowledge,
2. in screening operations where it is expected that the effects of all but a few of the factors will be negligible,
3. where blocks of experiments are run in sequence, and ambiguities remaining at an earlier stage of experimentation can be resolved by later blocks of experiments, and
4. when some factors that may interact are to be studied simultaneously with others whose influence can be described through main effects only.

Fractional factorial designs can be divided into three types with regard to their *power of resolution*, i.e. their degree of fractionation. The higher the degree of fractionation the more comprehensive the assumptions required to arrive at unequivocal interpretation of the system. Designs of resolution III, for example 2^{3-1} , are those in which no main effect is confounded with any other main effect, but main effects are confounded with two-factor interactions, and two-factor interactions with each other. In designs of resolution IV, for example 2^{4-1} , no main effect is confounded with any other main effect or two-factor interaction, but two-factor interactions are confounded with each other. Finally, in designs of resolution V, for example 2^{5-1} , no main effect or two-factor interaction is confounded with any other main effect or two-factor interaction, but two-factor interactions are confounded with three-factor interactions. Since in most real problems three- and higher-factor interactions can be safely neglected, a design of resolution V should be the design of choice. However, in order to reduce the number of runs required and thus keep within the economical bounds of most research and development projects, fractional factorial designs of resolution IV can be tolerated. The design 2^{8-4} discussed in Sec. 8.4.3 is of resolution IV. The confounding of two-factor interactions in this design leads to composite two-factor interaction, i.e. the sum of four two-factor interactions. Examples of these fractional factorial designs applied to 88WC12Co-, Ti-, 97Al₂O₃3TiO₂-, 85Fe15Si- and stellite coatings on mild and austenitic steel substrates will be shown in Sec. 8.4.3.

8.3.4 Box–Behnken Designs

Box–Behnken designs [8] are incomplete three-level factorial designs that allow estimation of the coefficients in a second-degree graduating polynomial. They employ subsets of the corresponding full three-level factorial, 3^p . For example, the three-factor design uses only 13 of the 27 points of the full factorial 3^3 with two extra replicates of the center points added, for a total of 15 experimental points of a spherical space-filling¹ and rotatable design. Another desirable feature of such designs with

¹ Note that the factorial designs are considered to have a 'cuboidal' or 'hypercube' factor space whereas the true response surface designs have a 'spherical' factor space.

$p > 4$ is the possibility to run it in separate blocks of points. Such *orthogonal blocking* permits subtraction of the effect of a shift of response between blocks, and thus removal of bias errors due to differences in extraneous variables not considered in the design. The 15 data points in the three-factor Box–Behnken design are five more than the minimum number of 10 required to estimate the coefficients of the design (3 linear main effects, 3 parabolic main effects, 3 two-factor effects, and 1 three-factor effect). Thus it provides five degrees of freedom for error. Orthogonal blocking is possible for designs from four up to ten factors. Rotatability is associated with the geometric properties of the design, i.e. the arrangement of the array of data points, except for the center point, to be at the mid-points of the edges or faces of a hypercube whose dimensionality is given by the number of factors considered. Hence all points are situated on a single sphere and are thus equidistant from the center. This means that the design is balanced by the mathematical momentum condition. The replicated center point allows estimation of the minimum factor significance, i.e. the inherent experimental error, and prediction of constant variances as a function of distance from the center.

It is good experimental strategy to employ such Box–Behnken-type designs at a rather advanced stage of experimentation when the number of potentially significant factors has been narrowed down to 3 to 6 continuous factors. As clearly pointed out by Bisgaard [4] even considering nonlinearity of responses in plasma-sprayed designs does not warrant, for reasons of experimental economy, three-level factorial designs in the initial stage of experimentation. Thus second-order effects should be dealt with exclusively when they actually show up in the set of data, and not only because the experimenter suspects that the system under investigation may show some global nonlinearity! When switching from two- to three-level designs any discrete, i.e. non-continuous factor effect must be considered constant. The response surface obtained through a Box–Behnken response surface design provides usually a high-quality prediction over a region where linear, parabolic (curvature) and two-factor interactions are needed to describe a response of the system, Y as a function of the coefficients of the independent input parameters X_i obtained by a full quadratic polynomial for p independent parameters:

$$Y = b_0 + \sum b_j X_j + \sum b_{jj'} X_j X_{j'} + \sum b_{jj} X_j^2, \quad (8-5)$$

with $j > j'$.

8.3.5 Designs of Higher Dimensionality

Three levels are the minimum number for each factor to describe accurately non-linear (curvature) effects. To add additional power of prediction to a Box–Behnken design, it is advisable to use more than three factor levels. One popular class of response surfaces are the *central composite* or Box–Wilson [24] designs that employ five levels for each factor. It is composed of a full two-level factorial 2^3 with added center points plus six star points outside the cube planes defined by the four points of the two-level factorial. The geometric shape of the resulting five-level design is a

tetrakisshexahedron whose 14 design points surround a k -time replicated center point. This polyhedron is 'cuboidally' spacefilling and can be described as the dual polytope of a cuboctahedral Dirichlet domain (Voronoi polyhedron).

8.4 Optimization of Coating Properties: Case Studies

8.4.1 Plackett–Burman (Taguchi) Screening Designs

Optimization of a novel (Ti, Mo)C–NiCo coating on mild steel (German steel number St38) was performed by vacuum plasma-spraying in an argon/hydrogen plasma using a 12-point 11-factor Plackett–Burman design (L_{12} -type according to Taguchi) [25]. The six factors varied at two levels (high and low) were: **1** = powder (agglomerate) grain size², **2** = plasma power, **3** = powder feed rate, **4** = plasmatron traverse speed, **5** = chamber pressure, **6** = spray (stand-off) distance. The plasma power, **2**, was not an independent parameter but obtained by an appropriate selection of the argon/hydrogen ratio and the current. The low value of **2** was 42 kW (argon: 48 l min⁻¹, hydrogen: 6 l min⁻¹, current: 800 A), the high value was 47 kW (argon: 48 l min⁻¹, hydrogen: 7 l min⁻¹, current: 900 A). The remaining factors and their levels were: **1** (–32 + 10 μ m; –63 + 32 μ m), **3** (0.5; 1 scale), **4** (4 m min⁻¹; 8 m min⁻¹), **5** (80 mbar; 100 mbar), and **6** (340 mm; 380 mm). Four responses Y_i were measured: surface roughness of the deposit (Y_1), microhardness (Y_2), porosity (Y_3) and fracture energy density (Y_4). The factors found to influence those responses at a level of confidence of 95% were **1** (positive effect for surface roughness and porosity, negative effect for fracture energy density) and **6** (positive effect for porosity, negative effect for fracture energy density). In addition, with the parameters **2**, **5** and **6** a full factorial design 2³ was run for the fine powder (–32 + 10 μ m) with increased ranges of **2** (38 kW; 53 kW) and **5** (100 mbar; 180 mbar) and a reduced range of **6** (200 mm; 300 mm) in order to minimize the coating porosity. For the low levels of **2** (38 kW), **5** (100 mbar) and **6** (200 mm) a coating porosity around 2% could be achieved with reasonably low surface roughness and a fracture energy density around 30 J mm⁻³. Problems occurred with a high heat transfer to the substrate that requires efficient substrate cooling.

Other recently reported optimization studies on plasma-sprayed coatings based on L_8 or L_{16} Taguchi designs relate to:

- NiCrAl/bentonite abrasible coatings (L_{16} design, 15 independent parameters, 3 dependent parameters: erosion resistance, tensile strength, hardness) [26]
- HVOF-sprayed Al–Si/polyester abrasible coatings (L_8 design, 5 independent parameters, 3 dependent parameters: hot erosion resistance, bond strength, hardness) [27]

² Here and in the following text the factors $X_1, X_2 \dots X_i$ will be denoted by **1, 2, ... i**.

- Thick thermal barrier coatings (TTBCs) (L_8 design, 7 independent parameters, 5 dependent parameters: erosion resistance, macrohardness, porosity, deposition efficiency, thermal shock resistance) [28]
- WC/Co-, $\text{Cr}_3\text{C}_2/\text{NiCr}$ - and $\text{Al}_2\text{O}_3/\text{TiO}_2$ coatings (L_8 design, 7 independent parameters, 4 dependent parameters: microhardness, Rockwell macrohardness, tensile strength, composition) [29].

8.4.2 Full Factorial Designs

Such designs are not very common in the literature since they are limited to a rather small subset of spray parameters. Only if enough knowledge of the system under investigation has been accumulated such designs are being applied to fine-tune the parameters of a decreased factor space (see Sec. 8.4.1).

A two-level five-factor full factorial 2^5 was employed by Hurng *et al.* [30] to evaluate the properties of a self-fluxing nickel-base alloy containing 15 to 18 mass% Cr and 5 mass% (Fe + C + B + Si) deposited by a hybrid APS/PTA (plasma transferred arc) process on mild steel. The five independent parameters and their ranges were: **1** plasma current (420 A; 460 A), **2** spray distance (15 mm; 17 mm), **3** powder feed rate (8; 12 wheel speed units), **4** plasmatron traverse speed (25 mm s^{-1} ; 35 mm s^{-1}) and **5** plasma transferred arc current (4; 6 scale units). Each parameter setting was repeated thus giving two sets A and B of 32 runs each. In addition, 15 experiments were run at the ‘working point’, i.e. the midpoint between the low and high values selected for each parameter.

The optimized dependent response parameters were the microhardness ($800 \pm 40 \text{ HV}_{0.3}$), the porosity ($2.1 \pm 1.5\%$) and an oxide content as low as 0.13%. The significant parameters for optimizing the microhardness were the plasma current **1** with an effect per unit of $-0.83 \text{ HV}_{0.3}$ per A, the two-factor interactions **12** (positive effect) and **45** (positive effect), and the spray distance **2** with an effect of about $11 \text{ HV}_{0.3}$ per mm. Thus $1 > 12 \geq 45 > 2$ (absolute). The significant parameters for optimizing the lumped together-values of coating porosity and percent oxide were the traverse speed **4** with 0.38 % per mm per s, the two-factor interaction **23** (negative effect) and the plasma transferred arc current **5** with an effect per unit of -0.32% per A. Thus $4 > 23 > 5$ (absolute).

This result shows clearly the problems such coating property predictions have when performed at an insufficient level of predicting power, i.e. only two-level design: the quite different factor significances for microhardness and porosity precludes an unambiguous optimization treatment. Microhardness is presumably much affected by porosity but the parameter with the highest significance for the former, the plasma current **1** does not at all show up in the response polynomial of the latter. Likewise, the parameter with the highest significance for the porosity, the traverse speed **4** is not part of the response polynomial of the microhardness. With the large number of experiments expended (79) a folded-over, i.e. replicated three-level five-factor Box–Behnken design could have been executed with a slightly increased total number of runs of 92. This design allows for the estimation of nonlinear effects that are to be expected in the system. On the other hand, a result comparable to that de-

scribed above would have been obtained with a mere 24 runs as a reflected five-factor 12-run Plackett–Burman or L_{12} Taguchi design that estimates main effects clear of two-factor interactions with 6 unassigned factors for determination of the minimum factor significance. It should be emphasized again that in the interest of experimental economy it is good practice to always start with a simple screening to weed out the weakly significant parameters, and only then follow up with a full factorial design.

A simple two-level three-factor full factorial design 2^3 with 2 center points added was used by Troczynski and Plamondon [31] to optimize the erosion rate, Rockwell A-macrohardness, density, thermal decomposition of WC, and surface roughness of 88WC12Co coatings deposited by APS at a plasma power of 24 ± 4 kW on mild steel. The independent parameters and their levels were hydrogen content in % in the argon/hydrogen plasma gas **1** $\{(2; 4) \pm 0.3\}$, spray distance **2** $\{(51; 127) \pm 2.5$ mm $\}$, and powder feed rate **3** $\{(30; 60) \pm 3$ g min $^{-1}$ $\}$. The choice of the independent parameters was as almost always a compromise, here between a limited experimental capability, a large number of variables potentially controlling the properties of the WC/Co coatings, and the practical relevance in industrial spraying operations. By plotting sections of the four-dimensional response hyperspaces $[1, 2, 3, Y_i]$ it was possible to define a set of robust conditions that resulted in optimized coating properties (erosion rate < 10 mg s $^{-1}$, hardness HRA > 40 , density > 9 g cm $^{-3}$, and W₂C content $< 7\%$ of initial amount of WC) insensitive to minor variations. These robust processing conditions were **1** = $2 \pm 0.5\%$ H₂, **2** = 76.2 ± 12.7 mm, and **3** = 60 ± 10 g min $^{-1}$. With this highly economical design a set of operating windows were obtained as shown in Fig. 8-4.

Optimization of the porosity of APS-tungsten coatings on 6061 aluminum substrates was done using a combination of statistical designs [32], e.g. a full factorial 2^3 with 4 center points, and a central composite design using a 2^3 full factorial plus 8 star points and 2 center points. The variables were **1** = total gas flow, **2** = second-

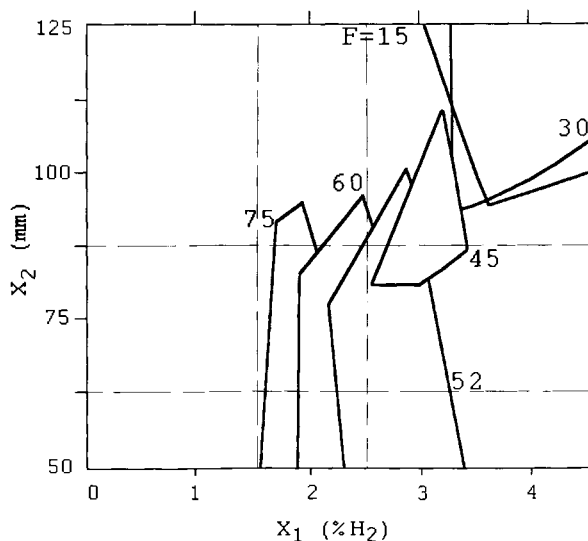


Figure 8-4. Response surface modification (RSM) optimization of an 88WC12Co coating to achieve an erosion rate < 10 mg s $^{-1}$, Rockwell A hardness > 40 , density > 9 g cm $^{-3}$. Shown are operating windows of the hydrogen content of the plasma gas in % and the stand-off distance in mm for powder feed rates F ranging from 15 to 75 g min $^{-1}$ [31].

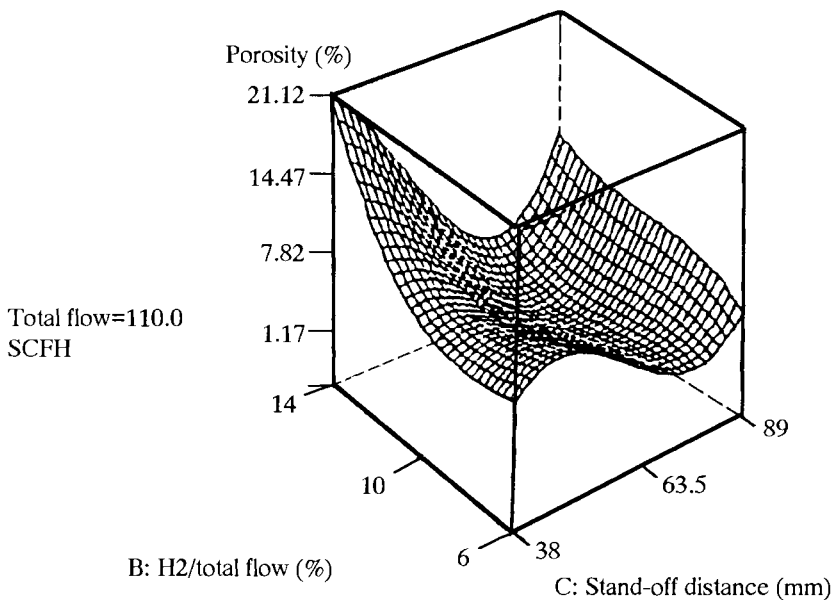


Figure 8-5. Optimization of the porosity of an APS–WC/Co coating on 6061 aluminum. The response surface of the porosity is displayed as a function of the ratio of the hydrogen/total gas flow (2), and the stand-off distance (3) for a total gas flow of 110 SCFH (approx. $3.1 \text{ m}^3 \text{ h}^{-1}$) [32].

ary(H_2)-to-total gas flow ratio and 3=stand-off distance. The average porosity measured ranged from 12.7 to 1.1%. The minimum porosity was obtained for 1 = 521 min^{-1} (110 standard cubic feet per hour (SCFH)), 2 = 11%, and 3 = 70 mm (2.75") as shown on the response surface (Fig. 8-5).

8.4.3 Fractional Factorial Designs

These designs permit a higher flexibility in terms of increasing the number of parameters under study. Although the number of plasma spray parameters that can potentially influence the coating properties is very large (≥ 150) it is common practice to consider only 8 to 12 parameters in statistical designs. Popular designs are 2^{8-4} fractional factorial designs of resolution IV.

8.4.3.1 Tungsten Carbide/cobalt Coatings

An example will be given of the optimization of 88WC12Co coatings deposited by APS (argon/helium plasma at Mach 2 velocities) onto low-carbon steel [33]. The eight selected parameters and their ranges were the plasma current 1 (700; 900 A), argon gas pressure 2 (0.34; 1.36 MPa), helium gas pressure 3 (0.34; 1.36 MPa), powder gas pressure 4 (0.34; 0.68 MPa), powder feed rate 5 (0.5; 2 scale value), powder

grain size **6** ($-45 + 5$; $-75 + 45 \mu\text{m}$), number of traverses **7** (5;15 for set 1 and 20;30 for set 2) and spray distance **8** (250; 450 mm). If all possible experiments would be executed, their total number would be 256 (2^8). In the present situation, however, only a fraction of the total, i.e. the 1/16 replicate was selected (2^{8-4}). Two sets of 16 spray runs each were performed. During the first set, the number of traverses was varied between 5 and 15; this produced relatively thin coatings with a maximum thickness of 80 μm . The data from this set were statistically evaluated to yield information on the main factor effects and synergistic two-factor interactions. The second set with the number of traverses varying between 20 and 30 resulted in coatings with a maximum thickness of 200 μm . The data from the second set were used to evaluate the microhardness and the cohesive strength of the coatings. The design allows the calculation of the eight main effects clear of the composite two-factor interactions E_i . The calculations are executed in Appendix C.

The statistical significance of the factor effects calculated analogous to the simple procedure outlined in Sec. 8.3.2 (see Appendix C) was checked against the minimum factor significance, $\{\min\} = \sigma_{\text{FE}} \times t_v^\alpha$, where $\sigma_{\text{FE}} = (1/n \sum E_i^2)^{1/2}$, t_v^α is the Student's t -value for a confidence level α of a double-sided significance test and v = degrees of freedom. All absolute factor effects larger than or equal to $\{\min\}$ were considered to be significant.

The composite two-factor interactions E_i were calculated in a similar fashion (see Appendix C). They are the unassigned factors that can be used to estimate the experimental error, i.e. the σ_{FE} value needed to calculate the minimum factor significance, $\{\min\}$. With the data obtained it follows that $\sigma_{\text{FE}} = (1/n \sum E_i^2)^{1/2} = (3592/7)^{1/2} = 22.6$, and $\{\min\} = 22.6 \times t(\alpha = 0.90, v = 7) = 22.6 \times 1.895 = 43$. This means, that all main factor effects whose absolute values are larger than 43 should be considered significant at a confidence level of 90%. Checking with the data in Appendix C, this is the case for **5** = 54 and **6** = 55 for thicker coating, i.e. those obtained from the second set of experiments with the number of traverses ranging between 20 and 30. Both effects have positive signs, i.e. the thickness of the coating increases with increasing powder feed rate, **5** and increasing spray distance, **8**. Short spray distances lead to overheating of the alloy powder thus causing thermal decomposition and/or reaction of the WC with the cobalt metal matrix forming η -carbides $\text{Co}_n\text{W}_m\text{C}$ (Fig. 5-17; [34]). Hence, the response polynomial of the thickness of plasma-sprayed 88WC12Co alloy coatings can be approximately expressed by the equation $d(\mu\text{m}) = 32 + 27X_5 + 28X_8$. For thinner coatings a slightly different picture emerges. In this case the significant factors affecting coating thickness are **6** (negative effect) $> \mathbf{8} > E_4, E_6$ (negative), $E_5 > \mathbf{7} > \mathbf{3}$; Fig. 8-6 shows the position of the experimental data points for the coating thickness in μm in a four-dimensional hypercube where the four axes of the cube are the factors **6**, **7**, **8** and **3**. The design consists of two nested cubes with $\mathbf{3} = -1$ and $\mathbf{3} = +1$. These 3D-cubes are also shown in Fig. 8-6 (bottom). Maximum thickness of the coatings can be obtained using fine powders, long spray distances, and high helium gas pressure. The complex statistical significance of the composite two-factor interactions $E_4 = \mathbf{15} + \mathbf{38} + \mathbf{26} + \mathbf{47}$, $E_5 = \mathbf{16} + \mathbf{78} + \mathbf{34} + \mathbf{25}$, and $E_6 = \mathbf{17} + \mathbf{23} + \mathbf{68} + \mathbf{45}$ may be somewhat deconvoluted by assuming that there exists at least one large component interaction involving factors with significant main effect in each composite interaction.

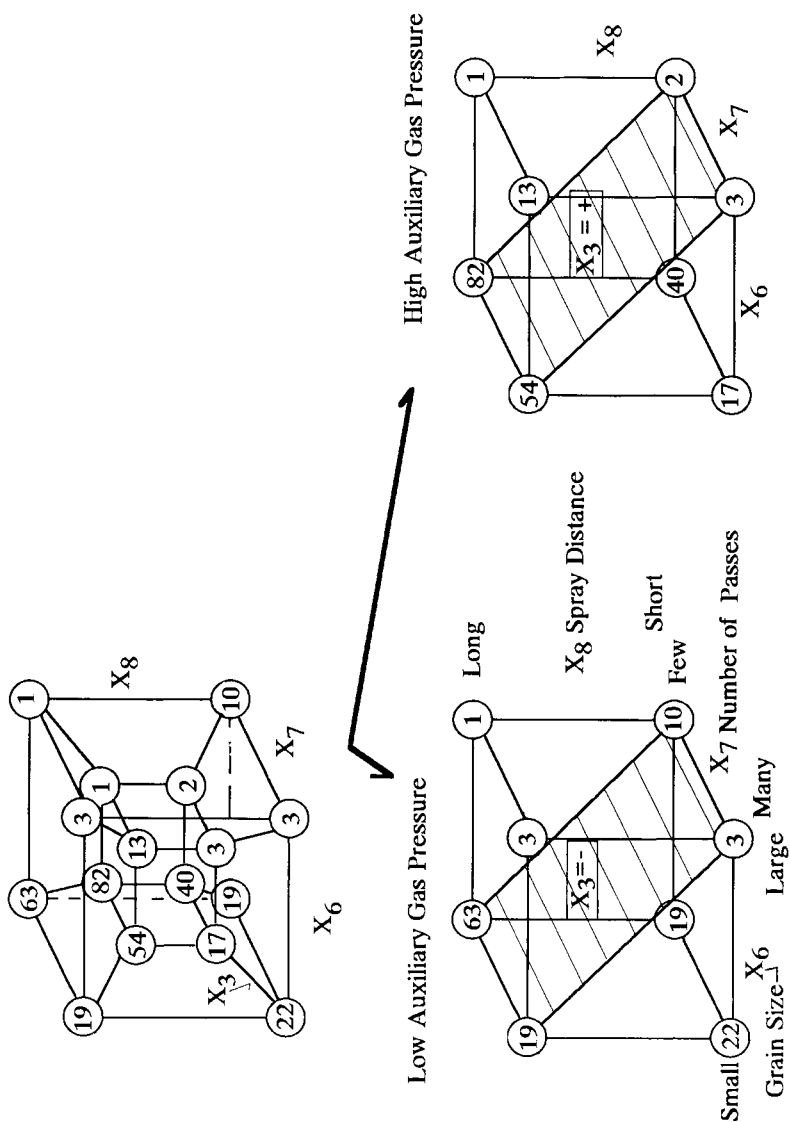


Figure 8-6. 4D-hypercube of optimization of the thickness of 88WC12Co coatings as a function of the auxiliary (helium) gas pressure, the powder grain size, the number of traverses, and the stand-off distance [33].

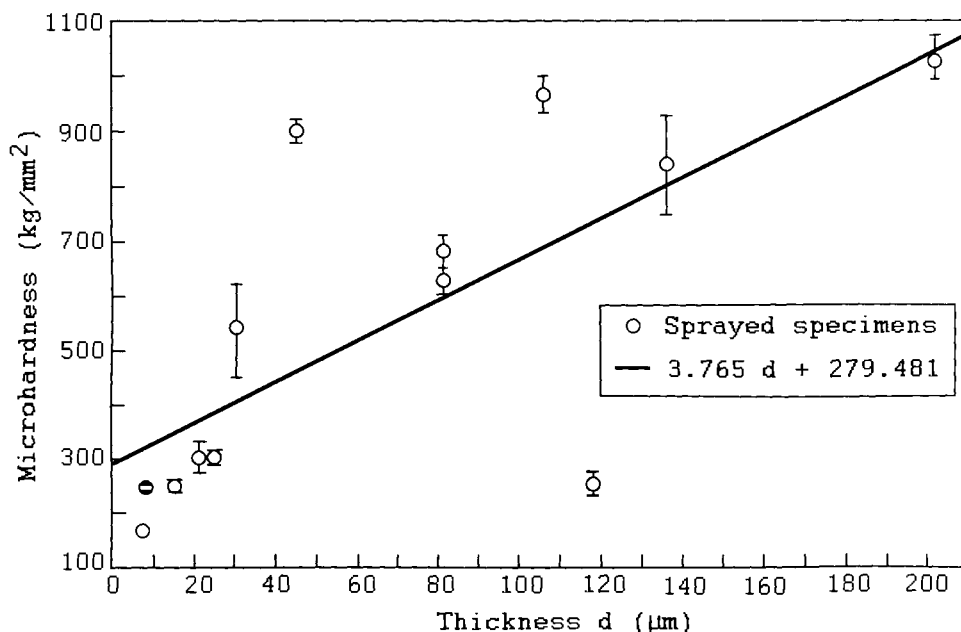


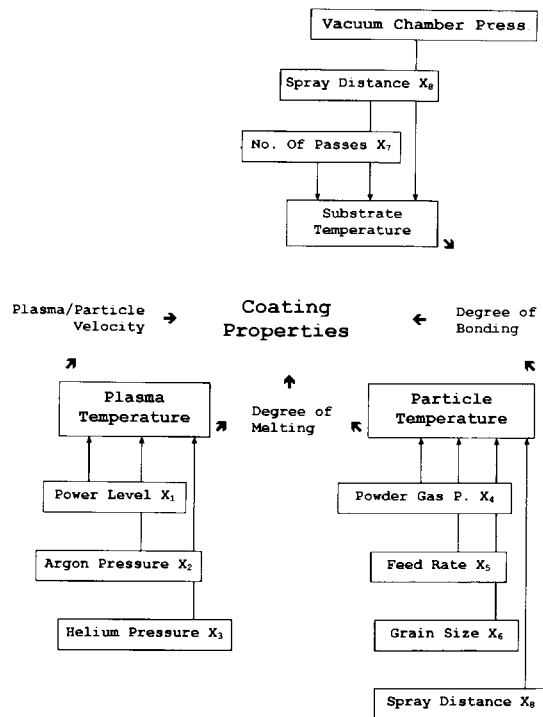
Figure 8-7. Quasi-linear relationship between microhardness ($\text{HV}_{0.2}$) and thickness for 88WC12Co coatings [33].

The most likely candidates are **38** for E_4 , **78** for E_5 , and **68** for E_6 . Additional experiments with a larger set of runs at a higher power of prediction would be required to resolve these ambiguities.

For the microhardness there exists only a weak significant factor, **8**. There is a quasi-linear relationship between coating thickness and microhardness (Fig. 8-7). The maximum microhardness obtained for coatings with thicknesses exceeding $200\ \mu\text{m}$ is $1200\text{HV}_{0.2}$ (75 HRC). The cohesive strength of the coatings exceeded $60 \pm 16\text{ MPa}$ and yielded a maximum value of 80 MPa . Additional scanning electron microscopy investigations were performed to obtain qualitative information on the porosity. The only significant parameter to describe the development of porosity is the powder grain size, **6**, i.e. fine powders produce higher coating porosity. Statistically nonsignificant results were obtained for the degree of densification; high plasma currents, **1** and a small powder grain size, **6** produced a higher degree of densification. These results are somewhat contradictory as increased densification should also produce a lower porosity. It may be, however, that overheating of the particles at short stand-off distances leads to vaporization, and the increased porosity simply reflects the eruption of gaseous decomposition products such as CO_2 generated by partial oxidation of tungsten carbide under formation of η -carbides [34].

In conclusion, the application of the statistical design matrix 2^{8-4} to 88WC/12Co coatings showed that the eight parameters selected as variables can be divided into highly significant ('soft'), and less or insignificant ('hard') parameters that can be

Figure 8-8. Plasma spray parameters 1 to 8 show a three-tiered hierarchy: plasma/particle velocity, degree of melting, and degree of bonding [33].



varied widely (see [31]). ‘Soft’ parameters for optimizing coating thickness are powder grain size and spray distance, i.e. parameters that determine the degree of melting of the particles. Typical ‘hard’ parameters are argon gas pressure, powder gas pressure and powder feed rate.

Figure 8-8 shows the three-tiered hierarchy of the selected plasma spray parameters. Third-level parameters are plasma/particle velocity, degree of particle melting, and degree of bonding of the coating to the substrate. These properties are influenced by the second-level parameters plasma temperature, particle temperature and substrate temperature. These in turn are determined by the eight first-level input parameters. This scheme illustrates once more that the fact that these parameters do not always act in the same directions (saddle points of the response surface), requires statistical multifactorial design to unravel the generally complex parameter interactions.

8.4.3.2 Ferrosilicon Coatings

A second case study concerns the optimization in terms of coating thickness and microhardness of an 85Fe15Si (Valco 3603.0, $-22 + 5 \mu\text{m}$) coating on carbon steel [35]. This material is known for its excellent corrosion resistance and may have applications in demanding environments such as those present in coal gasification where hydrogen sulfide leads to severe stress corrosion cracking. Samples were cut

from St 37 steel plate and mounted on a specially designed sample holder that permits cooling by water flowing through a thin copper pipe attached by hard soldering to the underside of the sample holder. The plasma spray equipment used to deposit the coatings was a conventional METCO system with a vibrating hopper, and a METCO 9M plasmatron. Spraying was performed with an argon/hydrogen plasma gas. A fractional factorial design 2^{8-4} was selected whose factors and their levels were as follows: **1** plasma current (300;500 A), **2** argon gas flow (100;140 scale value), **3** hydrogen gas flow (2;4 scale value), **4** substrate cooling³ (no;yes), **5** ammonia shroud⁴ (no;yes), **6** traverse speed (20;30 m min⁻¹), **7** substrate roughness (0.45; 1.1 μm), and **8** stand-off distance (80;120 mm). Constant factors were the anode (GH 732), powder feed tube (A), powder spray nozzle (2), powder feed rate (60 g min⁻¹), number of preheating cycles (3), number of spray traverses (3) and overlap (5 mm). The main factor effects **1** to **8** as well as the composite two-factor interactions E_1 to E_7 were estimated for the coating thickness (Y_1) and the microhardness (Y_2). The significant main effects for coating thickness were **4** (negative) and **6** (positive), i.e. the coating thickness is maximized (175 μm) on a preheated substrate with increasing traverse speed. There is a conspicuously large negative composite two-factor interaction, $E_2 = \mathbf{13} + \mathbf{27} + \mathbf{46} + \mathbf{58}$ (see Appendix C). This can be rather easily explained by the large value of the (negative) **46** two-factor interaction involving the two significant main effects **4** and **6**.

The significant main effects for the microhardness were **3** (positive), **4** (negative) and **8** (negative), i.e. the microhardness is maximized (325 kPa) at a short stand-off distance on a preheated substrate with increasing hydrogen flow rate (plasma enthalpy). Since it could be shown that for the optimization of the microhardness only three of the original eight selected parameters were significant, the 2^{8-4} fractional factorial design can be reduced to a replicated 2^3 full factorial design in variables **3**, **4** and **8**. Hence the assumption has been made that the remaining factors are essentially inert. However, the rather large standard deviation of the replicated microhardness values showed that this simplifying assumption cannot be upheld. For example, **1** is almost at the level of significance and may account for the variation of the replicated values. Thus the factor **1** behaves like a perturbation of the 3D-response surface in **3**, **4** and **8**, and it must be concluded that larger plasma arc currents, i.e. higher plasma temperatures will also increase the microhardness of 85Fe15Si coatings. Plotting the microhardness in a 4D-hypercube design (Fig. 8-9) in **1**, **3**, **4** and **8** shows clearly that the associated response surface has a saddle in the **34** plane for low and high level variations of **1**.

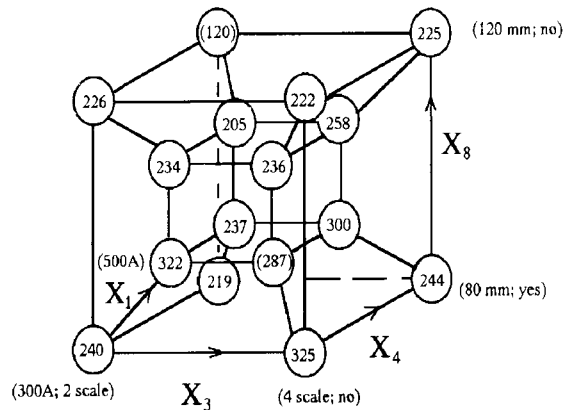
In conclusion, optimized microhardness values for 85Fe15Si coatings can be obtained by:

- substrate preheating,
- increased flow rate of high-enthalpy gases, e.g. hydrogen,

³ 'No' substrate cooling means substrate preheating.

⁴ Ammonia was used as a shroud gas since the 85Fe15Si coating was developed as a bond coat for a plasma-sprayed silicon nitride-based high temperature erosion resistant coating. Ammonia was supposed to counteract the thermal decomposition of silicon nitride during spraying [35].

Figure 8-9. Geometric 4D-representation of a 2^{8-4} design in variables 1, 3, 4 and 8 to estimate the microhardness of a 85Fe15Si coating. The numbers refer to HV_{0.2} values in kPa [35].



- short stand-off distances, and
- high plasma arc current.

Under these conditions the porosity of the coatings will also be minimized, and adhesion to the substrate will be maximized.

8.4.3.3 Alumina/titania Coatings

Similar coating optimization has been performed for alumina–titania plasma-sprayed coatings applied to pump plungers operating at elevated temperature and as protective coatings against hot gas erosion of petrochemical processing equipment [36]. As above, a 2^{8-4} fractional factorial design of resolution IV was selected with 1 plasma current (850;950 A), 2 argon gas pressure (345;517 kPa), 3 helium gas pressure (276;414 kPa), 4 substrate preheating (23;200 °C), 5 powder feed rate (4.5;5.5 r.p.m.), 6 roughening grit size (80;40 mesh), 7 number of traverses (20;50) and 8 stand-off distance (76;127 mm). Coating thickness was found to be significantly influenced by 2, 7 and 8. Figure 8-10 shows the 2^3 design cube with the results of the replicated coating thickness measurements. Figure 8-11 shows a different way to express parameter significance. The coefficients obtained by calculation identical to those shown in Appendix C have been plotted on a probability net. If the coefficients would only vary in a random fashion then their plot should give a straight line (Gaussian distribution). Deviation from this straight line signifies significant parameter effect. Figure 8-11 shows that the thickness of alumina–titania (97/3) coatings is significantly influenced by the argon gas pressure, 2 and the spray distance, 8 in a negative way, but positively influenced by the number of passes, 7, the powder feed rate, 5 and a two-factor composite interaction, E_3 (positive effect) whose determining contributions are presumably the two-factor interactions 28 and 57. In Fig. 8-12 it is shown that the interaction 28 has a large difference in slope at low and high levels of 7 with a cross-over at high 7. On the other hand, the probability plots of the coefficients of the second-order polynomial response equations for the microhardness (Vickers test, HV_{0.3}; Fig. 8-13) and the abrasion mass loss determined

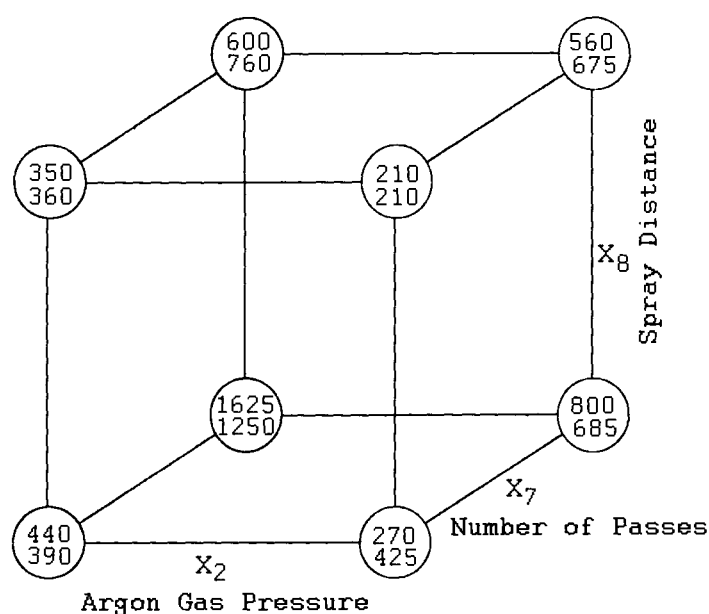


Figure 8-10. Optimization of the thickness of alumina/titania coatings as a function of argon gas pressure 2, number of traverses 7, and stand-off distance 8 [36].

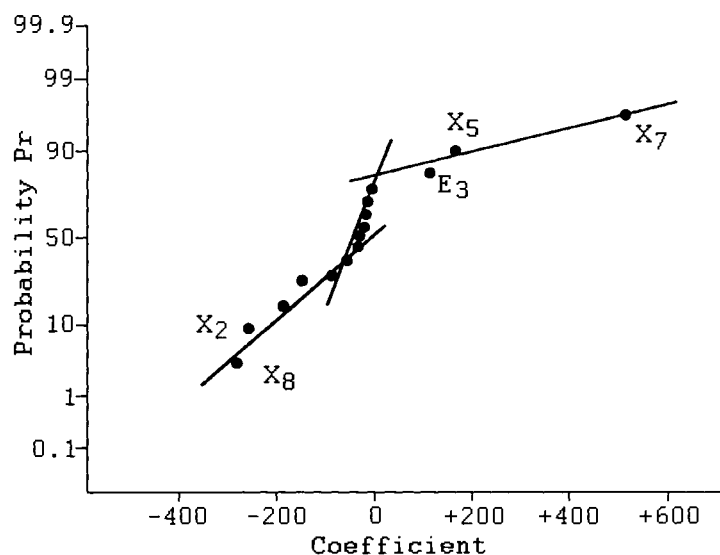


Figure 8-11. Probability distribution of the coefficients of the polynomial equation obtained for the thickness of alumina/titania coatings [36].

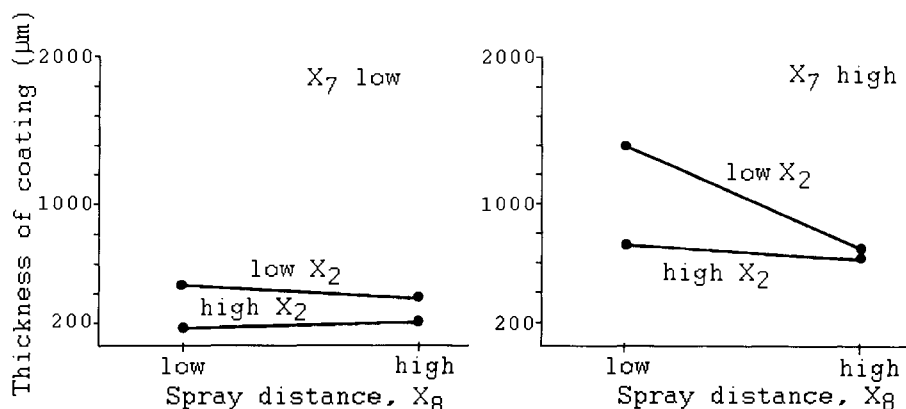


Figure 8-12. The two-factor interaction 28 is negligible for few traverses ($7 < 20$) but strong for many traverses ($7 > 50$) [36].

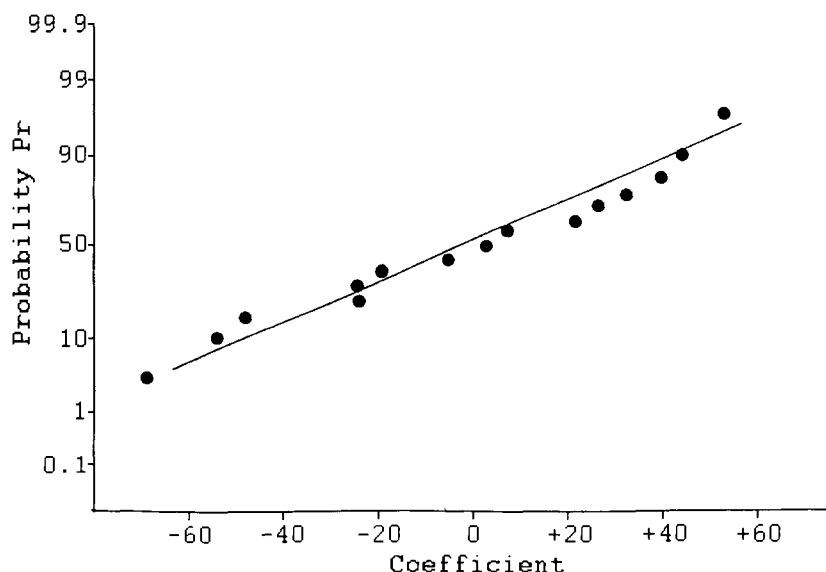


Figure 8.13. Probability distribution of the coefficients of the polynomial equation obtained for the microhardness of alumina/titania coatings, showing random, i.e. statistically nonsignificant factor effects [36].

by the ASTM G 65 test (Fig. 8-14) show random behavior thus indicating that in both cases the properties are not significantly influenced by the selected factors. The microhardness increases linearly (correlation factor 0.61) with coating thickness according to a limiting equation $HV_{0.3} = ad + b$, where $a = 120 \text{ kg mm}^{-3}$, $b = 974 \text{ kg mm}^{-2}$, and $d = \text{thickness (mm)}$. The abrasion mass loss is inversely proportional (correlation factor -0.89) to the coating thickness and obeys the equa-

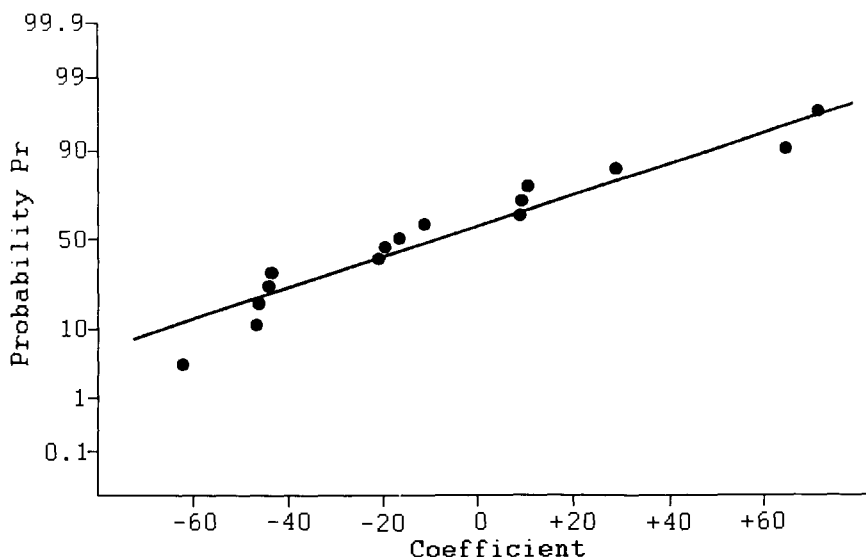


Figure 8-14. Probability distribution of the coefficients of the polynomial equation obtained for the abrasion mass loss (ASTM G65) of alumina/titania coatings, showing statistically nonsignificant factor effects [36].

tion $\Delta m = c/d$ where $c = 45.3 \text{ mg mm}^{-1}$ and $d = \text{thickness (mm)}$. Figure 8-15 shows that there is also an inverse relationship between abrasion mass loss and microhardness that can be expressed by the power function $\Delta m = A(\text{HV}_{0.3})^{-B} [\text{kg}]$ where $A = 4.3 \times 10^{24}$ and $B = 9.5$ (correlation factor -0.64).

In conclusion, application of a two level fractional factorial design 2^{8-4} to a set of $97\text{Al}_2\text{O}_3\text{3TiO}_2$ coatings on low-carbon steel (A 569) surfaces showed that the eight parameters selected could be divided into highly significant or 'soft', and less or nonsignificant 'hard' parameters. 'Soft' parameters to describe the coating thickness are the stand-off distance 8, the number of traverses 7, and the argon gas pressure 2. Typical 'hard' parameters are arc current, preheating temperature and grain size of the grit blasting material.

8.4.3.4 Stellite Coatings

Another example deals with stellite 6 (28Cr1C4W1Si, bal. Co) coating deposited by a PTA surfacing process on mild steel (SIS 2172) bars by Herrström *et al.* [37]. A 2^{6-2} fractional factorial design was used in the parameters, 1, plasma current (100;130 A), 2, argon gas flow (1;3 l min⁻¹), 3, powder gas flow (2;4 l min⁻¹), 4 oscillation frequency (82;90 min⁻¹), 5 weld speed (5;7 cm min⁻¹) and 6 stand-off distance (6;14 mm). Dependent parameters estimated were the percentage dilution, the hardness HV_{30} , and the width and the height of the deposit in mm. The hardness of the PTA deposit depends significantly with $2 > 6 > 1 \gg 16 + 45$, the width of the de-

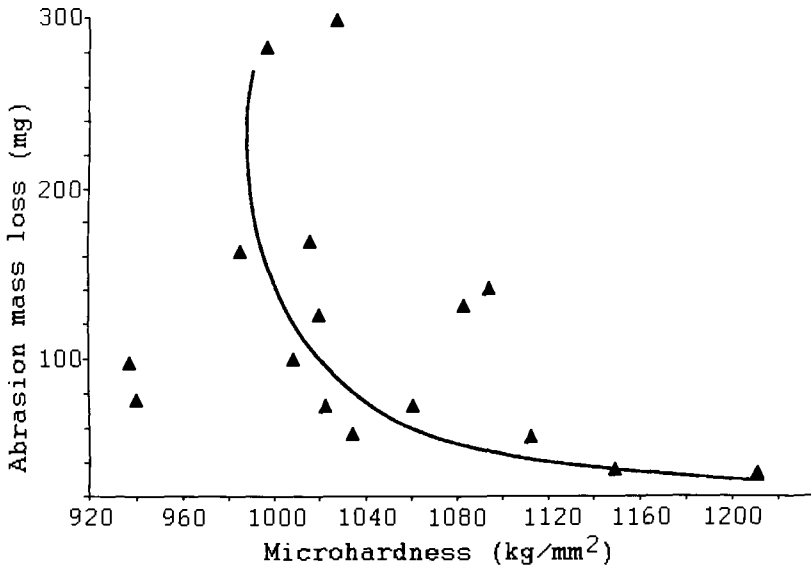


Figure 8-15. Inverse relationship between abrasion mass loss and microhardness of alumina/titania coatings [36].

posit shows $4 > 2$, and the height $1 > 2$. The dilution depends significantly at a confidence level $< 95\%$ on the parameters $2 > 1 \gg 6$. It should be mentioned that the responses Y are not independent of each other. So the hardness depends not only on the dilution but also on the microstructure and the cooling rate that were not explicitly parts of the experimental design. At the working point, i.e. at an intermediate parameter level ('0') the following optimized responses were found: hardness $424.6 \pm 3.78 \text{ HV}_{30}$, dilution $6.84 \pm 0.64\%$, width $15.24 \pm 0.30 \text{ mm}$, and height $2.84 \pm 0.29 \text{ mm}$.

8.4.3.5 Titanium Coatings

Work by Lugscheider *et al.* [38] on vacuum plasma-spraying of Ti coatings on 1.4571 and 1.4541 austenitic steel substrates employed an L_8 Taguchi matrix with four parameters varied. These parameters and their levels were the plasma current **1** (605; 655 A), argon gas flow **2** (33; 43 standard liter per minute (SLPM)), vacuum chamber pressure **4** (144; 164 mbar) and powder feed rate **6** (6.8; 10.8 g min^{-1}). The parameters **3** (hydrogen gas flow; 6.5 SLPM), **5** (spray distance; 280 mm), **7** (plasma transferred arc current; 0 A) and **8** (sputter distance 320 mm) were kept constant at the levels indicated. The eight runs performed actually constitute an 2^{8-5} matrix. Two additional runs with parameters **1** and **2** changed in the directions indicated by the fractional factorial design, and parameters **4** and **6** kept at their zero levels, i.e. midway between the upper and lower parameter levels led to the desired minimum porosity of 1.3% [39]. The other optimized dependent parameters were the micro-

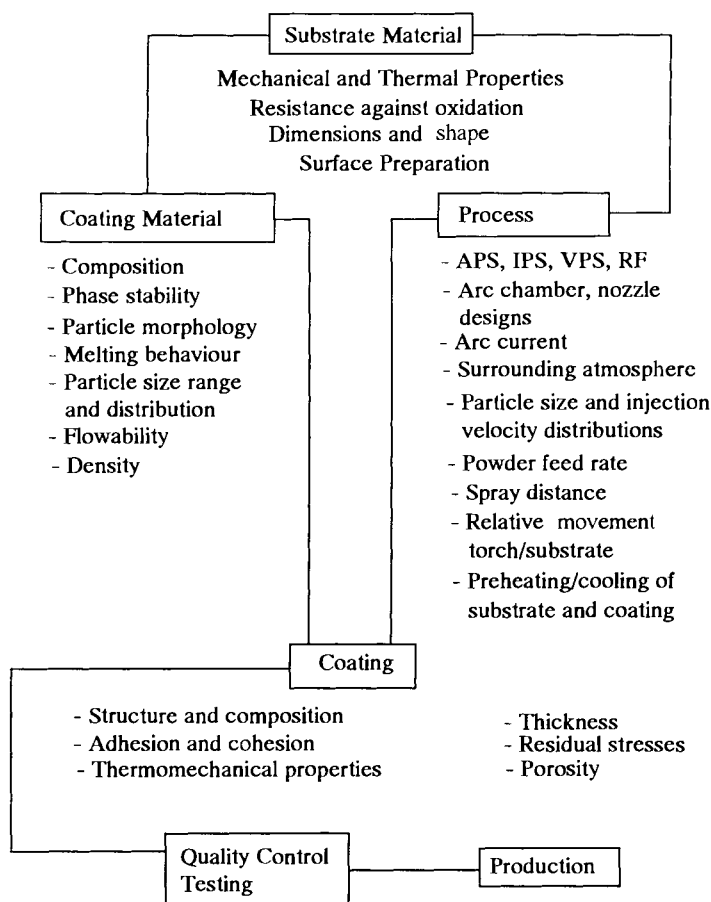


Figure 8-16. Main aspects of plasma spraying considering substrate–coating–process interactions.

hardness ($218 \pm 37 \text{ HV}_{0.05}$), adhesion strength obtained by DIN 50 160 ($75 \pm 4 \text{ N mm}^{-2}$), and the traverse bending strength by DIN 50 111. The significant parameters for this optimization were 2 (negative effect) \gg 14 $>$ 1.

8.5 Future Developments

Figure 8-16 shows the main aspects of plasma spraying that have to be considered in order to produce advanced metal, ceramic or composite coatings with high in-service performance. Most of the aspects listed therein have been dealt with rather exhaustively.

Thermal spray research and development of advanced materials for high performance applications is increasing rapidly, and many developments are being commercialized now. As an indication of this rapid development it should be mentioned that over 80% of the advances that have been made over the last 80 years have been made in the last two decades! Equipment and process advances have typically led the technology in the past. Increasingly, materials and process control (SPC), and novel applications will lead in the next 10 years.

Future developments in the advanced materials coating field can be characterized and evaluated in terms of their economic feasibility by looking at different technology support and development strategies [40]. Figure 8-17 shows that wear and thermal barrier coatings are level I strategies that deploy current technologies to improve the competitive performance of small companies or create new companies. Bio-ceramic and diamond coatings are level II strategies that focus on the development of innovative applications of new technological discoveries. Finally, low friction coatings, high-temperature superconducting, and silicon nitride coatings are level III strategies whose efforts are still concentrated on basic research leading up to the discovery of new technologies. Those new technological breakthroughs expected for the future will predominantly assist large companies, and attract completely new industries [43].

The main areas of contemporary developments will be automotive coatings with high rate, low cost processing, while aerospace applications are triggering the advance of the technology for novel thermal barrier coatings, spray forming and composite materials processing.

Advances are being typically made in the following areas [41]:

- materials, process, and equipment;
- control devices and automated robotic handling;
- use of SPC with resulting close process monitoring;
- accumulation of data bases and development of expert systems;
- HVOF processing;
- engineered powder production; and
- composite and intermetallic spray forming.

Thermal spray processing education and training needs to be implemented and managed on a broader base. Collaboration with industry in the resource and manufacturing sectors will lead increasingly to strategic alliances that enable industry to produce more competitively and environmentally compatibly. Process control, including modeling of complex plasma-particle-substrate interactions, on-line process diagnostics, and development of novel coatings with improved performance are areas rich in research needs and opportunities.

Such areas can be predicted by application technology mapping [42]. Marketers look for applications of materials, and then determine the performance needs for particular applications. These data are mapped against the value-in-use estimate and the customer's ability to pay (Fig. 8-18). The *military* have clearly a high ability to pay for sophisticated materials and coatings, or products with a high value-in-use, for example piezoelectric, ferroic and superconducting coatings for range finders and

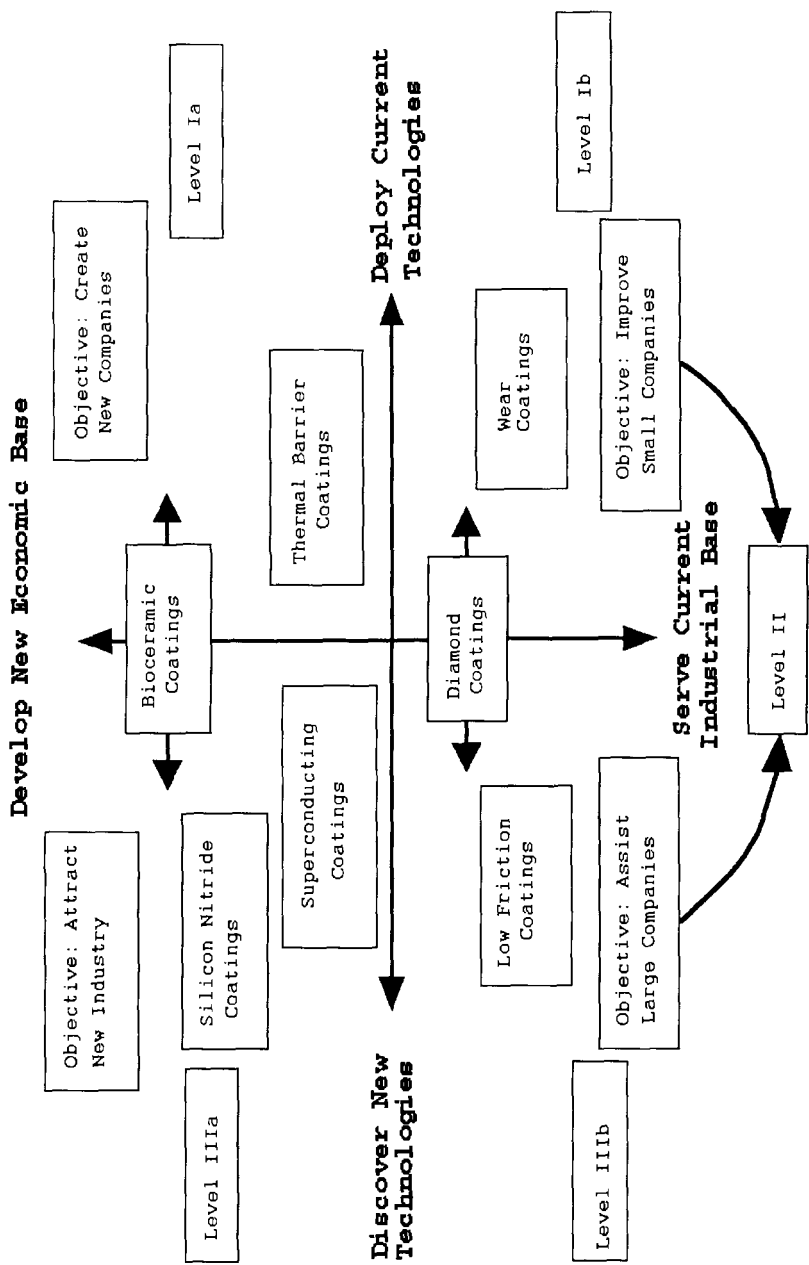


Figure 8-17. Technology support and development strategies applied to various types of coatings [43].

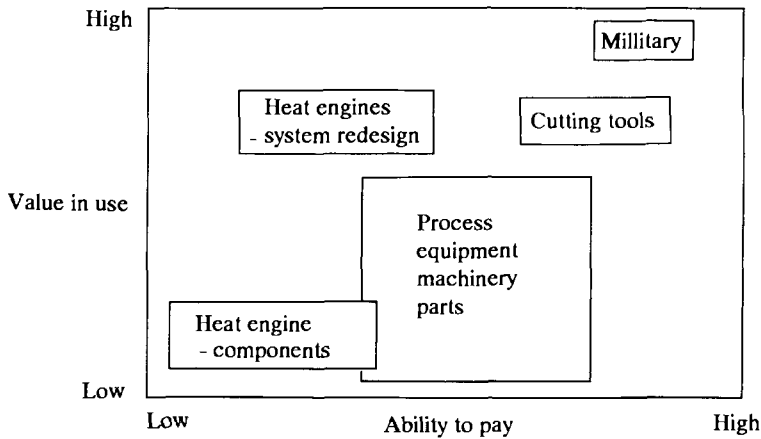


Figure 8-18. Application technology mapping for coatings [42].

surveillance systems. Titanium nitride, titanium carbide, and diamond coatings for ceramic *cutting tools* are high-value-added but nevertheless cost-competitive because of their superior wear performance in numerically controlled high-speed machining of tough and hard steels, and superalloys. On the other hand, *heat engine components* such as ceramic turbochargers, thermal barrier coatings (TBCs) and a variety of automotive sensors based on functional ceramic coatings and thin films have a low value, and the ability to pay for it by the car manufacturer is also low in order to maximize profit. New developments are presently being considered such as thick thermal barrier coatings (TTBCs) for diesel engines to replace water cooling by air cooling systems. The middle ground of Fig. 8-18 is occupied by wear-resistant parts for nonautomotive markets, i.e. *process equipment and machine tools*. In this area a new strong driving force is evolving that is geared towards first-generation materials to improve process efficiency and overall productivity in the manufacturing and resource industries [43].

In conclusion, the future of advanced materials coatings applied by plasma spray technology looks very bright. There are, however, problems still to be solved.

Technical problems include optimization of plasmatron design, powder size and composition, rheological and flow properties of powders, overspray losses and surface preparation. Quality control procedures must be developed or improved, and implemented for ceramic, metal and composite coatings to standardize impact testing, hardness testing, shear and bending testing, cavitation-erosion testing, slurry abrasion testing etc. Most of all, reliable and reproducible tests must be developed to measure the adhesion strength of the coatings to the substrate. Finally, the development of computer codes is necessary that model the forces acting on the coating/substrate interface. The objective is to develop coatings that sustain in-film compressive loads during service, thus improving adherence to the substrate and, in turn, maximizing the service life of the coated equipment.

There is also the considerable challenge of improving the image of thermal spray

coatings as a viable, reliable und immensely versatile option available to design engineers. Although it is widely recognized that plasma-sprayed coatings can provide many successful answers to engineering problems, its level of awareness in industry and government has to be raised [43].

Thermal spray technology is emerging as an important tool of increasingly sophisticated surface engineering technology. Initially developed as a simple and relatively crude surfacing tool, thermal and plasma spraying, respectively is now considered a powerful and flexible materials processing method with a high potential of development [44]. It appears that the return on investment in this area of surface engineering is excellent, and that small and medium-sized enterprises can hugely benefit from entering a market segment that by many is considered the *materials technology of the 21st century!*

At the end of this treatise on plasma-sprayed coatings the following final statement should be made. Strict quality control of well established coatings, and close attention to the design and testing of coating/substrate systems as a single synergistic entity, combined with the development of novel structural and functional coatings using improved automated equipment and comprehensive data bases and expert systems, will secure plasma spray technology a substantial market niche in the immediate future beyond the year 2000.

References

- [1] H. Holleck, *Surf. Eng.* **1991**, 7, 137.
- [2] S. Sampath, H. Herman, N. Shimoda, T. Saito, *MRS Bull.* **1995**, January, 27.
- [3] D. B. Marshall, T. Noma, A. G. Evans, *Commun. Am. Ceram. Soc.* **1982**, 65, C-175.
- [4] S. Bisgaard, *Proc. 3rd NTSC*, Long Beach, CA, USA, 20–25 May **1990**; p. 661.
- [5] R. B. Heimann, *Proc. First All-Alberta Appl. Stat. Biometr. Workshop. AECV91-P1*, Edmonton, Alberta, Canada, 18–19 October **1990**, p. 87.
- [6] E. Lugscheider, M. Knepper, DVS, Düsseldorf **1991**, 136, p. 88.
- [7] R. L. Plackett, J. P. Burman, *Biometrika* **1946**, 33, 305.
- [8] G. E. P. Box, D. W. Behnken, *Technometrics*, **1960**, 2, 455.
- [9] G. E. P. Box, W. G. Hunter, J. S. Hunter, *Statistics for Experimenters*, Wiley, NY, USA, **1978**.
- [10] W. E. Deming, *Out of the Crisis*, MIT Press, Cambridge, MA, USA, **1986**.
- [11] G. Taguchi, S. Konishi, *Taguchi Methods, Orthogonal Arrays and Linear Graphics*, American Supplier Institute, **1987**.
- [12] P. Whitcomb, *Design-Expert™*, version 3.0, Stat-Ease Inc., 2021 East Hennepin, #191, Minneapolis, MN 55413.
- [13] J. W. Tukey, *Ann. Math. Stat.* **1962**, 33, 1.
- [14] C. Daniel, *Applications of Statistics to Industrial Experimentation*, Wiley, NY, USA, **1976**.
- [15] W. G. Cochran, G. M. Cox, *Experimental Designs*, Wiley, NY, USA, **1957**.
- [16] DuPont de Nemours & Co, *Strategy of Experimentation*, **1975**.
- [17] E. De Bono, *The use of Lateral Thinking*, Penguin Books, Harmondsworth, **1970**.
- [18] H. Bandemer, A. Bellmann, *Statistische Versuchsplanung*, 4th ed., Teubner, Stuttgart, Germany, **1994**, p. 133.
- [19] S. I. Satterthwaite, *Technometrics* **1959**, 1, 111.
- [20] G. E. P. Box, N. R. D. Draper, *Empirical Model Building and Response Surface Methodology*, Wiley, NY, USA, **1987**.

- [21] F. Yates, *The Design and Analysis of Factorial Experiments*, Imperial Bureau Soil Sci., Techn. Commun., **1937**, 35.
- [22] J. S. Hunter, *Technometrics* **1966**, 8, 177.
- [23] G. E. P. Box, J. S. Hunter, *Technometrics* **1961**, 3(3), 311.
- [24] G. E. P. Box, K. B. Wilson, *J. Roy. Stat. Soc. B* **1951**, 13, 1.
- [25] S. Thiele, Mikrohärte, Mikrostruktur und Haftung vakuum-plasmagespritzter TiC/Mo₂C/Ni, Co-Verbundschichten. Unpublished diploma thesis, Freiberg University of Mining and Technology, June **1994**.
- [26] E. R. Novinski, A. J. Rotolico, E. J. Cove, *Proc. 3rd NTSC*, Long Beach, CA, USA, 20–25 May **1990**; p. 151.
- [27] T. Chon, A. Aly, B. Kushner, A. Rotolico, W. L. Riggs, *Proc. 3rd NTSC*, Long Beach, CA, USA, 20–25 May **1990**; p. 681.
- [28] J. E. Nerz, B. A. Kushner, A. J. Rotolico, *Proc. 3rd NTSC*, Long Beach, CA, USA, 20–25 May **1990**, p. 669.
- [29] J. Walter, W. L. Riggs, *Proc. 3rd NTSC*, Long Beach, CA, USA, 20–25 May **1990**, p. 729.
- [30] T. C. C. Hurng, M. B. C. Quigley, R. L. Apps, *Proc. 2nd Int. Conf. on Surface Engineering*, Stratford-upon-Avon, UK, 16–18 June **1987**, p. 413.
- [31] T. Troczynski, M. Plamondon, *J. Therm. Spray Technol.* **1992**, 1(4), 293.
- [32] D. J. Varacalle, L. B. Lundberg, B. G. Miller, W. L. Riggs, *Proc. 14th ITSC'95*, Kobe, Japan, 22–26 May **1995**, p. 377.
- [33] R. B. Heimann, D. Lamy, T. Sopkow, *J. Can. Ceram. Soc.* **1990**, 59(3), 49.
- [34] K. Hajmrlé, M. Dorfman, *Mod. Dev. Powder Metall.* **1985**, 15/17, 409.
- [35] R. B. Heimann, *Development of Plasma-Sprayed Silicon Nitride-Based Coatings on Steel*, Research Report to NSERC and EAITC, Canada, 15 December **1992**.
- [36] R. B. Heimann, D. Lamy, T. N. Sopkow, *Proc. 3rd NTSC*, 20–25 May **1990**, Long Beach, CA, USA, p. 491.
- [37] C. Herrström, H. Hallén, A. Ait-Mekideche, E. Lugscheider, *Proc. TS'93*, Aachen **1993**, DVS 152, p. 409.
- [38] E. Lugscheider, P. Lu, B. Hauser, D. Jäger, *Surf. Coat. Technol.* **1987**, 32, 215.
- [39] E. Lugscheider, P. Lu, *Proc. Int. Conf. Plasma Science Technol.*, Beijing, China, 4–7 June 1986; Science Press, Beijing, China, **1986**, p. 250.
- [40] Center for Economic Competitiveness. *Assessment of Alberta Technology Centers*. SRI International, **1990**.
- [41] R. W. Smith, R. Novak, *PMI*, **1991**, 23(4), 231.
- [42] S. K. Sutliff, *Trans. 4th Workshop CUICAC*, Toronto, Ontario, Canada, 25–26 May **1987**.
- [43] R. B. Heimann, *Proc. Adv. Mater.* **1991**, 1, 181.
- [44] E. Lugscheider, H. Eschnauer, U. Müller, Th. Weber, *PMI*, **1991**, 23(1), 33.

Appendix A: Dimensionless Groups

Dimensional analysis is a key step in modeling processes [1, 2]. There are usually fewer dimensionless groups than there are physical quantities (Buckingham's rule) [3]. When the model is evaluated or displayed, the dimensionless groups are the correct axes to choose (see, for example Fig. 4-18). It should be emphasized that dimensionless groups should always be used for exponential, logarithmic, or power law arguments since failure to do so may lead to pseudo-constants without physical significance [3].

Because of their ability to simplify complex modeling problems, dimensionless groups are frequently used in chemical engineering to solve complex equations of heat and mass transfer. In particular, equations of heat, mass and impulse transfer ubiquitously occurring in the description of plasma spray processes and numerical solutions of modeling approaches can be deduced from existing solutions of geometrically similar systems [4]. The term 'geometric similarity' refers to the interchangeability of streamlines and boundaries of systems of widely varying dimensional extension by linear scaling laws. Motion of fluids such as a plasma gas are dynamically similar when the solutions of the related dimensionless transfer equations are identical. For example, the simplified Navier–Stokes equation

$$\rho(\delta v/\delta t) = \rho(v \cdot \nabla)v - \nabla p + \eta \nabla^2 v + f, \quad (\text{A-1})$$

where v = mass average velocity (barycentric velocity), p = plasma gas pressure, and η = plasma gas viscosity, can be transformed to its dimensionless version by using the free-stream plasma velocity V , a characteristic length L and a typical pressure p_0 to normalize $v(x, y, z)$ and p by setting

velocity $W = v/V$,

length $X = x/L$, $Y = y/L$, $Z = z/L$, and (A-2)

pressure $P = p/p_0$.

Substituting the dimensionless ratios into Eq. (A-1) yields

$$\rho(V^2/L)(W \cdot \text{grad})W = -(p_0/L) \text{grad}(P) + (\eta V/L^2) \nabla^2 W \quad (\text{A-3})$$

$$\text{or} \quad (W \cdot \text{grad})W = -(p_0/\rho V^2) \text{grad}(P) + \text{Re}^{-1}(\nabla^2 W), \quad (\text{A-3a})$$

with $\text{Re} = VL/\eta$.

It should be noted that the second term on the right hand side of Eq. (A-3a) contains all the parameters that govern the fluid dynamics of a plasma jet. Dynamic similarity is assured if for two geometrically similar systems A and B, $Re(A) = Re(B)$. The similarity principle was discovered by Reynolds and has overriding importance for any modeling approach in fluid dynamics [5].

The most important dimensionless groups used in modeling of plasma heat and mass transfer equations can be conveniently divided into groups describing momentum-, heat-, and mass transfer, and materials constants.

Momentum transfer

Reynolds number $Re = VL/\nu$ (inertia force/viscous force)

Euler number $Eu = \Delta p/\rho V^2$ (fluid friction)

Grashof number $Gr = L^3 g \gamma \Delta T / \nu^2$ (bouyancy force/viscous force)

Heat transfer

Fourier number $Fo = \kappa \Delta T / L^2$ (heat transfer by diffusion)

Péclet number $Pe = VL/\kappa = Re \times Pr$ (bulk heat transfer/conductive heat transfer)

Rayleigh number $Ra = L^3 g \gamma \Delta T / \nu \kappa = Gr \times Pr$ (free convection)

Nusselt number $Nu = hL/k = Re \times St$ (total heat transfer/conductive heat transfer)

Stefan number $St = \sigma L T^3 / k$ (heat transfer by radiation)

Mass transfer

Fourier number $Fo^* = D \Delta T / L^2 = Fo / Le$ (unsteady state mass transfer)

Péclet number $Pe^* = VL/D = Re \times Sc$ (bulk mass transfer/diffusive mass transfer)

Grashof number $Gr^* = L^3 g \beta' \Delta x / \nu^2$ (mass transfer at free convection)

Nusselt number $Nu^* = kL/\rho D = Sh$

Materials constants

Prandtl number $Pr = \nu/\kappa = Pe/Re$

Schmidt number $Sc = \nu/D = Pe^*/Re$

Lewis number $Le = \kappa/D = Sc/Pr$

References

- [1] P. Bridgeman, *Dimensional Analysis*, 2nd edn., York University Press, New Haven, CT, USA.
- [2] E. Isaacson, M. Isaacson, *Dimensional Models in Engineering and Physics*, Wiley, NY, USA, 1975.
- [3] M. F. Ashby, *Mater. Sci. Technol.*, **1992**, 8, 102.
- [4] F. Rosenberger, *Fundamentals of Crystal Growth I*, Springer, Berlin, **1979**, p. 267f.
- [5] D. F. Boucher, G. E. Alves, *Chem. Eng. Progr.* **1959**, 55, 55.

Appendix B: Calculation of Temperature Profiles of Coatings

The following treatment has been adapted from the work by Houben [1]. It provides the calculations required to arrive at the temperature profiles through Mo and AISI-316 coatings, respectively deposited onto a low carbon steel substrate as shown in Fig. 5-12. The calculations are based on the Neumann–Schwartz equation [2].

B.1 Heat Conduction Equations

For the three regions identified in the coordinate system of Fig. 5-10 the three heat conduction (Fourier) equations can be expressed by

$$\partial^2 \Theta_0 / \partial x^2 - (1/a_0) \partial \Theta_0 / \partial t = 0 \quad \text{for } x \leq 0 \text{ (solid substrate)} \quad (\text{B-1a})$$

$$\partial^2 \Theta_1 / \partial x^2 - (1/a_1) \partial \Theta_1 / \partial t = 0 \quad \text{for } 0 \leq x \leq X(t) \text{ (solid deposit)} \quad (\text{B-1b})$$

$$\partial^2 \Theta_2 / \partial x^2 - (1/a_2) \partial \Theta_2 / \partial t = 0 \quad \text{for } x \geq X(t) \text{ (liquid deposit)}, \quad (\text{B-1c})$$

where Θ = temperature and a = thermal diffusivity.

The boundary conditions are $\Theta_0 = T_{s0}$ (20 °C) as $x \rightarrow -\infty$,

$$\Theta_0 = \Theta_1 \quad \text{as } x = 0.$$

$$\Theta_1 = \Theta_2 \quad \text{as } x = X(t)$$

For thermal equilibrium conditions at the interfaces it follows that

$$k_0(\partial \Theta_0 / \partial x) = k_1(\partial \Theta_1 / \partial x) \quad \text{as } x = 0 \quad (\text{B-3})$$

$$k_1(\partial \Theta_1 / \partial x) - k_2(\partial \Theta_2 / \partial x) = L\rho(dX/dt) \quad \text{as } x = X(t), \quad (\text{B-4})$$

where L = latent heat of melting.

For the special case indicated in Fig. 5-10 ($\Theta_2 = T_3 = T_m$ for $x \geq 0$) the Eq. (B-4) simplifies to

$$k_1(\partial \Theta_1 / \partial x) = L\rho(dX/dt) \quad \text{as } x = X(t). \quad (\text{B-4a})$$

B.2 Solutions of the Equations

B.2.1 Substrate Temperature Profile

Assumption: $\Theta_0 = T_{s0} + \alpha[1 + \operatorname{erf}(x/(4a_0t)^{1/2})]$. (B-5)

The quantity α is the so-called contact conductivity at the interface substrate/solid deposit ($x = 0$) and is defined as $\alpha = (k_1 \rho_1 c_1)^{1/2}$, where k = thermal conductivity, ρ = density, and c = specific molar heat. It should be emphasized that the solution shown in Eq. (B-5) satisfies both Eq. (B-1a) and, because of $\Theta_0 \rightarrow T_{s0}$ as $x \rightarrow -\infty$, the first boundary condition. The error function erf is as usually defined as $\operatorname{erf} z = \int (2/\pi^{1/2}) \exp(-z^2) dz$.

B.2.2 Deposit Temperature Profile

Assumption: $\Theta_1 = T_{s0} + \beta + \gamma \operatorname{erf}(x/(4a_1t)^{1/2})$. (B-6)

The quantity β is the contact conductivity at the interface solid/liquid deposit ($x = X(t)$), and γ the ‘contact’ diffusivity at the free interface receiving a constant stream of molten particles. Eq. (B-6) satisfies Eq. (B-1b), and also satisfies the second boundary condition if $\beta = \alpha$ ($\Theta_0 = \Theta_1$ as $x = 0$). Then Eq. (B-6) can be rewritten as

$$\Theta_1 = T_{s0} + \alpha + \gamma \operatorname{erf}(x/(4a_1t)^{1/2}). \quad (\text{B-6a})$$

To establish the required connection between α and γ the Eqs. (B-5) and (B-6) will be differentiated to yield

$$\begin{aligned} \partial\Theta_0/\partial x &= \alpha[(\partial/\partial x) \operatorname{erf}(x/(4a_0t)^{1/2})] \\ &= \alpha(2/\pi^{1/2}) \exp(-x^2/4a_0t)(1/(4a_0t)^{1/2}) \\ &= [\alpha/(\pi a_0t)^{1/2}] \exp(-x^2/4a_0t). \end{aligned} \quad (\text{B-7})$$

For $x = 0$ it follows that

$$(\partial\Theta_0/\partial x)_{x=0} = \alpha/(\pi a_0t)^{1/2}. \quad (\text{B-7a})$$

Analogously one obtains

$$(\partial\Theta_1/\partial x)_{x=0} = \gamma/(\pi a_1t)^{1/2}. \quad (\text{B-7b})$$

Substituting Eqs. (B-7a) and (B-7b) into (B-3) yields

$$k_0(\alpha/(\pi a_0t)^{1/2}) = k_1(\gamma/(\pi a_1t)^{1/2}).$$

With $\alpha/\gamma = B$, and $a = k/\rho c$ one obtains

$$B = (k_1 \rho_1 c_1)^{1/2} / (k_0 \rho_0 c_0)^{1/2}. \quad (\text{B-8})$$

With Eq. (B-8), Eq. (B-6a) can be expressed as

$$\begin{aligned} \Theta_1 &= T_{s0} + \gamma[(\alpha/\gamma) + \operatorname{erf}(x/(4a_1t)^{1/2})] \\ &= T_{s0} + \gamma[B + \operatorname{erf}(x/(4a_1t)^{1/2})]. \end{aligned} \quad (\text{B-9})$$

For $\Theta_1 = \Theta_2 = T_m$ (as $x \geq X(t)$) we obtain the explicit solution of the heat transfer equation at the interface liquid/solid deposit as

$$T_m - T_{s0} = \gamma[B + \operatorname{erf}(x/(4a_1t)^{1/2})]. \quad (\text{B-10})$$

With the assumption

$$X = p(4a_1t)^{1/2} \quad \text{or} \quad t = X^2/4p^2a_1 \quad (\text{B-10a})$$

(solution of the first-order differential equation of heat transfer) it follows that

$$dX/dt = p(a_1/t)^{1/2}. \quad (\text{B-11})$$

With Eq. (B-7) for $x = X(t)$, Eq. (B-4a) can further be expressed by

$$k_1(\gamma/(\pi a_1 t)^{1/2}) \exp(-X^2/4a_1 t) = L\rho (dX/dt) \quad (\text{B-12})$$

and with (Eq. B-11) as

$$k_1(\gamma/(\pi a_1 t)^{1/2}) \exp(-X^2/4a_1 t) = L\rho p(a_1/t)^{1/2}. \quad (\text{B-13})$$

From Eqs. (B-10 and 10a) it follows that

$$\gamma = (T_m - T_{s0})/[B + \operatorname{erf}(X/(4a_1t)^{1/2})] = (T_m - T_{s0})/(B + \operatorname{erf} p). \quad (\text{B-14})$$

Inserting Eqs. (B-14) and (B-10a) into Eq. (B-13) yields

$$(k_1/(\pi a_1 t)^{1/2})[(T_m - T_{s0})/(B + \operatorname{erf} p)] \exp(-X^2/4a_1 t) = L\rho p(a_1/t)^{1/2} \quad (\text{B-15})$$

$$\text{or} \quad (k_1/(\pi a_1 t)^{1/2})[(T_m - T_{s0})/(B + \operatorname{erf} p)] \exp(-p^2) = L\rho p(a_1/t)^{1/2}. \quad (\text{B-15a})$$

If the density of the molten particles equals the density of the solid material ($\rho = \rho_1$), Eq. (B-15a) can be expressed as

$$(k_1/(\pi a_1 t)^{1/2})[(T_m - T_{s0})/(B + \operatorname{erf} p)](1/(a_1/t)^{1/2}) = (L\rho_1 p) \exp(p^2), \quad (\text{B-16})$$

and finally, because $c_1 = k_1/\rho_1 a_1$,

$$(B + \operatorname{erf} p)p \exp(p^2) = c_1(T_m - T_{s0})/L(\pi)^{1/2}. \quad (\text{B-17})$$

Eq. (B-17) can be used to determine the constant p from the energy balance at the solidification front. It can also be taken from a nomogram provided by Kuijpers and Zaat [2]. With this one can also determine the *real temperature profiles*.

B.3 Real Temperature Profiles

From Eq. (B-8) it follows that $\alpha = \gamma B$, and with Eq. (B-14) one obtains

$$\alpha = [B(T_m - T_{s0})]/[B + \operatorname{erf} p]. \quad (\text{B-18})$$

Inserting Eq. (B-18) into Eq. (B-5) yields the *real substrate temperature profile*

$$\Theta_0 = T_{s0} + \{[B(T_m - T_{s0})]/[B + \operatorname{erf} p]\}\{1 + \operatorname{erf}(X/(4a_0t)^{1/2})\}. \quad (\text{B-19})$$

Likewise, the *real solid deposit temperature profile* becomes

$$\Theta_1 = T_{s0} + \{(T_m - T_{s0})/[B + \operatorname{erf} p]\}\{B + \operatorname{erf}(X/(4a_1t)^{1/2})\}. \quad (\text{B-20})$$

On rewriting the Eqs. (B-19) and (B-20) yield their final expressions:

$$(\Theta_0 - T_{s0})/(T_m - T_{s0}) = [B/(B + \operatorname{erf} p)][1 + \operatorname{erf}(X/(4a_0t)^{1/2})] \quad (\text{B-19a})$$

and

$$(\Theta_1 - T_{s0})/(T_m - T_{s0}) = [1/(B + \operatorname{erf} p)][B + \operatorname{erf}(X/(4a_1t)^{1/2})]. \quad (\text{B-20a})$$

These equations should be compared with the approximate expression obtained for transient heat conduction in solid spheres as shown earlier:

$$(T_m - T_R)/(T_m - T_1) = f(\text{Bi}, \text{Fo}) = f[\alpha\Theta/r^2] = f[a_1t/r_0^2] \quad (\text{4-23})$$

References

- [1] J. M. Houben, Relations of the adhesion of plasma sprayed coatings to the process parameters size, velocity and heat content of the spray particles. Ph.D. Thesis, Technical University Eindhoven, The Netherlands, **1988**.
- [2] T. W. Kuijpers, J. H. Zaat, *Met. Technol.* **1974**, March, 142.

Appendix C: Calculation of Factor Effects for a Fractional Factorial Design 2^{8-4}

In this example, calculations will be shown for estimating factor effects for the dependence of the thickness of a plasma-sprayed 88WC12Co coating on the eight selected plasma parameters and their ranges (Table C-1). To avoid bias (systematic) errors the 16 experimental runs to be performed were randomized. This randomized fractional two-level factorial design is shown in Table C-2.

The 2^{8-4} design chosen is a 1/16 replicate of a full 2^8 factorial of resolution IV that has the power to estimate the eight main factor effects X_i clear of each other, and clear of composite two-factor interactions E_i ¹. The effects of higher-order interactions can usually be safely neglected. Composite effects of the sum of four two-factor interactions, however, can be estimated from the unassigned factors. If only weak or no interactions exist, the effects of unassigned factors can be used to estimate the experimental (statistical) error, i.e. the minimum significant factor effect. The arrangement of the coded parameter levels in the design matrix (Table C-3) follows Yates' standard order.

Tables C-3 and C-4 show the numerical evaluation of the results for the main factor effects X_i and the composite two-factor interactions E_i . First the sum $\sum(+)$ of all responses Y (thickness of coating) on the '+' level is calculated. Then the $\sum(-)$ of all responses Y on the '-' level is calculated. The factor effect is the difference Δ of the two sums, divided by the number of '+' (or '-') signs in each column. The coefficients, C , of the parameters in the polynomial response equation are obtained by dividing

¹ The confounding pattern of the composite two-factor interactions E_i is as follows:

$$\begin{aligned} E_1 &= X_1X_2 + X_3X_7 + X_4X_8 + X_5X_6 = \mathbf{12 + 37 + 48 + 56} \\ E_2 &= \mathbf{13 + 27 + 58 + 36} \\ E_3 &= \mathbf{14 + 28 + 36 + 57} \\ E_4 &= \mathbf{15 + 38 + 26 + 47} \\ E_5 &= \mathbf{16 + 78 + 34 + 25} \\ E_6 &= \mathbf{17 + 23 + 68 + 45} \\ E_7 &= \mathbf{18 + 24 + 35 + 67} \end{aligned}$$

Table C-1. Plasma spray parameter and their ranges used to estimate the factor effects on coating thickness and microhardness.

	Plasma Spray Parameter	Ranges
X_1	Plasma arc current	700–900 A
X_2	Argon gas pressure	0.34–1.36 MPa
X_3	Helium gas pressure	0.34–1.36 MPa
X_4	Powder gas pressure	0.34–0.68 MPa
X_5	Powder feed rate	0.50–2 (scale value)
X_6	Powder grain size	(–45 + 5)–(–75 + 45) μm
X_7	Number of passes 1st set	5–15
	2nd set	20–30
X_8	Spray distance	20–45cm

Table C-2. Fractional two-level factorial design in variables 1 to 8 and the response Y (coating thickness) and its standard deviation.

Run #	X_1	X_2	X_3	X_4	X_5	X_6	X_7	X_8	Resp. Y (μm)	σ (μm)
1	700	0.34	0.34	0.68	2	Coarse	20	45	118	79
2	900	0.34	0.34	0.34	0.5	Coarse	30	45	16	8
3	700	1.36	0.34	0.34	2	Fine	30	45	203	111
4	900	1.36	0.34	0.68	0.5	Fine	20	45	57	25
5	700	0.34	1.36	0.68	0.5	Fine	30	45	82	35
6	900	0.34	1.36	0.34	2	Fine	20	45	138	87
7	700	1.36	1.36	0.34	0.5	Coarse	20	45	30	12
8	900	1.36	1.36	0.68	2	Coarse	30	45	82	44
9	900	1.36	1.36	0.34	0.5	Fine	30	25	7	4
10	700	1.36	1.36	0.68	2	Fine	20	25	108	104
11	900	0.34	1.36	0.68	0.5	Coarse	20	25	65	30
12	700	0.34	1.36	0.34	2	Coarse	30	25	16	10
13	900	1.36	0.34	0.34	2	Coarse	20	25	26	21
14	700	1.36	0.34	0.68	0.5	Coarse	30	25	9	12
15	900	0.34	0.34	0.68	2	Fine	30	25	30	13
16	700	0.34	0.34	0.34	0.5	Fine	20	25	22	19

the factor effect by two. Factor significance is checked against the minimum factor significance, $\{\min\} = \sigma_{FE} t_{\alpha, df}$ where $\sigma_{FE} = [(1/n) \sum E_i^2]^{1/2}$ with $t_{\alpha, df}$ = Student's t -value for a confidence level α of a double-sided significance test and df = degrees of freedom. All absolute factor effects larger than $\{\min\}$ are considered to be statistically significant.

Note that the second half of the main effect design matrix (Table C-3) is the mirror image of the first half, and that the two halves of the composite two-factor inter-

Table C-3. Computing of main factor effects according to Yates' algorithm.

Run	Main	X_1	X_2	X_3	X_4	X_5	X_6	X_7	X_8	Y
1	+	—	—	—	+	+	+	—	+	118
2	+	+	—	—	—	—	+	+	+	16
3	+	—	+	—	—	+	—	+	+	203
4	+	+	+	—	+	—	—	—	+	57
5	+	—	—	+	+	—	—	+	+	82
6	+	+	—	+	—	+	—	—	+	138
7	+	—	+	+	—	—	+	—	+	30
8	+	+	+	+	+	+	+	+	+	82
9	+	+	+	+	—	—	—	+	—	7
10	+	—	+	+	+	+	—	—	—	108
11	+	+	—	+	+	—	+	—	—	65
12	+	—	—	+	—	+	+	+	—	16
13	+	+	+	—	—	+	+	—	—	26
14	+	—	+	—	+	—	+	+	—	9
15	+	+	—	—	+	+	—	+	—	30
16	+	—	—	—	—	—	—	—	—	22
$\Sigma(+)$	1009	421	522	528	551	721	362	445	726	
$\Sigma(-)$	0	588	487	481	458	288	647	564	283	
$\Sigma\Sigma$	1009	1009	1009	1009	1009	1009	1009	1009	1009	
Δ	1009	—167	35	47	93	433	—285	—119	443	
Effect	63	—21	4	6	12	54	—36	—15	55	
c	b_0	—11	2	3	6	27	—18	—8	28	

action design matrix are identical (Table C-4). From Table C-4 the minimum factor effect can be calculated as follows:

$$\sigma_{FE} = [(1/n) \sum E^2]^{1/2} = (3592/7)^{1/2} = 22.6 \quad (\text{C-1a})$$

$$\{\min\} = \sigma_{FE} t_{\alpha=0.90, df=7} = 22.6 \times 1.895 = 43. \quad (\text{C-1b})$$

Thus, all factor effects whose absolute values are larger than 43 are significant at a confidence level of 90%. From Table C-3 it follows that X_5 (powder feed rate) and X_8 (stand-off distance) are the only significant main factor effects. This holds true even when the confidence level is increased to 95%. There are no significant composite two-factor interactions (Table C-4). Both main factor effects have positive signs, i.e. the coating thickness increases with increasing powder feed rate and increasing spray distance. Hence the response polynomial can be roughly expressed by the equation

$$d[\mu\text{m}] = 63 + 27X_5 + 28X_8. \quad (\text{C-2})$$

Table C-4. Computing of composite two-factor interactions.

Run	E_1	E_2	E_3	E_4	E_5	E_6	E_7	Y
1	+	+	-	-	-	+	-	118
2	-	-	-	-	+	+	+	16
3	-	+	+	-	+	-	-	203
4	+	-	+	-	-	-	+	57
5	+	-	-	+	+	-	-	82
6	-	+	-	+	-	-	+	138
7	-	-	+	+	-	+	-	30
8	+	+	+	+	+	+	+	82
9	+	+	-	-	-	+	-	7
10	-	-	-	-	+	+	+	108
11	-	+	+	-	+	-	-	65
12	+	-	+	-	-	-	+	16
13	+	-	-	+	+	-	-	26
14	-	+	-	+	-	-	+	9
15	-	-	+	+	-	+	-	30
16	+	+	+	+	+	+	+	22
$\Sigma(+)$	410	644	505	419	604	413	448	
$\Sigma(-)$	599	365	504	590	405	596	561	
$\Sigma\Sigma$	1009	1009	1009	1009	1009	1009	1009	
Δ	-189	279	1	-171	199	-183	-113	
Effect	-24	35	0	-21	25	-23	-14	
c	-12	18	0	-11	13	-12	-7	

Plasma- Spray Coating

by. Robert B. Heimann

Copyright© VCH Verlagsgesellschaft mbH. 1996

Index

- Abbot curve 158f
- Abel's inversion 79
- ablation of particles 104f
- abrasion
 - gouging abrasion 268
- acoustic emission (AE) 267
- adhesion number 269
- adhesive 229, 249ff
- adiabatic diesel engine 15
- advanced structural ceramics 3, 4
- aerospace industry 2, 8, 209
- application technology mapping 311
- Archimedes' method 166
- Archimedes' technique 247
- automated image analysis 165
- automotive industry 2, 8
 - ceramic engine parts 5
- Basset–Boussinesq–Oseen equation 101, 103
- Basset history term 101, 104
- bearings 15
- behavior surface 125f
- bench-scale test 277
- Bennett equation 57
- Bernoulli method 150
- Bernoulli's theorem 82
- Biot modulus 217
- Biot number 109, 112
- bipolar plate 235
- blades 15
- boiler tubes 8, 15, 196, 274
- boilers 196
- Boltzmann number 125f
- Bougue number 126
- Bragg angle 171
- Bragg equation 171
- Buckingham's rule 317
- Burner Rig test 220, 279ff
- calender rolls 15
- cathode fall 45
- cathode layer 45
- cavitation erosion 183, 202, 220, 268
- centrifugal pumps 183, 202
- ceramic properties
 - chemical stability 14
 - coefficient of thermal expansion 14
 - fracture toughness 14
 - hardness 14
 - heat conductivity 14
 - high porosity 14
 - thermal stability 14
- characteristic temperature 109
- Charpy impact test 189
- chemical bonding type 286
- chemical corrosion 183, 191, 202, 206, 279
- chemical processing 2
- choke nozzles 183f, 187
- Clausius–Clapeyron's equation 147
- Cline–Anthony model 220
- coating application 15
 - abradable coating 15
 - bioceramic coating 2, 8, 14, 164, 224ff, 311f
 - biomedical coating 15
 - chemical barrier coating 8
 - cocking 15
 - corrosion 15
 - corrosion-resistant coatings 181ff
 - diamond coating 14
 - electrocatalytic coating 14
 - electromagnetic interference 15
 - erosion protection 15

- friction properties 15
- functional ceramic coating 313
- functional coatings 181, 199
- functional plasma-sprayed coatings 232
- high temperature-coating 10, 11
- hot gas erosion 15
- HT-superconducting (HTSC) coatings 232f
- hypervelocity oxyfuel gun (HVOF) 10
- superconducting coating 14
- thermal and chemical barrier coatings 209ff
- thermal barrier bioceramic coatings 100
- thermal barrier coating (TBC) 8, 10, 97, 131, 132, 164, 177, 178, 201, 248, 259, 277, 287, 311ff
- thermal barrier top coating 207
- thick thermal barrier coating 297
- tribological coating 183, 210
- vacuum plasma spraying/low pressure plasma spraying 10
- wear application 15
- wear barrier coating 8, 311f
- wear control 15
- wear-resistant coatings 161, 164, 181ff, 208
- yttria-partially stabilized zirconia coatings 209ff
- coating composition 23
- AISI-316 stainless steel 152ff
- AlN 288
- Al-Si/polyester 296
- Al₂O₃ 112, 131, 181, 199, 253, 285ff
- Al₂O₃/TiO₂ 259, 297
- Al₂O₃/2.5% TiO₂ 172
- 97Al₂O₃3TiO₂ 294
- alumina 8, 21, 63, 70, 77, 80, 83, 91, 97, 101, 102, 109-111, 119, 128-130, 132-134, 142, 148, 149, 177, 201, 202ff, 211, 218, 223, 268
- alumina-titania 210, 268, 305ff
- B₄C 112, 181
- Bi-Sr-Ca-Cu-oxide 232
- C₃P³ 224
- CaO-SiO₂-ZrO₂ 223
- calcium phosphate 224
- η -carbide 168, 184ff, 201, 300, 302
- carbides 93, 97, 168, 181, 199
- cemented carbides 182, 201
- ceramic coating 2, 3, 6, 8, 14, 15
- ceramic membranes 15
- chemical coatings 6
- chromium 8, 164, 167, 201, 204ff, 258ff
- chromium carbide 94, 168, 196ff
- chromium carbide-nickel-chromium (Cr₃C₂-NiCr) composites 21, 268
- chromium oxide 235, 268
- CoCrAlY 131, 211
- CoCrNiW 199
- cobalt 10, 97
- composite coating 14
- composite materials 100
- copper 122-124
- CrB₂ 200
- 94Cr5Fe1Y₂O₃ 235
- Cr₂AlC 183
- Cr₂O₃ 181, 285
- Cr₃C₂ 181, 182
- Cr₃C₂/NiCr 297
- Cr₃C₂-25% NiCr 264f
- 80Cr₃C₂/20(NiCrMo) 275
- 62Cr₃C₂25W₂C5TiC4Ni3Mo1Cr 200
- Cr₃O₄ 205
- Cr₇C₃ 182, 196, 199
- Cr₂₃C₆ 182
- Cr_xC_y 191
- CT 227
- CT₂ 227
- density 97
- diamond 181, 207ff
- diamond coating 2, 14, 311ff
- diamond films 7
- diamond-like coating 15
- dicalcium silicate 223
- FeCrAlY 199
- 85Fe15Si 140, 294, 303
- FeTi 200f
- ferrosilicon 303ff
- fluorapatite 226
- gallium arsenide 7
- glass-based coating 6
- graded coating 23, 132
- graded metal-ceramic coating 178
- H-phases 183
- hafnium nitride 174
- Hastelloy 205
- HfC 182
- hydroxyapatite 15, 155, 156, 224ff
- Inconel 205
- indium phosphide 7
- indium tin oxide 6
- iron 10, 97
- kaolin 131
- LaCoO₃ 233, 236
- LaCrO₃ 235

- LaMnO₃ 233
- LaSrMnO₃ 233
- (La,Sr)(Ni,Co)O₃ 236
- MCrAlY 218
- M₆C 184
- M₁₂C₄ 184
- metal-ceramic composites 21
- metal coating 14, 15, 93, 166
- metal composites 21
- metallic coatings 205ff
- MoC_{1-x} 182
- MoO₂ 205
- Mo₂C 181, 182, 285
- molybdenum 91, 93, 112, 138, 142, 151ff, 168, 181, 205, 208, 253
- Nb 205
- NbC 181, 182
- Nb/Hf 206
- 89Nb10Hf1Ti 206
- Ni 211, 233
- Ni alloy-Al₂O₃ 235f
- Ni alloy-CSZ 235
- NiAl 100, 207
- NiAl-ZrO₂ 233
- Ni-Al₂O₃ 233
- NiCoCrAlY 181, 205, 207, 214, 218
- NiCr 254, 293
- NiCrAl/bentonite 296
- NiCrAlMo 259
- NiCrAlMo/ Al₂O₃-TiO₂ 262
- NiCrAlY 62, 214, 223
- NiCrAl/Y-PSZ 288
- Ni-Cr-10B-Si 183
- 73Ni15Cr4Si4Fe3B1C 186ff
- Ni₃Al 207
- nickel 10, 97, 112
- nickel aluminide 165, 167, 172, 198, 218
- nickel-base alloy 297
- nitrides 168
- nonferrous metals 10, 93, 94
- organic paint coating 6
- oxide coating 201ff
- oxides 93
- oxyhydroxyapatite 226
- partially stabilized zirconia (PSZ) 200
- perovskite 236
- polymer coating 8
- polymers 165
- Resistive CM 192
- Resistive CS-40 192
- Resistive HT-6A 192
- SiAlON 276, 285
- SiC 276, 288
- SiO₂ 112
- Si₃N₄ 276, 285
- silica 218
- silicon nitride 83, 311f
- spinel 236
- stabilized zirconia 15, 177, 201
- stainless steel 254
- steel 93, 94, 112
- stellite 308
- Stellite 6 192
- superalloys 15, 205
- superconducting coating 2, 15, 311
- Ta 112, 181, 205, 206
- TaC 112, 181, 182, 285
- TAFALOY 45CT 206
- 90Ta10W 206
- tetracalcium phosphate 226ff
- Ti 181, 205, 294
- 92.5Ti5Al2.5Fe 206
- TiB₂ 200f, 285
- TiC 112, 168, 181, 182, 285ff
- (Ti,Mo)C/NiCo 174, 271, 293, 296
- TiN 112, 285ff
- TiO₂ 181
- Ti₂AlC 183
- tin oxide 6
- titanium 8, 168, 194, 309
- titanium carbide 8, 191ff, 313
- titanium nitride 174, 313
- tricalcium phosphate 15
- tungsten 94, 131, 168, 208, 257, 298
- tungsten carbide 267
- tungsten carbide/cobalt coatings 183f, 299ff
- tungsten carbide-cobalt (WC-Co) composites 21
- UO₂ 112
- VN 288
- VC 182
- W 112, 181, 205
- WC 181, 182, 285ff
- 88WC12Co 186ff, 293, 294, 298, 323
- WC/Co coating 168, 268, 297
- WC/Co(Ni) 169
- W₂C 182
- Y-Ba-Cu-oxide 232
- yttria 211
- yttrium 99
- zirconia 8, 21, 83, 97, 99, 117, 207, 233,

- 259, 267
- zirconia–NiCrAlY 276f
- ZrC 112, 182
- ZrO₂ 112
- t-ZrO₂/α-Al₂O₃ 174
- ZrO₂ · Y₂O₃ 131
- ZrO₂–8wt% Y₂O₃–NiCrAlY 249
- coating diagnostics 153
- adhesion of coatings 167f
- adhesion strength 313
- Almen-type test 174ff
- area law of mixture 264f
- back wall echo 258
- blind hole test 170, 177
- chemical adhesion 167
- dry sand-rubber wheel abrasion test 271, 273
- four-point bending test 267
- interface echo 259, 261
- macrobonding 167
- macroroughness 157, 167
- macroscopic stresses 169
- measurement of porosity 165
- mechanical anchorage 167
- mesoscopic stresses 169
- microbonding 167
- microroughness 157
- microscopic stresses 169
- microstructure 153, 155, 161, 163, 165
- particle velocity 164
- peel test 255f
- physical adhesion 167
- pin-hole test 254
- residual stresses 169ff, 174ff
- roughness 159, 161
- a-scan diagram 258
- c-scan diagram 258ff
- scratch energy density 271
- scratch test 255ff, 263
- shear test 254f
- sin²ψ-technique 171
- surface roughness 155ff, 160, 161, 167, 174, 199, 269, 296
- tensile test 248ff, 259
- thermal wave scanning 259f
- three-point bend test 267
- (Ti,Mo)C–NiCo 255
- ultrasonic signal 255ff
- ultrasonic test 257ff
- wipe test 156
- coating properties 10
- abrasion resistance 187, 203, 271
- adhesion 142, 153, 161, 285
- adhesion strength 1, 97, 100, 148, 161, 202, 226, 248ff, 261
- adhesive bonding 137
- bending strength 211
- bond strength 246, 248ff
- chemical changes 168
- chemical properties 247, 275
- coating 142
- coating adhesion 229
- coating cohesion 169
- coating density 19
- coating porosity 137, 217, 229
- cohesion 91, 142, 148
- cohesive bonding 137
- cohesive strength 248ff, 262, 300
- composite hardness 263f
- corrosion resistance 203, 212, 214
- density 97
- electronic conductivity 6
- erosion resistance 199, 212, 223, 296f
- fatigue 97, 196, 209
- ferroic coating 311
- fractal approach 1
- fracture toughness 4, 100, 161, 202, 205, 211, 218, 224, 266f, 271, 285
- frictional properties 158, 161, 183, 191
- functional properties 23
- hardness 100, 161, 296f
- hot corrosion resistance 223
- Knoop indentation test 262
- low-cycle 277
- low cycle fatigue 206
- macrohardness 97
- macrohardness test 261ff
- mechanical properties 23, 247f, 277
- mechanical strength 4
- microhardness 187, 191, 202, 205, 212, 267, 296f, 300, 302, 304
- microhardness test 261ff
- microporosity 148
- microstructure 1, 23, 203, 207, 229, 263, 267, 268, 277
- oxidation resistance 187, 212, 214
- piezoelectric coating 311
- piezo- or ferroelectric properties 6
- porosity 97, 99, 157, 161, 164, 212, 263, 296f, 297, 302
- residual stress 1, 201, 202, 213ff, 229,

- 263, 267, 268
- Rockwell hardness 184, 186
- Rockwell hardness test 262
- superconducting coating 311f
- tensile strengths 91, 262, 296f
- thermal fatigue 277
- tribological properties 247, 268
- Vickers hardness 263
- Vickers indentation test 262
- wear resistance 97, 192, 196, 202, 203, 223
- coating techniques 3ff
- chemical vapor deposition (CVD) 2, 7, 207, 285
- diffusion coating 184, 196ff, 206
- electron-beam deposition 23
- electron-beam physical vapor deposition 206
- evaporation 7
- ion implantation 7
- laser ablation 7, 207
- magnetron sputtering 7
- physical vapor deposition (PVD) 2, 7, 285, 287
- plasma-assisted vapor deposition 35, 207
- RF sputtering 225
- sol–gel technique 2, 6, 94, 165
- sputtering methods 7
- color temperature 80
- combustion gas
- acetylene 17, 21, 194, 208
- butane 17
- chemical energy 17
- ethane 194
- internal enthalpy 48
- methane 194, 207
- propane 17, 21, 194
- propylene 196
- combustor can 15, 275
- component test 277
- concrete bridges 15
- concrete floors 15
- conservation 48
- conservation equations 55, 121f
- of continuity 121
- of energy 48, 121, 144, 145
- of mass 48, 144, 145
- of momentum 48, 57, 121, 144, 145
- species conservation 121
- construction industry 2
- continous wave photothermal radiometry 261
- control surface 125f
- convection–diffusion equation 117
- Coriolis forces 57
- corrabrasion 204
- Coulter Counter 247
- cracking furnace tubes 15
- critical current density 233
- cross-correlation function (CCF) 88
- crucible test 279ff
- crystal growth kinetics 137
- cutting tools 182, 208, 285, 313
- cytotoxic response 226
- Dean test 279, 281
- decarburization 181ff, 199, 201
- degree of crystallinity 226
- delamination 214, 216, 220
- dense loading conditions 101, 119ff, 124
- dental prostheses 15
- deposition efficiency 19, 21, 77, 94, 97, 100, 139, 297
- deposition rates 23
- deposition time 139
- design of
 - data bases 10
 - equipment 10
 - expert systems 10
 - software 10
 - spray powder 10
- design of coatings 285ff
- design of experiments 243ff
- Box–Behnken design 290, 294f, 297
- central composite design 295
- confounding pattern of two-factor interactions 323
- factorial design 293f
- four-dimensional hypercube 300f, 304
- fractional factorial design 293f, 299ff, 305, 323ff
- full factorial design 293, 297f
- limited response surface experiment 290
- minimum factor significance 291, 300, 324f
- minimum significant factor effect 323
- multifactorial analysis 243
- multifactorial design 303
- orthogonal blocking 295
- Plackett–Burman design 289ff, 296, 298
- power of resolution 294
- precision ratio 292
- response surface 299, 303, 304
- response surface methodology 289f

- rotatability 295
- statistical design of experiments (SDE) 10, 97, 288
- statistical experimental strategy (SES) 244
- statistical multifactorial experimental designs 184
- supersaturated design 290
- Taguchi design 289, 296, 298
- two-level factorial analysis 289
- Wheeler’s test 292
- Yates algorithm 293
- Yates order 293
- diamond indenter 263, 272
- diamond penetrator 262
- dielectric breakdown strength 202
- Dietzel equation 170, 178
- dimensionless groups 125, 317f
- Dirac delta function 151
- drag coefficient 103ff, 108, 149
- drag force 69, 101, 104, 149
- dwelt time 119

- ease of melting parameter 112, 113
- elastic modulus 288
- electrical conductivity 50, 60
- electrochemical machining 235
- electrode 35, 42, 47, 61, 62, 64, 68–70, 231
 - anode 46, 54, 55, 60, 62, 63, 74, 233, 235
 - cathode 46, 50, 52, 54, 60, 63, 91, 233, 235
 - cold cathode 46
 - contamination 61, 64
 - hot cathode 46
- electron emission 46, 50–52, 60
 - field emission 46
 - thermal emission 46
 - thermionic emission 41, 50–52
- electron mobility 50, 57
- electron work function 41, 50–52, 60
- electron-gas interactions 27
- electronics industry 2
- Elenbaas–Heller equation 48
- emission coefficient 79
- emission intensity 80
- emissivity 77, 80, 121, 125, 126, 259
- energy economy 126
- energy efficiency 127
- energy transfer process 22, 24, 27ff, 137
- Euler flow equation 57
- Euler number 318
- evaporation constant 119f
- extrusion dies 15

- fast Fourier transformation (FFT) analyzer 88
- Fick’s law 150, 167
- finite element 155
- finite element analysis 214, 216
- flame torch 19, 48
 - D-Gun system 17
 - hypervelocity oxyfuel gun (HVOF) 17, 21
 - Jet Kote system 17
 - oxyacetylene torches 17
- flight distance 141
- Fourier analysis 163
- Fourier number 112, 143, 318
- fractals
 - ballistic model 138, 159
 - box counting method 161f
 - characteristic correlation length 160
 - correlation length 163
 - density correlation function 161
 - dilatation symmetry 158
 - fractal dimension 158–161, 163, 167
 - fractal properties 154, 158
 - fracture profile analysis (FPA) 163
 - height difference correlation function 160
 - mass correlation function 163
 - mass fractals 158
 - percolative scaling 161
 - self-affinity 160
 - self-similarity 158
 - slit island analysis (SIA) 163
 - surface fractals 158
- friction coefficient 269
- functional gradient materials 287

- gas turbine 10, 11, 15, 62, 209, 211–213, 275, 279, 287
- gas turbine blades 132
- gas turbine vanes 15
- Gauss’ principle 165
- Gerdien arc 63, 69
- Grashof number 125, 318
- grey body radiation 80
- Grey probe 81f

- Hall Flow Funnel 247
- He–Ne laser 130
- heat conduction in solid spheres 111, 322
- heat conduction potential 114ff
- heat diffusion equation 140

- heat flow 139
- heat flux potential 48
- heat flux ratios 118
- heat loss 61
 - convection 61
 - conductive heat losses 221
 - convective heat losses 175
 - radiation 61
 - radiative heat losses 221
- heat sinks 15
- heat transfer 22, 41, 81, 101, 106ff, 119, 137
 - between plasma and particles 132
 - convective energy transfer 122
 - equation of heat transfer 317
 - Fourier's law 149
 - from particles to substrate 149
 - from plasma to particles 38, 50
 - heat flux 61, 64
 - heat transfer catastrophe 122ff
 - heat transfer equation 141, 142, 150, 152
 - heat transfer model 177
 - low loading conditions 106
 - modeling 127
 - radiative energy transfer 122
 - rates 60
 - to substrate 151
- heat transfer coefficient 106, 108, 125
- heat transfer equations 113ff
- hip prostheses 224
- Hooke's law 170
- Hugoniot adiabat 145f
- hydrogen arc 48f, 70
- hydrogen plasma jet 101

- I–U* characteristic 45
- indentation size effect 263, 266
- immersion test 279
- interface parameter 266
- intermission time 137, 140, 141
- internal combustion engine 2, 15
- ion beam dynamic mixing 225

- Jönsson–Hogmark model 264f
- Joule heating 46

- Kaufman stability criterion 68
- Knudsen number 104, 108

- ladles 15, 275
- Langmuir probe 35
- Laplace operator 150

- laser anemometer 81
- laser Doppler anemometry (LDA) 83ff, 101, 128
- laser irradiance 218f, 221
- latent heat of evaporation 118
- latent heat of fusion 109
- latent heat of melting 142
- lattice deformation 171
- Laval nozzle 74, 76, 88, 236
- Lewis number 318
- life-cycle curve 8
- Lorentz force 43, 52, 57, 58, 69, 125
- low-loading condition 113, 119

- Mach number 144, 236
- magnetic pinch 57, 64
- manufacturing industry 2
- marker and cell method 142
- Marsh's relation 266
- mass loss by vaporization 113
- mass transfer coefficient 113
- Maxwell distribution 31, 36–38
- Maxwell equation 48, 121
- Menstruum process 200
- mercury pressure porosimetry 165f
- metal properties
 - coefficient of thermal expansion 14, 169f, 174, 201, 218, 229
 - creep 277
 - creep strength 13
 - ductility 13
 - fatigue strength 13
 - flexural strength 13
 - fracture toughness 14
 - heat conductivity 14
 - porosity 14
- microelectronics industry 2
- microwave 44
- mining toll 15
- modulus of elasticity 170, 174, 178, 216, 217, 224, 267
- momentum transfer 22, 100ff, 108
 - from particles to substrate 141
 - from plasma to particles 50, 132
 - modeling 127

- Nabarro–Herring creep 217
- Navier–Stokes equation 57, 106, 121, 125, 317
- Nelson–Riley extrapolation function 174
- Neumann–Schwartz equation 319

- Neumann–Schwartz parameter 140
- Newton's law 104, 144
- Newton momentum equation 175
- nonlinearity 124, 174
- Nusselt number 108, 114, 125, 318

- Ohm's law 44, 48
- Ollard–Sharivker test 253
- Orowan–Petch relation 271
- orthopedic prostheses 15
- osmotic filtering 15
- osteogenesis
 - bonding osteogenesis 224
 - contact osteogenesis 224
 - distance osteogenesis 224
- oxygen sensor 82

- particle–substrate interactions 137ff
- particle diagnostics 128
 - particle emission 80
 - particle emissivity 108
 - particle flux 133
 - particle inertia 101
 - particle number density 128, 132f, 138, 141
 - particle number flux 78
 - particle temperature 104, 108, 109
 - particle temperature distribution 78
 - particle velocity 88, 101, 102, 106, 147, 149
 - particle velocity distribution 78, 130
 - plasma jet residence time 108f
 - residence time of the particles 231
 - temperature 128, 131, 132
 - velocity 128ff
 - wipe test 147, 154
- particle erosion 183
- particle impact 137, 142, 143, 147
 - catastrophic fragmentation 149
 - contact face perimeter 146
 - degree of flattening 155
 - elastic pressure 145
 - flattening ratio 141, 142, 248
 - hot spots 148
 - impact angle 142, 276
 - impact velocity 141
 - Mexican hat shape 138, 140
 - pancake shape 138
 - particle deformation 139
 - particle splats 137
 - rarefaction wave 147f
 - shock front 145, 146, 148
 - shock heating 147
 - shock pressure 141, 146, 147
 - shock wave 137, 144, 147, 164
 - stress wave 144
 - thermal pressure 145, 146
- Péclet number 143, 318
- photon correlator 84
- pin-on-disc apparatus 268
- piston 15, 210
- Pitot tube 81f
- plasma–particle interactions 1, 91ff
- plasma 77, 226
 - characteristic plasma parameter 48
 - charge carrier 27, 41, 44, 46, 50
 - charge distribution 27
 - classification 31, 33, 35
 - cold plasmas 31, 35
 - d.c. plasmas 50
 - Debye screening length 35
 - definition 27, 30
 - electrical field strength 28, 52
 - electric plasma 34
 - electromagnetic plasma 34
 - electron density 31, 33–36
 - electron temperature 32, 33, 35, 40, 44, 48
 - equilibrium compositions 38
 - equilibrium conditions 48
 - equilibrium distribution 39
 - equilibrium plasma 35, 38, 40
 - heavy particle temperature 32, 35, 48
 - high density plasma 35
 - high frequency oscillation 28
 - isothermal plasma 38
 - local thermal equilibrium 50, 125
 - local thermodynamic equilibrium 32, 77
 - low density plasmas 32
 - magnetic field 35
 - magnetic field strength 32, 35, 125
 - magnetic plasma 34
 - medium density plasmas 32, 34
 - modeling of the plasma spray process 1
 - neutrality 27, 28
 - nonequilibrium plasma 35, 40
 - nonisothermal plasma 44
 - plasma energy 37, 121, 227
 - plasma enthalpy 38, 155, 184
 - plasma state 27, 34, 38
 - plasma temperature 32
 - R.F. plasmas 50
 - scalar plasma 35
 - self-confinement 57

- solid state plasma 35
- subnormal discharge 46
- temperature 35
- tensorial plasma 34, 35
- thermal plasma 32, 35, 48
- three-fluid plasma 35
- two-fluid plasma 35
- Vlasov plasma 32
- plasma arc 17
- plasma arc properties
 - AJD mode 55
 - anode fall 46, 60
 - anode jet 52, 54, 55
 - anode region 55, 56
 - arc cathode 46
 - arc column 50, 52
 - arc current 82
 - arc discharge 46, 50
 - cathode fall 46, 50
 - cathode jet 52, 54, 55
 - characteristic 68
 - CJD mode 55
 - current density 50, 55
 - electron current 50
 - modeling of arc column 48
 - plasma column 42, 43, 55, 72
 - positive column 46, 50
 - positive-ion current 50
 - potential distribution 46, 47
 - space charge 46, 47, 50, 51
 - structure of the arc column 50
 - thermal boundary 46
 - wall-stabilized 50
- plasma arc stabilization 68ff
 - convection-stabilized arc 68, 69
 - electrode-stabilized arc 69
 - gas-sheath stabilized plasma 69
 - gas-stabilized arc 63, 68
 - magnetically-stabilized jet 70
 - by thermal pinch 64
 - vortex stabilized arc 69
 - wall stabilized arc 68
 - water-stabilized arc 63
- plasma chemical synthesis 37
- plasma diagnostics 77ff
 - enthalpy measurement 77
 - fringe mode measurement 84
 - multiwavelength pyrometry 128
 - spectroscopic measurement of plasma temperature 80
 - spectroscopic methods 77
 - temperature measurement 77, 78
 - two-color pyrometry 132
 - two-wavelengths pyrometry 80
 - velocity measurement 77, 78, 81–83
- plasma etching 35
- plasma gas
 - air 64
 - argon 19, 38, 39, 55, 64, 77, 82, 109, 110, 114, 116, 207, 296
 - argon/hydrogen 128, 155, 296
 - collision ionization 38, 43, 44
 - dependent discharge 45
 - discharge characteristic 45
 - dissociation 38
 - drift velocity 44, 50
 - energy content 40
 - flow rates 82
 - gas ionization 38
 - gas velocity 101
 - heat conduction 52
 - helium 38, 130, 192
 - hydrogen 19, 55, 109, 110, 114, 116, 192, 207
 - independent discharge 45
 - ionization 38, 40, 41, 55
 - ionization energy 40, 45
 - ionization frequency 44
 - nitrogen 19, 38, 39, 55, 77, 109–111, 114, 116
 - oxygen 79
 - photoionization 38
 - Saha–Eggert equation 40
 - specific heat 41
 - thermal conductivity 117
 - viscosity 103
 - volume ionization 45
- plasma generation 38ff
 - abnormal glow discharge 46
 - a.c. discharge mode 44
 - adiabatic compression 43
 - arc cathode 46
 - ballistic compressor 42, 43
 - d.c. discharge mode 44
 - dependent discharge 44
 - discharge current 45
 - electron beam plasma generator 43
 - gas discharges 44
 - glow cathode 45, 46
 - glow discharge 45, 46
 - impulse mode 44
 - independent discharge 44

- laser radiation 44
- magnetic compression 57
- magnetic plasma confinement 41
- MHD generator 41
- pinch 52
- Θ -pinch apparatus 42, 43
- z-pinch apparatus 42, 43, 57, 58, 125
- plasma focus 42, 43
- plasma furnace 40, 42
- Q engine 41, 42
- quiet plasma 41
- shock tube 42, 43
- shock wave 43
- plasma jet 17, 21, 43, 52, 57, 70ff, 79, 81–83, 86, 91, 94, 101, 106, 119, 124, 125, 132, 139, 149
- eddies 74, 75, 77, 91, 125, 134, 208
- electrical potential field 22, 100
- enthalpy distribution 70, 74
- heat content 19
- jet core 80, 84
- laminar 75
- modeling 101
- momentum transfer 101
- plasma core 74
- quasi-laminar jets 74
- quasi-laminar plasma 77
- ring vortex 73
- temperature distribution 71, 73, 80
- turbulence 101, 104, 125, 133, 134
- turbulent plasma 60, 70, 72, 74, 75, 84, 86, 88, 91, 103, 208
- velocity distribution 71, 72
- plasma parameters 28ff
 - characteristic distance 31, 35, 36
 - collision cross-section 30, 31
 - collision frequency 28, 31, 36
 - collision path length 30, 31, 36 see also mean free path length
 - Coulomb logarithm 30
 - cyclotron path 32
 - Debye screening length 28–31, 36
 - Debye sphere 29, 30
 - elastic collision 30
 - electron temperature 31
 - heavy particle temperature 31
 - inelastic collision 30
 - Landau length 28, 29 see also critical distance
 - Langmuir oscillation 43
 - Langmuir plasma frequency 28, 31, 36
 - see also collision length
 - Larmor radius 32, 36
 - Larmor rotation 32
 - macroscopic plasma parameters 70
 - Maxwell-Boltzmann distribution 30
 - mean free collision paths 32
 - mean free path length 28, 30, 108
 - microscopic parameters 28
 - particle velocity 143
 - particle viscosity 184
 - plasma condition 32, 34
 - plasma density 81, 82
 - plasma parameter 29, 32
 - plasma pressure 30, 57, 101, 317
 - plasma temperature 77, 80, 82, 104, 108, 114, 118, 119, 122, 128, 184
 - plasma velocity 70, 82, 84, 86, 101, 102, 113, 125, 126, 128, 231, 317
 - plasma viscosity 81, 113, 125, 317
 - relaxation time 31
 - temperature gradient 70, 81, 126, 129
- plasma spheroidizing 37, 94
- plasma spray parameters 20, 21, 23
 - design factors 97
 - argon gas pressure 324
 - chamber pressure 227, 296ff
 - feed rate 128
 - particle-size distribution 97
 - plasma arc current 324
 - plasma power 128, 155, 227, 229, 296ff
 - powder feed rate 227, 296ff, 324
 - powder gas pressure 324
 - spray distance 324
 - stand-off distance 128, 155, 227, 229, 296ff
 - substrate temperature 227, 229
 - traverse speed 296ff
- divergence 77
- gas pressure 19
- grain size 19
- injection angle 19
- powder feed rate 19
- powder gas pressure 19
- power input 19
- spray atmosphere 19
- spray distance 19
- spray divergence 19
- stand-off distance 77
- traverse rate 19

- plasma spray particles
 - injection of powders 91
- plasma spray powder
 - powder injection 64, 70, 74, 92
- plasma surface modification 35
- plasma/thermal spray powder
 - injection 133, 186
 - injection probe 133
 - powder characteristics 95, 96, 246
 - powder microstructure 95
 - powder morphology 95
 - size distribution 94, 97, 99, 138, 247
- plasmatron 8, 17–19, 43, 48, 50, 55ff, 62, 67–69, 72, 76, 77, 84, 91, 99, 119, 127, 137, 139, 186, 190, 194, 231, 287, 304, 313
 - arc discharge generator 57, 59
 - arc-welding configuration 61
 - electrode plasma (EP) 59
 - electrodeless plasma (ICP) 59
 - electrodeless plasmatron 65
 - inductively-coupled plasma (ICP) devices 63, 67
 - inductively-coupled plasmatron 66, 122, 123
 - inductively-coupled torch 64
 - nontransferred arc 63
 - nontransferred electrode plasmatrons 59, 60
 - nontransferred plasma 59, 62
 - transferred arc 61–63
 - transferred electrode plasmatrons 61
 - transferred plasma 59
- plasmatron electrode 66
- plungers 183, 202
- point counting 165
- Poisson's law 50
- Poisson ratio 170, 171, 174, 177, 178
- post-spraying treatment
 - hot isostatic pressing 14, 165, 218, 229
 - infiltration 14, 165, 218
 - laser densification 14
 - laser-glazing 202, 218
 - laser surface densification 165
 - laser surface remelting 218
 - post-spray grinding and polishing 202
 - pulsed laser sealing 223
 - reactive laser treatment 223
 - sealing 218
- Prandtl number 108, 125, 318
- printing rolls 15
- PSI model 121
- pump plungers 15
- PVD sputter targets 15
- quality control 243ff, 248, 313
 - coating quality 24
 - continuous improvement 243, 245
 - management style 243, 245
 - plasma spray powders 98
 - qualification procedure 245f
 - quality coating 244, 248
 - quality function deployment (QFD) 10, 97, 244
 - quality philosophie 243ff
 - quality tools 243f
 - statistical experimental design 212
 - statistical process control (SPC) 10, 97, 122, 244, 311
 - statistical quality assurance (SQA) 244
 - statistical quality control (SQC) 244
 - Taguchi analysis 122
 - total quality management 94, 225, 243ff
- Raman shift 231
- random walk influence 134
- Rankine–Hugoniot equation 144f
- rapid solidification 288
- rapid solidification technology 141, 167, 223
- Rayleigh number 125, 318
- reactive plasma processing 66
- reciprocating pumps 183, 202
- resorption resistance 226, 232
- Reynolds number 64, 81, 101, 103, 104, 114, 318
- Richardson–Dushman equation 51
- Riemann–Hugoniot catastrophe 125
- Ryshkevich–Duckworth equation 271
- saturation current 44
- Schmidt number 114, 318
- Schottky correction 51
- Schumann–Runge bands 79
- screening test 277
- self-sharpening 203f
- service life prediction 279
- Sharivker/Ollard test 249f
- Sherwood number 114
- shot peening 175
- shrouds 15
- solid oxide fuel cells (SOFC) 233ff
- solid-particle erosion (SPE) 187, 198, 271, 274

- solidification time 137, 140, 141, 147, 149, 152
- SPE resistance 196
- specific heat flux 114, 117
- spray powder production
 - agglomeration 94, 100, 196
 - arc-fuse/crush powders 97, 99
 - arc-fuse/spray-dry 97f
 - atomization 94, 97
 - chemical cladding 100
 - compositing 100
 - fluidized bed sintering 94
 - fusing/melting 94
 - fusion and crushing 97
 - gas-atomized particles 97, 100
 - hollow-spherical-powder (HOSP) 97, 99
 - hydrogen pressure-reducing powder coating (HYPREPOC) 100
 - spray drying 94
 - water-atomized particles 97, 99, 100
- spraying parameters 10
- stagnation enthalpy 81
- statistical design of experiments (SDE) 246
- steel bridges 15
- Stefan–Boltzmann coefficient 126
- Stefan–Boltzmann constant 108
- Stefan–Kutateladze group 142f
- Stefan number 125, 318
- Stokes equation 104
- strain gauges 170
- strain to fracture (STF) 267
- stress corrosion cracking 196
- substrate
 - AISI 304 199
 - AISI 410 199
 - AISI 422 198
 - AISI 5150 steel 186
 - aluminum 6, 167, 172, 224, 225, 253
 - 6061 aluminum 298f
 - austenitic steel 177, 294, 309
 - austenitic superalloy 209
 - bioactive glasses 224
 - carbon 224
 - carbon fiber composites 181
 - carbon steel 303
 - cast iron 6
 - ceramics 8
 - CK 45 287
 - Co–Cr alloys 224
 - copper 6, 164, 206, 258ff
 - Cr₇C₃ 263
 - ferritic steel 177
 - graphite 181
 - Hastelloy X 199, 207
 - hot-rolled sheet steel (A 569) 202
 - Inconel 617 213ff
 - Inconel 800 199, 207
 - low-carbon steel 140, 152f, 299
 - MCrAlY 209
 - metal foil 255
 - mild steel 187, 253, 271, 293, 294, 296–298, 308
 - Ni-based superalloy 217
 - nickel 6
 - PWA 1460 206
 - SiC 263
 - stainless 6
 - 304 stainless steel 177, 223, 224
 - steel 6, 8, 139, 151, 152, 167, 168, 174, 181, 183, 208, 293
 - St 37 steel 172f
 - substrate heating 19
 - superalloys 6, 206
 - surface roughness 19
 - tantalum 224
 - Ti6Al4V 226, 229
 - TiO₂ 263
 - titanium 224–226
 - vanadium alloys 8
 - VC 263
 - WC/Co 203f
 - zirconia 224
- superconductivity 233
- superheaters 15
- surface-tension gradient 220f
- Taber apparatus 268
- thermal conductivity 152, 161, 216, 220, 320ff
 - contact thermal conductivity 151, 320ff
 - mean boundary layer thermal conductivity 113
 - of the particles 109
 - of plasma gas 109
 - substrate with higher thermal conductivity 142
- thermal diffusion (heat conduction) equations 152
- thermal diffusivity 112, 150, 220, 319ff
- thermal pinch 55
- thermal spray powder 94

- thermal spraying methods 1, 2, 8ff, 17ff, 21ff
 - air plasma spraying (APS) 17, 19, 21–23, 94, 183, 187, 192, 196, 199, 205, 226, 248, 297
 - arc spraying 22
 - arc wire-spraying 127
 - controlled atmosphere plasma spraying 17
 - D-Gun 21, 22, 143, 144, 183, 196, 198
 - detonation gun techniques 94
 - electric arc spraying 93
 - electric arc wire-spraying 19, 22
 - flame spraying 8, 22, 93, 183, 205
 - high power plasma spraying 17
 - hypervelocity oxyfuel gun (HVOF) 21, 22, 94, 143, 144, 168, 183, 192, 205, 226, 231
 - inductive plasma spraying (IPS) 21, 22
 - inductively-coupled RF plasma 130
 - inert gas plasma spraying (IGPS) 17, 23
 - Jet Kote system 21, 22
 - laser spraying 19
 - low pressure laser spraying (LPLS) 22
 - low pressure plasma spraying (LPPS) 17, 19, 104, 132, 165, 183, 206, 248
 - oxyacetylene torch 22
 - plasma transferred arc (PTA) 297
 - PTA surfacing 308
 - radio-frequency spraying (RF) 21
 - reactive plasma spraying 183, 192ff
 - RF ICP 231, 233, 235
 - RF-plasma spraying 22
 - SPS 17
 - underwater plasma spraying (UPS) 19, 23, 183
 - vacuum plasma spraying (VPS) 17, 21–23, 94, 156, 183, 196, 199, 205, 226
- thermionic work function 53
- thermophoresis 129
- thermophoretic effect 101
- time-resolved infrared radiometry 259
- Townsend coefficient 44, 45
- Townsend discharge 45, 46
- Townsend ignition condition 45
- tribomaterials 269f
- tundishes 15, 275
- turbine blade 274
- turbine vanes 15
- ultimate tensile strength (UTS) 206
- ultrafiltration 15
- valves 15, 210, 223, 274
- Washburn equation 166
- water electrolyzers 236
- wear mechanisms
 - abrasive wear 269ff, 274
 - adhesive wear 269f
 - erosive wear 271
 - flank wear 287
 - long-term fatigue wear 271, 273
- Weibull modulus 178, 268
- welding process 127, 137
- Wheatstone bridge 170
- X-ray small angle scattering 165
- Young's modulus 171, 175, 177, 198, 211, 249

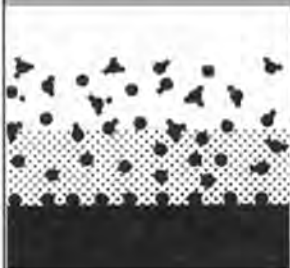


Rees, W.S., Jr. (ed.)

CVD of Nonmetals

1996. 400 pages with 100 figures and 60 tables. Hardcover. ISBN 3-527-29295-0

Written by leading experts in the field, this handbook offers an up-to-date, critical survey of this burgeoning field of research. Technological issues as well as new scientific results are discussed and the viability of the method, both technically and economically, is compared with other deposition techniques available.



Jones, A.C./O'Brien, P.

CVD of Compound Semiconductors Precursor Synthesis, Development and Applications

1996. 450 pages. Hardcover. ISBN 3-527-29294-2

Chemical growth methods of electronic materials are the keystone of microelectronic device processing. This book details the chemistry of the precursors used in the deposition of various materials and makes the science and technology of deposition accessible to the materials scientist.



Chemical Vapor Deposition (CVD)

ISSN 0948-1907

6 issues per year

CVD is published every two months as a special section of the world's leading material science journal **Advanced Materials**. The deposition of thin films of metal, ceramics, and semiconductors using CVD, their characterization, related vacuum technology and equipment, and related aspects of surface science are core areas covered in this journal.

Our standard setting stringent referee system on all papers submitted guarantee high quality papers from renowned experts around the globe.

Don't miss out on the latest results, developments and trends in your field.

Order your free sample copy!

Get the hottest peer
review research results on
chemical vapor deposition!

